NASA SP-207

BASIC AERODVNAMIC NOISE RESEARCH

A conference held at NASA Headquarters,
Washington, D. C., July 14-15, 1969

Edited by
IRA R. SCHWARTZ

Scientific and Technical Information Division
OFFICE OF TECHNOLOGY UTILIZATION 1969
NATIONAL AERONAUTICS AND SPACE ADMINISTRATION
Washington, D.C.

General Chairman

I. R. SCHWARTZ, *NASA, Office of Advanced Research and Technology*

Session Chairmen

H. T. NAGAMATSU, *General Electric Research and Development Center*
W. R. SEARS, *Cornell University*
P. J. WESTERVELT, *Brown University*
H. S. RIBNER, *University of Toronto*

Panel Members

P. E. DOAK, *Lockheed-Georgia Co.*
H. T. NAGAMATSU, *General Electric Research and Development Center*
H. S. RIBNER, *University of Toronto*
W. R. SEARS, *Cornell University*
J. E. FFOWCS WILLIAMS, *Imperial College, England*

For Sale by the Superintendent of Documents,
U.S. Government Printing Office, Washington, D.C. 20402
Price $2.25
Library of Congress Catalog Card Number 76-603960

PREFACE

The increasing requirements of aviation during recent years have necessitated the building of larger aircraft structures and engines. With the advent of larger and more powerful engines, aerodynamic noise has become a serious community problem. Although this problem has been with us for many years, it has not yet been solved, partly because of its many complexities, and partly because there has been only a very limited basic research program to complement the technological development programs.

A better understanding of the mechanisms of noise generation, propagation, and attenuation will ultimately provide the scientific and technological tools needed for substantial advancements in aerodynamic noise abatement. Several NASA Centers—Ames, Langley, Lewis, and Marshall—and NASA Headquarters' contractors have been involved in such programs for a number of years.

Accordingly, a Basic Aerodynamic Noise Research Conference was held at NASA Headquarters, Washington, D.C., on July 14–15, 1969, the proceedings of which are reported in this NASA Special Publication. The purpose of the meeting was to determine the future directions for basic noise research related to aircraft propulsion systems. In particular, the objectives of the meeting were to review the status of the university and industry basic noise research programs, to survey the programs at the NASA Centers, to determine those areas of research that appear to be the more pressing ones, and to discuss which, if any, of the various avenues of research appear to be the most promising ones with regard to our understanding of noise generation and propagation and, hence, inlet duct, rotating fan, and exhaust jet noise reduction and control.

Thus, to inform the scientific community on the most recent accomplishments in basic aerodynamic noise research and to further stimulate the growth of new ideas and understanding, 31 invited papers were presented at the conference and are published in these proceedings. These covered theoretical and experimental aspects of jet exhaust, rotating fan, inlet duct, and boundary layer noise research, and experimental diagnostic techniques. In addition, a major portion of the second day of the meeting was devoted to discussions by a panel composed of five of the participants and open discussion and remarks from the 200

attending scientific and engineering specialists who meticulously summarized the highlights of the program presentations and defined the directions that seemed to be most fruitful for future basic aerodynamic noise research. Their remarks at the conference and subsequent invited letters, which elaborated on their remarks, are also published in these proceedings.

The attendees were welcomed by Dr. Hermann H. Kurzweg, Director of the Research Division, NASA Office of Advanced Research and Technology, who discussed NASA's interests in Basic Aerodynamic Noise Research. C. W. Harper, Deputy Associate Administrator for Aeronautics, NASA Office of Advanced Research and Technology, and C. R. Foster, Director of Noise Abatement, Office of Secretary of Transportation, presented introductory remarks.

We were fortunate to have Dr. Henry Nagamatsu, Prof. Herbert Ribner, Prof. William Sears, and Prof. Peter Westervelt serve as session chairmen. They performed an admirable task of maintaining an informal conference atmosphere. We are grateful to the panel members: Dr. Phil Doak, Dr. Henry Nagamatsu, Prof. Herbert Ribner, Prof. William Sears, and Prof. Ffowcs Williams for their remarks and expertise in stimulating the open discussion from the general attendance.

IRA R. SCHWARTZ

CONTENTS

Page

PREFACE iii
I. R. Schwartz

Session I – JET NOISE RESEARCH

H. T. NAGAMATSU, *Chairman*

JET NOISE RESEARCH 3
John E. Ffowcs Williams

THE RELATION OF THE CONVECTIVE DECAY OF TURBULENT EDDIES TO THEIR FAR-FIELD SOUND PATTERN 11
C. E. Wooldridge and D. C. Wooten

SUPERSONIC JET NOISE THEORY AND EXPERIMENTS 17
H. T. Nagamatsu, R. E. Sheer, Jr., and G. Horvay

EDDY-MACH WAVE NOISE FROM A SIMPLIFIED MODEL OF A SUPERSONIC MIXING LAYER.. 53
H. S. Ribner

NOISE REDUCTION FROM INTERACTING COAXIAL SUPERSONIC JET FLOWS. 63
Darshan S. Dosanjh, Amr N. Abdelhamid, and James C. Yu

ENTROPIC EFFECTS IN SOUND GENERATION 103
Abraham C. Peter

EFFECT OF DUCT HEATING ON JET AND FAN NOISE 113
Harry E. Plumblee

ATTENUATION OF PLANE WAVES OF SOUND BY SUSPENSION OF RESONATING PARTICLES 137
Lee Arnold and Simon Slutsky

OPTICAL MEASUREMENTS OF SOUND SOURCE INTENSITIES IN JETS.. 147
L. N. Wilson, F. R. Krause, and K. A. Kadrmas

JET-ORIFICE-SURFACE INTERACTION NOISE.. 161
R. C. Potter

ACOUSTIC SPECTRA FROM TURBULENT JETS 177
William C. Meecham

Session II – FAN NOISE RESEARCH

W. R. SEARS, *Chairman*

DIRECT CORRELATION OF FLUCTUATING LIFT WITH RADIATED SOUND FOR AN AIRFOIL IN TURBULENT FLOW 189
P. J. F. Clark and H. S. Ribner

Page

SOME ASPECTS OF DISCRETE FREQUENCY NOISE GENERATION IN AXIAL-FLOW FANS 191
Ramani Mani

REFLECTION AND TRANSMISSION OF OBLIQUE SOUND WAVES BY A BLADE ROW 223
Roy Amiet and W. R. Sears

RESPONSE OF AN INFINITE WING TO AN OBLIQUE SINUSOIDAL GUST: A GENERALIZATION OF SEARS' PROBLEM 231
L. T. Filotas

UNSTEADY AIRFOIL RESPONSE 247
Robert A. Arnoldi

A STUDY OF FAN-COMPRESSOR NOISE GENERATION 257
M. J. Benzakein

SOME FEATURES OF AN EDGE-TONE FLOW FIELD 275
K. Karamcheti, A. B. Bauer, W. L. Shields, G. R. Stegen, and J. P. Woolley

PROPAGATION AND ATTENUATION OF SOUND IN A SOFT-WALLED ANNULAR DUCT CONTAINING A SHEARED FLOW 305
P. Mungur and H. E. Plumblee

Session III – INLET DUCT NOISE, BOUNDARY LAYER NOISE, DIAGNOSTIC TECHNIQUES

P. J. WESTERVELT, *Chairman*

BASIC AIRCRAFT NOISE RESEARCH AT THE LANGLEY RESEARCH CENTER 331
Philip M. Edge, Jr., and Harvey H. Hubbard

DESCRIPTION OF HYPERSONIC BOUNDARY LAYER NOISE FLIGHT MEASUREMENT PROGRAM 337
Harold B. Pierce and William H. Mayes

PROPAGATION OF WAVES IN AN ACOUSTICALLY LINED DUCT WITH A MEAN FLOW ... 345
Edward J. Rice

CURRENT UNDERSTANDING OF HELMHOLTZ RESONATOR ARRAYS AS DUCT BOUNDARY CONDITIONS 357
John F. Groeneweg

ACOUSTIC RESEARCH ACTIVITIES AT MARSHALL SPACE FLIGHT CENTER 369
Gilbert A. Wilhold

ONE-SHOT MEASUREMENTS OF THE DECAY OF SUPERSONIC AERODYNAMIC TURBULENT STRUCTURES 389
B. H. Funk and H. A. Cikanek, Jr.

NOISE MEASUREMENTS IN WIND TUNNELS 399
David H. Hickey, Paul T. Soderman, and Mark W. Kelly

SURFACE-PRESSURE FLUCTUATIONS ASSOCIATED WITH AERODYNAMIC NOISE 409
Charles F. Coe

OPTIMUM LINING CONFIGURATIONS 425
H. K. Liu and A. J. Martenson

SPECTRAL TECHNIQUES IN JET NOISE THEORY 435
S. P. Pao and M. V. Lowson

MATHEMATICAL ASPECTS OF NONLINEAR WAVE PROPAGATION 451
Ervin Y. Rodin

Page

INVESTIGATION OF PRESSURE PROBE RESPONSE IN UNSTEADY FLOW 455
T. E. Siddon

Session IV—PANEL AND OPEN DISCUSSION

H. S. RIBNER, *Chairman*

PANEL DISCUSSION

SOME COMMENTS ON POSSIBLE BACK-REACTION EFFECTS OF ACOUSTIC FIELDS ON AERODYNAMIC SOUND SOURCES 469
P. E. Doak

COMMENTS ON NOISE GENERATION BY HIGH-SPEED FAN BLADES 473
John E. Ffowcs Williams

COMMENTS ON SUPERSONIC JET NOISE 475
H. T. Nagamatsu

COMMENTS ON STATUS AND PROBLEM AREAS IN JET NOISE RESEARCH 477
H. S. Ribner

GENERAL REMARKS 485

I

JET NOISE RESEARCH

Chairman: **H. T. NAGAMATSU**

JET NOISE RESEARCH

John E. Ffowcs Williams
Imperial College
London, England

INTRODUCTION

The jet-noise problem can be simulated in a low-speed, easily visualized analogous facility, i.e., gravity waves on shallow water induced by turbulent flow. These waves are in general dispersive, with the wave speed of the very short waves tending toward zero. Surface-tension effects tend to make very short waves travel quickly, and at a particular water depth, 0.48 cm, surface-tension effects almost cancel the natural gravity wave dispersion to give a medium in which all but the very shortest waves travel at a constant speed of around 20 cm/sec. Small regions of turbulent flow in shallow water cause surface waves to radiate in a manner closely analogous to sound waves propagating from turbulence in air. Of course, the waves spread in two dimensions rather than three, and this feature brings about a certain restriction in the scope of the analogy. The details of the simulation have been worked out by Ffowcs Williams and Hawkings (ref. 1), who show that the exact equations of motion can be written as a quadrupole-driven, inhomogeneous, two-dimensional equation for the surface wave amplitude, with the main quadrupole term being the fluctuating Reynolds stresses. Apart from the two-dimensional aspect, this is an exact analogy with Lighthill's (ref. 2) equation for aerodynamic noise. The main difference caused by the two-dimensionality is that the 8th-power law of Lighthill is replaced by a 7th-power law in the water analogy, but in all essential qualitative aspects the simulation is complete. At Imperial College we have built a shallow water table, 14 ft by 9 ft in dimension, and have recently completed an experimental investigation into the quantitative aspects of how well the jet-noise problem is simulated in this facility.

THE ESSENTIALS OF THE JET-NOISE PROBLEM SIMULATION

Jets emerge from a nozzle in a somewhat turbulent condition, so the possibility exists that the mass flow out of the nozzle is unsteady. An

unsteady mass flow is the essential element of an acoustic monopole, the field of which decays with distance as $\sqrt{\lambda/r}$, r being the distance traveled and A the characteristic wavelength.

At the source, the pressure, or its shallow-water analog, surface height, is of the order of the fluctuating dynamic head ρu^2 so that the pressure in the distant field p varies as

$$p \sim \rho u^2 \left(\frac{\lambda}{r}\right)^{1/2} \tag{1}$$

The length scale in the flow is typically the nozzle scale l so that the typical frequency w is set by the velocity and this length scale

$$\omega \sim \frac{u}{l} \tag{2}$$

Waves propagate from the nozzle with this frequency at the constant wave speed c so that the wavelength A is

$$\begin{aligned} \lambda &\sim \frac{c}{\omega} \sim \frac{c}{u} l \\ \lambda &\sim \frac{l}{M} \end{aligned} \tag{3}$$

where M is the effective mach (Froude) number of the flow. At low mach numbers, the length scale in the radiation field is very much greater than that in the source field so that the equivalent sources are acoustically compact. By inserting this value of the wavelength in equation (I), we can derive the scaling law for the monopole term associated with unsteady mass efflux from the nozzle

$$p \sim \rho u^2 M^{-1/2} \left(\frac{l}{r}\right)^{1/2} \tag{4}$$

$$p^2 \sim \rho^2 u^4 M^{-1} \frac{l}{r} \tag{5}$$

This is the two-dimensional analog of the three-dimensional simple source expression

$$p^2 \sim \rho^2 u^4 \frac{l^2}{r^2} \tag{6}$$

This simple source term is, however, likely in both the model and in full scale to be very small because the mass-flow rate into, and therefore out of, the nozzle, is essentially steady. Turbulence can cause the mass-flow rate across any one section of the nozzle to be instantaneously high, but this must be compensated for at all instants by adjacent sink regions

so that the source-sink combination constitutes a dipole with axis normal to the jetstream. The field if a dipole is essentially $l \cdot \mathrm{V}$ times the field of the constituent simple sources, and because the length scale in the radiation field is l/M, $l \cdot \mathrm{V}$ is equivalent to multiplication by the factor $l/(l/M)$, or simply M. The field of the constituent simple sources is given in equation (4) so that the nozzle-located dipole field associated with nozzle exit turbulent flow induces a radiation pressure

$$p \sim \rho u^2 \cdot M^{1/2} \cdot \left(\frac{l}{r}\right)^{1/2} \tag{7}$$

or

$$p^2 \sim \rho^2 u^4 M \cdot \frac{l}{r} \tag{8}$$

This is the two-dimensional analog of the three-dimensional dipole result

$$p^2 \sim \rho^2 \cdot u^4 \cdot M^2 \cdot \frac{l^2}{r^2} \tag{9}$$

Of course, if the mach number M is not small, the source region is not compact, and each simple-source constituent element of the nozzle dipole is heard independently. Then equation (5) describes the nozzle turbulence-induced field.

Both the source mechanisms referred to are completely separate from the usual sources in the jet-mixing regions. They are caused by the nozzle exit flow and are basically more efficient than the usual sources at low enough speed. There is mounting evidence that these sources are present in the low-speed jet flows of modern turbofan engines.

On emerging from the nozzle, the jet flow mixes with the environment with a high degree of turbulence. This free turbulence is acoustically equivalent to a quadrupole distribution whose field is $(\mathrm{I} \cdot \mathrm{V})$ times the elementary dipole fields. Again $l \cdot \mathrm{V}$ is equivalent to multiplication by the mach number M. Equation (7) gives the basic dipole result, so that the pressure induced by free turbulence is proportional to

$$p \sim \rho u^2 \cdot M^{3/2} \left(\frac{l}{r}\right)^{1/2} \tag{10}$$

and

$$p^2 \sim \rho^2 u^4 M^3 \frac{l}{r} \tag{11}$$

Again, if the mach number M is not small, the elementary sources are not closely packed relative to the wavelength and each simple source field is again heard essentially independently. Then equation (5) describes the turbulence induced field at high mach number.

A more detailed theory (ref. 1) can describe the details of the transition from low to high speed, but the essential elements are as I have outlined.

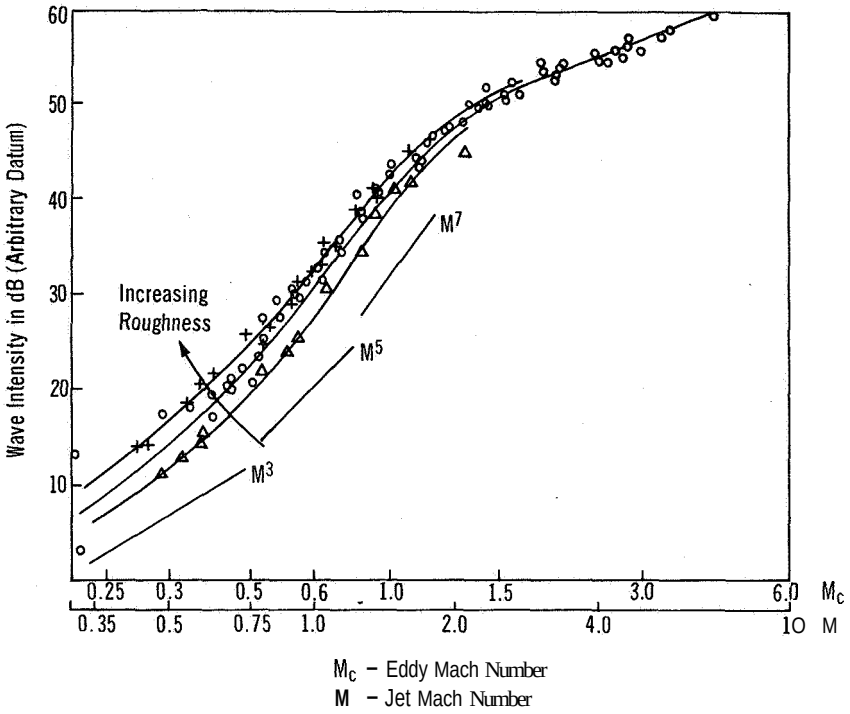

FIGURE 1.—Comparison of experimental and theoretical points.

These are the basic results which Webster at Imperial College has been able to verify in considerable detail in his experimental survey.[1]

Figure 1[2] shows experimental points superposed on the detailed theoretical prediction. It is seen that the experiment bears out the theoretical ideas with an accuracy of ± 2 dB over a dynamic range of 10^5. This agreement gives, I believe, considerable hope that this method of simulating more subtle aspects of the aerodynamic noise problem will have an important role in future. Both the flow and the wave field are very easily visualized as is apparent in figure 2, also taken from Webster's paper.

The flow in the simulation experiments is not reliably modeled as the Reynolds number is extremely small and there is a strong constraint on any turbulence because of the small depth of the water layer. But in the jet experiment these constraints do not seem to be significant, at least as far as the wave field is concerned. One is tempted to infer from the simulation certain gross features of full-scale flows. The area that is currently most exciting concerns the possibility of well-ordered motion in the turbulent jet. In the water table, jets often become turbulent.

[1] This paper will be published in the Journal of Fluid Mechanics.

[2] Fig. 1 is taken from Webster's paper.

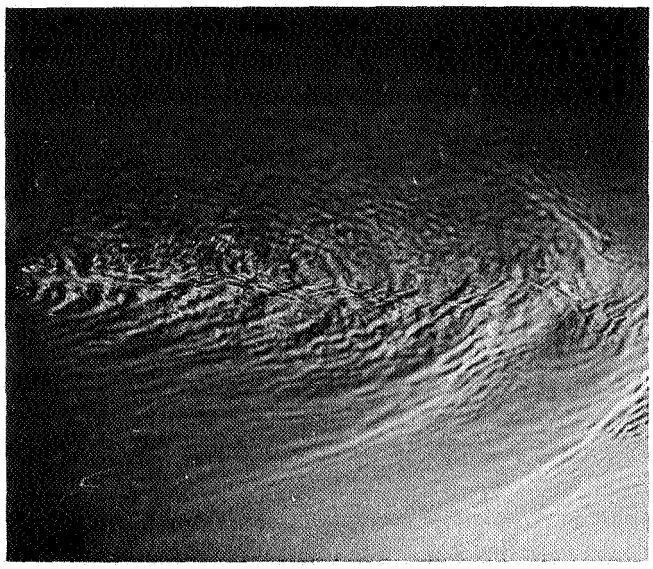

FIGURE 2.—Rough-nozzle jet flow, $M=6$.

The turbulent flow then develops an instability resulting in a highly ordered perturbatiop field. Such an instance is shown in figure 3. Presumably the turbulent jet is subject to the effective viscosity based on an eddy diffusivity, so the effective Reynolds number of the flow, in both simulation and real life, is very low. Distinct, highly ordered instabilities are commonplace to low Reynolds-number flows; thus, that highly turbu-

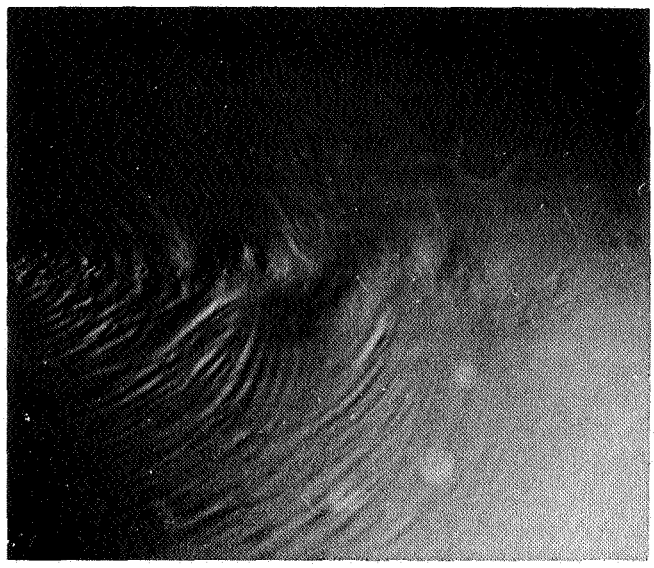

FIGURE 3.—Rough-nozzle jet flow, $M=2$.

lent jets may well display organized structures. There is some evidence that this is so and that the organized motion can be exploited to either control the radiated sound directly or to induce very rapid jet breakdown to reduce the length, and hence noisiness, of a very-high-speed jet. This general area is obviously one that will be thoroughly worked in the near future and is at this moment, I believe, very exciting especially because it is a new and untried idea.

POSSIBLE SOUND SOURCES IN THE DIRECTION OF AIRCRAFT MOTION

I turn now to a completely different aspect of aircraft noise that is currently receiving attention for the first time. That aspect concerns sources of sound associated with the jet and its environment that can radiate preferentially in the direction of aircraft motion. I remind you that the majority of jet noise is thought to come from turbulent eddies traveling in the direction opposite to the aircraft and radiating preferentially away from the aircraft because their efficiency is in inverse proportion to a power of the wavelength, which is reduced by the Doppler effect in the direction ahead of eddy motion. To find a source that radiates preferentially in the direction of aircraft motion requires, presumably, the identification of a source system attached to the aircraft and moving with it so that the Doppler factor can reduce the wavelength ahead of the aircraft and cause the source to radiate with increased efficiency in that direction when the aircraft moves. There seems to me to be three distinct possibilities for identifying such sources. The first is a source system attached to any steady shock system in a choked jet. The second is the source system associated with nozzle-exit turbulence I have referred to before. These dipole sources are fixed in the aircraft reference frame and move with it and must therefore radiate preferentially upstream. The third possibility is that there is an as yet imperfectly understood effective source system located along sharp solid edges, like the nozzle lip or the trailing edges of the wing. A first study of the influence of such sharp edges (ref. 3) near turbulent flow indicates they bring about the scattering to a propagating mode of the basic nonpropagating Bernoulli pressure field. At low speeds this effect appears to be a large one, at least if the radiation problem is posed, as Hall has done, as a diffraction problem. In that event there is a singularity at the sharp edge that has a profound effect on the radiation field. This singularity may or may not be relevant. Viscous effects would, of course, inhibit a true singularity, and the bulk effect of viscosity may be that an effective Kutta condition is applied to the sharp edge. Such a step would undoubtedly alter Hall's conclusions. This general question of what condition should be applied to sharp edges of surfaces in turbulent flow **is**

important. It has a profound effect on the sound-generating mechanisms and is relevant to a very large variety of problems.

REFERENCES

1. FFOWCS WILLIAMS, J. E.; AND HAWKINGS, D. L.: Shallow Water Wave Generation by Unsteady Flow. J. Fluid Mech., vol. 31, 1968, pp. 779–788.
2. LIGHTHILL, M. J.: On Sound Generated Aerodynamically. I. General Theory. Proc. Roy. Soc. London, ser. A, vol. 211, 1952.
3. HALL, L. R.: Ph. D. Thesis, London University, 1969.

371-986 0-LT-70—2

THE RELATION OF THE CONVECTIVE DECAY OF TURBULENT EDDIES TO THEIR FAR-FIELD SOUND PATTERN*

C. E. Wooldndge and D. C. Wooten
Stanford Research Institute
Stanford, Calif.

This paper outlines a series of experiments that are designed to answer several unresolved questions concerning the interpretation of jet noise. Particular attention will be paid to the coherent pressure field in the subsonic jet that extends across the entire jet. Hot-wire measurements of the large eddies at the inner edge of the mixing region will be used to estimate the potential flow fluctuations induced in the core. Convection speed and decay rate measurements of various eddy sizes will also be carried out.

SYMBOLS

a	speed of sound
d	diameter of jet
I	radiated intensity (energy) of sound
M_c	mach number of convected turbulence
p	pressure
p_{ij}	fluid stress tensor
r	distance from observer to point of sound emission
t	time
T_{ij}	tensor defining pressure-wave behavior in turbulent region
v	velocity component
V_j	jet outlet velocity
x	space coordinate
$\mathbf{X}$	vector describing path from point of sound emission to observer
$\mathbf{Y}$	vector describing dimensions of flow
θ	angle between direction of flow motion and direction to observer
δ_{ij}	Kronecker delta
ρ	density
τ	retarded time
μ	viscosity

Subscripts

i, j, k	notation indicating tensor components
j	jet
0	ambient conditions

*Supported by NASA, OART under contract no. NASW 1938.

INTRODUCTION

Aerodynamic noise is generated by turbulent mixing of the high-velocity engine exhaust jet with the ambient air; i.e., the noise is independent of the particular internal engine characteristics. This independence is evidenced by the fact that cold jets exhibit the same general noise characteristics, except for appropriate scaling factors, as do combustion-generated exhaust jets (refs. 1 and 2). It should be pointed out that the total sound power radiated from subsonic jets does not exceed approximately 0.1 percent of the total jet power, and except for special cases, the total power radiated from supersonic jets does not exceed a maximum of approximately 1 percent of the total power (ref. 3). This effectively means that the inverse problem of the effect of the noise field on the structure of the jet can be disregarded, at least for the first order.

In general, the jet exhaust can be separated into two basically different regions. The first is the region in which the jet core persists, i.e., the longitudinal region in which the shear or vorticity layer, originating from the jet boundary, has not yet penetrated to the jet centerline; the second is the downstream region of profile similarity. Each region contributes in a different way to the overall sound power of the jet. The region near the nozzle exit, where the jet core is still present, contributes most of the sound and has a characteristically higher frequency content than does the downstream region (ref. 4). In fact, about 80 percent of the sound is generated in the region up to about eight jet diameters from the nozzle exit.

The functional relationship between the radiated sound power and the parameters describing the jet characteristics is given by (ref. 5)

$$I \approx \frac{\rho_j^2 V_j^8}{\rho_0 a_0^5} d^2 \tag{1}$$

It is evident from the above relation that the jet velocity is the dominant parameter determining radiated acoustic power. It has been verified experimentally (ref. 5) that the acoustic power radiated from subsonic jets varies with the jet exit velocity raised to a power varying from the sixth to the eighth, with the square of the jet diameter, and with something less than the square of the jet density (ref. 3) depending on where the jet density is evaluated; i.e., as the nozzle exit value or as some average value across the jet at some particular longitudinal station downstream of the exit.

BACKGROUND

The fundamental mathematical relationships between noise produced by a jet and the turbulence within it were derived by Lighthill in his papers on aerodynamically generated sound (refs. 3, 4, 6, and 7). He considered the effect of a fluctuating fluid flow occupying a limited part

of a very large volume of fluid, the remainder of which is at rest. The wave equation for the entire medium may be written in tensor form as (ref. 6)

$$\frac{\partial^2 \rho}{\partial t^2} - a_0^2 \frac{\partial^2 \rho}{\partial x_i \, \partial x_i} = \frac{\partial^2 T_{ij}}{\partial x_i \, \partial x_i} \tag{2}$$

where $T_{ij} \equiv 0$ outside the embedded fluctuating region, and

$$T_{ij} = \rho v_i v_j + p_{ij} - a_0^2 \rho_0 \delta_{ij} \tag{3}$$

within the embedded region.[1] The stress tensor p_{ij} is given in terms of the velocity field as

$$p_{ij} = p\delta_{ij} + \mu \left(-\frac{\partial v_i}{\partial x_j} - \frac{\partial v_j}{\partial x_i} + \frac{2}{3} \frac{\partial v_k}{\partial x_k} \delta_{ij} \right) \tag{4}$$

where δ_{ij} is the Kronecker delta, equal to unity if $i=j$, and zero otherwise. Lighthill (ref. 4) shows that at moderate mach numbers (i.e., subsonic) the dominant term in the tensor T_{ij} is the momentum flux term $\rho v_i v_j$.

The momentum flux can vary from point to point, but for a given volume in the absence of solid boundaries, the momentum ρv_i that is entering at one point on the free boundary of the volume must be balanced by momentum leaving from other points on the boundary. Therefore, the momentum flux term should generate sound in the same manner as two canceling acoustic dipoles, which represent an acoustic quadrupole.

At a distance $\mathbf{X}_r$ which is large compared to a flow dimension $\mathbf{Y}_r$ the second spatial derivative of T_{ij} can be replaced by a second time derivative, allowing the solution to equation *(2)* to be written in terms of a retarded potential as (ref. 6)

$$p - p_0 = \frac{x_i x_j}{4\pi a_0^4 r^2} (1 - M_c \cos\theta)^{-3} \int_V \frac{\partial^2}{\partial \tau^2} T_{ij} (\mathbf{Y}, \tau) dV(\mathbf{Y}) \tag{5}$$

where V is the volume containing the embedded fluctuating fluid flow, r is the absolute value of $\mathbf{X}$ minus Y, and τ is the retarded time $(t - r/a_0)$. The pressure p_0 is a background reference value. The integral must be taken with retarded times so that only the sound arriving instantaneously from different parts of the volume Vis summed at the point of interest.

The value of the integral can be estimated (see Lighthill (ref. 4)) by making use of the fact that, in a turbulent flow, fluctuations are well correlated at points in the same vicinity but uncorrelated at points more remote from each other. This yields a picture of turbulent flow divided into regions such that the quadrupoles in any one region are perfectly correlated with one another, but uncorrelated with quadrupoles in any

[1] The usual summing convention on repeated indices is implied here.

other region. The overall intensity (energy) is made up of the sum of the mean square pressure contributions from each of the uncorrelated source regions. Williams (ref. 8) has shown that the total number of quadrupoles must be multiplied by a factor $(1-M_c \cos\theta)$ to give that number whose radiation energies arrive at a given point at the same time. Therefore the directional distribution of intensity carries a factor $(1-M_c \cos\theta)^{-5}$, which would be absent in the case of sound generated by stationary quadrupoles.

Recent measurements by Davies, Ko, and Bose (ref, 9) have shown that a coherent pressure field having a wavelength that is long compared to the thickness of the mixing layer extends from the subsonic jet axis to the near field outside the jet. Their measured distribution of turbulent and pressure intensities is reproduced in figure 1, and the observed axial convection velocity is shown in figure 2. The discrepancy between the convection velocity and the mean velocity, especially in the inner half of the mixing region near the core, is shown to occur because the pressure wave is traveling at 0.6 of the core velocity throughout the entire region. This work suggests additional experiments to determine the mechanism by which a coherent pressure wave is generated by the turbulent field and thus to understand why the convection velocity of the pressure wave is 0.6 of the jet core velocity.

MEASUREMENTS OF THE JET STRUCTURE

The presence of a coherent pressure wave containing most of its energy at a fixed Strouhal number suggests the generation of the wave in the

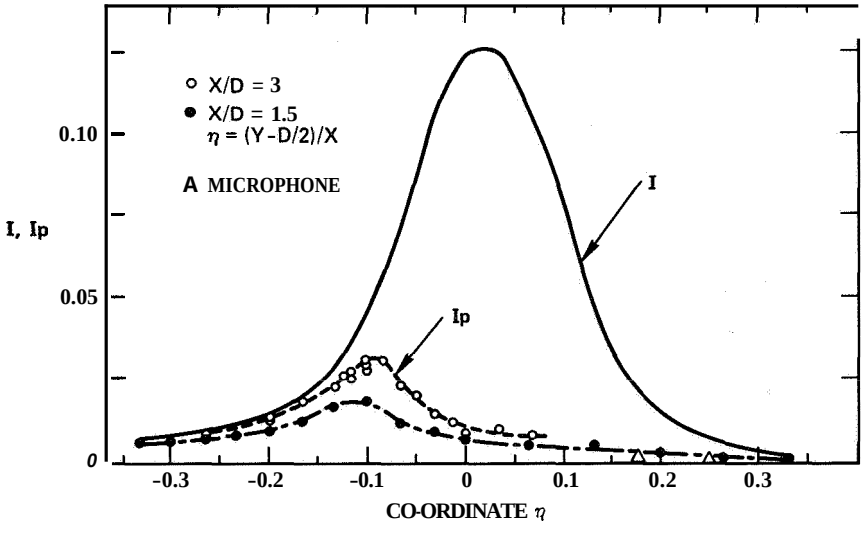

FIGURE 1.—Distribution of turbulent and pressure intensities (from Davies, Ko, and Bose, ARC C.P. 989,1967).

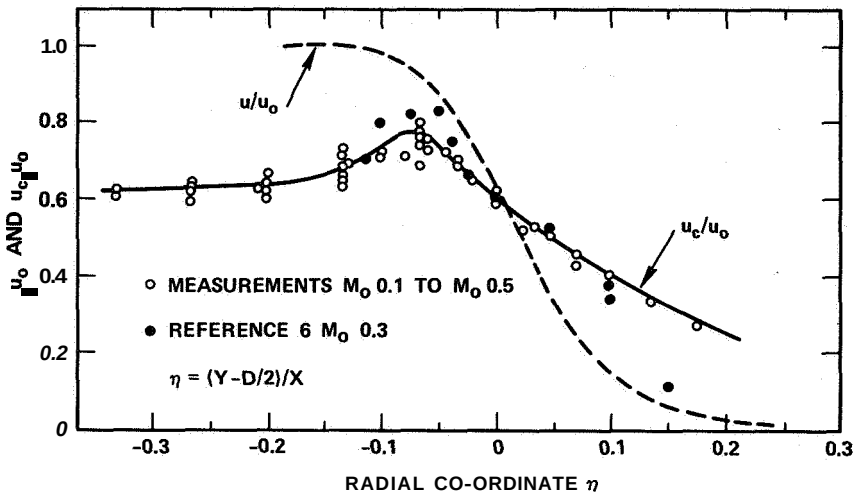

FIGURE 2.—Radial distribution of axial convection velocity along rays, η = constant (from Davies, Ko, and Bose, ARC C.P. 989, 1967).

confined core of the jet by potential flow fluctuations induced by the convection of the large eddies that protrude from the mixing region into the core. Thus the first measurements to be carried out will consist of a hot-wire anemometer measurement of the convection velocity of these large eddies that are observed as intermittent turbulence at the inner edge of the mixing region of a subsonic jet. To induce an effective potential flow in the core, it is likely that these eddies will take the shape of doughnutlike vortex rings propagating away from the jet lip; i.e., the intermittency on opposite sides of the core should be correlated. This picture implies that both the frequency and the convection velocity of the pressure wave are determined by the large-eddy behavior. The fact that the pressure wave is coherent across the entire jet implies that only generation within the confined core is of primary importance.

In order to change either the amplitude or the frequency of the generated noise, the mixing pattern at the boundary of the core must be changed. It may be possible to change the mixing pattern by modification of the boundary layer at the edge of the jet, just before it leaves the nozzle by suction or injection, depending on the sound-generating mechanism. Another possibility is modification of the sound generation by injection of evaporating droplets. The fact that selective frequencies may be damped by choice of the appropriate droplet sizes (ref. 10) offers an interesting possibility for modification of the sound-producing eddies.

Additional hot-wire measurements will be carried out at several longitudinal stations to determine the nondimensional spectral distribution of energy as well as the decay rate of various eddy sizes at the local

convection speed. The objective will be to determine whether and how the characteristic' turbulent scale and the characteristic decay time change with distance from the jet outlet.

CONCLUDING REMARKS

In this paper a series of experiments designed to provide additional understanding of the coherent pressure field observed by other investigators is described. The experimental results will be used to generate a model of the pressure fluctuations induced in the potential core of the jet and their subsequent transmittal to the far field.

REFERENCES

1. TYLER, J. M.; AND PERRY, E. C.: Jet Noise. Pratt & Whitney Aircraft Inst. Rept. 451, 1954.
2. SANDERS, N. D.; AND CALLAGHAN, E. E.: Recent NACA Investigations of Noise Reduction Devices on Full-Scale Jet Engines. Report on NACA Conference on Some Problems of Aircraft Operation. NACA Lewis Center, Cleveland, 1954.
3. LIGHTHILL, M. J.: Jet Noise, AIAA J., vol. 1, July 1963, pp. 1507–1517.
4. LIGHTHILL, M. J.: On Sound Generated Aerodynamically. II. Turbulence as a Source of Sound. Proc. Roy. Soc. (London, ser. A, vol. 222, 1954, pp. 1–32.
5. HARRIS, C. M.: Handbook of Noise Control. McGraw-Hill Book Co., Inc., 1957.
6. LIGHTHILL, M. J.: On Sound Generated Aerodynamically. I. General Theory. Proc. Roy. Soc. (London), ser. A, vol. 211, 1952, pp. 564–587.
7. LIGHTHILL, M. J.: Sound Generated Aerodynamically. Proc. Roy. Soc. (London), ser. A, vol. 267, 1962, pp. 147–182.
8. WILLIAMS, J. E. F.: Some Thoughts on the Effects of Aircraft Motion and Eddy Convection on the Noise from Air Jets. Aeron. and Astronaut. Rept. 155, Univ. of Southampton, 1960.
9. DAVIES, P. O. A. L.; KO, N. W. M.; AND BOSE, B.: The Local Pressure Field of Turbulent Jets. Aeronaut. Research Council C.P. No. 989, London, 1967.
10. MARBLE, F. E.: Some Gasdynamic Problems in the Flow of Condensing Vapors. Astronaut. Acta, vol. 14, 1969, pp. 585–614.

SUPERSONIC JET NOISE THEORY AND EXPERIMENTS*

H. T. Nagamatsu and R. E. Sheer, Jr.
General Electric Research and Development Center
Schenectady, N.Y.
and
G. Horvay
University of Massachusetts
Amherst, Mass.

From the available experimental data for supersonic jets of various diameters and total temperatures, the supersonic core length and the supersonic length were determined as functions of the jet mach number. The variations of the acoustic power output per unit length of the supersonic jets were evaluated from the acoustic measurements for small jets over a mach-number range of 1.0 to 2.5. These measurements indicated that the largest source of noise occurred just ahead of the transition region from supersonic to subsonic velocities on the axis. Using the empirical relationship of the supersonic length as a function of mach number, the linear variation of the acoustic radiation per unit length in the supersonic region, and the subsonic turbulent decay for the acoustic power, an equation for the overall acoustic power output for supersonic jets was developed by Nagamatsu and Horvay. Overall sound-power levels for supersonic jets over the velocity range of 900 to 19700 fps and corresponding mach-number range of 0.85 to 3.7 were correlated with the Nagamatsu-Horvay theory. As predicted analytically, the decrease in the jet density with increasing jet temperature causes a large reduction in the sound generation for constant supersonic mach number. The exponents α and β in the Nagamatsu-Horvay theory were evaluated as functions of mach number for parallel flow and convergent nozzles.

*The research was supported in part by NASA Headquarters, Office of Advanced Research and Technology, Research Division.

SYMBOLS

A	cross-sectional area
c_a	velocity of sound in ambient air
c_j	velocity of sound in jet
D	jet diameter
dB	decibel
$F(M_j)$	function in Nagamatsu-Horvay theory
$f_0(M_j)$	acoustic power output per unit exit diameter at jet exit
$g_0(M_j)$	acoustic power output per unit exit diameter at supersonic core tip
I	acoustic intensity
kHz	frequency in 1000 Hz
l	eddy correlation radius
l_c	jet core length
l_s	supersonic length
L_c	nondimensionalized jet core length, l_c/D
L_s	nondimensionalized supersonic length, l_s/D
m	mass flux
M	mach number
M_c	eddy convective velocity mach number
M_j	jet mach number
M_{j_a}	jet mach number relative to ambient
$\bar{p}$	rms pressure
r	radius from jet centerline
T_{ij}	quadrupole strength
T_{t_j}	jet total temperature
U_j	jet velocity
v_c	eddy convective velocity
V_e	eddy volume
w	sound power per unit length
w_d	sound power per unit diameter length
w_m	maximum sound power per unit length
W	sound power
x	axial distance from jet exit
α	exponent for sound power per unit length at jet exit
β	exponent for sound power per unit length at sonic point
γ	ratio of specific heats
θ	angle
ρ_a	density of ambient air
ρ_j	density of jet
σ	exponent in Nagamatsu-Horvay theory
ω	frequency

INTRODUCTION

The development of supersonic airplanes for commercial and military use requires knowledge regarding efficient methods for decreasing supersonic jet exhaust noise during takeoff at airports located in metropolitan areas of the world. For the supersonic transports being developed, the problem of jet-noise reduction is very difficult because of the large thrust required for takeoff and transonic acceleration and the supersonic jet exhaust velocities. To reduce this exhaust noise, some knowledge of the mechanism and the location of the noise sources in supersonic jets must be obtained. But, even for subsonic jets, the actual location of the noise sources within the jet from the turbulent fluctuations has not been well defined. For supersonic jets, the available experimental data are very limited, and the relationship between the noise generation from the supersonic region and the radiation to the far field is not too well understood. The present theoretical and experimental investigations were undertaken to obtain additional flow and acoustic information from subsonic to supersonic jet exhaust velocities for the purpose of determining the differences and similarities in the acoustic characteristics of subsonic and supersonic jets. It was also hoped that with better knowledge regarding the source of acoustic radiation from supersonic jets, an efficient method of reducing the jet exhaust noise will be developed.

For subsonic jet exhaust velocities, Lighthill developed a theory (refs. 1 and 2) for predicting the acoustic power output from a subsonic turbulent jet by relating the fluctuating turbulent stress tensor in the flow field to its acoustic field. Gerrard (ref. 3) investigated the noise produced by a subsonic jet over a mach number range of 0.398 to 0.995 with a 1-in.-diameter jet and found that the observed noise field was qualitatively in agreement with Lighthill's theory. One of the early experimental studies of subsonic jets with different gases was conducted by Lassiter and Hubbard (ref. 4) at a jet mach number of 0.9 with Freon, air, and helium as the working gas to evaluate the effects of jet velocity, density, and turbulence level on the noise level. The same authors in reference 5 extended the experimental investigation of the plain jet to supersonic exhaust velocities at various air temperatures. Additional experimental investigations of subsonic jet flow noise were conducted by Mollo-Christensen (refs. 6 and 7) with a 1-in.-diameter nozzle. Their results were similar to those of Gerrard, and they found that the emitted sound depended upon the structure of the boundary layer at the nozzle exit for subsonic velocities. Eldred (ref. 8) summarized the noise-generation data for rockets and jets and found that the overall acoustic power output measurements agreed with the eighth-power law of Lighthill over an exhaust velocity range of 650 to approximately 2000 fps for rockets and

turbojets. At the higher velocities the observed acoustic power output varied more slowly than the eighth power, as predicted by the supersonic jet-noise theory of Nagamatsu and Horvay (ref. 9).

Various experimental hot-wire investigations (refs. 10 to 14) have been conducted to determine the characteristics of turbulence within the subsonic jets that had been shown by Lighthill to be sources of acoustic radiation. The hot-wire anemometers were used to determine the intensity of turbulence, correlation coefficients, and spectra of turbulence for subsonic jets of various diameters. Recently Davies and colleagues (ref. 13) have used hot-wire measurements to study the pressure field associated with the turbulent shear flows from subsonic jets. They were able to separate the hot-wire output into the output caused by the turbulent and pressure field components. From these measurements they determined the radial distribution of turbulent and pressure intensity. Hot-wire measurements of fluctuating turbulent stresses in the mixing layer of a two-dimensional jet were made by Jones (ref. 14) to aid in understanding the aerodynamic noise generation from subsonic jets.

The noise from a supersonic jet has been studied by a few investigators with small jets. Powell (ref. 15) was able to correlate the loud "screech" from room-temperature supersonic jets with the schlieren photographs of the jets. These photographs indicated that the sound waves of ultrasonic frequency were caused by the transition of the initially laminar boundary layer to turbulence. Near-field and far-field noise surveys for solid-fuel rockets have been conducted by Mayes and colleagues (ref. 16). With these rockets the exhaust velocities were close to 8500 fps, but the jet mach number varied from 2.65 to 4.07. Near-field surveys indicated that the sound-pressure level increased monotonically from the jet exit and that the highest pressure occurred about 20 exit diameters downstream of the nozzle near the transition from supersonic to subsonic flow. Potter and Jones (ref. 17) observed similar phenomena for a small nitrogen jet at room temperature with an exit mach number of 2.49 and corresponding velocity of 1800 fps. They were able to determine the acoustic power generated per unit length of the jet flow by the use of a large reverberation chamber. The acoustic power distribution increased from the jet exit, and the peak acoustic power generation occurred approximately 20 diameters downstream, which was just ahead of the sonic location. Recent investigations by Nagamatsu and colleagues[1] with a convergent nozzle operated over a jet mach-number range of 0.60 to 1.40 have also indicated the nearly linear increase in the acoustic radiation per unit length from the jet exit to the sonic location for supersonic jets. Also, the impact pressure fluctuations along the axis indicated maxi-

[1] H. T. Nagamatsu, R. E. Sheer, Jr., and M. S. Gill: Flow and Acoustic Characteristics of Subsonic and Supersonic Jets from Convergent Nozzles. NASA CR in progress.

mum fluctuations just ahead of the sonic point for supersonic jets.

Ribner (ref. 18) investigated, by the application of Lighthill's theory, the spatial distribution of the noise source along a subsonic jet. By assuming similar profiles in the mixing region, the acoustic power emitted by a slice of jet was essentially constant with distance in the initial mixing region of four diameters as postulated by Lighthill (refs. 1 and 2). Farther downstream in the fully turbulent jet, the acoustic power decreased very rapidly, x^{-7} or faster. A detailed discussion of the generation of sound by subsonic turbulent jets is presented in reference 19.

The detailed understanding necessary for predicting the noise-generating mechanism of supersonic jets is not as well developed as the Lighthill theory for a subsonic jet. Phillips (ref. 20) proposed a theory to describe the generation of sound by turbulence at supersonic mach numbers. The sound radiated as eddy mach waves, and this mechanism of generation became dominant at high mach numbers. The acoustic power increased approximately as $M_j^{3/2}$ for $M_j > 1$, a contrast with the M_j^8 variation found by Lighthill for $M_j < 1$. Williams (ref. 21) also considered the noise from supersonic jets and extended Lighthill's theory for the sound radiated from turbulent flow to deal with the transonic and supersonic ranges of eddy convection speeds. For these conditions the theory predicts the strength of the sound waves from the supersonic jet to be proportional to M_j^3 while the experimental observations of Laufer (ref. 22) for supersonic turbulent boundary layer on a flat plate was M^4. Williams in his analysis did not consider the large difference in the location of the main noise generation region for supersonic jets, as found by Mayes (ref. 16), Potter (ref. 17), and Nagamatsu,[2] compared to subsonic jets.

Recently, Ollerhead (ref. 23) and Plumblee (ref. 24) have attempted to develop semiempirical prediction methods for determining the near-field noise and the overall sound power level for turbojets and rocket engines with supersonic exhaust velocities. Ollerhead, using the concept of a discrete finite number of sound sources for supersonic jets, established an approximate expression for the sound pressure level distribution. Plumblee (ref. 24) derived a semiempirical relationship for predicting the near-field and far-field sound-pressure levels from supersonic jets with the jet temperature and mach number as the controlling parameter. These analyses do not predict the actual acoustic power generated per unit length of the supersonic jet flows as determined by Potter (ref. 17) and Nagamatsu.[3] An analysis of the acoustic power output from supersonic jets has been developed by Nagamatsu and Horvay (ref. 9) by considering the aerodynamic and acoustic characteristics

[2] Ibid.

[3] Ibid.

for supersonic exhaust velocities. Dosanjh and his colleagues (ref. 25) have been investigating the sound generation and reduction of noise from small supersonic jets.

This paper will discuss the status of experimental and theoretical results for the acoustic and flow characteristics of supersonic jets. Some of the experimental aerodynamic and acoustic data obtained for a convergent nozzle operated over a mach-number range of 0.60 to 1.40 will be summarized and correlated with other published literature.[4] The main concepts and equations for the supersonic jet noise theory of Nagamatsu and Horvay (ref. 9) will be presented and the theory correlated with the available acoustic data for supersonic jets.

SUPERSONIC JET CHARACTERISTICS

Fluid Mechanics

One of the most significant aerodynamic differences between the subsonic and supersonic jet is the length of the primary core, defined as the distance from the jet exit to the location on the axis where the initial jet velocity still exists as shown in figure 1. For subsonic jet ex-

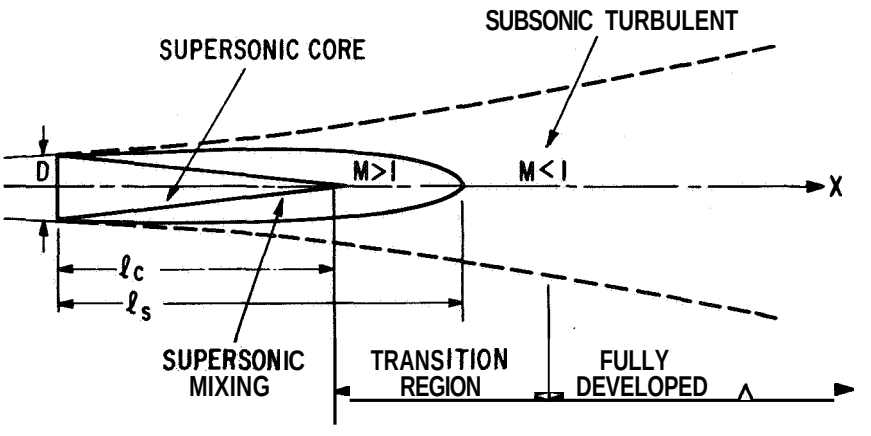

FIGURE 1.—Parallel-flow supersonic jet expanded to ambient pressure.

haust velocities (refs. 10 and 26),[5] the core length is approximately four diameters as assumed by Lighthill (refs. 1 and 2) in his analysis. The experimental data for the uniform core region as a function of jet exhaust mach number are presented in figures 2 and 3. Surrounding the supersonic core region, there is a region in which turbulent mixing occurs at supersonic velocities as indicated in figure 1. Beyond this supersonic region, subsonic turbulent mixing is taking place.

[4] Ibid.
[5] Ibid.

The axial mach number and velocity distributions for a convergent jet have been determined from the impact pressure and total temperature surveys for various jet mach numbers.[6] Over the jet mach-number range of 0.60 to 1.0, the axial variations of flow mach number with distance from the jet exit were quite similar with the uniform mach number on the axis extending approximately 5 diameters instead of the 4 diameters assumed by Lighthill. Downstream of the core region, the velocity decreases very rapidly in the transition region where the fully developed turbulent jet is being established. In the fully established turbulent jet region the velocity continues to decrease with distance. For supersonic jet mach numbers of 1.2 and 1.4, the flow mach number on the axis over the initial portion of the jet is not constant as in subsonic jets. This difference is the result of the presence of shock bottles for supersonic jets from a convergent nozzle as shown optically[7] and analyzed in reference 27. It can be seen in figure 2 that the location of the sonic point

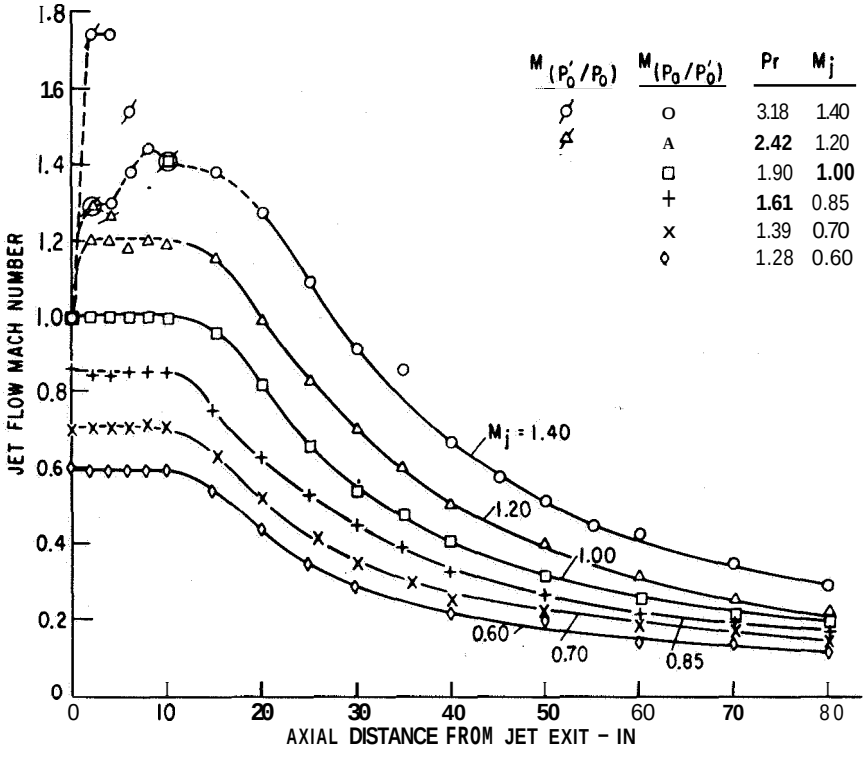

FIGURE 2.—Variation of flow mach number along the jet axis with distance for convergent nozzle.

[6] Ibid.
[7] Ibid.

on the jet axis moves downstream with the supersonic mach number. Also, because of the presence of the shock bottles, the supersonic jets from a convergent nozzle do not mix rapidly with the ambient air. Once the flow mach number on the jet axis becomes sonic, the velocity decays similarly to the subsonic jets.

The jet core and supersonic lengths for supersonic exhaust velocities for various jet diameters and temperatures are presented in figure 3. Warren (ref. 26) conducted an extensive axial survey over a jet exhaust mach-number range of 0.60 to 2.6 at different temperatures. He used contoured nozzles to produce parallel flow at the nozzle exit for supersonic mach numbers. For this condition there is a supersonic core region as indicated in figure 1. Both Potter (ref. 17) and Eggers (ref. 28) investigated the flow regimes for parallel-flow supersonic jets, and their results for the core and supersonic lengths are presented in this figure. Also,

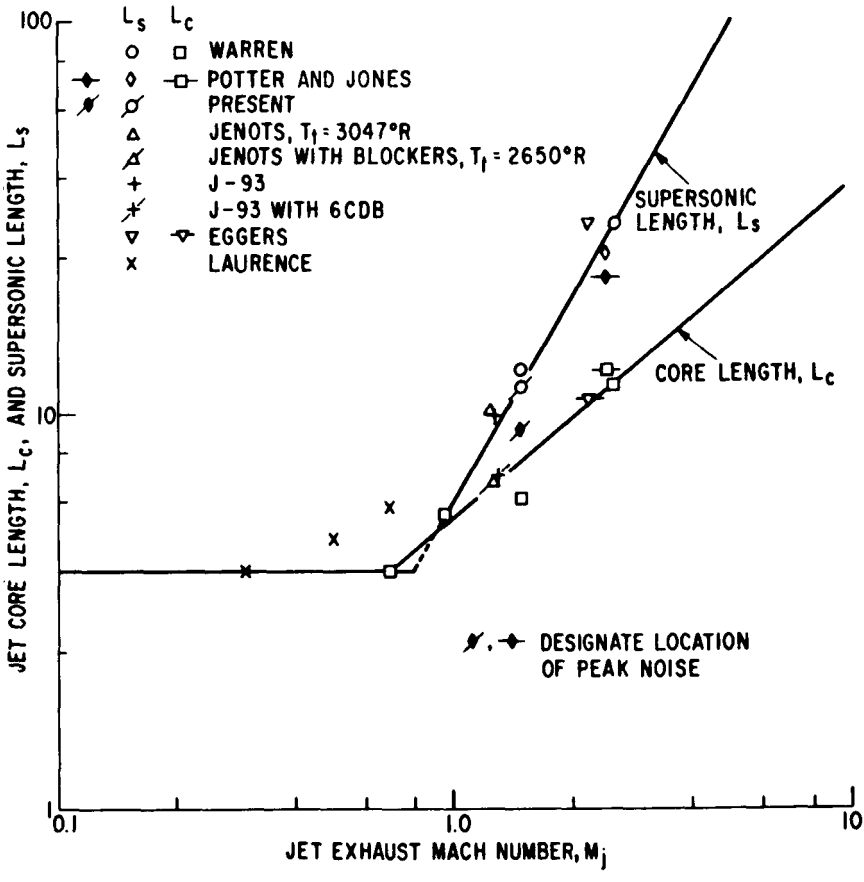

FIGURE 3.—Jet core length and supersonic length as function of jet mach number.

the results from both a 4-in. diameter and a J–93 jet engine convergent nozzles at high exhaust temperatures are included. Because the data from various jets at different temperatures and diameters do correlate well for the core and supersonic lengths in figure 3, for supersonic exhaust velocities the jet mach number is the dominant physical parameter and governs the flow phenomena. For subsonic jets the core lengths determined by Laurence (ref. 10) are also presented and agree approximately with the results for a convergent jet presented in figure 2 for subsonic mach numbers.

Based upon the experimental data for the core length relative to the nozzle-exit diameter, an empirical relationship between the core length and the jet mach number was derived in reference 9 as

$$L_c = l_c/D = 5.22\ M_j^{0.9} + 0.22 \tag{1}$$

This is the L_c curve in figure 3 and is slightly different from that derived empirically in reference 23. It is assumed for jet mach numbers less than 0.7 that the core length is identical to the mixing region length assumed by Lighthill (refs. 1 and 2) so that

$$L_c = 4 \qquad 0 < M_j < 0.7 \tag{1a}$$

Ollerhead (ref. 23) provides a somewhat different curve, which does not make use of all the recent experimental data.

In figure 3 the length of the supersonic region relative to the jet diameter as a function of the jet mach number is given by

$$L_s = l_s/D = 5M_j^2 + 0.8 \tag{2}$$

The available experimental data for air jets at room temperature, rocket exhausts, high-temperature jet engines, and for jet-exit diameters from 1 to 30 in. agree reasonably well with this empirically established equation. It is seen that temperature and gas composition have little effect upon the supersonic length in terms of the jet exhaust mach number.

Acoustic Characteristics of Subsonic and Supersonic Jets

Potter and Jones (ref. 17) were able to determine experimentally the location of the maximum noise-generation region for a mach-2.49 nitrogen jet exhaust at room temperature. A perfectly expanded contoured nozzle with an exit diameter of 1 in. was operated at a correct pressure ratio with a parallel flow. By moving this jet into and out of a large reverberation room and measuring the reverberant sound-pressure

371-986 O-LT-70—3

level, the acoustic power distributions were determined as a function of the distance of the nozzle from the orifice in the wall. The acoustic power per unit length of the jet flow was determined by differentiating the resultant acoustic power curves and is presented in figure 4. The maximum acoustic power generation is located approximately 20 exit diameters from the nozzle, which is just ahead of the supersonic core tip. It is apparent from this figure that the initial mixing region of a parallel-flow supersonic jet is a very low producer of noise because of the thin mixing layer around the jet and that a constant acoustic power per unit length, as postulated for a subsonic jet, is not relevant for a supersonic jet. In the initial region, the slope of the acoustic distribution curve varies linearly with x, and in the subsonic region beyond the supersonic tip, the acoustic power generation per unit length is proportional to x^{-6}, which is close to the $x^{-6}l^{-1}$ variation observed for subsonic jets.

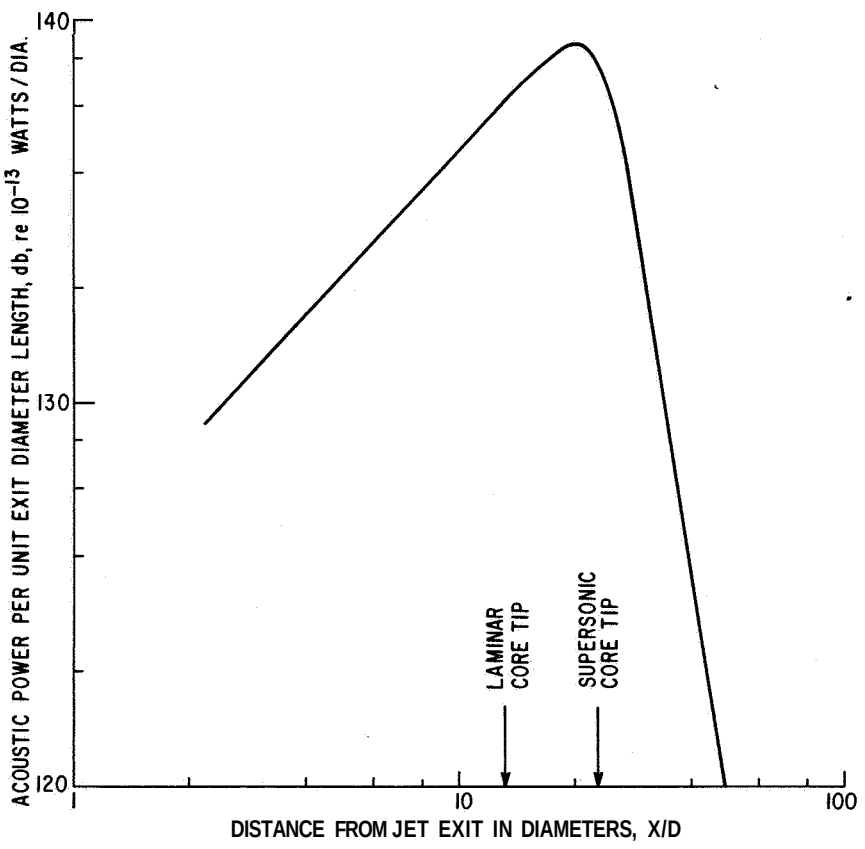

FIGURE 4.—Acoustic power generated per unit length of the jet (ref. 17).

A small &in.-diameter quartz piezoelectric pressure transducer with a response time of approximately 20 psec has been used to measure the impact pressure fluctuations along the axis for a convergent nozzle with an exit diameter of 2 in., corresponding to the mach-number distribution in figure 2.[8] The rms values of the pressure fluctuations were obtained over an axial distance of 80 in. from the jet exit for various jet mach numbers and are presented in figure 5. Over the subsonic mach-number range of 0.60 to 1.0, the variations of the impact pressure fluctuations with distance were quite similar with peak fluctuations occurring approximately 9 diameters from the jet exit. In the initial core region of approximately 5 diameters (fig. 2), the pressure fluctuations are quite small compared to the peak value. From the axial velocity distributions, it appears that the peak impact pressure fluctuations occur in the region where the primary jet is completely mixed with the surrounding gas, which corresponds to the adjustment region defined by Lighthill (refs. 1 and 2). After this region the jet decays as a fully established turbulent jet, and the impact pressure fluctuations decay monotonically with distance and are quite similar over the subsonic jet mach-number range of 0.60 to 1.0.

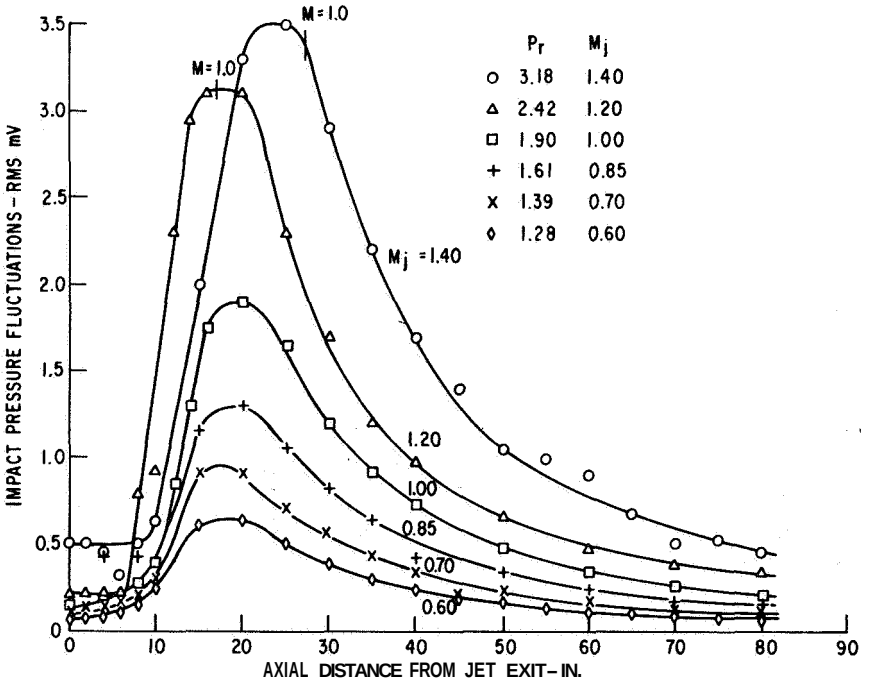

FIGURE 5.—Impact pressure fluctuations along the jet axis for convergent nozzle.

[8] Ibid.

As the jet velocity was increased to supersonic mach numbers, the peak impact pressure fluctuations became greater than those observed for subsonic jets (fig. 5), and the location of the peak fluctuations was in the vicinity of the sonic velocity location on the axis. At a jet mach number of 1.4 the peak fluctuations occurred just ahead of the sonic point, which is approximately 13 diameters from the jet exit. Evidently the impact pressure fluctuations at the normal shock waves in the shock bottles for convergent nozzles are not large compared to the fluctuations presented at the end of the supersonic flow region. After the location of the peak fluctuations for supersonic jets, the flow velocity (fig. 2) and the impact pressure fluctuations decreased continuously like the subsonic jets.

Directivity of Far-Field Sound

The overall sound pressure levels have been determined from the microphone measurements on a 10-ft radius from the exit of a 2-in.-diameter convergent jet and are presented in figure 6.[9] For subsonic jet velocities the variations of the overall sound-pressure level with angular position were quite similar with the maximum pressure level at an angular position of 19.1°, and the pressure monotonically decreased with increas-

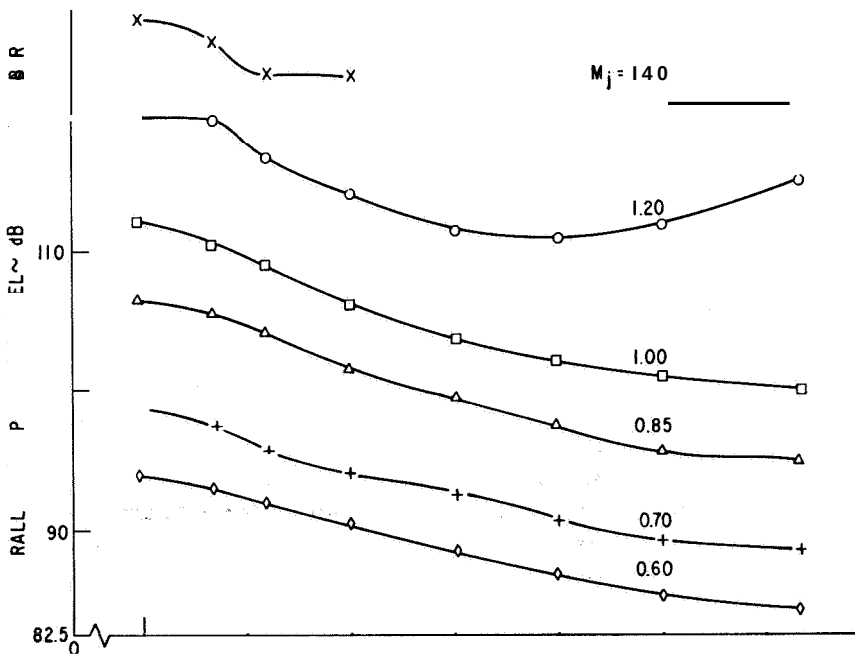

FIGURE 6.—Overall sound-pressure level as a function of angular position from jet axis for different jet mach numbers.

[9] Ibid.

ing angle. With room-temperature subsonic jets, similar variations of the overall sound pressure level with angular position were observed by other investigators. In references 3, 4, and 7, it was found that the directional characteristics of the sound field consisted of apparent sound sources for low and high frequencies. The angle of maximum intensity decreased with frequency, indicating the directivity distributions and the spectra of high and low frequencies are different with smooth transition between them.

For supersonic jets the far-field directivity patterns are different from those observed for subsonic jets as shown in figure 6. The maximum overall sound pressure levels were located close to the jet axis for supersonic mach numbers and decreased to the 43.8° location. Beyond this angular position the sound intensity remained nearly constant for a mach 1.4 jet. This type of sound-pressure-level distribution is the result of the occurrence of eight shock bottles at this mach number with corresponding large acoustic radiation from each bottle as discussed in reference 25. Both convergent and contoured nozzles with the same throat diameter and pressure ratio for a jet mach number of 1.5 were investigated in reference 29. It was observed that the overall sound-power level decreased with angular position from the jet axis for the contoured nozzle because of the lack of shock bottles.

Sound Power Spectra

From microphone measurements at eight angular positions[10] the spectra of the acoustic power output of the 2-in.-diameter convergent jet per 1/3-octave frequency band for a jet mach-number range of 0.60 to 1.4 are shown in figure 7. With the available tape recorder, the power spectra were obtained over a frequency range of 40 Hz to 16 kHz. There is appreciable scatter at frequencies below approximately 100 Hz. For these lower frequencies the wavelength is becoming greater than the 10-ft radius for the microphone, and consequently the acoustic data will be in the near field at these lower frequencies, which causes the scatter as well as the increase in the apparent acoustic power output. Gerrard (ref. 3) had obtained the power spectra for a small jet at room temperature over a mach-number range of 0.316 to 1.0 and obtained the spectra over a frequency range of 150 Hz to 9 kHz. Over this frequency range his spectra are quite similar to those presented in figure 7.

For subsonic exhaust velocities there is no noticeable change in the frequency of the maximum power as indicated in figure 7. Even at a supersonic mach number of 1.2, the power spectrum is very similar to that observed for subsonic jets. At the highest mach number of 1.4, the maximum power occurred at a higher frequency than that for the sub-

[10] Ibid.

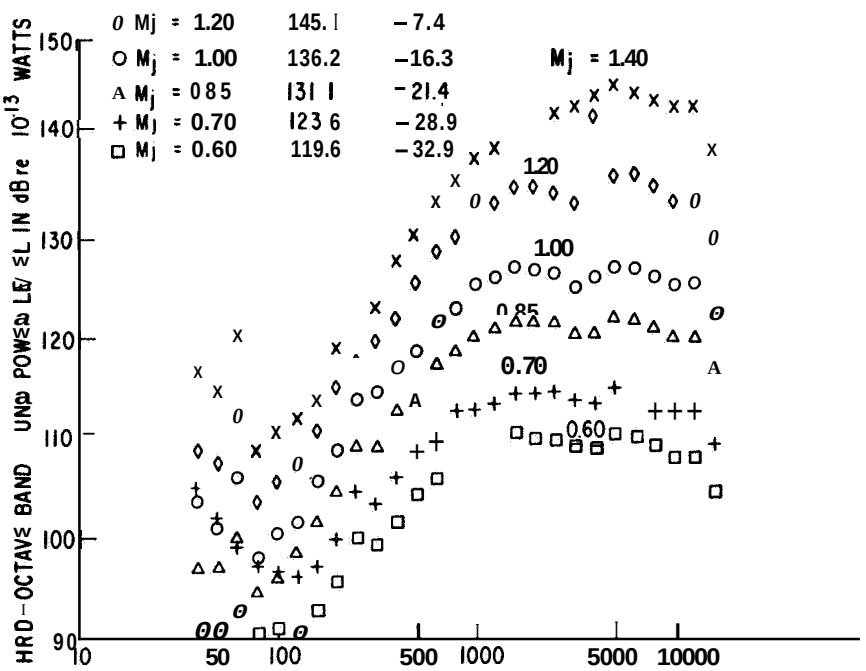

FIGURE 7.—Comparison of sound-power spectra for plain convergent jet at various mach numbers.

sonic jets. Acoustic data for a mach-1.4 jet was obtained also with a tape recorder with a frequency response up to 80 kHz, and the power spectrum from these data agreed with that observed with the regular tape recorder over the frequency range of 40 Hz to 16 kHz. For frequencies greater than 16 kHz, the power continuously decreased indicating that nearly all of the acoustic power is contained in frequencies below 16 kHz for the 2-in.-diameter jet. Comparison of the sound-power spectra in figure 7 between subsonic and supersonic jets indicates that the change in the power spectrum from subsonic to supersonic jet velocities is rather gradual and not as drastic as the overall sound pressure level shown in figure 6.

Near-Field Sound-Pressure Levels

By locating the microphone at various radial distances from the 2-in.-diameter convergent nozzle exit, the variations in the near-field pressure fluctuations with axial distance from the jet exit have been

determined[11] for jet mach numbers of 0.60 to 1.4 and are presented in figure 8 for the microphone located at two nozzle diameters from the periphery of the jet exit. For subsonic jet mach numbers of 0.60 to 1.0, the variations of the sound-pressure level with axial distance were quite similar, indicating the same type of acoustic radiation from subsonic jets as well as for a sonic jet. From the axial impact pressure surveys for these mach numbers, it is noted that the core region extends to approximately 5 diameters as indicated in figure 2. But the near-field sound-pressure level increased with distance beyond the core region for subsonic jets. This is reasonable because the sound pressure at a particular radial and axial distance is influenced by the acoustic radiation from the upstream and downstream portion of the jet for subsonic exhaust velocities. Hence, the near-field pressure level should increase with distance over the initial region from the jet exit as shown in figure 8.

The distributions of the near-field sound-pressure levels with radial and axial distances from the jet exit are presented in figure 8 for supersonic jet mach numbers of 1.2 and 1.4. It is apparent in this figure that

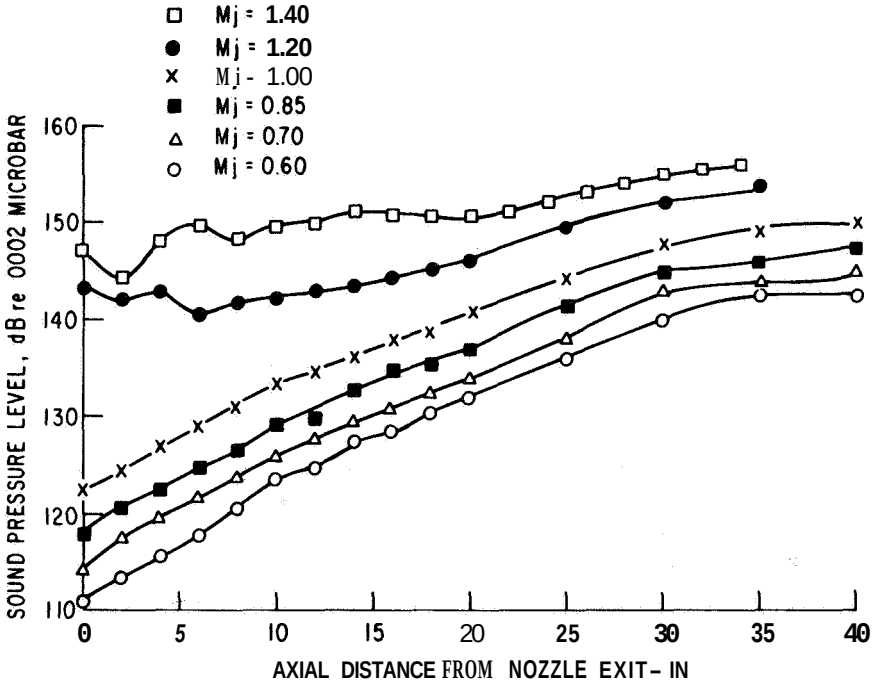

FIGURE 8.—Near-field overall sound-pressure level as a function of jet mach number and axial distance at 2 diameters from nozzle exit.

[11] Ibid.

the sound-pressure variations with axial distances are very different than those observed for subsonic jets. The greatest difference between the subsonic and supersonic jets occurred at the jet-exit location. Also, the rate of increase in sound-pressure level with distance was much less for the supersonic jet, and there were more fluctuations in the sound-pressure levels for supersonic jets because of the presence of mach waves from the jet boundary. Lassiter and Hubbard (ref. 5) also investigated the effects of the jet velocity on the near-field sound-pressure variation with axial distance for a hot jet and observed a similar type of near-field sound-pressure variation as indicated in figure 8.

From these sound-pressure measurements in the near field, the acoustic intensity and the acoustic power transmitted through a cylindrical surface have been calculated to obtain information regarding the acoustic radiation characteristics for subsonic and supersonic jets.[12] The intensity of the acoustic radiation at the microphone radial location is given by

$$I=\frac{\bar{p}^2}{\rho_a c_a} \tag{3}$$

where $\bar{p}$ is the rms sound pressure. By assuming that the sound emission from the circular jet is axially symmetric, the sound-power transmission per unit length through a cylindrical surface containing the microphone in terms of unit jet diameter length is

$$w_d=\frac{D}{\rho_a c_a}\int_0^{2\pi}\bar{p}^2 r\, d\theta \tag{4}$$

Using these equations, the acoustic power transmission through the cylindrical surfaces surrounding the jet have been calculated,[13] and the results for supersonic mach numbers for a radial location of two nozzle diameters are presented in figure 9. The acoustic power distributions for these supersonic mach numbers are quite different from those observed for subsonic jets. The acoustic power transmission per unit length in the axial direction is not continuous, but can be approximated by a linear variation up to the sonic location as indicated in figure 9. For a jet mach number of 1.2, the scatter from the linear approximation is small compared to that existing for the mach 1.4 jet because of the stronger shock waves existing for the higher mach numbers.

To obtain some information regarding the acoustic power radiation from a convergent nozzle, the acoustic power per unit exit diameter

[12] Ibid.
[13] Ibid.

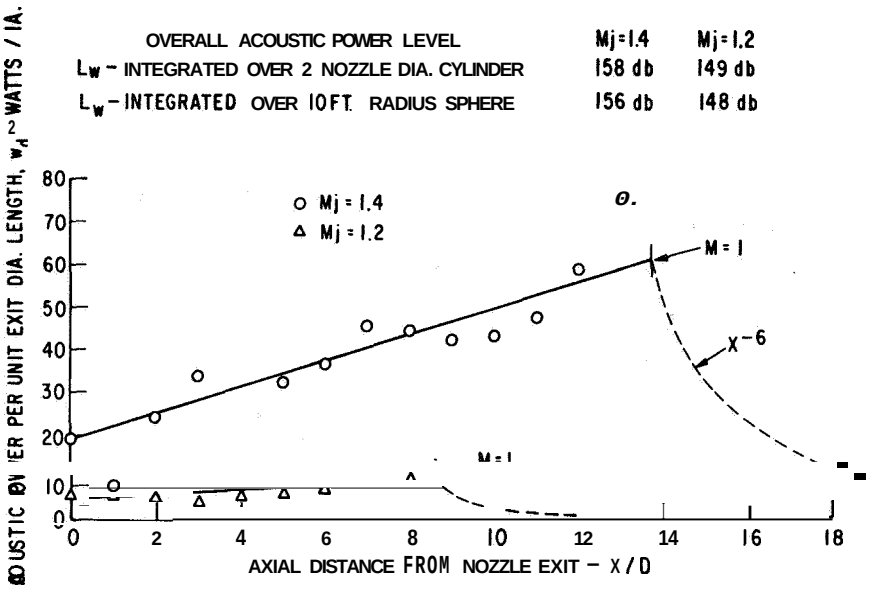

FIGURE 9.—Acoustic power per unit length of jet obtained with microphone traverse parallel to jet axis at two nozzle diameters from nozzle periphery.

length for various jet mach numbers has been calculated.[14] The acoustic power distributions presented in figure 9 were integrated to obtain the overall acoustic power level for supersonic jets by

$$W = \int_0^{l_s} w 2\pi r\, dx + \int_{l_s}^{\infty} w 2\pi r l_s^6 x^{-6}\, dx \tag{5}$$

where $r = 2.5$ D and l_s is the supersonic length. It is assumed for a supersonic jet downstream of the supersonic region, in the subsonic jet mixing region, that the acoustic power distribution would vary as x^{-6}, the same variation as assumed by Lighthill for subsonic jets. The overall power levels calculated by equation (5) for jet mach numbers of 1.2 and 1.4 were 149 and 158 dB, respectively. From the microphone measurements on a 10-ft radius, the corresponding far-field overall acoustic power levels were 148 and 156 dB, respectively. These results indicate a surprising agreement between the overall acoustic power level determined from near-field and far-field measurements for supersonic jets. This excellent agreement may be the result of two factors. First, at these supersonic mach numbers the sound-power spectra (fig. 7) indicate that the

[14] Ibid.

frequency for the peak power was approximately 5 kHz with a corresponding wavelength of 0.22 ft. Thus, the microphone was located approximately 1.5 times the wavelength from the jet periphery. The second factor is the result of the existence of mach waves for supersonic jets as shown in references 17, 25, and 27. Thus, in the near-field location the microphone will be influenced primarily by the mach waves and the sound waves from the region of the jet upstream of the microphone location. The sound emission from the region of the jet downstream of the microphone will be highly attenuated or will not reach the microphone because of the supersonic jet velocity.

SUPERSONIC JET-NOISE THEORY

Subsonic Jet-Noise Theory of Lighthill

Lighthill (refs. 1 and 2) used experimental and dimensional analysis to evaluate the expression for the acoustic power output per unit volume of low-speed jets. He assumed that in the mixing region (fig. 10), the fluctuations of terms like $\rho u_i u_j$ in the quadrupole strength expression T_{ij} is proportional to ρU^2 and changes slowly with x. The typical frequency ω of the turbulent eddy decreases as U/x and the typical eddy volume V_e increases as x^3. By using these approximations, the acoustic power output per unit volume in the mixing region is seen to vary as

$$\frac{\rho_j^2 U_j^8}{\rho_a c_a^5 x} \tag{6}$$

Because the volume per unit length increases with x, the acoustic power emitted per unit length of subsonic jet should remain constant in the mixing region as shown in figure 10, and the overall sound power up to $x=4D$ is found to be proportional to

$$\frac{\rho_j^2 U_j^8 D^2}{\rho_a c_a^5} \tag{7}$$

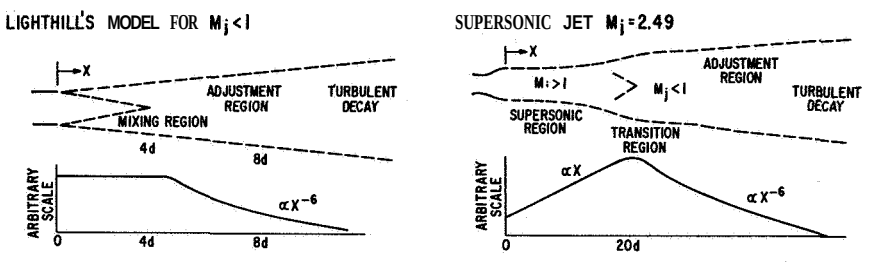

FIGURE 10.—Comparison of subsonic and supersonic jet aerodynamic and acoustic characteristics.

This is Lighthill's (refs. **1** and *2)* eighth-power law for a subsonic jet.

Beyond the mixing region $x > 4D$, the fluctuations in the quadrupole strength T_{ij} decrease with a corresponding decrease in the sound emitted per unit length of the jet. For locations beyond $8D$, the velocity decreases as x^{-1} and the acoustic power output per unit length falls off as $x^{-6}\, l^{-1}$, where l is the eddy correlation radius. For large distances 1 is proportional to x, but it vanes little up to $20D$. Thus, in the fully developed turbulent jet, the acoustic power outputs decay as $x^{-6}\, l^{-1}$, which was also shown by Ribner in reference **19.**

Lighthill in reference **2** derived an equation for the overall sound power for subsonic jets based upon dimensional analysis and experimental acoustic data as

$$W = 10^{-4}\,\frac{1}{2}\,\frac{\rho_a U_j^8 A}{c_a^5} \tag{8}$$

and it was assumed that the jet density ρ_j equals the ambient density ρ_a and that A is the cross-sectional area of the jet. To account for the differences in the physical state of the jet with that of the ambient gas, equation (8)can be expressed as

$$W = 10^{-4}\,\frac{m}{2}\,\frac{\rho_j}{\rho_a}\left(\frac{c_j}{c_a}\right)^5 c_j^7 M_j^7 \tag{8a}$$

where $m = \rho_j U_j A$, the mass flow of the jet.

By assuming the sound emitted from the mixing region $0 \leq x \leq 4D$ to be constant and the fully developed turbulent decay region as $4D \leq x < \infty$, the overall acoustic power output can be expressed as

$$W = \int_0^{4D} w_m\, dx + \int_{4D}^{\infty} w_m (4D)^6 x^{-6}\, dx \tag{9}$$

where w_m is the sound emission per unit length in the initial mixing region. As shown in reference **9,** the acoustic power output per unit diameter length in the mixing and turbulent decay regions can be expressed as

$$w_{d_m} = \frac{10^{-4}}{9.6}\, m\,\frac{\rho_j}{\rho_a}\left(\frac{c_j}{c_a}\right)^5 c_j^2 M_j^7 \qquad 0 \leq x/D \leq 4 \tag{10}$$

and

$$w_d = \frac{10^{-4}}{9.6(4^{-6})}\, m\,\frac{\rho_j}{\rho_a}\left(\frac{c_j}{c_a}\right)^5 c_j^2 M_j^7 (x/D)^{-6} \qquad 4 \leq x/D < \infty \tag{11}$$

These equations for the sound emission from subsonic jets will be correlated with acoustic measurements.

Supersonic Jet-Noise Theory of Nagamatsu and Horvay

An analysis of the acoustic power output for fully expanded supersonic jets was made by Nagamatsu and Horvay by considering the flow and acoustic characteristics in reference 9. The idealized supersonic flow model used in the analysis is shown schematically in figures 1 and 10. In the latter figure, Lighthill's acoustic model for a subsonic jet is presented together with the Potter and Jones (ref. 17) model for a parallel-flow jet with supersonic exhaust velocity. A similar type of acoustic distribution has been observed for a convergent nozzle at jet mach numbers of 1.2 and 1.4.[15] The results are presented in figure 9. The basic differences between the subsonic and supersonic jets are apparent from figure 10. The supersonic mixing region extends over a large distance as given by equation (2) and at a mach number of 2.49, it is slightly greater than 20 diameters, while for low-speed jets this is approximately 4 diameters, as assumed by Lighthill. The second difference is that the acoustic power output per unit length is not constant in the mixing region for supersonic jets but increases linearly with distance. When the jet has become fully turbulent and subsonic, the acoustic power output in the turbulent decay region varies approximately as x^{-6} for supersonic jets as in the subsonic case. Therefore, this is one part of Lighthill's subsonic jet noise theory that can be utilized for the analysis of supersonic jets.

It was assumed in the analysis by Nagamatsu and Horvay (ref. 9) that the peak acoustic radiation, given by equation (2), per unit length of the supersonic jet was located at the supersonic core tip, even though the experimental data of Potter and Jones (ref. 17) for a jet mach number of 2.49 and Nagamatsu and colleagues[16] at a mach-1.4 jet indicated that the peak output was located slightly ahead of the sonic location on the axis. The peak impact pressure fluctuations for supersonic jets were found in reference 29 to occur just ahead of the sonic location on the axis as indicated in figure 5.[17]

With this assumption, the overall sound power output from a supersonic jet can be expressed as a sum of the acoustic contributions from the supersonic region $0 \leqslant x \leqslant l_s$ and the subsonic turbulent decay region $l_s \leqslant x < \infty$ by

$$W = \int_0^{l_s} w\, dx + \int_{l_s}^{\infty} w\, dx \tag{12}$$

where w is the acoustic power output of a jet slice of unit length and is

[15] Ibid.
[16] Ibid.
[17] Ibid.

a function of x for given jet exhaust conditions. This may be written with $w_d = wD$ as

$$W = \int_0^{L_s} w_d \, d(x/D) + \int_{L_s}^{\infty} w_d \, d(x/D) \tag{12a}$$

where L_s is the supersonic core length given by equation (2) and figure 3.

For the supersonic region, it will be assumed that the acoustic power output per unit exit diameter will vary linearly as indicated in figures 4, 9, and 10 and will be expressed as

$$w_d = f_0(M_j) + \frac{g_0(M_j) - f_0(M_j)}{L_s} x/D \qquad 0 \leq x/D \leq L_s \tag{13}$$

where $f_0(M_j)$ and $g_0(M_j)$ are the acoustic power output per unit exit diameter length at the jet exit and at the supersonic core tip L_s, respectively. Both of these quantities are primarily functions of the supersonic jet exit mach number M_j.

The additional requirement that must be observed is that as the jet mach number approaches unity, the equation for the overall sound power output transforms into the Lighthill equation (10). Thus, at a jet exhaust mach number of unity both $f_0(M_j)$ and $g_0(M_j)$ must reduce to the value based upon Lighthill's result

$$f_0(M_j) = g_0(M_j) = w_m D = \frac{10^{-4}}{9.6} m \left(\frac{\rho_j}{\rho_a}\right) \left(\frac{c_j}{c_a}\right)^5 c_j^2 M_j^7 \qquad M_j \leq 1.0 \tag{14}$$

and this quantity will be assumed to be constant over the subsonic mixing region $0 \leq x/D \leq 4$. Conditions of equation (14) will be satisfied if the acoustic power output per unit diameter length at the jet exit is given by

$$f_0(M_j) = \frac{10^{-4}}{9.6} m \left(\frac{\rho_j}{\rho_a}\right) \left(\frac{c_j}{c_a}\right)^5 (c_j^2 M_j^7) M_j^{-\alpha} \qquad M_j > 1.0 \tag{15}$$

and at the end of supersonic region by

$$g_0(M_j) = \frac{10^{-4}}{9.6} m \left(\frac{\rho_j}{\rho_a}\right) \left(\frac{c_j}{c_a}\right)^5 (c_j^2 M_j^7) M_j^{-\beta} \qquad M_j > 1.0 \tag{16}$$

Both of these expressions contain the subsonic acoustic power output in the mixing region given by equation (14), and the exponents α and β in these equations must be determined from experimental observations.

These constants reveal the variation of $f_0(M_j)$ and $g_0(M_j)$ as a function primarily of the jet mach number, although the jet and ambient physical conditions are also included. With this assumed type of variation of the acoustic power output at the exit and the sonic region, the desired conditions of transforming to the subsonic expression, equation **(14),** are satisfied.

By substituting equations **(2), (15),** and **(16)** into equation **(13),** the variation of the acoustic power output per unit diameter in the supersonic region $0 \leqslant x/D \leqslant L_s$ is given by

$$w_d = \frac{10^{-4}}{9.6} m \left(\frac{\rho_j}{\rho_a}\right) \left(\frac{c_j}{c_a}\right)^5 (c_j^2 M_j^{7-\alpha}) \left[1 + \frac{M_j^{\alpha-\beta} - 1}{5M_j^2 + 0.8}\right] x/D \tag{17}$$

and the acoustic power output from the supersonic region, $0 \leqslant x/D \leqslant L_s$ can be obtained by substituting into equation (12*a*). Downstream of the supersonic core tip region, as indicated in figures **1, 3,** and **10,** it was assumed by Nagamatsu and Horvay (ref. **9)** that a fully developed turbulent jet exists in the subsonic region for $x/D > L_s$. The acoustic power per unit length of the jet in the subsonic region was assumed to be proportional to

$$w = x^{-6} \tag{18}$$

with the turbulent correlation radius l assumed constant. The peak acoustic power output per unit diameter length of the jet at the beginning of the subsonic region was assumed to be the value given at the end of the supersonic region (eq. **(16)).** From this value at the end of the supersonic region L_s the power output per unit diameter length was assumed to vary in the subsonic region $L_s \leqslant x/D < \infty$ as indicated in figures **4, 9,** and 10, by

$$w_d = \frac{10^{-4}}{9.6} m \left(\frac{\rho_j}{\rho_a}\right) \left(\frac{c_j}{c_a}\right)^5 (c_j^2 M_j^{7-\beta}) (5M_j^2 + 0.8)^6 (x/D)^{-6} \tag{19}$$

where α and β are exponents that must be evaluated from experimental acoustic data.

By substituting equations **(17)** and **(19)** into equation (12*a*), the acoustic power outputs from the supersonic and subsonic regions for supersonic jets can be evaluated as well as the total overall sound power output by

$$W = \frac{10^{-4}}{9.6} m \left(\frac{\rho_j}{\rho_a}\right) \left(\frac{c_j}{c_a}\right)^5 (c_j^2 M_j^2)(5M_j^2 + 0.8)\left(\frac{M_j^{-\alpha} + M_j^{-\beta}}{2} + \frac{M_j^{-\beta}}{5}\right) \tag{20}$$

Thus, the total acoustic power output from a supersonic jet is a function of the jet mach number, density, and sound velocity for both the jet and the ambient gas. Also, the constants α and β are parameters that must be determined from the experimental acoustic measurements from supersonic jets. Some of the values determined for parallel flow and convergent nozzles will be presented in the latter section of this paper. This equation for the sound-power output from supersonic jets derived by Nagamatsu and Horvay (ref. 9) contains the length of the supersonic region, variation of the acoustic power outputs at the jet exit and at the supersonic core tip, and the decay of fully turbulent subsonic jet. These equations were used to analyze the sound emission from supersonic jets. The analyses by Phillips (ref. 20) and Williams (ref. 21) for supersonic jets do not take into consideration the observed aerodynamic and acoustic characteristics for supersonic jets.

To determine the effects of jet mach number, velocity, and total temperature for air as a working fluid, equation (20) was evaluated in reference 9 by assuming that the compressed and heated air expanded isentropically and with parallel flow to the ambient condition. It was also assumed as a first approximation that the ratio of the specific heats γ was constant and equal to 1.40, and the ambient condition was taken as pressure of 14.7 psia and temperature of 60° F. For the initial evaluation of equation (20) to predict the overall sound power levels from supersonic jets, the values $\alpha = 6.2$ and $\beta = 2.4$ for equations (15) and (16) were determined from the Potter and Jones (ref. 17) results for $M_j = 2.49$ as a first approximation.

With these values the acoustic power distributions were calculated from equation (20) as a function of distance from the jet exit and total temperature for a constant exit mach number and are presented in figures 11(*a*) and 11(*b*). For a jet mach number of unity (fig. 11(*a*)), the acoustic power distribution was constant over the initial 5.8 diameters before decreasing as x^{-6} for the range of total temperature from 520° to 3500° R. It is apparent in this figure that increasing the jet total temperature with the corresponding increase in the jet velocity for sonic mach number has a pronounced effect upon the acoustic radiation per unit length of the jet. But at higher jet mach numbers, the acoustic power distribution increased over an appreciable distance as given by equation (2), before decreasing as x^{-6} (fig. 11(b)) for a jet mach number of 1.5. The acoustic power distribution increases with distance from the jet exit to the peak value at the sonic location. In reference 9 the calculated results for other supersonic jet mach numbers and total temperatures are presented.

In figures 12(*a*) and 12(*b*), the acoustic power distribution for different supersonic jet mach numbers with constant total temperatures of 520°

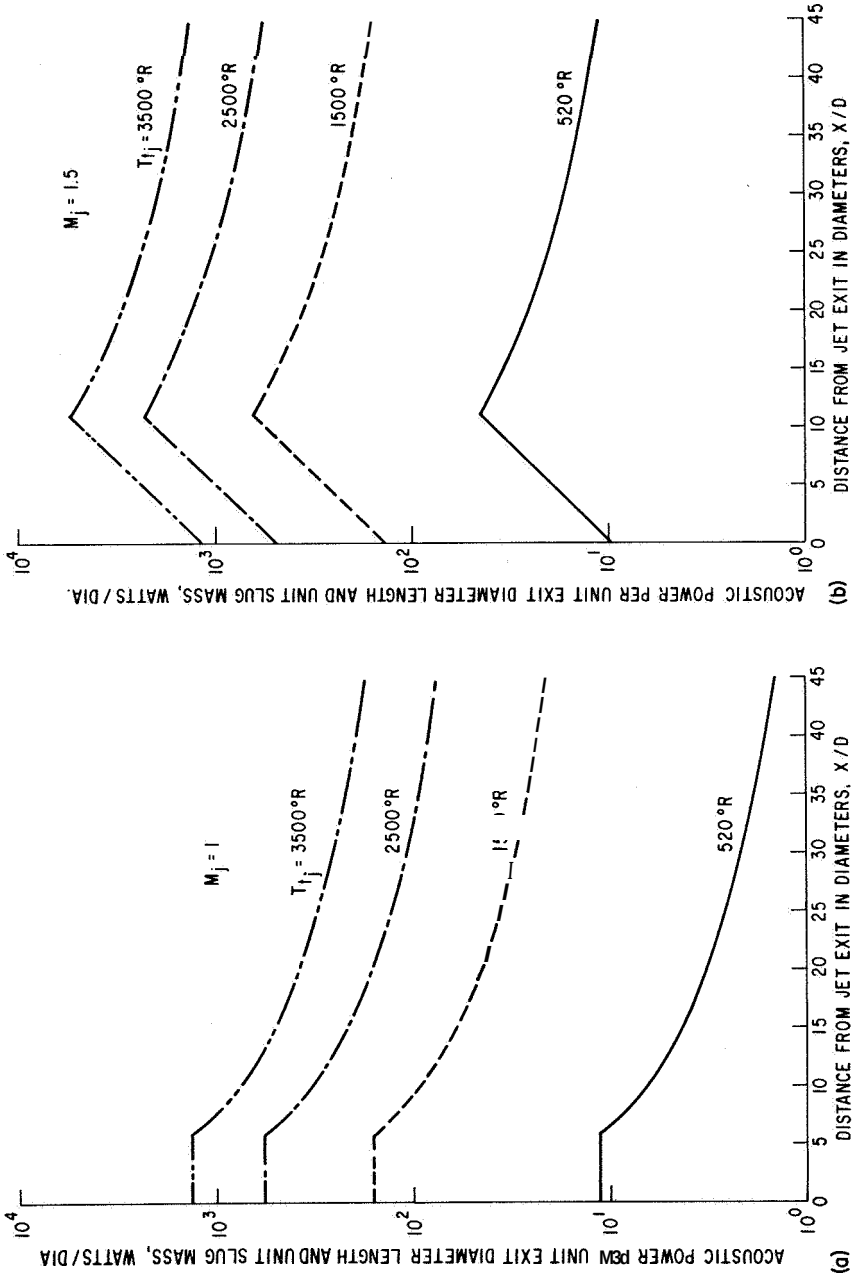

FIGURE 11.—Acoustic power generated per unit length of the jet for jet mach number of (*a*) 1.0 and (*b*) 1.5.

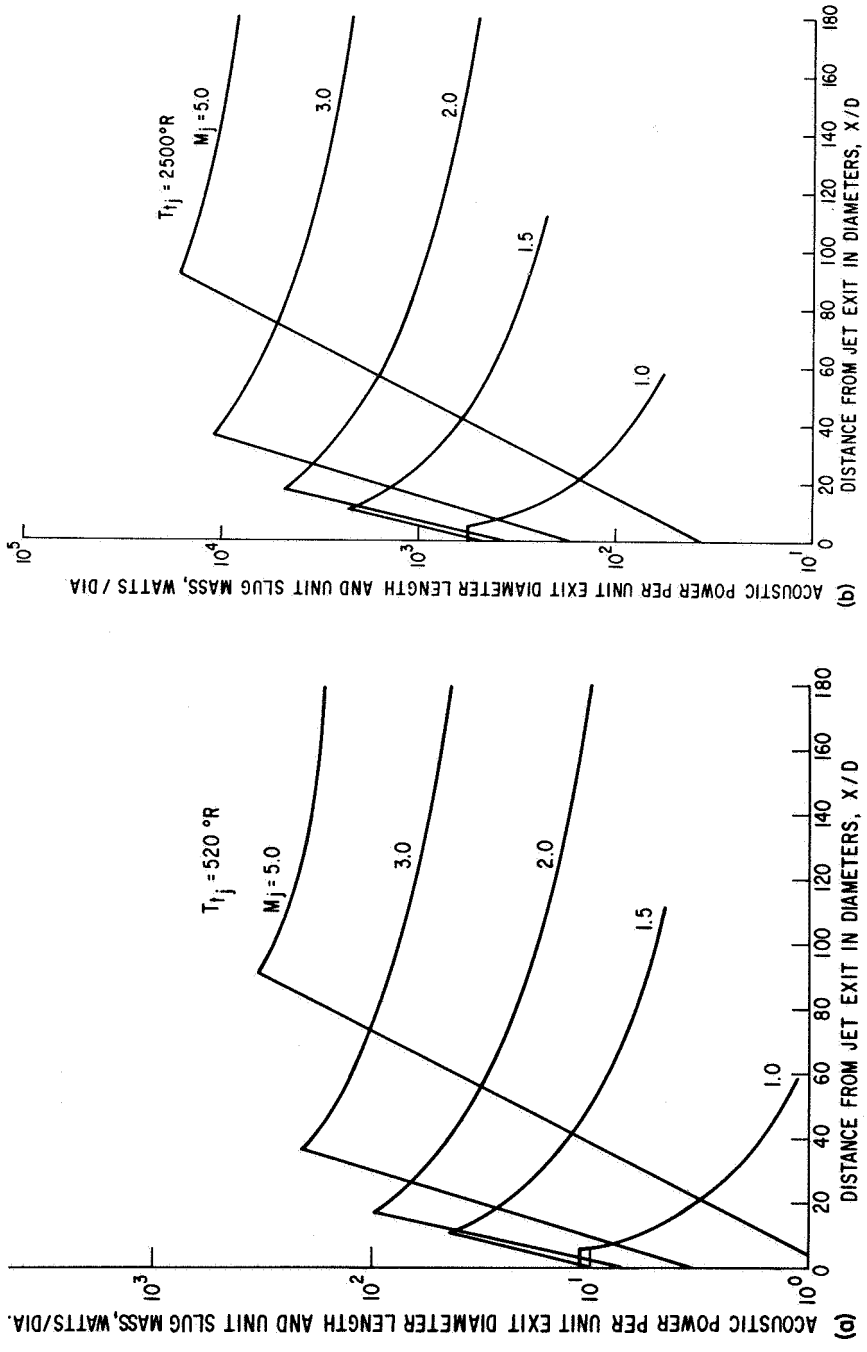

FIGURE 12.—Acoustic power generated per unit length of the jet for jet total temperature of (*a*) 520° R and (*b*) 2500° R.

and 2500° R are presented as a function of the distance from the jet exit. From these figures the effect of jet mach number upon the acoustic power distribution and the location of the peak sound radiation is very large for both total temperatures of 520° and 2500° R. For supersonic jets, the jet mach number is governed by the ratio of the jet total pressure to the ambient pressure at the jet exhaust, while the jet exhaust velocity depends upon the jet pressure ratio and the total temperature. The results for jet mach number 5.0 must be considered as an approximation because the supersonic core length was determined from equation (2), and the shielding effects of the mach waves from the jet periphery were not considered.

In figures 13(*a*) and 13(*b*) the overall sound power levels in dB with respect to 10^{-13} W for a unit slug mass given by equation (20) is plotted as a function of mach number and velocity for different jet total temperatures. When the overall acoustic power output is plotted as a function of mach number (fig. 13(*a*)), the curves are quite similar for the jet total temperature range of 520° to 3500° R. Also, in this figure the value of the overall acoustic power given by Lighthill in equations (8) and (8*a*) are plotted for the total temperature of 1500° R. Both values are higher for supersonic mach numbers than the curve determined from equation (20). When the overall sound power levels are plotted in terms of the exhaust velocity (fig. 13(*b*)), the curves for each total temperature condition are nearly straight lines with the slope decreasing with the total temperature (ref. 30). For these curves the subsonic portions, where equation (20) does not apply, are plotted as dashed lines. For a total temperature of 520° R, the Lighthill equation (8*a*) with density correction overestimates the sound power level in the supersonic region. The highest exhaust velocity of 5900 fps was attained for the case of 3500° R total temperature and mach number 5, which is extremely large for an air-breathing propulsion system.

CORRELATION OF NAGAMATSU AND HORVAY SUPERSONIC JET-NOISE THEORY WITH EXPERIMENTAL DATA

Evaluation of Exponents α and β

The overall sound power levels for a 2-in.-diameter convergent nozzle with unheated air were determined in reference 29 for a parallel-flow mach-1.5 jet with a throat diameter of 2 in.[18] These experimental data for the acoustic power levels were used to evaluate the exponents α and β for the Nagamatsu-Horvay theory (ref. 9) in equations (15) and (16). The theoretical curves for the acoustic powers were calculated for $\alpha = 6.2$

[18] Ibid.

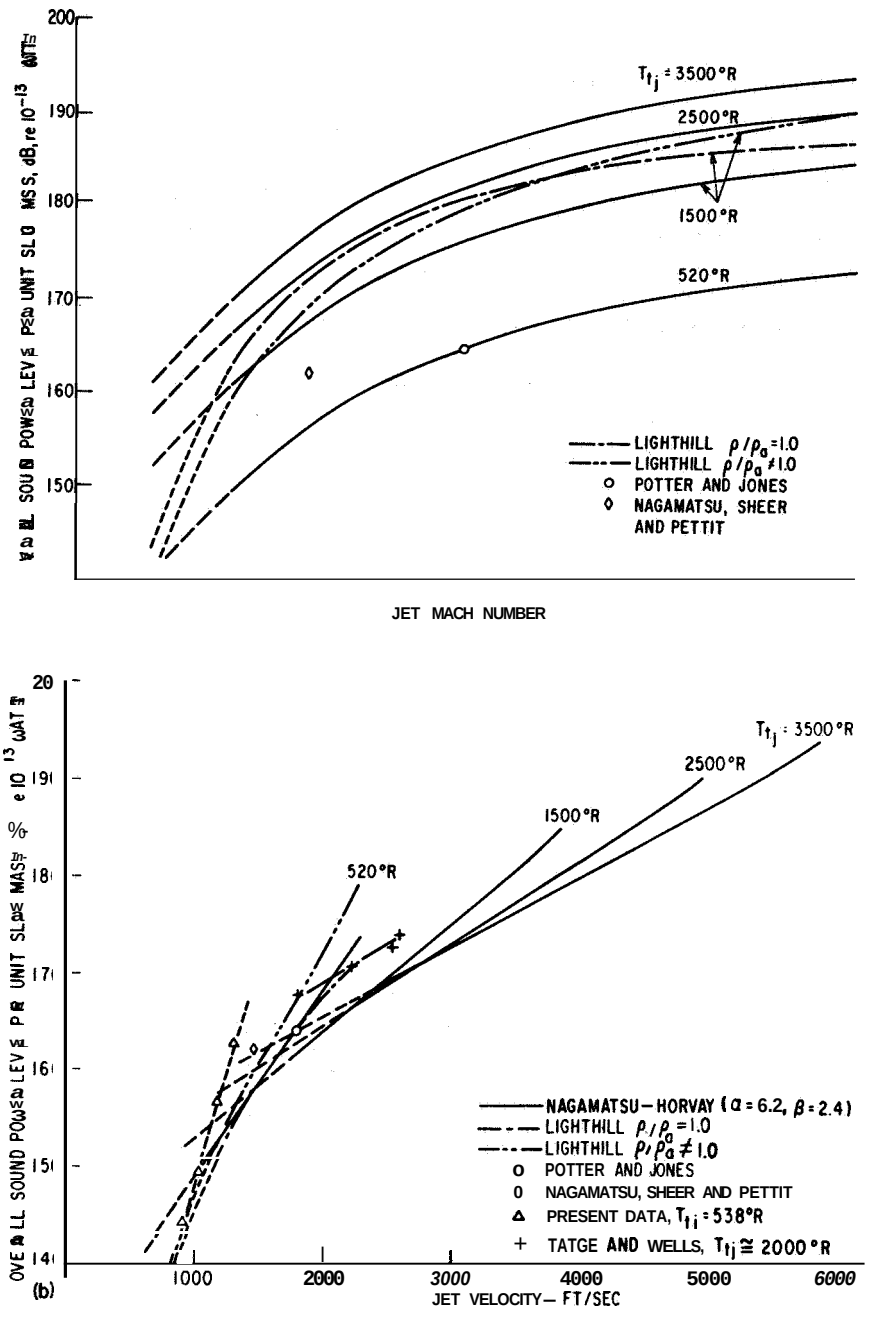

FIGURE 13.—Overall sound-power level in dB per unit slug mass as function of
(*a*) jet mach number and
(*b*) jet velocity.

and $\beta = 2.4$ based upon Potter and Jones data as a first approximation. In figure 13(*b*) the experimental results for the acoustic power levels from a convergent 2-in.-diameter jet with ambient total temperature are compared with the theoretical curves. At the **sonic** jet mach number, the calculated value agreed well with the experimental observation, but for supersonic mach numbers the calculated values were less than the experimental data. From the acoustic measurement at a mach number of 1.4 the values of α and β were determined to be 0.356 and -1.17, respectively, and are presented in figure 14. Similarly the values of α and β were found to be 0.229 and -0.962 for a jet mach number of 1.2.

In figure 14 the values of the exponents α and β for the Nagamatsu and Horvay supersonic jet noise theory are presented as a function of the

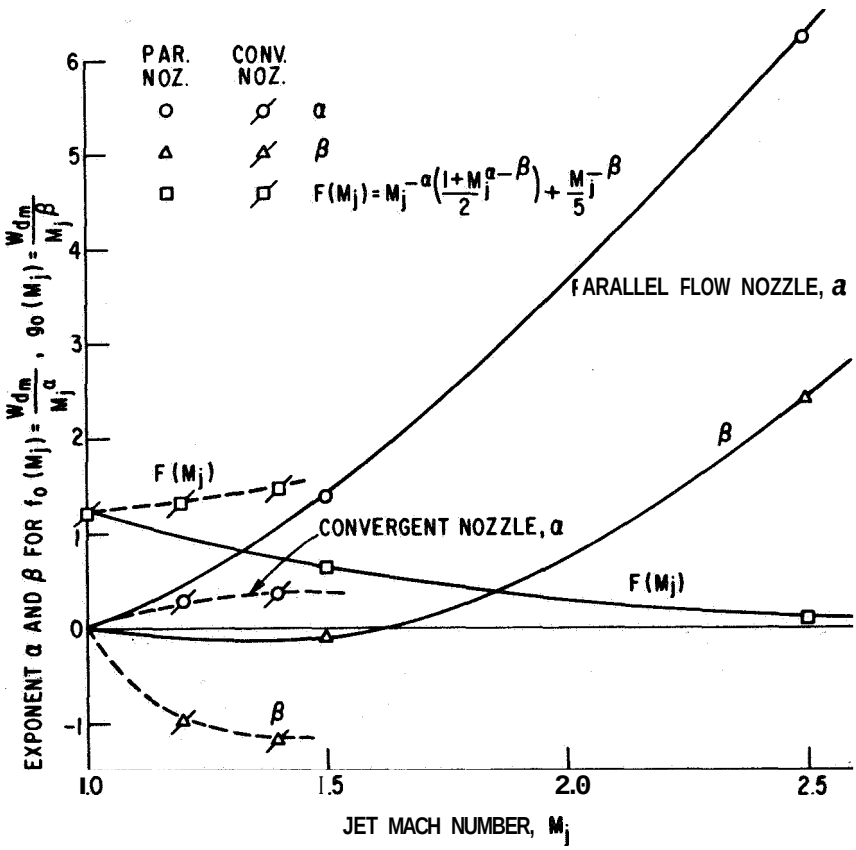

FIGURE 14.—Values of exponents α and β of Nagamatsu-Horvay supersonic jet-noise theory as function of jet mach number for parallel-flow and convergent nozzle with $T_{tj} = 520°$ R.

jet mach number for convergent and parallel-flow nozzles. The function given by

$$F(M_j)=\frac{M_j^{-\alpha}+M_j^{-\beta}}{2}+\frac{M_j^{-\beta}}{5} \tag{21}$$

from equation (20) also is presented in this figure. A contoured nozzle (ref. 29) with a throat diameter of 2 in. and exit mach number of 1.5 was used to determine the values of α and β. The values for a parallel nozzle with exit mach number of **2.49** were determined from reference 17. Because the supersonic flow from a convergent nozzle contains shock bottles (refs. 25 and **27**),[19] while there is no such shock system for parallel-flow nozzles, the values of the exponents α and β should depend upon the type of nozzle as indicated in figure **14.** Also, the value of $F(M_j)$ is greater for the convergent nozzle than the parallel-flow nozzle because of the existence of shock bottles with additional noise sources as discussed by Dosanjh (ref. **25).** Additional experiments will be conducted to define the variation of α, β, and $F(M_j)$ with mach number for different types of nozzles and at various temperatures.

Overall Sound Power Levels

Because the results from the models in the firing ranges at high velocities indicate that the weak waves from the turbulent boundary layers are drastically attenuated by the bow shock wave, it was assumed in reference **9** that the sound waves for hypersonic jet exhaust velocities will be attenuated by the shock wave produced by the hypersonic eddies. These stronger waves will be propagated close to the mach angle relative to the jet axis given by

$$\cos e=\frac{1}{M_c} \tag{22}$$

where $M_c=v_c/c_a$ is the eddy convective velocity mach number relative to the ambient velocity of sound. To account for the shock waves that will be produced by the eddies from hypersonic jets, the acoustic power output per unit diameter length at both the nozzle exit and at the end of the supersonic region was modified by Nagamatsu and Horvay (ref. **9)** to include the jet mach number relative to the ambient velocity of sound. With this assumption, the acoustic power output at the jet exit as given by equation (15) becomes

$$f_0(M_j)=\frac{10^{-4}}{9.6}\,m\,\frac{\rho_j}{\rho_a}\left(\frac{c_j}{c_a}\right)^5 c_j^2 M_j^7\,\frac{M_j^{-\alpha}}{M_j^{\sigma}} \tag{23}$$

[19] Ibid.

NASA SP-207

BASIC AERODYNAMIC NOISE RESEARCH

A conference held at

NASA HEADQUARTERS

Washington, D. C.

July 14–15, 1969

NATIONAL AERONAUTICS AND SPACE ADMINISTRATION

and at the end of the supersonic region as given by equation **(16)** becomes

$$g_0(M_j) = \frac{10^{-4}}{9.6} m \frac{\rho_j}{\rho_a} \left(\frac{c_j}{c_a}\right)^5 c_j^2 M_j^{\alpha} \frac{M_j^{-\beta}}{M_{j_a}^{\sigma}} \tag{24}$$

where M_{j_a} is the ratio of the jet velocity to the ambient velocity of sound, and σ is a constant that must be determined from experiments, such as for nuclear reactors and hydrogen rockets. In reference **9** the values of σ for the hydrogen-oxygen rocket data of Smith and Brown (ref. 31) and for the nuclear reactor rocket data of Manhart and colleagues (ref. **32)** were evaluated and used to calculate the overall sound power levels as functions of jet mach number and jet velocity (figs. **15(*a*)** and **15(*b*)).**

The experimental overall sound power levels per unit slug mass were obtained over a velocity range of 900 to **19 500** fps and corresponding jet mach-number range of 0.85 to **3.7** and are presented in figures **15(*a*)** and **15(*b*).** In these figures the values of $\alpha = 6.2$ and $\beta = 2.4$ were used in equation **(20)** together with values of $\sigma = 2.1$ for the hydrogen-oxygen rocket and $\sigma = 2.5$ **for** the nuclear rocket with hydrogen in equations **(23)** and **(24).** When the overall sound power levels are plotted as a function of jet mach number (fig. **15(*a*)),** the curves for the air at total temperatures of **520**" and **2500**" **R** are quite similar to those calculated for hydrogen-oxygen and nuclear rockets even though the jet velocity is different by an order of magnitude for these different working gases. Potter and Jones (ref. **17)** nitrogen data at a jet mach number of **2.49** falls on the calculated curve because the values of the exponents α and β in equation **(20)** were determined from their results. The acoustic result for a parallel flow nozzle (ref. **29)** with an exit mach number of 1.5 and ambient total temperature lies above the analytical curve and the values of a and β given in figure **14** for this mach number must be used in equation **(20)** to obtain agreement.

The acoustic data for a convergent nozzle operated over a jet mach number of 0.60 to **1.4,** obtained by Nagamatsu, Sheer, and **Gill,**[20] are presented as a function of the jet velocity in figure **15(*b*).** The total temperature of the jet was at room temperature, and the previous results (ref. **29)** for a parallel-flow nozzle with a mach number of **1.5** were obtained under the same jet conditions as indicated in this figure. The slope of the experimental data for the convergent nozzle is steeper than that calculated from equation **(20)** with $\alpha = 6.2$ and $\beta = 2.4$. **Also,** the results of Tatge and Wells (ref. **30)** for air heated to approximately **2000**" R and jet mach number range of 0.87 to **1.%** are presented in figure **15(*b*).** The experimental data fall above the theoretical curve calculated with $\alpha = 6.2$ and $\beta = 2.4$ in equation **(20),** but the slope **is** reasonably close to the

[20] **Ibid.**

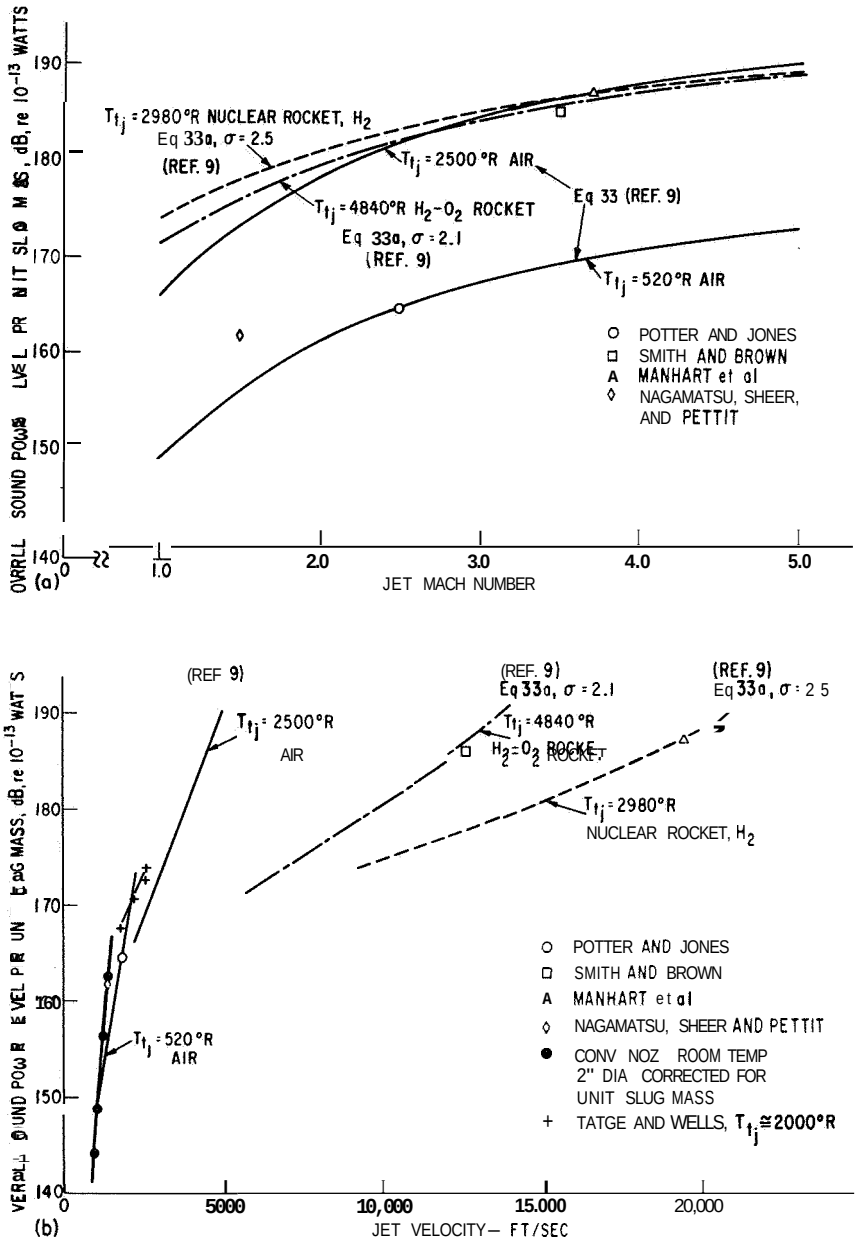

FIGURE 15.—Overall sound power level in dB per unit slug mass for different gases and temperatures as function of
(a) jet mach number and
(6) jet velocity.

calculated curve. Acoustic data for a hydrogen-oxygen rocket (ref. 31) at an exhaust velocity of 12 600 fps, and for a nuclear reactor rocket (ref. 32) with hydrogen at an exit velocity of 19 500 fps are also presented in this figure. These calculated curves must be considered as an approximation for the prediction of the overall sound power levels at these extremely high velocities until additional experimental acoustic data are obtained to evaluate the exponent σ in equations (23) and (24).

CONCLUSIONS

From the available experimental data for the jet exit diameter range of 1 to 30 in. and total temperature range of 520° to 3200° R, the supersonic core lengths, distance over which the jet exit velocity still exists on the axis, and the supersonic lengths, where the axial mach number is sonic, were determined as functions of the jet mach number. It was observed that the total temperature of the jet was of secondary importance compared to the mach number even though the velocity of the high-temperature jet was much higher than the cold jet for a given mach number. The constants in the equations for the supersonic core and sonic lengths were evaluated from the experimental data.

The variations of the acoustic power output per unit length of the supersonic jets were evaluated from the acoustic measurements for small jets over a mach number range of 1.0 to 2.5. These measurements indicated that the largest source of noise occurred just ahead of the transition region from the supersonic to subsonic velocities on the axis. At the jet exit the acoustic radiation per unit length was much less than that at the end of the supersonic region. After the jet velocity became subsonic, the acoustic radiation decayed as x^{-6}, similar to that observed for the fully developed subsonic jet.

Using the empirical relationship of the supersonic length as a function of mach number, the linear variation of the acoustic power radiation per unit length in the supersonic region, the acoustic power output per unit length at the jet exit and at the sonic point, and the subsonic turbulent decay for the acoustic power, an equation for the overall acoustic power output for supersonic jets containing several unspecified constants was developed by Nagamatsu and Horvay. As a first approximation these constants were determined from the experimental results for the mach-2.49 jet. For hypersonic jet exhaust mach numbers relative to the ambient velocity of sound, the overall acoustic power output equation was modified by including the hypersonic mach number for the shielding effects of mach waves.

The acoustic power outputs per unit diameter length were calculated by the use of the Nagamatsu-Horvay supersonic jet noise theory for jet mach numbers of 1 to 5 and total temperature range of 520° to 3500° R

with air as the working gas. Similar calculations were made for hydrogen-oxygen and nuclear hydrogen rocket jets with total temperatures of 4840° and 2980° R, respectively.

Overall sound power levels for supersonic jets with room temperature and approximately 2000° R total temperatures were correlated with the supersonic jet noise theory of Nagamatsu and Horvay. For a given jet mach number but for different total temperatures, the experimental overall sound power level variation with jet velocity decreased in the slope as predicted by the theory. The decrease in the jet density with increasing jet temperature has a large effect upon the sound generation from supersonic jets.

Based upon the experimental acoustic data for convergent and parallel-flow nozzles at supersonic mach numbers, the exponents α and β in the Nagamatsu-Horvay theory were evaluated as functions of mach number. The overall sound power level at a given supersonic mach number for the convergent nozzle was greater than that observed for a parallel flow nozzle because of the presence of shock bottles.

The overall sound power levels for air jets, hydrogen-oxygen, and nuclear hydrogen rockets with a mach number range of 0.85 to 3.7 with corresponding velocity range of 900 to 19 700 fps were correlated with the supersonic jet-noise theory. When the acoustic power levels were plotted as a function of jet mach number, the overall power level curves for the mach-number range of 1 to 4 were quite similar for the above different gases in the supersonic jets. But when presented in terms of the jet velocity, there was a large decrease in the acoustic power with velocity because of the decrease in the jet density and the shielding effects of mach waves at hypersonic jet mach numbers relative to the ambient velocity of sound.

Additional aerodynamic and acoustic measurements for supersonic jets should be obtained to increase the knowledge regarding the noise generation from high-velocity jets. Also, the exponents α and β in the supersonic jet noise theory of Nagamatsu and Horvay should be determined for various jet temperatures, velocities, and gases.

REFERENCES

1. LIGHTHILL, M. J.: Sound Generated Aerodynamically. Proc. Roy. Soc., ser. A, vol. 267, 1962, pp. 147–182.
2. LIGHTHILL, M. J.: Jet Noise. AIAA J., vol. 1, no. 7, 1963, pp. 1507–1517.
3. GERRARD, J. H.: An Investigation of the Noise Produced by Subsonic Air Jet. J. Aeron. Sci., vol. 23, 1956, pp. 855–866.
4. LASSITER, L. W.; AND HUBBARD, H. H.: Experimental Studies of Noise From Subsonic Jets in Still Air. NACA TN 2757, 1952.

5. LASSITER, L. W.; AND HUBBARD, H. H.: The Near Field Noise of Static Jets and Some Model Studies of Devices for Noise Reduction. NACA Rept. 1261, 1954.

6. MOLLO-CHRISTENSEN, E.; AND NARASIMHA, R.: Sound Emission From Jets at High Subsonic Velocity. J. Fluid Mech., vol. 8, 1960, pp. 49–60.

7. MOLLO-CHRISTENSEN, E.: Jet Noise and Shear Flow Instability Seen From an Experimenter's Viewpoint. Trans. ASME, Paper no. 67, APM-C, 1966.

8. ELDRED, K. M.: Correlation and Prediction of Turbojet and Rocket Noise. Rept. no. TR–56–652, AD 110667, USAF Wright Air Development Center, 1956.

9. NAGAMATSU, H. T.; AND HORVAY, G.: Supersonic Jet Noise. Rept. 69–C–161, GE Research and Development Center, 1969.

10. LAURENCE, J. C.: Intensity, Scale and Spectra of Turbulence Mixing Region of Free Subsonic Jet. NACA Rept. 1292, 1956.

11. DAVIES, P. O. A. L.; FISHER, M. J.; AND BARRATT, M. J.: The Characteristics of the Turbulence in the Mixing Region of a Round Jet. J. Fluid Mech., vol. 15, 1963, pp. 337–367.

12. CHU, W. T.: Turbulence Measurements Relevant to Jet Noise. UTIAS Rept. 119, Inst. of Aerospace Sci., 1966.

13. DAVIES, P. O. A. L.; KO, N. W. M.; AND BOSE, B.: The Local Pressure Field of Turbulent Jets. Aeronaut. Research Council, CP no. 989, 1967.

14. JONES, I. S. F.: Fluctuating Turbulent Stresses in the Noise-Producing Region of a Jet. J. Fluid Mech., vol. 36, pt. 3, 1969, pp. 529–543.

15. POWELL, A.: The Noise of Choked Jets. J. Acoust. Soc. Am., vol. 25, 1953, pp. 385–389.

16. MAYES, W. H.; LANFORD, W. E.; AND HUBBARD, H. H.: Near Field and Far Field Noise Surveys of Solid Fuel Rocket Engines for a Range of Nozzle Exit Pressures. NASA TN D–21, 1959.

17. POTTER, R. C.; AND JONES, J. H.: An Experiment to Locate the Acoustic Sources in a High Speed Jet Exhaust Stream. Wyle Laboratories Rept., 1967.

18. RIBNER, H. S.: New Theory of Jet Noise Generation, Directionality and Spectra. J. Acoust. Soc. Am., vol. 31, 1959, pp. 245–246.

19. RIBNER, H. S.: The Generation of Sound by Turbulent Jets. Vol. 8 of Advances in Applied Mechanics. Academic Press, Inc., 1964.

20. PHILLIPS, O. M.: On the Generation of Sound by Supersonic Turbulent Shear Layers. J. Fluid Mech., vol. 9, pt. 1, 1960, pp. 1–28.

21. WILLIAMS, J. E. F.: The Noise From Turbulence Convected at High Speed. Phil. Trans. Roy. Soc. London, ser. A, vol. 255, 1963, pp. 479–503.

22. LAUFER, J.: Aerodynamic Noise in Supersonic Wind Tunnels. J. Aerospace Sci., vol. 28, 1961, pp. 685–693.

23. OLLERHEAD, J. B.: On the Prediction of the Near Field Noise of Supersonic Jets. NASA CR–857, 1967.

24. PLUMBLEE, H. E., JR.: The Effect of Exhaust Temperature on the Noise Generation. Lockheed-Georgia Co. Rept., 1967.

25. DOSANJH, D. S.; AND MONTEGANI, F. J.: Reduction of Noise From Underexpanded Axisymmetric Jet Flows Using Radial Jet Flow Impingement. AIAA Paper no. 68–81, 1968.

26. WARREN, W. R.: An Analytical and Experimental Study of Compressible Free Jets. Ph. D. dissertation, Princeton Univ., 1957.

27. LOVE, E. S.; GRIGSBY, C. E.; LEE, L. P.; AND WOODLING, M.: Experimental and Theoretical Studies of Axisymmetric Free Jets. NASA TR–6, 1959.

28. EGGERS, J. M.: Velocity Profiles and Eddy Viscosity Distribution Downstream of a Mach 2.2 Nozzle Exhausting in Quiescent Air. NASA TN D–3601, 1966.

29. NAGAMATSU, H. T.; PETTIT, W. T.; AND SHEER, R. E., JR.: Some Flow and Acoustic Characteristics of a Shrouded Supersonic Jet. Rept. 69-C-156, GE Research and Development Center, 1969.

30. TATGE, K. B.; AND WELLS, R. J.: Model Jet Noise Study at Alplaus Facility. Rept. 61GL25, GE Engineering Laboratory, 1961.

31. SMITH, E. B.; AND BROWN, W. L.: Acoustic Scale-Model Tests of High-speed Flows. Rept. CR-66-75, Martin Marietta Corp., 1966.

32. MANHART, J. K.; ET AL.: An Acoustic Study of KIWI-B Nuclear Rocket. NASA CR-370, 1966.

EDDY-MACH WAVE NOISE FROM A SIMPLIFIED MODEL OF A SUPERSONIC MIXING LAYER*

H. S. Ribner
University of Toronto
Canada

A simplified flow model is presented for simulating features of noise generation by supersonic jets and rockets. Eddy mach waves appear as a consequence of balancing internal and external pressures, and noise power may be estimated.

Specifically, the turbulent mixing layer of a supersonic jet is modeled as a layer of two-dimensional square eddies; this separates the main flow U_j from fluid at rest and moves at an intermediate speed. (In an improved model the square eddies are replaced by a turbulent flow layer constrained by plain interfaces.) Because of unopposed internal pressures, the interfaces that were initially plane will ripple slightly so that mach waves arise and effect a pressure balance. The mach-wave noise pattern, as well as the acoustic energy flux, is readily calculated.

In an example simulating a round rocket jet the effective mixing layer area is taken to be 6π (diameters)*, the rms eddy velocity is $0.1U_j$, and U_j = six times external sound speed. The efficiency (noise power/flow power) comes out to be about 1/3 percent, which is of the order of measured values for rocket noise.

SYMBOLS

c	sound speed
D	jet diameter
f	frequency of eddy mach waves
I	acoustic energy flux per unit area normal to mixing layer
k	wave number (2π/wavelength)
L	edge length of square cells (eddies)
M	mach number based on external sound speed (U/c_o)
n	effective length of mixing region (diameters)
p	perturbation pressure ($p_{abs} - p_o$)
U	local mean flow speed
u, v	components of local perturbation velocity
x, y	coordinate frame (x alined with flow)
w	rms (spatial average) velocity in square eddies

*This research was sponsored by the Air Force Office of Scientific Research, Office of Aerospace Research, U.S. Air Force, under AFOSR grant no. 67-0672A.

β $\sqrt{M_m^2-1}$
θ angle with horizontal of normal to mach waves
ψ stream function
ρ density
η efficiency (noise power/flow power)

Subscripts

abs absolute
j main jet flow
m mixinglayer
o ambient (outside jet)

INTRODUCTION

The present paper studies a simplified flow model simulating features of eddy-mach-wave generation in the noise from supersonic jets and rockets. Shadowgraphs show these mach waves emanating from the turbulent mixing layer that separates the core of the jet from the ambient fluid. This mixing layer is not of constant width, but continually spreads in the downstream direction. It can be described loosely in terms of irregular unsteady eddies that defy precise description.

In this model the irregularity and the spreading are suppressed in a deliberate oversimplification. The mixing layer is postulated as an array of square flow cells (models of eddies) convected at the supersonic mean flow speed of the layer. It is thought that some broad features of the physical processes responsible for noise generation are retained and displayed very simply.

THE MODEL

The square eddy model of the mixing layer is shown in figure 1. The eddy flow is given by

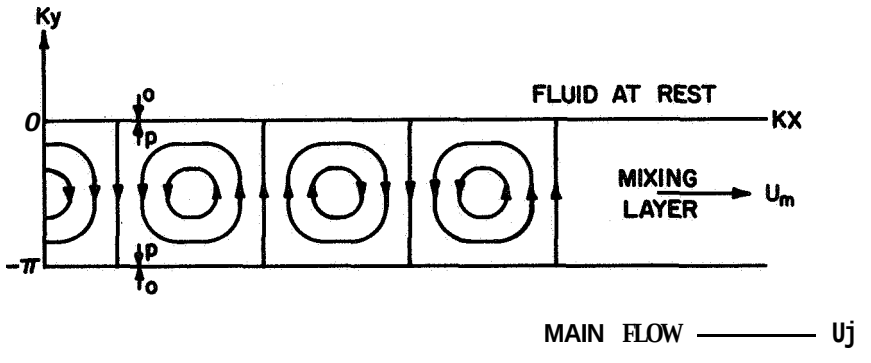

FIGURE 1.—Model simulating features of rocket noise generation. Turbulent mixing layer is simulated by an array of square eddies. Notice unbalanced pressures across plane interfaces.

$$u=\frac{w}{\sqrt{2}}\cos kx\cos ky$$
$$v=\frac{w}{\sqrt{2}}\sin kx\sin ky \tag{1}$$

with stream function

$$\$=\frac{w}{k\sqrt{2}}\cos kx\sin ky \tag{2}$$

Here w is the rms velocity in the cell and the wave number k is related to the layer thickness L by $kL=\pi$. (The layer may be generalized to n cells thickness if desired using $kL=nn$; the physical arguments will be unaltered.) It is assumed that w is small enough that the eddy flow, and not the main flow, may be considered incompressible for simplicity. The pressure field in this layer would be, if constrained between rigid plane boundaries $ky=0, -\pi$ so that equation (1) holds accurately

$$p_{\text{abs}}=\frac{\rho_m w^2}{2}(\cos 2ky-\cos 2kx)+\text{constant} \tag{3}$$

by integration of Euler's equations. The average value of this pressure field along the boundaries $ky=0, -\pi$ is taken to match the ambient pressure p_o. The perturbation pressure $p_{\text{abs}}-p_o$ is then

$$p=-\frac{\rho_m w^2}{2}\cos 2kx \tag{4}$$

along the boundaries of the model mixing layer.

The boundaries, however, are not rigid and are not capable of supporting the pressure difference p of equation (4). On removing the artificial constraint of rigidity, the boundaries will deform into ripples that, because of their downstream motion, will generate mach waves (fig. 2). An equilibrium can be specified in which the mach-wave pressure field will balance the eddy pressure field value of equation (4).

It will be justified a posteriori that the distortion is so small that the errors introduced into equations (1) to (4) are negligible. Then the pressure enforced in the wave field is merely the value of equation (4) at the interface $y=0$, and for $y\geqslant 0$ it is

$$p=-\frac{\rho_m w^2}{2}\cos 2k(x+\beta y) \qquad \beta=\sqrt{M_m^2-1} \tag{5}$$

which corresponds to mach waves inclined as dictated by the mach number $M_m=U_m/c$ (ref. 1).

Equations (1) to (5) apply in a frame of reference moving in the positive

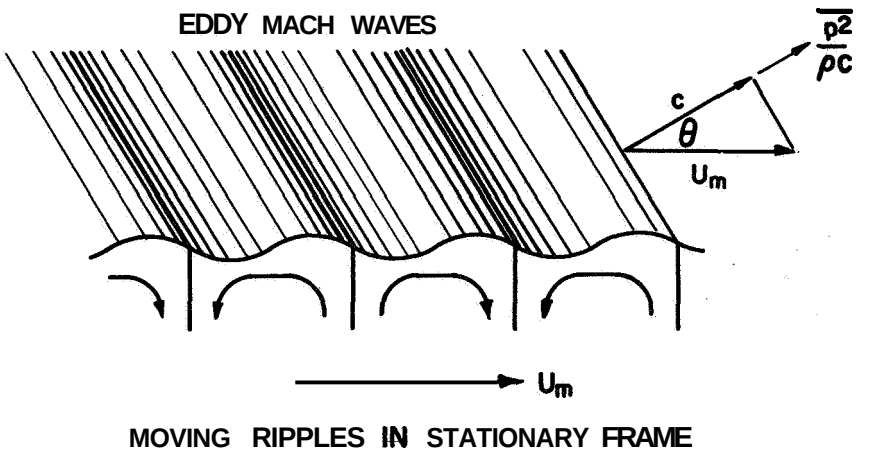

FIGURE 2.—Model simulating features of rocket noise generation. Traveling ripples develop in interfaces and generate eddy mach waves (noise); wave amplitude is such as to achieve a pressure balance across interfaces.

x-direction with the ripple speed U_m. In a stationary frame, equation (5) becomes

$$p=-\frac{\rho_m w^2}{2}\cos 2kx(x-U_m t+\beta y) \tag{6}$$

which exhibits the mach waves as moving sound waves. The waves move past a fixed point with speed U_m, giving rise-to frequency

$$f=kU_m/\pi=U_m/L$$

The sound pressure given by equation (5) or (6) in this mach-wave field by our physical argument matches the eddy pressure field at the boundary of the mixing layer; we may call the latter the near field of the simulated turbulent jet. The mach waves thus extend the near-field pressures to the radiation field.

RIPPLE AMPLITUDE

We now explore whether the ripple amplitude is small compared with the eddy edge length L, as has been assumed. The boundary conditions are

(*a*) The pressure must be equal on opposite sides of the rippled interface. This condition is met by equations (5) and (6).

(b) The streamline slopes must be equal on opposite sides in the ripple-attached reference frame.

Condition (b) will be automatically enforced when we choose the ripple

amplitude compatible with the mach-wave pattern (5); it is given by (ref. 1)

$$\frac{dy}{dx}=-\left[\frac{p\beta}{\rho_o U_m^2}\right]_{y=0} \tag{7}$$

$$=\frac{1}{2}\frac{\rho_m}{\rho_o}\left(\frac{w}{U_m}\right)^2 \beta \cos 2kx$$

$$y=\frac{1}{4k}\frac{\rho_m}{\rho_o}\left(\frac{w}{U_m}\right)^2 \beta \sin 2kx \tag{8}$$

Since $kL=\pi$, the ripple amplitude is

$$y_{\max}=\frac{\beta}{4\pi}\frac{\rho_m}{\rho_o}\left(\frac{w}{U_m}\right)^2 L \tag{9}$$

in terms of the rms turbulence level w/U_m. As a severe test case, let $w/U_m=\frac{1}{3}$ (an upper limit), $M_m=3$ (or $\beta=2\sqrt{2}$), $\rho_m/\rho_0=1$. Then

$$y_{\max}=0.025\ L \tag{10}$$

This confirms that the ripple amplitude is very much less than the eddy length L. The distortion of the initial square shape may thereby be neglected insofar as its effect on the internal pressure and velocity fields is concerned. This neglect is not wholly defensible at the higher turbulence velocities at which the assumption of incompressible internal flow becomes poor.

ACOUSTIC ENERGY FLOW

The flux of acoustic energy through unit area is $\overline{p^2}/\rho_o c_o$ in a direction normal to the mach waves. The vertical component in figure 2 is

$$I=\frac{\overline{p^2}}{\rho_o c_o}\sin \theta$$

The mean-square pressure is $\rho_m^2 w^4/8$ from equation (6), and $\sin\theta=\sqrt{M_m^2-1}/M_m=\beta/M_m$, giving

$$I=\frac{\rho_m^2 w^4}{8\rho_o}\frac{\sqrt{M_m^2-1}}{U_m} \tag{11}$$

as the flux of acoustic energy through the unit area normal to the mixing layer.

371-986 0-LT-70—5

NOISE FROM ROUND JET

We will curve the plane mixing layer, equations (1) to (3), into a cylinder to simulate the mixing layer of a round jet (fig. 3). Because our model is at best a crude one, we shall assume that the energy flux per unit area, equation (11), is still approximately valid.

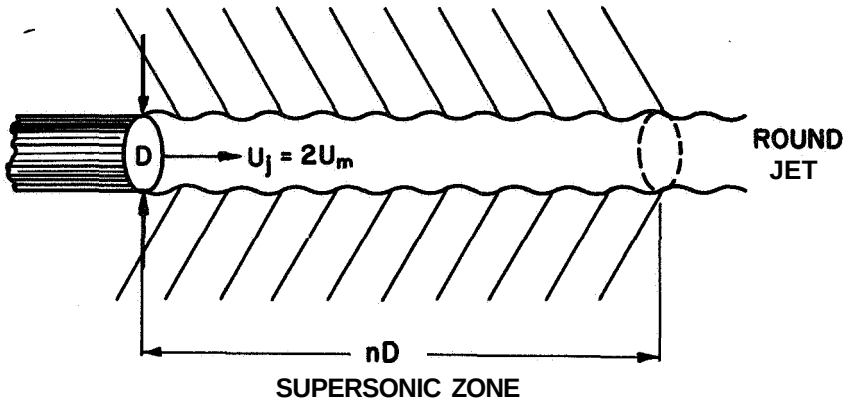

FIGURE 3.—Model simulating features of rocket noise generation. Geometry for estimating ratio (noise power-jet flow power) for simplified rocket jet.

The effective length of the supersonic mixing layer will be taken as n diameters, giving a total surface area $nD \cdot \pi D$. The acoustic power radiated from this area will then be

$$\text{noise power} = \pi n D^2 I \tag{12}$$

By comparison the mechanical power expended in the kinetic energy of the jet flow will be

$$\text{flow power} = \frac{\pi D^2}{8} \rho_j U_j^3 \tag{13}$$

The ratio (noise power/flow power) is the acoustical efficiency

$$\eta = 2n \frac{\rho_m^2}{\rho_o \rho_j} \left(\frac{w}{U_j}\right)^4 \sqrt{(U_j/2c_o)^2 - 1} \tag{14}$$

where the mean speed U_m of the mixing layer has been taken to be $(\frac{1}{2})U_j$.

EXAMPLE AND DISCUSSION

In an example intended to simulate crudely a rocket jet, it will be convenient to approximate ρ_m as a geometric mean density. The example

specifications are

$$n=6 \qquad U_j=6c_o \qquad w=0.1U_j \qquad \rho_m^2/\rho_o\rho_j=1$$

Insertion into equation (14) yields the acoustical efficiency as

$$\eta=0.0034 \qquad \text{or 0.34 percent} \tag{15}$$

It is rather striking that this is of the order of magnitude of measured efficiencies of rocket jet-noise generation.

Other proposed mechanisms for the noise generation, for example, the Lighthill quadrupole model with supersonic convection factor, do predict comparable efficiencies[1] (refs. 2 and 3). Thus the present model cannot be affirmed as necessarily simulating a dominant mechanism of noise generation by supersonic jets. The physical arguments with support of the example results suggest it may be an, important mechanism.

The equations employed herein, as applied to the specified flow model, are as accurate as the Lighthill equations for flow noise in their general form, and are more accurate than the usual solution with the constant density approximation. The approximation is in the flow model, not in the mathematics.

IMPROVED FLOW MODEL

It is possible to improve the model to better simulate features of a turbulent mixing layer while still retaining the basic simplicity. In the improved model we replace the square eddies by random turbulence, retaining the plane interfaces. To show that this is possible, consider that a semi-infinite uniform flow with superposed turbulence and its mirror image will be separated by a plane stream surface. In the model we remove the image flow and replace it by fluid at rest. As in the square eddy model, unopposed pressures on the plane interface will cause it to ripple and develop mach waves to effect a pressure balance.

The pressure field, in either the simulated layer or the mach-wave field, is no longer sinusoidal but random. If we make a Fourier analysis, the square-eddy solution behaves like a single sinusoidal Fourier component of this more general pattern. The mach-wave pressure field will now have a broadband spectrum in place of the former single line or pure tone. However, the results for mean-square pressure and noise-generating efficiency will be unaltered, assuming postulated turbulence is a frozen convected pattern.

---

[1] J. E. Ffowcs Williams: Some Open Questions on the Jet Noise Problem. Dept. of Mathematics, Imperial College, London, 1967. Unpublished paper.

The improved model still differs from a real turbulent mixing layer in retaining quasi-planar interfaces. Nevertheless it would seem that a mechanism rather like the one proposed in this paper is operative in the real flow and generates eddy mach waves. The role of these waves is to match the near-field pressures and extend them to the radiation field. The virtue of the model is the conceptual simplicity of the generation process and the ease with which predictive formulas can be extracted.

COMPARISON WITH OTHER MODELS

The Lighthill model as extended by Ffowcs Williams[2] or by Ribner (ref. 3) deals with a supersonic mixing layer in terms of the source-motion Doppler effect. This is embodied in a convection factor that multiplies the intensity that would occur for unconvected eddy sound sources. The emission has the character of mach waves, with peak intensity normal to the mach cones of the moving eddies.

The eddy-sound sources are identified as perturbations of the Reynolds stresses or rate of momentum flow. These generate a near field (pseudo-sound) and a far field. The convection factor dictates the eddy-mach-wave character of the far field, but it does not apply to the near field because the moving eddies emit into locally comoving fluid.

Thus the extended Lighthill theory predicts both the near field and the far field in terms of perturbations of rate of momentum flow in the eddies, together with eddy convection effects. An integral formalism is used, and it is as accurate as the turbulence description fed into it.

Another important model is that of Phillips (refs. 3 and 4). His eddy-sound sources, equivalent to Lighthill's in their total emission, are identified as products of pairs of velocity gradients. (These can be related to the deformation of fluid elements.) The method of solution applied to a supersonic shear layer leads directly to eddy mach waves as the far field; the near field is not obtained, although in principle it could be.

In the dilatation theory (refs. 3 and 5) the eddy-sound sources are identified as the volume fluctuations of fluid elements in response to the near-field pressure. This leads to an integral relating the far-field pressure to (essentially) the near-field pressure. In this respect it resembles the present model, although sharing the rigor of the Lighthill formalism. But in the present model, the connection is much more direct—a matching, in fact.

The present model, like the others, predicts both near-field and far-field sound from the turbulence flow field properties. But the turbulence is highly idealized, and the continuous shear in the mixing layer is

[2] Ibid.

idealized into two planar slip surfaces. The greater simplicity appears in both the physics and mathematics of the mach wave generation process.

REFERENCES

1. LIEPMANN, H. W.; AND ROSHKO, A.: Elements of Gasdynamics. John Wiley & Sons, Inc., 1957, p. 426.
2. LIGHTHILL, M. J.: Wright Brothers Lecture. Jet Noise. AIAA J., vol. 1, no. 7, July 1963, pp. 1507–1517.
3. RIBNER, H. S.: The Generation of Sound by Turbulent Jets. Vol. 8 of Advances in Applied Mechanics. Academic Press, Inc., 1964, pp. 103–182.
4. PHILLIPS, O. M.: On the Generation of Sound by Supersonic Turbulent Shear Layers. J. Fluid Mech., vol. 9, 1960, pp. 1–28.
5. RIBNER, H. S.: Aerodynamic Sound From Fluid Dilatations. A Theory of the Sound From Jets and Other Flows. UTIA Rept. 86, Inst. Aerospace Studies, Univ. of Toronto, 1962.

NOISE REDUCTION FROM INTERACTING COAXIAL SUPERSONIC JET FLOWS*

Darshan S. Dosanjh, Amr N. Abdelhamid, and James C. Yu
Syracuse University
Syracuse, N.Y.

Far-field and near-field noise from interacting coaxial high-speed jet flows has been investigated experimentally in a fully anechoic chamber to assess the use of interacting coaxial jets as a potential abatement technique for supersonic jet noise. **A** number of arrangements of the inner and outer coaxial nozzles were used. With the outer convergent annular nozzle operated at somewhat higher pressure ratio than the inner convergent-divergent nozzle, the radiated overall acoustic power level from the combined interacting jet flows was found to be lower than that from the outer annular jet alone by 10 dB, and the maximum reduction in peak sound pressure level was recorded to be 11 dB (re 2×10^{-4} μbar). The corresponding near-field sound pressure surveys of the individual jets and their comparison with those of the combined interacting jet flows revealed the effects of the interaction between the outer and the inner jet flows to be a downstream shift, spatial extension, and weakening of strong noise sources normally located near the jet exit; redistribution of the emitted acoustic power per unit length of the interacted jets; and elimination of discrete, intense acoustic components. The pitot pressure surveys and shadowgraphic data of the interacting coaxial jet flows recorded at the operating conditions at which maximum noise reduction was achieved indicated replacement of the repetitive shock structure in the outer annular jet flow, effectively, by a single oblique shock; appearance of normal shock front located just downstream of the inner nozzle exit; and modifications of the mean mach-number distributions and velocity profiles. Possible dependence of the observed noise reduction on these flow changes is discussed; and the acoustic power contributions from flow regions with shock structure, supersonic and subsonic turbulent mixing regions, and fully developed turbulent flow regions are deduced.

*This research was supported by **NASA** grant no. **NGR** 33–022–082.

INTRODUCTION

The advent of the jet-propelled aircraft brought in its wake an associated jet-noise problem, which has been the subject of serious scientific and engineering research for the past two decades. Substantial progress has already been made in understanding and limiting the noise radiated by subsonic jet flows. However, more recent developments such as the supersonic aircraft, which requires more powerful turbojet engines for propulsion, and the space-age booster rocket engines have escalated the nature and magnitude of the jet-noise problem, thus pointing toward an even greater need for continued research and development in this field. To develop any acceptable and successful practical noise-abatement technique, one must first locate and understand the nature of all the contributing noise sources in subsonic and/or supersonic jet flows; then guided by this knowledge and understanding, one must devise techniques to make these noise-generating sources less effective. This approach necessitates a systematic study of the far-field noise, the near-field noise, the noise sources and their mechanisms in the shear flow regions, mixing and turbulent nature of the jet flows, shock structure, shock-turbulence interaction, and general fluid mechanical behavior of the subsonic and supersonic jet flows.

The mechanisms responsible for subsonic jet-noise generation are now understood reasonably well. This understanding has been greatly promoted by Lighthill's (refs. 1 and 2) theory of noise generated from turbulent jet flows and its subsequent improvements (refs. 3 and 4) and variations (ref. 5). On the basis of these and related studies (ref. 6), it is well established that the major noise sources in subsonic jets are located in the turbulent mixing region, which in subsonic flows usually extends from nozzle exit to 4 or 5 diameters downstream. In this region the acoustic intensity is predicted to be proportional to the eighth power of the mean jet-exit velocity, and the acoustic power generated per unit length of the jet flow is constant. The major factors contributing to noise generation from subsonic turbulent flows are the intensity and the scale of turbulence. In devising practical and successful techniques to reduce noise from subsonic jet flows, it is advantageous, therefore, to reduce the jet-exit mean velocity, to reduce mean shear by enhancing flow entrainment by the jet flows, and to shorten the extent of the mixing region by accelerating the mixing process. Practical noise-abatement techniques for subsonic jet exhausts for which some of these practices have been successfully used are the mixing nozzles, such as the multitubed and corrugated nozzles, and the high bypass ratio turbofan engines. In the multitubed exhaust system the shielding of the acoustic sources in the flow from inner exhaust tubes by the flow from outer ring of exhaust tubes also plays an important role in yielding reduced noise levels.

However, the current knowledge of the noise-generating mechanisms in supersonic jet flows is inadequate. This is especially true for underexpanded or overexpanded jet flows, in which the presence of standing shock systems is a significant complicating factor. Various investigators have made contributions to the study of various aspects of possible noise-generating mechanisms in high-speed flows, such as the eddy mach-wave radiation (refs. 4 and 7), interaction of shock waves with basic flow disturbances (refs. 8 to 12), shock oscillation (ref. 13), and flow resonance phenomena (ref. 14). Extensive experimental research on noise from high-speed jet flows and engine exhausts has also been carried out by many investigators at a number of research establishments (refs. 14 to 26). Examples of supersonic jet-noise-abatement techniques investigated so far are modifications of nozzle exit geometry (ref. 15), ejector shroud (ref. 27), and extended plug and center-core flow nozzles (refs. 28 and 29).

Based on the results of some of these investigations, it is evident that besides the usual acoustic sources present in subsonic flows, additional acoustic sources come into play in supersonic jet flows. Some of these acoustic sources are the mach-wave radiation (refs. 4 and 7) associated with turbulence eddies convected supersonically relative to the ambient fluid, shock-turbulence interaction (refs. 8 and 9), shock oscillations (refs. 13 and 23), and flow resonance (ref. 14).

Furthermore, from a practical standpoint, if a potential noise abatement technique is to be attractive, it should not result in an unacceptable thrust loss. Therefore, in addition to retaining the flow characteristics that have been shown to lead to noise reduction in subsonic jet flows, any successful abatement technique for supersonic jet noise should modify, weaken, or eliminate some or all of these additional noise sources present in supersonic flows without resulting in any serious thrust loss. One obvious method of modifying the prominent noise sources in a free supersonic jet exhaust is to interact it just downstream of the nozzle exit with a secondary free supersonic jet flow. Since both of the jet flows are supersonic, their mutual interaction will not influence and disturb the upstream flow at the nozzle exits. If this interaction between a primary and a secondary jet leads to the elimination or weakening of some or all of the important acoustic sources in supersonic jet flows enumerated above, noise reduction should result. Dosanjh and Montegani (refs. 24 and 25) and Dosanjh and Yu (ref. 26) first studied acoustic and flow characteristics of underexpanded sonic and supersonic jet flows radially impinged upon by a lower energy jet. The observed noise reduction, though modest at the operating conditions used, did prove the feasibility of the flow impingement and interaction as a potential technique for noise abatement from supersonic jet exhaust flows. It became

apparent, however, that the use of the radial flow for impingement represents a loss of useful power. Therefore, impingement and/or interaction downstream of the jet exits between two coaxial free jet flows, which are both thrust producing, suggested itself. These interacting coaxial jet flows may be fully expanded, underexpanded, or overexpanded.

If any such arrangement of the impinging and/or interacting supersonic free jet flows is to be successful as an effective and practical approach to noise abatement, it should meet some or all of the following criteria:

(1) The net thrust from the interacting jets should in the limit equal the sum of the thrusts produced by the individual jets. This can be best realized only if both jets are thrust producing and if flow interactions between free supersonic flows take place downstream of the nozzle exits.

(2) The extent of the individual supersonic flow regions should be reduced in the combined interacting jet flows. This may be achieved by two possible methods: *(a)* The repetitive shock structure in the free supersonic jet flows can be considerably modified, or (b) strong shocks can be induced as a result of the mutual impingement and/or interaction of two or more jets. These methods expedite the change of the free jet flows from supersonic to low subsonic speeds.

(3) The effective mean shear near the exit of each jet flow should be reduced by interaction.

(4) The effectiveness of the mixing region as a noise source should be diminished. Commonly, this is achieved by an acceleration of mixing, thus shortening the extent of the mixing region.

(5) The shielding of the noise sources in the inner flow should be enhanced by interaction of coaxial jet flows.

To achieve some or all of these desirable flow changes and the expected noise reduction without any serious thrust loss, noise investigations with coaxial nozzle arrangements were recently undertaken. The acoustical data and the corresponding flow characteristics of the individual jets were compared with those from the combined interacting high-speed jets. Useful information on the location, nature, modification, and relative importance of the basic acoustic sources responsible for generation of noise from high-speed jet flows has been obtained.

EXPERIMENTAL FACILITY

Coaxial Nozzle Arrangements

The nozzle arrangements used in these investigations are shown in figures 1(*a*), 1(*b*), and 1(*c*). These consist of (1) an inner convergent-divergent 12" conical nozzle of throat diameter $D_t = 0.375$ in. and exit diameter $D_e = 0.482$ in.; (2) an outer annular convergent nozzle of inner

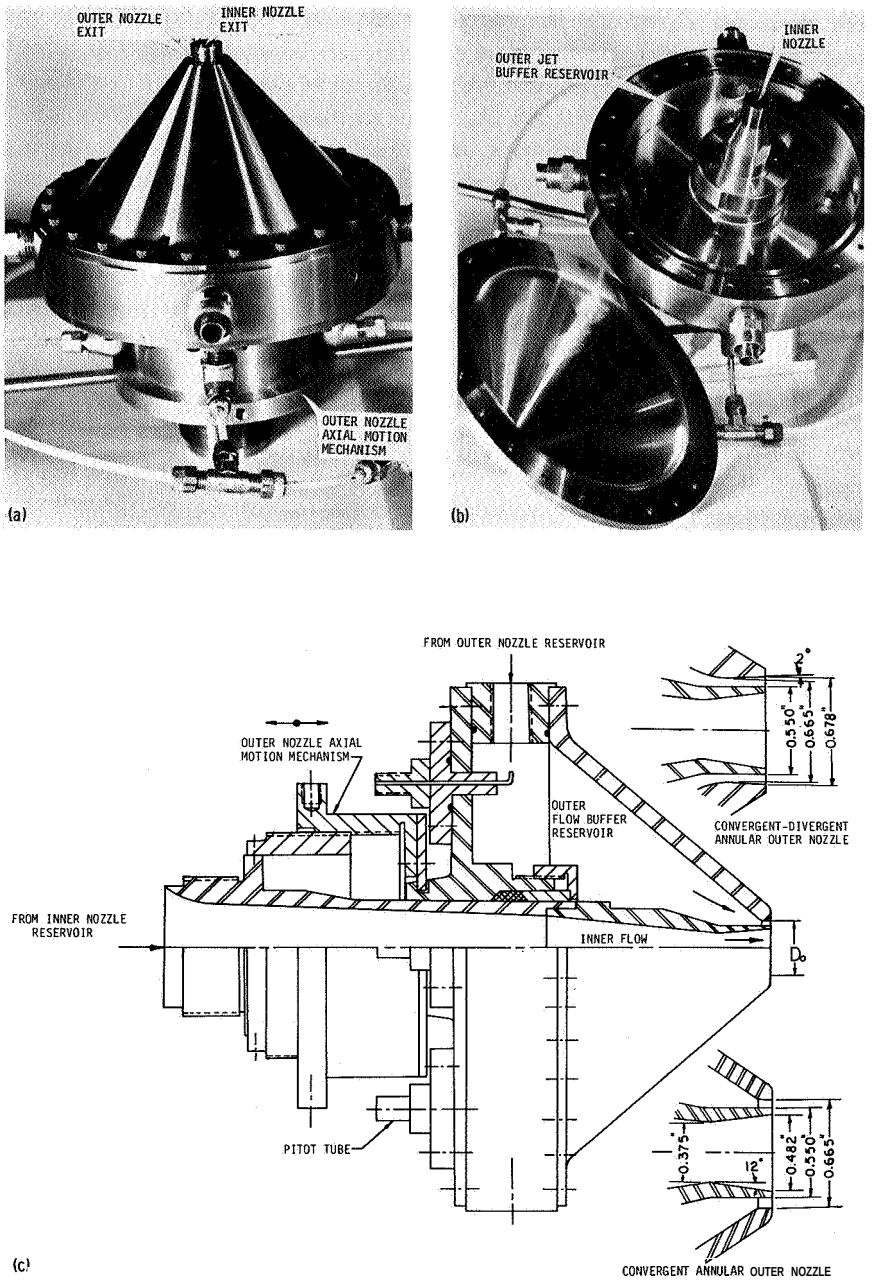

FIGURE 1.—Nozzle assembly:
(*a*) external view,
(*b*) internal view, and
(*c*) details of nozzle arrangement.

exit diameter $D_i = 0.550$ in. and outer diameter $D_o = 0.665$ in.; (3) or keeping the inner nozzle the same as in (1), use instead an outer annular convergent-divergent 2" conical nozzle with inner exit diameter $D_i = 0.550$ in., throat diameter $D_t = 0.665$ in., and exit diameter $D_e = 0.678$ in.

With these nozzle geometries, the throat area of all three nozzles is the same. The outer nozzle can slide in the axial direction on the inner nozzle, and therefore the distance between inner and outer jet nozzle exits is easily controllable. In this study, however, the inner and outer nozzles were adjusted so that their exits were in the same plane (fig. 1(*c*)). The two jet flows are supplied through two separate settling chambers so that stagnation pressures for each jet flow are independently adjustable. The stagnation temperatures of both jets were measured and found to be about equal to ambient temperature. For the mode of operation of the nozzle arrangements discussed here,[1] the outer nozzle was operated at comparatively higher pressure ratios, while flow through inner nozzle was used as a secondary jet flow and was operated at comparatively lower pressure ratios. Both the inner and outer jet flows were directed in the same direction, and both are thrust producing.

Optical Investigations

Spark shadowgraphs of three jet flows over a range of operating conditions were recorded: (1) inner jet flow alone, (2) outer jet flow alone, and (3) interacting inner and outer jet flows. Detailed description of the optical system employed has been reported in references *24* and *25*.

Total and Static Pressure Survey

Total pressure surveys were conducted both in the subsonic and supersonic regions of coaxial jet flows. These total pressure data were used to determine the mach-number distribution as well as the velocity profiles at various cross sections of the coaxial jet flows. The physical dimensions of the pitot tube used were outside diameter (o.d.) = 0.02 in. and inside diameter (i.d.) = 0.01 in. Movement of the pitot tube was controlled by a traversing assembly that consisted of a capacitor-driven motor, a potentiometer, and a digital voltmeter.

To calculate flow mach numbers and velocity profiles, one of the assumptions made was that the static pressure in the shock-free flow downstream of the observed shock structure in the combined jet flows is equal to the ambient pressure. The validity of this assumption was verified by a static-pressure probe traverse. The static-pressure probe

[1] These nozzle arrangements were also operated with the inner nozzle at a higher pressure ratio than the outer nozzle. The noise reduction in this mode of operation was modest (2½ dB). The details of this phase of the experimental measurements are not presented here.

had an o.d. = 0.03 in. with four static pressure holes located four probe diameters downstream from the blunt tip and 90° apart around its circumference.

Acoustical Instrumentation

Far-field overall sound-pressure levels and spectrum measurements of the radiated noise as well as near-field sound-pressure surveys of interacting jet flows were conducted in a fully anechoic chamber. Detailed descriptions of the chamber and the acoustical instrumentation used are available in references 24 and 25. The 1/8-in. condenser microphone model 4138 by B&K was adapted to replace the B&K 1/4-in. condenser microphone model 4135 used in the previous investigations (refs. 24 and 25). The specifications of the 1/8-in. microphone are a frequency range of 30 Hz to 140 kHz and a dynamic range of 76 to 184 dB.

Near-field Traversing Mechanism

The microphone traversing mechanism used for near-field sound pressure survey is shown in figure 2. Essentially it consists of two traversing components that can be displaced in two mutually perpendicular directions: one along the axial direction of the jet flows; the other

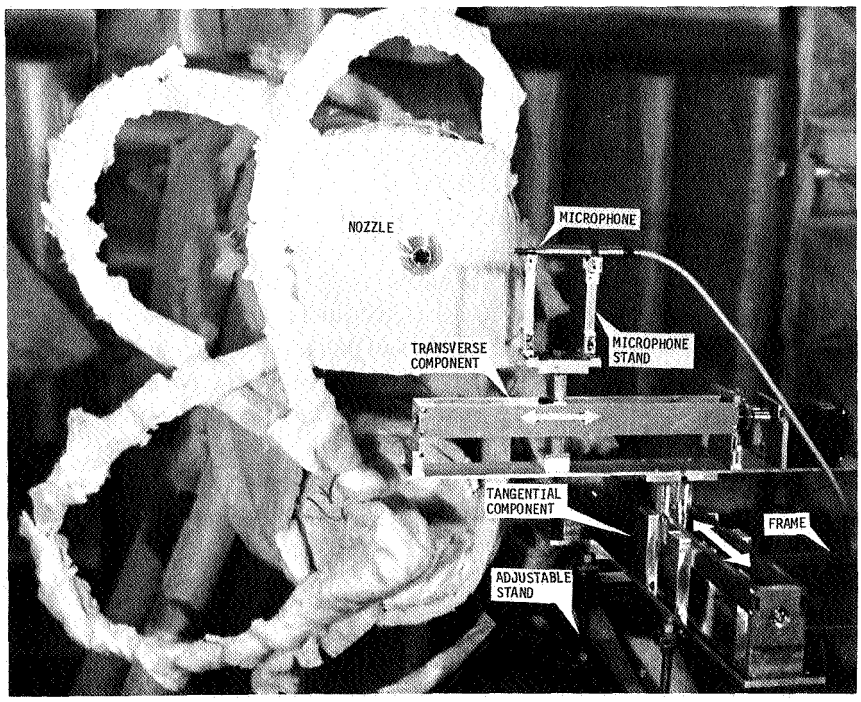

FIGURE 2. — Arrangement of the near-field traversing mechanism in the anechoic chamber.

in the transverse direction. Capacitor-driven instantly reversible single-phase instrument motors are used as drivers. An electrical contact assembly and an electromagnetic counter registers the precise location within **0.005** in. of the center of microphone diaphragm. The entire traversing mechanism is mounted on a portable hollow-steel frame. During noise measurement, the frame as well as the traversing mechanism are well covered by sound-absorbing fiber glass.

EXPERIMENTAL, RESULTS AND DISCUSSION

Far-field Noise Investigation

Outer Annular Convergent Nozzle

For comparison with the interacting coaxial jet flows, the overall acoustic power level and directivity characteristics of jet flows issuing from two single nozzles operated at ratios of reservoir pressures to ambient pressures ranging from **3.04** to **7.80** were determined. The single nozzles were a convergent' nozzle of exit diameter **0.375** in. having the same throat area as the inner and outer nozzles and the outer annular convergent nozzle without the inner secondary flow.

The overall acoustic power levels of jet flows issuing from these nozzles, curves A and B in figure **3,** are practically the same. Typical directionalities of convergent and outer annular convergent nozzles individually operated at pressure ratio $=3.04$ are shown as curves A and B in figure **4.**

For outer annular convergent nozzle operating pressure ratios ξ_O of **3.04, 3.72, 4.40, 5.08, 5.76,** and **7.80,**[2] the overall acoustic power level and directionality of the interacting coaxial jet flows were determined at various inner jet operating pressure ratios ξ_I.[3] Significantly, at each of the operating outer jet pressure ratios, as the operating pressure ratio of the inner jet is increased, the overall acoustic power level of the sound emitted from the coaxial combined jet flows decreased to a minimum and then increased. This typical variation of the overall acoustic power level for $\xi_O=3.04$ is shown in figure **5.** For operating pressure ratios of **2.43** for the inner jet, the overall acoustic power level of the combined coaxial jet flows was reduced by 10 dB below the power level of the outer jet flow alone operated at pressure ratio $\xi_O=$ **3.04.** At these operating conditions, comparison between the directionality characteristics of the sound emitted from the combined coaxial jet flows and the sound from the outer jet flow alone is shown as curves B and *C* in

---

[2] ξ_O, the ratio of outer jet reservoir pressure P_{TO} and ambient pressure P_a.

[3] ξ_I, the ratio of inner jet reservoir pressure P_{TI} and ambient pressure P_a. $\xi_I=1$ means inner jet flow is not operated.

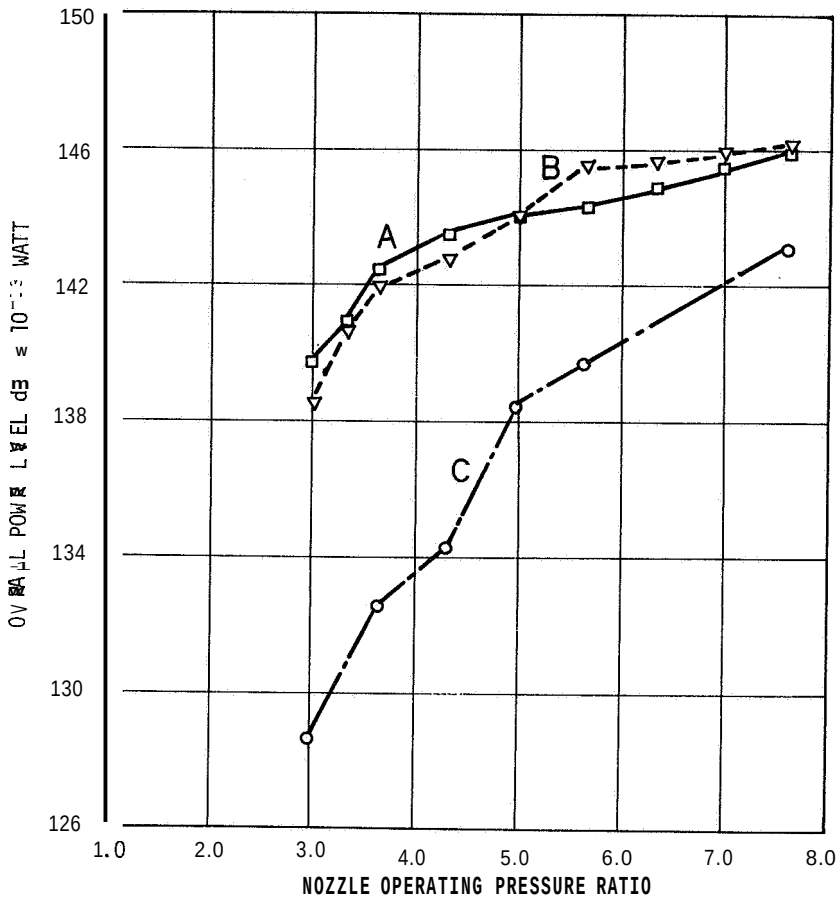

FIGURE 3.—Overall power level versus nozzle operating pressure ratio: *A*. convergent nozzle; *B*. outer annular nozzle: convergent; C. combined coaxial jet flows at operating conditions corresponding to minimum noise (outer annular nozzle: convergent).

figure **4.** The difference between the maximum measured sound-pressure level for the outer jet flow alone and that of the interacted coaxial jet flow is 11 dB. Thus, in addition to having an overall power decrease, there occurs also an attenuation of the noise radiation in the direction of the peak. This is desirable because one of the more important aspects of the emission from an acoustic source, as far as abatement of noise is concerned, is the acoustic intensity at the observer rather than the integrated power radiated over all directions.

The overall acoustic power level of the outer annular convergent jet flow alone and the minimum overall power levels achieved with the interacting coaxial combined jet flows are compared in figure **3,** for outer jet pressure ratios ξ_O ranging from 3.04 to 7.80. The inner jet pressure

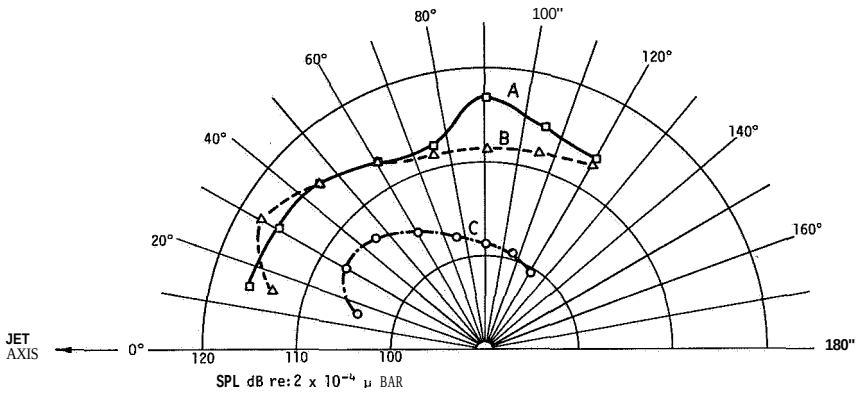

FIGURE 4. — Overall sound pressure directionality: *A*. convergent nozzle, operating pressure ratio= 3.04; *B*. outer annular convergent nozzle alone, ξ_O=3.04; C. combined coaxial jet flows ξ_O = 3.04, ξ_I = 2.43 (outer annular nozzle: convergent).

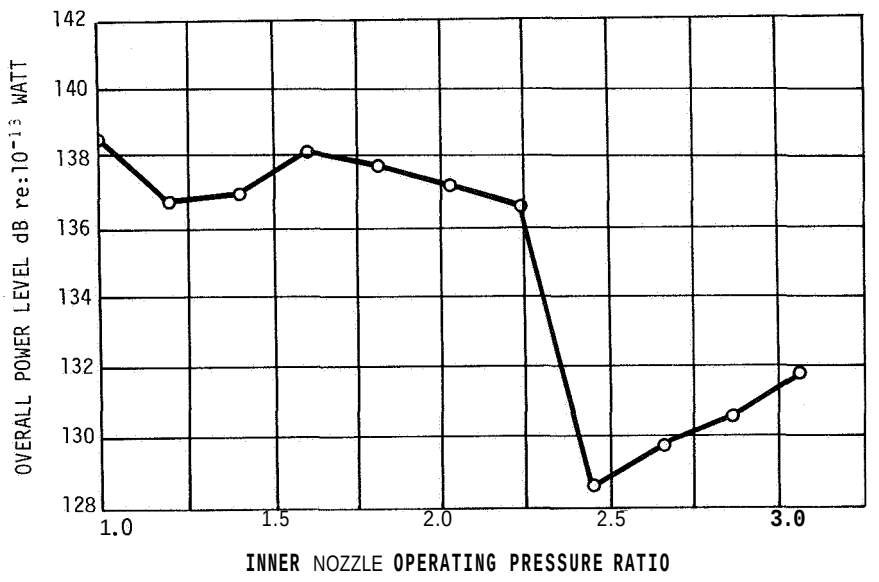

FIGURE 5. — Typical variation of overall acoustic power level with inner nozzle operating pressure ratio, outer annular nozzle: convergent, ξ_O = 3.04.

ratios ξ_I required to achieve these minimum acoustic power levels at different outer jet operating pressure ratios ξ_O are shown in figure 6. It is evident that significant noise reductions, of the order of 6 dB and higher, are achieved for outer jet pressure ratios ξ_O up to 5.08. Furthermore, it is worth noting that at all inner jet operating pressure ratios indicated in figure 3, the total noise radiated by the combined jets is lower than that from the outer jet alone and the required inner jet

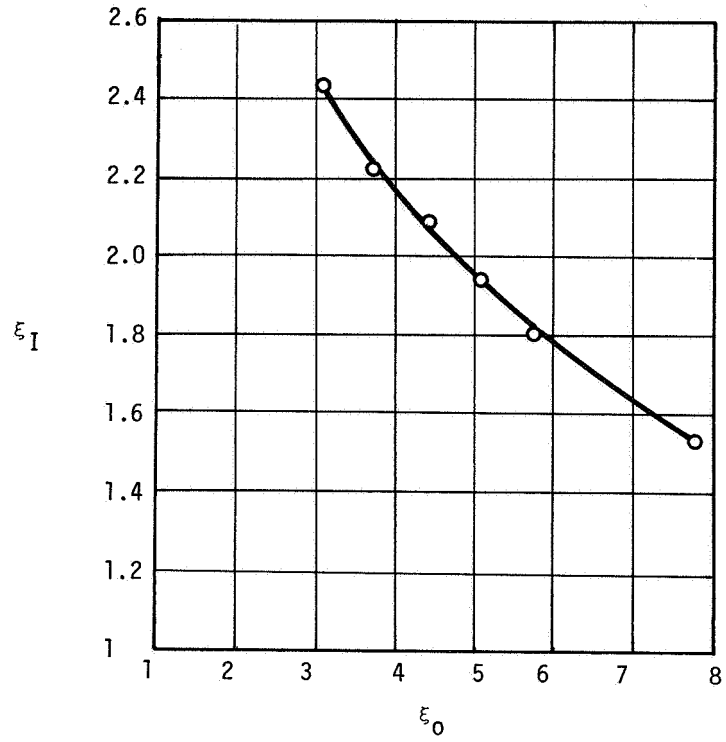

FIGURE 6.—Variation of inner nozzle pressure ratio ξ_I with outer nozzle pressure ratio ξ_O for minimum noise operation.

pressure ratios to achieve the minimum acoustical power levels decreases as the outer jet reservoir pressure is increased. The basic fluid mechanical reasons behind these observations are discussed in the sections on optical observations and mach-number distributions and velocity profiles of coaxial jet flows.

Spectral analyses of the noise radiated from the outer jet alone and from the coaxial interacting combined jet flows at operating conditions corresponding to the minimum overall acoustic power level were undertaken at 1/3 octave bandwidth (fig. 7).

The 1/3 octave power spectra of the noise generated by the outer annular jet flow alone at a pressure ratio $\xi_O = 3.04$ ($\xi_I = 1$) exhibits two discrete peaks at 40[4] and 80 kHz. These discrete spectral peaks are eliminated at operating conditions ($\xi_O = 3.04$ and $\xi_I = 2.43$) corresponding to the minimum emitted noise from the interacting jet flows. More

[4] From shadowgraphs (fig. 10), the average wavelength of the discrete acoustic wave packets was measured to be 0.35 in. (frequency ≃ 38 kHz).

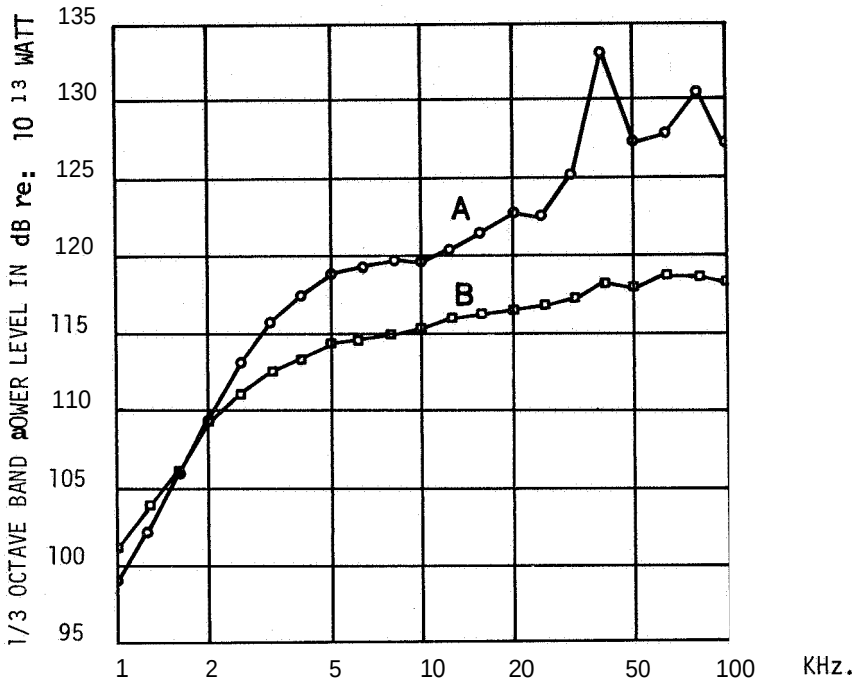

FIGURE 7.—⅓-octave band power spectra: *A*. outer annular nozzle: convergent, $\xi_O = 3.04$; *B*. combined coaxial jet flows (minimum noise operation), $\xi_O = 3.04$, $\xi_I = 2.43$.

importantly, such use of the interacting inner jet flow attenuates the broadband noise over almost the entire spectral range, with somewhat greater attenuation at higher frequency bands. The frequency range of the acoustical instrumentation available limited the experimental observations to a maximum of 100 kHz. It is likely, however, that the nature of the spectral characteristics of the emitted noise from the outer jet flow alone and from the combined jet flows, as shown in figure 7, would not have changed significantly if the measurements were to be extended to frequencies higher than 100 kHz. In that case, the overall noise reduction may even be somewhat enhanced. This instrumentation-imposed limitation can be rectified either by using larger jet exits, thus reducing the higher frequency content of the emitted noise, and/or by using acoustic instrumentation with higher frequency response. Testing of both of these remedies is planned.

Outer Annular Convergent-Divergent Nozzle

The outer annular convergent nozzle was replaced by an annular convergent-divergent nozzle of design exit mach number $M_e = 1.4$ operated at a design pressure ratio of $\xi_O = 3.20$. The variation of the over-

all acoustic power level with inner jet operating pressure ratio ξ_I is shown in figure 8 for outer jet reservoir pressure ratios of 3.20, 3.72, and 4.40. A maximum reduction in the overall acoustic power level of about 7 dB was achieved at $\xi_O = 3.20$ and $\xi_I = 2.63$. A typical comparison between the directionality characteristics of the noise radiated from the outer supersonic jet flow alone at design operating conditions ($\xi_O = 3.20$) and those of the interacting combined coaxial jet flows at maximum observed noise reduction ($\xi_O = 3.20$ and $\xi_I = 2.63$) is shown in figure 9. This comparison shows clearly that, similar to the arrangement with an outer convergent annular nozzle, significant reduction in measured sound-pressure level is achieved over all azimuthal angles.

Optical Observations

Outer Annular Convergent Nozzle

To establish the correspondence between the observed reduction in emitted noise and the modifications in the flow field of the interacting

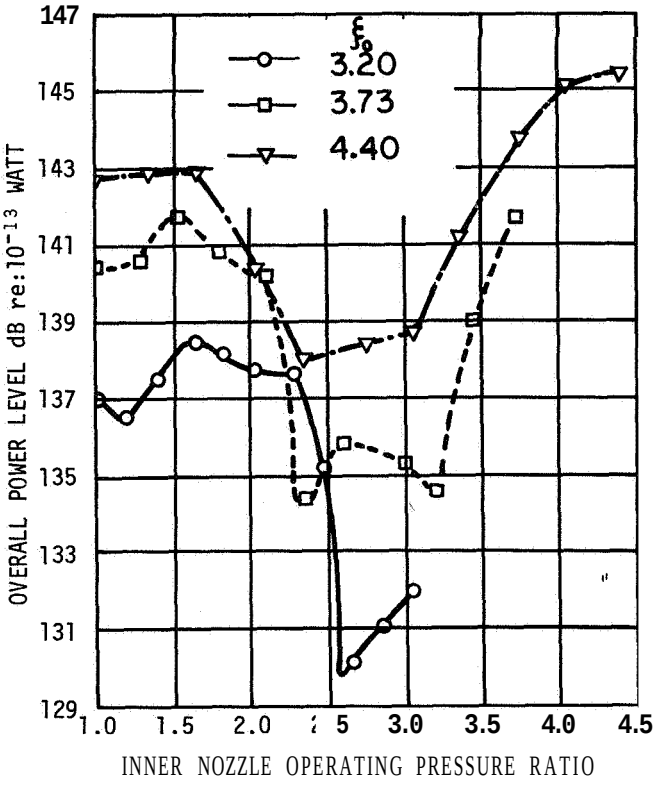

FIGURE 8.—Variation of overall acoustic power level with inner nozzle operating pressure ratio, outer annular nozzle: convergent-divergent.

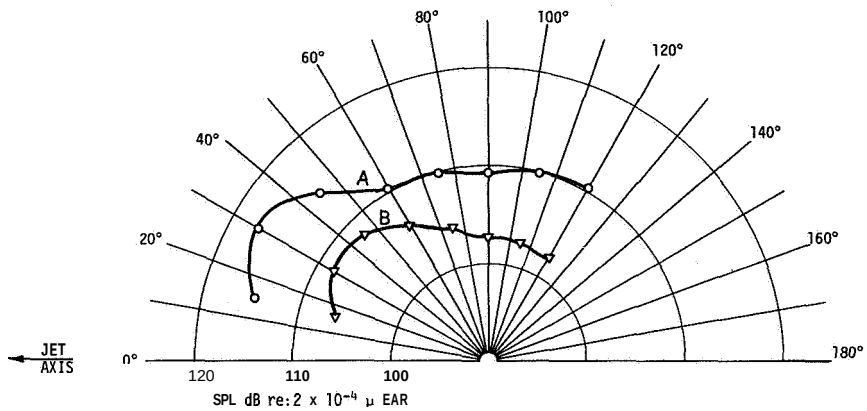

FIGURE 9.—Overall sound pressure directionality: *A*. outer annular nozzle: convergent-divergent, $\mathcal{E}=3.20$; *B*. combined coaxial jet flows, $\xi_O=3.20$, $\mathcal{E}=2.63$ (outer annular nozzle: convergent-divergent).

coaxial jet flows and to determine the possible locations of the dominant noise sources, shadowgraphs of the jet flows were recorded at systematically varied operating conditions for outer jet flow alone with operating pressure ratios ξ_O ranging from 3.04 to 7.80, for inner jet flow alone with

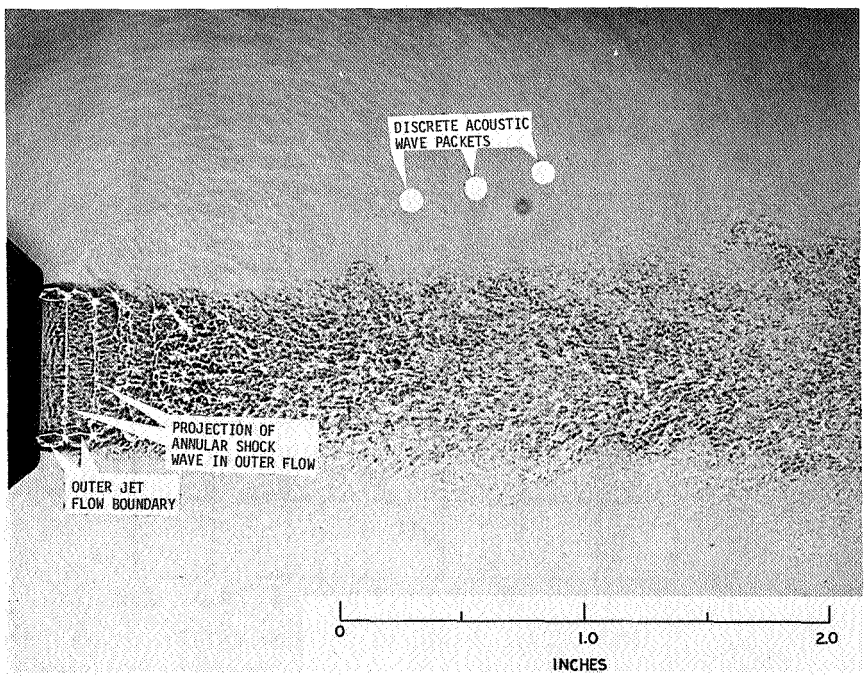

FIGURE 10.—Typical shadowgraph of outer annular convergent nozzle flow alone, $\xi_O=3.04$.

operating pressure ratios ξ_I ranging from **1.34** to 7.80, and interacting coaxial jet flows. The shadowgraphic data recorded for the outer converging annular jet flow alone operated at a pressure ratio of 3.04 is shown in figure 10; data for the inner converging-diverging jet flow operated at a pressure ratio of **2.43** in figure **11;** and data for the combined interacting coaxial jet flows operated at these individual jet pressure ratios, in figure **12.** Comparisons of these data show extensive differences in both the flow characteristics and shock structure.

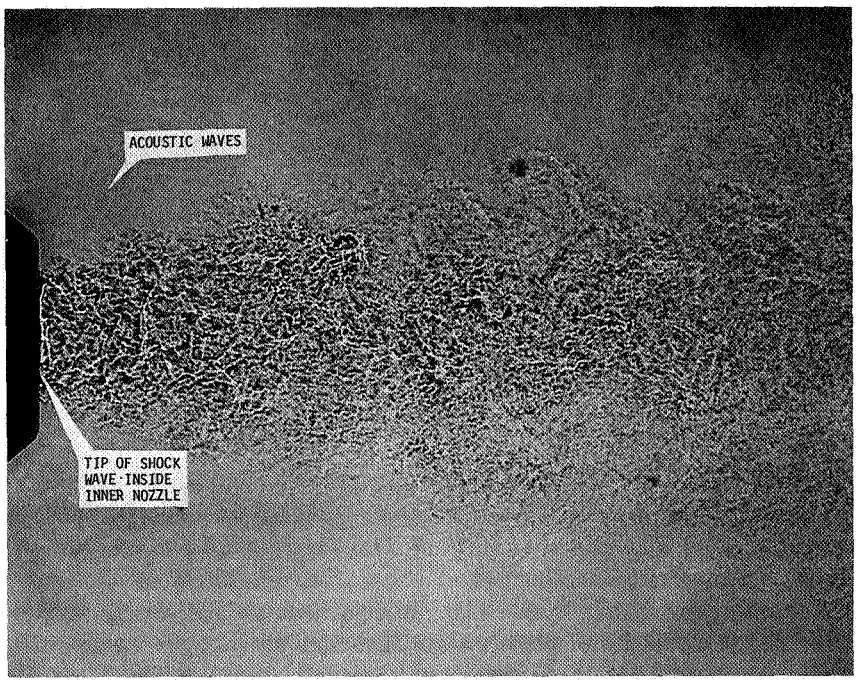

FIGURE 11.—Typical shadowgraph of inner jet flow alone, $\xi_I = 2.43$.

The underexpanded annular convergent outer jet flow alone operating at a pressure ratio of 3.M has the following characteristics (fig. 10): The annular jet flow is first deflected toward the axis of symmetry because of the lower pressure in the cavity at the inner nozzle exit. This gross flow deflection continues up to a downstream axial location of $X/D_0 = 0.7$, where the annular jet flow reaches the centerline. Downstream of this location the jet flow spreads. The supersonic portion of the flow as evidenced from the undulations in the shape of the jet-flow boundary and the total pressure survey as discussed in the section on mach-number distributions and velocity profiles of coaxial jet flows extends to about $X/D_0 = 3$.

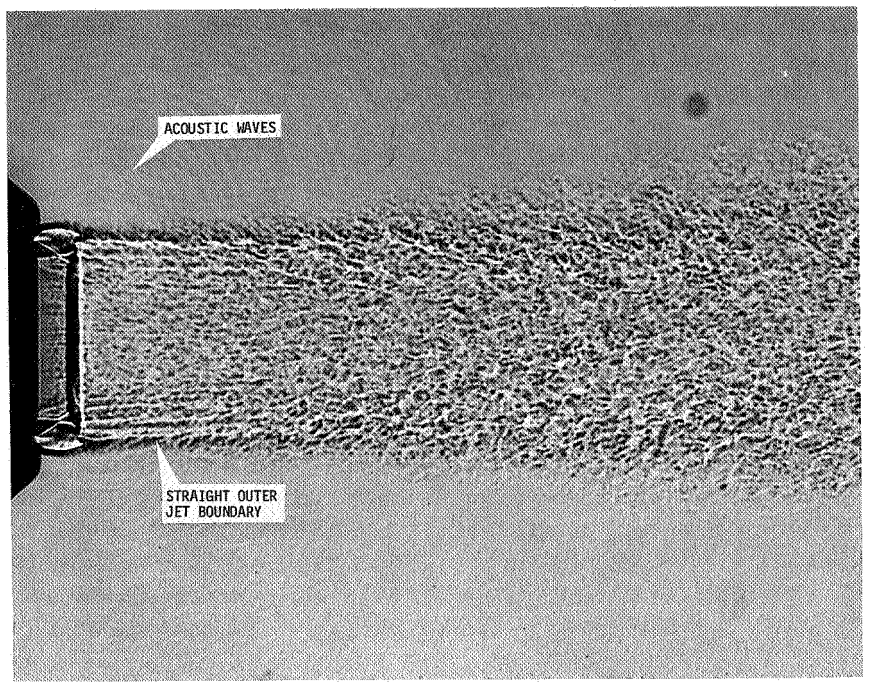

FIGURE 12.—Typical shadowgraph of coaxial jet flows at minimum noise operation, $\xi_O=3.04$, $\xi_I=2.43$.

The jet flow issuing from the inner converging-diverging nozzle alone operated at a pressure ratio of **2.43** (fig. **11**) does not show any shock structure outside the nozzle except for the tip of shock structure visible just at the nozzle exit. This is because the design [5] pressure ratio, i.e., the ratio between the reservoir pressure and the static pressure at nozzle exit of the inner convergent-divergent nozzle, was 7.80. Due to the off-design operating pressure ratio, the flow seems to separate inside the nozzle. For the coaxial jet flows, however, the static pressure in the cavity between the inner and the outer jet flows just downstream of the nozzle exits becomes progressively less than the ambient pressure for increasing operating pressure ratios ξ_O and ξ_I. As a result, the effective operating pressure ratio of the inner nozzle approaches the design pressure ratio. The flow from the inner nozzle when operated at $\xi_I=2.43$ does not appear to separate inside the nozzle.

The combined coaxial jet flows operated at pressure ratios of **3.04** for outer jet and 2.43 for inner jet **(fig. 12)** may be divided into two

[5] This implies that nozzle-exit pressure is equal to the pressure of the receiving medium surrounding the nozzle exit.

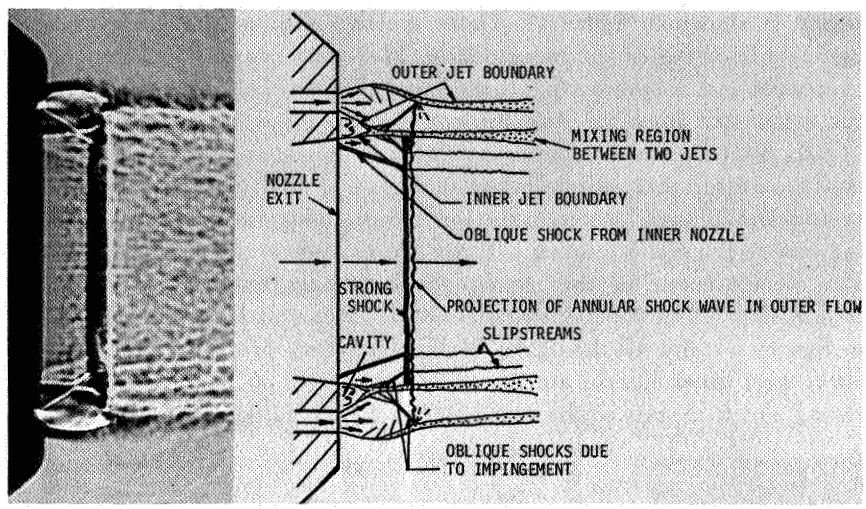

FIGURE 13.—Shock structure and flow details of interacting coaxial jet flows near nozzle exits, $\xi_O = 3.04$, $\xi_I = 2.43$.

regions: a flow region that extends from the nozzle exits to about $X/D_0 = 0.16$ downstream of the exit, and a flow region that extends downstream of this location. The coaxial jet flows in the first region are supersonic and contain several shock fronts in the outer as well as in the inner jet flows. Schematic representation of the flow field in this

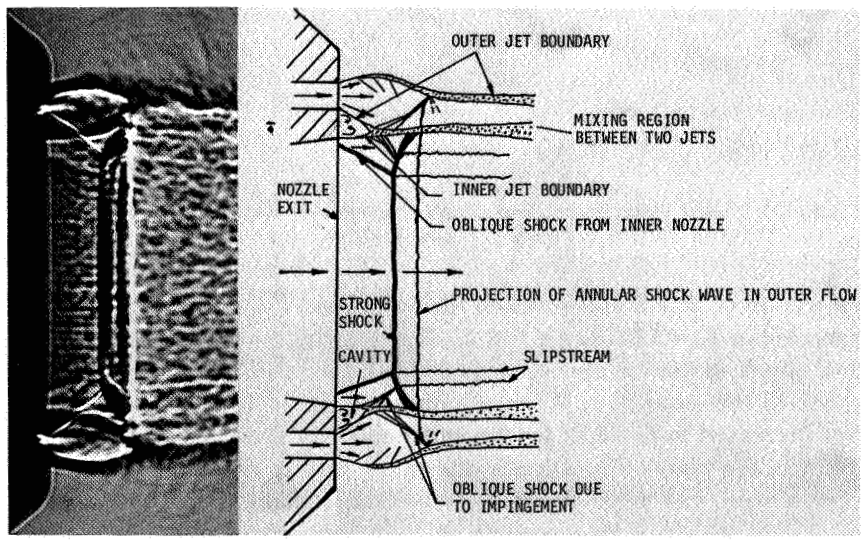

FIGURE 14.—Shock structure and flow details of interacting coaxial jet flows near nozzle exits, $\xi_O = 3.72$, $\xi_I = 2.36$.

region is shown in figure **13.** There are two oblique shock waves that emanate from inside the inner nozzle. The inner nozzle flow is therefore overexpanded, assuming that these shocks adjust their strength to match the nozzle-exit pressure with the cavity pressure surrounding the inner nozzle. **A** strong shock system consisting of these two oblique interacting shocks, a mach disk and reflected shocks, is formed. Such a strong shock system would have formed in the inner flow, though at a different operating reservoir pressure, even without the existence of the outer jet flow. The development of the strong shock system and the downstream progression of the standoff distance of the mach disk is further illustrated in figures **14** and 15. In figure **14** the operating pressure ratios of the outer and inner nozzle are $\xi_O = 3.72$ and $\xi_I = 2.36$, respectively. The strong shock system in the inner flow is clearly formed upstream of the

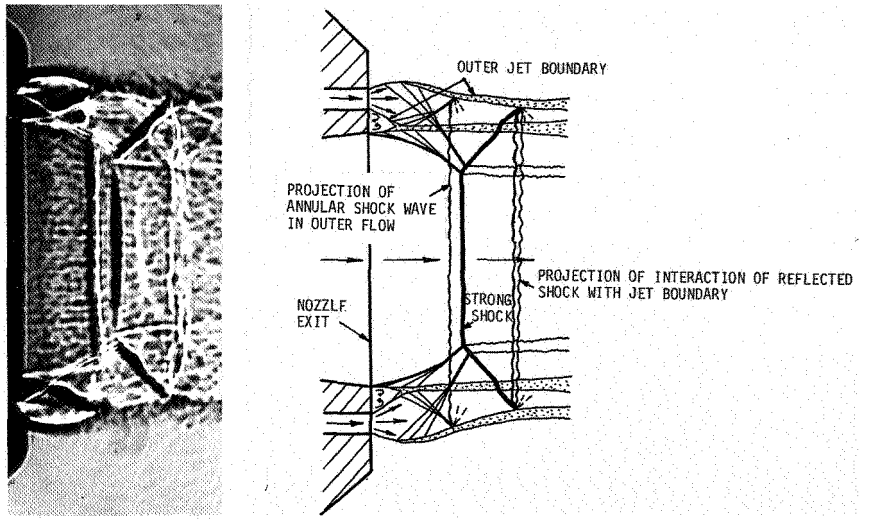

FIGURE 15.—Shock structure and flow details of interacting coaxial jet flows near nozzle exits, $\xi_O = 3.04$, $\xi_I = 3.52$.

projection of an annular shock in the outer flow. For the coaxial jet flows operated at $\xi_O = 3.04$ and $\xi_I = 2.43$ (fig. 13), the mach disk of the inner flow shock system is almost coplanar with the projection of the annular shock in the outer flow. When the inner nozzle operating pressure ratio was increased to $\xi_I = 3.52$ for the same outer jet pressure ratio $\xi_O = 3.04$ (fig. 15), the standoff location of the mach disk in the inner flow moves downstream with respect to the projection of the annular shock in the outer flow. In all of these variations of the operating conditions and the shock structure, the inner and outer supersonic jets impinge at an oblique angle just downstream of the jet exits. The boundaries of the two jet

flows therefore meet and interact locally. Essentially, the individual jet flows deflect into themselves and generate compression waves that emanate from the region of interaction of the two jet boundaries. These compression waves coalesce and form two additional oblique shock waves (fig. **13).** These shocks have several important effects on the inner and outer jet flows. The additional oblique shock in the inner flow affects the standoff distance and size of the mach disk as well as the configuration of the reflected shocks in the inner flow. The additional oblique shock in the outer flow eliminates the repetitive shock structure in the outer annular jet flow (fig. **12).** The outer jet boundary of the coaxial jet flows downstream of the shock seems to be fairly straight, indicating that the static pressure in this region is almost equal to the ambient pressure. Beyond a downstream distance of $X/D_0=2$, the combined coaxial jet flows spread and behave as a single jet. The behavior of the outer jet boundary of the combined flows in this shock-free region appears to be very similar to a properly expanded supersonic jet flow.

The observed development of the coaxial jet flows, as the inner jet reservoir pressure is increased, is illustrated in a set of shadowgraphs shown in figure **16.** Beyond inner jet operating pressure ratio $\xi_I=1.20$, the outer jet does not deflect toward the axis. The cellular structure in the outer jet flow, however, is still present. The effective operating pressure ratio of the inner nozzle is well below the design value, and the flow separates inside the nozzle. When the inner jet reservoir pressure ratio is increased so that $\xi_I=1.82$, a wiggled shock wave appears from the inner nozzle exit, indicating that the flow **in** the inner nozzle has become supersonic but still separates inside the nozzle because of the large adverse pressure gradient associated with the shock structure. This coaxial jet-flow pattern remains the same as the reservoir pressure of the inner nozzle is increased until the static pressure in the cavity between the inner and outer jets is low enough[6] to yield an effective pressure ratio resulting in an unseparated flow from the inner nozzle. This type of flow pattern has been observed at an inner jet nozzle operating pressure ratio $\xi_I=2.43$. Under these operating conditions, the inner and the outer jet flows impinge on each other obliquely and result in the extensive modification of shock structure discussed before. This flow pattern corresponds to the observed maximum noise reduction.

Outer Convergent-Divergent Nozzle

Similar coaxial jet-flow patterns have been observed when the outer annular convergent nozzle was replaced by an annular convergent-

---

[6] **Experimental measurements of the cavity pressures as well as attempts to reduce the size of the cavity and its possible adverse effects on thrust of the combined coaxial jets are planned.**

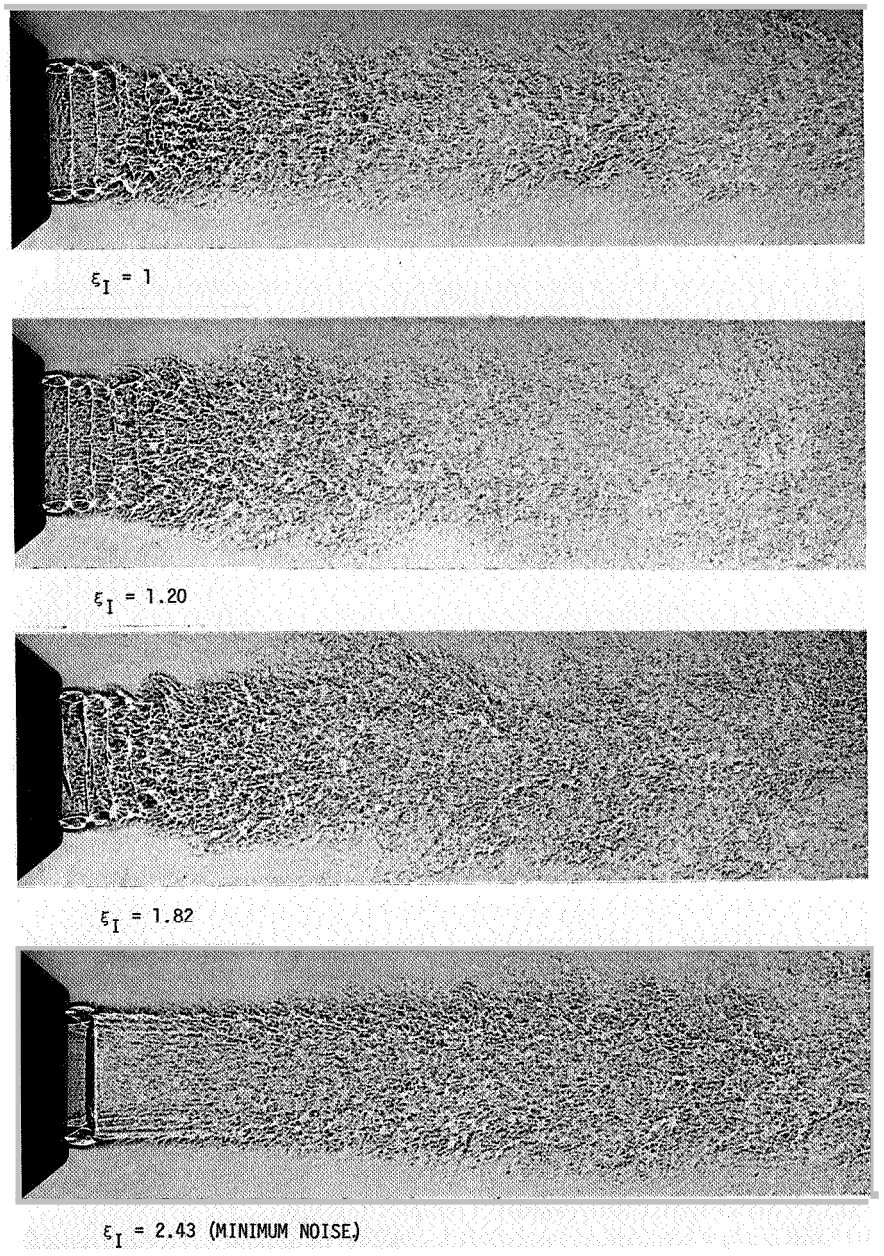

FIGURE 16.—Typical development of shock structure with inner nozzle operating pressure ratio, outer annular nozzle: convergent, $\xi_O = 3.04$.

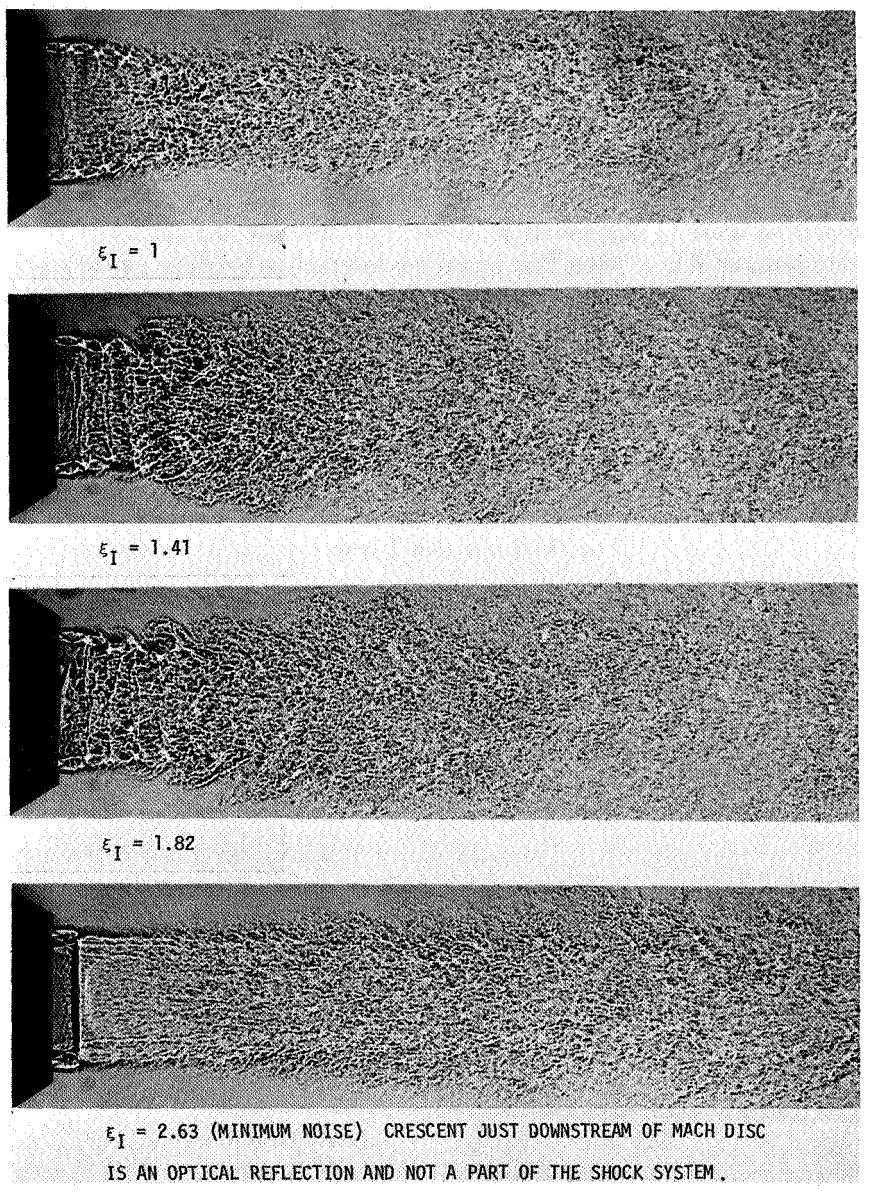

FIGURE 17.—Typical development of shock structure with inner nozzle operating pressure ratio, outer annular nozzle: convergent-divergent, $\xi_O = 3.20$.

divergent nozzle. This is evident from the set of shadowgraphs shown in figure 17. When the coaxial jet flows are operated at $\xi_O = 3.20$ and $\xi_I = 2.63$, the overall acoustic power level is about 7 dB below the level of the outer jet alone operated at $\xi_O = 3.20$. It should be pointed out that

the flow and shock pattern at $\xi_O = 3.20$ and $\xi_I = 2.63$ that corresponds to the maximum observed noise reduction are similar to those observed at maximum noise reduction conditions when the outer annular convergent nozzle was used (fig. 12). This flow and shock pattern was observed when the inner and outer flows obliquely impinge and interact just downstream of the nozzle exit.

It was pointed out earlier that repetitive shock structure is a significant source of noise in supersonic jet flows. The acoustic and shadowgraphic data presented here show that by proper interaction between two or more high-speed coaxial jet flows, the repetitive shock structure can be eliminated. However, the observed noise reduction is not entirely the result of the elimination of the repetitive shock structure alone. To examine the effect of coaxial flow interaction on other possible noise sources in supersonic jet flows, the following preliminary fluid mechanical measurements were attempted.

Mach-Number Distributions and Velocity Profiles of Coaxial Jet Flows

Pitot pressure surveys were conducted in outer jet alone and in the combined coaxial jet flows operated at $\xi_O = 3.M$ and $\xi_I = 2.22$ or 2.43. Data were recorded at $X/D_0 = 1.5$, 3, 4, 5, 6, 7.5, and 12 downstream of the nozzle exit where the flows were either slightly supersonic or sub-

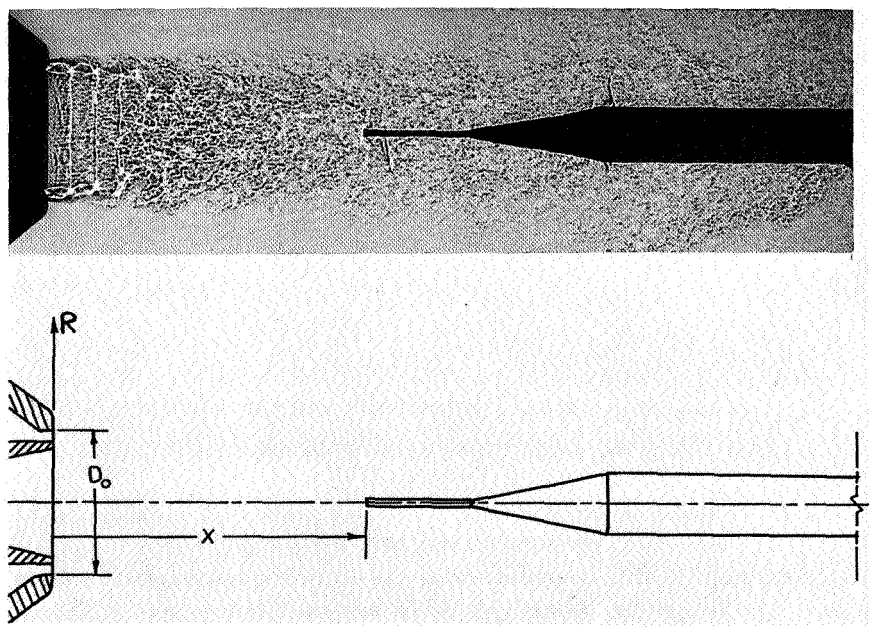

FIGURE 18.—Axial and radial location of pitot tube.

sonic (fig. 18). For the operating pressure ratios used, the pitot-tube bow shock, if it exists at these locations, is relatively weak. Therefore the measured pitot pressures were assumed to be equal to the local total pressures. Furthermore, the static pressure at flow sections $1.5D_0$ and further downstream of the exists is assumed to be constant and equal to the ambient pressure. This assumption is supported by the shape of the jet boundary (no curvature), as evident in shadowgraphic data (fig. 12) and by static pressure measurements in this flow region, which indicated a maximum difference of only 0.45 psi between the measured local static pressure and the surrounding ambient pressure. Such an error in the assumed static pressure would result in a maximum error of about 3 percent in the calculated mach number. The stagnation temperatures of the inner and outer jet flows were measured to be almost equal to the ambient temperature. With these assumptions, the local static temperatures and velocities were calculated.

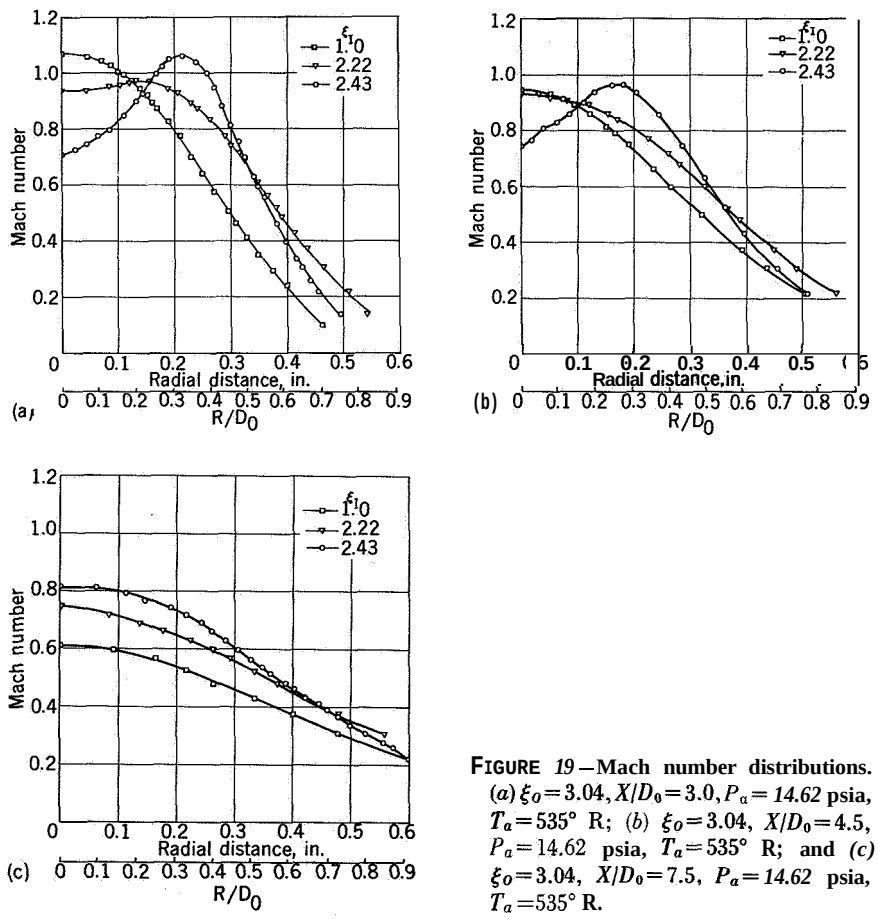

FIGURE *19*—**Mach number distributions.** (*a*) $\xi_0=3.04, X/D_0=3.0, P_a=14.62$ psia, $T_a=535°$ R; (*b*) $\xi_0=3.04$, $X/D_0=4.5$, $P_a=14.62$ psia, $T_a=535°$ R; and (*c*) $\xi_0=3.04$, $X/D_0=7.5$, $P_a=14.62$ psia, $T_a=535°$ R.

Comparisons between the mach-number distribution at various cross sections for the outer jet alone and for the interacting jet flows are shown in figure 19. At $X/D_0=3$, the core of the outer annular jet is filled and the flow at the axis has attained a mach number of **1.07** (fig. 19(a)). For the same axial location, the mach-number distribution corresponding to the operating conditions $\xi_O=3.04$ and $\xi_I=2.22$ is fuller at the centerline than for $\xi_O=3.04$ and $\xi_I=2.43$. At $X/D_0=4.5$ downstream (fig. 19(b)), the interacting jet flows operated at $\xi_O=3.04$ and $\xi_I=2.22$ have almost the same mach number at the centerline as for the outer jet flow alone operated at $\xi_O=3.04$. The combined jet flows operated at $\xi_O=3.04$ and $\xi_I=2.22$ or **2.43**, and the outer jet flow alone are all entirely subsonic at $X/D_0=4.5$. At $X/D_0=7.5$ (fig. 19(c)), the mach-number distribution for $\xi_O=3.04$ and $\xi_I=2.43$ exhibits a maximum value of 0.81 at the centerline. Axial mach-number distributions were also calculated (fig. 20) for three operating conditions: the outer converging annular jet alone at $\xi_O=3.04$, the coaxial jet flows at $\xi_O=3.04$ and $\xi_I=22$, and the coaxial jet flows at $\xi_O=3.04$ and $\xi_I=2.43$. For $3.75>X/D_0>1.5$, the axial mach number in the outer jet alone is supersonic. However, the mach-number distribution for this operating condition decays faster than for the other two operating conditions. The axial mach-number distributions for $\xi_O=3.04$ and $\xi_I=2.22$ or **2.43** are entirely subsonic for $X/D_0>1.5$.

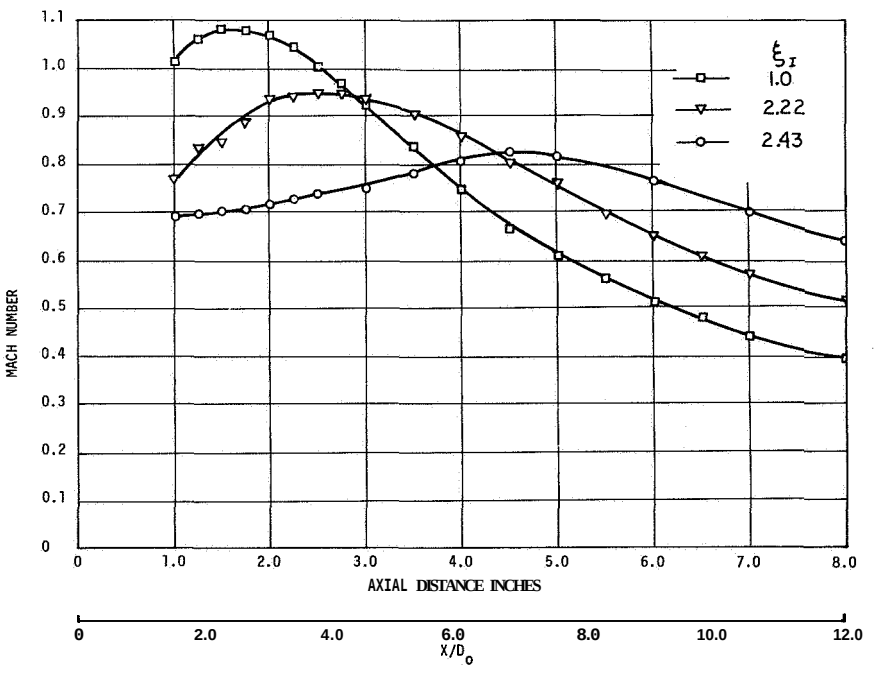

FIGURE 20.—Axial mach number distribution, $\xi_O=3.04$, $P_a=14.68$ psia, $T_a=535°$ R.

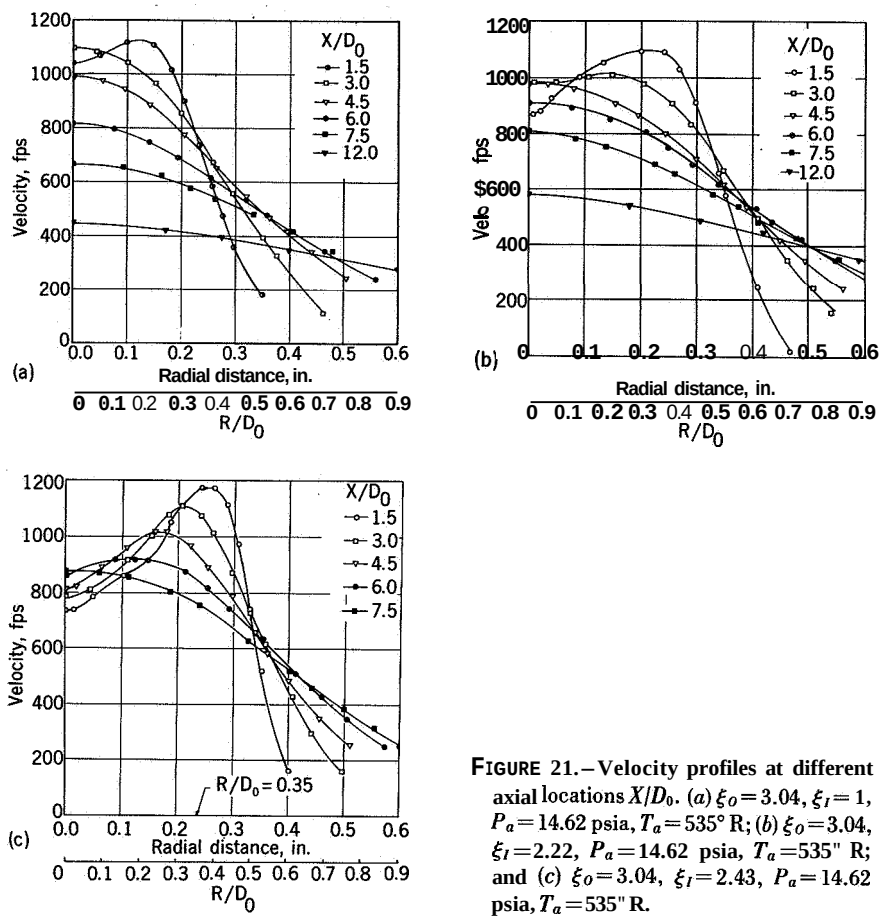

FIGURE 21.—Velocity profiles at different axial locations X/D_0. (*a*) $\xi_O=3.04$, $\xi_I=1$, $P_a=14.62$ psia, $T_a=535°$ R; (*b*) $\xi_O=3.04$, $\xi_I=2.22$, $P_a=14.62$ psia, $T_a=535°$ R; and (*c*) $\xi_O=3.04$, $\xi_I=2.43$, $P_a=14.62$ psia, $T_a=535°$ R.

Therefore, as a result of interaction, the interacting supersonic jet flows become subsonic closer to the jet exits than the outer jet flow alone.

The calculated velocity profiles for the same operating conditions are shown in figure **21.** These velocity profiles exhibit trends similar to those of the calculated mach-number distributions. Specifically, the state of fully developed turbulent jet flow was reached at a location farther downstream for $\xi_O=3.04$ and $\xi_I=2.43$, the minimum noise operating conditions, than for the other two operating conditions. However, in the range of $1.5<X/D_0<4$, the mach number or velocity profiles for the outer jet alone are fuller at the axis for $\xi_O=3.04$ and $\xi_I=2.22$ than for $\xi_O=3.04$ and $\xi_I=2.43$, the minimum noise operating conditions. The coaxial interacting jet flows operated at $\xi_O=3.04$ and $\xi_I=2.43$ exhibit a longer mixing region. (See table I.) This observation seems to contradict the common expectation that the shorter the mixing region, the lesser

TABLE I. – *Spatial Extent of Various Prominent Flow Regions, $\xi_O = 3.04$*

Flow region \ ξ_I	1	2.22	2.43
Supersonic mixing region with shock structure	$0.8 \geq X/D_0 \geq 0$	$0.9 \geq X/D_0 \geq 0$	$0.16 \geq X/D_0 \geq 0$
Supersonic mixing region without shock structure	$4.5 \geq X/D_0 > 0.8$	$3 \geq X/D_0 > 0.9$	$3 \geq X/D_0 > 0.16$
Supersonic mixing region	$4.5 \geq X/D_0 \geq 0$	$3 \geq X/D_0$ B O	$3 \geq X/D_0 \geq 0$
Subsonic mixing region	([a])	$4.5 \geq$ XIDo > 3	$7.5 \geq X/D_0 > 3$
Overall mixing region [b]	$4.5 \geq X/D_0 \geq 0$	$4.5 \geq X/D_0 \geq 0$	$7.5 \geq X/D_0 \geq 0$
Fully developed turbulent region [c]	$X/D_0 > 4.5$	$X/D_0 > 4.5$	$X/D_0 > 7.5$

[a] For $\xi_I = 1$, mean velocity similarity was established at about the same location where the flow becomes subsonic. Hence the extent of subsonic mixing region could not be determined.

[b] Defined as the region from nozzle exit to the location where the velocity distributions of the interacted flows become similar.

[c] Defined as the region in which the velocity distributions of the interacted flows are similar.

the noise. Furthermore, near-field noise studies presented in the section on distributions of acoustic power show that noise emitted from flow regions where there are no shock waves is less for $\xi_O = 3.04$ and $\xi_I = 2.43$ than for either the outer jet alone or $\xi_O = 3.04$ and $\xi_I = 2.22$.

Thus it is evident that besides eliminating the repetitive shock structure, the interaction between the coaxial high-speed jet flows significantly modifies the mach number and velocity profiles of the noise-producing flow regions, yielding substantial noise reduction. The turbulence characteristics of either the individual or the interacting jet flows have not been measured so far. However, it is surmised that the observed noise reduction is partly the result of favorable modification in the turbulence characteristics of the interacting jet flows.

In these studies, the modification of prominent features of the interacting jet flows and the associated dominant acoustic sources that resulted in the observed noise reduction have not yet been fully explored. An optimization of the noise reduction by proper design and use of the coaxial nozzle arrangement whereby more effective impingement and/or interaction is induced between the inner and the outer jet flows is now under consideration.

NEAR-FIELD SOUND-PRESSURE SURVEY[7]

To locate the dominant noise sources in the interacting coaxial jet flows as well as to determine their spatial distribution, spectral contents, and general acoustic behavior, a sound-pressure survey was conducted in the near-noise field with outer jet flow operated at $\xi_O = 3.04$, and inner jet flow operated at $\xi_I = 1$, 2.22, and 2.43, respectively? The boundary of the coaxial jet flows was determined from shadowgraphs recorded at these operating conditions. A maximum jet spread of approximately 9" occurred when the outer jet was operated at $\xi_O = 3.04$ and inner jet at $\xi_I = 2.22$. To avoid possible effects of intermittence and psuedosound on the sound pressure measured in the near field, a 10" boundary for sound-pressure measurement was used from $X/D_0 = 0$ to $X/D_0 = 8$. For $X/D_0 > 8$, the boundary of measurement was selected to be 15". To measure sound pressure, a 1/8-in. microphone was traversed along the boundary of measurement in a horizontal plane containing the axis of coaxial jet flows. The axis of the microphone was oriented so that it was perpendicular to the axis of coaxial jet flows. The range of the microphone traverse in the radial direction was from the boundary of measurement to $R/D_0 = 15$. In the axial direction the range of traverse was from the nozzle exit to $X/D_0 = 20$. Correction of the random incidence of sound waves on the microphone diaphragm was not considered necessary because of the omnidirectionality of the 1/8-in. condenser microphone.

Spatial Distribution of Overall Sound Pressure

The near-field contours of overall sound pressure level for the outer jet operated at $\xi_O = 3.M$ alone and inner jet operated at $\xi_I = 2.22$ and 2.43, respectively, are given in figure 22.

When the outer jet was operated alone at $\xi_O = 3.04$, it is seen (fig. 22(a)) that a strong acoustic source region extends from $X/D_0 = 0.2$ to $X/D_0 = 0.8$ adjacent to the 10" measuring boundary. The standoff distance of the four visible annular shocks in the outer jet measured from shadowgraphs were $X/D_0 = 0.20$, 0.41, 0.67, and 0.85, respectively. The sound-pressure levels recorded when the microphone was successively placed near the shock tips of the repetitive shock structure were approximately the same, and the average source strength was 164 dB. These measurements indicate that the existence of shock structure in the supersonic jet flow is responsible for strong noise emission. The direction of maximum sound propagation was estimated by calculating the average gradient of sound-pressure level along rays extended from the center of the strong

[7] Near-field noise investigations reported here were conducted primarily by James Yu, one of the authors of this report.

[8] $\xi_I = 1$ means inner jet is not operated.

371-986 0-LT-70—7

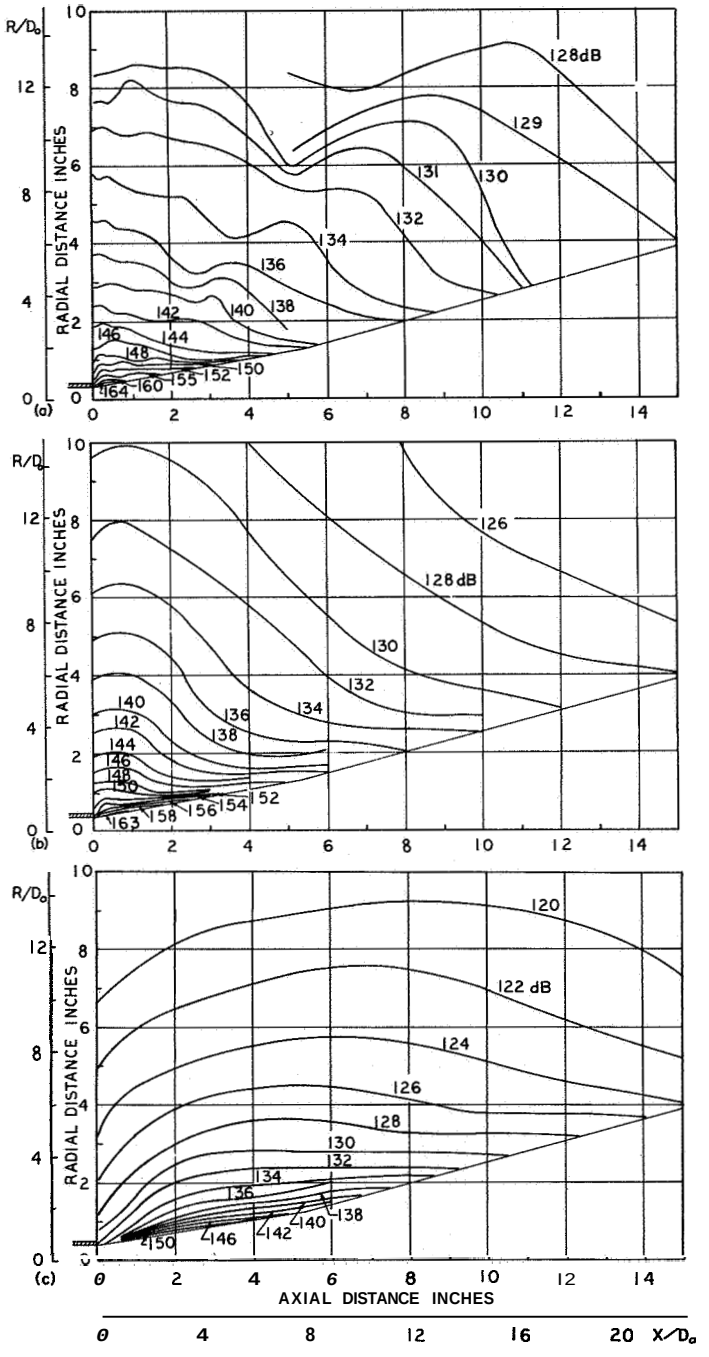

FIGURE 22.—Near-field contours of overall sound pressure level. (a) $\xi_0=3.04$, $\xi_1=1.0$; (b) $\xi_0=3.04$, $\xi_1=2.22$; and (c) $\xi_0=3.04$, $\xi_1=2.43$.

source region. The direction was determined to be within a 30" to **45**" azimuthal angle. The crests that appeared on each constant sound-pressure contour are indications of the passage of intense sound.

Two groups of crests can be seen in figure 22(a). The first group lies between ***30***" and **45°,** which also coincides with the direction of maximum sound propagation. The second group is bounded by 80" and **105".** To identify these strong sound emissions, the far-field spectral directionality patterns were examined. These are shown in figure ***23.*** It is seen that a discrete sound emission at a 40-kHz **⅓-octave** band has its primary directional peak at a 30" azimuthal angle, with the secondary directional peak along a **105**" azimuthal angle. The second harmonic of this discrete emission peaked at about a **90**" azimuthal angle. It suggests that the presence of crests on constant sound-pressure contour lines was caused by the passage of this strong discrete sound and its second harmonics.

With the inner jet operated at $\xi_I = 2.22$, the near-field sound pressure changed extensively (fig. 22(b)). The constant sound pressure level (SPL) contours exhibit a smoother pattern. A strong source region, of average strength **163** dB, extended from $X/D_0 = 0.3$ to $X/D_0 = 0.9$ along the **10**" measuring boundary. The standoff distance of the three visible shock structures were measured to be $X/D_3 = 0.16$ for the strong shock in the inner jet flow and $X/D_3 = 0.35$ and **0.57** for the annular shock structures in the outer jet flow. The directions of propagation of strong sound emissions were determined to be within a 30" to **45**" azimuthal angle and an **85**" to **95**" azimuthal angle. The **85**" to **95**" direction agreed with the directional peak of discrete sound emissions at center frequencies of **50** kHz and ***63*** kHz, measured from far-field spectral directivity. It seemed that with the introduction of the inner jet flow, the discrete sound emission in the downstream directions was eliminated or shifted to the direction normal to the axis of coaxial jet flows.

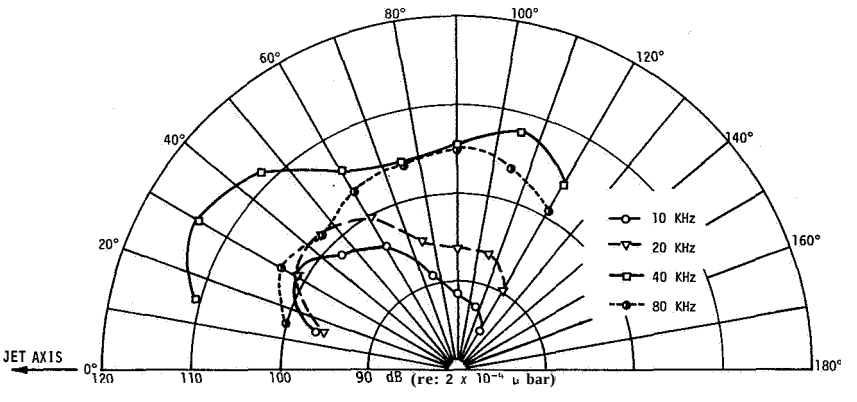

FIGURE 23.—Far-field spectral sound pressure directionality, $\xi_O = 3.04$, $\xi_I = 1.0$.

At outer jet operating pressure ratio $\xi_O = 3.04$ and inner jet operating pressure ratio $\xi_I = 2.43$, where the maximum noise reduction was observed from far-field measurement, the contours of sound pressure in the near field exhibit a considerably modified pattern. (See fig. 22(*c*).) Predominantly, the sound field is generated by an extended source region located downstream of the exit. This extended source region of strength 150 dB extends from $X/D_0 = 1$ to $X/D_0 = 6.2$. The corresponding shadowgraphic data reveal that in the combined jet flows, the locations of the single annular shock in the outer flow and the strong shock in the inner flow are almost coplanar at $X/D_0 = 0.16$. It indicates that the strong sources associated with the repetitive shocks observed at $\xi_I = 1$ and 2.22, respectively, were eliminated and replaced by an extended but reduced strength source region downstream of the single strong shock system. The direction of maximum sound propagation was determined to be approximately a 30° azimuth angle. The comparative rate of sound-pressure decay along rays from the center of the extended source was very gradual as the ray angle increased or decreased from the direction of maximum propagation. This observed characteristic agrees with the overall sound-pressure directionality recorded in the far field.

Near-field Sound-Pressure Distribution Along Boundary of Measurement

The sound-pressure distribution along the measurement boundary for the outer jet operated at $\xi_O = 3.M$ and inner jet operated at $\xi_I = 1$, 2.22,

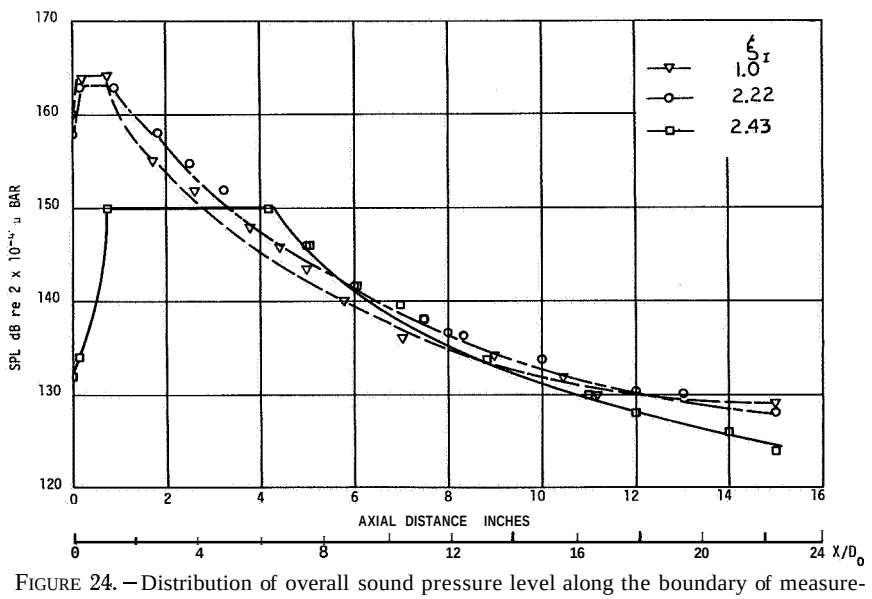

FIGURE 24. — Distribution of overall sound pressure level along the boundary of measurements, $\xi_O = 3.04$.

and **2.43,** respectively, are given in figure **24.** Major differences among the three distributions occur between $X/D_0 = 0$ and $X/D_0 = 4.5$. The sound-pressure distributions $\xi_I = 1$ and $\xi_I = 2.22$ are similar except for the strong source region. However, the reduction in source strength for the inner jet operated at $\xi_I = 2.43$ is quite striking. For example, near the nozzle exit, the sound pressure levels are **27** dB lower than those for $\xi_I = 1$ and **2.22.** The strength of the strong source was reduced by about **14** dB. Near the location of shock structure in the combined jet flows, the sound pressure for $\xi_I = 2.43$ was only **132** dB, while for $\xi_I = 1$ and **2.22,** sound pressures were **163** and **164** dB, respectively. The decay of sound pressure along the measurement boundary starts at $X/D_0 = 0.7$ downstream of the nozzle exit for $\xi_I = 1$ and **2.22.** However, for $\xi_I = 2.43$, it starts at $X/D_0 = 6.2$. It is worth noting that at $\xi_I = 2.43$, the noise level generated by shock waves in the combined jet flows is relatively insignificant. (See table 11.) This suggests that possible noise-generating mechanisms such as shock-turbulence interaction and shock oscillations are not important sources of noise in the combined jet flows at this operating condition. Because the shock fronts are located just downstream of the nozzle exit, and the mixing effects are not yet dominant, it is likely that the turbulence level of the jet flows upstream of the shocks is relatively low. The contribution from shock turbulence interaction therefore may be small. Also, at the operating pressure ratios $\xi_O = 3.04$ and $\xi_I = 2.43$, the repetitive shock structure has been eliminated. Thus, any possible shock oscillations that may exist in a more complex repetitive shock structure are not present.

TABLE 11.—*Percent Contributions of Acoustic Power Emitted From Various Prominent Flow Regions, $\xi_O = 3.04$*

[In percent]

Flow regions / ξ_I	1	2.22	2.43
Supersonic mixing region with shock structure.	37	29	Less than 1
Supersonic mixing region without shock structure.	53	47	30
Shock structure alone	27.5	15	Less than 1
Supersonic mixing region	62.5	61	30
Subsonic mixing region	([a])	13	60
Overall mixing region	62.5	74	90
Fully developed turbulent region	10	11	9
Total power emitted (W and dB re 10^{-13} W).	11.5 W (140.6 dB)	16.6 W (142.2 dB)	3.5 W (135.4 dB)

[a]

Near-field Sound-Pressure Spectra Along the Boundary of Measurement

Sound-pressure spectra were recorded in the near field at various locations along the boundary of measurement for $\xi_O = 3.04$ and the inner jet operated at $\xi_I = 1$, 2.22, and 2.43, respectively. It was found that discrete sound emission occurs for inner jet pressure ratios $\xi_I = 1$ and 2.22. At $\xi_I = 1$ (fig. 25(a)), discrete emissions at 40 kHz were recorded at all measuring stations along the measuring boundary. The maximum intensity of these discrete emissions was about 160 dB in the shock region and decreased gradually as the microphone was moved downstream and away from the shock region. The second harmonic of this discrete emission was recorded within $X/D_0 = 0$ and $X/D_0 = 2.2$. The relative contribution of these discrete components were evaluated by comparing the overall SPL with discrete components, and with the discrete components discounted. The difference was about 6 dB. When the inner jet was operated at $\xi_I = 2.22$, two discrete peaks at 50 kHz and 63 kHz were observed in the near-field spectra (fig. 25(b)). The 50-kHz peak was recorded at only one microphone location, while the 63-kHz peak persisted at locations much farther downstream. The maximum level of these discrete emissions was about 4 dB lower than that observed for the outer jet alone.

In supersonic jet flows containing shock structure, discrete sound emissions often exist (refs. 14, 23, and 25). In reference 14, it was observed that if an acoustic feedback loop exists among repetitive shock patterns, the discrete emission and its second harmonics are the prominent features of noise emission, if the second harmonics propagate normal to the jet axis. This seemed to be the case for $\xi_I = 1$. As the inner jet flow was introduced at $\xi_I = 2.22$, no harmonics were observed. This indicates that the inner flow must have the effect of interrupting the feedback loop because the emission frequencies of discrete tone were shifted from 40 kHz and 80 kHz to 50 kHz and 63 kHz. From the fact that the 50-kHz peak is observed at only one X/D_0 at which the shock structure of inner jet flow was located, it seems that this discrete emission could be attributed to the inner jet flow. In figure 25(c), the near-field sound pressure spectra taken at $\xi_I = 2.43$ are given. It is seen that the spectra at all measuring positions are wideband in nature. The maximum spectral peak of about 145 dB was recorded at $X/D_0 = 2.2$. The observed elimination of discrete tone at $\xi_I = 2.43$, as reported in the section on the outer annular convergent nozzle and which is also discussed in the next section, was found to be responsible for only a fraction of the noise reduction observed at these operating pressure ratios. The majority of the noise reduction was attributable to the modification in the mixing region and the elimination of the repetitive shock structure.

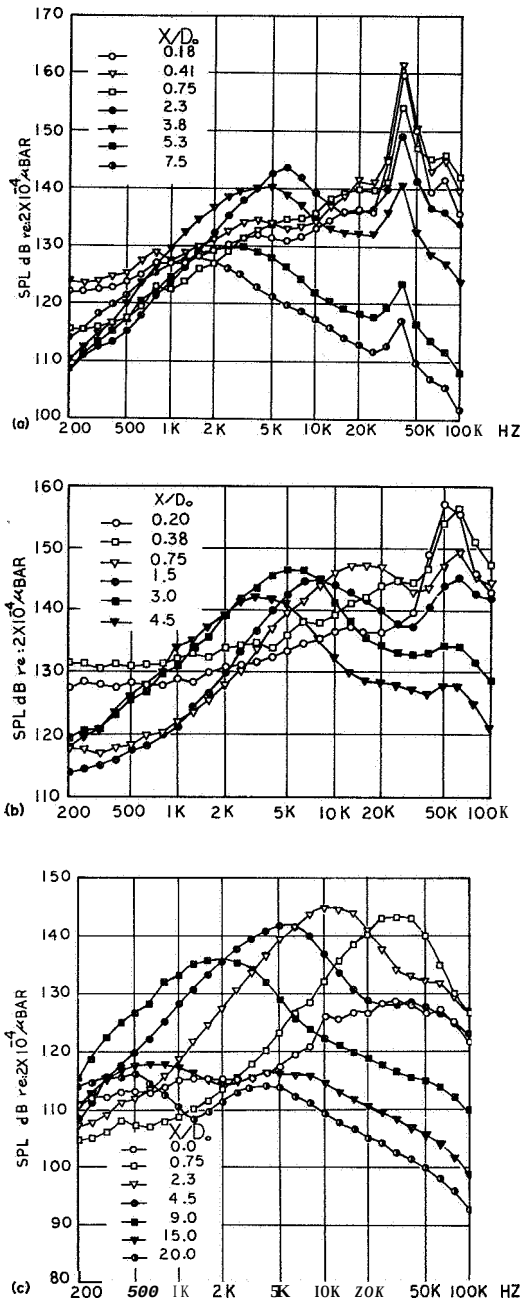

FIGURE 25.—Near-field sound pressure spectra. *(a)* $\xi_0 = 3.04$, $\xi_1 = 1.0$; *(b)* $\xi_0 = 3.04$, $\xi_1 = 2.22$; and (c) $\xi_0 = 3.04$, $\xi_1 = 2.43$.

Distributions of Acoustic Power

Total acoustic power emitted by the interacting jet flows was determined from near-field sound-pressure measurements. The measurement boundary of near-field sound-pressure surveys was carefully selected with the aid of shadowgraphic data to avoid any possible induction effects but still stay close enough to the local acoustic sources that the contributions from neighboring acoustic sources are of only secondary importance. However, it is still possible that in the near field, the microphone may have recorded part of the nonpropagating hydrodynamic fluctuations. The calculated results are shown in figure 26, where the differential acoustic powers emitted are plotted against the downstream distance. For $\xi_O = 3.04$ and $\xi_I = 1$ or 2.22, the major sound-producing regions are limited to $X/D_0 = 3.0$, where the flow is supersonic and contains repetitive shock structure. For $\xi_O = 3.04$ and $\xi_I = 2.43$, at which maximum noise reduction is observed, it is seen that the major part of the overall sound power is generated from the flow region extending from $X/D_0 = 1.75$ to $X/D_0 = 7.5$. It is important to point out that the flow region of the combined jets extending from the nozzle exits to 1 diameter downstream, in which a nonrepetitive strong shock system exists, contributes only a negligible amount to the total acoustic power.

The total acoustic powers integrated from near-field data were found to be on the average 5 dB higher than those recorded in the far field.

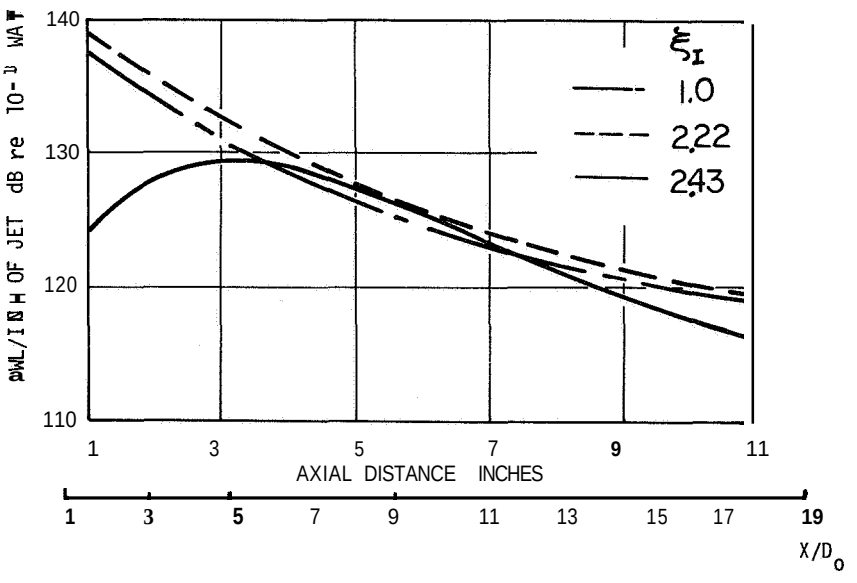

FIGURE 26.—Distribution of power emitted per unit length of the interacting coaxial jet flows.

The possible induction near-field effect mentioned above may be a contributing factor. Also there is likely to be some attenuation because of the absorption of the high-frequency components emitted by the acoustic sources. However, because the major noise-producing region extends only a few jet diameters downstream of the exit and in this part of the jet flow intermittence is less pronounced, the corresponding pseudosound or induction effect may be less serious than in the downstream turbulent decay region. Therefore, some pertinent characteristics of the noise sources can be deduced from this preliminary differential acoustic power data obtained.

The differential acoustic power from slices of interacting coaxial jet flows was calculated by using sound-pressure data and the corresponding frustum surface area at the boundary of measurement. As a first approximation, the acoustic power so calculated was assumed to represent the radiated power. This assumption admittedly neglects any possible contributions from the induced near-field effect as well as the variations with frequency of the direction of principal radiation. At least partial justification of this assumption is provided by fair agreement between the far-field integrated acoustic power and the acoustic power integrated along the boundary of measurement in the near field. The spatial extent of different flow regions determined from pitot pressure measurements and optical records is illustrated in figure 27. The results are summarized in table I. The corresponding percent contributions to the overall acoustic power emitted for different operating conditions are deduced and summarized in table II. The percent contributions from "supersonic mixing region with shock structure" (table II, "Flow region A") are calculated from the boundary sound-pressure measurements taken adjacent to the flow region containing shock structure. The contributions from "supersonic mixing region without shock structure" {table II, "Flow region B") are obtained from sound-pressure data recorded along the boundary of measurement that is adjacent to the flow region extended from downstream of the mixing region with shock fronts to the apex of the sonic boundary in the outer jet flow. The noise contributions that may be attributed to the presence of "shock structure alone" (table II, "Flow region C") were deduced from the power emitted by flow region A by subtracting from it the power emitted by the supersonic mixing alone in region A. This was roughly approximated by linear extrapolation from known contributions and the extent of region B. Then the acoustic power emitted by "supersonic mixing region" (table 11, "Flow region D") is obtained by adding contributions of flow region B and the difference of contributions from flow regions A and C. The contributions from the "subsonic mixing region" (table II, "Flow region E") represent the noise produced in the flow region that extends from the axial location of the

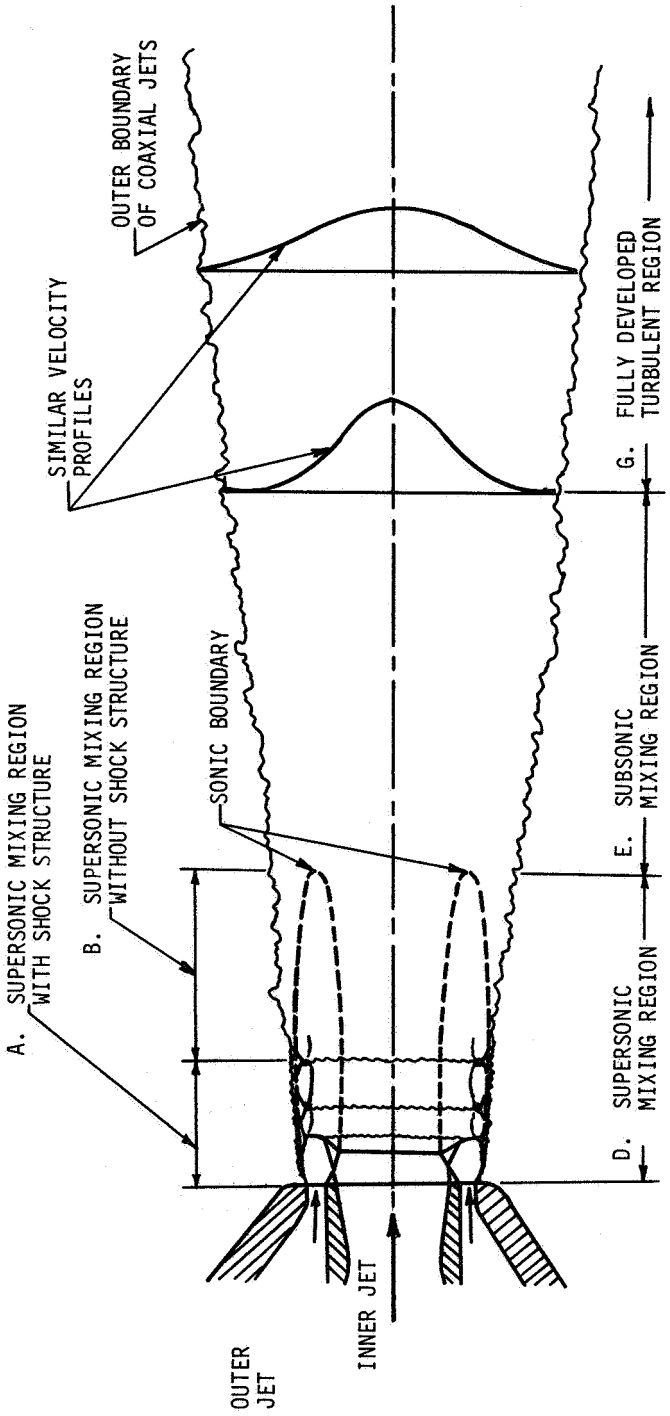

FIGURE 27.—Illustration of typical flow regions in interacting coaxial supersonic jet flows.

apex of sonic boundary to the axial location beyond which velocity profiles become similar. (See fig. 27.) The sum of flow regions **D** and **E** yields the "noise contributions from overall flow mixing" (table 11, "Flow region F"). Finally, the noise from "fully developed turbulent region" (table II, "Flow region G") is calculated from the sound-pressure data recorded at the beginning of the similar velocity profile to the location where the sound-pressure levels dropped by 10 dB. From table **11,** it is obvious that the interactions between the inner and outer jet flows result in variations in percent power distribution from different parts of the jet flows. These effects include drastic reductions in the noise attributable to the presence of shock fronts in the flow, and reduction in the contribution from supersonic mixing and a relative increase in noise emitted by the subsonic mixing region. The overall relative contribution from mixing is increased. Also, the emitted power from fully developed turbulent region remains the same for all operating conditions used and is lower than the 20-percent contribution commonly predicted by subsonic jet-noise theory. Besides these effects, shock waves in supersonic jet flows do contribute a substantial portion of overall noise, but it can be made relatively insignificant by properly affecting shock locations, their spacings, and strengths by jet-flow interactions.

It is seen from table II that for $\xi_I = 2.43$, the relative contribution from jet mixing is 90 percent and the possible shock contribution amounts to only less than **1** percent. However, it is interesting to note that on absolute basis, this **90** percent contribution from an extended mixing region is still much lower than the corresponding contribution from shorter mixing regions for $\xi_I = 1$ or **2.22.** These observations lead to the conclusion that related noise-generating mechanisms such as shock-turbulence interaction and shock oscillation are greatly suppressed, and the absolute contributions from the mixing regions are also reduced by proper flow interaction.

CONCLUSIONS

It has been shown that substantial reductions in noise emitted by supersonic jet flows can be achieved by the use of interacting coaxial high-speed jet flows. These noise reductions result from favorable modifications of the dominant acoustic sources in the interacting coaxial jet flows caused by mutual impingement and/or interaction between the inner and outer supersonic jet flows downstream of the nozzle exits. If both of the coaxial jet flows are supersonic, their impingement and/or interaction downstream of the nozzle exits should neither disturb the nozzle flows at the exits nor influence the thrust-producing capabilities of the individual nozzles. Thus the use of interacting coaxial supersonic jet flows offers a potentially practical method for abatement of supersonic jet noise.

REFERENCES

1. LIGHTHILL, M. J.: On Sound Generated Aerodynamically. I. General Theory. Proc. Roy. Soc. (London), ser. A, vol. 211, 1952, pp. 564–587.
2. LIGHTHILL, M. J.: On Sound Generated Aerodynamically. 11. Turbulence as a Source of Sound. Proc. Roy. Soc. (London), ser. A, vol. 222,1954, pp. 1–32.
3. FFOWCS WILLIAMS, J. E.: Some Thoughts on the Effects of Aircraft Motion and Eddy Convection on Noise of Air Jets. Aeronaut. Astronaut. Rept. 155, Univ. of Southampton, 1960.
4. FFOWCS WILLIAMS, J. E.: The Noise From Turbulence Convected at High Speed. Phil. Trans. Roy. Soc. (London), ser. A, vol. 255, 1963, pp. 469–503.
5. RIBNER, H. S.: Aerodynamic Sound From Fluid Dilations. UTIAS Rept. no. 86, 1962.
6. RIBNER, H. S.: On Generation of Sound by Turbulent Jets. Volume 8 of Advances in Applied Mechanics. Academic Press, Inc., 1964, pp. 103–182.
7. PHILLIPS, O. M.: On the Generation of Sound by Supersonic Turbulent Shear Layers. J. Fluid Mech., vol. 9, pt. 1, 1960.
8. LIGHTHILL, M. J.: On the Energy Scattered From the Interaction of Turbulence With Sound or Shock Waves. Proc. Cambridge Phil. Soc., vol. 49, pt. 3, July 1953.
9. RIBNER, H. S.: Acoustic Energy Flux From Shock-Turbulence Interaction. UTIAS Rept. no. 108, July 1967.
10. HOLLINGSWORTH, M. A.; AND RICHARDS, E. J.: On the Sound Generated by the Interaction of a Vortex and a Shock Wave. FM 2371, British A.R.C. 18257,1956.
11. DOSANJH, D. S.; AND WEEKS, T. M.: Sound Generated by Shock-Vortex Interaction. AIAA J., vol. 5, no. 4, 1967.
12. DOSANJH, D. S.; AND HAMERNIK, R.: Interaction of an Advancing Shock Front With a Concentrated Heat (Entropy) Source. J. Pbys. Fluids (Supplement), Apr. 1969.
13. HAMMITT, A. G.: The Oscillation and Noise of Overpressured Sonic Jet. J. Aerospace Sci., vol. 28, 1961, pp. 675–684.
14. POWELL, A.: On the Mechanism of Choked Jet Noise. Proc. Phys. Soc. (London), sec. B, vol. 66, 1953, pp. 1039–1056.
15. WESTLEY, R.; AND LILLEY, G. M.: An Investigation of the Noise Field From a Small Jet and Methods for Its Reduction. Rept. no. 53, College of Aeronautics, Cranfield, England, Jan. 1952.
16. MULL, H. R.; AND ERICKSON, J. C., Jr.: Survey of the Acoustic Near-Field of Three Nozzles at a Pressure Ratio of 30. NACA TN 3978, Apr. 1957.
17. MAYES, W. H.; LANFORD, W. E.; AND HUBBARD, H. H.: Near-Field and Far-Field Noise Surveys of Solid Fuel Rocket Engines for a Range of Nozzle Exit Pressures. NASA TN D–21, 1959.
18. KEAST, D. N.; AND MAIDANIK, G.: Studies of the Near-Field Noise Properties of a Small Air Jet. Rept. no. 1272, Bolt, Beranek & Newman, Inc., NASA STAR no. N 66–24941, Feb. 1966.
19. LOWSON, M. V.: Shadowgraph Visualization of Noise From Cold Supersonic Jets. Rept. WR 67–3, Wyle Laboratories, Jan. 1967.
20. POTTER, R. C.; AND JONES, J. H.: An Experiment to Locate the Acoustic Sources in a High Speed Jet Exhaust Stream. Paper presented at the 74th meeting, Acoustical Society of America (Miami Beach, Fla.), Nov. 1967.
21. HOWES, W. L.: Similarity of Far Noise Fields of Jets. NASA TR–R–52, 1960.
22. NAGAMATSU, H. T.; AND HORVAY, G.: Supersonic Jet Noise. Rept. no. 69–C–161, Mechanical Engineering Laboratory, GE Co., Schenectady, N.Y., Apr. 1969.
23. WESTLEY, R.; AND WOOLLEY, J. H.: An Investigation of the Near-Noise Fields at a Choked Axisymmetric Air Jet. Rept. no. LR–506, NASA STAR no. N 69–10531,1968, NRC (Canada).

24. DOSANJH, D. S.; AND MONTEGANI, F. J.: Reduction of Noise From Underexpanded Axisymmetric Jet Flows Using Radial Jet Flow Impingement. AIAA J., vol. 7, no. 3, Mar. 1969, pp. 458–464.
25. MONTEGANI, F. J.; AND DOSANJH, D. S.: Noise From Underexpanded Axisymmetric Converging Jet Flows Interacted With Radially Impinging Annular Jet Flows. Rept. no. ME/Aerospace 1085–1208F, Syracuse University Research Institute, Dec. 1967.
26. DOSANJH, D. S.; AND YU, J. C.: Noise From Underexpanded Axisymmetric Jet Flows Using Radial Jet Flow Impingement. AFOSR–UTIAS Symposium on Aerodynamic Noise, Univ. of Toronto Press, 1969.
27. MIDDLETON, D.: The Noise of Ejectors. R&M no. 3389, British A.R.C., 1965.
28. PERNET, D. F.: Experimental Noise Investigation of Model Nozzles. TR no. AFAPL-TR–64–138, IIT Research Institute, Dec. 1964.
29. MOORE, H. B.; AND CLINCH, J. M.: Application of Extended Plug Nozzle Noise Suppression Theory to a Small Turbojet Engine. Tech. Rept. of Williams Research Corp., NASASTAR no. N66–19871, Aug. 7,1965.

ENTROPIC EFFECTS IN SOUND GENERATION*

Abraham C. Peter
North American Rockwell Corp.
Downey, Calif.

SYMBOLS

a	isentropic speed of sound
c_p	specific heat at constant pressure
c_v	specific heat at constant volume
D	nozzle diameter
E_p	$e^{-(S-S_0/c_p)}$
E_v	$e^{-(S-S_0/c_v)}$
F_i	body forces vector
f	friction coefficient
h	enthalpy
$J P$	thermodynamic function as defined
M	mach number
p	pressure
ρ	density
R	gas constant
S	entropy
T	temperature
t	time
U_i	velocity vector
x_i	space coordinate
α	entropic propagation speed
β_p^2	process function
γ	adiabatic exponent, c_p/c_v
A	finite increment
δ_{ij}	Kronecker delta
ε	small parameter
θ	angle, as defined
τ_{ij}	viscous part of the stress tensor

***This work has been supported by the Unsteady Gas Dynamics Branch of MSFC in Huntsville, Ala.**

i, j, k	directional subscripts
o	initial conditions, isentropic variations at the beginning of the J-process, used as subscript
s	stagnation conditions, $\frac{d}{dt}=\frac{\partial}{dt}+U_j\frac{\partial}{\partial x_j}$

Even though the problem of entropic effects of gases includes a much broader field than that of sound generation, the phenomenon of high-speed aerodynamic noise can be viewed as a physical process in which acoustic excitations appear as a byproduct **of** energy degradation in dissipative compressible fields. The basic characteristic of such entropic flows is their dependence upon past history. In application to gas dynamics and, specifically, to the problem of sound generation, these historical effects tend to magnify the influence of certain local gradients. **As** a consequence, gradient terms, whose contribution is greatly enhanced by virtue of previous history rather than local phenomena, appear in the differential equations of motion. To put it simply: what has happened before may, under certain conditions, be more important than what is happening now. It will subsequently be demonstrated that for the case of high-speed gas flows, the conditions referred to above are near sonic or supersonic flow conditions.

THE J_p AND S FUNCTIONS

The current discussion of the subject of entropic effects in sound generation is based upon the concept of the thermodynamic J_p-function, which for a calorically perfect gas is defined by the equation

$$dJ_p=\beta_p^2\left[\mathrm{dp}-\frac{\rho}{\gamma_p}\mathrm{dp}\right]-\mathrm{dp} \tag{1}$$

An alternative and useful form of this equation may also be written:

$$dJ_p=-\frac{\beta_p^2}{c_p}\rho\, dS-dp \tag{2}$$

We consider next the case of an entropic process in which the thermodynamic function J_p is held constant. Integration of equation **(1)** or (2), in which the quantity β_p^2 is regarded as a parameter, yields the following relations (ref. **1):**

$$\beta_p^2=\frac{a_o^2}{\gamma-1}\left[\frac{\left(\frac{p}{p_o}\right)^{\gamma-1/\gamma}-1}{E_p-1}\right] \tag{3}$$

which may also be written using the perfect gas relation:

$$\beta_p^2=\frac{a_0^2}{\gamma-1}\left[\frac{\quad}{E_p-1}\right] \tag{4}$$

Equations (3) and (4) define the entropic process parameter β_p^2. The corresponding entropic work integral takes the following form:

$$\int\frac{dp}{\rho}=-\int\frac{S_p^2}{C_p}dS \tag{5}$$

It will be also useful to introduce the concept of an entropic propagation speed α_p^2 defined by equation (6):

$$\alpha_p^2=\left[\frac{\partial p}{\partial \rho}\right]_j \tag{6}$$

Combination of equations (1) and (6), in conjunction with the perfect-gas relations, allows the evaluation of the quantity α_p^2 in terms of entropy, the parameter β_p^2, and the isentropic speed of sound:

$$\alpha_p^2=\frac{(\gamma-1)\,\beta_p^2\left[\exp\left(-\frac{S-S_o}{c_p}\right)-1\right]+\alpha_o^2}{\gamma\left[\exp\left(-\frac{S-S_o}{c_p}\right)-1\right]+\frac{a_o^2}{\beta_p^2}+1} \tag{7}$$

It should be noted that as the entropy gradient tends to zero in the limit, the entropic function α_p^2 reduces to the isentropic speed of sound.

The Equations of Motion

With these preliminaries, it is possible to express the equations of motion in terms of the thermodynamic functions J_p and S (ref. 1), a procedure that is rather lengthy and for our purposes quite unnecessary. It will suffice to stipulate immediately that we are looking at processes that may be represented by straight lines in the J_p–S-plane.[2] In application to the flow noise problem, we consider two regions. The first is a highly perturbed region with a possible appearance of moderate shock waves. This region is embedded in a second region of quiescent fluid excited acoustically by the entropic effects of the perturbed region.

[2] This implies a far-field noise analysis. (See ref. 2.)

371-986 0-LT-70—8

Under these conditions, the thermodynamic J_p-function varies simply as the negative pressure function in the isentropic region and is held constant in the entropic dissipative region.

The resulting differential equation obtained by cross-differentiation of the continuity and momentum equations, and elimination of the acceleration terms from the latter, yields the following results. For the case of the isentropic region where interacting nonlinear velocity fluctuations and viscous effects are inadmissible, the equation reduces to

$$\frac{d^2}{dt^2}\left[\ln\left(\frac{p}{p_o}\right)\right]-\frac{\partial}{\partial x_i}\left\{a_o^2\frac{\partial}{\partial x_i}\left[\ln\left(\frac{p}{p_o}\right)\right]\right\}=0 \tag{8}$$

On the other hand, in the entropic region where all dissipative and nonlinear terms contribute, the governing equation becomes

$$\frac{1}{c_v}\left\{\frac{d}{dt}\left(\frac{\beta_p^2}{\alpha^2}\frac{ds}{dt}\right)-\beta_p^2\nabla^2 s\right\}=-\gamma\frac{\partial u_i}{\partial x_j}\frac{\partial u_j}{\partial x_i}+\gamma\left\{\frac{\partial}{\partial x_i}\left[\frac{1}{\rho}\frac{\partial}{\partial x_j}(\tau_{ij})+F_i\right]\right\} \tag{9}$$

Finally, when the dissipative region acts as an excitation source propagating acoustic waves into the isentropic region, equation (9) serves as a forcing function to that in equation (8), so that the resulting expression takes on the following form:

$$\frac{d^2}{dt^2}\left[\ln\left(\frac{p}{p_o}\right)\right]-\frac{\partial}{\partial x_i}\left[a_o^2\frac{\partial}{\partial x_i}\ln\left(\frac{p}{p_o}\right)\right]=\frac{1}{c_v}\left[\frac{d}{dt}\left(\frac{\beta_p^2}{\alpha^2}\frac{ds}{dt}\right)-\beta_p^2\nabla^2 s\right]$$
$$-\gamma\frac{\partial}{\partial x_i}\left[\frac{1}{\rho}\frac{\partial}{\partial x_j}(\tau_{ij})+F_i\right]+\gamma\frac{\partial u_i}{\partial x_j}\frac{\partial u_j}{\partial x_i} \tag{10}$$

Equation (10), which represents the wave equation governing acoustic emissions from an entropic J_p-region, may be reduced to that used in classical approaches by letting the entropy gradients vanish, in which case the resultant expression reduces to that derived by Phillips (ref. 3):

$$\frac{d^2}{dt^2}\left[\ln\left(\frac{p}{p_o}\right)\right]-\frac{\partial}{\partial x_i}\left\{a_0^2\frac{\partial}{\partial x_i}\left[\ln\left(\frac{p}{p_o}\right)\right]\right\}$$
$$=\gamma\frac{\partial u_i}{\partial x_j}\frac{\partial u_j}{\partial x_i}-\gamma\frac{\partial}{\partial x_i}\left[\frac{1}{\rho}\frac{\partial}{\partial x_j}(\tau_{ij})+F_i\right] \tag{11}$$

Similarly, Lighthill's form of the acoustic wave equation may be obtained by the use of isentropic pressure-density relations.

However, even though the equation governing the entropic wave generation reduces to the form used in classical investigations, it is evident that

this equivalence holds true for isentropic pressure variations only. On the other hand, the analytical aspects of the J_p-process are specifically aimed at the inclusion of entropic effects and emphasize the energy degradation terms of the forcing function, As a consequence, processes that include, among others, unsteady shock fluctuations as well as high-speed frictional phenomena, are reflected in the nonisentropic terms of the governing equation.

MAGNIFICATION EFFECTS OF THE ENTROPIC TERMS

First of all, it is noted that the two entropic terms appearing in the forcing function of the wave equation (10) are of the form $\beta_p^2 \Delta S$. These will be considered for the case of shock application as well as that of frictional flows.

An engineering application of the wave equation to the acoustic emission of unsteady shocks has been initiated by the author (ref. 1). In this acoustic analogy, the process parameter β_ρ^2 becomes a function of the initial states of transition:

$$\beta_\rho^2 = \frac{\dfrac{a_o^2}{\gamma-1}\left\{\left(\dfrac{2\gamma M_o^2 \sin^2 8-(\gamma-1)}{\gamma+1}\right)^{\frac{\gamma-1}{\gamma}}-1\right\}}{\left\{\left(\dfrac{(\gamma+1)M_o^2 \sin^2 8}{(\gamma-1)M_o^2 \sin^2\theta+2}\right)\left(\dfrac{\gamma+1}{2\gamma M_o^2 \sin^2\theta-(\gamma-1)}\right)^{\frac{1}{\gamma}}-1\right\}} \tag{12}$$

Here M_o is the initial transition mach number and 8 is the angle of inclination of the shock wave.

Now as $M_o^2 \sin^2 8$ approaches unity so that $M_o^2 \sin^2\theta = 1+\epsilon$, it can be readily verified that

$$\lim_{\epsilon\to 0} \beta_p^2 = 0\left(-\frac{1}{\epsilon^2}\right)$$

Moreover, because the entropy variation through a weak shock is of third-order variation in E, it follows that the entropic work increment is of first-order variation even for the case of weak shock waves.

Another typical example of entropic magnification effects is the application of the thermodynamic J_p-process to the problem of frictional and compressible duct flows. For this simple one-dimensional flow, the momentum equation takes on the following form:

$$d\left[\frac{1}{2}U^2+\frac{\gamma R}{\gamma-1}T\right]=\frac{\beta_p^2}{C_p}dS-2\frac{f}{D}U^2\,dx \tag{13}$$

This equation is based upon a thermodynamic process that is represented by straight lines, as the fluid particles move from some initial state A to some finite state B, in the J_p–S-plane.

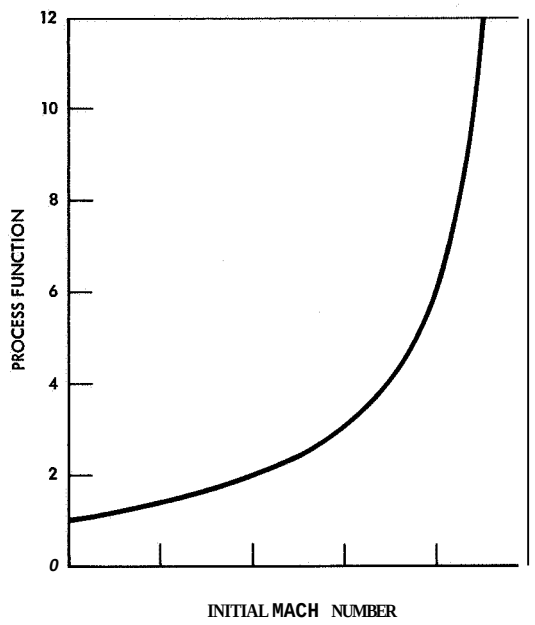

FIGURE 1.—Process functions versus initial mach-number subsonic flow.

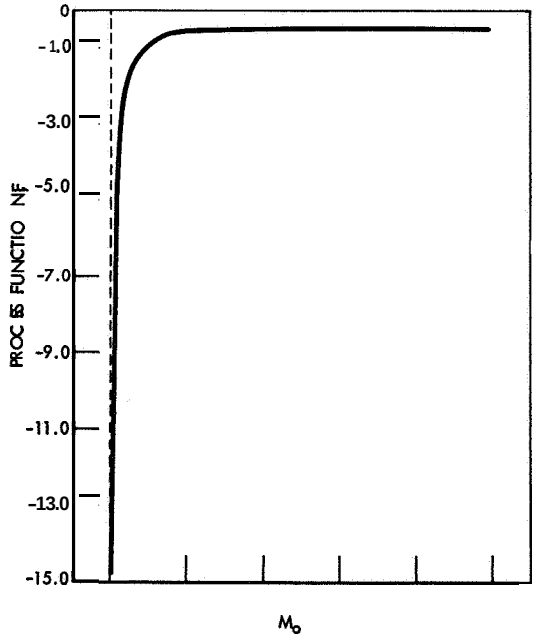

FIGURE 2.—Process functions versus initial mach-number supersonic flow.

It should be noted that equation (13) still admits of two degrees of freedom with respect to the thermodynamic processes considered.

An application of this equation to the case of isothermal duct flows duplicates the results of classical approaches (ref. 4). However, for adiabatic flows, this is not the case.

In the first place, the left-hand side of equation (13) vanishes identically in adiabatic frictional flows, regardless of whether or not the process is reversible or irreversible. This results in the simplified form of the momentum equation given by

$$\frac{\beta_p^2}{\sim} dS = 2 \frac{f}{\sim} U^2 \, dx \tag{14}$$

Next, the process parameter β_p^2 may be evaluated by using the remaining equations of motion coupled with the caloric equation of state.

The resulting differential equation takes on the following form:

$$\left\{ \frac{\left(\frac{M_o^2}{M^2}\right)^{\frac{\gamma-1}{2\gamma}} \left(\frac{1+\frac{\gamma-1}{2} M_o^2}{1+\frac{\gamma-1}{2} M^2} \right)^{\frac{\gamma-1}{2\gamma}} - 1}{\left(\frac{M_o^2}{M^2}\right)^{\frac{\gamma-1}{2\gamma}} \left(\frac{1+\frac{\gamma-1}{2} M^2}{1+\frac{\gamma-1}{2} M_o^2} \right)^{\frac{\gamma+1}{2\gamma}} - 1} \right\} \left[\frac{1-M^2}{1+\frac{\gamma-1}{2} M^2} \right] \frac{a_o^2}{\gamma M^2} \, dM^2 = 4 \frac{f}{D} U^2 \, dx \tag{15}$$

Here, the subscript o denotes the intial isentropic condition from which the J_p-process starts, in accordance with the previous formulation.

When the initial conditions are reflected by stagnation flow so that the initial mach number M_o vanishes, equation (15) reduces to the classical form:

$$\left[\frac{1-M^2}{1+\frac{\gamma-1}{2} M^2} \right] \frac{dM^2}{\gamma M^4} = 4 \frac{f}{D} dx \tag{16}$$

However, for each finite initial mach number, the contribution of the entropic effects to frictional phenomena is greater than that represented by this classical equation. Some aspects of this magnification effect can be obtained from the plotted data.

Figure 1 represents the initial jump conditions caused by the duct-entrance phenomena for the case of subsonic flow. It is noted that as the initial mach number approaches unity, the magnitude of this jump tends to infinity. However, differential equation (16) has no singularity there because the entropy differential has a zero at the sonic point and the two cancel out.

Figure 2 depicts the initial contribution of the entropic process for

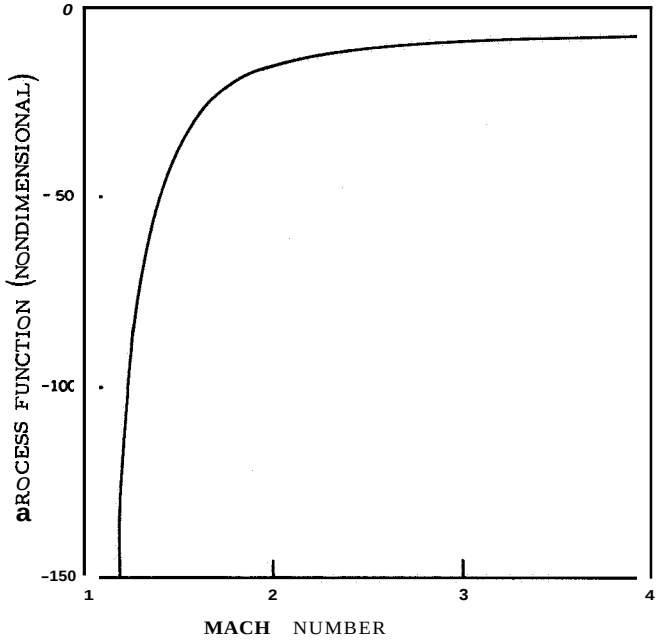

FIGURE 3.—Process function versus initial mach-number shock transition.

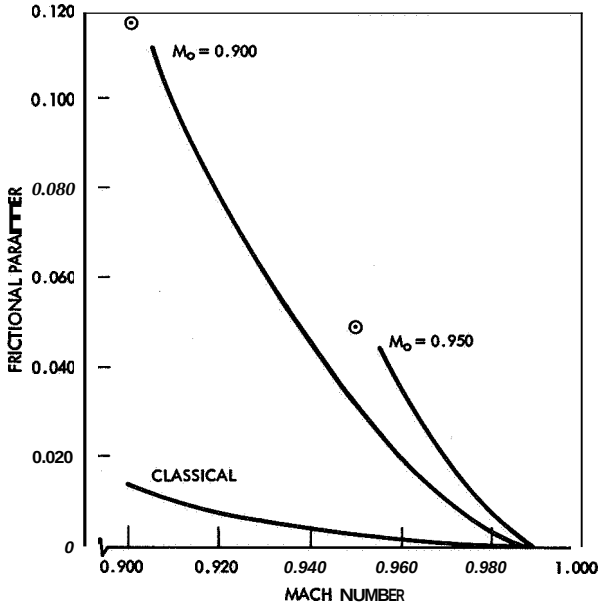

FIGURE 4.—Frictional effects near sonic conditions.

the case of supersonic flow. In this case, the process parameter is negative and tends to negative infinity as sonic conditions are approached. As in the previous case, the complete differential equation is finite at the sonic point.

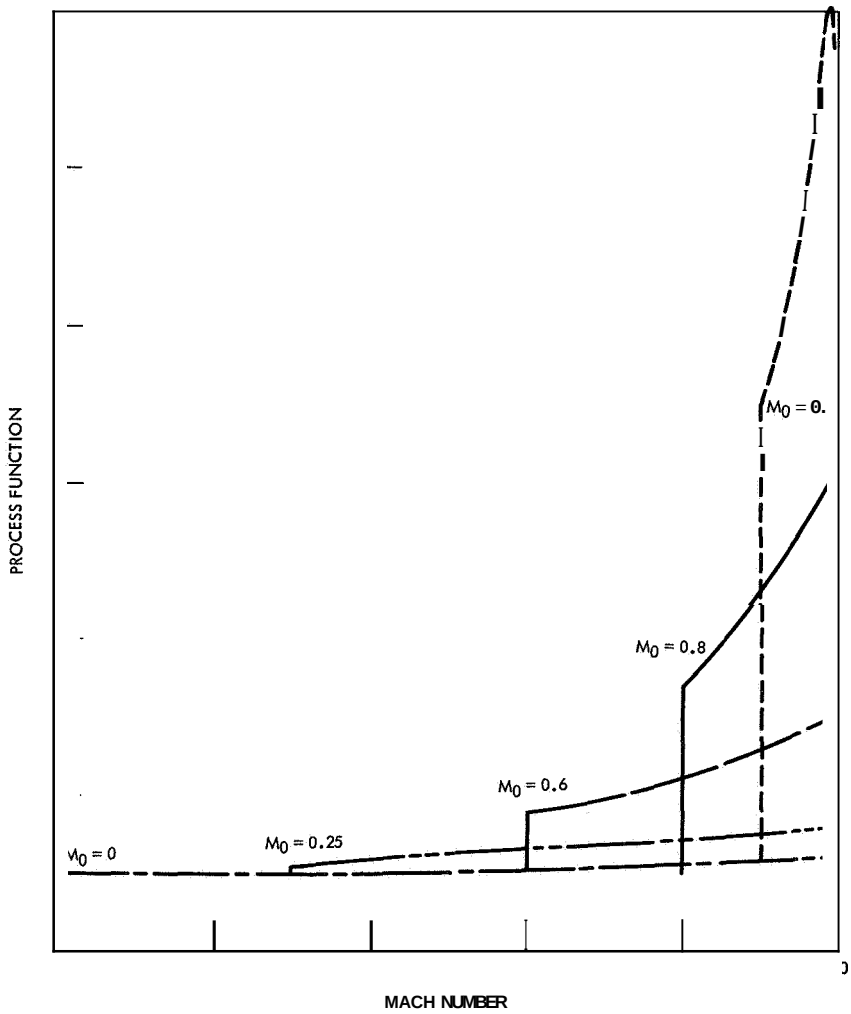

FIGURE 5.—Process functions versus mach number for various initial conditions.

Figure 3 represents the corresponding values of the entropic effects based on shock transition values. It is seen that the curve is similar to that of figure 2, but its corresponding numerical values are different.

Figure 4 compares the frictional effects of entropy generation to the classical solution of the problem. The initial isentropic mach numbers

considered here are $M_o=0.9$ and $M_o=0.95$. Obviously, the classical solution, having no historical effects, is the same for all initial isentropic mach numbers.

Figure 5 represents the variation of the process parameter β_p^2 as a function of local mach number for various initial conditions. It is seen that as the initial isentropic mach number increases, the successive frictional flow gradients also increase.

The preceding discussion of entropic effects in gases has been presented as a factual consequence of the J_p-process formulation. The author has also obtained the pertinent thermodynamic J_v-function whose resultant J_v-process admits of the following entropic work integral:

$$\int p d\left(\frac{1}{\rho}\right)=-\int \frac{\beta_v^2}{C_p} ds \tag{17}$$

where

$$\beta_v^2=-\frac{a_o^2}{\gamma-1}\left[\frac{E_v \frac{T}{T_o}-1}{E_v-1}\right]$$

In future publications, the extremum properties of these entropic work integrals will be discussed and it will be shown that under certain conditions

$$d\left(\frac{p}{\rho}\right)=\left[\frac{(E_v-E_p)^2}{(E_v-1)^2 \frac{E_p}{C_p}-(E_p-1)^2 \frac{E_v}{C_v}}\right] dT \tag{18}$$

This equation suggests that a perfect gas may be degraded when subjected to high entropy gradients.

These considerations illustrate the nature of entropic effects and their historical importance in flow development. Its application to the flow-noise problem indicates that the triggering mechanism of high-speed noise depends to a large extent upon past history and, therefore, upon the irreversible characteristics of the nozzle in question. If so, it appears that local mach-number effects are not sufficient to model high-speed noise generation.

REFERENCES

1. PETER, A. C.; AND COTTRELL, J. W.: An Investigation To Define the Propagation Characteristics of a Finite Amplitude Pressure Wave. NASA CR 735, 1967.
2. PETER, A. C.: Non-Isentropic Acoustic Wave Generation. J. Acoust. Soc. Am., vol. 45, 1968, 339(A).
3. PHILLIPS, O. M.: On the Generation of Sound by Supersonic Turbulent Shear Layers. J. Fluid Mech., vol. 9, pt. I, 1960, pp. 1–28.
4. PETER, A. C.: Non-Isentropic Finite Amplitude Wave Generation. SD69–108, Apr. 1969.

EFFECT OF DUCT HEATING ON JET AND FAN NOISE*

Harry E. Plumblee
LockheedGeorgia Co.
Marietta, Ga.

It was established in **1952** (ref. **1)** that jet density has a significant effect on radiated sound power and sound-pressure directivity, with a series of experiments on helium, air, and Freon jets. A later series of tests (ref. **2)** established the effect of jet temperature on jet sound-pressure level. As a result of the reference **3** tests, it was hypothesized that jet heating could be used to reduce radiated jet noise because it was observed that increasing jet temperature, at constant velocity, resulted in decreased radiated sound-pressure level. It was further hypothesized that a burner introduced in the fan duct of a fanjet engine (aft of the fan compression stage) might reduce radiated fan noise because the fan-generated noise must propagate through the high-temperature region prior to radiation.

This paper summarizes the previous work and describes a series of tests in which temperature effects on jet noise were determined quantitatively, and the effect of pure-tone propagation through a high-temperature jet flow was evaluated qualitatively.

It was found that, at low temperatures, the jet sound power is linearly proportional to jet density, but that at temperatures above approximately 1000" R, the decrease is predicted to be markedly greater than the linear relationship. At **3500**" R, the prediction technique indicates a reduction in jet sound power of the order of 6 to 8 dB more than expected from the linear relationship.

It was also shown that the effect of the high-temperature flow on a pure tone propagating through the flow is similar to that of a tuned vibration absorber; **i.e.,** at certain frequencies, the sound is amplified, and at others it is highly attenuated.

*Supported by contract **NAS1-8443, NASA** Langley Research Center.

SYMBOLS

A	exhaust area
c	speed of sound
$DI(\theta)$	directivity index
I	sound intensity
M	mach number
$\bar{p}$	root-mean-square sound pressure
PWL_N	sound-power level for l-in. nozzle
r	distance from source location to field point, nondimensionalized to nozzle exit diameter
T	total temperature in °R
T_S	exit static temperature in °R
V	exit plane velocity
θ	angle from field point to jet thrust axis, referenced to nozzle exit plane
ρ_j	jet density (static)
ρ	atmospheric density
τ	thrust
ω	radial frequency

INTRODUCTION

This program, an experimental study of temperature-density effects on radiated jet and fan noise, was initiated because of the continued and ever-increasing interest in both describing aircraft engine noise-generating mechanisms and devising means of reducing that noise. Although the experiments described here are by no means complete, the results presented are perhaps interesting enough to stimulate further research in the area.

Primarily, this paper describes results from two independent jet-noise experiments which explore temperature effects (refs. 2 and 3). It then exploits an empirically derived (ref. 2) expression for predicting jet noise to extend the range of the reference 3 experiments to provide an estimate of effects of high temperatures, at relatively low velocity, on radiated sound-power level. The paper also suggests the possibility of using high-temperature burning in a fan duct as a means of selectively filtering fan-generated pure tones, as discussed in reference 4.

TEMPERATURE EFFECTS ON AIRCRAFT ENGINE NOISE

It is now well known that pure-tone noise can virtually be eliminated in the design of a fan engine. Many basic research experiments have shown how this is to be accomplished. The next generation of turbofan engines (RB–211, JT9D, CF6) will incorporate many of these design

improvements for noise reduction, and NASA Lewis is going still farther in designing two quiet engines that may essentially eliminate annoying pure-tone radiation. However, many of these design features result in a degradation of performance, and tradeoff studies involving engine weight, performance, and noise output might well show that an engine designed for maximum performance at minimum weight prior to the noise-elimination design would fare just as well as the low-noise design. Also, once the pure-tone noise is effectively reduced into the jet-noise floor, jet noise must then be reduced before further improvements in noise output can be achieved.

This study, then, was aimed at investigating the effect of duct heating as a new method of reducing both fan-noise and jet-flow noise. The research was essentially divided into two separate experiments: one to determine the effect of temperature on jet noise, and the other to show the effect of temperature on fan noise.

Temperature Effects on Jet Noise

Prior to this work, several studies have been conducted to show the effects of density on radiated jet noise. Notably, Lassiter and Hubbard (ref. 1) tested helium, Freon, and air jets and demonstrated that radiated mean-square sound pressure at 90° to the jet-exhaust centerline was proportional to the square of density. Other studies concluded that jet density, when controlled by temperature, was a relatively ineffective factor in changing jet power. For instance, Rollin (ref. 5) concluded that sound power was unaffected by jet density, and Regier (ref. 6) came to essentially the same conclusion.

However, a more recent set of tests by Plumblee (ref. 2), using measurements from a free-field jet, indicated that sound pressure at 90° to the jet axis was proportional to jet density to a power varying from 1.6 to slightly over 2, depending on the velocity. The reference 2 tests formed the basis for the study reported here, and results from the reference 2 analysis are used in a later section of this report to discuss trends.

It is well known that radiated sound power in a jet engine is proportional to jet velocity raised to a power somewhere between 3 and 8, depending on the nature of the jet flow. Whatever the power might be, it is better to run the temperature-effect tests at constant velocity to eliminate the very significant sound pressure variations with minor velocity variations. It is also wise to conduct the tests with several nozzles to average out peculiarities in the data that can be attributed to individual nozzles.

To accomplish these aims (ref. 3), a model jet was installed in the Lockheed-Georgia Co. Research Laboratory anechoic room, and the air and temperature control system was equipped with pneumatic servo-

controls. Hot air was supplied from a propane burner located outside the laboratory and was exhausted through a muffler in the ceiling of the anechoic room. Four nozzles were tested with diameters ranging from **0.9** to 2.00 in. Sound pressure was measured at 12 positions along an arc in the far-field exhaust quadrant centered at the nozzle-exit-plane centerline. The measured sound pressure was then used to calculate radiated sound power.

Effect of Velocity on Total Acoustic Power

Before trying to ascertain the effect **of** temperature, it was necessary to establish what velocity law the model jet was following, since the 8th-power law is not always found in practice. For instance, in reference ***2,*** something closer to a 6th-power law was experimentally determined. Also, reference 7 reported a 6th-power law for a full-scale turbojet. Figures 1 and 2 are plots of the sound-power level, showing the functional relationship with exit velocity for all four nozzles and two different exit static temperatures. The solid lines are 8th power. From examination of the data in these two charts, it is justifiable to specify 'an 8th-power velocity law for the tests in this analysis.

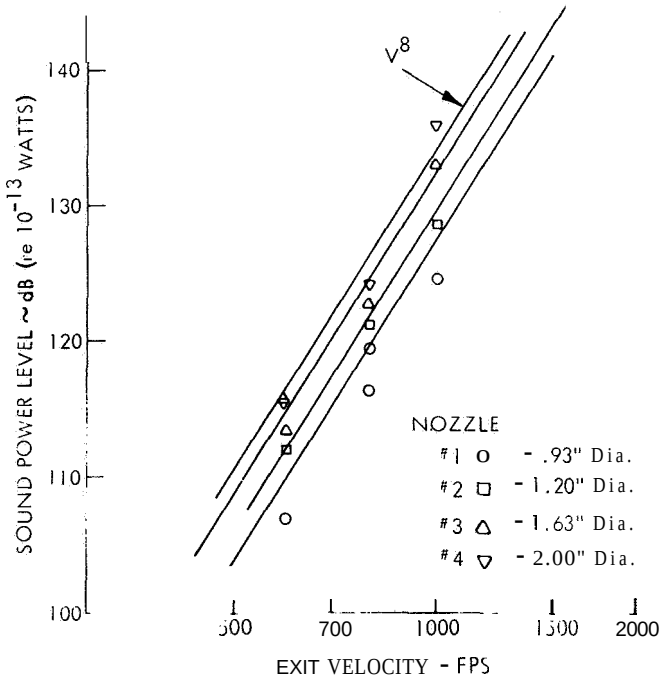

FIGURE 1.—Effect *of* velocity *on* sound power level, exit temperature 540° R.

The 8th-power trend lines for each nozzle are separated by 10 log A_n/A_4, where A_n/A_4 is the ratio of nozzle area referenced to the largest nozzle area. It is observed that all the data are fairly accurately separated by the nozzle area ratio, except for the smallest nozzle.

Effect of Temperature on Total Acoustic *Power*

If an existing engine were equipped with a duct burning system purely as a means of reducing jet noise, assuming this is possible, it would be vital to constrain two principal variables: velocity, which is directly related to sound power generation, and thrust, which is a primary indicator of performance. If the radiated sound power is then normalized to velocity and thrust, any variations in the normalized sound power with temperature could be directly attributed to temperature.

Figure 3 is a plot of measured sound-power level normalized to $\rho_j A V^8$, which is equivalent to τV^6. It is concluded from the composite data shown in figure 3 that sound power is linearly proportional to jet density for the range of temperature of the tests reported here. The variations in the data are attributed primarily to mean pressure fluctuations during the data acquisition. However, because these variations are significant

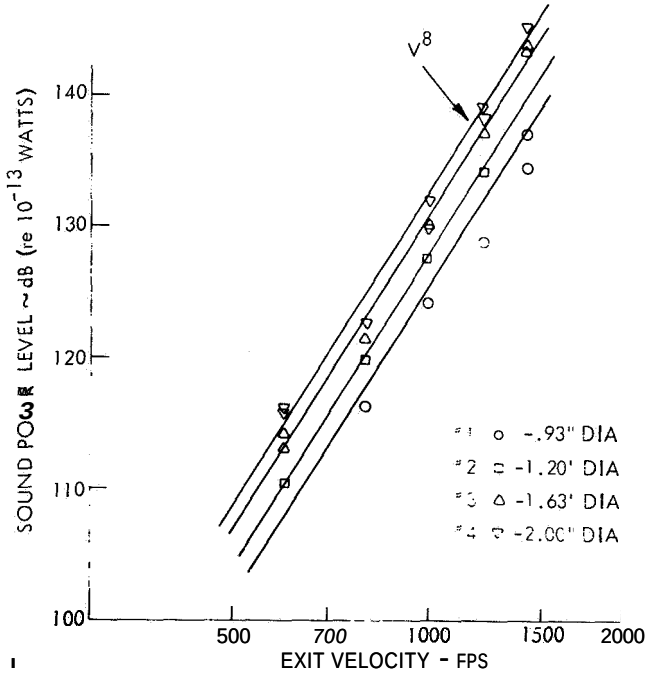

FIGURE 2.—Effect of velocity on sound power level, exit temperature 900° R.

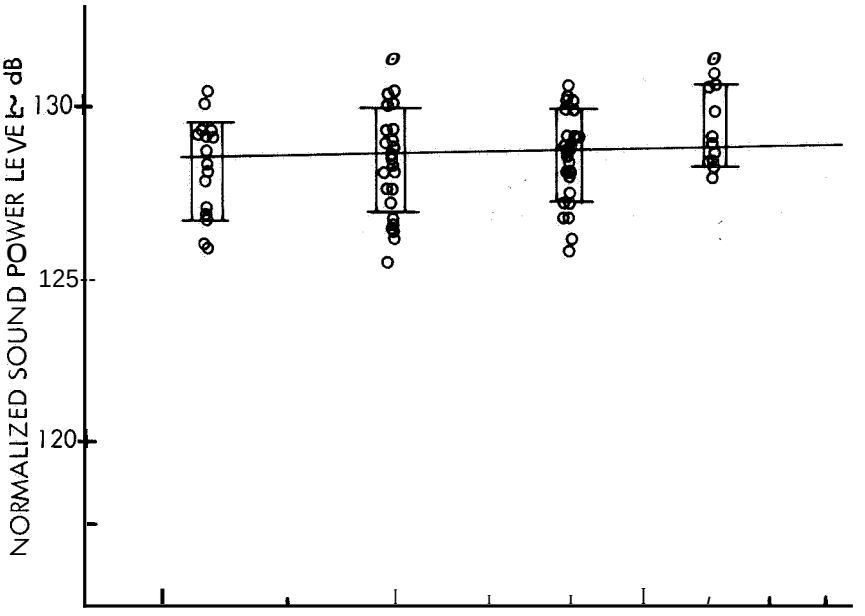

enough to introduce doubt concerning the trend, other available data are studied in the following discussion.

Also, because it was not possible to make tests at higher temperatures in the anechoic room because of valving and room cooling difficulties, the only practical way to determine the temperature effect at higher temperatures was to refer to previous tests. In reference **2,** a series of tests was conducted at temperatures as high as **2800"** R static temperature. Velocities ranged as high as 3700 fps and as low as **880** fps. All the data are in terms of sound pressure level (SPL), and an empirical relationship is given for calculating SPL at any point in the near or far field.' It is possible to determine total sound power from the results of reference **2** if intensity ($I=\bar{p}^2/\rho c$ is assumed) is numerically integrated over a reference sphere. The formula for mean square pressure is

[1] There is an error in ref. **2** that could lead to misuse of the data. On p. 15, table I, the temperature given is total temperature and the speed of sound and velocity were mistakenly calculated based on total temperature instead of static temperature. It should also be observed that the prediction formula for sound pressure requires total temperature instead of static temperature.

$$\bar{p}^2=\frac{KT^sM^n(1+\alpha^2+M^2)^{5/2}\ (1+\cos^4\theta)\left(\frac{c_1}{r^2}+\frac{c_2}{r^4}+\frac{c_3}{r^6}\right)}{\left[\left(1-\frac{M\cos\theta}{1+c_6e^{-c_7r}}\right)^2+\alpha^2M^2\right]^{5/2}\left(1+\frac{c_4e^{-c_5\theta}}{1+c_6e^{-c_7r/4}}\right)} \tag{1}$$

For large values of r, the nondimensional (nondimensionalized to nozzle exit diameter) field distance (say $r>20$), several terms may be discarded from this expression. On assuming large r, the equation becomes

$$\bar{p}^2=\frac{c_1KT^sM^n(1+\alpha^2M^2)^{5/2}(1+\cos^4\theta)}{r^2[(1-M\cos\theta)^2+\alpha^2M^2]^{5/2}(1+c_4e^{-c_5\theta})} \tag{2}$$

For calculating overall sound pressure, the parameters in the equation are

$$\left.\begin{aligned} c_1&\equiv M^{2.34}\\ KT^sM^n&=4.63\times10^{-8}T^{1.54}M^4\\ \alpha^2&=0.823M^{-1.24}\left(\frac{T}{1000}\right)^{-2.3+1.47M}\\ c_4&=45.76M^{2.11}\left(\frac{T}{1000}\right)^{3.37-2.39M}\\ c_5&=12.8M^{-1.82}\left(\frac{T}{1000}\right)^{-1.79+1.16M}\end{aligned}\right| \tag{3}$$

This expression was evaluated for power level in a small digital computer program. The results of the power-level calculations are shown in figure 4. The power-level data are plotted against temperature for curves of constant velocity, which correspond to the velocity points for the tests discussed earlier in the report. It is quite evident that, at temperatures up to 1200° R or 1500" R, the assumption that power is inversely proportional to jet temperature is matched by the prediction method. However, at higher temperatures, the prediction technique indicates that sound power falls off much more rapidly so that, at 3000° R, reductions are found that are larger by 5 to 6 dB than would be achieved with an inverse-temperature law. This prediction of reduction requires more discussion.

It appears from the prediction technique (fig. 4) that significant reductions in radiated sound power are possible by heating the jet to static temperatures of the order of 2500" R to 3000° R at relatively low velocities. To examine this in more detail, the velocity range of figure 4 is expanded in figure 5. Along with the constant velocity curves, constant mach-number curves are also plotted corresponding to the reference 2 tests. All the predictions below the mach-0.8 curve at temperatures greater than 1100" R are then extrapolated and certainly would require

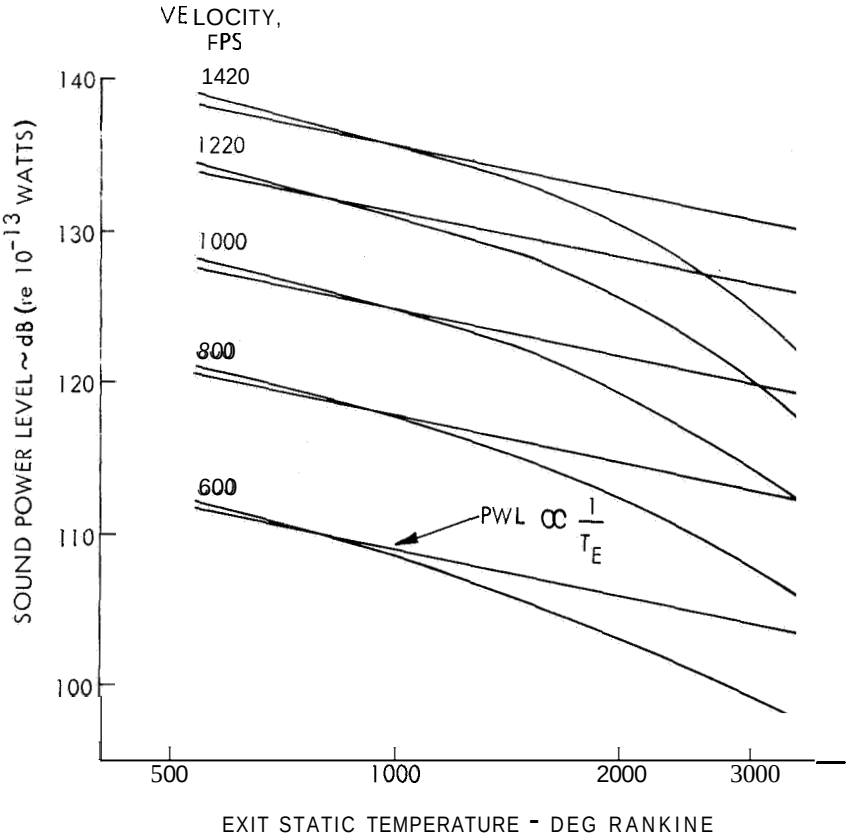

FIGURE 4.—Effect of jet temperature on total sound power for 1-in. nozzle (ref. 2).

validation for proof. If the effect of temperature at constant exhaust mach number is examined, the prediction indicates different effects, depending on the mach-number value. At subsonic mach numbers, the slope of the curve for constant mach number decreases at high temperatures, while at high mach numbers, the slope is almost constant (proportional to $T^{1.5}$).

It is instructive to compare the prediction method with the data from which the method was derived to show the scatter and also with the data from the reference 3 tests. The data used in the derivation of the prediction method are shown by the solid symbols. All the data are within 3 dB of the predicted power levels. Also, the data from the reference 3 tests are shown as mean values with the calculated standard deviation. Here again, the comparison is within ±3 dB in all cases. However, before the prediction method could be used with confidence in the temperature

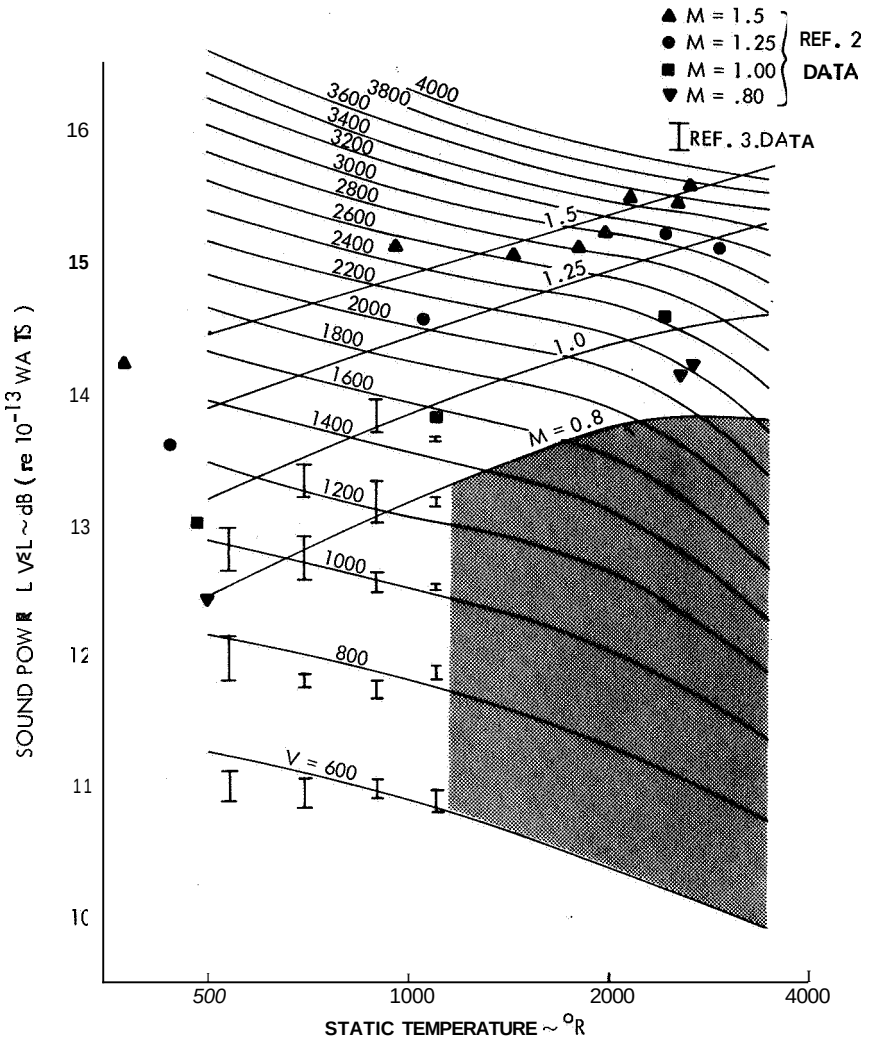

FIGURE 5.—Effect of jet velocity, mach number, and static temperature on total sound power including measured data and reference 2 prediction method.

region greater than 1100°R for mach numbers less than 0.8, more experimental data are required to verify the trends. This region on the plot is shown as a shaded area. Semrau (ref. 8) ran a series of tests with high-temperature jets, covering approximately the same mach-number–temperature range as the data from which the prediction method discussed here was developed. Figure 6 is a presentation of power level, as measured by Semrau, plotted against static temperature for constant exhaust

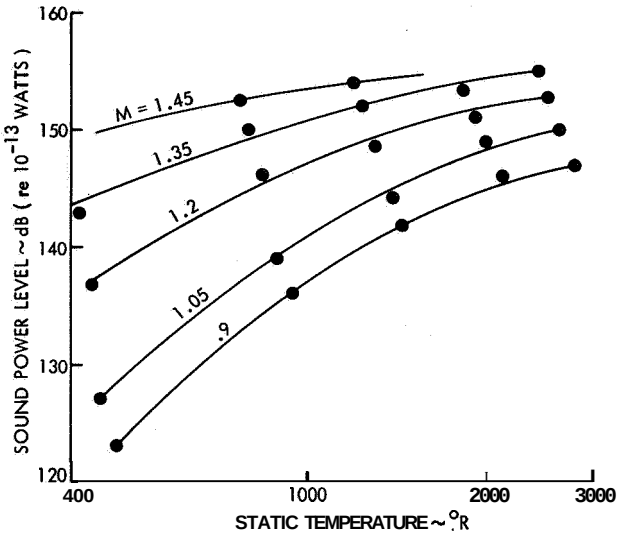

FIGURE 6.—Effect of mach number and static temperature on radiated sound power level (based on Semrau's data, ref. 8).

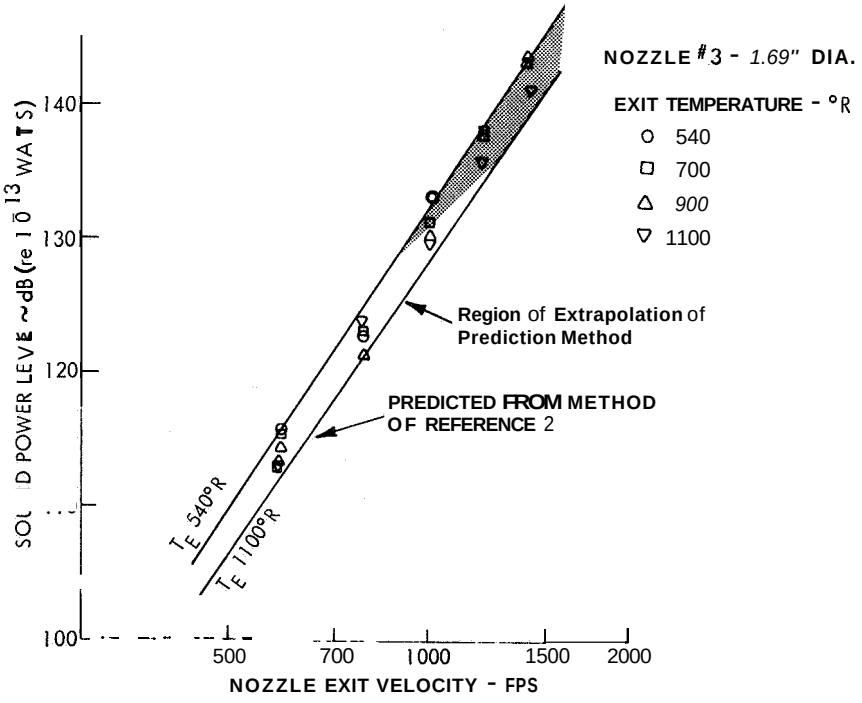

FIGURE 7.—Comparison of measured sound power level and prediction method.

mach number. Without comparing absolute values (they differ by as much as 7 dB), it is observed that the slope of the curve for constant mach number decreases as temperature is increased. This effect is more predominant at low mach number, which is essentially the same trend as shown by the prediction method portrayed in figure 5.

As a further check on the validity of the prediction method outside the range of the data used to derive the method, power levels were calculated for individual test points of the reference 3 tests by Haddle. These calculations, as well as the measured data, for the 1.69-in.-diameter converging nozzle are shown in figure 7. The overlap range for the prediction-method data and Haddle's data is shown as a shaded area in the

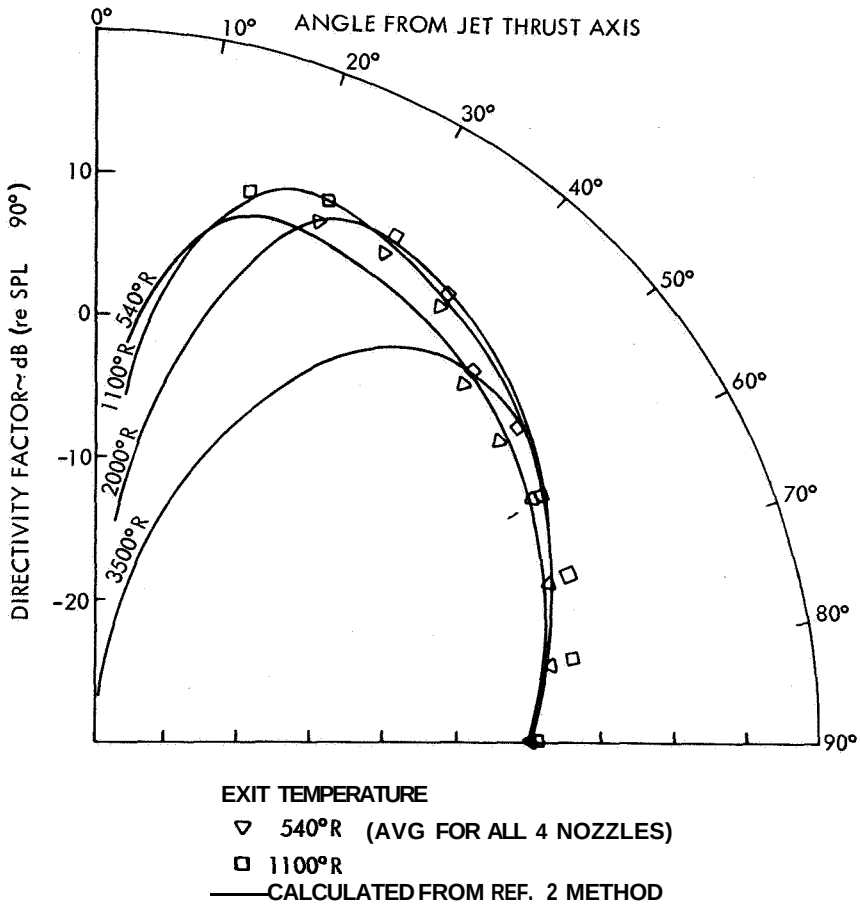

FIGURE 8.—Effect of temperature on directivity factor, comparison of prediction method with measured data, exit velocity 1000 fps.

upper right-hand side of the plot. All the data below this shaded area represent an extrapolation of the prediction method. The comparison is quite acceptable; the maximum error is only 2 to 3 dB, and the mean deviation is considerably less.

Therefore, up to this point, the comparison seems to be fairly accurate for overall sound-power level, but because the reference 2 prediction technique was actually developed for both near- and far-field sound pressure, a comparison of measured and predicted sound-pressure fields would be more indicative of the accuracy of the prediction method. At this point, instead of comparing actual SPL, directivity will' first be examined. Figure 8 shows calculated directivity at a jet velocity of 1000 fps for a wide range of temperatures. The measured data are taken from the reference 3 tests. The SPL normalized to SPL at 90" is plotted for four different temperatures, and the measured directivity is shown for 540" R and 1100° R. Here, the comparison for the prediction and measured data is considered to be quite satisfactory, and the trends attributed to temperature change based on the measured data are reasonably predicted.

So, to summarize the effect of temperature on jet noise, in the range where data exist, there are some significant reductions in noise with increasing temperature. The prediction method developed from these data adequately predicts sound power and overall sound-pressure level outside the range for which it was developed at temperatures below 1100" R. If the prediction method is used at higher temperatures for the range of fan-engine-exhaust velocities, significant reductions in jet noise are predicted. However, more data should be obtained in this velocity-temperature range.

Prediction Method for Calculating Community Noise

Because of the apparent accuracy of the prediction method in its applicable range, a simplified design procedure has been developed. It involves using figure 5 to determine sound-power level and figure 9, which gives directivity indices, for determination of various velocities and temperatures. The directivity indices in figure 9 have been plotted so that there is a constant difference between PWL and SPL at 90". The formula for determining SPL is then

$$\mathrm{SPL} = PWL_N + DI(\theta) - 20 \log r + 6 \tag{4}$$

where r is distance nondimensionalized to nozzle-exit diameter and is not to be less than 20 diameters, $DI(\theta)$ is directivity factor determined from figure 9, and PWL_N is power level for a 1-in.-diameter nozzle.

To determine the angular distribution of far-field jet noise using equation (4), first determine the normalized power level from figure 5. This

requires exhaust plane static temperature and exhaust velocity, or exhaust local mach number (referenced to sound speed in the flow). If total temperature and mach number are known, figure 10 can be used to determine static temperature. Figure 11 is useful for determining relationships between velocity, mach number, and static temperature. Once power level is determined, find the directivity curve in figure 9

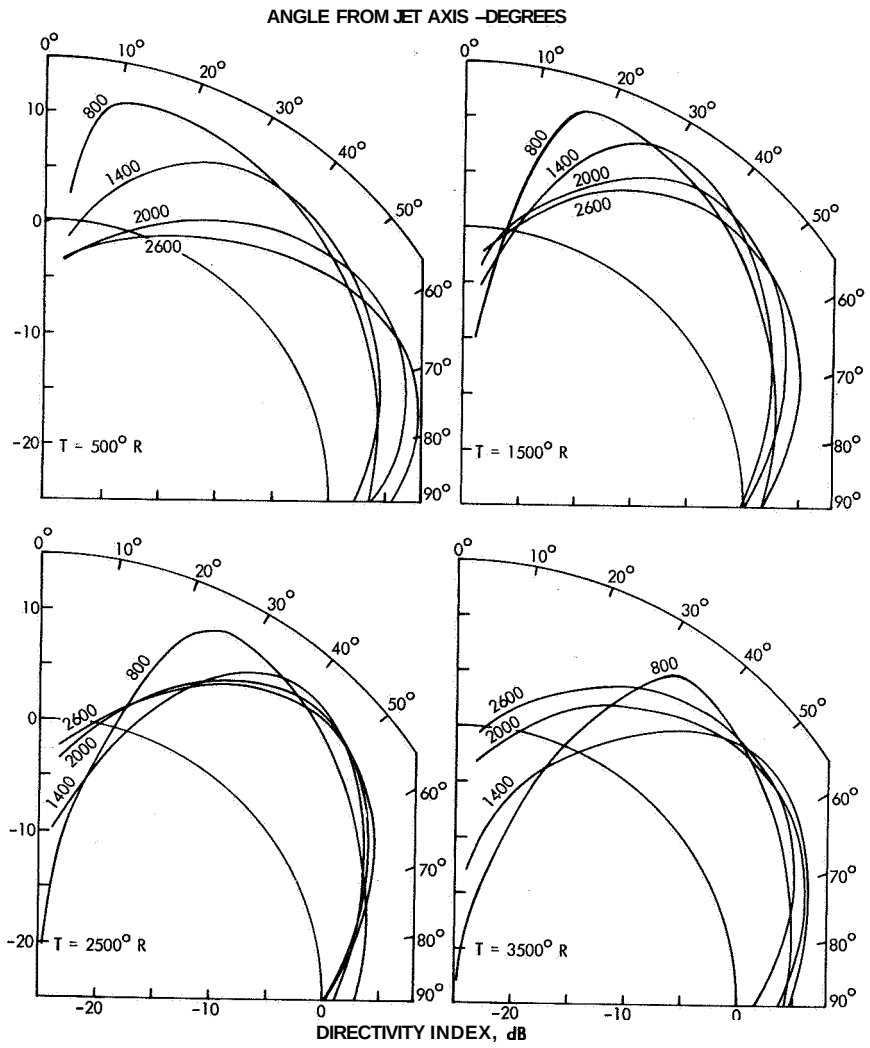

FIGURE 9.—Generalized directivity indices for determining effects of temperature and velocity.

that most closely approximates the exhaust condition (or interpolate between the curves) and determine a directivity factor. Then determine the distance factor from figure 12. Finally, these factors are combined as indicated in equation **(4).**

This prediction method is only for overall SPL and, of course, no correction is given for high-frequency attenuation with distance. Also, spectra are not given in the prediction method. References 2, 3, and ***8*** can be used to obtain estimates of the effects of temperature on spectra.

Effects of Temperature on Simulated Fan Noise

It was speculated that the addition of heat to the bypass air of a fan-engine exhaust would not only change the character of the jet noise but

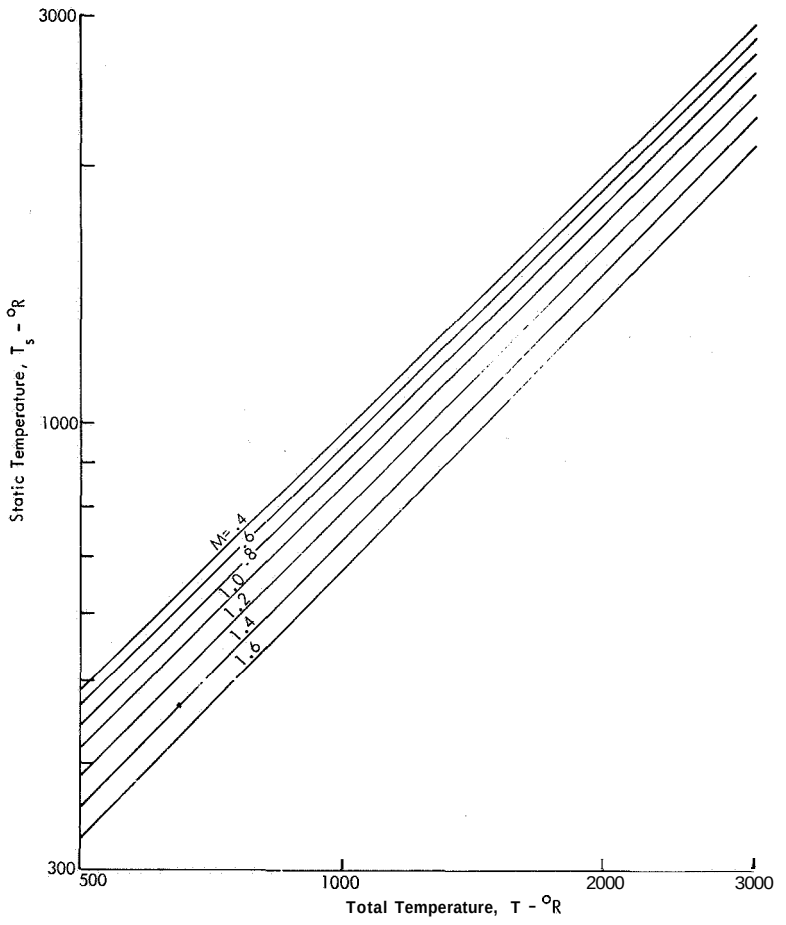

FIGURE 10.—Static temperature functional relationship with mach number and total temperature (variation of specific heat, γ, for air with static temperature used).

would also significantly affect the propagation of fan tones through the heated region. The only sure way to determine the effects would involve testing of a full-scale or model fan engine or development of a theory. Precluding these efforts because of expense, it was possible to get a qualitative laboratory evaluation of the effect.

Schematically, the proposed modification to an engine would be as shown in figure 13(*a*). A diffuser would be added to the fan duct to slow the fan air, fuel would be injected, and burning would occur. An acoustic schematic of the engine (fig. 13(*b*)) shows that fan noise is generated in

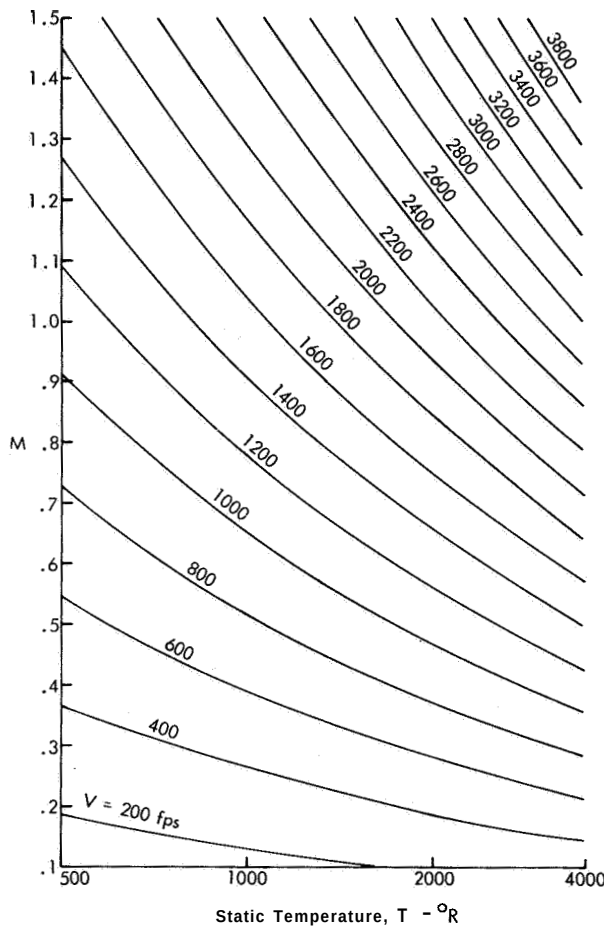

FIGURE 11.—Variation of mach number with static temperature and velocity (variation of specific heat, γ, for air with static temperature variations used).

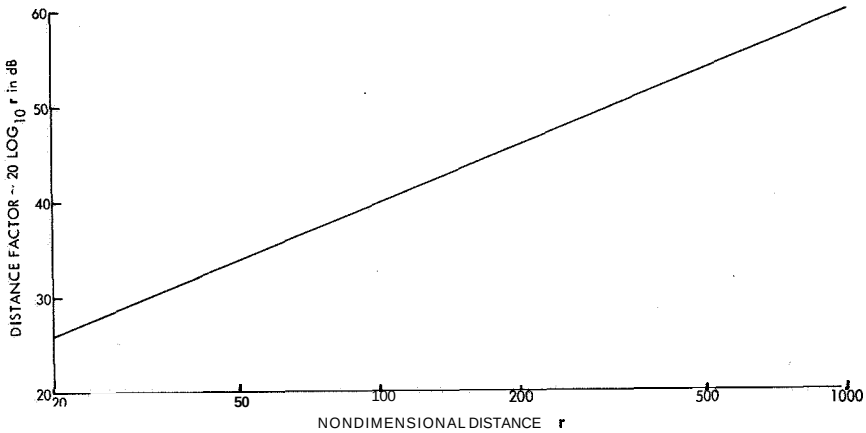

FIGURE 12.—Distance factor for use with jet-noise-prediction procedure.

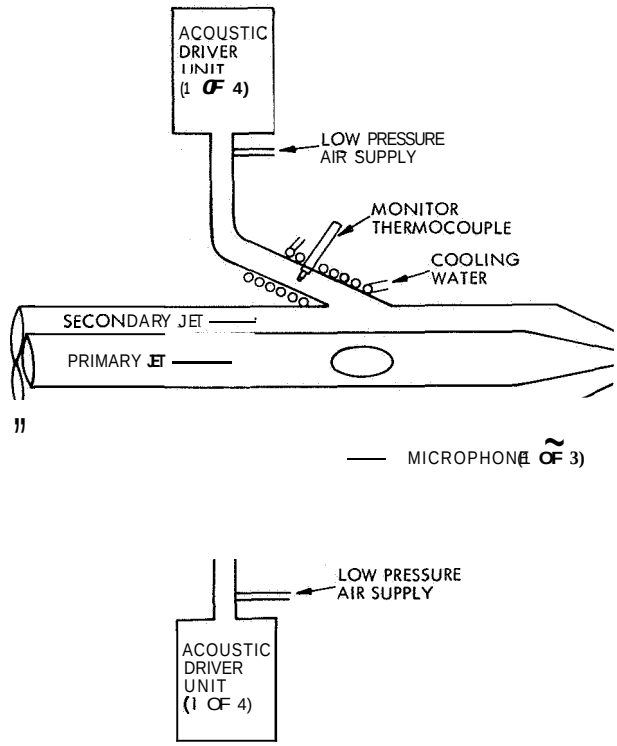

FIGURE 14.—Schematic of test set up to evaluate effect of bypass air heating on pure-tone sound radiation.

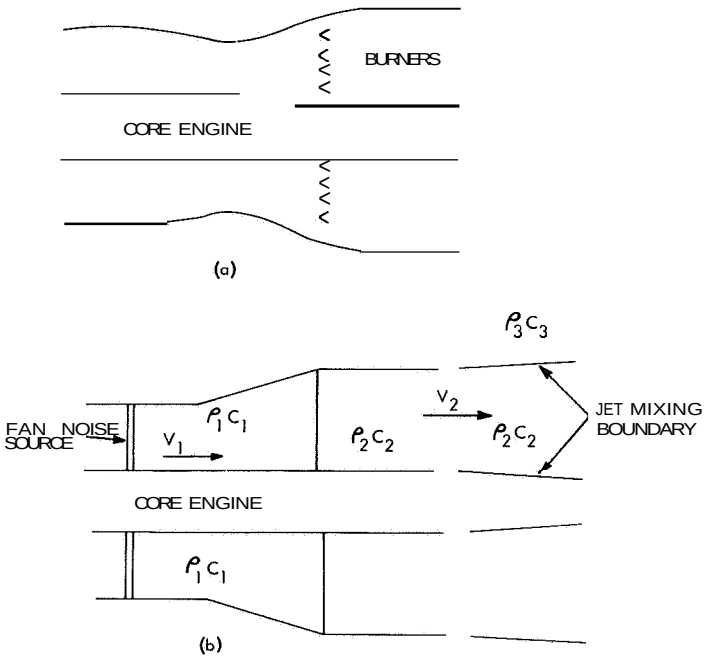

FIGURE 13.—Schematic of fan engine with duct burning.

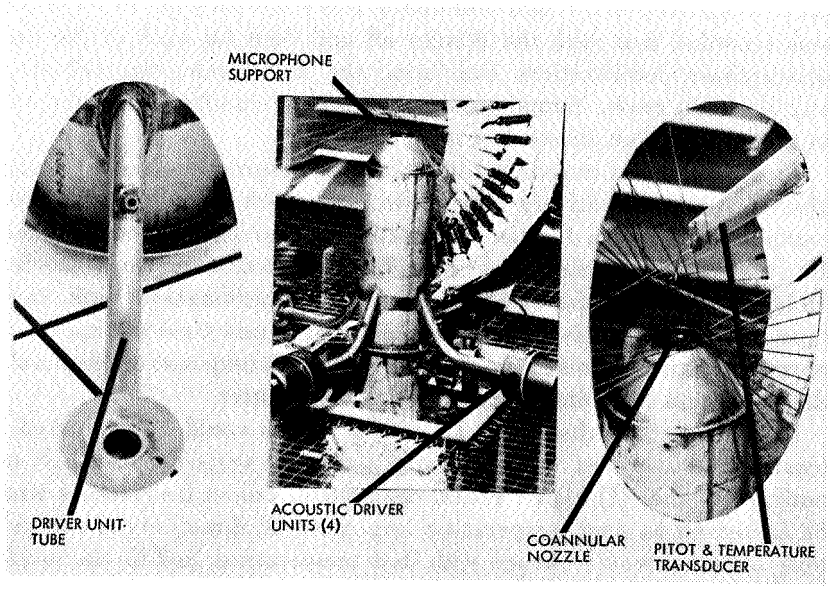

FIGURE 15.—Model jet nozzle set up for determining temperature effects on radiated pure-tone noise.

medium 1, which then must refract through the burning boundary into medium 2, and later through the jet mixing boundary and into medium 3.

A simple experiment was designed to obtain order-of-magnitude effects of the high-temperature region on pure-tone propagation. In this experiment, a coannular jet was constructed in an anechoic room. The temperature of both the primary and secondary air jets could be individually controlled from ambient temperature to approximately 800° F. The secondary jet was constructed, as shown in figures 14 and 15, and four acoustic driver units were used to introduce pure tones into the secondary flow upstream of the nozzle exit plane.

Tests were run wherein the secondary air temperature was varied, while flow mach number was held constant. Another series of tests was run with secondary temperature varied at constant velocity. The constant mach-number runs were made because mach number is the parameter in duct-mode propagation theories. With constant mach number, all duct effects should be eliminated except for those attributed to temperature. The results of these tests are described below.

Effect of Secondary Flow Temperature on Pure-Tone Propagation Data Analysis

For each flow and temperature condition tested (ref. 4), radiated sound-pressure level was recorded in the far field at six angular positions, beginning at 15° and continuing every 15° through 90°. The SPL was recorded first with the drivers off and then for each of the three driver-phase combinations simulating the (0,0) mode, the (1,0) mode, and the (2,0) mode. Sound-pressure level was simultaneously recorded in three of the four driver-unit tubes.

A pure tone was introduced into the nozzle during the tests. During a given test run, the drivers were set into one of the three possible phase combinations, and a frequency sweep was made from 400 Hz to 8000 Hz, with constant electrical input to the acoustic drivers. All data, including the oscillator signal, were recorded on magnetic tape. In the tape playback analysis, a narrowband analyzer was used to improve the pure-tone signal-to-noise ratio, and the frequency response of the annular-duct radiation field was displayed on an $x-y$ plotter.

It was expected that three individual effects could be evaluated, at least qualitatively, as a result of the pure-tone tests described. It was anticipated that (1) higher order, duct-mode, cut-on frequencies would be increased as duct temperature increases; (2) directivity of the pure-tone radiation would change with flow temperature; and (3) the level of the pure-tone wave propagating through the high-temperature medium would change with temperature. These effects are discussed later.

Effect of Temperature on Higher Acoustic Duct Mode Cut-on Frequency

It can be shown theoretically that duct mode cut-on frequencies are proportional to the speed of sound in the duct (or the square root of duct temperature). Therefore, an increase in duct temperature results in an increase in duct cut-on frequency. This fact could be particularly useful if the fan happened to be generating a pressure distribution that was predominately propagating in a mode at or just above its cut-on frequency. If the cut-on frequency of this mode were raised by duct heating to a frequency greater than the frequency of the fan-pressure distribution, it was speculated that a significant attenuation could be evidenced in the radiated noise.

This behavior was verified to some extent in one phase of the testing. For instance, when alternate driver units were out of phase, a (2,0) mode pressure distribution was simulated. For this pressure pattern, as frequency is increased, the point at which significant pure-tone radiation begins is the cut-on frequency of the (2,0) mode. First, it is interesting to show the radiation characteristics of the duct-nozzle combination in the (2,0) mode without any flow and at ambient temperature. Figure 16 shows the normalized radiation response of the test duct when excited by a simulated (2,0) mode pressure distribution. To normalize the radiated

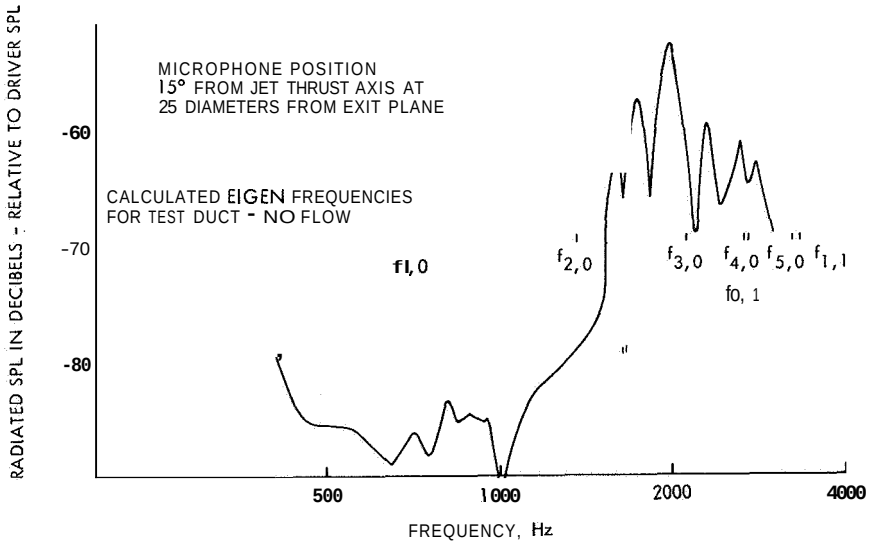

FIGURE 16.—Radiation response of annular test duct. Driving pressure phased to excite (2,0) mode. No-flow–ambient temperature condition calculated cutoff frequencies from appendix 111, Sofrin and Tyler (ref. 9) for hub-tip ratio of 0.5.

SPL, the SPL measured in one of the acoustic driver-unit tubes was subtracted from the radiated SPL. This gives the radiated SPL for a constant-amplitude sound pressure at the source. Of course, it makes no assumption about interaction of the thermal barrier and the source output.

Referring again to figure **16,** it is observed that significant radiation at a point **15°** from the jet axis begins at approximately **1550** Hz for no-flow and ambient temperature in the duct. The calculated cut-on frequency (using the tables in ref. 9) for an infinite-length annular duct with a **0.5** hub-tip ratio, in the (2,0) mode, is **1360** Hz. This is approximately 200 Hz lower than the measured value, but the test duct was fitted with a conical nozzle that reduced the 8-in. duct diameter to **3.5** in. The addition of the smaller diameter conical nozzle would certainly tend to increase duct cut-on frequencies. The shape of the normalized radiated SPL is similar at all six angular microphone positions but varies somewhat in amplitude.

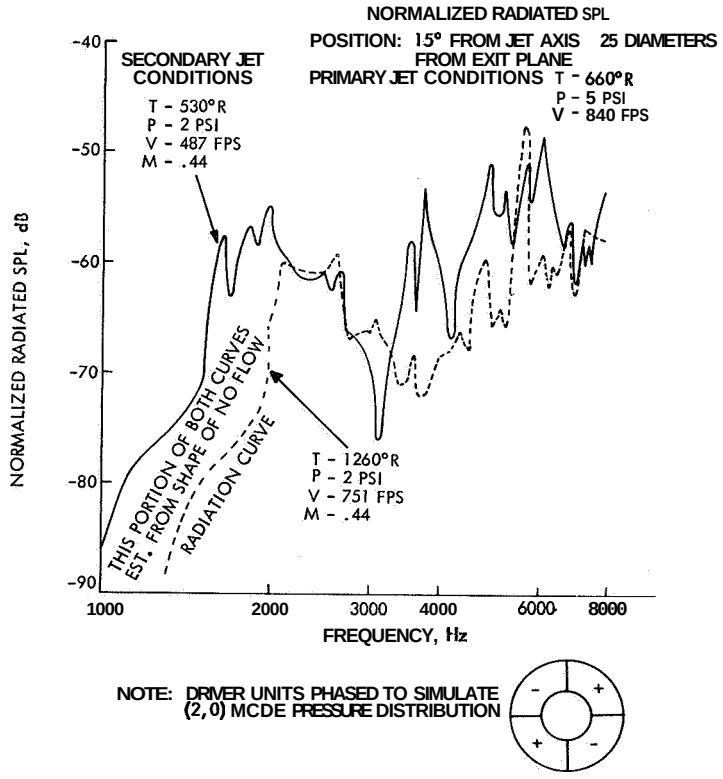

FIGURE 17.—Radiated pure-tone sound pressure showing effect of temperature on duct mode cut-on frequency and on level.

Next, to show the effect of flow and temperature on the (2,0) mode cut-on frequency, the normalized radiated SPL is shown in figure 17 at the same field position as in figure **16.** Here, the radiated pure-tone level became lost in the jet noise at about 1550 Hz for the **530**" R case and at 2000 Hz for the **1260**" R case. Therefore, the shape of the cutoff curve was superimposed from the no-flow condition. Examining the response of the duct at constant mach number, it is evident that increasing temperature increases cut-on frequency. From the theory, with an increase in temperature from 530" to **1260**" R (at the indicated velocities, a static temperature ratio of **1213/510),** the frequency should increase by the square root of the temperature ratio, **1.54.** The actual increase of the (2,0) mode cut-on frequency is approximately **1.3.**

Effect of Heating on Radiated Pure-Tone SPL

To show the effect of heating on radiated SPL, the difference between normalized radiated SPL for the ambient and **800°F** cases is determined. Representative plots are shown in figures **18, 19,** and 20 at three angular positions 25 diameters from the exit plane. The difference plot is shown from a frequency beginning at the (2,0) mode cut-on frequency for the high-temperature case. Below this frequency, the difference can only be

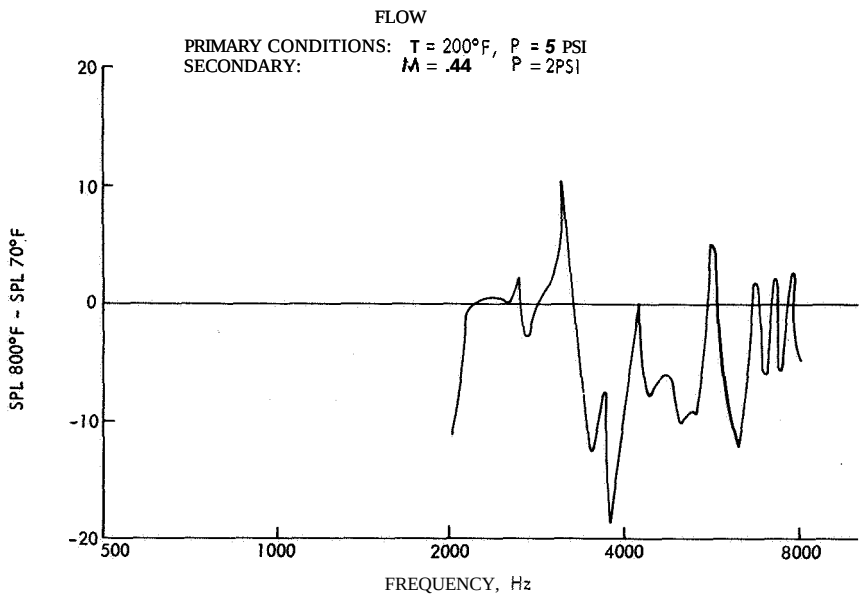

FIGURE 18.—Effect of temperature on radiated pure-tone sound-pressure level, 15" from jet thrust axis. Difference between radiated sound-pressure level for cold and hot jet with superimposed pure tone in (2,0) mode. Measurement 15" from centerline

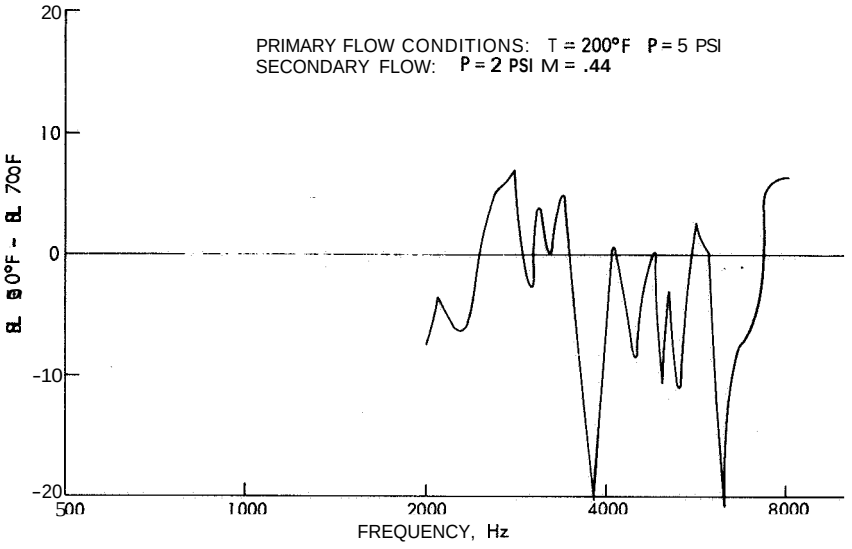

FIGURE 19.—Effect of temperature on radiated pure-tone sound-pressure level, 45° from jet thrust axis. Difference between radiated sound-pressure level for cold and hot jet with superimposed pure tone in (2,0) mode. Measurement 45° from centerline.

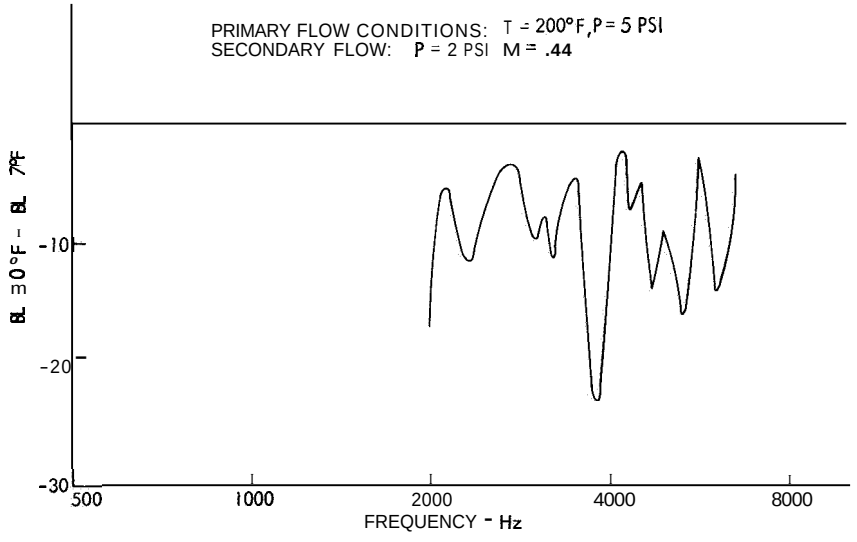

FIGURE 20.—Effect of temperature on radiated pure-tone sound-pressure level, 90° from jet thrust axis. Difference between radiated sound-pressure level for cold and hot jet with superimposed pure tone in (2,0) mode. Measurement 90° from centerline.

estimated but is of the order of 20 dB, down to the cut-on frequency of the (2,0) mode at ambient temperature. Below this frequency, the difference curve would be meaningless. The difference curves show that, over the greater part of the frequency range, SPL is reduced (of course, remember that these data are referenced to a constant source level—if the increase in temperature changes the source output noise level, these trends are also subject to change). If a frequency is carefully chosen, large reductions in pure-tone level can be achieved, but obviously for other frequencies, an increase would be observed in radiated SPL. Only at a point 90° to the jet axis does the increase in temperature show an attenuation across the complete frequency spectrum. Therefore, it is difficult to draw firm conclusions based on these data concerning the effect of temperature on the attenuation (or gain) in level of a pure tone refracting through a moving, high-temperature layer of air. However, the meaningful result is that large reductions apparently can be obtained at selected frequencies.

Effects of temperature on pure-tone directivity were not accurately determined from the experiments because measurements were made at only six angular positions. More data and an analysis are necessary before further comments can be made.

The pure-tone measurements then show that reductions of fan noise could presumably be achieved by propagating the pure tones through a high-temperature region. These reductions would be attributed to impedance mismatch between the source, high-temperature flow, and ambient medium. Refraction and convection would play a large part in redirecting the sound, and it is possible that the finite dimensions of the high-temperature region could be used to advantage in selectively filtering the pure tones.

CONCLUSIONS

Effects of temperature on jet noise have been shown by experiment. A prediction method developed from the experimental data indicates the possibility of significant noise reductions at high temperatures and low velocities, but more data are required to validate the magnitudes of reduction. Comparison with Semrau's data validates the predicted trends with temperature

A useful graphical prediction method is given for far-.field jet noise, including jet-temperature effects.

It is also shown that a possibility exists for selectively and significantly reducing pure tones that propagate from the fan through a high-temperature region in the fan duct and then into the ambient atmosphere.

REFERENCES

1. LASSITER, L. W.; AND HUBBARD, H. H.: Experimental Studies of Noise From Subsonic Jets in Still Air. NACA TN 2757,1952.
2. PLUMBLEE, H. E.; BALLENTINE, J. R.; AND PASSINOS, B.: Near Field Noise Analyses of Aircraft Propulsion Systems With Emphasis on Prediction Techniques for Jets. AFFDL–TR-67–43, Aug. 1967.
3. HADDLE, G. P.; WYNNE, G. A.; AND MATHIS, J. T.: Test to Determine the Relationship Between Jet Exhaust Temperature and Radiated Jet Noise. ER–9571, Lockheed-Georgia Co., May 1969.
4. PLUMBLEE, H. E.; WYNNE, G. A.; AND ZINN, B. T.: Effect of Jet Temperature on Jet and Pure Tone Noise Radiation. NASA CR 1472, 1969.
5. ROLLIN, V. G.: Effect of Temperature on Jet Noise Generation. NACA TN 4217, Mar. 1958.
6. REGIER, A. A.: Why Do Airplanes Make Noise? SAE Trans., vol. 63, 1955, p. 275.
7. HERMES, P. H.; AND SMITH, D. L.: Measurement and Analysis of the J57–P21 Noise Field. AFFDL–TR–66–147,1967.
8. SEMRAU, W. R.: Research on Jet Noise Generation and Suppression. AD 636805, GE Co., Apr. 1964.
9. TYLER, J. M.; AND SOFRIN, T. G.: Axial Flow Compressor Noise Studies. SAE Trans., vol. 70, 1962, p. 309.

ATTENUATION OF PLANE WAVES OF SOUND BY SUSPENSION OF RESONATING PARTICLES

Lee Arnold and Simon Slutsky
New York University
New York, N.Y.

A theoretical investigation has been initiated at New York University under the sponsorship of the NASA Langley Research Center for the determination of the influence of solid-particle seeding on jet exhaust noise. The influence of small concentrations of slender flexible rods or filaments on acoustic wave attenuation and stability of parallel shear flows is being considered and is briefly discussed here.

SYMBOLS

a	radius of rod cross section
c	speed of sound
c_2	coefficient of viscous damping for elastic attachment of M_2 to rod
f	flexural mode shape of rod
k_2	spring constant
m	total mass of seeding particle, m_0+M_2
m_0	mass of rod (or filament)
M_2	mass of particle attached to rod
N	particle number density
q	generalized coordinate for vibrating rod
R	half length of rod
u, v	perturbation velocity components of gas
u_0, v_0	perturbation velocity components of particles
κ'	Stokes parameter
μ	coefficient of viscosity
ρ_a	mass density of gas
ρ_0	particle mass density
τ	relaxation time
ω	frequency of disturbance
Ω	angular velocity of rod

371-986 0-LT-70 —10

INTRODUCTION

As the noise generated by compressor, turbine, and fan blades, and other internal noise mechanisms is made more tolerable by the use of liners and other solutions, the problem of quietening the noise generated in the engine jet exhaust will become more urgent. There are three ways of influencing exhaust noise: exit geometry, acoustic seeding, and solid-particle seeding. The engine companies have shown that to gain significant quietening from exit geometry without performance degradation is an unprofitable approach. The work statement covering New York University's efforts includes acoustic and solid-particle seeding. Until now, only solid-particle seeding has been considered.

Since the beginning of the century, various investigators have considered the influence of the presence of solid particles on the propagation of sound waves in a gas. More recently, Saffman (ref. 1) has considered the influence of such seeding on flow stability, and Michaels (ref. 2) has considered the influence on Kelvin-Helmholtz instability.

It has been shown that the effect of rigid-particle seeding on sound attenuation and flow instability is trivial for practical concentrations of particles. However, it is believed, and somewhat verified by analysis, that if particles respond as deformable bodies, the effect is major. For example, if the particles are assumed to have the form of slender elastic rods, major effects can be obtained at their resonant frequencies. In addition, because the particles in a shear flow will be spinning at a rate corresponding to the local vorticity, an additional dynamic effect corresponding to centrifugal loading results. Although the spinning produces a broadening of the frequency spectrum for which beneficial effects are gained, it is believed that unless additional dynamic features are introduced, particle concentrations would be too large for effective silencing. Analysis indicates that in addition to the degrees of freedom associated with spinning and flexible vibration, it is necessary that an additional mass be attached to the rod by an elastic element. It is believed that this coupled system will be the means of effecting attenuation of acoustic waves and flow stabilization over an appreciable frequency range.

In studies of the influence of rigid particles in gas flows, it is found that the primary dissipative mechanism is that associated with Stokes viscous reaction, corresponding to relative gas-particle motion. It is found that the influence of such particles is negligible. It can be shown that a positive damping associated with the motion of elements attached to a rotating system can result in extremely large damping (or even negative damping) relative to fixed space. A fluctuating spinning rod or filament in a perturbed viscous gas experiences such an effect. Thus it is believed that much greater dissipative effects can be obtained from a rotating flexible particle than from a rigid particle.

GAS-PARTICLE INTERACTIONS

The purpose of the following analysis is to determine the influence of dynamically responding particles on the generation and propagation of noise created in a shear layer. The influence of rigid particles has been considered by various investigators who have shown that practical concentrations of rigid particles only slightly affect the attenuation and stability mechanisms that might be responsible for noise generation.

Two basic mechanisms acted as stimuli for the present investigation. First, it is known that in the case of the propagation of waves in crystal lattices composed of diatomic molecules each having an atom unbound to the other molecules, there is a stopping band of frequencies for which signals are cut off. Each of the nonmolecularly bound atoms acts as a dynamic absorber. It is hoped that the presence of flexible particles in the gas may exhibit some of this same stopping-band effect. Second, it is known that a rotating, flexible rod to which is attached another concentrated mass by a spring support can be very effective in the absorption or emission of energy associated with external disturbances. An essential feature is that a dissipative element, such as a viscous damper, be attached to the rotating system, but it has been found that the presence of such positive viscous damping can cause the instability of such a system over a large frequency range. Therefore great care must be taken in designing such particles for purposes of absorbing acoustic energy, for they may be beneficial in certain frequency ranges but not in others. The mechanism referred to here has been considered in the study of the phenomenon of helicopter-ground resonance. In this case, there is a large energy transfer from the helicopter powerplant and an exchange of lateral disturbances into rotational ones, This mechanism has been investigated by Lee Arnold Associates.[1]

In the case of the helicopter rotor, the viscous damping is obtained from a hydraulic damper at each blade's drag hinge. For a spinning, flexing particle, however, it is shown that the viscous damping is obtained by the Stokes effect caused by relative particle-gas motion. In all previous studies of the effect of rigid particles, the Stokes effect has been assumed to be the primary dissipative mechanism.

Another analogy of what might be expected can be seen in the transfer of the diffusive, translatory energy of gas particles, which is a measure of the gas temperature, into the energy associated with the internal degrees of freedom of the rotation, vibration, and dissociation of the molecules.

---

[1] Lee Arnold Associates, Inc.: Ground Resonance Analysis— Model YH–16B Conversion Helicopter (prepared for the Piasecki Helicopter Corp.). Mar. 1965 (unpublished).

In addition to the internal mode dissipation, the usual rigid-particle Stokes dissipation is still operative but may be enhanced for resonating elements.

Attaching an additional mass element to each filament is required for the filaments to respond to wavelengths that are large compared to their length and to broaden the stopping band.

It can be shown that for both propagation and stability, the maximum attenuation and stabilization possible with solid-particle seeding is trivial. It appears that seeding is not a solution to jet-exhaust silencing, unless the dynamic influences associated with deformable particles resulting in irreversible transfer from translatory propagating modes to nontranslatory modes can be controlled.

THEORETICAL DEVELOPMENT

We consider the behavior of a parallel, two-dimensional flow separated into three domains, with the undisturbed flow in the x-direction having velocity ranges

$$U(y)=\begin{cases} U_0=\text{constant} & y\geqslant d \\ U_0\dfrac{y}{d} & -d\leqslant y\leqslant d \\ -U_0 & y\leqslant -d \end{cases} \tag{1}$$

as shown in figure 1. The region $-d\leqslant y\leqslant d$ contains flexible particles of number density N and mass m. At a point (x, y) at time t, a unit volume contains N particles in the shape of straight rods (or filaments) spinning at the rate

$$\Omega=-\frac{1}{2}\frac{dU}{dy}=-\frac{1}{2}\frac{U_0}{d} \tag{2}$$

The center of the rod is assumed to be moving with the velocity $u=U(y)$ and $v=0$; i.e., with the velocity of the fluid particles at (x, y). When the flow is disturbed, the midpoint of the rod has velocity components $U(y)+u_0$, and v_0, and the rod takes the form shown in figure 2. In figure 2 it is assumed that only one flexural mode of the rod is excited. This mode has a shape $f(r)$, and associated with the motion is a generalized coordinate $q(t)$. Attached elastically to the midpoint of the rod is a mass M_2. The elastic attachment is isotropic, and the deflection of M_2 relative to the midpoint of the rod is (x_2, y_2). It is also assumed that the transverse flow across the rod because of disturbed motion is adequately described by Stokes' viscous forces over a circular cylinder at small Reynolds numbers (ref. 3). If $u^{(n)}$ is the lateral component of the perturbed gas velocity at a point r of the rod, and $u_0^{(n)}$ is the lateral component of the rod velocity, the resistance per unit length according to Stokes is

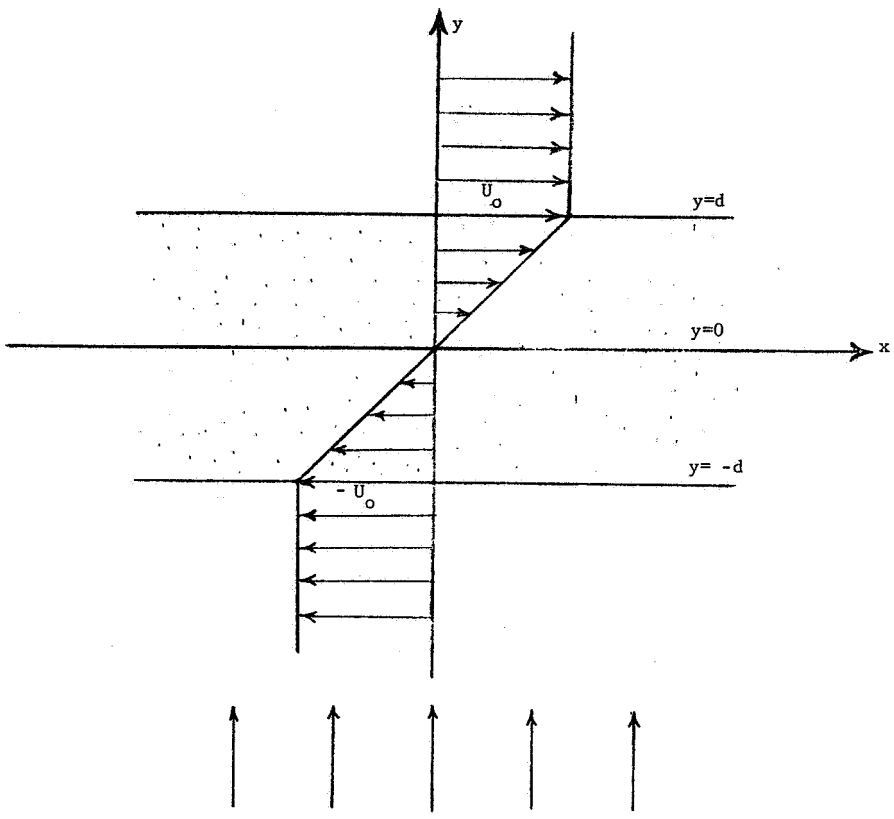

FIGURE 1.—Acoustic field.

$$\kappa'[u^{(n)}-u_0^{(n)}] \tag{3}$$

where

$$\kappa'=C\mu a \tag{4}$$

C is a constant, μ is the viscosity, and a the cross-sectional radius. The resistive force per unit volume at a point r is

$$\kappa[u^{(n)}-u_0^{(n)}] \tag{5}$$

where

$$\kappa=N\kappa' \tag{6}$$

From the kinematics of particle motion, it is found that the average resistances per unit volume are $\kappa(u-u_0)$, $\kappa(v-v_0)$, and $\bar{\kappa}\dot{q}$ corresponding to the x, y, and lateral directions, respectively, and

$$\bar{\kappa}=2\kappa\int_0^R f^2\,dr \tag{7}$$

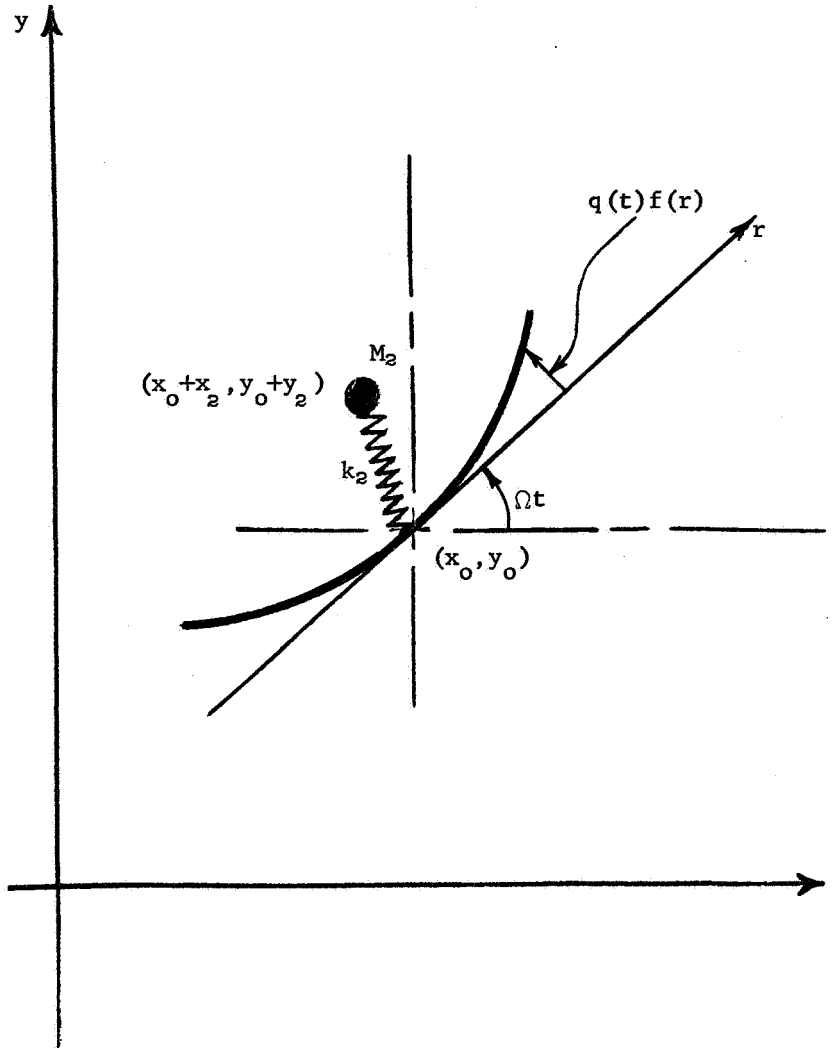

FIGURE 2.—Form of the rod when flow is disturbed.

Based on this model the equations of motion take the form

$$\rho_a\left(\frac{\partial u}{\partial t}+U\frac{\partial u}{\partial x}+U'v\right)=-\frac{\partial p}{\partial x}+\mu\nabla^2 u+\kappa(u_0-u) \tag{8}$$

$$\rho_a\left(\frac{\partial v}{\partial t}+U\frac{\partial v}{\partial x}\right)=-\frac{\partial p}{\partial y}+\mu\nabla^2 v+\kappa(v_0-v) \tag{9}$$

$$\frac{\partial \rho}{\partial t}+\rho_a\left(\frac{\partial u}{\partial x}+\frac{\partial v}{\partial y}\right)=0 \tag{10}$$

$$p = c^2\rho \tag{11}$$

$$\rho_0\left(\frac{\partial u_0}{\partial t} + U\frac{\partial u_0}{\partial x} + U'v_0\right) + \rho_1\frac{\partial^2 x_1}{\partial t^2} + \rho_2\frac{\partial^2 x_2}{\partial t^2} = \kappa(u - u_0) \tag{12}$$

$$\rho_0\left(\frac{\partial v_0}{\partial t} + U\frac{\partial v_0}{\partial x}\right) + \rho_1\frac{\partial^2 y_1}{\partial t^2} + \rho_2\frac{\partial^2 y_2}{\partial t^2} = \kappa(v - v_0) \tag{13}$$

$$\eta\left[\frac{\partial^2 x_1}{\partial t^2} + 2\Omega\frac{\partial y_1}{\partial t} - \Omega^2 x_1 + \omega_0^2 x_1 + \frac{\bar{\kappa}}{m_2}\left(\frac{\partial x_1}{\partial t} + \Omega y_1\right)\right] = -\frac{1}{2}\left(\frac{\partial u_0}{\partial t} + U\frac{\partial u_0}{\partial x} + U'v_0\right) \tag{14}$$

$$\eta\left[\frac{\partial^2 y_1}{\partial t^2} - 2\Omega\frac{\partial x_1}{\partial t} - \Omega^2 y_1 + \omega_0^2 y_1 + \frac{\bar{\kappa}}{m_2}\left(\frac{\partial y_1}{\partial t} - \Omega x_1\right)\right] = -\frac{1}{2}\left(\frac{\partial v_0}{\partial t} + U\frac{\partial v_0}{\partial x}\right) \tag{15}$$

$$\left(\frac{\partial^2 x_2}{\partial t^2} + \omega_2^2 x_2 + \frac{c_2}{M_2}\frac{\partial x_2}{\partial t}\right) + \left(\frac{\partial u_0}{\partial t} + U\frac{\partial u_0}{\partial x} + U'v_0\right) = 0 \tag{16}$$

$$\left(\frac{\partial^2 y_2}{\partial t^2} + \omega_2^2 y_2 + \frac{c_2}{M_2}\frac{\partial y_2}{\partial t}\right) + \left(\frac{\partial v_0}{\partial t} + U\frac{\partial v_0}{\partial x}\right) = 0 \tag{17}$$

where

$$\eta = \frac{m_0 m_2}{m_1^2} \tag{18}$$

$$m_i = 2\int_0^R f^i(r)\rho(r)\,dr \tag{19}$$

$$\left.\begin{aligned} \rho_1 &= Nm_1 \qquad \rho_2 = NM_2 \\ \rho_0 &= Nm = N(M_2 + m_0) \end{aligned}\right\} \tag{20}$$

$$\omega_2 = \sqrt{k_2/M_2} \tag{21}$$

Neglecting viscous diffusion, that is, assuming the only dissipation is due to Stokes effect, the above equations yield

$$\frac{\partial^2 v}{\partial t^2} + \frac{\kappa}{\rho_a}(1 - \kappa m)\frac{\partial v}{\partial t} - c^2\frac{\partial^2 v}{\partial y^2} = 0 \tag{22}$$

This yields solutions of the form $v = e^{i(\omega t - \beta y)}$ where

$$\beta = \frac{\omega}{c}\sqrt{1 + i\frac{\kappa m - 1}{\omega\tau}} \tag{23}$$

and where $\tau = \rho_a/\kappa$ is the relaxation time corresponding to the relative particle-gas motion.

For a rigid particle

$$\kappa m = \frac{1}{1 + i\omega\tau\rho_0/\rho_a} \tag{24}$$

and

$$\beta = \frac{\omega}{c}\sqrt{1 + \frac{\rho_0}{\rho_a}\frac{1 - i\omega\tau\rho_0/\rho_a}{1 + (\omega\tau\rho_0/\rho_a)^2}} \tag{25}$$

The maximum attenuation occurs for $\omega\tau\rho_0/\rho_a = 1$, which yields

$$\beta_{\max} = \frac{\omega}{c}\sqrt{1 + \frac{\rho_0}{\rho_a}\frac{1 - i}{2}} \tag{26}$$

For $\rho_0/\rho_a \ll 1$

$$\beta_{\max} \doteq \frac{\omega}{c}\left[1 + \frac{1 - i}{4}\frac{\rho_0}{\rho_a}\right] \tag{27}$$

and

$$v \sim e^{i\omega\left[t - \left(1 + \frac{1}{4}\frac{\rho_0}{\rho_a}\right)\frac{y}{c}\right]} \cdot e^{-\frac{1}{4}\frac{\omega}{c}\frac{\rho_0}{\rho_a}y} \tag{28}$$

Thus, for rigid particle seeding, we obtain a trivial attenuation for practical values of

$$\frac{\omega}{c}\frac{\rho_0}{\rho_a}$$

Repeating the above analysis for the flexible, rotating particles, one obtains a decay factor

$$\beta = \frac{\omega}{c}\sqrt{1 + \left(\frac{\rho_0}{\rho_a}\right)_A \frac{1 - i\omega\tau(\rho_0/\rho_a)_A}{1 + [\omega\tau(\rho_0/\rho_a)_A]^2}} \tag{29}$$

where $(\rho_0/\rho_a)_A$ is an apparent density ratio that is complex in form and is given by

$$\left(\frac{\rho_0}{\rho_a}\right)_A = \frac{\bar{\rho}/\rho_a + (1 + i\omega\tau)[(\bar{\rho}/\rho_a)^2 - (B\rho_1/\rho_a)^2]}{1 + (1 + i\omega\tau)\rho/\rho_a - iBU'\tau\rho_1/\rho_a} \tag{30}$$

where

$$\bar{\rho} = \rho_0 + A\rho_1 + H\rho_2 \tag{31}$$

$$A=\frac{-\omega^2}{2\eta}\frac{\left(\omega^2+\Omega^2-\omega_0^2-i\omega\frac{\bar{\kappa}}{m_2}\right)}{\left(\omega^2+\Omega^2-\omega_0^2-i\omega\frac{\bar{\kappa}}{m_2}\right)^2-\left[\Omega\left(2\omega-i\frac{\bar{\kappa}}{m_2}\right)\right]^2}$$

$$B=\frac{-\omega^2}{2\eta}\frac{\Omega\left(2\omega-i\frac{\bar{\kappa}}{m_2}\right)}{\left(\omega^2+\Omega^2-\omega_0^2-i\omega\frac{\bar{\kappa}}{m_2}\right)^2-\left[\Omega\left(2\omega-i\frac{\bar{\kappa}}{m_2}\right)\right]^2} \tag{32}$$

$$H=\frac{-\omega^2}{\omega^2-\omega_2^2-i\omega\frac{c_2}{M_2}}$$

It is the term $[(\bar{\rho}/\rho_a)^2-(B\rho_1/\rho_a)^2]$ that controls the mechanism for large energy transfer. The expression $(\rho_0/\rho_a)_A$, which replaces ρ_0/ρ_a in β, includes both a magnification of density and dissipation.

The density magnification can be seen for the case $A=B=0$, $H\neq 0$ for which we find that because H can be very large close to resonance and

$$\beta_{\max}=\frac{\omega}{c}\sqrt{1+\frac{1-i}{2}\left[\frac{\rho_0}{\rho_a}+H\frac{\rho_2}{\rho_a}\right]} \tag{33}$$

in a narrow frequency range, even for small ρ_0/ρ_a and ρ_2/ρ_a, attenuation can be very large. It is believed that the effect of rotation, i.e., A and $B\neq 0$, will cause a broadening of the frequency band.

Studies of Kelvin-Helmholtz instability indicate very similar effects on stabilization through seeding.

Experimental work is continuing to determine the influence of the described particle on critical Reynolds number, Lighthill multipole strength, and shear flow stability, as well as the influence of other irreversible dissipative mechanisms, such as acoustically induced chemical effects.

Studies are in progress for determining materials that can obtain the desired particle dynamic characteristics.

An experimental program for testing these ideas is being formulated and, hopefully, will be initiated in the near future.

REFERENCES

1. SAFFMAN, P. G.: On the Stability of Laminar Flow of a Dusty Gas. J. Fluid Mech., vol. 13, 1962, pp. 120–128.
2. MICHAELS, D. H.: Kelvin-Helmholtz Instability of a Dusty Gas. Proc. Cambridge Phil. Soc., vol. 61, 1965, pp. 569–571.
3. LAMB, H.: Hydrodynamics. Dover Pub., Inc., 1945, pp. 614–616.

OPTICAL MEASUREMENTS OF SOUND SOURCE INTENSITIES IN JETS

L. N. Wilson
IIT Research Institute
Chicago, Ill.
and
F. R. Krause and K. A. Kadrmas
NASA Marshall Space Flight Center
Huntsville, Ala.

Direct measurements of local sound source intensities in turbulent jets are being attempted using an optical cross-correlation technique. It has been shown that optical crossbeam measurements can be related directly to the volume integral describing the source strength. This paper represents a study of this relationship. The application and limitations of the technique are discussed in detail, with reference to Lighthill's and, in particular, Ribner's mathematical formulations. The latter formulation is particularly suited to crossbeam measurements because it expresses source strengths in terms of volume integrals of mass density fluctuations. Area integrals of density fluctuations are being attempted using a new infrared crossbeamed system. Progress to date on subsonic jets with this system shows promise of giving the desired density dependence. Measurements were made using the CO_2 absorption band at 4.3 μm. This type of measurement should be applicable to estimations of mach-wave emission.

SYMBOLS

$\mathbf{x}_f$	position vector (x_f, y_f, z_f)
$\mathbf{x}$	position vector (x, y, z)
$\boldsymbol{\xi}$	vector in direction of far-field observer (ξ_1, ξ_2, ξ_3)
$\boldsymbol{\xi}$	vector in direction of flow (ξ, η, ζ)
$\bar{\rho}$	mean density
ρ	fluctuating density
m_f	fluctuating mass fraction
k	absorption coefficient
$\bar{P}$	mean pressure
P	fluctuating pressure
$\bar{\mathbf{u}}$	mean velocity vector $(\bar{u}, \bar{v}, \bar{w})$
a_0	ambient speed of sound

a	local speed of sound
ι	fluctuating signal
Z	mean signal
l	path angle
τ	retarded time
U_c	turbulence convection speed

Subscripts

A, B	radiation beams of the crossed-beam system
a	contribution from absorption
s	contribution from scattering

INTRODUCTION

The mathematical formulation of the jet-noise problem (refs. 1 and 2) has given us considerable insight into scaling laws associated with noise production, but little progress has been made in experimental verification of the predicted sound-source strengths. The actual sound-source intensities as predicted by the theory are given in terms of turbulence flow properties that are extremely difficult to measure and even then must be incorporated into a complicated volume integral expression involving retarded time differences between statistical variables. Some attempts (refs. 3 and 4), with a measure of success, have been made in estimating sound-source strengths from hot-wire measurements in low-speed jet flows where the transformation to a moving frame of reference allows retarded times to be ignored to a good degree of approximation. At high speeds, this approximation is invalid; in fact a singularity occurring at the sonic convection condition results in a prediction of infinite acoustic power radiated. A different type of noise source then dominates, and sound radiates from the jet in a manner analogous to mach-wave propagation (ref. 5).

An instrumentation technique, called the crossed-beam correlation method, has been recently developed (ref. 6) that automatically performs an area integral of pertinent turbulent properties. This technique is similar in form to that required for a direct estimate of sound-source intensity (ref. 7), and thus affords us the opportunity of measuring a part of the sound-source volume integral directly. This paper covers the application of the technique to the mach-wave emission expected from supersonic jets and discusses progress thus far on the experimental verification.

ANALYTICAL DEVELOPMENT

Sound-Source Intensities

Ffowcs Williams (ref. 5) has shown that, where turbulent jet convection speeds are in excess of the ambient speed of sound

$$M_c = \frac{U_c}{a_0} > 1$$

a pronounced finite sound peak occurs at $\cos\theta = 1/M_c$, where θ is the angle between the line to the observer and the flow direction (fig. 1).

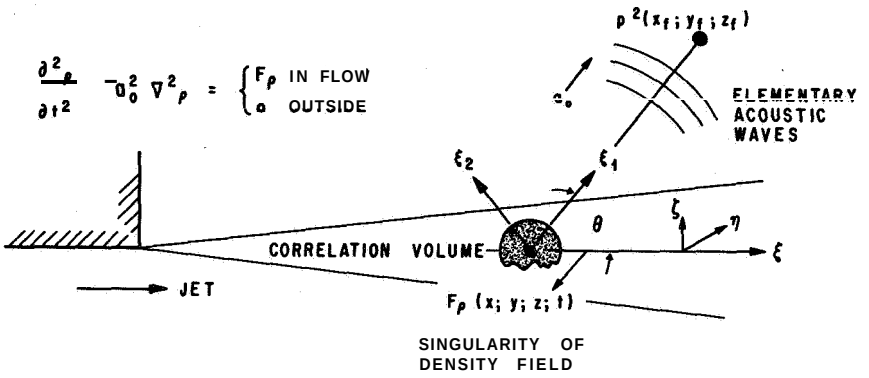

FIGURE 1.—Sound generation in jets, extension of acoustic waves into flow.

Because this is the direction at which mach waves would emanate from supersonic bodies moving at a mach number M_c, the emission is analogous to the mach-wave emission from supersonically moving eddies, the latter behaving somewhat like solid bodies. The intensity of acoustic radiation is then determined by the "shape" of the bodies; i.e., by the density gradient through the eddy. The sound source in this case is sourcelike (monopole, whereas in subsonic flow the sound source is quadrupole in nature. The sound-source strength is then determined, through suitable mathematical manipulation, by density correlations in a fixed frame of reference, thus removing the complication resulting from measurements being required in the moving frame of reference as happens in the case of quadrupole noise. The far-field sound-source intensities can be given by the equation

$$F(\mathbf{x}) = \int \left\langle F_\rho(\mathbf{x}, t) F_\rho\left(\mathbf{x} + \boldsymbol{\xi}, t - \frac{\xi_1}{a_0}\right)\right\rangle d\boldsymbol{\xi}$$

obtained by integration over ξ of the timelag derivatives of

$$\left\langle \underset{\text{Paint}}{\rho(\mathbf{x}, t)} \underset{\text{Area}}{\int \rho\left(\mathbf{x} + \boldsymbol{\xi}, t - \frac{\xi_1}{a_0}\right) d\xi_2\, d\xi_3} \right\rangle$$

the product mean value of gas density fluctuations.

The far-field acoustic radiation from the shear layer of a turbulent jet is then predicted to be

$$\langle P^2 \rangle = \frac{1}{16\pi^2} \int \frac{(x_f - x)^2 (y_f - y)^2}{|\mathbf{x}_f - \mathbf{x}|^6} \{\partial \bar{u}/\partial y\}^2 S(\mathbf{x})\ d\mathbf{x} \tag{1}$$

where

$$S(\mathbf{x}) = \int \left\langle \frac{\partial \rho}{\partial t}\left(\mathbf{x}, t - \frac{|\mathbf{x}_f - \mathbf{x}|}{a_0}\right) \frac{\partial \rho}{\partial t}\left(\mathbf{x} + \xi, t - \frac{|\mathbf{x}_f - \mathbf{x} - \xi|}{a_0}\right)\right\rangle d\xi \tag{2}$$

$S(\mathbf{x})$ is considered here to be the acoustic source strength per unit volume of turbulence. The other terms in the equations, apart from the mean velocity gradient, are dependent upon the relative position of the observer and the sound source. The velocity gradient can be measured independently of the source integral by other standard measurements. Ffowcs Williams writes the correlations in terms of the pressure gradients by assuming locally isotropic conditions is $\boldsymbol{p} = (1/a^2)P$. This technique requires a knowledge of the local speed of sound in the shear layer. If, however, we can measure density fluctuations directly, this approximation and requirement is not necessary. Ffowcs Williams also shows that the sound-source integral is more properly written in a frame of reference alined with and perpendicular to the mach-wave direction of propagation.

Croesed-Beam Principle

The operation of the crossed-beam technique has been described elsewhere and will therefore be discussed only briefly here. In principle, two narrow beams of selected wavelength radiation are positioned so that they intersect at a point in the region of interest in the jet. If the beam intensity for each beam is modulated by a process that is linearly related to the local gas-density fluctuations, then the intensities can be expressed by

$$i_A = I_A \int (km_f)\, d\eta = I_A \int \rho\ d\eta \tag{3}$$

$$i_B = I_B \int (km_f)\, d\zeta = I_B \int \rho\ d\zeta \tag{4}$$

where i_A, i_B, I_A, and I_B are the fluctuating and mean signals, respectively, for each of the two beams A and B. If the two signals are cross-correlated over a sufficiently long integration time, the product mean value $\langle i_A i_B \rangle$ will give information concerning only the fluctuations common to each beam; i.e., in the intersection region. In this way, local information on turbulence has been obtained without the necessity of inserting physical probes into the flow field (ref. 6). From a more intuitive viewpoint (fig. 2), we might consider turbulence as consisting of discrete

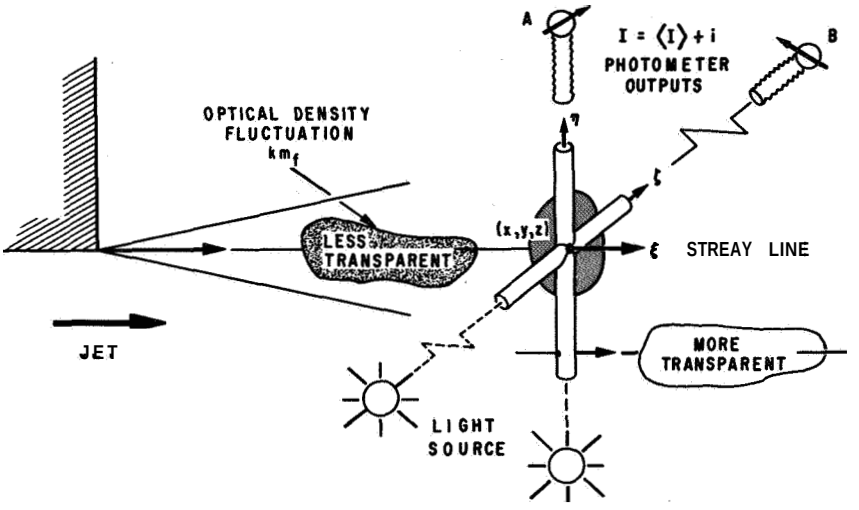

FIGURE 2.—Optical approximation of sound source intensities.

$$\frac{\langle i_A \cdot i_B \rangle}{\langle I_A \rangle \langle I_B \rangle} = \int \langle \rho(x, y, z, t) \rho(x, y+\eta, z+\zeta, t) \rangle \; d\eta \, d\zeta$$

X-Beam Correlation Point—area product mean value of optical density fluctuations

eddies that are more or less transparent to the beams of radiation than the surroundings. As an eddy passes through a beam of radiation, the light intensity at the detector changes. When the two detector outputs are cross-correlated, only the information concerning eddies passing through the beam intersection point is retained. Signal fluctuations caused by source instabilities, detector noise, etc., are normally uncorrelated, although these contributions do affect the overall signal-to-noise ratio of the system (ref. *8).*

Cross-correlation of equations (3) and (4) gives

$$G(\mathbf{x}) = \frac{\langle i_A i_B \rangle}{\langle I_A \rangle \langle I_B \rangle} = \iint \langle \rho(x, y+\eta, z, t) \rho(x+\xi, y, z, t+\tau) \rangle d\eta \, d\zeta \quad (5)$$

where i_A and i_B are correlated with an arbitrary time delay τ between signals and ξ is a displacement of beam B relative to beam A in the direction of U_c. This equation expresses the correlation between two line integrals. If we can write equation (5) as

$$G(\mathbf{x}) = \iint \langle \rho(x, y, z, t) \rho(x+\xi, y+\eta, z+\zeta, t+\tau) \rangle d\eta \, d\xi \quad (6)$$

or

$$G(\mathbf{x}) = \langle \rho(x, y, z, t) \iint \rho(x+\xi, y+\eta, z+\zeta, t+\tau) \, d\eta \, d\zeta \rangle \quad (7)$$

Point Area

then we are dealing with the correlation between the area integral of points in a plane ($x+\xi=$ constant) with an outside point (x, y, z). Such a cross-correlation has been assigned the term "point-area correlation," and is the type occurring in equation (1).

If the turbulent flow is everywhere homogeneous, then the point-area formulation is obviously proper. If departures from homogeneity are pure odd functions of space coordinates about the point (x, y, z), then these departures tend to integrate out and the point-area formulation is still valid. In any event, the final proof of the point-area correlation assumption can come only from experiment. Two tests for this proof, discussed in detail in reference 8, are summarized here.

(1) The spatial resolution of the measurements across streamlines should be limited only by the outside "point," which, in practice, is the optical beam diameter.

(2) Since the cross-correlation of signals i_A and i_B will correspond only to contributions from turbulent fluctuations normal to the beam plane, the energy spectrum should approximate the three-dimensional spectrum of turbulence. This is in contrast to a two-point hot-wire measurement of the so-called one-dimensional spectrum that contains contributions carried by crossflow components. As a result, the energy spectrum for crossed-beam data should approach a $-11/3$ variation in the high-frequency portion.

Therefore, assuming the validity of the point-area correlation approximation, equation (7) in abbreviated fashion becomes

$$G(\mathbf{x})=\int\int\langle\rho(\mathbf{x}, t)\rho(\mathbf{x}+\xi, t+\tau)\rangle\, d\eta\, d\zeta \tag{8}$$

Application to Sound-Source Intensity Measurements

The similarity between equation (1) and equation (8) is striking. It would appear that only one further integration (point area to point volume) is required to obtain the sound-source intensity. There are, however, two main points to be considered carefully in making the comparison: The radiation extinction process must be directly gas density dependent and time derivative and not space derivative correlations are required, and the correct retarded time difference must be used. We will now consider these two points in greater detail.

Extinction Process

Several extinction processes have been used in crossed-beam studies in the past. These include scattering from natural and artificial tracers and the use of the absorption of air in the ultraviolet portion of the spectrum (Schumann-Runge bands of oxygen). Each of these has proven to be unacceptable for sound-source measurements although they are

useful in other turbulence parameter studies. More recently, instrumentation has been developed to measure absorption by naturally occurring CO_2 in air using the near-infrared portion of spectrum. The fundamental vibration band of CO_2 near $4.3\mu m$ is the most promising because of the absence of water vapor absorption in this region. Only naturally occurring CO_2 can be used, because only then will the optical fluctuations measured be truly representative of the gas density fluctuations in the jet. The use of the infrared spectrum also reduces the contributions to the signal fluctuations from ever-present particle contaminants in the flow.

The extinction process in general can be written as

$$\begin{aligned} i+I &= I_0 \exp\left[-\int(\bar{\rho}+\rho)\,dl\right] \\ &= I_0 \exp\left[-\int\bar{\rho}\,dl\right]\exp\left[-\int\bar{\rho}\,dl\right] \\ &= I \exp\left[-\int\rho\,dl\right] \end{aligned}$$

Now, for small perturbations

$$\exp\left[-\int\rho\,dl\right]=1-\int\rho\,dl$$

Thus

$$i=-I\int\rho\,dl$$

which is the form presented in a previous section.

It should be repeated at this point that ρ is analogous to km_f. This means that a comprehensive study must be made using a unique absorption calibration cell to determine the dependence of k on the static and dynamic pressure and static temperature. Therefore, knowing $\partial k/\partial P$ and $\partial k/\partial T$, the experimenter can choose the optimum wavelength and bandpass settings in the absorption band to discriminate against the temperature dependence of k. These experiments can be made only in a controlled environment free of a contribution caused by scattering to the observed signal.

In principle then, it is feasible to use infrared absorption by naturally occurring CO_2 for the measurement of gas-density fluctuations. The preliminary results are given in the next section.

Time-Derivative Requirements and Retarded Time Effects

The point-area correlation in equation (6) must be in terms of the time derivatives of the gas-density fluctuations in order to obtain an experimentally accessible form of equation (1).

For stationary time series, the correlation of time derivatives is identical with the timelag differentiation of the correlation:

371-986 0-LT-70—11

$$\left\langle \frac{\partial \rho(\mathbf{x}, t)}{\partial t} \frac{\partial \rho(\mathbf{x}+\boldsymbol{\xi}, t+\tau)}{\partial t} \right\rangle = \frac{\partial^2 \langle \rho(\mathbf{x}, t)\ \rho\ (\mathbf{x}+\boldsymbol{\xi}, t+\tau) \rangle}{\partial \tau^2} \tag{9}$$

$$\frac{\partial^2 G(\mathbf{x})}{\partial \tau^2} = \iint \frac{\partial^2 \langle \rho(\mathbf{x}, t)\ \rho(\mathbf{x}+\boldsymbol{\xi}, t+\tau) \rangle}{\partial \tau^2} d\xi_2\, d\xi_3 \tag{10}$$

$$S(\mathbf{x}) = \int \frac{\partial^2 G(\mathbf{x})}{\partial \tau^2}\, d\xi_1 \tag{11}$$

We can also simplify the retarded times in equation **(1)** by the approximation

$$|\mathbf{x}_f - \mathbf{x}| - |\mathbf{x}_f - \mathbf{x} - \boldsymbol{\xi}| \simeq {}_{41} \tag{12}$$

The order of timelag differentiation and space integration (eq. **(11))** may be interchanged in the special coordinate system $\boldsymbol{\xi} = (\xi_1, \xi_2, \xi_3)$, where the planes $\xi_1 =$ constant are parallel to the mach-wave fronts that are generated at the source point **x,** the reason being that retarded times are constant along such planes within the far-field approximation. This type of crossed-beam orientation is possible, but does not alleviate the problem since θ is not known a priori.

The time delay for the orientation in figure 2 is

$$\tau = \frac{\xi_1}{a_0} = \frac{\xi}{U_c}$$

This time delay is also precisely that which allows an eddy to move from the upstream beam to the downstream beam along a streamline in a reference frame oriented in the flow direction $\boldsymbol{\xi} = (\xi, \eta, \zeta)$. In other words, the retarded time is correct for the area near the common streamline, but away from the streamline τ is a function of the particular points η and ζ. In the first approximation, the contributions should cancel as in the case for crossflow components. Therefore, we can write equations **(10)** and **(11)** as

$$\frac{\partial^2 G(\mathbf{x})}{\partial \tau^2} = \iint \frac{\partial^2 < \rho(\mathbf{x}, t) \rho(\mathbf{x}+\boldsymbol{\xi}, t+\tau)}{\partial \tau^2} d\eta\, d\zeta \tag{13}$$

$$S(\mathbf{x}) = \int \frac{\partial^2 G(\mathbf{x})}{\partial \tau^2}\, d\xi \tag{14}$$

and

$$|\mathbf{x}_f - \mathbf{x}| - |\mathbf{x}_f - \mathbf{x} - \boldsymbol{\xi}| \simeq \xi \tag{15}$$

Because $S(\mathbf{x})$ is an experimentally accessible quantity under the above assumptions, sound-source intensities can be measured.

EXPERIMENTAL STUDIES

The first tests[1] conducted with the infrared crossed-beam system were made in the shear layer at an axial location of $X/D=4$ of a subsonic jet *so* that comparisons could be made with more standard measuring

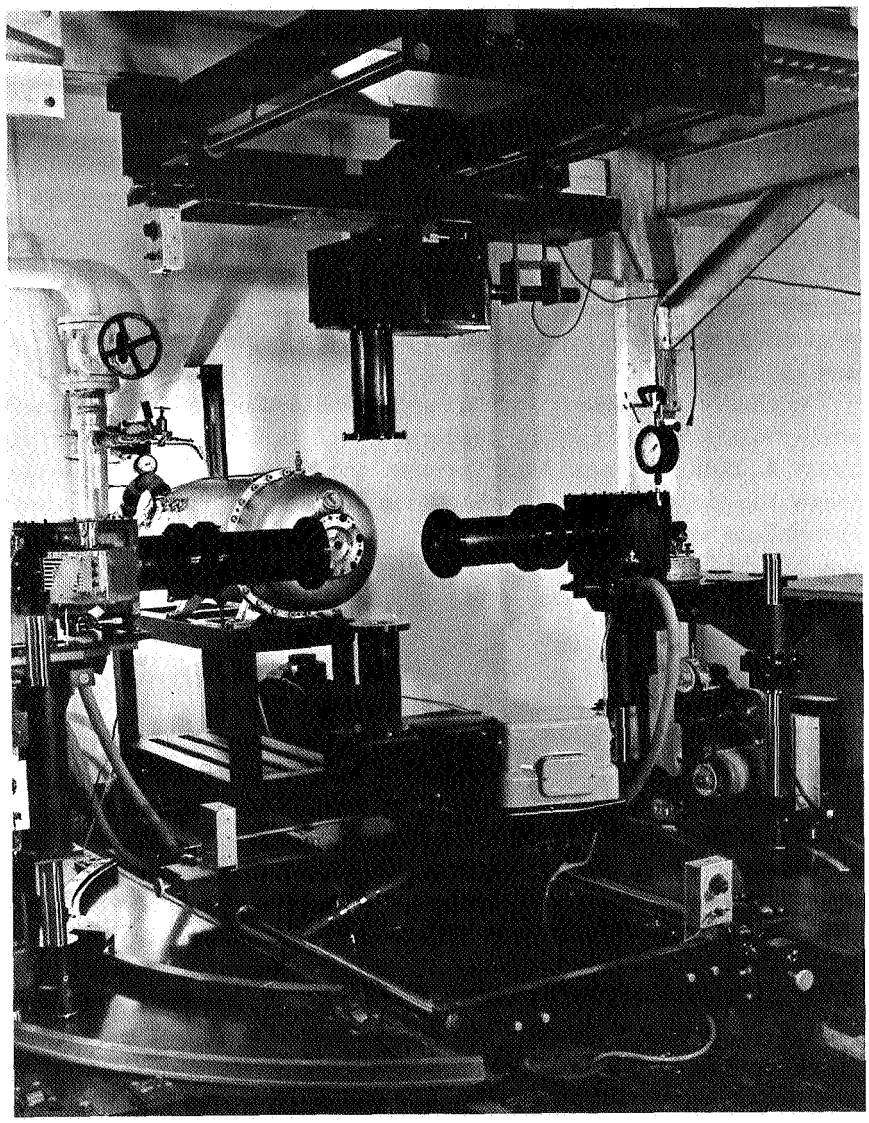

FIGURE 3.—The 1-in.-diameter subsonic jet facility and infrared crossed-beam system.

[1] The data presented here were kindly supplied by Dr. R. J. Damkevala of IIT Research Institute.

techniques. A photograph of the 1-in.-diameter subsonic jet facility and infrared crossed-beam system is shown in figure 3.

The radiation sources currently in use are glowbars operating at a temperature of 1100° K (equivalent blackbody temperature). Cassegrainian optics are used to focus the radiation from the sources into the jet-flow field with an image dimension of 2 mm in the flow direction and 1 mm in the transverse direction. The radiation is then collected, using similar optics, and refocused on the entrance slit of a McPherson model 218 monochromator. The experimenter can then choose the center wavelength and bandpass settings desired in the 4.3-μm absorption band of CO_2. The bandwidth initially used was typically 0.08 μm. The radiation level is monitored at the exit slit of the monochromator by using LN_2 cooled indium-antimonide detectors. The fluctuating signals obtained are amplified and recorded for a detailed analysis. Simultaneously, the signals are reduced on line using a PAR correlator. A computer program is available to reduce the digitized data tapes to obtain the correlations and spectra.

The cross-correlations (zero beam separation) and mean levels obtained while traversing the spectral region from 4.1 to 4.5 μm are shown in figure 4. Both the mean-level traverse and cross-correlation traverse follow the shape of the CO_2 absorption curve as expected, but cross-correlations were recorded outside the absorption band where the absorption should fall to zero. It is felt that this is caused by the contribution from scattering to the total signal because the jet is contaminated by

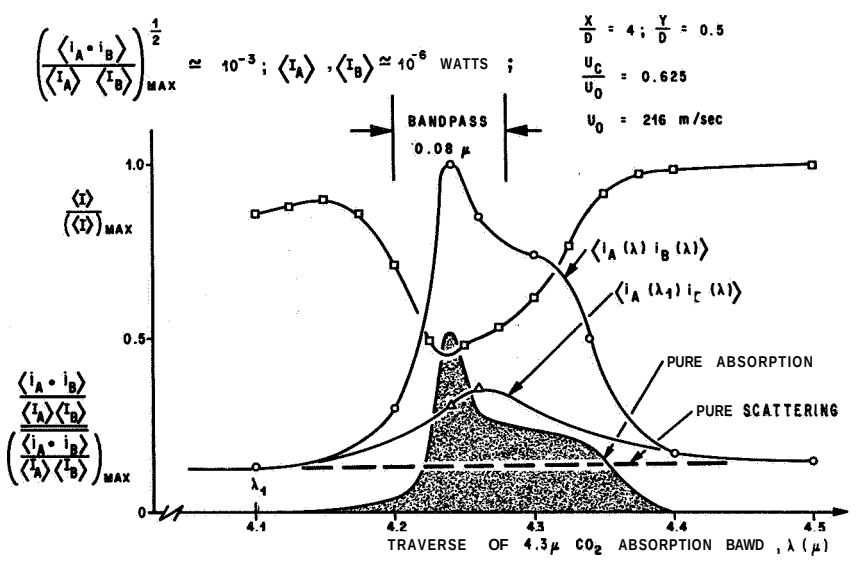

FIGURE 4. – Relation between optical and gas density fluctuations.

oil mist from the compressors. In this case, the signal is obviously not entirely due to CO_2 absorption, and therefore some method must be devised to treat this type of problem.

If we consider the fluctuating signals of beam A and beam B to be composed of contributions due to absorption and scattering, then

$$i_A(\lambda, \ldots) = i_{A_a}(\lambda, \ldots) + i_{A_s}(\lambda_1, \ldots)$$

and

$$i_B(\lambda, \ldots) = i_{B_a}(\lambda, \ldots) + i_{B_s}(\lambda_1, \ldots) \tag{16}$$

where we have assumed that the scattering contribution is a linear continuum across the absorption band and can thus be approximated at λ_1.

The cross-correlation of the two composite signals yields

$$\begin{aligned}\langle i_A(A, \ldots) i_B(A, \ldots)\rangle &= \langle i_{A_a}(\lambda, \ldots) i_{B_a}(A, \ldots)\rangle \\ &+ \langle i_{A_a}(\lambda, \ldots) i_B(Ai, \ldots)\rangle + \langle i_{A_s}(\lambda_1, \ldots) i_{B_a}(\lambda, \ldots)\rangle \\ &+ \langle i_{A_s}(\lambda_1, \ldots) i_{B_s}(\lambda_1, \ldots)\rangle\end{aligned} \tag{17}$$

Therefore, to obtain

$$\langle i_{A_a}(\lambda, \ldots) i_{B_a}(\lambda, \ldots)\rangle$$

we must know the three remaining terms on the right-hand side of equation (17).

By definition,

$$Q_{aa}(\lambda, \lambda) = \frac{\langle i_{A_a}(\lambda, \ldots) i_{B_a}(\lambda, \ldots)}{\langle I_A\rangle\langle I_B\rangle} \tag{18}$$

and

$$Q_{ss}(\lambda_1, \lambda_1) = \frac{\langle i_{A_s}(\lambda_1, \ldots) i_{B_s}(\lambda_1, \ldots)\rangle}{\langle I_A\rangle\langle I_B\rangle} \tag{19}$$

Also

$$\begin{aligned}Q_{as}(\lambda, \lambda_1) &= \frac{\langle i_{A_a}(\lambda, \ldots) i_{B_s}(\lambda_1, \ldots)\rangle}{\langle I_A\rangle\langle I_B\rangle} \\ &= \frac{\langle i_{A_s}(\lambda_1, \ldots) i_{B_a}(\lambda, \ldots)\rangle}{\langle I_B\rangle\langle I_B\rangle}\end{aligned} \tag{20}$$

because both processes are governed by the turbulence convection and are thus well correlated. Now, setting beam A at λ_1 and beam B at A, cross-correlating the two signals, we get

$$\frac{\langle i_A(\lambda_1, \ldots)\, i_B(\lambda, \ldots)\rangle}{\langle I_A\rangle\langle I_B\rangle} = Q_{as}(\lambda, \lambda_1) + Q_{ss}(\lambda_1, \lambda_1) \tag{21}$$

or

$$Q_{as}(\lambda, \lambda_1) = \frac{\langle i_A(\lambda_1, \ldots) \, i_B(\lambda, \ldots)\rangle}{\langle I_A\rangle\langle I_B\rangle} - Q_{ss}(\lambda_1, \lambda_1) \tag{22}$$

Finally, we can write

$$Q_{aa}(\lambda, \lambda) = \frac{\langle i_A(\lambda, \ldots) \, i_B(\lambda, \ldots)\rangle}{\langle I_A\rangle\langle I_B\rangle} - 2\,\frac{\langle i_A(\lambda_1, \ldots) \, i_B(\lambda, \ldots)\rangle}{\langle I_A\rangle\langle I_B\rangle} + Q_{ss}(\lambda_1, \lambda_1) \tag{23}$$

which is the contribution due to absorption only (fig. 4).

Figure 5 shows a radial profile measured at a center wavelength of $\lambda = 4.24\,\mu$m. The resolution of the crossed-beam system may be assessed by comparing the width of this intensity peak with the shear layer width. The consistent variation of the two-beam product mean value is evidence of resolution capabilities and supports the earlier contention of the validity of the point-area correlation concept.

Fourier transforms performed on the cross-correlations are presented in figure 6. Once again the point-area concept appears to be supported by experimental evidence because the high-frequency portion of the spectrum does approximate the $-11/3$ power law very well.

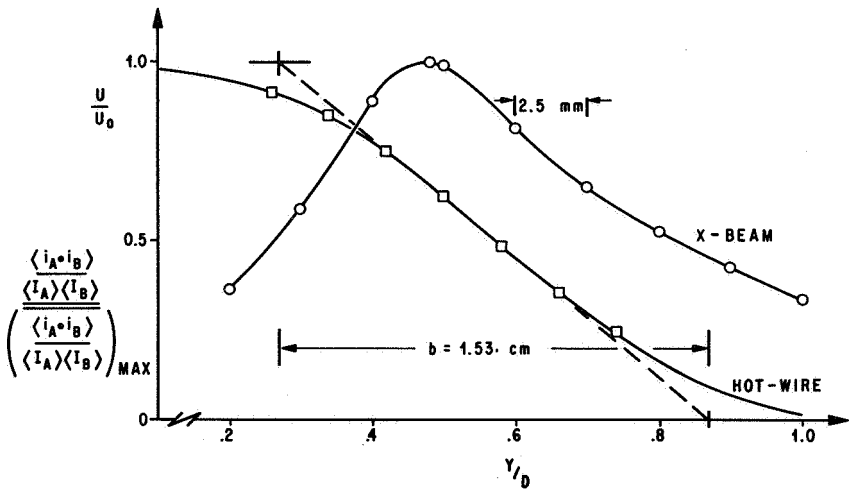

FIGURE 5.—Sound source location in a subsonic jet.

$U_0 = 216$ m/sec,

$\frac{X}{D} = 4$ cm, $D = 2.54$ cm,

$\langle I_A\rangle, \langle I_B\rangle \simeq 10^{-6}$ W,

$\left(\frac{\langle i_A \cdot i_B\rangle}{\langle I_A I_B\rangle}\right)^{1/2}_{max} - 10^{-3}$

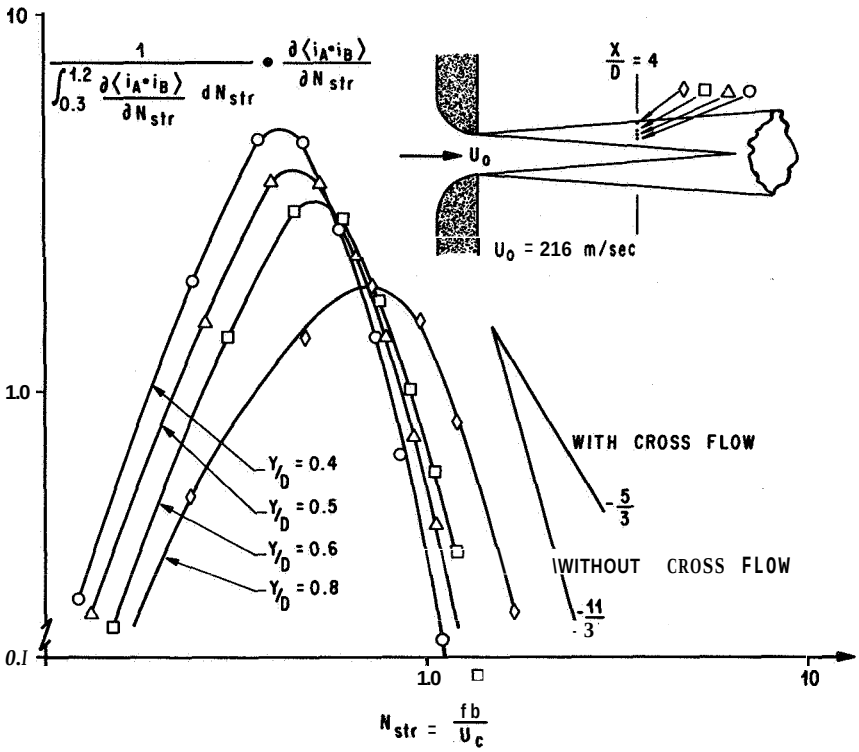

FIGURE 6.—Three-dimensional point spectra in a jet.

CONCLUSIONS AND FUTURE PLANS

The very promising first results presented in this paper have given confidence that the crossed-beam technique will allow measurements of sound-source intensities to be made in jet flows. Toward that end, experiments are being initiated to measure two-beam correlations in a heated subsonic jet, and measurements have already begun in a specially designed absorption calibration cell to verify analytical predictions with regard to understanding pressure and temperature effects. These measurements are to be made by varying the absorber mass, static and dynamic pressure, and static temperature independently.

With this information and the already proven ability to obtain at a distance point-area correlations that are not accessible to probe instruments, the crossed-beam system will have the potential of locating and measuring, for the first time, the turbulent sound-source intensities in jet flows. Such measurements, taken without disturbing the flow, will not only lend support to analytical predictions but also aid in the design and evaluation of noise-suppression devices.

REFERENCES

1. LIGHTHILL, M. J.: On Sound Generated Aerodynamically. I. General Theory. Proc. Roy. Soc., ser. A, vol. 211,1952, p. 1107.
2. LIGHTHILL, M. J.: On Sound Generated Aerodynamically. 11. Turbulence as a Source of Sound. Proc. Roy. Soc., ser. A, vol. 222, 1954, p. 1148.
3. CHU, W. T.: Turbulence Measurements Relevant to Jet Noise. UTIAS Rept. no. 119, 1966.
4. JONES, I. S. F.: Fluctuating Turbulent Stresses in the Noise Producing Region of a Jet. J. Fluid Mech., vol. 36, no. 3, 1969.
5. FFOWCS WILLIAMS, J. E.; AND MAIDANIK, G.: The Mach Wave Field Radiated by Supersonic Turbulent Shear Flows. J. Fluid Mech., vol. 24, no. 4, 1965.
6. FISHER, M. J.; AND KRAUSE, F. R.: The Crossed-Beam Correlation Technique. J. Fluid Mech., vol. 28, no. 4, 1967.
7. KRAUSE, F. R.; AND WILSON, L. N.: Optical Crossed-Beam Investigation of Local Sound Generation in Jets. Proceedings of the Conference on Noise Alleviation of Large Subsonic Jet Aircraft. NASA SP–189, 1968.
8. FISHER, M. J.; AND DAMKEVALA, R. J.: Fundamental Considerations of the Crossed-Beam Correlation Technique. NASA CR–61252, 1969.

JET-ORIFICE-SURFACE INTERACTION NOISE*

R. C. Potter
Wyle ***Laboratories, El Segundo, Calif.***

When an experimental program for isolating and identifying acoustic source regions within high-speed jets was extended to slower flows, noise was generated by the interaction of the jet flow with the orifice and wall through which it was passing. This sound was studied within a reverberation room and an anechoic room using two cold air jets run at velocities up to 950 fps. The turbulent jet mixing flow itself, examined with a hot-wire anemometer, was apparently unchanged. The effects of various orifice sizes, surface areas surrounding the orifices, and surface finishes were studied in terms of the measured total acoustic power generated, directivity, and spectra. The results are reported, and provisional explanations of this mechanism of noise generation are proposed.

INTRODUCTION

This study is the result of a previous experimental program to determine the acoustic source distribution in jet flows (refs. 1 and 2). The original experimental technique consisted of directing a jet flow through an orifice into a reverberation room (fig. 1). The jet was initially positioned so that the whole jet flow was contained within the room. Then, the reverberant sound-pressure level and spectrum gave a measure of the level and spectrum of the jet acoustic power, once the room absorption characteristics had been considered. By moving the jet out of the room in progressive increments and including an adjustment of the orifice size, the acoustic power generated by that part of the flow contained within the room could by determined. Differentiation of these results against distance along the jet flow gave the distribution of acoustic source strength within the jet flow.

The experiment was first completed for a high-speed cold nitrogen jet of nozzle-exit diameter of 1 in. and exit mach number 2.49. The results obtained were very encouraging. However, during this experiment, some

*This work is supported by NASA Marshall Space Flight Center, under contract NAS **8–21060.**

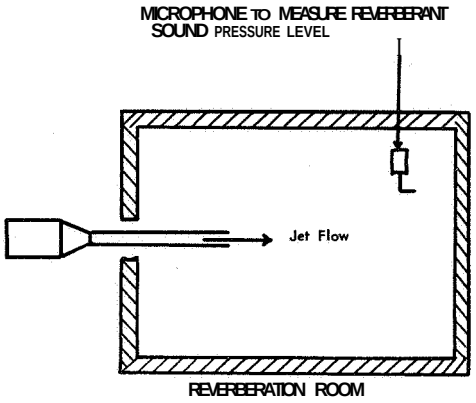

FIGURE 1.—Experimental technique for measurement of acoustic source distribution in a jet flow.

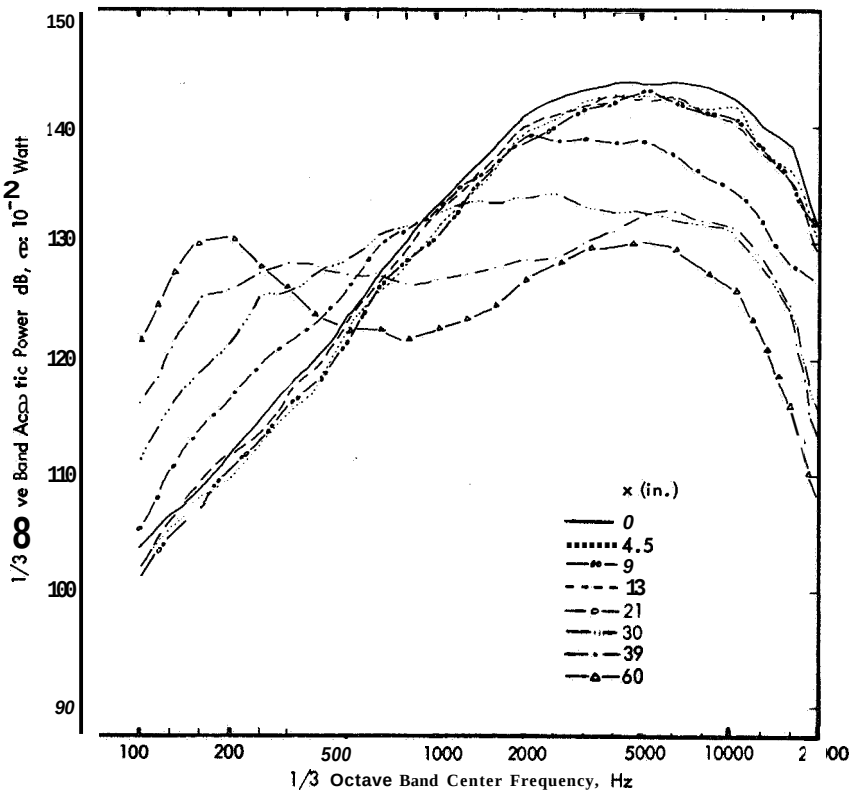

FIGURE 2.—Measured acoustic power spectrum, initial experiment, jet into reverberation room.

extra noise was observed to be generated at the large nozzle-exit-to-orifice spacings, and a set of typical results is shown in figure 2. The values plotted are for acoustic power measured within the room as the nozzle was withdrawn.

Initially, at the point where the entire jet was contained within the room, $(x=0)$, where x is the distance of the nozzle exit from the orifice plate, the 1/3-octave-band spectrum shows the complete power spectrum of the total noise generated by the jet. As the jet nozzle was moved progressively away from the orifice, the initial mixing flow was isolated outside the reverberation room, and the power measured within the room did not change significantly. Once the separation distance between the nozzle exit and the orifice plate set in the wall of the room increased beyond 10 nozzle-exit diameters $(x=10$ in.), the levels measured, and hence the acoustic power generated within the room, started to drop. This initial drop is noted at the high frequencies near the peak frequency of the total jet noise generated.

As the separation was increased further, the high-frequency acoustic power continued to decrease, but an increase in the low-frequency sound was observed. This noise is obviously in addition to the jet mixing noise, as the levels exceed the initial values of the jet sound power alone measured at zero separation.

In this first experiment, the interest was in the source distribution of the jet sound power generated by the mixing flow. Therefore, it was feasible to eliminate this extra sound, and in fact, the analyses of references 1 and 2 only considered the sound power generated at frequencies greater than 500 Hz.

The next stage of the program was to extend this experiment to the case of a subsonic jet. It may be queried as to why the program started with a supersonic jet, the reason being the controversy regarding acoustic-source distribution that existed for high-speed jet mixing flows (refs. 3, 4, and 5). The acoustic-source distribution of subsonic jets was understood to be the basis of the theoretical analysis of Ribner (ref. 6) at this time. However, with the increased interest in jet-engine silencers for large subsonic aircraft and the achieved decrease in compressor noise, the understanding of sound generation by subsonic jet flows again has become critical.

The experiment was set up with a subsonic 2.5-in. exit diameter jet flow, and three immediate effects were observed. The orifice-jet interaction noise, which is how we shall refer to this phenomenon, increased significantly relative to the noise of the jet alone. The frequency shifted relative to the jet noise toward the peak frequency of the jet noise, and finally the effect occurred at small jet nozzle exit to orifice spacings. In fact, as the jet was drawn out of the room, the reverberant sound-

pressure levels measured within the room increased, and the experiment became completely unworkable. Therefore, a series of experiments were conducted to study this effect, and the preliminary results and conclusions are presented in this paper.

MEASUREMENT OF JET-ORIFICE PLATE INTERACTION SOUND POWER

The rig was rearranged as shown in figure 3 so that the jet was contained wholly within the room. Plates, 24 in. by 24 in., with various-sized orifices, were set up on a trolley so that the plate could be traversed down the jet flow. The reverberant sound-pressure level was measured within the room and plotted automatically against distance of the orifice from the nozzle using on $x-y$ plotter. The levels observed within the octave bands were also obtained, and figure 4 shows some typical results. The origin for the ordinate has been shifted for each octave band to avoid overlaying the results.

The test conditions for the experimental results shown were jet exit velocity, 482 fps; jet exit nozzle diameter, 2.5 in.; and orifice diameter, 5 in. In this case, the reverberation level caused by the jet alone was

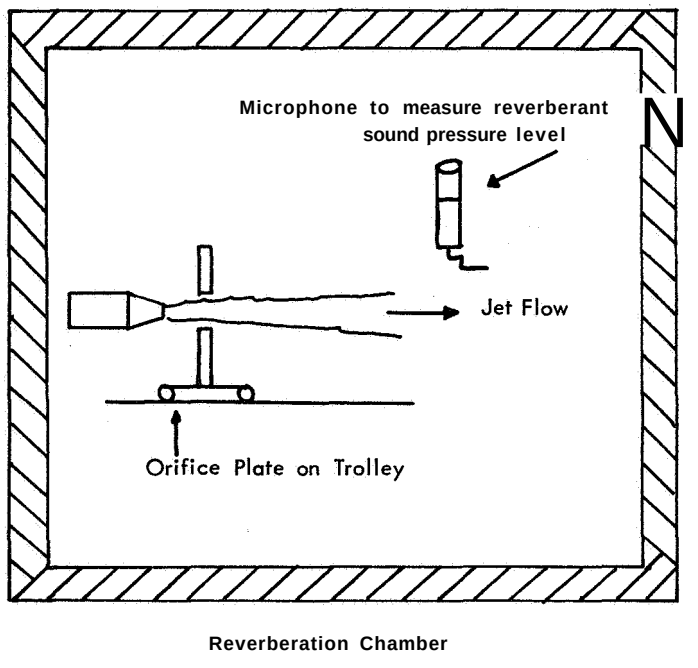

FIGURE 3.—Experimental setup to measure jet-orifice interaction noise.

held constant, and so the increase in levels shown in figure 4 was directly due to the jet-flow-orifice interactions.

It should be explained that this noise is not the result of the jet flow impinging directly on the plate itself. The jet was observed, both visually and by measurement with hot-wire anemometers, to pass through the orifice cleanly at positions where a substantial noise increase was observed. As a measure of the interference, the location of the various orifice plates that caused an increase of 1 dB over the jet-noise reverberant sound-pressure level alone was observed, and the results are plotted in figure 5. Each result shown is for a different-size orifice, and apparently the position that causes this increase in sound expands from the jet lip at a much greater angle than the rate of the jet spread.

Figure 6 shows the dependence of this jet-orifice noise on the velocity of the jet. The results are for a single orifice of diameter 5 in. located 3 in. downstream from the jet nozzle exit, which is 2.5 in. in diameter. The results are all plotted to some arbitrary origin. For all the octaves, the sound power caused by the orifice noise (obtained by subtracting the

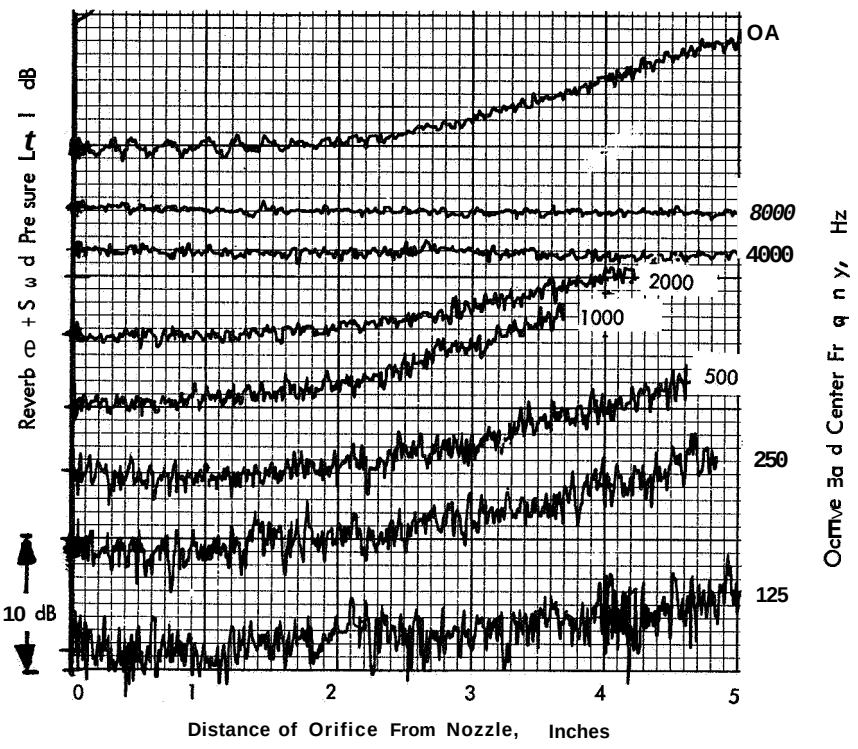

FIGURE 4. – Jet-orifice noise, effect of orifice location.

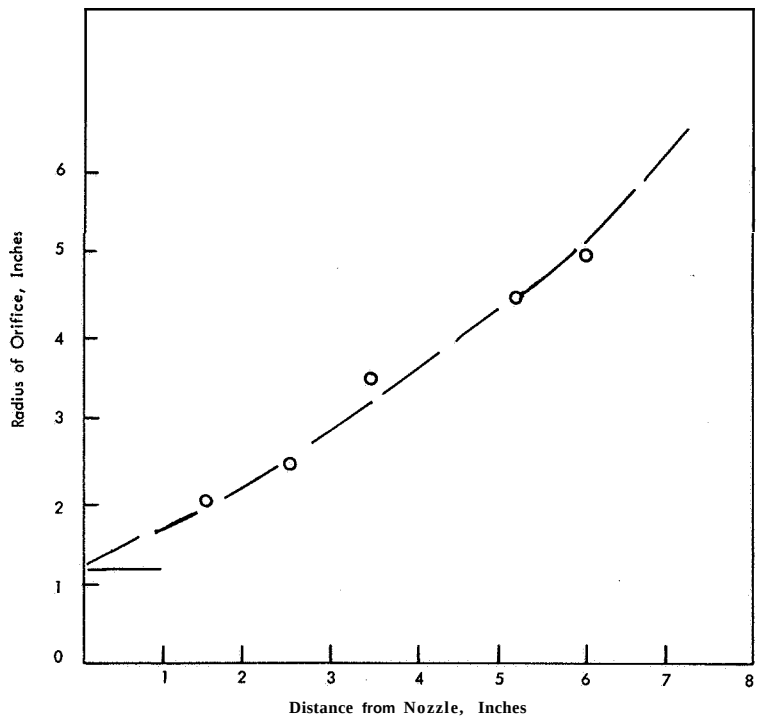

FIGURE 5.—Location of orifice to cause fig. 1 dB increase in reverberant sound-pressure level.

jet noise from the total noise measured) increases following a U^6 law within the experiment limitations. The U^6 line is also shown on this figure for comparison.

SOUND-POWER DIRECTIVITY AND SURFACE EFFECTS

The following experiment was, therefore, set up as shown in figure 7. A cold model jet flow was positioned within an anechoic room, and plates with orifices were set around the jet. In this case, the model jet was 0.75 in. in exit diameter and the orifices and plates were correspondingly scaled to match the previous experiment. The far-field sound created by the various combinations was measured at 5" intervals over a range of angles from 20" to 120" to the jet axis by using a moving microphone boom. An automatic octave-band analyzer was incorporated to obtain a complete octave-band spectrum at 5" intervals around the jet.

Some of the parameters that were varied in the experiments, for which results will be presented, are two different orifice sizes, two different

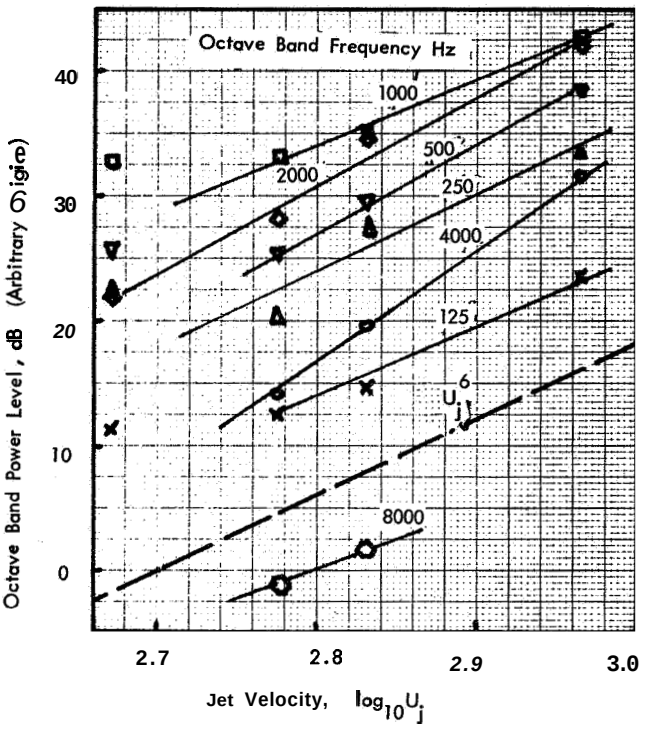

FIGURE 6. – Jet-orifice noise dependence on jet velocity.

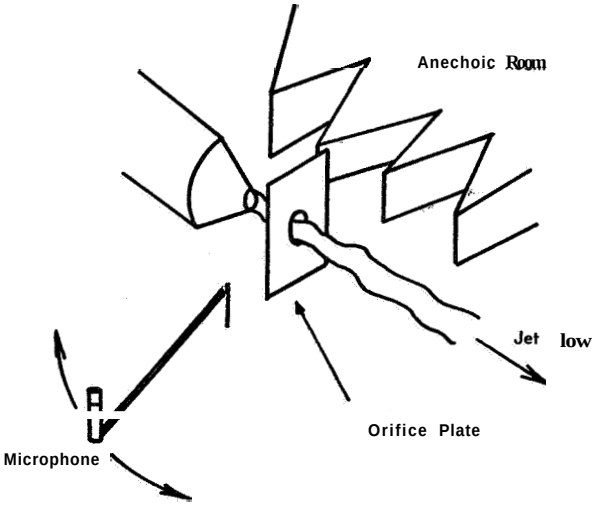

FIGURE 7. – Experimental setup for directivity measurements.

jet velocities (482 and 896 fps), and two different plate sizes. The first plate was scaled directly, based on nozzle-exit diameter, from the plates used in the previous experiment. The second plate was chosen to be over twice as big as the original plate. In both cases, the plates were square to match the previous plates used and for ease of mounting. The initial results obtained with these two different-size plates, the one some 15 nozzle-exit diameters on a side and the second some 40 nozzle-exit diameters on a side, showed no significant difference in the sound field measured. The next stage of the experiment involved placing absorbing foam on the surfaces of the plate in an effort to absorb the local near-field pressures and to prevent any reaction with the plate's surfaces. Foam was placed first on the downstream side of the plate; i.e., the side of the plate away from the nozzle exit. Next, the foam was placed on the upstream side of the plate, the side of the plate facing toward the jet nozzle exit, by simply reversing the plate. Finally, the foam was applied to both sides of the plate.

The foam used in these experiments was 0.5-in.-thick porous foam that when placed on a solid surface had a measured impedance of about seven times that of air at frequencies of 1000 Hz and above. The jet,

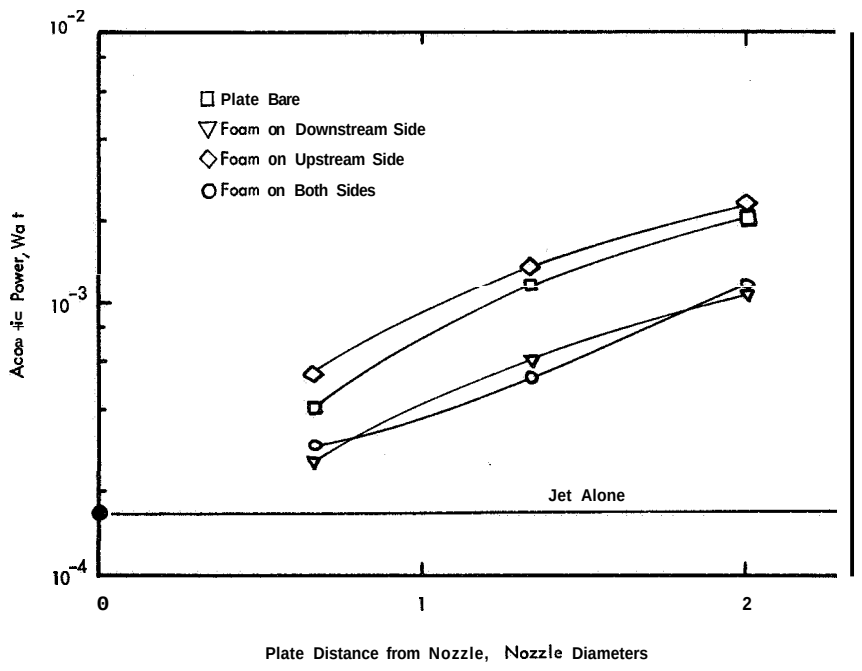

FIGURE 8.—Acoustic power generated by jet-orifice interaction and showing the effect of foam addition to plate surfaces.

as previously stated, was 0.75 in. in diameter, and when run at a velocity of just over 450 fps, produced noise that peaked in the 2000- to 4000-Hz range.

Figure 8 shows the results for overall acoustic power generated within the forward 90° quadrant (measured with respect to the jet-flow direction); i.e., in the space where the majority of the jet noise is radiating. The results for the jet noise alone are shown by the solid symbol, and the bottom axis on the figure indicates the position of the plate along the jet flow. The results for the plate alone show how the sound power increases as the plate is positioned further downstream from the jet nozzle exit and indicate that the jet boundary is getting nearer the orifice edge. Adding foam to the downstream side of the plate, the side away from the nozzle, produced some noise reduction, as shown by the triangle symbol. The addition of foam on the upstream side gives the results indicated by the diamonds, and shows that the sound, in effect, is the same as when no foam was present. Foam on both sides of the plate produced results that are similar to the case of foam on the downstream side only.

Figure 9 gives the results of overall sound-pressure level measured by the boom as it traversed around the jet and orifice plate; the symbols

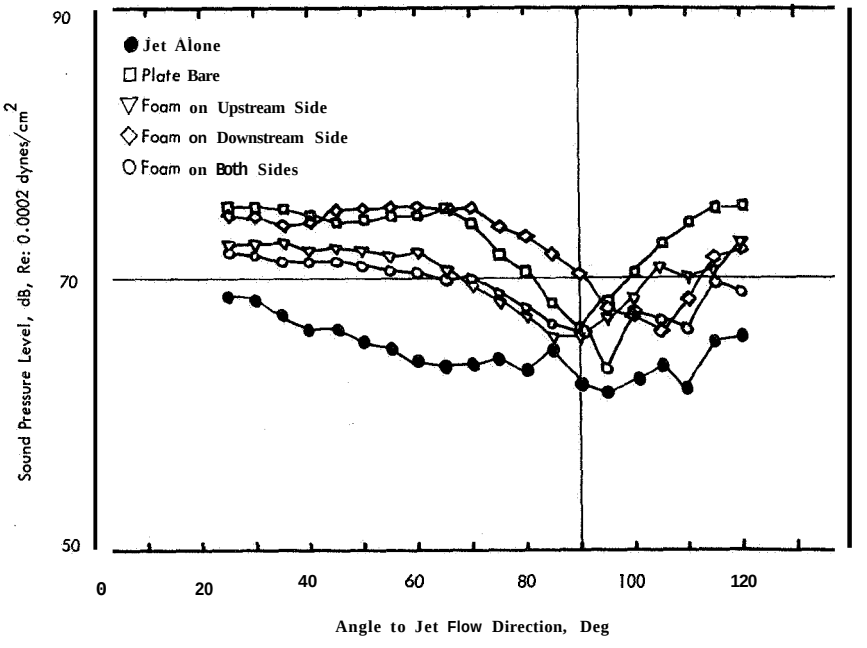

FIGURE 9.—Directivity of sound field, overall sound pressure level.

371-986 0-LT-70—12

used are the same as for figure 8. These results are all for the plate 1 in. (or 1.3 exit diameters) from the nozzle, with an orifice in the plate of 2 jet exit diameters, and with the jet operated at 482 fps. Adding foam to the downstream side of the plate shows a reduction in the sound pressure measured in the downstream arc, with a smaller reduction observed in the upstream arc, 90° to 120° behind the nozzle exit. The addition of foam on the upstream side of the plate does reduce the level in the segment behind the nozzle, but has no effect on the levels measured from 20° to 90°. When both sides were treated, the results showed a maximum reduction in both arcs; first, as measured for the downstream foam, and then as measured for the upstream foam.

Figure 10 shows similar results for the 500-Hz octave band sound-pressure levels. These values indicate that the plate increases the sound pressure level, but the foam causes little effect at this low frequency, with the treated and untreated plate showing similar results. Figure 11 presents the results of the 1000-Hz octave band and again indicates little effect caused by the addition of foam. However, the results do show a very pronounced directivity effect to all cases. It is believed that at this frequency the plate becomes more significant because its half width is

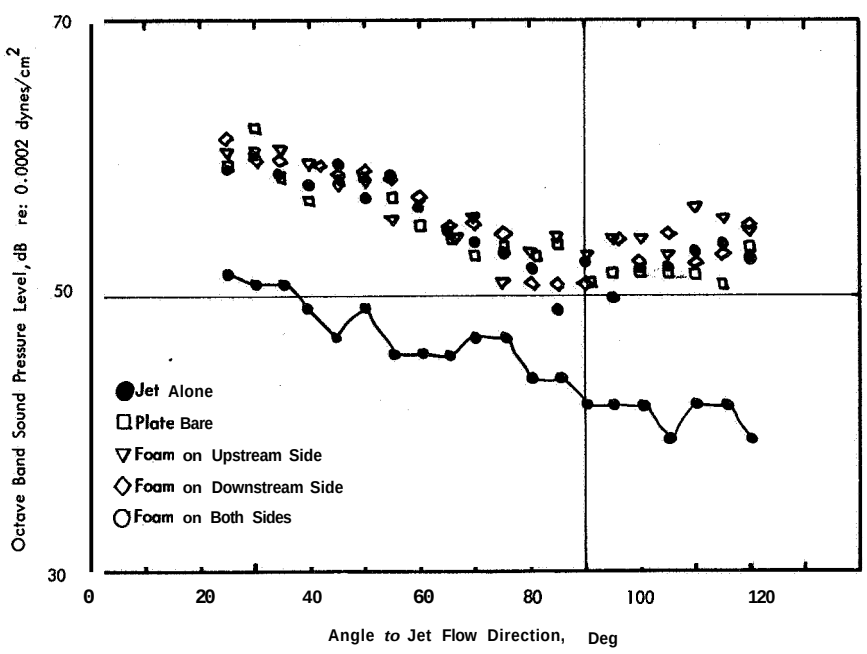

FIGURE 10.—Directivity of sound field, 500-Hz octave band.

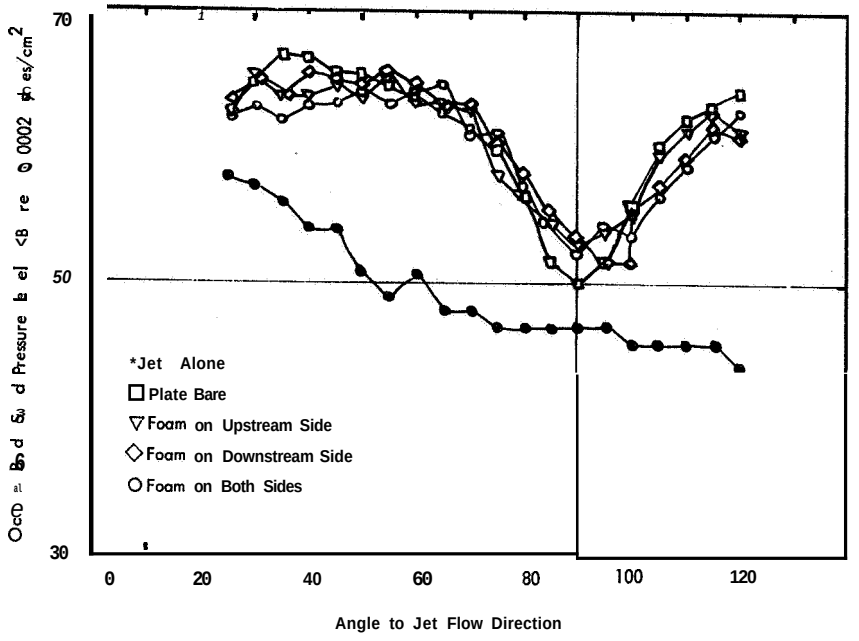

FIGURE 11.—Directivity of sound field, 1000-Hz octave band.

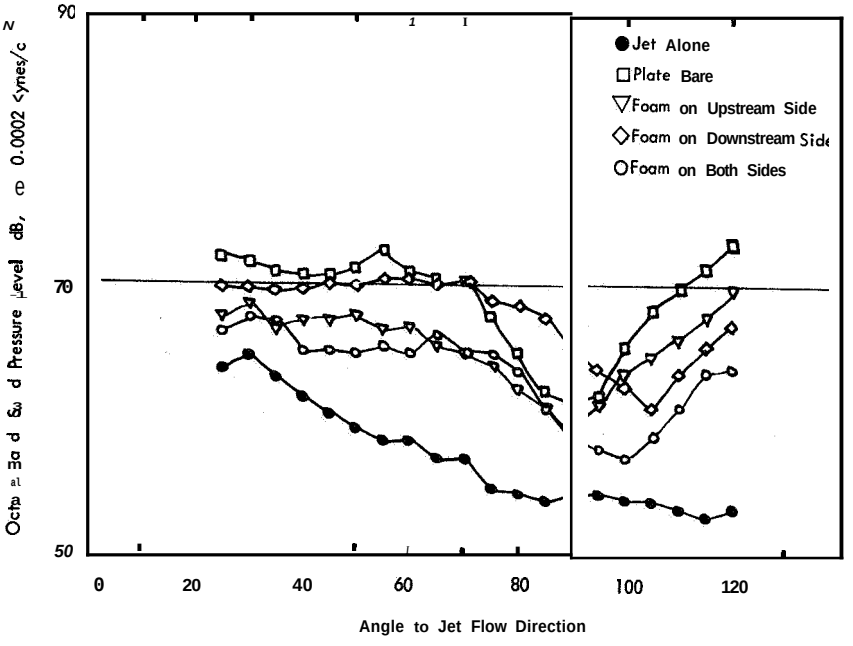

FIGURE 12.—Directivity of sound field, 2000-Hz octave band.

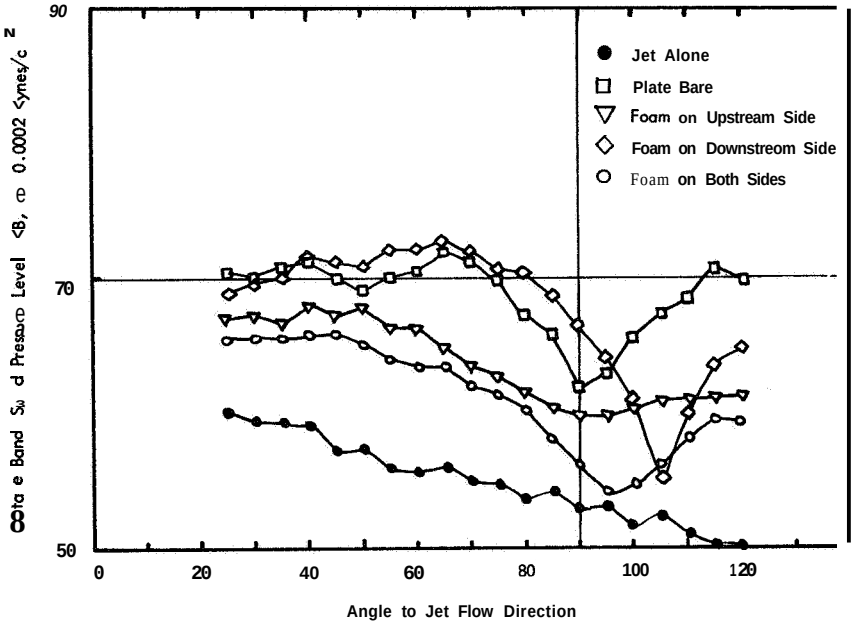

FIGURE 13.—Directivity of sound field, 4000-Hz octave band.

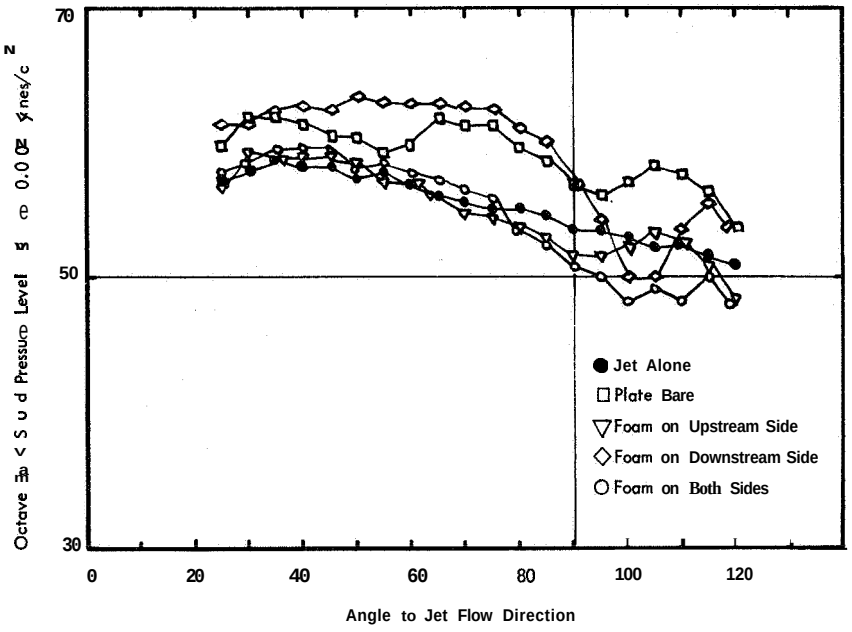

FIGURE 14.—Directivity of sound field, 8000-Hz octave band.

about 1 ft, the wavelength at **1000** Hz, although the thin foam is still operating at a frequency too low to cause any significant effect.

Figure 12 shows similar results for the 2000-Hz octave band, though now it is possible to see the effect of the foam. The results for the downstream arc are less than the results for no foam added. The levels for the upstream arc are reduced in turn when foam is added to the upstream side. However, the levels still do not approach those of the jet alone.

Figure **13** shows the results for the 4000-Hz octave band and gives a similar effect, except here the foam is even more efficient.

Figure **14** shows the 8000-Hz octave band. It should be remembered that the spectrum of the jet alone peaks at a frequency much below this value. These results show two differences from the previous figures. First, the increase caused by the bare plate is not so great as previously measured; second, the foam addition brings the levels down to the results measured for the jet alone.

Figure **15** shows these results plotted as octave band power in the forward hemisphere; i.e., in the initial 90° measured from the jet flow

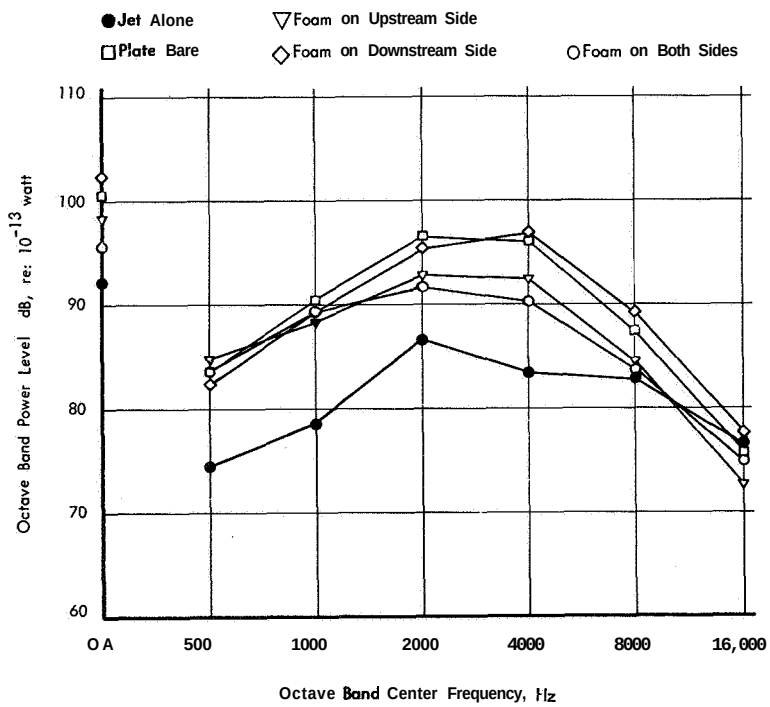

FIGURE 15.—Spectrum of total sound in the forward hemisphere (0 to 90° to the jet flow direction).

direction. These results show how the plate causes **10** dB more power at the low frequencies up to the jet-noise peak frequencies. At the highest frequencies, little increase is observed. The results also show how the foam absorbs the high-frequency sound; further, the directional plots show a very pronounced directivity in midfrequencies and the results assume a classic dipole-type radiation, with sound radiated in both directions.

POSSIBLE NOISE-GENERATION MECHANISMS

Three proposed mechanisms for this jet-orifice noise generation were examined. The first idea examined was that the local near-field pressures, which normally will not radiate, are forced to radiate sound by interacting with the plate's surface. Because this sound will be expected to follow a U^6 law, and the addition of foam **on** the plate's surface will be expected to remove this effect, at least at frequencies where the foam could act, this idea looked most promising. However, the main drawback of such a hypothesis is that the frequencies affected are not those of the local near-field pressure fluctuations. At the locations considered, the near-field pressures contain mostly very high frequencies, greater than the peak frequency of the jet noise alone. However, the jet-orifice interaction noise is generated at frequencies less than the peak frequencies of the jet noise itself.

The second idea suggested that, although the jet mixing flow itself did not touch the orifice, the jet did, in fact, actually induce a small flow through the orifice. This flow will be unsteady, and the resulting mass-flow fluctuations will radiate sound similar to a piston in a surface, thus producing monopole noise generation. Calculations suggested that a rms velocity fluctuation of about **2** fps is all that is required to produce the results shown here at **2000 Hz.** This sound is generated much more efficiently than the aerodynamic mixing noise, so it is possible that it could dominate over the jet noise at low jet velocities. The frequencies will be fixed by the frequencies of the air fluctuations through the orifice, and these will be driven in turn by the outer mixing flow of the jet, which does contain low frequencies. Therefore, the results can be expected to show an increase in sound at frequencies lower than the jet noise as measured. However, the effect of adding foam to the plate's surface should be negligible and, in these experiments, a distinct reduction in noise was noted.

A final theory suggests that the plate splits the noise-generating region within the jet flow that originates the resultant sound field to form a more efficient noise-producing system. Figure **16,** for example, shows a longitudinal quadrupole and an observer at a position ***P*,** where a

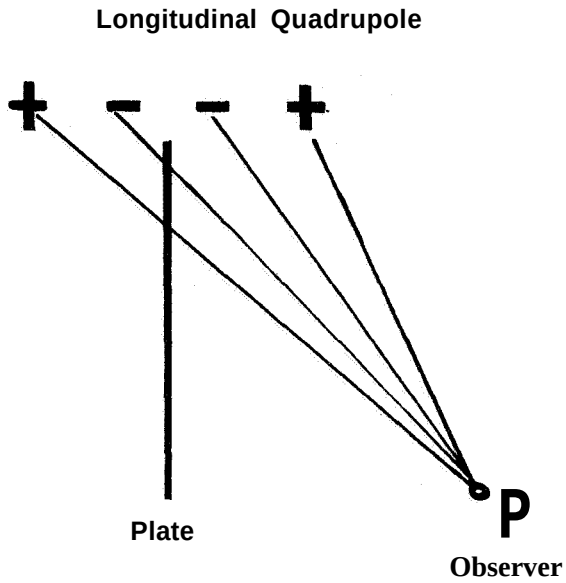

FIGURE 16.—Plate-splitting of quadrupole.

resulting pressure, caused by this longitudinal quadrupole, is the result of the addition of the four fields. Placing a plate so that it acts to eliminate two elements of the quadrupole means that the observer at P in effect sees a dipole, which is a much more efficient noise generator. It may also be considered that the plate reduces the correlation length over which the convective disturbances radiate to produce the sound received by the observer. Cutting off part of this correlation length results in a smaller correlation volume locally. However, with a large part of the low correlation volume eliminated, a stronger, more coherent source and a resulting increased sound pressure at the observer would be produced.

CONCLUSIONS

The interaction of a jet flow passing cleanly through an orifice has been examined in terms of the additional noise generated. The experimental program is proceeding and producing results that, unfortunately, only tend to confuse the determination of the noise-generation mechanism. Several mechanisms have been suggested and certain results of the experiments have tended to confirm different points of the postulated mechanisms. The experiments are continuing with the insertion of microphones in the plate surfaces to measure the fluctuating pressure on the plate itself.

REFERENCES

1. POTTER, R. C.; AND JONES, J. H.: An Experiment to Locate the Acoustic Sources in a High Speed Jet Exhaust Stream (Preliminary Results). J. Acoust. Soc. Am., vol. 42, no. 5, 1967.
2. POTTER, R. C.: An Investigation To Locate the Acoustic Sources in a High Speed Exhaust Stream. Research Staff Rept. WR 68–4, Wyle Laboratories, 1968.
3. FFOWCS WILLIAMS, J. E.: The Noise From Turbulence Convected at High Speed. Phil. Trans. Roy. Soc. London, ser. A, vol. 255, 1963.
4. ELDRED, K. M.; ET AL.: Suppression of Jet Noise With Emphasis on the Near Field. Rept. ASD–TDR–62–578, Wright-Patterson Air Force Base, 1963.
5. LARGE, J. B.: The Development of Engineering Practices in Jet, Compressor and Boundary Layer Noise. AFOSR–UTIAS Symposium on Aerodynamic Noise, Univ. of Toronto Press, 1969, pp. 43–67.
6. RIBNER, H. S.: On the Strength Distribution of Noise Sources Along a Jet. Rept. 51, Inst. of Aerophysics, University of Toronto, 1958.

ACOUSTIC SPECTRA FROM TURBULENT JETS

William C. Meecham"
University of California
Los Angeles, Calif.

One of the interesting and important problems involving turbulent jets is that of determining the spectrum of the radiated sound. This has proved to be a difficult theoretical problem because the space-time correlation of the velocity is central in the prediction of such sound characteristics. In this work we use the following assumptions in the development. First we suppose, as is often the case in turbulence measurements, that the turbulent fluid has approximately gaussian statistical characteristics. Then we suppose that the space-time characteristics for the needed second-order velocity correlation can be obtained by assuming that the fluid is approximately in frozen flow. From these assumptions the higher frequency sound-power spectrum is obtained in terms of an integral over the turbulence energy spectrum. For the familiar energy spectrum $k^{-5/3}$, it is found that the sound spectrum behaves like $\omega^{-4/3}$. For the often-measured energy spectrum k^{-2}, the sound spectrum behaves as ω^{-2}.

INTRODUCTION

A problem in connection with turbulent jets that is of considerable interest is that of determining the spectrum of the acoustic radiation. The problem of predicting sound spectra from isotropic turbulence was considered previously (ref. 1). The fundamental work in aerodynamic sound from turbulence is contained in the work of Lighthill (ref. 2).

Some general remarks can be made concerning acoustic radiation from a turbulent jet. First, it is known that the bulk of the energy in the turbulent motion will reside in the large-scale eddies. It is also known that the number and size of these large eddies is dependent upon the manner in which the turbulence is produced. Thus we can expect that the large-scale characteristics (energy range) of the turbulence depend upon details of the jet generation process. Because most of the acoustic radiation comes from the large-scale eddies, we can say at the outset that the total acoustic power produced by a given turbulent motion

*The author is also a consultant with Bolt, Beranek & Newman, Inc.

will depend upon the manner in which the turbulence is generated. Concerning the spectrum of the turbulence, one can say that because the large-scale eddies produce the low-frequency sound, the low-frequency end of the power spectrum will depend upon the driving mechanism of the turbulence (the jet characteristics). The high-frequency end of the spectrum, on the other hand, may be somewhat independent of the driving forces. This high-frequency sound is produced by the rapid fluctuations in the turbulent fluid. One plausible model of the sound-generation process suggests that the small-scale eddies give rise to the high-frequency components of the power spectrum. This view is adopted here.

We shall first briefly review the pertinent theory of aerodynamic sound. It will be seen that the crucial quantity in determining the sound radiated is the fourth-order space-time correlation of the velocity fluctuation within the turbulent jet, at least in low-fluctuation mach number jets. It is known for homogeneous turbulent processes, for example, wind-tunnel experiments, that the velocity fluctuations are in many important characteristics near-gaussian. In particular within experimental error the even moments of the velocity fluctuation are related to one another as they would be for a gaussian process (ref. 3). Incidentally, the same work has shown that odd moments in dimensionless form are typically of an order of a few percent. Furthermore, it has been found that the velocity fluctuations at a single point are gaussian to within experimental error (ref. 4). Indeed, these wind-tunnel experiments have shown that the processes are nearly gaussian in the way described (that is, the even moments related to one another as they would be for a gaussian process), even for space-time correlations. We shall assume that jet flows behave similarly and use the relationship between fourth-order and second-order velocity correlations that would be obtained if the process were exactly gaussian.

Concerning the time characteristics of the correlations, we proceed in the following manner. First we know that if we take measurements of a transporting turbulent flow, measuring at a fixed point or points, we find that the time changes are primarily the result of the transport process itself. This characteristic of the process is one regularly observed in turbulent flows, at least homogeneous turbulent flows, and has often been called frozen turbulence in the literature. We shall assume that the time correlations for smaller eddy characteristics of the second-order velocity correlation are governed primarily by the transport process as indicated.

Use of these two simplifying assumptions, in the order indicated, will permit us to calculate the high-frequency end of the spectrum for the sound radiated by the turbulent jet. These assumptions are discussed in more detail later. They lead to the prediction of sound spectra depend-

ent upon the spatial energy spectrum of the turbulence within the jet. If we assume that the energy spectrum is the Kolmogoroff spectrum $E(k) \sim k^{-5/3}$, we obtain a power spectrum for the sound falling off at the high-frequency end as $\omega^{-4/3}$. On the other hand, if we use for the energy spectrum of the turbulence $E(k) \sim k^{-2}$, a spectrum often observed experimentally for lower Reynolds number flows, we obtain a power spectrum for the sound falling off like ω^{-2}. Whatever else may be said for the approximations necessary for this calculation, it will be seen that the resulting spectra are not inconsistent with experimental results for the sound radiated by turbulent jets.

REVIEW OF THE THEORY OF SOUND FROM JETS

Consider a volume V of turbulent fluid in jet. The turbulent fluid is assumed to be essentially the same as that surrounding the turbulent region, which we shall assume to be at rest. In addition, it will be assumed that the motion is statistically stationary, i.e., the statistical properties of the flow do not depend upon the time. The size of the jet is taken to be of order L, where order is the diameter of the jet exit. The large, energy-containing eddies are also of order L. As stated above, we assume that the velocity fluctuations are smaller than c_0, the velocity of sound in the undisturbed fluid. Ordinarily this condition is satisfied even for jets whose mean flow is transonic. We leave for later work the effects of refraction, which are the result of either temperature effects in the jet or the shear characteristics of the jet. In any event, effects may not be important for the high-frequency end of the sound spectrum, though of course they do affect the spatial distribution of the sound (ref. 5).

Starting from the Navier-Stokes equation we use the index summation convention throughout

$$\frac{\partial u_i}{\partial t}+u_i\frac{\partial u_i}{\partial x_j}=-\frac{1}{\rho}\frac{\partial \rho}{\partial x_i}+\nu\left[\nabla^2 u_i+\frac{1}{3}\frac{\partial}{\partial x_i}\nabla\cdot\mathbf{u}\right] \tag{1}$$

and the equation of continuity

$$\frac{\partial \rho}{\partial t}+\frac{\partial}{\partial x_j}(\rho u_j)=0 \tag{2}$$

Lighthill (ref. 2) has obtained the following expression for the density fluctuations at a point r caused by the turbulent motion

$$\begin{aligned}\Delta\rho(\mathbf{x},t)&=\rho(\mathbf{x},t)-\rho_0\\&=\frac{\rho_0}{4\pi c_0^2}\int_V d\mathbf{y}\int dt'\,\frac{\delta(t'-t+|\mathbf{y}-\mathbf{x}|/c_0)}{|\mathbf{y}-\mathbf{x}|}\frac{\partial^2 u_i' u_j'}{\partial y_i \partial y_j}\end{aligned} \tag{3}$$

where the u_i' are the fluctuation velocity components of the fluid at the point y and the time t', and ρ_0 is the mean density. There are possible cross-terms, which could also serve as sources, involving fluctuations and mean flow terms. Ribner's work (ref. 5) suggests these terms are of the same order. In the present work we treat only fluctuation terms. In obtaining equation (3), it has been assumed that the effects of temperature and viscosity on the propagation of sound are negligible. The velocity components associated with the acoustic waves are small compared with the turbulent velocity and u' is assumed small compared with c_0, hence in equation (3) the u_i' are taken to be the velocity components associated with the incompressible turbulent motion. The integration over y is thus confined to the volume V. We are interested in the sound field far from the turbulent region. From equation (3) by performing the t' integration, integrating by parts in y, and dropping terms of order $(y/x)^2$, we obtain

$$\Delta\rho(\mathbf{x}, t) = \frac{\rho_0}{4\pi c_0^4}\frac{x_i x_j}{x^2}\frac{\partial^2}{\partial t^2}\int_V d\mathbf{y}\, u_i' u_j' \left(\mathbf{y}, t - \frac{|\mathbf{x}-\mathbf{y}|}{c_0}\right) \tag{4}$$

Based upon our assumption that u' is small, we may in the usual way neglect retardation effects. Then the time correlation of the distant density change is, using the assumed statistical stationarity and hence time averages

$$\langle \Delta\rho(t)\, \Delta\rho(t-\tau)\rangle = \frac{x_i x_j x_k x_l}{x^4}\frac{\rho_0^2 \bar{V}}{(4\pi c_0^4 x)^2}\frac{\partial^4}{\partial \tau^4}\int d\xi Q_{ij,kl}(\boldsymbol{\xi}, \tau) \tag{5}$$

with the fourth-order correlation defined by

$$Q_{ij,kl}(\boldsymbol{\xi}, \tau) \equiv \langle u_i' u_j'(\mathbf{y}, t) u_k' u_l'(\mathbf{y}+\boldsymbol{\xi}, t+\tau)\rangle \tag{6}$$

In obtaining equation (5) from equation (4) we have made the simplifying assumption that the turbulent jet is locally and statistically homogeneous. We permit a variation in turbulence intensity, however, leaving the following definition of the effective volume of turbulence (used in eq. (5)):

$$V \equiv \int d\mathbf{y}[\langle u'^8(\mathbf{y})\rangle / \langle u'^8(\mathbf{y}_0)\rangle] \tag{7}$$

Here y_0 is a point near the core of the jet where the turbulence intensity is greatest. The eighth power of u' is used as a weighting function because in equation (5) the estimated time derivative is proportional to u' which in conjunction with equation (6) suggests a form like that of equation (7). In fact, the 8th power is a reflection of the Lighthill 8th-power law. It shows the known fact that the volume of turbulence effec-

tive in sound production is only effective in the region where the turbulence intensity is a maximum. The coefficients $\mathbf{x}$ in equation *(5)* give the well-known quadrupole source characteristic.

The sound intensity magnitude in the direction $\mathbf{x}$ $I(\mathbf{x})$ emitted by the turbulence is proportional to this correlation (5) for $\tau=0$. The power spectrum $I(\mathbf{x}, \omega)$ is related to its Fourier transform. Thus

$$I(\mathbf{x})=\frac{c_0^3}{\rho_0}\langle\Delta\rho(\mathbf{x}, t)\Delta\rho(\mathbf{x}, t)\rangle \tag{8}$$

$$I(\mathbf{x}, \omega)=\frac{c_0^3}{2\bar{u}\rho_0}\int_{-\infty}^{\infty} d\tau e^{i\omega\tau}\langle\Delta\rho(\mathbf{x}, t)\Delta\rho(\mathbf{x}, t-\tau)\rangle \tag{9}$$

Inserting equation (5) we find

$$I(\mathbf{x})=\frac{\rho_0\bar{V}}{6\pi^2x^2c_0^5}\frac{x_ix_jx_kx_l}{x^4}\int d\xi\left[\frac{\partial^4}{\partial\tau^4}Q_{ij,kl}(\xi, \tau)\right]_{\tau=0} \tag{10}$$

and

$$I(\mathbf{x}, \omega)=\frac{\rho_0\bar{V}}{32\bar{u}^3x^2c_0^5}\frac{x_ix_jx_kx_l}{x^4}\int d\xi\int_{-\infty}^{\infty} d\tau\, e^{i\omega\tau}\frac{\partial^4}{\partial\tau^4}Q_{ij,kl}(\xi, \tau) \tag{11}$$

It is clear from equations (10) and (11) that we need the time characteristics of the velocity correlation to discuss the radiated sound. To continue the discussion, further assumptions are needed, as outlined in the introductory section.

USE OF THE NEARLY NORMAL AND FROZEN-FLOW ASSUMPTIONS TO OBTAIN THE SPECTRUM

As suggested, it is known that subsonic, wind-tunnel turbulence is in certain characteristics, nearly normal (gaussian) (ref. *3)*. In particular, it was found for the space and time delays measured that to good approximation

$$Q_{ij,kl}(\xi, \tau)=Q_{ij}(0, 0)Q_{kl}(0, 0)+Q_{ij}(\xi, \tau)Q_{jl}(\xi, \tau)+Q_{il}(\xi,\tau)Q_{jk}(\xi, \tau) \tag{12}$$

There is not so much statistical evidence for free jets as there is for wind tunnels, but we shall assume that equation (12) holds approximately in our jet problem as well. Adjacent to jet boundaries we may have to take turbulence intermittency into account in later refinements of this work. Assumption (12) has been used by Stein (ref. *6)* in the treatment of geo-

physical problems involving the aerodynamic generation of acoustic-gravity waves. Stein, however, used a quite different approach to the determination of the time characteristics than that to be suggested here.

Our program now consists of substituting equation **(12)** into equations **(10)** and **(11).** Evidently, to proceed, we shall need an estimate of the second-order, space-time velocity correlation Q_{ij}. For this purpose, we employ the frozen-flow hypothesis as discussed above. Frenkiel and Klebanoff (ref. **3)** have found this assumption to be a good approximation for wind-tunnel turbulence. As remarked, we shall focus attention on the smaller eddy structure to determine the higher frequency sound spectrum characteristics. Adopting a frozen-flow hypothesis enables us to approximately determine the space-time correlation from a simple space correlation of the velocity fluctuations. If we suppose that the small eddies are transported on larger eddies, we can deduce the space-time correlation as follows:

$$Q_{ij}(\boldsymbol{\xi}, \tau) \cong \int Q_{ij}(\boldsymbol{\xi}+\mathbf{U}\tau)P(\mathbf{U})\, d\mathbf{U} \tag{13}$$

In equation (13), Q_{ij} in the integral is the simple second order space-correlation for the velocity fluctuations. Here U is the large-eddy locally observable velocity. As indicated, to obtain the space-time correlation, one must weigh this with the probability distribution of the large-eddy velocity, here $P(\mathbf{U})$. It is known for wind tunnel experiments (ref. **4)** that the distribution of the velocity is, to a good approximation, gaussian. We shall once again extend those experiments by hypothesis to include velocity distributions in jets. Thus we propose to use for the probability density, ignoring anisotropic complications,

$$P(\mathbf{U}) = (2\pi U_0^2)^{3/2}\, e^{-U^2/2U_0^2} \tag{14}$$

where U_0^2 is the mean-square velocity fluctuation. It is convenient to use the Fourier transform of the simple space correlation defined as follows:

$$Q_{ij}(\mathbf{Z}) = \int \Phi_{ij}(\mathbf{k})\; e^{i\mathbf{k}\cdot\mathbf{z}} d\mathbf{k} \tag{15}$$

Substituting equation **(15)** into equation **(13)** and changing the variable of integration in equation (13), we find

$$Q_{ij}(\boldsymbol{\xi}, \tau) = \int \Phi_{ij}(\mathbf{k})\; \exp\left[i\boldsymbol{\xi}\cdot\mathbf{k} - \frac{U_0^2\tau^2}{2} k^2\right] d\mathbf{k} \tag{16}$$

Obviously, we cannot expect equation **(16)** to be a valid approximation

for the largest eddies within the turbulence, for the idea that the space correlation is transported on the energy-containing eddies would then lose its meaning. However, the result seems fairly plausible for the smaller eddies, in which we are mainly interested.

Consider now the quantity needed for equations (10) and **(11)**

$$\frac{x_i x_j x_k x_l}{x^4} \frac{\partial^4}{\partial \tau^4} Q_{ij,\,kl}(\xi, \tau) \tag{17}$$

which is to be obtained from equation (12) and following work. Examining equation (12), we see that the differentiation removes the first term. Furthermore, because of symmetry, the second and third terms will be equal after substitution. For equations **(10)** and **(11)** we see that we need the integral over ξ. Taking these simplifications into account, we substitute equation **(16)** into equation (12) and that in turn into equation (11), perform the time-Fourier transform, and obtain the result

$$I(\mathbf{x}, \omega) = \frac{\rho_0 \bar{V}}{2c_0^5} \frac{\omega^4}{x^2} \frac{x_i x_j x_k x_l}{x^4} \int \left(\frac{\pi}{U_0^2 k^2}\right)^{1/2} e^{-\omega^2/4U_0^2k^2} \cdot \Phi_{ik}(\mathbf{k})\ \Phi_{jl}(-\mathbf{k})\ d\mathbf{k} \tag{18}$$

Equation (18) is obtained by integrating the inner integral in equation **(11)** four times by parts. For @-functions that are algebraic, and for even more general classes of functions, we see that significant contributions to the integral in equation (18) occur for the smaller eddies; that is, for $k > \omega/U_0$.

This is consistent with our assumption that the higher frequencies in the sound spectrum come from the smaller eddies (larger wave numbers). In turbulence experiments it has been found (ref. **4)** that these smaller eddies can be expected to be approximately statistically isotropic. In such a case the tensor Φ_{ij} can be written

$$\Phi_{ij}(\mathbf{k}) = \frac{E(k)}{4\pi k^4} (k^2 \delta_{ij} - k_i k_j) \tag{19}$$

where E is the usual energy spectrum function. Substituting equation (19) into equation (18), summing as indicated, and carrying out angular integration, we obtain

$$I(\mathbf{x}, \omega) = \frac{\rho_0 \bar{V} \omega^4}{c_0^5} U_0 \frac{1}{15\sqrt{\pi} x^2} \int_0^\infty k^{-3}\, e^{-\omega^2/4k^2U_0^2}\, E^2(k)\, dk \tag{20}$$

The resulting radiated field at these higher frequencies is isotropic under our simplifying assumptions. Of course, refraction effects within the jet

can be expected to upset such a simple result for the spatial distribution of the radiated sound. Doppler effects caused by the motion of the sources in the jet exist. Side effects cause intensity changes but will not affect the frequency dependence, in most cases, of the higher frequency end of the sound spectrum.

We now substitute some familiar energy spectra into equation (20). For the smaller eddies, measurements show that the energy spectra are algebraic

$$E(k) \sim c_\alpha k^{-\alpha} \tag{21}$$

Substituting equation (21) into equation (20) and using standard integrals (ref. 7), we obtain for the expected high-frequency sound spectrum

$$I(x, \omega) = \frac{\rho_0 \bar{V}^{16}}{15x^2 c_0^5} U_0^3 \left(\frac{2U_0}{\omega}\right)^{2\alpha-2} c_\alpha^2 \frac{\Gamma(2\alpha+2)}{\Gamma(\alpha+3/2)} \tag{22}$$

where Γ is the familiar gamma function. Recent measurements taken in very large Reynolds-number flows have shown a five-thirds-law spectrum; i.e., $\alpha = 5/3$ in equation (21). Using dimensional reasoning and standard turbulence results (ref. 4), we find for the constant

$$C_{5/3} = K_{5/3} U_0^2 k_0^{2/3}$$

where $K_{5/3}$ is a dimensionless constant of order unity and k_0 is the wave number at the energy spectrum maximum. Substituting in equation (22), we find that $I(x, \omega) \sim \omega^{-4/3}$ for this presumed energy spectrum function. Earlier, lower Reynolds-number flows gave a measured energy spectrum function for higher wave frequencies, falling off, as k^{-2}. The constant C_2 in this case turns out to be $K_2 U_0^2 k_0$ where again K_2 is a dimensionless constant of order unity. Substituting in equation (22), we find $I(x, \omega) \sim \omega^{-2}$. Both of these spectra have divergent integrals at low frequencies, indicating a not-unexpected failure of the assumptions in that frequency range. It was noted in the introduction that it is likely the sound-frequency spectrum at low frequencies will be strongly dependent upon the geometrical form of the jet itself. Thus, we can expect these lower frequency characteristics to vary considerably from one jet experiment to another.

Many experiments involving air jets, jet engines, and rockets, for example, reference 8, have yielded spectra that fall off as ω^{-1} to ω^{-2} on the high-frequency side. Thus, the results obtained here involving the use of a nearly normal assumption together with a frozen-flow assumption seem to be consistent with many jet-noise measurements. Finally,

we might remark that the combination of assumptions amounts to a view that the noise is generated by the higher frequency sources being rotated by the energy-containing eddies. This is perhaps reminiscent of the familiar model used in the treatment of propeller noise.

REFERENCES

1. MEECHAM, W. C.; AND FORD, G. W.: Acoustic Radiation From Isotropic Turbulence. J. Acoust. Soc. Am., vol. 30, 1958, pp. 318–322.
2. LIGHTHILL, M. J.: Sound Generated Aerodynamically. Proc. Roy. Soc., ser. A, vol. 267, 1962, pp. 147–182.
3. FRENKIEL, F. N.; AND KLEBANOFF, P. S.: Higher-Order Correlations in a Turbulent Field. Phys. Fluids, vol. 10, 1967, pp. 507–520.
4. BATCHELOR, G. K.: Homogeneous Turbulence. Cambridge University Press, 1953.
5. RIBNER, H. S.; AND MACGREGOR, G. R.: The Elusive Doppler Shift in Jet Noise. Sixth International Congress on Acoustics, vol. IV, 1968, pp. 97–100.
6. STEIN, R. F.: Generation of Acoustic and Gravity Waves by Turbulence in an Isothermal Stratified Atmosphere. Solar Phys., vol. 2, 1967, pp. 385–432.
7. MAGNUS, W.; AND OBERLIETTINGER, F.: Special Functions of Mathematical Physics. Chelsea Pub. Co., 1949.
8. COLE, J. N.; VON GIERKE, H. E.; KYRAZIS, D. T.; ELDRED, K. M.; AND HUMPHREY, A. J.: Noise Radiation From Fourteen Types of Rockets in the 1,000 to 130,000 Pounds Thrust Range. WADC TR 57–354, 1957.

371–986 O-LT-70 – 13

II

Fan Noise Research

Chairman: **W. R. SEARS**

DIRECT CORRELATION OF FLUCTUATING LIFT WITH RADIATED SOUND FOR AN AIRFOIL IN TURBULENT FLOW*

P. J. F. Clark and H. S. Ribner
University of Toronto
Canada

An airfoil in turbulent flow is thought to radiate sound in consequence of its fluctuating lift. The instantaneous sound and lift should be connected by Curle's equation, which describes sound radiation from a rigid surface in contact with turbulent flow. It follows that the crosscorrelation of sound and lift should be related in a corresponding way to the lift autocorrelation. Such correlations were measured in the present investigation of an airfoil in a jet flow, and the Curle relationship was verified semiquantitatively. The predicted comparative shapes of the correlation curves were found; the comparative magnitudes showed a 27-percent (2.7-dB) discrepancy. This small discrepancy is attributed to model vibration, which falsely enhanced the lift signal via inertial loading. This small discrepancy is attributed to model vibration, which falsely enhanced the lift signal via inertial loading. The work answers in part questions that have been raised as to the applicability of Curle's equation. Further, it confirms that a rigid surface in contact with a turbulent flow need not be inherently passive—a reflector of sound—but can be an active generator of sound.

*A complete version will appear as a short paper in the Journal of the Acoustical Society of America.

SOME ASPECTS OF DISCRETE FREQUENCY NOISE GENERATION IN AXIAL-FLOW FANS*

Ramani Mani
General Electric Co.
Schenectady, N.Y.

This paper summarizes solutions to two classical problems arising in studies of blade passing frequency noise from fans and compressors. The first concerns the problem of estimating noise generated from a blade row caused by fluctuating forces induced on it because of the presence of a neighboring row. The special feature of the present solution in this case is that moving medium effects are incorporated. The second problem is concerned with the propagation of sound waves generated from one row through an adjacent row. A critical experiment to verify aspects of the first analysis is described. The experiment proved useful both in verifying major results of the noise-generation theory and in indicating further areas of research.

SYMBOLS

a	representative radius of fan annulus
A	amplitude of pressure waves
B	number of rotor blades
c	speed of sound
$\mathbf{F}$	force
j	$\sqrt{-1}$
k	wave number in axial direction
l	blade chord length
m	integer, number of tangential lobes
M	mach number
n	harmonic of blade passing frequency
$\mathbf{n}$	unit wave normal
p	pressure
$\mathbf{q}$	vector velocity

* This work has been supported by: Aircraft Engine Group of the GE Co., FAA under contract FA–SS-67–7, and the GE Research and Development Center.

$\mathbf{r}$	position vector
r	radial coordinate, also integer
$R(r)$	combination of Bessel functions whose gradient vanishes at hub and tip
s	spacing between blades
S	number of stator blades
t	time
U	axial velocity
V	swirl velocity
$\mathbf{v}$	velocity of moving medium
Y	tangential coordinate
z	axial coordinate
β	axial mach number
γ	swirl mach number
ξ	orientation of force
δ	Dirac delta function
Δ	constant
ϕ	angular coordinate in cylindrical coordinate system
λ	wavelength
ρ	density
θ	phase factor
ω	frequency, radii per sec
Ω	rotor frequency, radii per sec

Abbreviation

GA	geometrical acoustics

Subscripts

0	steady state
1	upstream
2	downstream
$+$	upstream
$-$	downstream
A	amplitude factor
r	rotor, also radial component
s	stator
t	at the tip
Y	tangential component
z	axial component
ϕ	ϕ-component

Superscripts

$'$	unsteady quantity
1	upstream
2	downstream

INTRODUCTION

The present paper is a summary of recent work at the GE Research and Development Center on blade passing frequency noise generated from fans and compressors. Much of this work has been reported elsewhere (refs. **1,** 2, 'and **3)** and the purpose of the present note is to present abbreviated versions of these analyses in a logical sequence and to clearly indicate their relevance to the compressor noise problem.

The author acknowledges gratefully the assistance of **M.** J. Benzakein, W. ***G.*** Cornell, and **N.** J. Lipstein of the GE Co. in various aspects of the work reported herein. ***G.*** Horvay (formerly of the GE Co. and now of the University of Massachusetts) collaborated with the author on the work reported in the section on an approximate theory of sound propagation through blade rows.

GENERATION OF NOISE FROM A BLADE ROW

Many previous works (ref. **4)** have pointed out the importance of interaction between moving and stationary rows in axial flow machines as an important source of pure-tone noise. Perhaps the most striking evidence for this is that the pure-tone noise decreases as the axial separation between the rows is increased. In the present section we shall develop a two-dimensional analysis to predict the amounts of acoustic energy, at the blade passing frequency and its harmonics, radiated upstream and downstream of a blade row because of its interaction with a neighboring row. Some papers have appeared on this subject (ref. 5) but a treatment of the noise-generation problem that includes the effects of flow is not known to the author. Our purpose is twofold: first, to indicate the linearization of the basic equations necessary to yield a tractable problem applicable to flow situations in present axial-flow fans; second, to develop concrete expressions for the noise generated.

Our concern in this paper is with aerodynamic sound. The basic theory is Lighthill's work (ref. **6),** but for blade passing noise, the most pertinent theory is the extension of Lighthill's theory by Curle (ref. **7)** to include the effects of solid boundaries. Curle showed that the influence of solid boundaries is equivalent to a distribution of acoustic dipoles, each representing the force with which unit area of the solid boundary acts upon the fluid. Experimental information on the tip-speed dependence of blade passing noise has identified the unsteady forces exerted by the blades on the fluid as the dominant source of noise. The significance of Curle's results is that if the fluid flow through a fan were solved exactly and the unsteady forces exerted by the solid surfaces on the fluid were known, the contribution of the solid surfaces to the noise could be found by placing on the surfaces acoustic dipoles equal to the unsteady forces.

Such an exact solution of the unsteady flow through a fan is, however, far from available, and hence one has to resort to procedures of linearization and consideration of the most likely noise sources to achieve tractable problems.

Linearized Equations for the Unsteady Quantities

The basic flow through an axial flow fan as calculated by present design methods is a steady, axisymmetric flow. Since high efficiencies are attained by present-day fans designed on this basis, we may reasonably assume this to be the dominant part of the flow through a fan. We consider unsteady flow quantities as small perturbations about this basic flow.

Euler's equations for an ideal compressible fluid are

$$\frac{\partial \rho}{\partial t} + \nabla \cdot (\rho \mathbf{q}) = 0 \tag{1}$$

and

$$\frac{\partial \mathbf{q}}{\partial t} + (\mathbf{q} \cdot \nabla)\mathbf{q} = -\frac{1}{\rho} \nabla p + \mathbf{F} \tag{2}$$

Consider a decomposition of (1) and (2) of type

$$\mathbf{p} = \rho_0 + \mathbf{p}' \tag{3}$$

where ρ_0 is independent of time and $\mathbf{p}'$ is time dependent, and the unsteady quantities are regarded as one order smaller than the steady quantities.

The zeroth-order equations are

$$\nabla \cdot (\rho_0 \mathbf{q}_0) = 0 \tag{4}$$

and

$$(\mathbf{q}_0 \cdot \nabla)\mathbf{q}_0 = -\frac{1}{\rho_0} \nabla p_0 + \mathbf{F}_0 \tag{5}$$

The first-order equations are

$$\frac{\partial \rho'}{\partial t} + \nabla \cdot (\rho' \mathbf{q}_0 + \rho_0 \mathbf{q}') = 0 \tag{6}$$

and

$$\frac{\partial \mathbf{q}'}{\partial t} + (\mathbf{q}_0 \cdot \nabla)\mathbf{q}' + (\mathbf{q}' \cdot \nabla)\mathbf{q}_0 = -\frac{1}{\rho_0} \nabla p' + \frac{\rho'}{\rho_0^2} \nabla p_0 + \mathbf{F}' \tag{7}$$

Equations (6) and (7) are the usual starting points of the study of the acoustics of a moving, nonhomogeneous medium (ref. 8). Even these linear equations are difficult to handle in their present form. For example it is not possible to assume that $\mathbf{q}'$ is irrotational or that the unsteady field is isentropic without further simplification. We are interested in discrete frequency sound, and we will use the approximations of geometrical acoustics (ref. 7, ch. 2, sec. 7). Geometrical acoustics (GA) is a high wave number or short-wavelength approximation in which one disregards spatial gradients of the steady-state quantities in equations (6) and (7) (and in any further spatial differentiations of eqs. (6) and (7)). With this simplification it is not surprising that one ends up with a field equation for p' very similar to the one obtained by considering a constant steady-state field. The main purpose of introducing the notion of GA is to consider how valid this notion is in the variable property steady-state flow fields in axial flow fans, and to take account within this approximation of changes in steady-state properties across the row.

Thus we may rewrite equations (6) and (7), using GA as

$$\frac{\partial \rho'}{\partial t} + (\mathbf{q}_0 \cdot \nabla)\rho' + \rho_0(\nabla \cdot \mathbf{q}') = 0 \tag{8}$$

and

$$\frac{\partial \mathbf{q}'}{\partial t} + (\mathbf{q}_0 \cdot \nabla)\mathbf{q}' = -\frac{1}{\rho_0}\nabla p' + \bar{F}' \tag{9}$$

Consider now the application of equations (8) and (9) to the fan-noise problem. We will neglect (in the cylindrical coordinate system of fig. 1) the radial component of $\mathbf{q}_0$. Guided by the work of Tyler and Sofrin

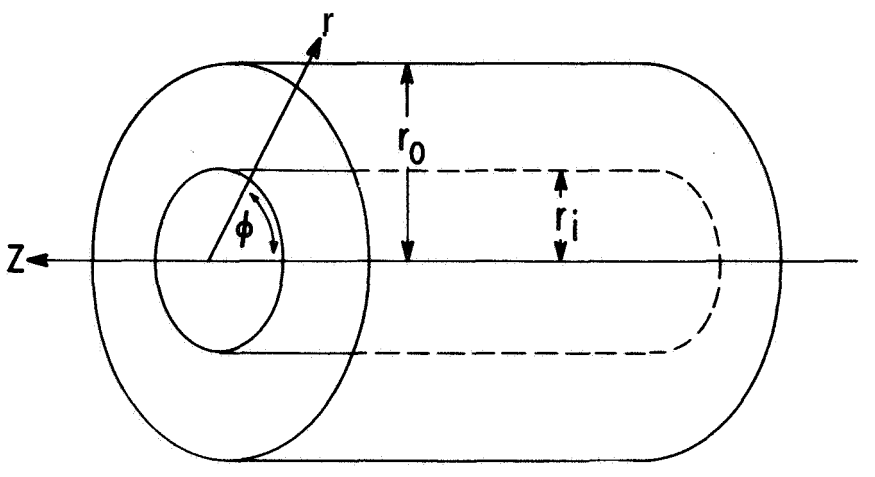

FIGURE 1.—Cylindrical coordinate system.

(ref. 9), consider solutions of q' whose z, ϕ, t-dependence is of type exp $j[m\phi+kz-\omega t]$ (i.e., waves periodic in ϕ, propagating along the axial direction and harmonic in time). Then

$$\left[-j\omega+jq_{0z}k+j\frac{m}{r}q_{0\phi}\right]\mathbf{q}'=-\frac{1}{\rho_0}\nabla p' \tag{10}$$

off the blade rows where $\mathbf{F}'=0$. Within the framework of **GA,** it is seen that $\mathbf{q}'$ is proportional to $\nabla p'$ and the requirement that q_r' vanish at the hub and tip translates into the condition that $\partial p'/\partial r=0$ at the hub and tip, which is the customary condition used in stationary acoustics. Finally to derive a single equation for the pressure, we take the divergence of equation (9), and substitute for $(\nabla\cdot\mathbf{q}')$ from equation (8), using always the approximation of **GA** to derive

$$\nabla^2 p'-\frac{1}{c_0^2}\frac{\partial^2 p'}{\partial t^2}-2\frac{(\mathbf{q}_0\cdot\nabla)}{c_0^2}\frac{\partial p'}{\partial t}-\frac{(\mathbf{q}_0\cdot\nabla)^2}{c_0^2}p'=\nabla\cdot\rho_0\mathbf{F}' \tag{11}$$

In reference 8 it is shown that within the approximations of **GA,** the unsteady field propagates isentropically and we have set

$$\frac{\partial p'}{\partial t}+\mathbf{q}_0\cdot\nabla p'=c_0^2\left[\frac{\partial\rho'}{\partial t}+\mathbf{q}_0\cdot\nabla\rho'\right]$$

$\rho_0\mathbf{F}'$ may be regarded as the unsteady force per unit volume.

Justification of the Approximation

Equation (11) has the same form as would have been obtained had we assumed a constant property, steady-state field. The only difference is that in GA one uses local values of $\mathbf{q}_0$, c_0, and ρ_0. It remains to consider how valid the notion of **GA** is for blade passing noise.

Consider, as a typical example, an estimate of the ratio of $|(\mathbf{q}'\cdot\nabla)\mathbf{q}_0|$ to $|(\mathbf{q}_0\cdot\nabla)\mathbf{q}'|$ in equation (7). We are considering solutions of $\mathbf{q}'$ of type $\mathbf{q}_A'$ exp $j\left(wt-\frac{2\pi}{\lambda}\theta\right)$, where A is the wavelength of sound, $\mathbf{q}_A'$ is an amplitude factor, and θ a phase factor. For plane waves in a stationary medium, **6** would be $\mathbf{n}\cdot\mathbf{r}$, where **n** is a unit normal to the wavefronts and **r** is the position vector. Thus $|\nabla\theta|$ is of order unity. Then

$$|(\mathbf{q}'\cdot\nabla)\mathbf{q}_0|\simeq q'\frac{\partial q_0}{\partial s}$$

where $\partial q_0/\partial s$ is a measure of the spatial gradient of q_0. Similarly

$$|(\mathbf{q}_0 \cdot \nabla)\mathbf{q}'| \simeq q_0 \left(\frac{2\pi}{\lambda}\right) |\nabla\theta| q'$$

Hence ratio $|(\mathbf{q}' \cdot \nabla)\bar{q}_0| \div |(\mathbf{q}_0 \cdot \nabla)\mathbf{q}'|$ is of order

$$\left[\left(\frac{\partial q_0}{\partial s}\right) \cdot \frac{\lambda}{2\pi}\right] \div q_0$$

or

$$\frac{(\Delta q_0)_{\frac{\lambda}{2\pi}}}{q_0}$$

where $(\Delta q_0)_{\frac{\lambda}{2\pi}}$ denotes the change of q_0 over a length $\lambda/2\pi$. Thus this admittedly crude estimate indicates that $(\mathbf{q}' \cdot \nabla)\mathbf{q}_0$ would be small compared to $(\mathbf{q}_0 \cdot \nabla)\mathbf{q}'$ if the change of q_0 over $\lambda/2\pi$ were small compared to q_0 itself. λ may be estimated as follows:

$$\lambda \sim \frac{2\pi c}{\omega} \sim \frac{2\pi c}{nB\Omega}$$

Let a denote a radius of the fan annulus at which the tip mach number is known, and let s denote the spacing between the blades at this radius. Then

$$\lambda \sim \frac{2\pi c a}{nB\Omega a} \sim \frac{s}{nM_t}$$

Assuming a solidity of the rows of unity, $\lambda = l/nM_t$, where l is the blade chord length. Now M_t ranges from about 0.75 to unity in present-day fans. Thus crudely we may say $\lambda = l/n$. For the fundamental tone the assumption that changes of q_0 over $1/2\pi$ of the chord are small is probably well justified. For the higher harmonics, linearization based on GA is even more justified.

We did not discuss the gradients of q_0 radially, because these are likely to be less severe than those axially by an order (1÷ aspect ratio of blades) and present-day fans use an aspect ratio of around 3.

Two-Dimensional Analysis: Expressions for Acoustic Power Upstream and Downstream of a Blade Row

The solution of equation (11) subject to equation (10) proceeds as follows. Regarding $\mathbf{q}_0$, assume for $q_{0\phi}$ a solid body rotation (i.e., $q_{0\phi} = r$) and take for q_{0z} some average value (different upstream and downstream of the row). Because $\partial p'/\partial r = 0$ at the hub and the tip and

$$p' \sim p'(r, z)e^{j(m\phi - \omega t)}$$

one assumes $p' = R(r) \exp j[kz + m\phi - \omega t]$, where R (r) is a combination of Bessel functions of order m whose gradient vanishes at the hub and tip (refs. 5 and **9).** A Fourier-Bessel analysis of the unsteady forces in the radial direction yields a decomposition of the three-dimensional problem of equation **(11)** into several two-dimensional problems; i.e., involving only z, ϕ, t.

In what follows, we shall restrict ourselves to a two-dimensional version of equation **(10).** The two-dimensional problem for acoustic power will be calculated at a representative radius of the fan annulus. The value of such analyses for high hub tip ratio machines, for example, greater than 0.75, has been pointed out by Morfey (ref. 5). We have chosen this as a starting point because we feel the introduction of the Bessel functions somewhat obscures the procedure of analysis that we wish to emphasize. All present analyses known to the author (refs. **10** to **13)** regarding the estimation of unsteady forces are on a two-dimensional basis. It makes little sense to push the acoustic analysis too far with only approximate methods available for the estimation of unsteady forces.

The theories of references **10** to **13** give amplitudes of unsteady lifts on blades based on potential and viscous wake interaction. All are based on incompressible flow, and the theory of reference **12** attempts to predict the unsteady lift distribution on the chord. With the large interrow separations used in present-day fans, it is probably true that most of the unsteady lift is because of viscous wake interaction. The theory in reference **12** predicts lift distributions peaked near the blade leading edges, and this theory has received some experimental support by Lefcort (ref. **14).** With the present knowledge of unsteady forces, the author feels that a good approximation to the unsteady forces in a blade row is to use a row of delta functions spaced apart by $(2\pi a/S)$ along an axial line, where a is the mean radius of analysis and S the number of vanes (see fig. 2). Consider a stator blade row with S vanes (spaced $2\pi a/S$ apart). At each vane, a force distribution acts which may be represented for the zeroth blade as

$$\mathbf{F}_{0_s}\delta(z)e^{-jnB\Omega t}\delta(y) \tag{12}$$

$\mathbf{F}_{0_s}$ is the unsteady lift obtained; e.g., as by the Kemp-Sears theory. The phase relation (ref. **10,** p. **492)** between the adjacent vanes implies that the force distribution at the mth blade is

$$\mathbf{F}_{m_s} = \mathbf{F}_{0_s}\delta\left(y - \frac{2\pi ma}{S}\right) e^{-jnB\Omega t\left(-\frac{2\pi m}{S\Omega}\right)} \delta(z) \tag{13}$$

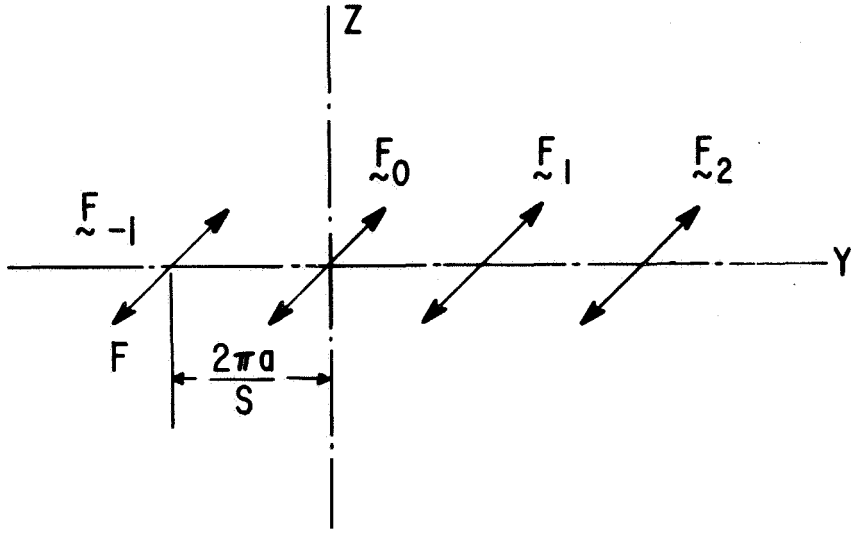

FIGURE 2.—Representation of forces by a row of delta functions.

$$= \mathbf{F}_{0_s}\delta\left(y-\frac{2\pi ma}{S}\right)e^{j2\pi mn\frac{B}{S}}e^{-jnB\Omega t}\delta(z) \tag{14}$$

Using the expansion formula

$$\delta(y-y_0)=\frac{1}{2\pi a}\sum_{r=-\infty}^{\infty}\exp\left[j\frac{r}{a}(y-y_0)\right]$$

We may show (ref. 9) that the sum of forces of type (14) from $m=O$ to $m=S-1$ is

$$\frac{S}{2\pi a}\mathbf{F}_{0_s}\delta(z)\sum_{k=-\infty}^{\infty}e^{j\left[(nB-kS)\frac{y}{a}-nB\Omega t\right]} \tag{15}$$

The k here is a dummy index of summation; $\mathbf{F}_{0_s}S/2\pi a$ is the unsteady blade force per unit transverse length. For the rotor, a very similar result holds; i.e., the unsteady forces combine in an axial plane to produce a force distribution (in a stationary frame of reference)

$$\delta(z)\mathbf{F}_{0_r}\frac{B}{2\pi a}\sum_{n=-\infty}^{\infty}e^{j\left[(nB-kS)\frac{y}{a}-nB\Omega t\right]} \tag{16}$$

n here is a dummy index of summation.

In using, e.g., the Kemp-Sears results, when considering an $(nB-kS)$ tangential mode from a stator, the unsteady force component of interest is the nth harmonic of the rotor blade passing frequency, while for the

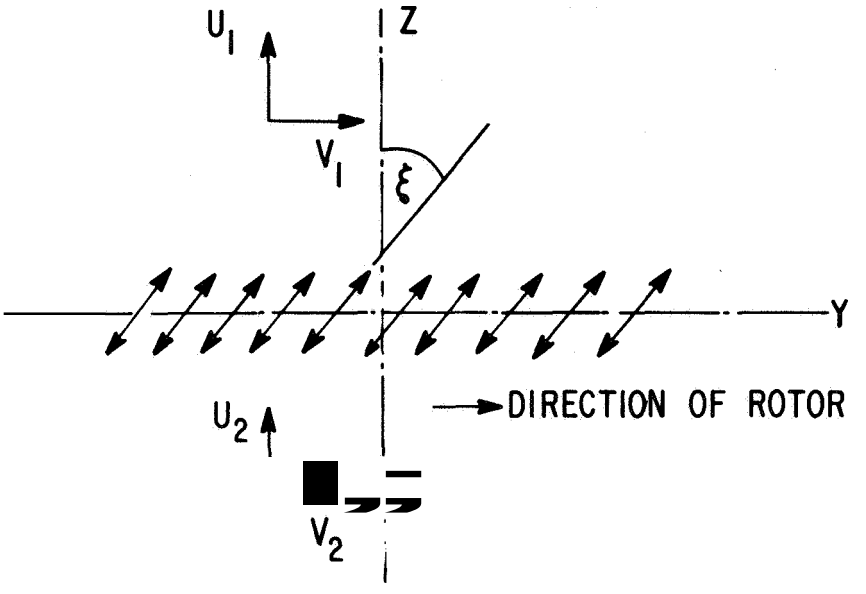

FIGURE 3.—Actuator disk scattering problem.

same mode from a rotor, the unsteady force component of the interest is the kth harmonic of stator blade passing frequency in a rotor-fixed frame. In the numerical calculations presented later, we have assumed that the unsteady lift has the same orientation as the steady-state lift, which is perpendicular to the vector mean velocity through the blade row in a blade-row-fixed frame of reference. We are now ready to formulate and solve the actuator disk scattering problem (fig. 3)

The steady-state axial velocities upstream and downstream of the blade row are U_1 and U_2 (note in axial-flow fans U_1 and U_2 would be negative), the steady-state swirl velocities are V_1 and V_2 (positive if taken in same sense as rotor motion). The problem is to determine acoustic waves produced upstream and downstream of such a blade row by an unsteady force distribution described by

$$F_z = F \cos(\xi)\delta(z) e^{j\left(m\frac{y}{a} - \omega t\right)} \tag{17}$$

$$F_y = F \sin(\xi)\delta(z) e^{j\left(m\frac{y}{a} - \omega t\right)} \tag{18}$$

F denotes $F_{0_s}S/2\pi a$ for a stator and $F_{0_r}B/2\pi a$ for a rotor. ξ denotes the angle the unsteady forces make with the axial direction, which will be assumed parallel to the steady-state lift in our calculations. Thus we have to solve for the pressure p' subject to

$$\nabla^2 p' - \frac{1}{c_{1,2}^2}\frac{\partial^2 p'}{\partial t^2} - 2\frac{U_{1,2}}{c_{1,2}^2}\frac{\partial^2 p'}{\partial z\,\partial t} - 2\frac{V_{1,2}}{c_{1,2}^2}\frac{\partial^2 p'}{\partial y\,\partial t} - \frac{U_{1,2}^2}{c_{1,2}^2}\frac{\partial^2 p'}{\partial z^2}$$
$$-\frac{V_{1,2}^2}{c_{1,2}^2}\frac{\partial^2 p'}{\partial y^2} - 2\frac{U_{1,2}V_{1,2}}{c_{1,2}^2}\frac{\partial^2 p'}{\partial z\,\partial y} = e^{j\left(m\frac{y}{a}-\omega t\right)}$$
$$\times F\left[\cos(\xi)\delta'(z) + j\sin(\xi)\cdot\frac{m}{a}\delta(z)\right] \tag{19}$$

where

$$\nabla^2 p' = \frac{\partial^2 p'}{\partial z^2} + \frac{\partial^2 p'}{\partial y^2}$$

and

$$\delta'(z) = \frac{\mathrm{d}}{dz}(\delta(z))$$

Subscript 1 on U, V, and c refers to upstream conditions and 2 to downstream conditions.

The interpretation of the foregoing problem is simple. We seek a

$$p' \sim p'(z)\ \exp\left[j\left(m\frac{y}{a} - \omega t\right)\right]$$

such that

(1) p' satisfies the homogeneous equations upstream and downstream; i.e., with the right-hand side of equation (19) equal to zero.

(2) There are outgoing waves up and downstream (we discuss this condition next).

(3) The solution for p' obeys jump conditions that are derived as follows. Integrate equation (19) twice with respect to z over an interval from $z = -\epsilon$ to $z = \epsilon$ and then take the limit as $\epsilon \to 0$. After one integration, the following terms on the left-hand side of equation (19) contribute. In what follows, subscript + refers to conditions at $z = 0_+$ and subscript − to conditions at $z = 0_-$:

$$\lim_{\epsilon\to 0}\int_{-\epsilon}^{\epsilon}\left[1 - \frac{U_{1,2}^2}{c_{1,2}^2}\right]\frac{\partial^2 p'}{\partial z^2}\,dz = \left[1 - \frac{U_1^2}{c_1^2}\right]\frac{\partial p'}{\partial z}\Bigg]_+ - \left[1 - \frac{U_2^2}{c_2^2}\right]\frac{\partial p'}{\partial z}\Bigg]_-$$
$$\lim_{\epsilon\to 0}\int_{-\epsilon}^{\epsilon} -2\frac{U_{1,2}}{c_{1,2}^2}\frac{\partial^2 p'}{\partial z\,\partial t}\,dz = -\left\{2\frac{U_1}{c_1^2}\frac{\partial p'}{\partial t}\Bigg]_+ - 2\frac{U_2}{c_2^2}\frac{\partial p'}{\partial t}\Bigg]_-\right\}$$
$$\lim_{\epsilon\to 0} -\int_{-\epsilon}^{\epsilon} 2\frac{U_{1,2}V_{1,2}}{c_{1,2}^2}\frac{\partial^2 p'}{\partial y\,\partial z}\,dz = -\left\{2\frac{U_1V_1}{c_1^2}\frac{\partial p'}{\partial y}\Bigg]_+ - 2\frac{U_2V_2}{c_2^2}\frac{\partial p'}{\partial y}\Bigg]_-\right\}$$

Because all other terms on the left-hand side do not involve gradients with respect to z, they do not contribute in the limit as $\epsilon \to 0$.

371-986 O-LT-70—14

On the right-hand side the term involving $\delta(z)$ alone contributes because

$$\lim_{\epsilon \to 0} \int_{-\epsilon}^{\epsilon} \delta(z)\, dz = 1$$

and

$$\lim_{\epsilon \to 0} \int_{-\epsilon}^{\epsilon} \delta'(z)\, dz = 0$$

Upon integrating a second time with respect to z on the left-hand side now only the term

$$\frac{\partial^2 p'}{\partial z^2}\left(1 - \frac{U_{1,2}^2}{c_{1,2}^2}\right)$$

yields a contribution:

$$p'_+\left[1 - \frac{U_1^2}{c_1^2}\right] - p'_-\left[1 - \frac{U_2^2}{c_2^2}\right]$$

because no other term on the left-hand side of equation (19) involves a gradient with respect to z twice. Now on the right-hand side the term involving $\delta'(z)$ alone contributes because

$$\lim_{\epsilon \to 0} \int_{-\epsilon}^{\epsilon} \left[\int^{z} \delta(\xi)\, d\xi\right] dz = 0$$

and

$$\lim_{\epsilon \to 0} \int_{-\epsilon}^{\epsilon} \left[\int^{z} \delta'(\xi)\, d\xi\right] dz = 1$$

where ξ is a dummy variable of integration. Summing up, the solution for p' obeys jump conditions at $z = 0$ as follows:

$$\left.\frac{\partial p'}{\partial z}\right]_+ \left(1 - \frac{U_1^2}{c_1^2}\right) - \left.\frac{\partial p'}{\partial z}\right]_- \left(1 - \frac{U_2^2}{c_2^2}\right) - 2\left\{\left.\frac{U_1}{c_1^2}\frac{\partial p'}{\partial t}\right]_+ - \left.\frac{U_2}{c_2^2}\frac{\partial p'}{\partial t}\right]_-\right\} - 2\left\{\left.\frac{V_1 U_1}{c_1^2}\frac{\partial p'}{\partial y}\right]_+ - 2\left.\frac{V_2 U_2}{c_2^2}\frac{\partial p'}{\partial y}\right]_-\right\}$$
$$= j \sin(\xi)\left(\frac{m}{a}\right) F e^{j[m(y/a) - \omega t]} \tag{20}$$

and

$$p'_+\left[1 - \frac{U_1^2}{c_1^2}\right] - p'_-\left[1 - \frac{U_2^2}{c_2^2}\right] = F \cos(\xi)\, e^{j(m(y/a) - \omega t)} \tag{21}$$

The assumption of outgoing waves amounts to ignoring reflected waves from discontinuities in the axial direction. The two major sources of

discontinuities are the open end of the duct and the presence of a neighboring blade row. Slutsky (ref. *15)* and Morfey (ref. 5) have shown that duct reflections are unimportant, except in a narrow range of frequencies around cutoff frequencies. Our analysis **will** be restricted to frequencies above cutoff. The presence of a neighboring row should be handled by using the present analysis along with an additional analysis of the reflection and transmission properties of a blade row.

The solution of equations (19), (20), and (21) proceeds as follows. Assume p' for $z > 0$ to be

$$A_+ \exp j\left[k_1 \frac{z}{a} + \frac{m}{a} y - \omega t\right] \tag{22a}$$

and for $x < 0$ to be

$$A_- \exp \left\{j\left[-k_2 \frac{x}{a} + m \frac{y}{a} - \omega t\right]\right\} \tag{22b}$$

Introducing axial mach numbers $\beta_1 = U_1/c_1$, $\beta_2 = U_2/c_2$, swirl mach numbers $\gamma_1 = V_1/c_1$, $\gamma_2 = V_2/c_2$, and tip mach numbers $M_t^1 = a\Omega/c_1$, $M_t^2 = a\Omega/c_2$, it is easily shown that

$$k_1 = \frac{-\beta_1(nBM_t^1 - m\gamma_1) + [(nBM_t^1 - m\gamma_1)^2 - m^2(1-\beta_1^2)]^{1/2}}{(1-\beta_1^2)} \tag{23a}$$

$$k_2 = \frac{+\beta_2(nBM_t^2 - m\gamma_2) + [(nBM_t^2 - m\gamma_2)^2 - m^2(1-\beta_2^2)]^{1/2}}{(1-\beta_2^2)} \tag{23b}$$

The jump conditions for p' give for A+ ,A-

$$A_+\{k_1(1-\beta_1^2) + 2\beta_1(nBM_t^1 - m\gamma_1)\} + A_-\{k_2(1-\beta_2^2) - 2\beta_2(nBM_t^2 - m\gamma_2)\} = \sin(\xi) mF \tag{24a}$$

$$A_+(1-\beta_1^2) - A_-(1-\beta_2^2) = \cos(\xi) F \tag{24b}$$

If we let

$$\begin{aligned} \Delta_+ &= (nBM_t^1 - m\gamma_1)^2 - m^2 \\ \Delta_- &= (nBM_t^2 - m\gamma_2)^2 - m^2 \end{aligned} \tag{25}$$

then

$$\frac{A_+}{F} = \frac{\cos(\xi) k_1 \Delta_- + k_1 k_2 \sin(\xi) m(1-\beta_2^2)}{(1-\beta_2^2)\Delta_+ k_2 + (1-\beta_1^2)\Delta_- k_1} \tag{26a}$$

$$\frac{A_-}{F} = \frac{-k_2 \cos(\xi)\Delta_+ + m \sin(\xi)(1-\beta_1^2) k_1 k_2}{(1-\beta_2^2)\Delta_+ k_2 + (1-\beta_1^2)\Delta_- k_1} \tag{26b}$$

In the special case that the change in velocity across the stage is negligible

$$\frac{A_+}{F}=\frac{-\cos(\xi)}{(1-\beta^2)}\frac{k_2}{k_1+k_2}\left[1+\frac{m\tan(\xi)}{k_1}\right] \tag{27a}$$

and

$$\frac{A_-}{F}=\frac{-\cos(\xi)}{(1-\beta^2)}\frac{k_2}{k_1+k_2}\left\{1-\frac{m\tan(\xi)}{k_2}\right\} \tag{27b}$$

where

$$\beta=\beta_1=\beta_2 \qquad \text{and} \qquad \gamma=\gamma_1=\gamma_2$$

For a moving medium, the intensity flux vector for plane harmonic waves (ref. 8) is shown by Blokhintsev to have a maximum amplitude

$$\frac{p_0^2}{\rho q c}(\mathbf{v}+c\mathbf{n})$$

where p_0 is the amplitude of the pressure wave, v is the vector velocity of the flowing medium, **n** is a unit normal to the wavefronts, and

$$q=c-\mathbf{v}\cdot\nabla\theta$$

where the pressure waves have the space-time dependence

$$\exp \mathrm{j}\left(\omega t-\frac{\omega}{c}\theta\right)$$

The z-component of the intensity flux vector gives the flux of energy per unit annular area radiated out of the compressor. The rms value of the axial component of the intensity flux vector is

Upstream:

$$\frac{A_+^2}{2\rho c}\frac{\left(\beta_1+\dfrac{k_1}{\sqrt{m^2+k_1^2}}\right)}{\left[1-\dfrac{k_1\beta_1+m\gamma_1}{nBM_t^1}\right]} \tag{28a}$$

Downstream:

$$\frac{A_-^2}{2\rho c}\frac{\left[-\beta_2+\dfrac{k_2}{\sqrt{k_2^2+m^2}}\right]}{\left[1-\dfrac{m\gamma_2-k_2\beta_2}{nBM_t^2}\right]} \tag{28b}$$

For the case of no flow, the author has verified that these results are identical to those of Morfey in section 6.5 of reference 5, if open end duct reflections are neglected.

The ratio of equations (28a) to (28b) gives the split of energy upstream and downstream of a row. The product of equations (28a) and (28b) with the compressor annulus gives the sound power generated up and downstream of a row.

AN EXPERIMENT TO VERIFY THE PREDICTIONS OF THE ANALYSIS

Details of Test

Clearly the theory above describes the discrete frequency sound field caused by the interaction of adjacent blade rows in terms of spiral modes as identified by Tyler and Sofrin (ref. 9) and relates the energy radiated in each of these modes to the unsteady blade force including the effects of a moving medium. The effectiveness of the force in generating a mode is critically dependent on the orientation of the spiral mode and the unsteady blade force vector.

To test the validity of the theory, a 54-blade axial compressor rotor was tested with an inlet cascade of either 41 or 82 thin cylindrical rods. The wakes from the rods interact with the rotor to cause spiral acoustic modes at design blade passing frequency.

The test rotor was a model of a jet-engine compressor, scaled to 6-inch o.d. and operated in a closed compressor acoustic test loop. Freon-12 was used as the working fluid to reduce running rpm at design conditions.

As shown in figure 4, the compressor consists of a single-stage 54-blade rotor and 55-blade outlet guide vane. The latter were displaced 5.1 stator chords downstream to minimize the acoustic radiation from rotor-stator interaction. The details of a similar compressor stage and the test loop have been previously described in a paper by R. J. Wells and J. M. McGrew (ref. 16). Complete details of the acoustic and aerodynamic instrumentation are given in reference 2.

Aerodynamic and acoustic tests were performed on four rod configurations as well as with all the rods removed. A view looking into the compressor inlet with rods retracted is shown in figure 5.

The four configurations tested are listed in table I along with some computed parameters descriptive of the wake generation.

TABLE I. —*Wake Interference Test Configurations*

Test series	Number of rods	Rod, diameter, in.	Orientation	x/c [a]	x/D [a]	$D\sqrt{x/D}$	$[1/\sqrt{x/D}]$
1	82	0.04	Radial	1.75	19.25	0.176	0.228
	41	.04	Radial	1.75	19.25	.176	.228
2	82	.02	Radial	.25	5.5	.047	.425
	41	.02	Radial	.25	5.5	.047	.425

[a] x = Distance rod C/L to rotor blade leading edge,
c = Rotor blade chord (0.440 in.).
D = Rod diameter.

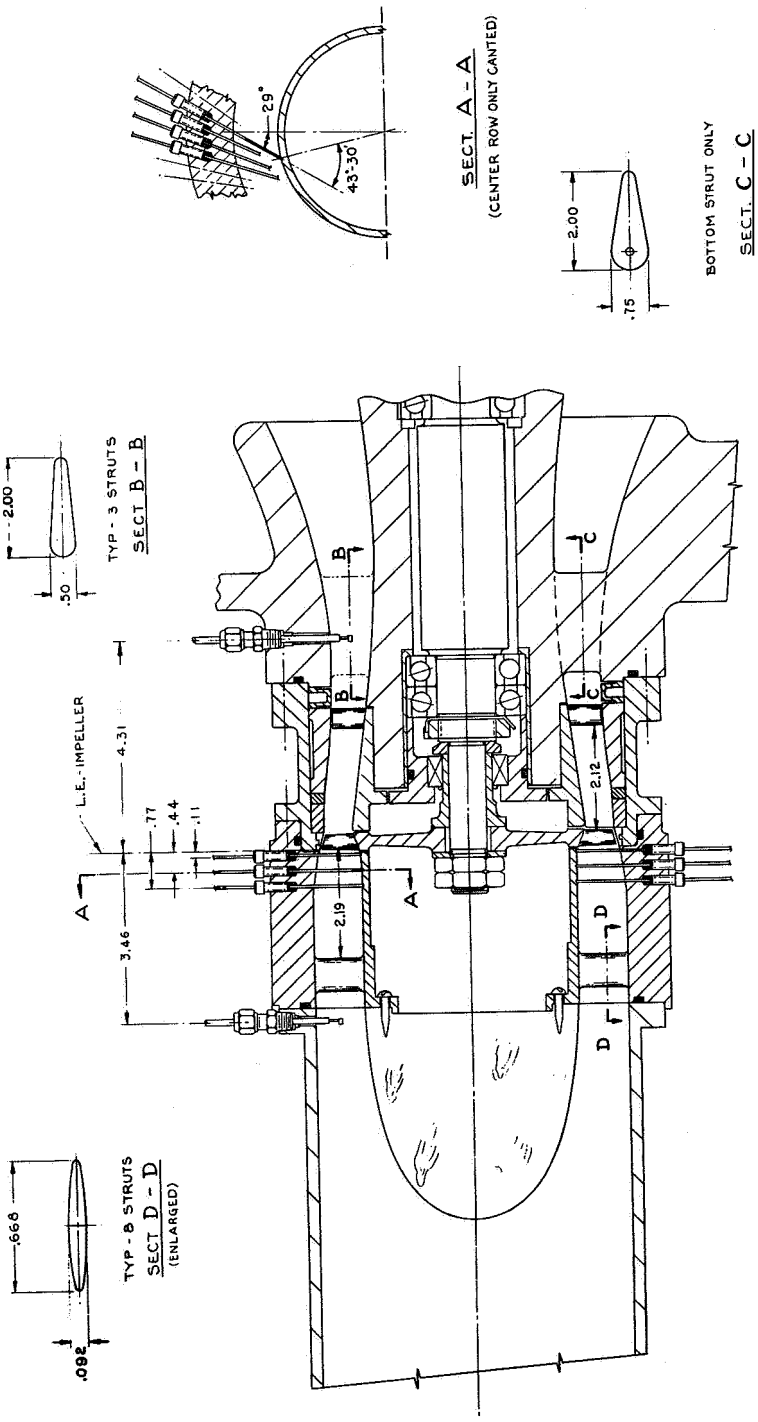

FIGURE 4.—Section view of model compressor.

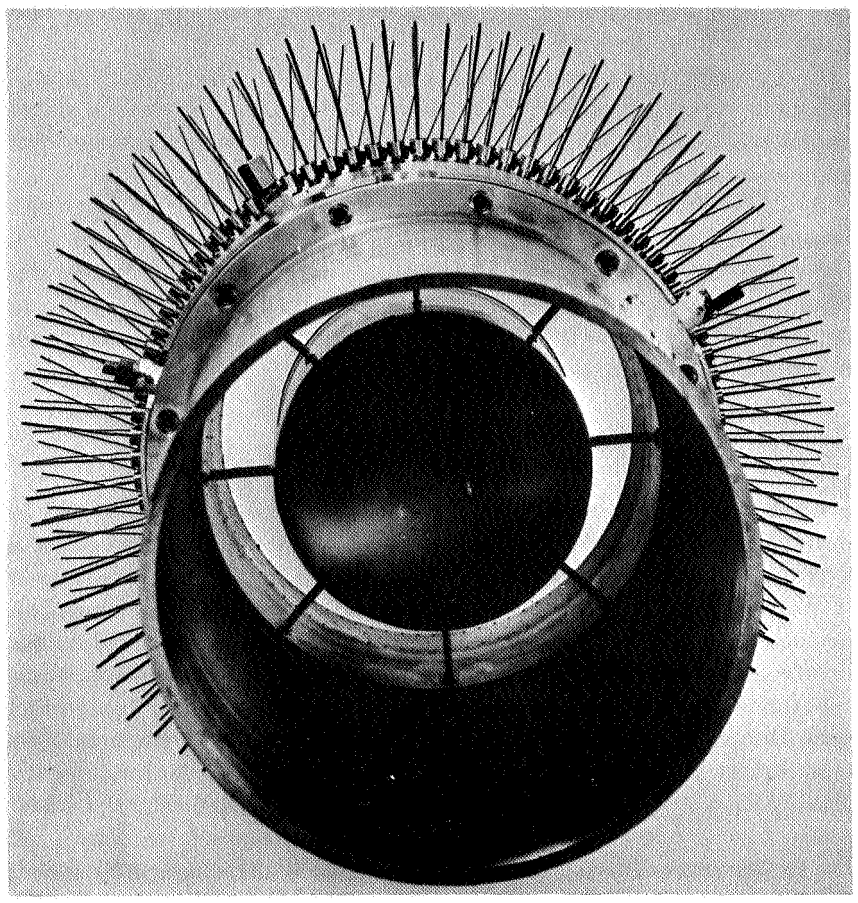

FIGURE 5.—Inlet view of compressor, all rods retracted.

Cylindrical rods were chosen as wake generators because their drag characteristics are well established and an array of small-diameter rods would have minimum dispersal effect on the transmission of waves upstream through them. The pitch-line blockage ranged from 0.20 for 82 rods of 0.04-in. diameter to a blockage of 0.05 for 41 rods of 0.02-in. diameter. At large distances downstream of a rod, the wake velocity profiles become similar, and the wake width as given by Schlichting (ref. 17) becomes proportional to $D\sqrt{x/D}$ and the centerline velocity defect proportional to $1/\sqrt{x/D}$. Values of these parameters for the test cases are given in table I. At the minimum axial spacing of 5.5 rod diameters, the wake characteristics are not self-similar, nor are the details well documented in the literature. Experiments at this spacing were necessary to assure sufficient excitation to achieve measurable

effects with a wake intensity characteristic of a closely spaced inlet guide vane rotor design.

Compressor performance data were obtained along approximately constant corrected speeds from 10 to 100 percent of design speed, and it was verified that the influence of the rods on compressor performance is small.

Acoustic data were taken by setting the throttle valve to produce a nominal design load and collecting data at constant speeds from 10 to 100 percent of design speed. The acoustic data reported in figures 6 to 13 are the total far-field energy radiated in the inlet and the exhaust in decibels relative to 10^{-13} W in a 0.1-octave band centered on the fundamental blade passing frequency.

Application of Acoustic Theory to Test Results

Each rotor blade experiences a periodic disturbance as it passes through a rod wake. As shown in reference 11, the principal effect is a perturbation in the lift force acting on the blade that, for the purposes of this analysis, is assumed to act normal to the blade stagger. This unsteady, periodic force in turn excites various acoustic modes identified in reference 9 from the symmetry of rotor-stator interaction and boundary conditions imposed by the inner and outer shrouds of the compressor duct. Denoting by B the number of rotor blades and by S the number of rods, it was shown in reference 9 that associated with the fundamental blade passing noise are tangential lobed patterns with $(B-kS)$ lobes, where k is any integer. Only a few of these lobed patterns propagate. For the present tests, $B=54$ and $S=41$ or 82. In the range of tip speeds studied for the 41–54 test, a $+13$ $(=54-41)$ and a -28 $(=54-2\times 41)$ lobed pattern propagate. For the 82–54 interaction, only a -28 $(=54-82)$ lobed pattern propagates.

In a rotor-fixed frame, an S-rod cascade produces unsteady lifts on the rotor at S, $2S$, $3S$, . . . times the rotor frequency. The unsteady lift on the rotor (in a rotor-fixed frame) at $k\cdot S$ times the rotor frequency produces a $(B-kS)$ lobed pattern spinning that produces fundamental blade passing frequency noise in a stationary frame of reference. In a rotor-fixed frame, the 41-rod cascade produces pulsations of lift on a rotor blade at $41, 2\times 41$, . . . times the rotor frequency. Because only a $+13$-lobed pattern and a -28-lobed pattern propagate, we are interested in unsteady lifts on the rotor caused by the rods at the first two harmonics of rod passing frequency in a rotor-fixed frame. Let these unsteady lifts be denoted by F_{41}^{1} and F_{41}^{2}. Similarly for the 82-rod cascade, propagating noise is produced by an unsteady force, which may be denoted by F_{82}^{1}.

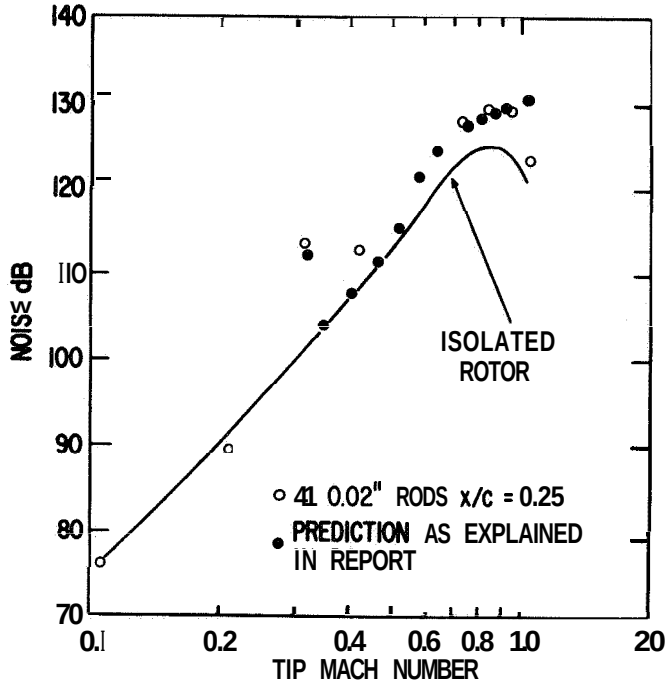

FIGURE 6.—41 rod test. Inlet, close spacing.

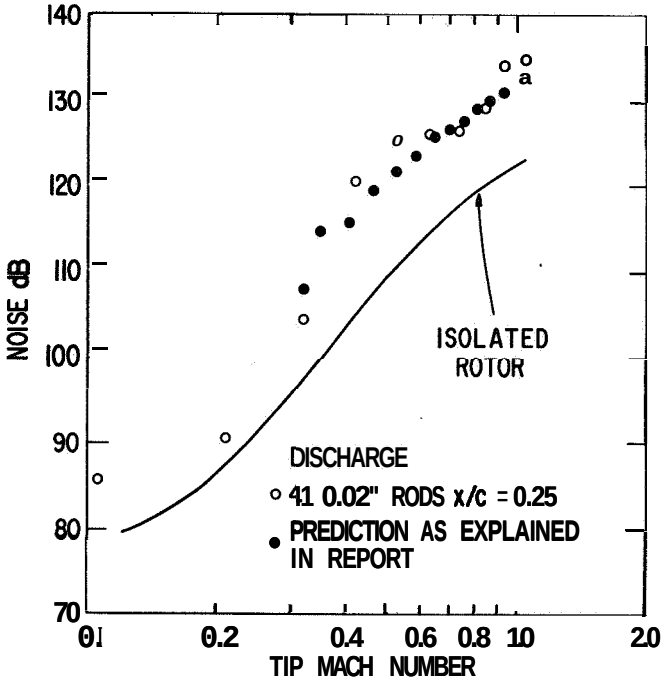

FIGURE 7.—41 rod test. Discharge, close spacing.

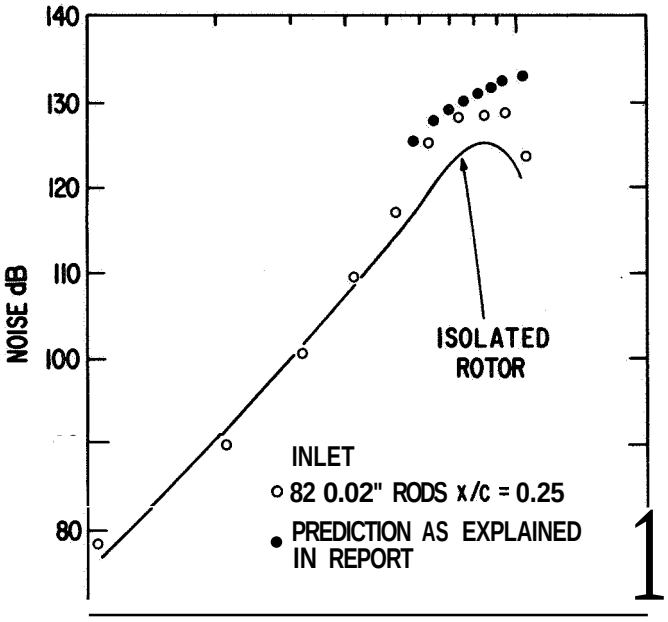
140
130
120
110
100
80
NOISE dB
ISOLATED
ROTOR
INLET
○ 82 0.02" RODS x/c = 0.25
● PREDICTION AS EXPLAINED
IN REPORT

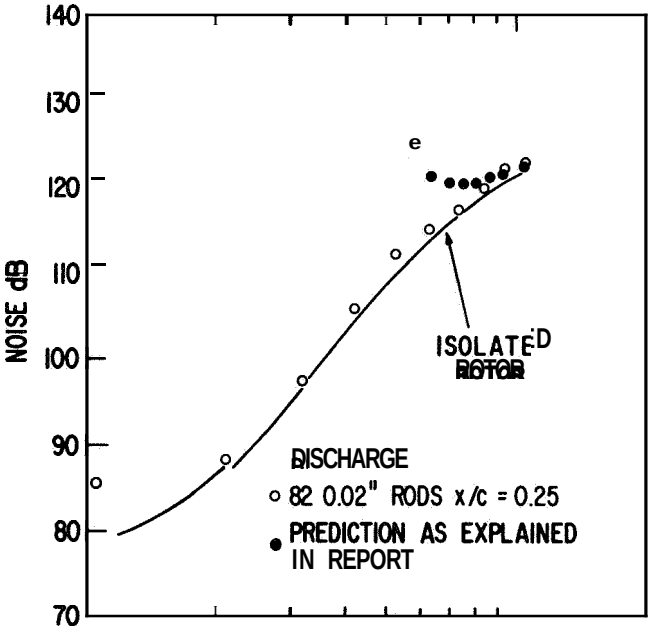
140
130
120
110
100
90
80
70
NOISE dB
ISOLATED
ROTOR
DISCHARGE
○ 82 0.02" RODS x/c = 0.25
● PREDICTION AS EXPLAINED
IN REPORT

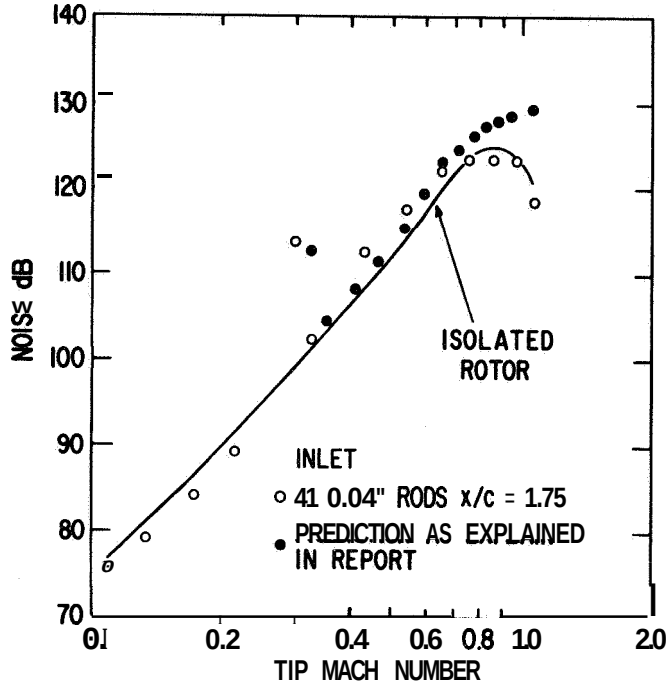

FIGURE 10.—41 rod test. Inlet, large spacing.

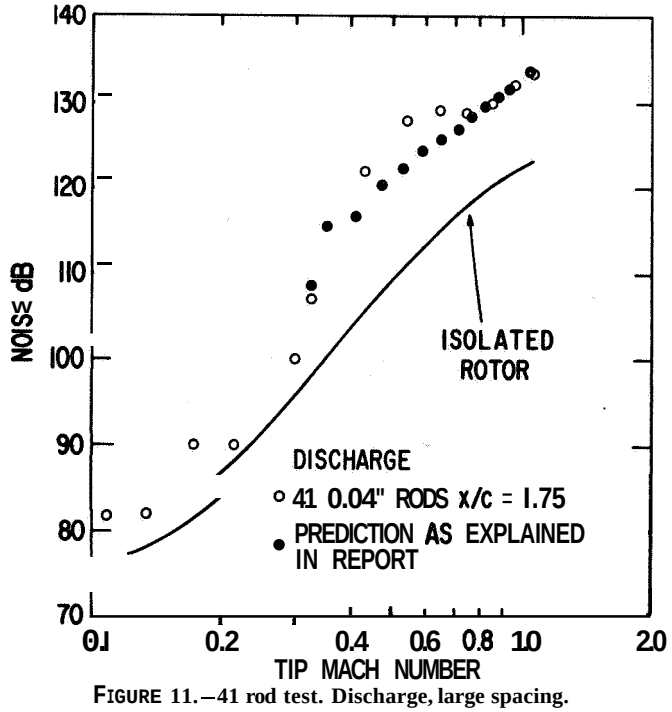

FIGURE 11.—41 rod test. Discharge, large spacing.

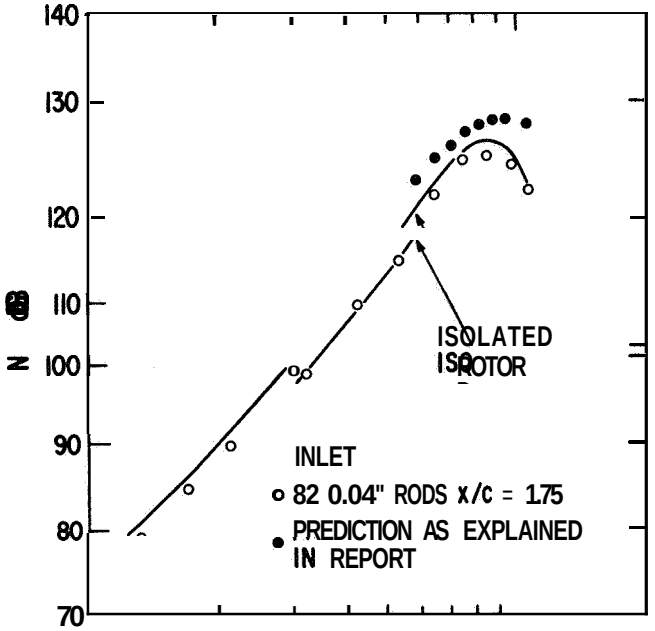
140
130
120
110
100
90
80
70
ISOLATED
ROTOR
INLET
82 0.04" RODS x/c = 1.75
PREDICTION AS EXPLAINED
IN REPORT

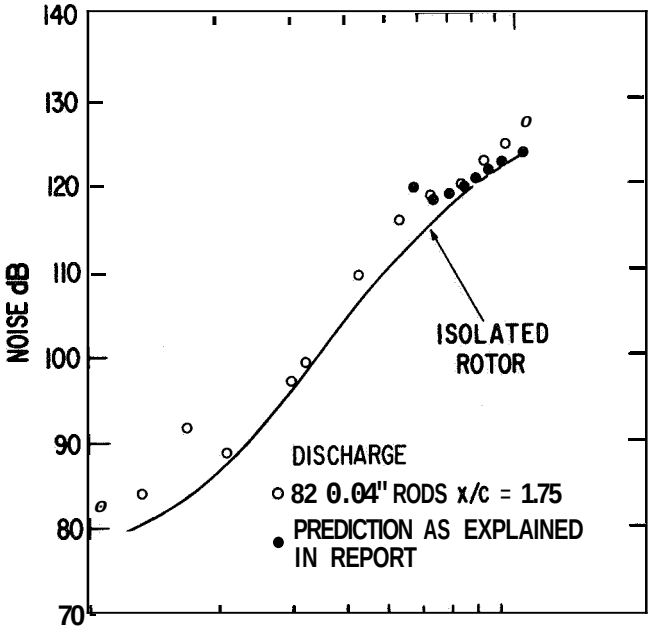
140
130
120
110
100
90
80
70
NOISE dB
ISOLATED
ROTOR
DISCHARGE
82 0.04" RODS x/c = 1.75
PREDICTION AS EXPLAINED
IN REPORT

The theory of reference 1 summarized in the first section of the present paper gives the amount of acoustic energy radiated upstream and downstream of a blade row in a particular acoustic mode, given the magnitude of unsteady force exciting the mode. The analysis given there was two dimensional, and it was applied to the present experiments at the mean pitch line conditions of the compressor annulus, assuming these conditions to be a representative average of conditions over the entire fan annulus. Because the model fan has a hub tip ratio of 0.74, this should

TABLE II. – *41–54 and* **82–54** *Interaction*

Blade tip mach no. M_t, plotted on abscissae of noise data	η_+	
	41–54	82–54
1.05	0.04732	0.1093
	.1567	.00047
.94	.4322	.....
	.1610	.....
.92	.....	.1241
	.....	.0022
.88	.0408	.....
	.1635	.....
.86	.....	.1336
	.....	.0042
.82	.038	.....
	.1664	.....
.80	.....	.1451
	.....	.0076
.76	.035	.....
	.1698	.....
.75	.....	.1594
	.....	.0136
.70	.031	.1777
	.1738	.0255
.64	.02689	.1982
	.1786	.0539
.58	.02184	.1707
	.1843	.1964
.53	.01586	.....
	.1912	.....
.47	.0089	.....
	.1998	.....
.41	.001827	.....
	.2106	.....
.35	.0055	.....
	.2191	.....
.32	.1659	.....
	.0573	.....

be a reasonable assumption. Equations (23), (25), (26), and (28) of the first section give efficiency factors of acoustic-noise production upstream and downstream that, along with the magnitude of unsteady force exciting the mode and dimensions of the fan annulus, yield acoustic-power contributions of the interaction. These power contributions should be added to those of the isolated rotor to obtain the total noise upstream and downstream. In table II we have tabulated the efficiency factors η_+ (upstream) and η_- (downstream). Only results above cutoff are presented. In calculating table 11, we have assumed that the pitch-line velocity triangles at the various tip speeds are similar to the one shown in figure 14; i.e., that the velocity triangles scale linearly with tip speed. To estimate the unsteady forces, the following extremely crude model was used. This model was resorted to because no information is known to the author giving details of velocity defects caused by cylinder wakes at the close spacings that were necessary in this investigation to obtain substantial interaction noise. The unsteady lifts were calculated by replacing the rods by airfoils of chord equal to rod diameter and drag coefficient $C_D = 1.00$ and then using the theory of reference 11. This concept is sketched in figure 15. The range of Reynolds' numbers of the rod in these tests is about $(1.95)(10^4)$ to $(13.49)(10^4)$, which justifies the use of $C_D = 1.00$. The unsteady lifts F^1_{41}, F^2_{41}, and F^1_{82} were calculated by this means. As indicated earlier, only interaction noise over and above isolated rotor noise is theoretically predicted by combining the theories of the first section and reference 11.

The isolated rotor noise contributions for inlet and discharge were tabulated for each speed from the experimental data. As a first try, the unsteady lift coefficients based on the model of figure 15 were directly

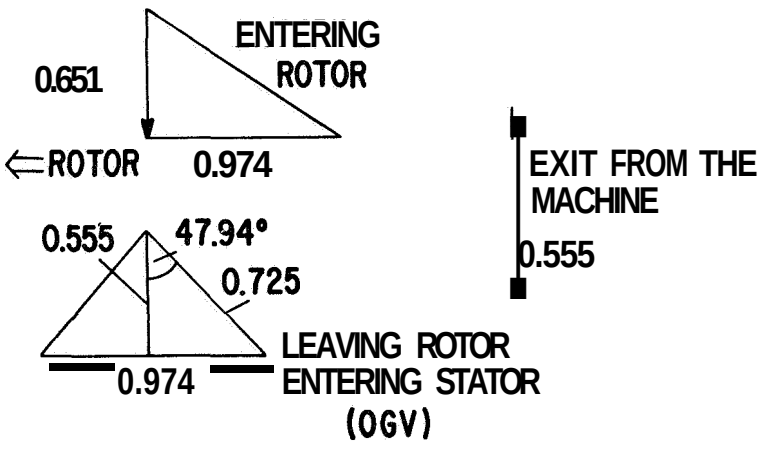

FIGURE 14.—Pitch-line velocity triangles in mach numbers at 100 percent design speed.

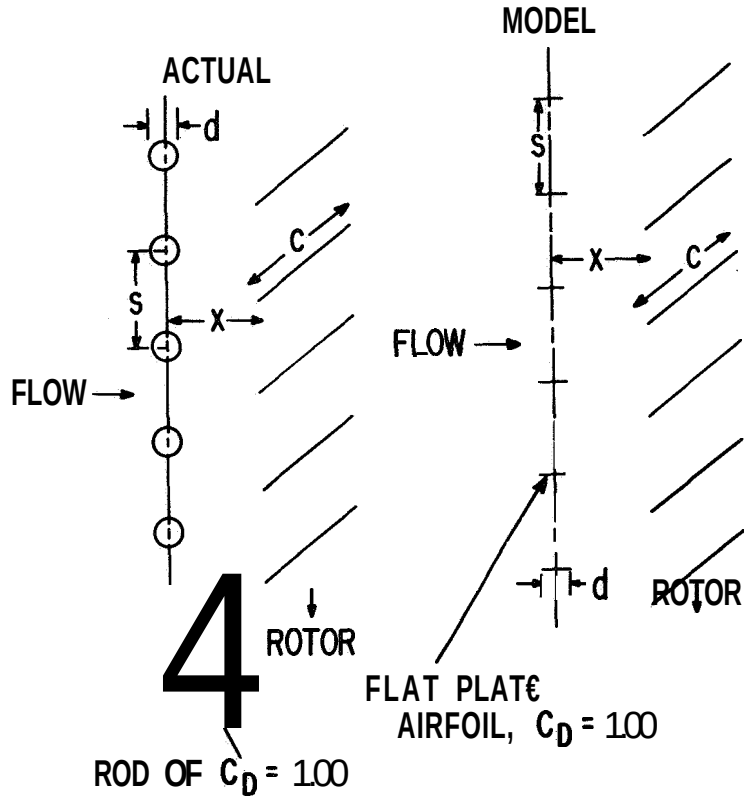

FIGURE 15.—Model used for interaction.

used to obtain unsteady lifts and, as indicated in the first section, interference noise outputs upstream and downstream. These were added to the isolated rotor levels to obtain total noise levels. These noise levels predicted the trends of the experimental data quite well, but were higher than the actual dB levels by almost a constant number of dB (both on inlet and discharge). This suggested reducing the unsteady force estimates by a factor of 1.5 for all the tests, and all noise levels were recalculated as before. These results are presented in figures 6 to 13. As far as the isolated rotor noise levels go, only faired curves through the experimental points are shown. The open symbols in figures 6 to 13 represent actual data points, and filled-in symbols the predictions as explained above.

It is seen that generally there is good agreement between the predictions and the results. Lest the significance of these predictions be misunderstood, we wish to reiterate their implication.

The unknown in the acoustic analysis of the first section is the unsteady force. For the 41-rod case, one needs F^1_{41} and F^2_{41}. For the 82-rod results, one needs F^1_{82}. The crude model of figure 15 along with reference 11 was

used to estimate F_{41}^{1}, F_{41}^{2}, and F_{82}^{1}. Reducing the values of F_{41}^{1}, F_{41}^{2}, and F_{82}^{1} by a factor of 1.5, the theory of the first section predicts the experimental noise levels reasonably well.

There are, of course, some interesting discrepancies between the experimental results and the predictions. These discrepancies seem to fall into two major groups. The first concerns systematic deviation, around cutoff, between theory and experiment in the 82-rod close spacing discharge noise data (fig. 9). As was discussed earlier, the analysis of the first section neglects reflections that would become important as we approach cutoff. Thus it seems worthwhile to explore more fully the open-end reflection coefficients of spinning modes in flowing media with inlet and discharge geometries typical of actual jet engines. This study should enable better prediction of noise just around cutoff.

The second discrepancy observable is that the actual inlet noise begins to drop off with high speeds, and the actual noise levels are much lower than predicted at high speeds. This tendency to drop off at high speeds is not observed on the exhaust. As the axial mach numbers in the compressor duct are still only around 0.55 (at $M_t = 1$), this does not appear to be a choking effect in the conventional sense. However, one can easily demonstrate that the effect of flow on noise generated in some axial plane at a particular frequency is to shorten the wavelength on the inlet and to raise it on the discharge. Thus spatial gradients in the sound field are much greater on the inlet than on the discharge. Viscous attenuation, which is related to the spatial gradients, is thus much higher on the inlet than on the discharge. These tendencies increase with increasing flow through the compressor and appear to provide plausible explanation of increasing attenuation with speed on the inlet and no attenuation on the discharge.

Thus the main conclusion of these experiments appears to be that the analysis of the first section is reasonably substantiated by the experimental results with the following two reservations:

(1) There is a need for better understanding of open-end reflections in a moving medium situation to enable better prediction of noise close to cutoff.

(2) The need for incorporation of some mechanism to explain the dropoff of inlet noise with high tip speed somewhat earlier than would be expected on grounds of choking of the inlet.

AN APPROXIMATE THEORY OF SOUND PROPAGATION THROUGH BLADE ROWS

Introduction

Because jet-engine fans and compressors consist of more than one row of vanes and blades, the noise generated at one row is impeded before

it reaches an observer by the presence of an adjacent row. A synopsis of an approximate calculation of sound transmission through blade rows is presented in the present section.

It should be pointed out immediately that the problem of noise generation from a row cannot really be studied in isolation from the problem of transmission through a row. The problems of estimation of unsteady forces and generation of noise should really be solved by including the presence of the whole jet-engine geometry; i.e., the presence of adjacent moving and stationary rows, inner and outer shrouds, open-end terminations, etc. The enormous complexity of such a solution suggests tackling the problem piecemeal. Thus the results of this section should be viewed as an attempt to shed light on the acoustic behavior of blade rows and how they impede the transmission of noise generated from an adjacent row.

The spiraling modes identified by Tyler and Sofrin (ref. 9) appear in a two-dimensional cascade plane picture as plane harmonic waves. The present section is thus concerned with the reflection and transmission of plane harmonic acoustic waves in a flowing medium by an infinite set of flat plates of arbitrary spacing and stagger. The velocity potential satisfies the wave equation in a flowing medium. The problem of solving this equation subject to the pertinent boundary conditions is converted into two consecutive Wiener-Hopf problems. The first problem is concerned with plane harmonic acoustic waves reflected by and transmitted through an infinite array of semi-infinite flat plates. The second problem considers the radiation and reflection of duct waveguide modes from the open ends of an infinite array of semi-infinite plates. By combining these two solutions, an approximate solution to the problem of sound transmission through a blade row is obtained.

Summary of Solution Procedure

As already indicated, we assume the following mechanism of the transmission process (fig. 16). The incident wave has a certain frequency ω and makes an angle θ with the blades. The blade row is idealized as a cascade of flat plates of arbitrary spacing and stagger with uniform subsonic flow through it ($|M|$ in fig. 16 is less than unity). Because the analysis is two dimensional, it should be applied at some suitable radius of the fan annulus. We always use a frame of reference fixed with respect to the blade row. Thus, there is no difference between a stationary and rotating blade row as far as the mathematical details go. However, because measurements are always made in a stationary frame of reference, appropriate transformations of frequency and energy need to be made when scattering by rotors is considered. These details are given in reference 3.

371-986 O-LT-70—15

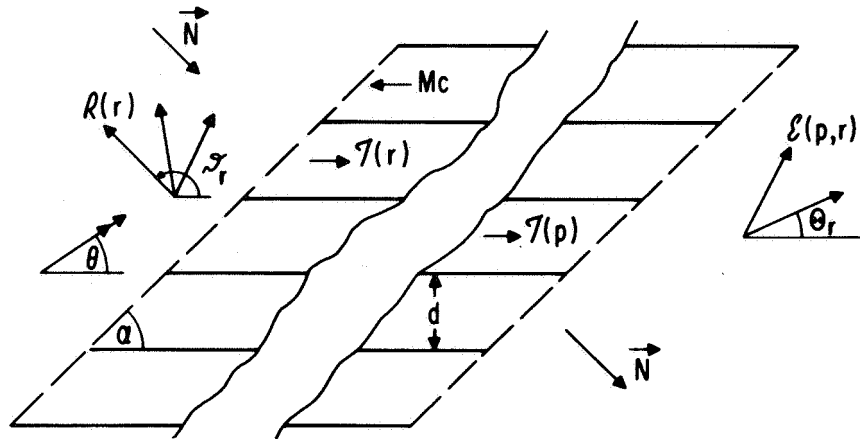

FIGURE 16.—Sound transmission through blade rows.

In the free space to the right and left of the blade row in figure **16,** plane harmonic waves are produced. In the blade row duct, waveguide-type solutions exist owing to the boundary conditions imposed by the blades. The wave incident from the right excites duct waveguide modes denoted by $T(r)$ in figure **16** and reflected waves in free space denoted by $R(r)$ in figure **16.** The orientations of the reflected waves are denoted by θ_r. Only propagating reflected wave and propagating duct waveguide mode amplitudes are calculated. The calculation of $T(r)$ and $R(r)$ is performed by the Wiener-Hopf method, assuming the blades extend to infinity on the right. In a second analysis, one considers propagating duct waveguide modes, denoted by $T(p)$ in figure **16,** advancing from the blade row to the left and emitting propagating plane wave denoted by $\epsilon(p, r)$. In this second analysis the blades are assumed to extend to infinity on the left, and the Wiener-Hopf method is used again. The orientation of the emitted waves is denoted by θ_r. **N** in figure **16** denotes a unit normal to the blade row. The analysis gives the component of the acoustic intensity flux vector in the direction of **N** associated with the various free-space acoustic waves in the reflected and emitted regions as a fraction of that of the incident wave. In the case of scattering by a rotor, appropriate transformation of these fractions and the frequency is carried out to obtain the results in a stationary frame of reference. The Kutta condition is assumed satisfied at the trailing edge in the analysis.

The following paragraphs summarize the main results of the analysis:

(1) Closed-form expressions are obtained for fractions of energy reflected and transmitted in various free-space propagating waves as a function of frequency of incident wave, stagger, spacing, and mach number of blade row. Scattering by both rotors and stators is considered (full details are given in ref. 3).

(2) A "specularly" reflected wave and an emitted wave coincident in orientation with the incident wave always appear. Higher order emission and reflection are also possible as the wavelength-blade spacing ratio decreases. Such higher order reflections and emissions are quite common in actual jet-engine applications.

(3) In case of higher order scattering by a stator, frequencies of the scattered waves are the same as the incident wave frequency. There is an alteration of lobe number, though the new lobe numbers are still given by the Tyler-Sofrin formula $(nB - kS)$. In case of higher order scattering by a rotor, the frequencies of the scattered waves are now harmonics of the blade passing frequency different from that associated with the incident wave.

(4) First, with regard to conservation of energy, it can only be checked in a frame of reference fixed with the scattering blade row because the scattering of acoustic waves by moving objects is not necessarily energy conserving. Second, even in a frame of reference fixed with respect to the scattering row, it should be noted that there is some kinetic energy in the shed wakes. We have not tried to calculate this kinetic energy, but there is partial conversion of incident acoustic energy into wake kinetic energy when moving medium effects are considered.

After completing this analysis, we came across a paper by S. Kaji and T. Okazaki on the transmission and reflection of plane harmonic acoustic waves by an infinite set of flat plates (ref. **18).** An oscillating doublet distribution is laid out on the blade chords whose strength is sought to cancel the normal velocity caused by the incident wave. By ingenious use of Poisson's summation formula, Kaji and Okazaki obtain the final results for the transmitted and reflected waves in a form identical to that of the present paper. They plot the amplitude of pressure ratios in figures 2 to 5 of their paper. In figures **17** to 19 of the present paper, we compare their results with our paper. The following points are noteworthy.

(1) Most of figures 2 to **4** of reference **18** are for waves eight times as long as the blade chord. This is somewhat outside the range of interest with regard to blade passing frequency noise in fans whose wavelength is of the order of the blade chord. The Wiener-Hopf approximation should get better as the chord appears longer compared to the wavelength. At any rate, figures **2** to **4** of reference **18** constitute a rather severe test of the Wiener-Hopf approximation.

(2) In reference 18 the numerical results are obtained by numerically solving a singular integral equation for the unsteady blade force and later integrating over the blade chords to obtain the far-field pressures. The advantage of the Wiener-Hopf method is that closed-form expressions are obtained for the reflection and transmission coefficients.

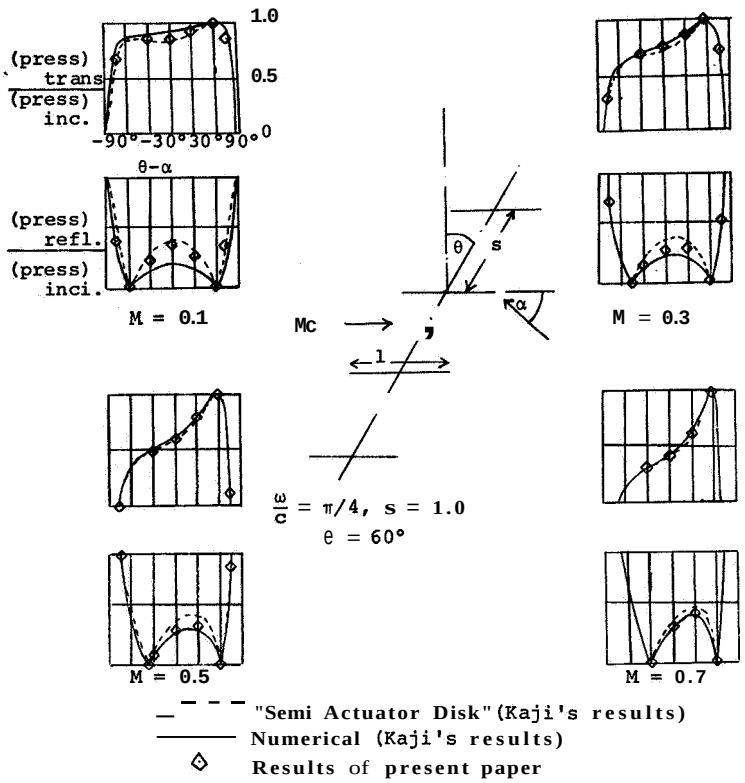

FIGURE 17.—Comparison with Kaji's results, effect of mach number.

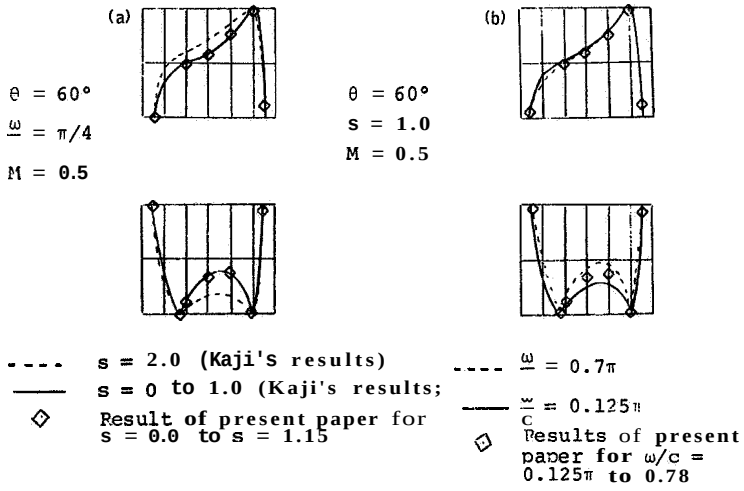

FIGURE 18.—Comparison with Kaji's paper on effect of *(a)* spacing and *(b)* frequency (same legend as fig. 7).

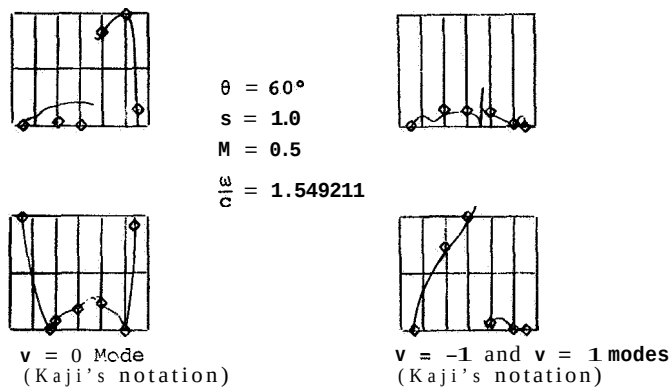

FIGURE 19.—Comparison with Kaji's paper for the superresonant cases (same legend as fig. 7).

For example, the Wiener-Hopf approximation of the cases in figures 2 to 4 of reference 18 is independent of spacing and wavelength and involves only sines and cosines of θ, a, and the mach number.

(3) The generally good agreement over broad ranges of incidence, spacing, wavelength, and mach number between Kaji and Okazaki's and our results may be taken as justification of the assumed basic mechanism of the transmission phenomena. We assume that the incident wave is reflected and excites duct waveguide modes as if the blades were semi-infinite to the right. The duct waveguide modes then reradiate as if the blades extend to semi-infinity on the left. Of course, to obtain a rigorous solution in this fashion, one should keep track of phases, nonpropagating modes, phase changes over the finite blade chord, and multiple reflections. The advantage of the approximation introduced in this section is that very simple, closed-form solutions are obtained. Both Kaji and Okazaki's and our approach neglect many features of the actual problem such as blade thickness and camber, turbulence in the passages, variable velocity of the flow, the three-dimensional nature of the actual problem, etc. The simplicity of the Wiener-Hopf approximation introduced in this paper seems worthwhile despite these various omissions.

REFERENCES

1. MANI, R.: Discrete Frequency Noise Generation From an Axial Flow Fan Blade Row. Paper no. 69–FE–12, Am. Soc. Mech. Engrs., 1969.
2. LIPSTEIN, N. J.; AND MANI, R.: Experimental Investigation of Discrete Frequency Noise Generated by Unsteady Blade Forces. Paper 69–WA–FE–22, Am. Soc. Mech. Engrs.
3. MANI, R.; AND HORVAY, G.: Sound Transmission Through Blade Rows. Rept. no. 69–C–104, GE Research and Development Center, Feb. 1969.

4. SHARLAND, I. J.: Sources of Noise in Axial Flow Fans. J. Sound Vib., vol. 1, no. 3, July 1964, pp. 302-302.
5. MORFEY, C. L.: Rotating Pressure Patterns in Ducts: Their Generation and Transmission. J. Sound Vib., vol. 1, 1964, pp. 60–87.
6. LIGHTHILL, M. J.: On Sound Generated Aerodynamically. I. General Theory. Proc. Roy. Soc., ser. A, vol. 211, 1952, pp. 564–587.
7. CURLE, N.: The Influence of Solid Boundaries Upon Aerodynamic Sound. Proc. Roy. Soc., ser. A, vol. 231, 1955, pp. 505-514.
8. BLOKHINTSEV, D. I.: Acoustics of a Nonhomogeneous, Moving Medium. NACA TM 1399, 1956.
9. TYLER, J. M.; AND SOFRIN, T. G.: Axial Flow Compressor Noise Studies. SAE Trans., vol. 70, pp. 309-332.
10. KEMP, N. H.; AND SEARS, W. R.: Aerodynamic Interference Between Moving Blade Rows. J. Aeron. Sci., vol. 20, no. 9, Sept. 1953, pp. 585–598.
11. KEMP, N. H.; AND SEARS, W. R.: The Unsteady Forces Due to Viscous Wakes in Turbomachines. J. Aeron. Sci., vol. 22, no. 7, July 1955, pp. 478–483.
12. MEYER, R. X.: The Effect of Wakes on the Transient Pressure and Velocity Distributions in Turbomachines. Trans. Am. Soc. Mech. Engrs., vol. 80, 1958, p. 1544.
13. LOTZ, M.; AND RAABE, J.: Blade Oscillations in One-Stage Axial Turbomachinery. J. Basic Eng., Trans. Am. Soc. Mech. Engrs., vol. 90, ser. D, no. 4, Dec. 1968, pp. 485–493.
14. LEFCORT, M. D.: An Investigation Into Unsteady Blade Forces in Turbomachines. J. Eng. Power, Trans. Am. Soc. Mech. Engrs., vol. 87, ser. A, no. 4, Oct. 1965, pp. 345–354.
15. SLUTSKY, S. L.: Discrete Noise Generation and Propagation by a Fan Engine. AFOSR–UTIAS Symposium on Aerodynamic Noise, Univ. of Toronto Press, 1969.
16. WELLS, R. J.; AND MCGREW, J. M.: The Use of Gases Other than Air in the Acoustic Testing of Model Compressors. Am. Soc. Mech. Engrs., no. 67–GT–22, 1967.
17. SCHLICHTING, H.: Boundary Layer Theory. McGraw-Hill Book Co., Inc., 1955.
18. KAJI, S.; AND OKAZAKI, T.: Study on Plane Sound Waves Passing through a Compressor Blade Row. Reports of the Sixth International Congress on Acoustics, Dr. V. Kohasi, ed., Paper no. F-5-1, 1968.

REFLECTION AND TRANSMISSION OF OBLIQUE SOUND WAVES BY A BLADE ROW*

Roy Amiet and W. R. Sears
Cornell University
Ithaca, N.Y.

A problem relating to the noise produced by axial flow compressors and fans is the reflection and transmission of propagating sound waves by a blade row. Such propagating waves, essentially helical in form, are produced, for example, by rotor-stator interaction. It is important to determine to what extent such sound is transmitted through another row of blades, upstream or downstream, and ultimately into the outside environment.

INTRODUCTION

In this investigation the usual approximation of plane flow will be made; that is, the blade row appears as an infinite lattice of two-dimensional airfoils. This, of course, implies that the actual air passage is annular and that the radius ratio of the blades is not large. In this approximation the propagating helical sound field appears as a train of propagating plane waves, whose angle relative to the blade row depends on the geometry of the helix. It will be assumed that the whole problem is one of small disturbances in a uniform, inviscid stream. Figure 1 shows the geometry of this flow and defines the symbols to be used. The incoming sound waves propagate with normal velocity equal to the speed of sound a_0, relative to the undisturbed stream, and carry velocity perturbations whose direction is normal to these waves and varies sinusoidally with the normal distance.

This problem has been attacked by Kaji and Okazaki (ref. 1) by a straightforward method of acoustic singularity distribution leading to a complicated integral equation. Mani and Horvay (ref. 2) used a cruder model, in which the blade chords are infinite, obtaining simpler analytical results, which appear to agree with those of Kaji and Okazaki, at least for a certain range of geometrical parameters and mach number.

*This work has been supported by the U.S. Air Force Office of Scientific Research under contract F44-620-69-C-0063.

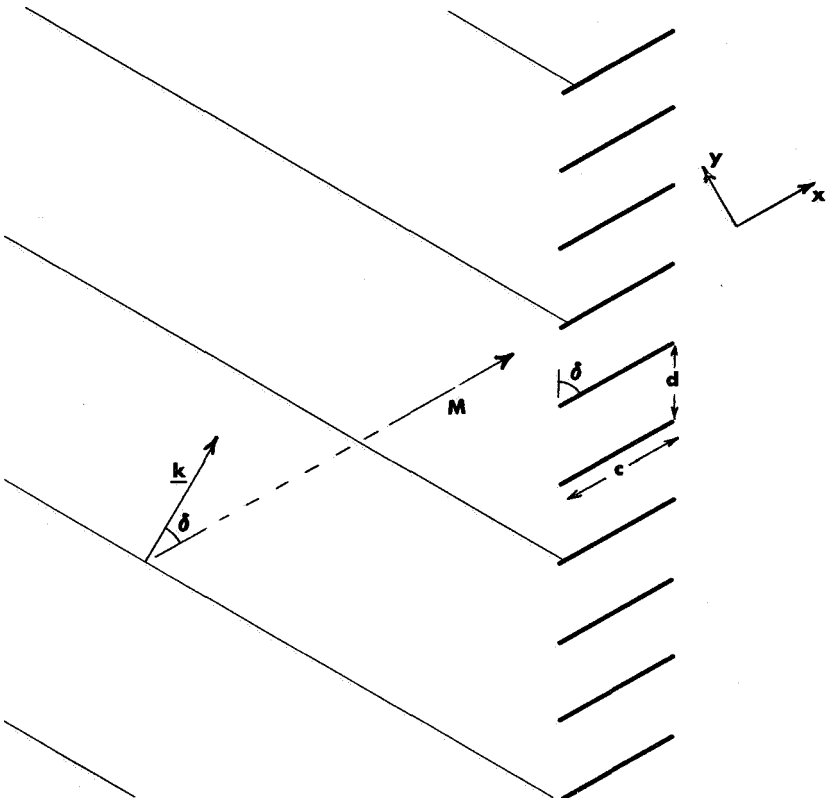

FIGURE 1.—Diagram showing blade-row and incident-wave geometry.

In the present paper, we report on a different approximation to the same problem; namely, one that draws upon a classical, steady-flow lattice for an estimate of the forces on the blades. To support this approximation, we consider first the application of the method of matched asymptotic expansions to aerodynamic-noise problems.

MATCHED ASYMPTOTIC EXPANSIONS IN AERODYNAMIC-NOISE PROBLEMS

The appropriate linearized equation for small perturbations of a uniform inviscid stream at mach number M is the familiar acoustic equation transformed by a Galilean transformation:

$$\frac{1}{a_0^2}\frac{\partial^2\phi}{\partial t^2}-\nabla^2\phi+\frac{2M}{a_0}\frac{\partial^2\phi}{\partial x\,\partial t}+M^2\frac{\partial^2\phi}{\partial x^2}=0 \tag{1}$$

where ϕ denotes the perturbation velocity potential.

Suppose that the wavelength of propagating sound produced is large

compared with the typical bodv dimension. Then there are two identifiable regions of flow dominated, respectively, by the acoustic wavelength and the body dimension. In other words, spatial gradients will be determined by these respective lengths, and spatial derivatives in equation (1) will be of different orders of magnitude in the two regions.

This is the kind of problem for which the method of matched asymptotic expansion is useful. The method consists of approximating appropriately to the equation of the problem in the two regions and then requiring that the approximations overlap consistently; i.e., are "matched." The result is a composite solution that is superior to either of the two approximations mentioned.

The process begins by writing equation (1) in dimensionless form, for plane flow in an x, y-plane, using for the reference time the parameter $1/\omega$, where $\omega/2\pi$ is the frequency of the body's motion, and for the reference length the body dimension c in the inner region and the length a_0/ω in the outer region. Thus, with

$$x = cx^i \qquad y = cy^i \qquad t = \tau/\omega \qquad \phi = \omega c^2 \phi^i \tag{2}$$

we obtain for the inner region

$$\nabla_i^2 \phi^i - M^2 \frac{\partial^2 \phi^i}{\partial x^{i2}} = 2M\epsilon \frac{\partial^2 \phi^i}{\partial x^i \, \partial \tau} + \epsilon^2 \frac{\partial^2 \phi^i}{\partial \tau^2} \tag{3}$$

where ϵ denotes $\omega c/a_0$, which is (except for a factor 2π) the length ratio mentioned above, assumed to be small.

The leading terms in equation (3) are $O(1)$ for small ϵ; a first approximation is obtained by neglecting terms of order ϵ and higher, and the result is the Prandtl-Glauert equation

$$\nabla_i^2 \phi^i - M^2 \frac{\partial^2 \phi^i}{\partial x^{i2}} \tag{4}$$

On the other hand, writing

$$x = a_0 x^\circ/\omega \qquad y = a_0 y^\circ/\omega \qquad t = \tau/\omega \qquad \phi = \omega c^2 \phi^\circ \tag{5}$$

we obtain for the outer region

$$\nabla_o^2 \phi^\circ - 2M \frac{\partial^2 \phi^\circ}{\partial x^\circ \, \partial \tau} - \frac{\partial^2 \phi^\circ}{\partial \tau^2} - M^2 \frac{\partial^2 \phi^\circ}{\partial x^{\circ 2}} = 0 \tag{6}$$

In other words, no terms of equation (1) can be neglected in the outer region, even for small ϵ. Solutions to equation (6), such as acoustic dipoles in a stream, are known.

We find, therefore, that the simplification afforded by the theory of matched asymptotic expansions is that the Prandtl-Glauert approximation can be used to describe the inner flow. Instead of distributing acoustic singularities in such a way as to satisfy the boundary conditions at the body (as Kaji and Okazaki have done, for example), one may approximate to the inner flow by using the Prandtl-Glauert theory in a quasi-steady way, and then match it to a flow consisting of acoustic singularities at large distances. Great simplification results, for the inner flow viewed from afar can be represented very simply in terms of transformed incompressible singularities. In fact, the nature of acoustic singularities is such that they are identical to the corresponding incompressible singularities near their origins. The matching procedure is therefore one of replacing the incompressible singularities of the inner field, one by one, with corresponding acoustic singularities.

Finally, we can exploit the well-known relationships between the successive singularities of an incompressible flow and such integrated quantities as total force, net efflux of fluid, etc. In many practical problems there is no net efflux, and the leading term is a dipole proportional to total force on the body. In such cases the consequences of the theory outlined above boil down to the following simple prescription: (1) calculate the total force on the body by use of Prandtl-Glauert theory, and (2) represent this force in an acoustic dipole. The sound field produced is the field of this dipole.

APPLICATION TO BLADE-ROW PROBLEMS

The extension of these considerations to problems wherein the body is actually an infinite array (lattice) of blades requires some thought, for one can question whether a quasi-steady approximation can ever be valid for unsteady flow involving an infinite array. In terms of the argument outlined above, one asks whether it is correct to use the blade chord or gap as the characteristic length in such a problem and if the characteristic length actually has become infinite. The answer is, of course, that the quasi-steady approximation is valid for sufficiently slowly varying flow. Specifically, the timelag for interference effects of nearby blades, whose presence is most important, must be small compared to the period of the motion. This is just the condition that has already been assumed, namely that ϵ is small.

In a blade-row problem, therefore, we calculate blade forces in the Prandtl-Glauert approximation, which means incompressible flow through a transformed lattice of blades whose chord, stagger angle, and spacing (fig. 1) are

$$c' = c/\beta \qquad \delta' = \tan^{-1}(\beta \tan \delta) \qquad \text{and } d' = d\,(\sin \delta / \sin \delta') \tag{7}$$

where $\beta^2 = 1 - M^2$.

APPLICATION TO THE SOUND-TRANSMISSION PROBLEM

In the particular case of the lattice impinged upon by oblique, plane, sinusoidal sound waves, as in figure 1, we must determine the blade forces, in the approximation just described, caused by the sinusoidal field of perturbation velocities carried by the propagating incident sound waves. In lieu of a more accurate theory of incompressible flow through a lattice with conditions varying sinusoidally along it, we shall approximate to these forces in a crude way; namely, by applying a classical infinite-lattice theory locally at every blade. This seems consistent with other approximations made here, for it assumes that the wavelength of the sinusoidal variation along the blade row is large compared to the chord.

ANALYSIS

Let the velocity potential of the disturbance field of the incident sound be

$$\Phi = B \cos\left[\omega t(1+M\cos\gamma) - \mathbf{k}\cdot\mathbf{r}\right] \tag{8}$$

The wave vector k in this expression is equal to $\omega a_0^{-1}(\mathbf{i}\cos y + \mathbf{j}\sin y)$, where i and j are unit vectors in the x- and y-direction, respectively. Thus ω is the circular frequency heard by an observer moving with the undisturbed flow; it is related to the frequency Ω of fluctuations at a blade as follows:

$$\omega(1+M\cos y) = \Omega \tag{9}$$

The resulting perturbation in blade angle of attack is then

$$\hat{\alpha} = (B\omega/a_0U)\sin y \sin\left[\omega t(1+M\cos y) - \mathbf{k}\cdot\mathbf{r}_0\right] \tag{10}$$

where $\mathbf{r}_0$ denotes the position on the blade row where the angle of attack is being measured and U is the stream speed.

The forces on the blades will now be determined from classical lattice theory (ref. 3). For small angles of attack they are

$$F_x = 0 \qquad F_y = 2\rho_0 U^2 d'(1+2\kappa/R)^{-1}\hat{\alpha} \tag{11}$$

where

$$\frac{\pi c'}{2d'} = \sin\delta' \ln\left(\frac{R+2\kappa\sin\delta'}{1-\kappa^2}\right) + \cot\delta' \tan^{-1}\left(\frac{2\kappa\cos\delta'}{R}\right) \tag{12}$$

ρ_0 is the density of the stream, and

$$R = \sqrt{\kappa^4 - 2\kappa^2\cos 2\delta' + 1} \tag{13}$$

These expressions give the total force on the blades in the transformed plane, which is equal to the total force on the actual blades, according to the Prandtl-Glauert transformation.

The distribution of the force over each blade is unimportant unless we wish to calculate the near field in detail. Thus, we have an array of discrete forces at spacing d along the blade row. These discrete forces produce the same far-field sound as a sinusoidal distribution having the same integrated force per half period. We therefore consider a distribution of forces continuous and sinusoidal along the blade row and sinusoidal in time.

To find the pressure field caused by such a distribution, the forces are replaced by dipoles, and the pressure fields caused by the dipoles are then integrated. Perhaps the easiest way to do this is to move one's coordinate system along the blade row at the proper speed to make the flow field stationary in time. One then has supersonic steady flow over a sinusoidal distribution of dipoles.

The resulting formula for the reflected pressure field P_r, expressed as a ratio to the pressure amplitude P_0 of the incident field, is

$$\frac{P_r}{P_0}=-\frac{|M|\sin\gamma[\sin(2\delta-\gamma)+M\sin 2\delta-M^2\sin^2\delta\sin\gamma]}{\beta(1+R/2\kappa)[\sin(\delta-\gamma)+M\sin\delta]\sqrt{1-M^2\sin^2\delta}}$$
$$\times\sin\left[\omega t(1+M\cos y)+(\omega/a_0)(x\sin 6-y\cos 6)\right.$$
$$\left.\times\frac{2\sin(\delta-\gamma)+2M\sin\delta}{1-M^2\sin^2 6}-(x\omega/a_0)\cos y-(y\omega/a_0)\sin\gamma\right] \quad (14)$$

Similarly, one finds for the pressure P_t in the transmitted field (including here the incident field upon which it is superimposed because it has the same spatial and temporal phase)

$$\frac{P_t}{P_0}=\left\{1-\frac{|M|\sqrt{1-M^2\sin^2\delta}\sin^2\gamma}{\beta(1+R/2\kappa)[\sin(\delta-\gamma)+M\sin\delta]}\right.$$
$$\times\sin[\omega t(1+M\cos y)-(x\omega/a_0)\cos\gamma-(y\omega/a_0)\sin\gamma] \quad (15)$$

Expressions have been given in equations **(12)** and **(13)** for the geometry factors R and κ. Also, the lattice-effect coefficient $4d'\kappa/\pi Rc'$ is plotted in reference **3.** The above results, for $M>0$, describe a wave traveling downstream and impinging upon the leading edge of the blade row, while for $M<0$, they describe a wave traveling upstream and impinging upon the trailing edge of the blade row.

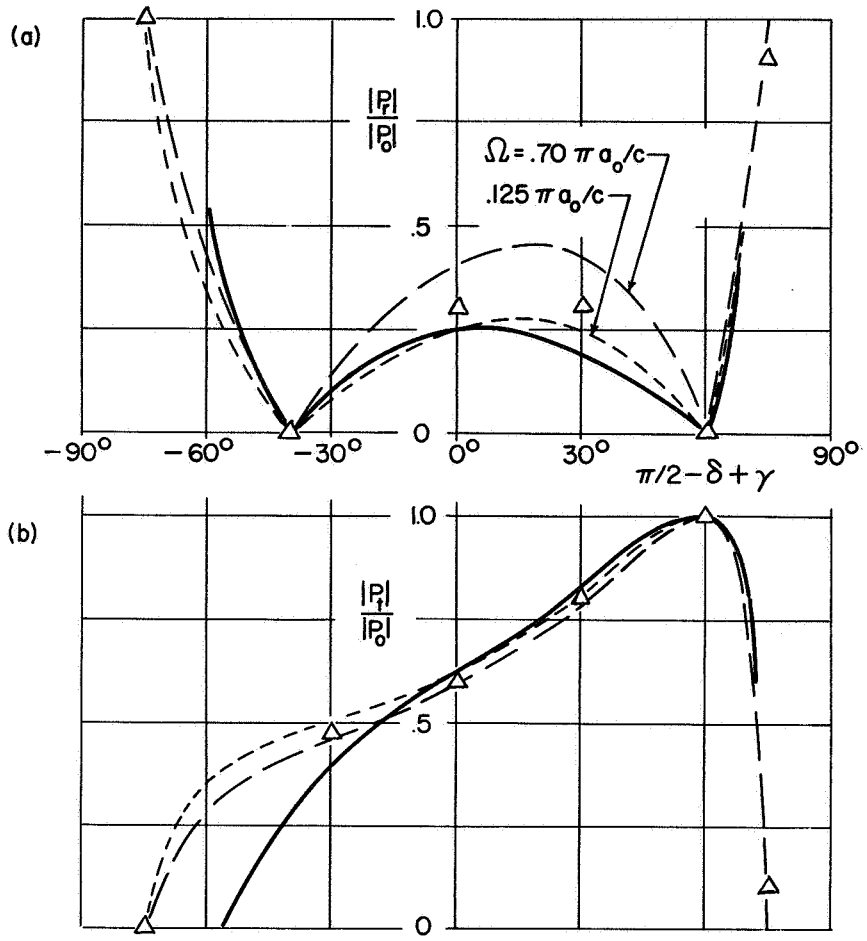

FIGURE 2.—(*a*) Amplitude of reflected pressure field. (*b*) Amplitude of transmitted pressure field. $M=-0.5$, $\delta=30°$, $c=d=1$. See note added in proof. ——— Amiet and Sears results; — — — results of reference 1 for dimensionless frequencies indicated; A results of reference 2.

RESULTS

Some numerical results for the case $M=-0.5$, $\delta=30°$, and $c=d=1$ are shown in figure 2 along with the results of Kaji and Okazaki for the frequencies $0.125\pi a_0/c$ and $\Omega=0.7\pi a_0/c$. (Note that the functions plotted in fig. 2 are independent of frequency according to the present approximation.) It is seen that reasonable agreement is achieved with these low-frequency results of Kaji and Okazaki over a considerable range of the incident angle γ. However, for large negative values of the abscissa, the agreement is poorer. It appears that our approximations result in an overestimate of the blade forces in this geometrical regime,

which is close to the limiting condition where the incident waves do not actually propagate upstream into the blade row.

NOTE ADDED IN PROOF

As this report goes to press, we have found a numerical error in the solid-line curves of figure 2. The correction increases slightly the values of reflected sound and decreases the values of transmitted sound. The publication schedule has not permitted the corrected curves to be included here.

REFERENCES

1. KAJI, S.; AND OKAZAKI, T.: Study on Plane Sound Waves Passing Through a Compressor Blade Row. Paper no. F–5–1, reports of the Sixth International Congress on Acoustics, V. Kohasi, ed., Aug. 1968.
2. MANI, R.; AND HORVAY, G.: Sound Transmission Through Blade Rows. GE Rept. no. 69–C–104, 1969.
3. WISLICENUS, G. F.: Fluid Mechanics of Turbomachinery. McGraw-Hill Book Co., Inc., 1947.

RESPONSE OF AN INFINITE WING TO AN OBLIQUE SINUSOIDAL GUST: A GENERALIZATION OF SEARS' PROBLEM*

L. T. Filotas
University of Toronto, Canada

An approximate closed-form expression is derived for the loading on a two-dimensional airfoil passing through an inclined sinusoidal gust. The expression, based on linearized incompressible lifting surface theory, is asymptotically exact in the limiting cases where the reduced frequency, which is proportional to the ratio of airfoil chord to gust wavelength, is either very small or very large. When the gust inclination is such that the nodal lines are perpendicular to the flight path, the resulting special case is a well-known problem of unsteady airfoil theory (Sears' problem). The pressure distribution obtained for this case has the form predicted by classical theory. The value for the lift, while not exactly identical to the Sears function, differs from it only slightly in the range of reduced frequency of order unity. Arguments indicating that the accuracy for the general case is of the same order are advanced.

*A more extensive treatment can be found in Report no. **139** of the University of Toronto Institute for Aerospace Studies. This research was carried out at the University of Toronto Institute for Aerospace Studies and was supported by the National Research Council of Canada under grant no. A2003 and by the Air Force Office of Scientific Research, Office of Aerospace Research, U.S. Air Force, under grant no. 67-0672A.

SYMBOLS

A	aspect ratio
a	constant
b_0	semichord measured perpendicular to the leading edge
b	$b_0 \cos \beta$
$C_i(z)$	cosine integral (ref. 1)
C_l	lift coefficient
$E(z)$	complete elliptic integral of the second kind (ref. 1)
$F(r, \theta)$	integral defined by eq. (5)
$H_n^{(2)}(z)$	Hankel function (ref. 1)
$I_n(z)$	modified Bessel function of the first kind (ref. 1)
$J_n(z)$	Bessel function of the first kind (ref. 1)
$K_n(z)$	modified Bessel function of the second kind (ref. 1)
$Ki_n(z)$	repeated integral of K_0 (ref. 1)
k_0	gust wave number
k	dimensionless wave number (reduced frequency) $=k_0 b_0$
k_1	chordwise wave number $=k \sin \beta$
k_2	spanwise wave number $= k \cos \beta$
l	local lift
$Q(t)$	kernel function, eq. (17a)
$Q_R(t)$	kernel function, eq. (18)
$S(k)$	Sears function
$Si(z)$	sine integral (ref. 1)
s	dimensionless distance along flight path $=U_0 t/b_0$
$T(k, \beta)$	generalized Sears function, eq. (26)
U_0	flight velocity
U	$U_0 \sec \beta$
u,v,w	velocity components
x,y,z	space coordinates
x_{cp}	center of pressure location in chords aft of the leading edge
α_0	angle of attack at midchord
β	gust inclination angle
$\delta(z)$	delta function
γ	vorticity discontinuity across wing
$\bar{\gamma}$	normalized vorticity $=\hat{\gamma}(b/\hat{\Gamma})$
ξ	chordwise variable
η	spanwise variable
ρ	density
Γ	circulation

Superscripts

$-$	nondimensionalized by b
$\sim$	nondimensionalized by b_0
$*$	complex conjugate
	amplitude of complex variable

INTRODUCTION

The sound radiated by a fan or compressor blade passing through a flow disturbance is the result of the fluctuating aerodynamic loading. Even though tip effects are usually negligible, calculations based on strip theory are questionable if the blade encounters large spanwise downwash gradients.

In the linearized case, a two-dimensional airfoil moving through an arbitrary flow disturbance responds only to the downwash pattern in its own plane. Expressed as a two-dimensional Fourier integral, this pattern can always be regarded as the superposition of elementary sinusoidal components. A single component is visualized as a corrugated sheet of downwash in the airfoil plane (fig. 1); the wavelength and inclination may assume all possible values; a special case ($\beta = \pi/2$ in fig. 1) is the well-known two-dimensional sinusoidal gust problem of Sears (ref. 2). The response to such a Fourier component is also of fundamental importance in the study of flight through atmospheric turbulence (refs. 3 and 4).

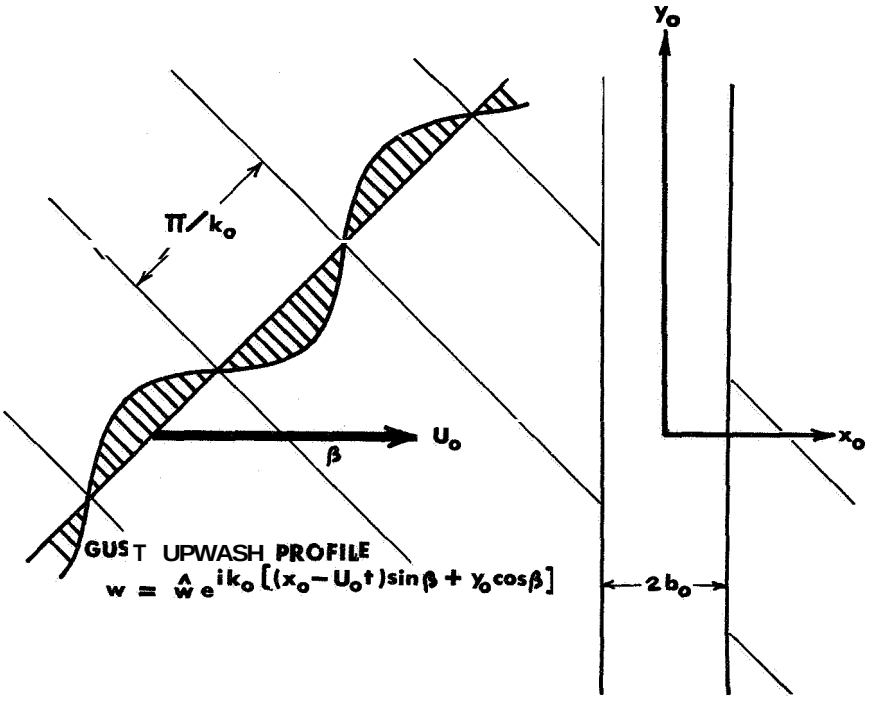

FIGURE 1.—Basic aerodynamic problem associated with the response *to* an *arbitrary* flow disturbance. An infinite wing in an inclined sinusoidal gust.

371-986 0-LT-70—16

Independently of the present work, J. M. R. Graham has recently obtained a numerical solution for this basic case.[1] For use as input to a more complex analysis, however, an approximate closed-form solution may be preferable. The special geometry allows a relatively simple closed-form approximation, one that preserves the most important features, to be obtained. The physical picture emerging from the present approach is also believed to clarify the numerical results.

THE EQUIVALENT STEADY PROBLEM

Relative to axes x_0, y_0 attached to the wing, the gust is convected downstream at the flight speed U_0. The upwash velocity in complex form is

$$w(x_0, y_0) = \hat{w}e^{ik_0[(x_0-U_0t)\sin\beta + y_0\cos\beta]} \tag{1}$$

The problem of finding the pressure distribution may be greatly simplified by a coordinate transformation. The time variation sensed by an observer on the wing is due to the uniform translation of the lines of constant phase along the span. If the observer were to move along the span with the trace velocity $V = U_0 \tan\beta$, the flow would appear steady. Alternately, the addition of a uniform transverse velocity $V = U_0 \tan\beta$ will not alter the perturbation pressure caused by the gust. This is illustrated schematically in figure 2. The flow resulting after the addition of the transverse component is shown to be equivalent to the steady flight of an infinite swept-wing (fig. 3).

The coordinate systems used are indicated in figure 4; the calculations are most conveniently done in the nonrectangular x, y-frame with the

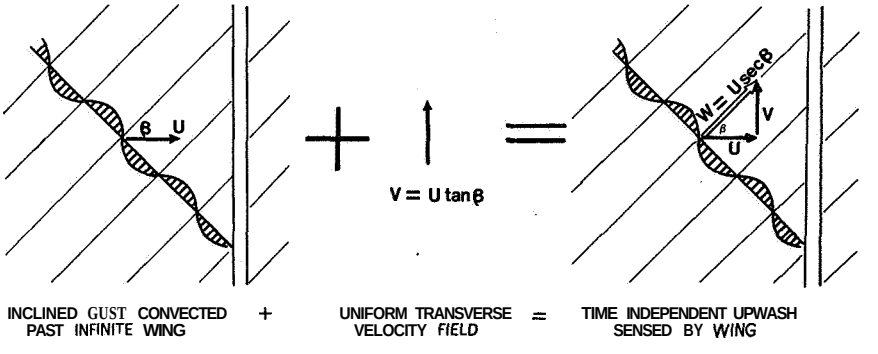

FIGURE 2.—Transformation to an equivalent steady problem by superposition of a uniform spanwise velocity.

[1] J. M. R. Graham: An Analytical Method of Calculating the Load on a Thin Rectangular Wing in an Arbitrary Incompressible Flow Field. Eng. Dept., Univ. of Cambridge, unpublished.

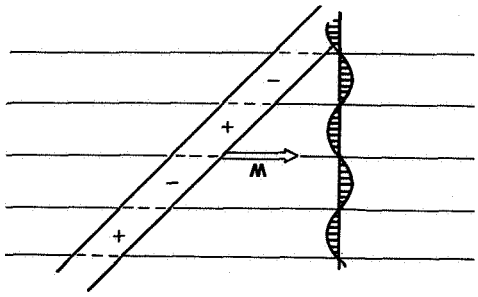

FIGURE 3.—Figure 2 redrawn to show equivalence with stationary flow past twisted sweptback wing.

y-axis along the span and the x-axis in the free stream direction. The relationship between the lift distribution in the original x_0, yo-frame and the surface vorticity $\gamma(x, y)$ in the moving frame is given by

$$l(x_0, y_0, t) = \zeta U_0 \sec\beta \gamma[x_0 \sec\beta, -y_0 - (x_0 - U_0 t) \tan\beta] \tag{2}$$

THE INTEGRAL EQUATION

Using the nondimensional variables defined in the list of symbols and assuming the form

$$\gamma(\bar{x}, \bar{y}) = \hat{\gamma}(\bar{x}) e^{-ik\bar{y}} \tag{3}$$

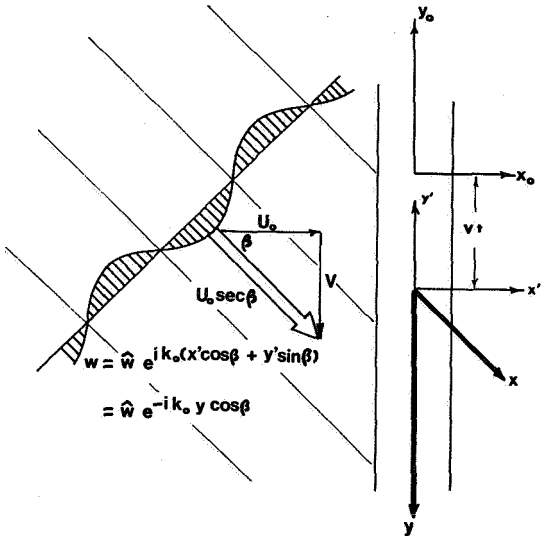

FIGURE 4.—Moving oblique reference frame.

it is possible to derive the integral equation

$$\hat{w}\cos\beta=\frac{k}{2\pi}\int_{-1}^{1}\left\{\frac{\pi}{2}+\frac{F[k(\bar{x}-\bar{\xi}),\beta]}{k(\bar{x}-\bar{\xi})}\right\}\hat{\gamma}(\bar{\xi})d\bar{\xi} \tag{4}$$

where

$$F(r,\theta)=-\frac{i}{2}e^{-ir\sin\theta}\int_{-\infty}^{\infty}\frac{\sqrt{t^2+(r\cos}}{t-r\sin\theta}e^{it}\,dt \tag{5}$$

The integral (5) can be expressed in closed form only for special values of the parameters but can be expanded in a converging series for general values.

THE TOTAL CIRCULATION

Defining the magnitude of the circulation as

$$\hat{\Gamma}=b\int_{-1}^{1}\hat{\gamma}(\xi)d\bar{\xi} \tag{6}$$

the relation

$$\hat{\Gamma}=\frac{2\pi\hat{w}\,bo}{\frac{\pi}{2}k+F(R,\beta)} \tag{7}$$

may be derived by averaging equation (4) over the chord. It is also precisely the result predicted by the Weissinger theory (ref. 5) for this situation. (See fig. 3.)

LOW- AND HIGH-FREQUENCY LIMITS

Eliminating $\hat{w}$ in equations (4) and (7), there results the somewhat simpler form

$$\int_{-1}^{1}F[k(\bar{x}-\bar{\xi}),\beta]\frac{\bar{\gamma}(\bar{\xi})}{\bar{x}-\bar{\xi}}d\bar{\xi}=F(k,\beta) \tag{8}$$

where

$$\bar{\gamma}(\bar{\xi})=\frac{b}{\hat{\Gamma}}\hat{\gamma}(\bar{\xi}) \tag{9}$$

is a normalized chordwise loading function such that

$$\int_{-1}^{1}\bar{\gamma}(\bar{\xi})d\bar{\xi}=1 \tag{10}$$

Expanding equation (8) for large and small values of k, there results

$$\int_{-1}^{1}\frac{\bar{\gamma}(\bar{\xi})}{\bar{x}-\bar{\xi}}d\bar{\xi}=1 \qquad k\to 0 \tag{11a}$$

$$\int_{-1}^{1} \frac{|\bar{x}-\bar{\xi}|}{\bar{x}-\bar{\xi}} \bar{\gamma}(\bar{\xi}) = 1 \qquad k \to \infty \tag{11b}$$

independent of the gust inclination β. These have the solutions

$$\bar{\gamma}(\bar{\xi}) = \frac{1}{\pi} \sqrt{\frac{1-\bar{\xi}}{1+\bar{\xi}}} \qquad k \to 0 \tag{12a}$$

$$\gamma(\xi) = \delta(\bar{\xi}+1) \qquad k \to \infty \tag{12b}$$

These equations mean that for very low frequency (or large wavelength), the response is quasi-steady; for very high frequency, the loading behaves as an impulse at the leading edge.

FORM OF THE COMPLETE SOLUTION

Because it does not seem likely that equation *(8)* can be inverted explicitly, we proceed heuristically by postulating a plausible form for ? that interpolates between the limiting forms (11a) and (11b). A suitable form that also satisfies the condition that the leading edge singularity must remain of the square root type for all k and β is

$$\bar{\gamma}(\bar{\xi}) = C \sqrt{\frac{1-\bar{\xi}}{1+\bar{\xi}}}\, e^{-ak\bar{\xi}} \tag{13}$$

To satisfy condition (10), the normalizing factor C must be

$$C = \frac{1}{\pi} \frac{1}{I_0(ak) + I_1(ak)} \tag{14}$$

The exponential factor in equation (13) crowds the distribution toward the leading edge for increasing k, equations (12) being identically satisfied if a is any arbitrary function of β with nonnegative real part.

From equation (5) it is apparent that in any exact solution of equation (8) the parameters k and β will appear in the combinations

$$k_1 = k \sin \beta \qquad k_2 = k \cos \beta \tag{15}$$

To insure that equation (13) is compatible with this observation in a relatively simple way, we must have

$$a = a_1 \sin \beta + a_2 \cos \beta \tag{16}$$

where a_1 and a_2 are now absolute constants, to be evaluated through detailed consideration of the cases $\beta = 0$ and $\pi/2$, respectively.

LINES OF CONSTANT UPWASH NORMAL TO THE LEADING EDGE ($\beta=0$)

For the case $\beta=0$ (fig. 5), the basic integral equation (4) may be written in the form

$$\hat{w}=\frac{1}{2\pi z}\int_{-1}^{1}\left\{\frac{\pi}{2}+\frac{Q\left(\frac{\bar{x}-\bar{\xi}}{z}\right)}{\left(\frac{\bar{x}-\bar{\xi}}{z}\right)}\right\}\hat{\gamma}(\bar{\xi})\,d\bar{\xi} \tag{17}$$

where

$$z=1/k$$

$$Q(t)=|t|\left[\frac{\pi}{2}-Ki_1(|t|)+K_1(|t|)\right]$$

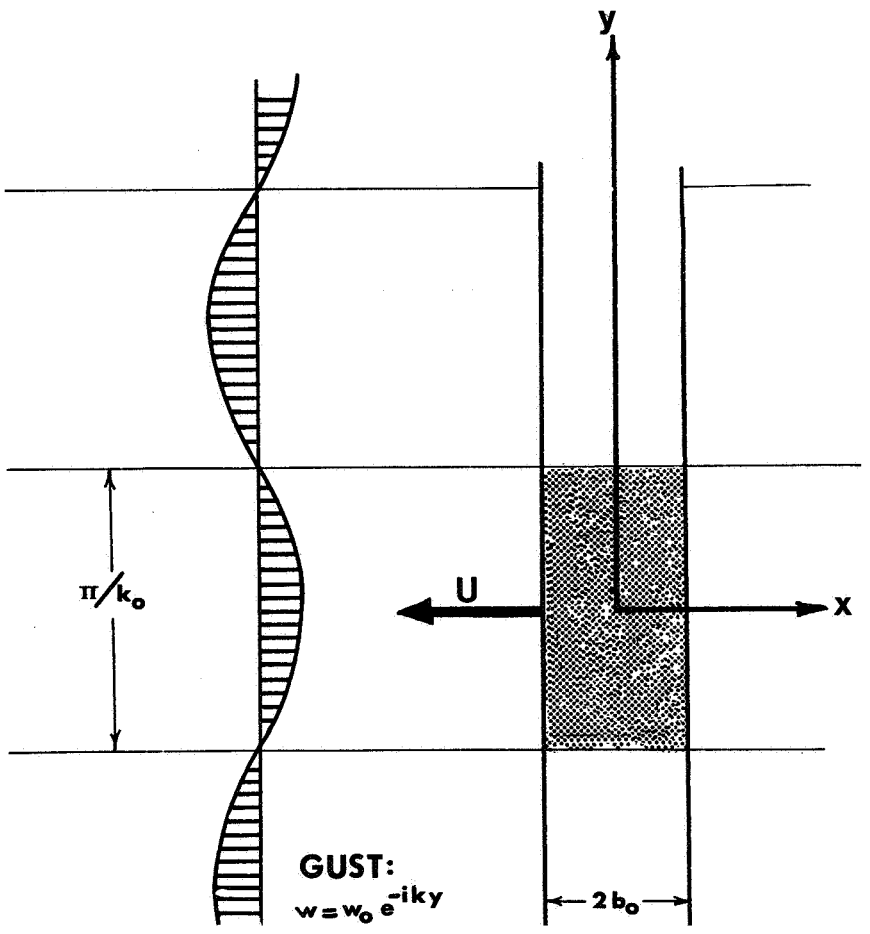

FIGURE 5.—Lines of constant upwash normal to the leading edge. $\beta=0$. Flow is stationary. Reduced frequency interpreted as an aspect ratio parameter.

We may note that the parameter z, which is the inverse of the reduced frequency, is proportional to the aspect ratio of a rectangular portion of wing cut out by successive nodal lines, as shown by the shaded area in figure **4.** An analogy between the loadings on the infinite sinusoidal wing considered herein and on a finite wing of aspect ratio $A=1/k$ may be demonstrated.

Consider an uncambered rectangular wing, twisted if necessary, with elliptical spanwise loading. An integral equation for the downwash on the centerline of such a wing has been derived by Wieghardt (ref. **6).** This equation can be written in the same form as equation *(17)* if z and Q are replaced by z_R and Q_R where

$$z_R = A$$
$$Q_R(t) = \sqrt{1+t^2}\, E[(1+t^2)^{-1/2}] \tag{18}$$

The analogous relationship between the parameters A and $1/k$ is evident. The asymptotic forms

$$\left.\begin{matrix} Q(t) \\ Q_R(t) \end{matrix}\right\} \sim 1 - t^2 \log |t| \qquad t \to 0 \tag{19}$$

$$\left.\begin{matrix} Q(t) \\ Q_R(t) \end{matrix}\right\} \sim \frac{\pi}{2} |t| \qquad t \to \infty \tag{20}$$

indicate that the chordwise loading on the infinite sinusoidal wing is precisely the same as that at the center section of an elliptically loaded finite wing of aspect ratio $1/k$ for both limits $k \to 0$ and $k \to \infty$. This same relationship must hold true to a very good approximation for the complete range of k, as demonstrated by figure 6. The kernel functions Q and Q_R are seen to be very good approximations to each other for the whole range of argument.

The constant a_2 in equation **(16)** may now be evaluated, for example, by stipulating that the center of pressure position for $k \to \infty$ be the same as that given by the Wieghardt equation for $A \to 0$.

For $k \to \infty$, the center of pressure position, in chords aft of the leading edge, is obtained from equation **(13),** with $a = a_2$, as

$$x_{cp} \sim \frac{1}{4a_2 k} \qquad k \to \infty \tag{21}$$

But for $A \to 0$, Wieghardt's equation gives the result (refs. **6** and *7)*

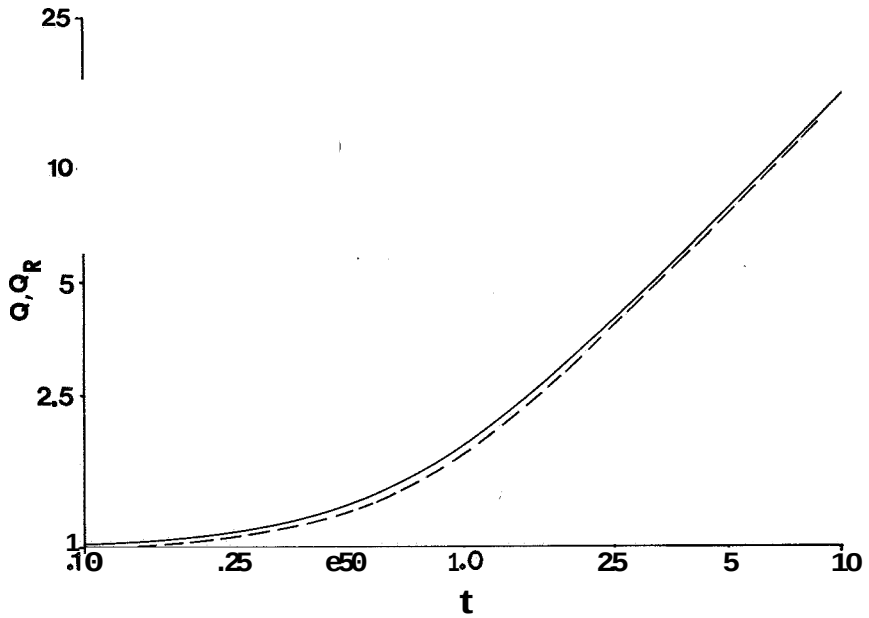

FIGURE 6.—Comparison of the kernel functions for the chordwise loadings on the infinite sinusoidal and analogous finite wings for the case $\beta = 0$.

$$x_{cp} \sim \frac{1}{4}A \qquad A \rightarrow 0 \tag{22}$$

Hence we take $a_2 = 1$. To show that this value is appropriate for the entire range of k, the center of pressure position using this value is compared with numerical solutions of Wieghardt's equation (ref. 8) on figure 7. The suitability of the assumed form, for this case at least, is apparent.

LINES OF CONSTANT PHASE PARALLEL TO THE LEADING EDGE (SEARS' CASE, $\beta = \pi/2$)

This case is most easily studied in the original x_0, yo-frame, where the flow approaches two-dimensional conditions as $\beta \rightarrow \pi/2$. The flow represents the flight of a two-dimensional airfoil through a stationary gust; but it is a well-known general result of two-dimensional theory that when an airfoil passes through any stationary gust whatever, the resulting pressure distribution must be proportional to the flat plate loading given by the square-root factor in equation (13). Using equation (2), it is found that the present theory can be made compatible with this observation is we take $a_1 = i$

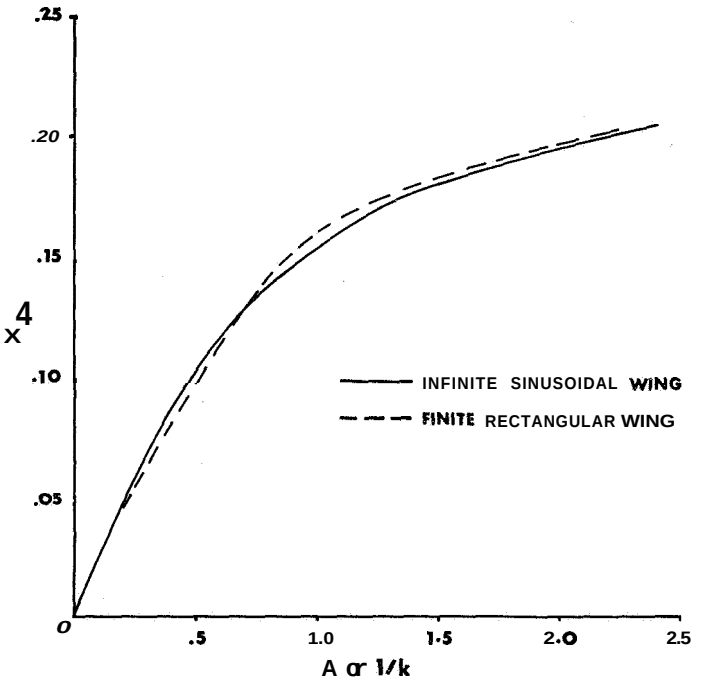

FIGURE 7.—Center of pressure location on the infinite sinusoidal and analogous finite wings.

FINAL RESULTS

Taking $a = \cos\beta + i \sin\beta$, equations (2), (3), and *(13)* give

$$l(x_0, y_0, t) = \frac{2\rho\hat{w}U_0}{\pi/2k + F(k, \beta)} \frac{e^{-k_2(\tilde{x}-i\tilde{y})-ik_1S}}{J_0(k_1-ik_2)+iJ_1(k_1-ik_2)} \sqrt{\frac{1-\tilde{x}}{1+\tilde{x}}} \tag{23}$$

where

$$\tilde{x} = x_0/b_0 \qquad \tilde{y} = y_0/b_0$$

$$S = U_0 t/b_0$$

Equation *(23)* shows that at any fixed instant of time, the spanwise loading is sinusoidal, with wavelength $2\pi/k_2$ and nodal lines perpendicular to the leading edge. The chordwise loading may be interpreted as having the same shape as that on the center section of an elliptically loaded rectangular wing of aspect ratio $1/k_2$. As time progresses, the whole pattern moves along the wing with speed $U_0 \tan\beta$.

The section lift coefficient obtained by integration of equation *(23)* may be written in the form

$$C_l = 2\pi T(k, \beta)\alpha_0, \tag{24}$$

where α_0 is the instantaneous angle of attack of the midchord line

$$\alpha_0 = \frac{\hat{w}}{U_0} e^{-i(k_1 S - k_2 \tilde{y})} \tag{25}$$

The lift-transfer function of generalized Sears function is given by

$$T(k, \beta) = \frac{1}{\pi/2k + F(k, \beta)} \frac{I_0(k_2) + I_1(k_2)}{J_0(k_1 - ik_2) + iJ_1(k_1 - ik_2)} \tag{26}$$

The magnitude and phase are plotted on figure *8*. The center of pressure position is

$$x_{cp} = \frac{1}{2k_2} \frac{I_0(k_2)}{I_0(k_2) + I_1(k_2)}$$

independent of the chordwise wave number k_1.

COMPARISON WITH SEARS FUNCTION

Taking $\beta = \pi/2$ in equation (26), we get the result

$$T(k, \pi/2) = \frac{1}{[J_0(k) + iJ_1(k)][\pi/2k + \cos k + kSik + i(kCik - \sin k)]} \tag{27}$$

Because of a sign difference in the definition of the gust waveform, equation *(27)* must be compared with the complex conjugate of the Sears function $S(k)^*$. This may be written in the form

$$S(k)^* = \frac{2}{\pi k} \frac{1}{H_0^{(2)}(k) + iH_1^{(2)}(k)} \tag{28}$$

The limiting results

$$\left.\begin{matrix} T(k, \pi/2) \\ S(k)^* \end{matrix}\right\} \sim 1 - \pi/2k - ik \ln k \qquad k \to 0 \tag{29}$$

$$\left.\begin{matrix} T(k, \pi/2) \\ S(k)^* \end{matrix}\right\} \sim \frac{1}{\sqrt{2\pi k}} e^{-i(k - \pi/4)} \qquad k \to \infty \tag{30}$$

confirm the claim that our solution is exact at both these limits. The comparison presented on figure *9* shows that equation *(27)* is a satisfactory approximation for all *k*.

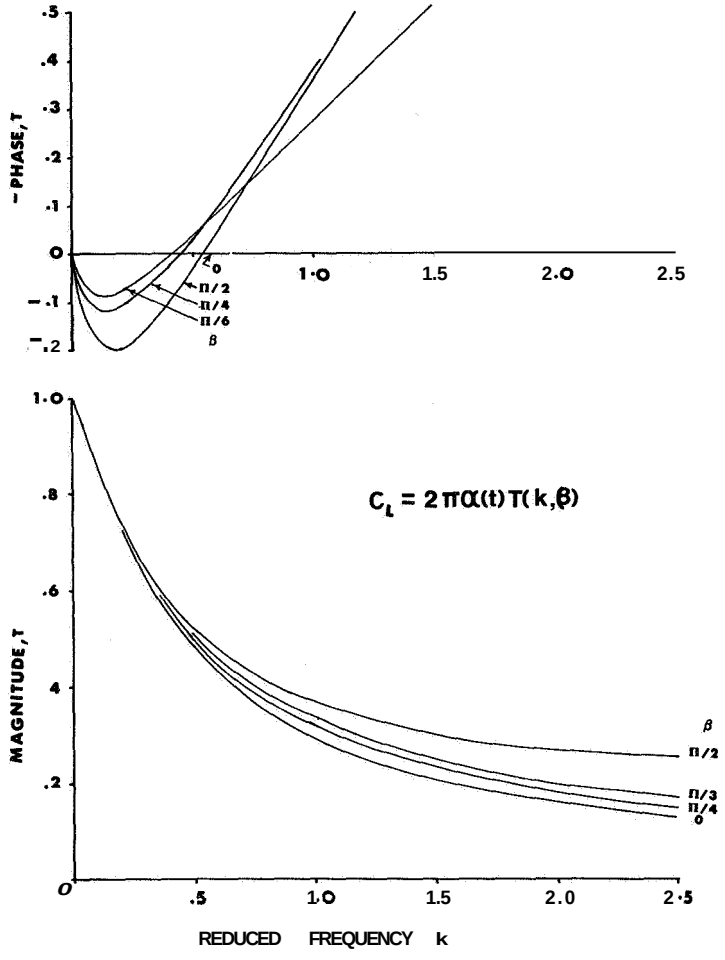

FIGURE 8.—Lift transfer function for an inclined sinusoidal gust.

DISCUSSION

The supposition that our result is a reasonable approximation to the exact solution of the linearized problem for all values of the parameters is verified by comparison with numerical results obtained by Graham.[2] Figure 10, for example, shows a comparison for the intermediate inclination angle $\beta = \pi/4$. It appears, in fact, that the comparison with Sears' case (fig. 9) exhibits the largest discrepancies.

The asymptotic relation obtained from equation (27)

[2] Ibid.

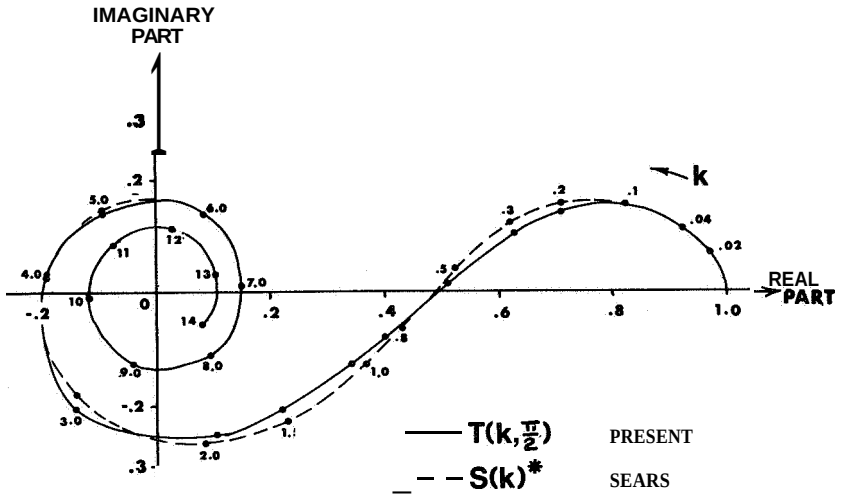

FIGURE 9.—Comparison with Sears' solution for the case $\beta=\pi/2$.

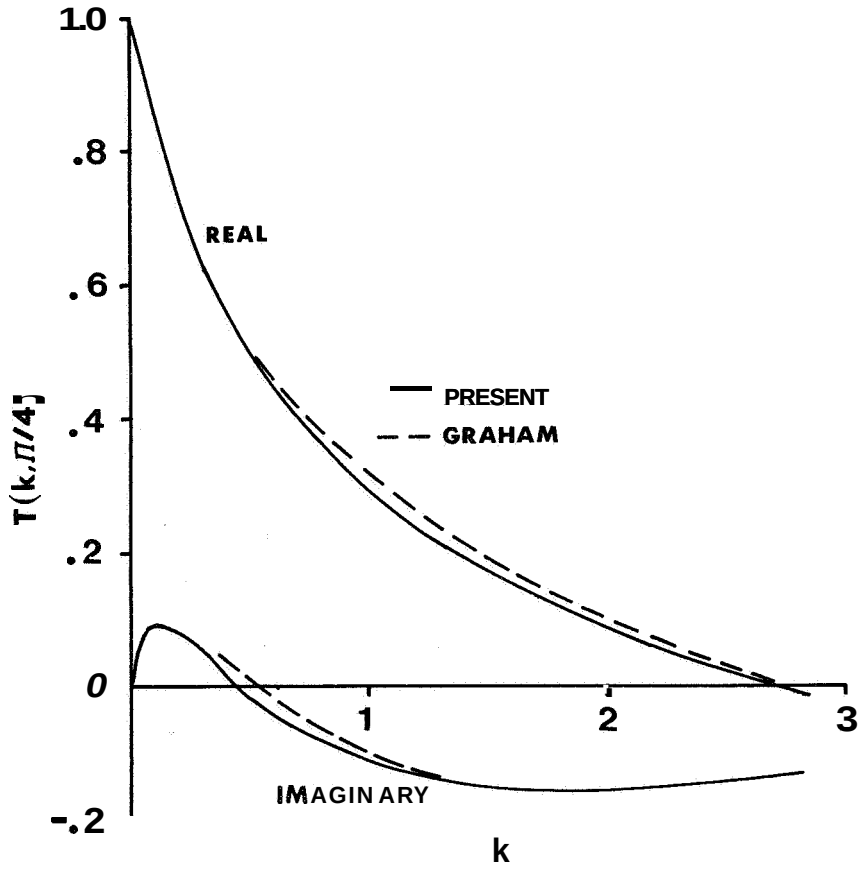

FIGURE 10.—Comparison with Graham's results for the case $\beta=\pi/4$.

$$T(k, \beta) \sim \frac{2}{\pi} \frac{e^{-i(k \sin \beta - \beta/2)}}{\sqrt{k(\sin^2 \beta + 4k \cos \beta)}} \qquad k \gg \sec \beta \tag{31}$$

shows that even for the infinite wing, a very slight three-dimensionality can change the behavior at large k from Sears' $k^{-1/2}$ to k^{-1}. Similarly, the invariance of the center of pressure position with reduced frequency is a particular limiting result true only for the strictly two-dimensional case.

These observations indicate the dangers inherent in the injudicious use of strip theory, even in situations that are very nearly two dimensional. They-are also pertinent to the response to turbulence at which the behavior at large k may contribute significantly to the mean square lift or moment.

A USEFUL APPROXIMATE FORM

Because an aim of the preceding analysis was to obtain an expression that would be convenient in routine calculations, it would be useful to further simplify equation (26). Recalling that the derivation consisted of patching together the exact low- and high-frequency expressions, we replace equation (26) by a simpler expression that reduces to the same limiting forms.

Consideration of equations (30) and (31) leads to an appropriate approximate form:

$$T(k, \beta) = \frac{e^{-ik\left[\sin \beta - \frac{\pi\beta(1+1/2 \cos \beta}{1+\pi k(1+1/2 \cos \beta}\right]}}{\sqrt{1+\pi k(1+\sin^2 \beta + \pi k \cos \beta)}} \tag{32}$$

This expression correctly predicts the high-frequency behavior as well as the low-frequency limit for all β. The behavior at very small k is not exactly identical to that of equation (26); however, for many applications this is not a serious deficiency.

For the case $\beta = \pi/2$, the magnitude reduces to an approximation originally suggested by Liepmann (ref. 4), the phase angle to an expression of Giesing et al. (ref. 9). In fact, except for very small k, the resulting expression is generally a better approximation to the Sears function than is equation (27). For other values of β, differences between equations (32) and (26) are slight.

REFERENCES

1. ABRAMOWITZ, M.; AND STEGUN, I. D. (eds.): Handbook of Mathematical Functions. Dover Pub., Inc., 1965.
2. SEARS, W. R.: Some Aspects of Non-Stationary Airfoil Theory and Its Practical Application. J. Aeron. Sci., vol. 8, no. 3, Jan. 1941, pp. 104–108.
3. RIBNER, H. S.: Spectral Theory of Buffeting and Gust Response: Unification and Extension. J. Aeron. Sci., vol. 23, Dec. 1956, pp. 1075–1077.

4. LIEPMANN, H. W.: On the Application of Statistical Concepts to the Buffeting Problem. J. Aeron. Sci., vol. 19, no. 12, Dec. 1952, pp. 793–800.
5. WEISSINGER, J.: The Lift Distribution of Swept Back Wings. NACA TM 1120, 1947.
6. WIEGHARDT, K.: Chordwise Load Distribution for a Simple Rectangular Wing. NACA TM 963, 1940.
7. LANDAHL, M.: Pressure Loading Functions for Oscillating Wings With Control Surfaces. AIAA J., vol. 6, no. 2, Feb. 1968, pp. 345–348.
8. LOMAX, H.; AND SLUDER, L.: Chordwise and Compressibility Corrections to Slender Wing Theory. NACA TN 2295, 1951.
9. GIESING, J. P.; STAHL, B.; AND RODDEN, W. P.: On the Sears Function and Lifting Surface Theory for Harmonic Gusts. Paper 5368, Douglas Aircraft Co., Mar. 1969.

ACKNOWLEDGMENT

The author gratefully acknowledges the supervision of Dr. H. S. Ribner who suggested the topic of this investigation.

UNSTEADY AIRFOIL RESPONSE

Robert A. Arnoldi
Pratt & Whitney Aircraft
East Hartford, Conn.

The analytical prediction of noise from fans and compressors tends to divide itself into separate aerodynamic and acoustic problems. Such an artificial division is probably caused by our ignorance of second-order interactions, but it is quite practical in view of the great si-nplifications in geometry required even for the divided problems. The aerodynamic problem quickly reduces to the prediction of unsteady airfoil response to gusts of various types. The response to a sinusoidal gust is applicable to blade-vane interaction, inflow distortion, and even to partially coherent turbulence excitation. Although a wide selection of sinusoidal gust response functions have been developed in connection with flutter and aeroelastic work, the acoustic analysis published to date has been restricted to the use of two-dimensional response for a thin, isolated airfoil at incompressible speeds. The purpose of the present study is to examine the available array of sinusoidal gust response functions, to comment on their relative importance to aeroacoustic analysis, and to suggest several important areas for improvement in this direction.

ISOLATED AIRFOIL RESPONSE

The aerodynamic analysis used in present fan-noise-prediction systems reduces to a quasi-steady calculations of fluctuating airfoil forces caused by transverse upwash and an assumption that the actual forces can be obtained by the use of the Sears function $S(k)$ (ref. 1) as a modifying factor. A very recent study (ref. 2) has extended this approach to include variations in streamwise velocity, deriving the Horlock function $T(k)$, which may be used in a manner analogous to $S(k)$, to modify the quasi-steady lift caused by the component of streamwise velocity fluctuations normal to the airfoil. The oscillating lift may then be expressed in terms of two additive components

$$L_v = \rho U b \frac{dC_l}{d\alpha} S(k) v \tag{1a}$$

and

$$L_u = \rho U b \frac{dC_l}{d\alpha} T(k) u\alpha \tag{1b}$$

where v and u are the oscillatory component velocity amplitudes (transverse and streamwise) of the sinusoidal gust as shown in figure **1** and where k is the reduced frequency $2\pi fb/U$ in terms of the semichord b. The range of k encountered for blade passage frequency response of gas turbines is from 0.5 to 5.0, considerably higher than the range that is of interest in flutter work. The two functions are related by

$$T(k) = S(k) + J_0(k) + iJ_1(k) \tag{2}$$

Here, the $S(k)$ modifies the response caused by that part of the horizontal gust that is transverse to the airfoil chord, and the term $J_0(k) + iJ_1(k)$ yields the effect of fluctuation in dynamic pressure on the otherwise steady lift as the gust passes.

In terms of interaction between blade rows due to viscous wakes as in reference **3** (where the composite wake is represented by a Fourier series with harmonic index m), the result of the inclusion of the Horlock function is to replace the use of $S(mk)$ in the final equation **(33)** of reference **(3)** by

$$H(mk) = S(mk) - \alpha \cot \delta T(mk)$$

as in equation **(37)** of reference **2.** For reasonable values of the incidence angle α and the wake angle δ relative to the downstream entrance flow, this is not a large correction.

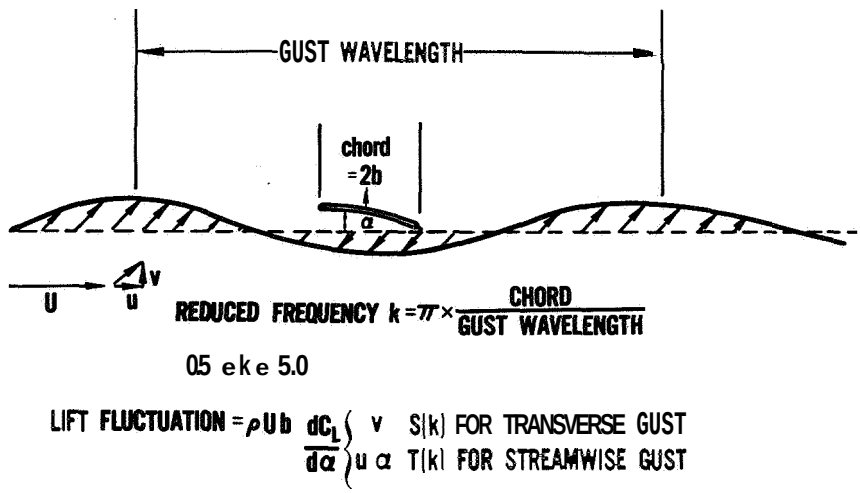

FIGURE 1.—Sinusoidal gust response of isolated airfoil.

Above a reduced frequency of 1.0, the following approximations are satisfactory:

$$S(k) \approx (2\pi k)^{-1/2} \exp\,(ik - i\pi/4) \tag{3a}$$

$$T(k) \approx 3S(k) \tag{3b}$$

It is important to note that the phase angle is related to the passage of the sinusoidal gust through the midchord position. Considerable simplification in this respect may be achieved by using the leading edge of the airfoil as a reference point because this involves multiplication by $\exp(-ik)$. The two functions are shown in figure 2 as vectors in the

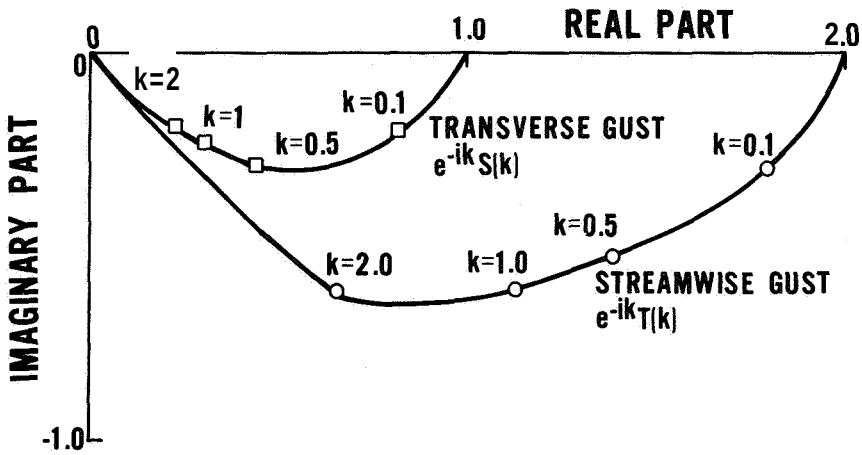

FIGURE 2.—Isolated airfoil response to sinusoidal gust, streamwise and transverse.

complex plane illustrating the validity of the approximations (3a) and (3b). In both cases, the airfoil response to a sinusoidal gust as it strikes the leading edge is immediate (in phase) for very low frequencies and approaches a constant phase lag of $\pi/4$ at higher frequencies (k of unit value or higher). This general behavior will be seen to persist as a general feature in such cases as cascades and compressible effects, although the asymptotic amount of phase lag varies in some cases.

It may be seen immediately that the usually small angle of incidence α results in small values of L_u relative to L_v unless the gust is primarily in the streamwise direction. For blade wakes of conventional compressors, in relation to their interaction with following vanes as shown in figure 3, substantial transverse components exist and L_v becomes the primary lift amplitude. For general turbulence from causes like IGV and strut wakes and wall boundary layers, the streamwise fluctuations are substantial and L_u cannot be ignored. The unsteady effect of interaction from adjacent blades in the same row varies from a negligible

371-986 0-LT-70—17

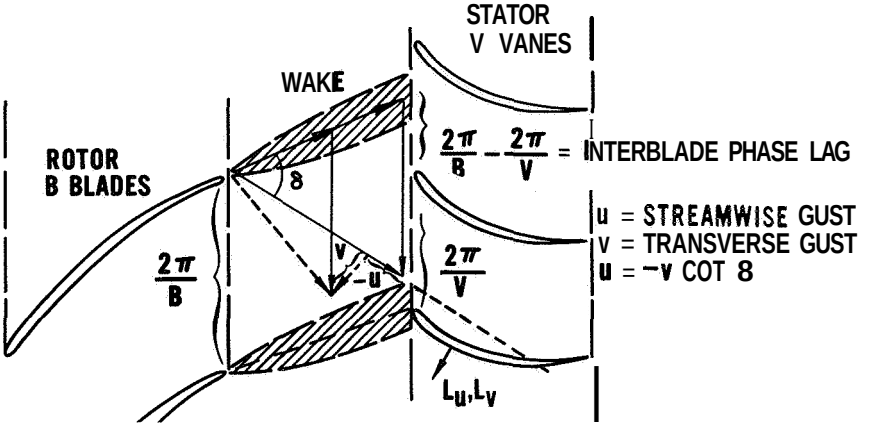

FIGURE 3.—Gust effect from rotor wake.

factor to a very large one and depends on reduced frequency, stagger angle, and interblade phase angle.

INCOMPRESSIBLE FLOW IN CASCADES

The interblade phase angle constitutes an expression of the timelag of the sinusoidal gust effect at one blade in relation to its occurrence at the next, as shown in figure 3. The analysis of the interaction involves fluctuations in the vorticity distribution on each blade, and the resultant effect of these fluctuations on the adjacent blade is very dependent on the geometrical factors mentioned above. Tabulated values of gust response functions have been given in reference 4 and are plotted in figures 4, 5, and 6.

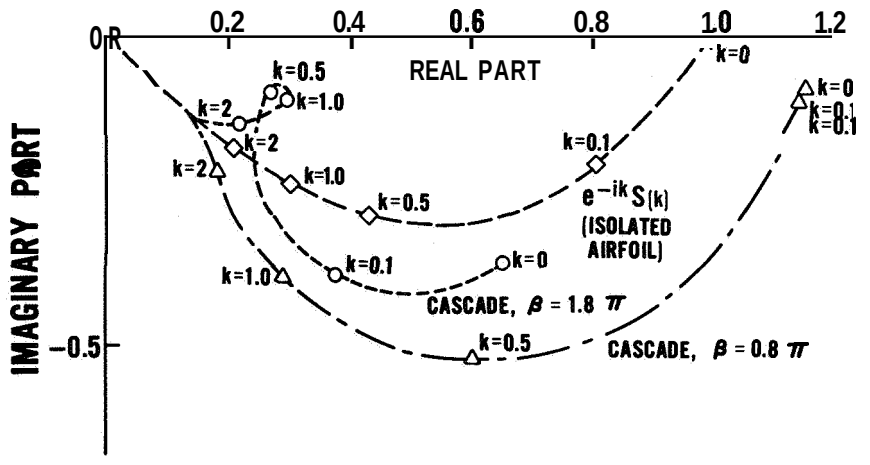

FIGURE 4.—Cascade response to sinusoidal transverse gust, extreme effects of interblade phase angle β, gap/chord = 1, stagger angle $\xi = 45°$.

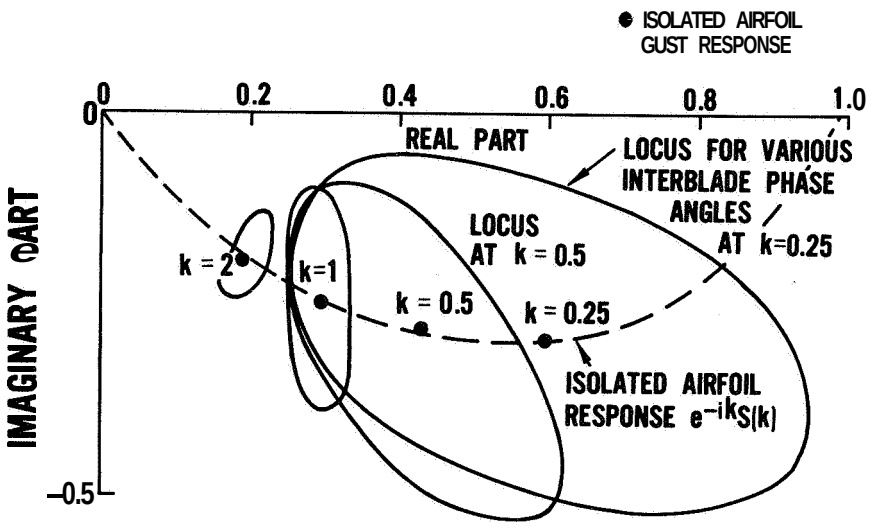

FIGURE 5.—Cascade response to sinusoidal transverse gust, effect of interblade phase angle at various reduced frequencies, $\xi=45°$, S/C=1.

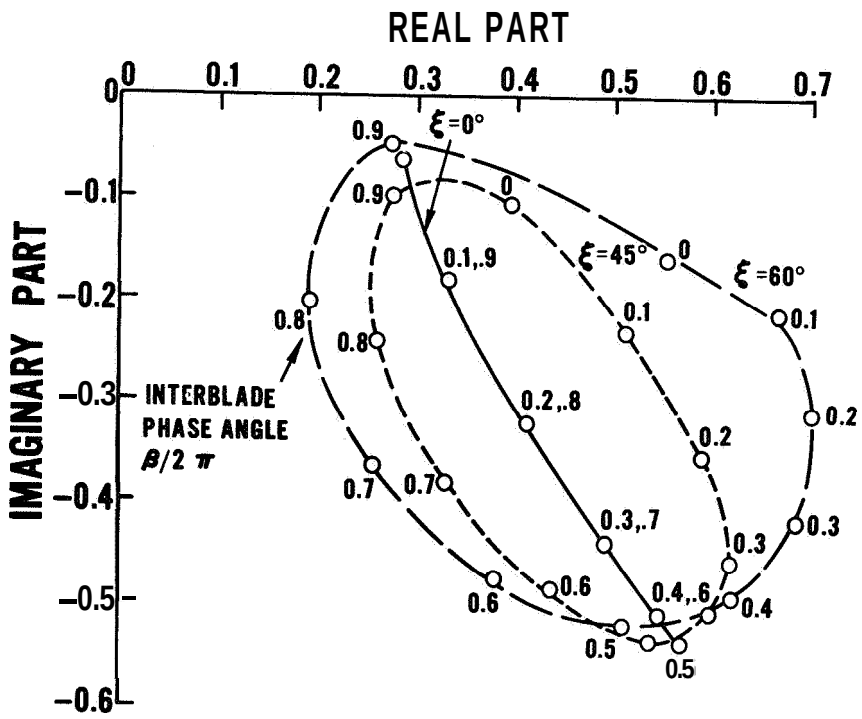

FIGURE 6.—Cascade response to sinusoidal transverse gust, effect of stagger angle ξ for S/C=1, $k=0.5$.

For reduced frequencies over 0.5, the phase lag of the airfoil response is least when the interblade phase angle is near zero and greatest when the phase angle is near π. The response and the interblade phase angle at which the maximum response occurs are strongly affected by the stagger angle ξ at low reduced frequencies (see fig. 6). At higher values of k, the cascade response approaches that of an isolated airfoil (figs. 4 and 5). It may be seen that the possible variation in response is greatest at reduced frequencies just on the lower border of the acoustic range near 0.5. Because the cascade effect can vary by a factor of 3 at this frequency, it is hardly negligible, and its variation with compressibility is of great importance.

At the same time, it is clear from figures 5 and 6 that the gust response is least for interblade phase angles of 1.6π to 2π, corresponding to a number of vanes that exceed a multiple of the blade number by 20 percent or less. This fact agrees with current practice in fan design, and the results are not greatly different from the isolated airfoil response at higher reduced frequencies. It would therefore appear that cascade effects are significant for aerodynamic noise, but that isolated airfoil functions may be used if reduced frequency and interblade phase angle limitations are properly observed.

STALL EFFECTS

The effect of blade loading near the stall point has not been investigated for sinusoidal gust response, although the flutter problem has prompted attention to be paid to its effect on translatory and pitching oscillations (see ref. 5). The expectation is that overshoot of the steady stall loading will occur, with the amount of loading depending strongly on reduced frequency and interblade phase angle. When stall occurs during the cycle, the deviation from a purely sinusoidal response constitutes higher harmonics of the gust frequency as well as a change in magnitude and phase of the fundamental response. If random turbulence is present, the amount of overshoot will probably vary from cycle to cycle and cause a corresponding random shift in nonsinusoidal response. This shift constitutes a probable source of broadband noise.

THREE-DIMENSIONAL EFFECTS

Lack of two-dimensionality in the sinusoidal gust response can manifest itself in at least two conditions of importance in compressor noise. The first consists of the spanwise variations in velocity that will normally cause any particular blade wake to distort and prevent the wake from striking all spanwise stations of the following vane simultaneously. This effect causes spanwise variations of the circulation to be induced in the vane, with the associated shedding of trailing vorticity, which is

oriented streamwise and therefore omitted from the two-dimensional gust analysis. A treatment of this case has been presented at this conference [1] and is compared with the two-dimensional function in figure 7.

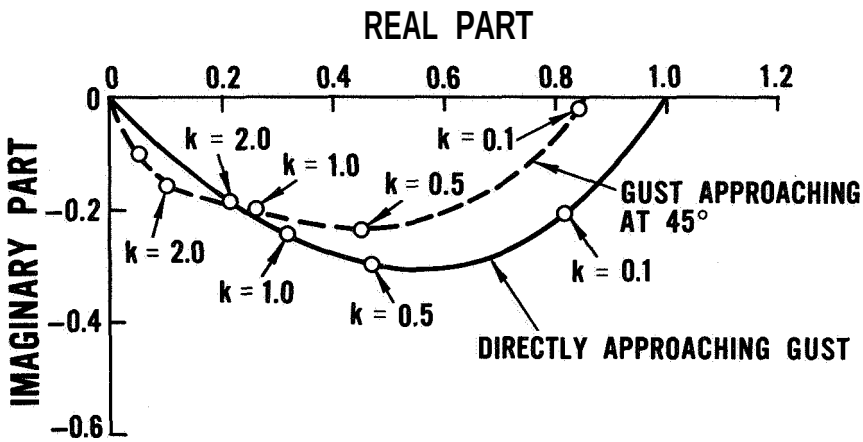

FIGURE 7.—Sinusoidal gust response of isolated airfoil, effect of obliquity of gust.

The second manifestation of three-dimensional effects occurs in the application of sinusoidal gust functions to the interaction of turbulence with the airfoil, where the lateral scale of the turbulence is insufficient for spanwise uniformity. In this case, the sectional response of an airfoil may be approximated by published values (ref. 6) calculated for wings of finite aspect ratio. This approximation does not properly account for the lack of spanwise coherence but does consider the induced downwash caused by the streamwise vorticity in the wake. Figure 8 shows the magnitude of the effect for a rectangular wing having an aspect ratio A of 4, for incompressible and supersonic flow, compared to the two-dimensional functions. The values are calculated from equations (32) and (70) of reference 6, which replace $S(k)$ in equation (la):

$$M=0:\ e^{ik}\left\{1-\frac{0.391ik}{0.285+ik}-\frac{0.609ik}{1.638+ik}\right\} \tag{4}$$

$$M>1:\ e^{ik}\left\{\frac{f_0(M,\bar{\omega})}{1-\frac{1}{2}\beta A}+\frac{\beta}{4M^2k^2A(1-\frac{1}{2}\beta A)}\left[1-e^{-i\bar{\omega}}\left(\cos\frac{\bar{\omega}}{M}+iM\sin\frac{\bar{\omega}}{M}\right)\right]\right\} \tag{5}$$

where

$$\bar{\omega}=2M^2k/\beta^2 \quad \text{and} \quad \beta^2=M^2-1 \tag{6}$$

[1] See p. 231.

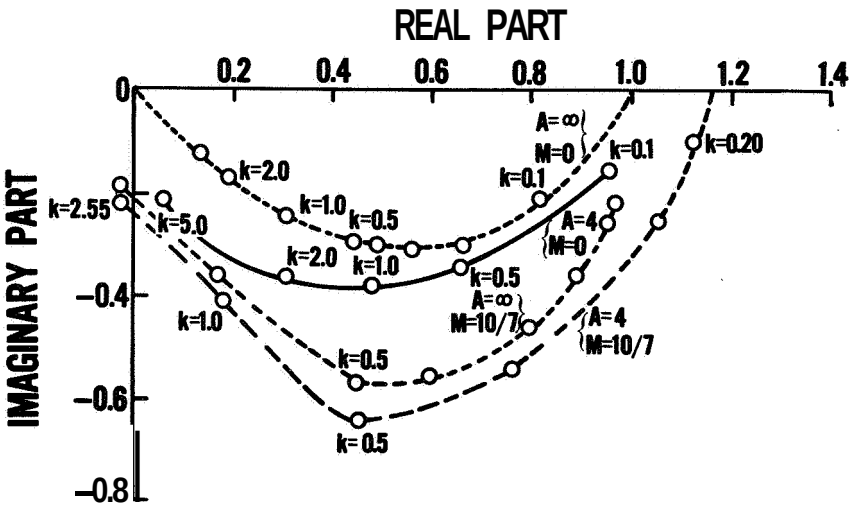

FIGURE 8.—Sinusoidal gust response of isolated airfoil, effect of compressibility and aspect ratio.

and f_0 is the Schwartz function, tabulated in reference 7:

$$f_0(M, \bar{\omega}) = \int_0^1 e^{-i\bar{\omega}x} J_0(\bar{\omega}x/M)\,dx \tag{7}$$

It should be emphasized that the variation of overall response with compressible flow and finite aspect ratio depends on $dC_l/d\alpha$ as well as on the gust response function. Equation (13.22) of reference 8 gives a compressibility correction based on Goethert's rule:

$$\left(\frac{dC_1}{d\alpha}\right)_{M,A} = \frac{1.8+A}{1.8+\beta A}\left(\frac{dC_2}{d\alpha}\right)_{M=0,A} \tag{8}$$

In commentary on figure 8, the effects of aspect ratio are considerable and in some respects, rather surprising; the implication is that coefficients for turbulence will also differ considerably from their two-dimensional counterparts. There appears to be a greater response for low aspect ratio in general, as well as a remarkable shift in phase angle at low reduced frequencies for supersonic flow. Experimental verification of these tendencies would be valuable.

AIRFOIL THICKNESS EFFECT

The effect of airfoil thickness may be approximately assessed by comparison of the calculated values of reference 9 for the Kuessner function (unsteady response to a sharp-edged gust). For thin airfoils

(qualitatively acceptable as an assumption for the 8.4 percent Mises airfoil presented in ref. 9), the sinusoidal gust function may be derived from the Kuessner function by the formula (ref. 6)

$$e^{-ik}S(k)=1+ik\int_0^\infty [k_2(s)-1]e^{-iks}ds \tag{9}$$

Following figure 8 of reference 9

$$k_2(s)\approx 1-0.24e^{-0.058s}-0.55e^{-0.364s}-0.17e^{-2.42s} \tag{10a}$$

which may be compared with the flat-plate response (ref. 6)

$$k_2(s)\approx 1-0.236e^{-0.058s}-0.513e^{-0.364s}-0.171e^{-2.42s} \tag{10b}$$

From equations (9) and (10a)

$$e^{-ik}S(k)\approx 1-\frac{0.24ik}{0.058+ik}-\frac{0.55ik}{0.364+ik}-\frac{0.17ik}{2.42+ik} \tag{11}$$

which is plotted in figure 9. The effect of thickness is seen to be small, and it may be concluded that other effects demand more immediate attention.

CONCLUDING REMARKS

In conclusion, the use of the Sears function as a measure of unsteady aerodynamic response in aeroacoustic problems will lead to discrep-

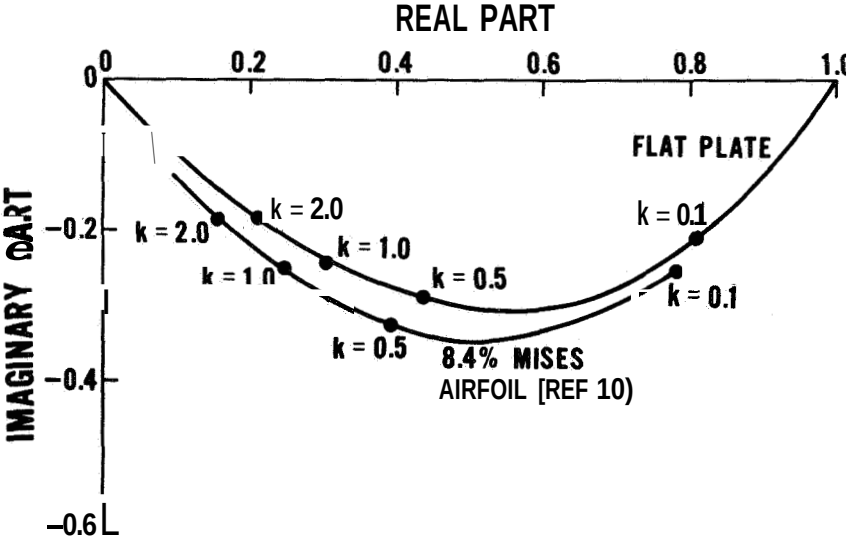

FIGURE 9.—Sinusoidal gust response of isolated airfoil, effect of thickness.

ancies of only a few decibels except in extreme cases. In general, other functions need be brought into noise prediction systems only if—

(1) Comparison is to be made of situations in which interblade phase angles are substantially different or in a range of critical sensitivity;

(2) Blade loading is near the stall region, so that nonsinusoidal response to a sinusoidal gust can be expected; and

(3) Unusually low reduced frequencies are characteristic of the system at the operating condition.

The most desirable extensions of available tabulated functions which will answer these needs are the combined effects of interblade phase angle with spanwise variation of sinusoidal gust phase, the effect of stall overshoot on sinusoidal gust response, and the effect of compressible flow velocities on the cascade gust response. With these in hand, the aerodynamic problems of noise prediction can be approached with the confidence that accuracy, at least equivalent to that inherent in the calculation of acoustic generation and propagation, is being provided.

REFERENCES

1. SEARS, WILLIAM R.: Some Aspects of Non-Stationary Airfoil Theory and Its Practical Application. J. Aeron. Sci., vol. **8**, Jan. 1941, pp. 104–108.
2. HORLOCK, J. H.: Fluctuating Lift Forces on Airfoils Moving Through Transverse and Chordwise Gusts. Am. Soc. Mech. Engrs., Paper 68–FE–28, 1968.
3. KEMP, NELSON H.; AND SEARS, W. R.: The Unsteady Forces Due to Viscous Wakes in Turbomachines. J. Aeron. Sci., vol. 22, 1955, p. 478.
4. WHITEHEAD, D. S.: Force and Moment Coefficients for Vibrating Airfoils in Cascade. R&M no. 3254, British A.R.C., Feb. 1960.
5. CARTA, F. O.: Unsteady Normal Force on an Airfoil in a Periodically Stalled Inlet Flow. J. Aircraft, vol. 4, Sept.–Oct. 1967, pp. 416–421.
6. DRISCHLER, J. A.: Calculation and Compilation of the Unsteady-Lift Functions for a Rigid Wing Subjected to Sinusoidal Gusts and to Sinusoidal Sinking Oscillations. NACA TN 3748, Oct. 1956.
7. GARRICK, I. E.; AND RUBINOW, S. I.: Flutter and Oscillating Air-Force Calculations for an Airfoil in a Two-Dimensional Supersonic Flow. NACA Rept. 846, 1946.
8. SHAPIRO, A. H.: The Dynamics and Thermodynamics of Compressible Fluid Flow. Ronald Press Co., 1953.
9. GIESING, J. P.: Nonlinear Two-Dimensional Unsteady Potential Flow With Lift. J. Aircraft, vol. 5, Mar.–Apr. 1968, pp. 135–143.

A Study of Fan-Compressor Noise Generation

M. J. Benzakein
General Electric Co.
Cincinnati, Ohio

An analytical model of the discrete frequency tone generation mechanisms in axial-flow fans and compressors is presented. The model is based on turbomachinery unsteady aerodynamics coupled with a duct acoustic field described in terms of spinning modes. A prediction method for the sound-power levels generated by a rotor alone, as well as by potential, wake, and vortex interactions between blade rows, is outlined. The results are presented in parametric form and indicate the effects of fan-compressor design, number of blades, vane-blade ratio, aerodynamic parameters, and blade-row spacing on pure-tone noise reduction. The analytical results are compared with experimental data obtained on different vehicles and are shown to be in good agreement.

SYMBOLS

A_{nm}	Fourier-Bessel coefficient
B	number of rotor blades
c	speed of sound
D	number of rotating line vortices
$f(r)$	radial distribution of unsteady tangential velocity
J_n, Y_n	first and second kind Bessel functions of order n
M	mach number
m	integer index
n	integer index or spinning mode number
$\hat{n}$	integer index
$\bar{n}$	integer indicator of the harmonic of blade passing frequency
P	pressure
PWL	sound-power level referenced to 10^{-13} W
$R_n(\lambda_{nm}r)$	Bessel cylinder function
R_0	duct outside radius
r, θ, z	polar coordinates
t	time
v	acoustic particle velocity

Γ	unsteady blade circulation
Y	see equation (2)
δ	impulse function
ζ	see equation (3)
η_{nm}	see equation (13)
λ_{nm}	eigenvalue
μ	radius ratio
ρ	density
ϕ	velocity potential

Subscripts

n	spinning mode number
m	radial mode number
z	axial direction
θ	tangential direction

INTRODUCTION

The advent of high bypass ratio turbofan engines introduced a new set of noise problems into commercial aviation. In the past few years the noise generated by jet aircraft has become increasingly annoying to communities in the vicinity of airports. Future exposure of populated areas to the noise generated by aircraft during takeoff and landing procedures may present the aircraft industry with additional problems unless quiet engine configurations can be developed.

For a long time the major source of noise in commercial jet aircraft was created by the hot exhaust of gases in pure jets and in low bypass ratio fans; however, in the last few years, with the advent of large bypass ratio turbofans, the so-called pure tones generated in fans and compressors at the blade passing frequency have been shown to be of high-level annoyance to the listener. This high-frequency noise has, therefore, become of primary importance to the propulsion design engineer. A major effort was undertaken to reduce turbomachinery noise to acceptable levels. It quickly became apparent that an effective and economically feasible noise reduction in fans and compressors could be accomplished only after a basic understanding of the noise-generation, transmission, and radiation mechanisms was obtained.

In the past most of the engineering effort was directed toward reducing the engine noise after the fact. The acoustician was presented with the final version of a fan and told to make it quiet. The only thing left to do at that time was to treat the inlet and exhaust duct with acoustic material and hope for the best. During the last few years, however, much research has been performed in the field of unsteady aerodynamics and noise

abatement. The object of this presentation is to show how a knowledge of the basic noise-generating mechanisms can be applied to the designs of quiet fans and compressors.

ANALYTICAL MODEL

The basic analysis of aerodynamic sound generation has been investigated by a number of theoreticians. Different theories have been presented, most of them agreeing with the fact that the interaction of the flow with a rigid body will produce a sound of a dipole nature. The strength of the dipole is a function of the lift fluctuations impacted on the body immersed in the flow. An analysis of these lift fluctuations and the associated unsteady circulations generated in a fan-compressor at the blade passing frequeney was conducted at General Electric. This analysis, based on turbomachinery unsteady aerodynamics, is described in some detail in reference 1. The results of this work are summarized below.

The solution of the wave equation in an annular duct in the presence of spinning modes of sound can be written as

$$\phi = \sum_{n=-\infty}^{+\infty} \sum_{m=0}^{\infty} A_{nm} e^{i(\zeta+\gamma)z} \cdot e^{in(\theta - M_n t)} R_n(\lambda_{nm} r) \tag{1}$$

where

ϕ	sound velocity potential
n	number of spinning lobes (diametral modes)
m	number of radial modes
A_{nm}	Fourier coefficient depending on noise generation mechanisms
M_n	circumferential mach number of a spinning lobe
M_n	$\bar{n}\frac{M_t}{n}B$
$\bar{n}$	harmonic number
M_t	blade tip mach number
B	number of blades
$R_n(\lambda_{nm} r)$	cylinder function satisfying the radial boundary conditions
λ_{nm}	eigenvalue satisfying the radial boundary conditions

and

$$\gamma = \frac{-nM_z(M_n - \bar{M}_\theta)}{1 - M_z^2} \tag{2}$$

$$\zeta = \frac{\sqrt{n^2(M_n - M_\theta)^2 - \lambda_{nm}^2(1 - M_z^2)}}{1 - M_z^2} \tag{3}$$

where

M_z axial flow mach number

M_θ circumferential mach number

Let us consider a rotating vortex line $\vec{v}$ (fig. 1) in the plane of the fan-compressor rotor ($z=0$). The tangential velocity at an angle θ will be

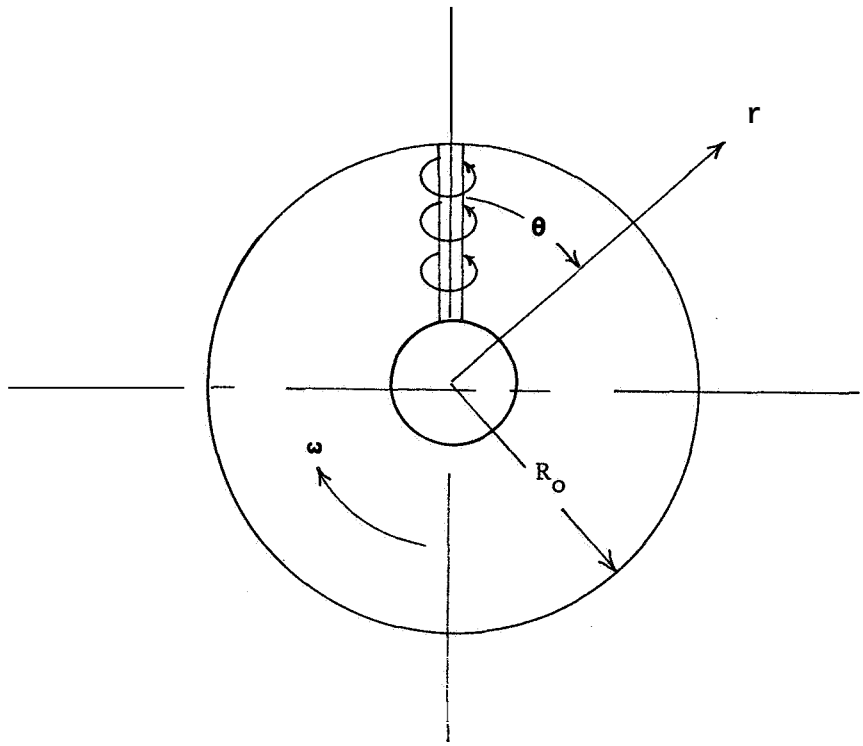

FIGURE 1.—Model of a rotating line vortex.

zero until the source is at the same angle. Then it may be assumed that the velocity jumps to a value $f(r)$. This can be expressed mathematically by writing

$$v=f(r)\delta(8-M_n t) \tag{4}$$

where $f(r)$ is the radial distribution of tangential velocity. The circulation at a given radius may be found by integrating

$$\Gamma(r)=R_0 c\int_0^{2\pi} vr\,d\theta \tag{5}$$

where $R_0 c$ is introduced to nondimensionalize the circulation. Then

$$\Gamma(r) = R_0 crf(r) \tag{6}$$

or

$$v = \frac{\partial\phi}{\partial\theta}_{z=0} = \frac{\Gamma(r)}{Rorc}\delta(\theta - M_n t) \tag{7}$$

Using the fact that $\mathbf{V} = \nabla\phi$, the final boundary condition can be expressed as

$$v_{z=0} = \frac{\Gamma(r)}{R_0 rc}\delta(\theta - M_n t) \tag{8}$$

If there are D such rotating line vortices, the boundary condition can be expressed as

$$\frac{\partial\phi}{\partial\theta}_{z=0} = \frac{\Gamma(r)}{R_0 c}\sum_{k=1}^{D}\delta\left(\theta - M_n t + \frac{2\pi k}{D}\right) \tag{9}$$

After some algebra we obtain

$$\Gamma(r)\sum_{k=1}^{D} e^{\frac{-i\hat{n}2\pi k}{D}} = R_0 c\sum_{n=-\infty}^{+\infty}\sum_{m=0}^{\infty} 4i\pi n A_{nm}\delta_{n\hat{n}}R_n(\lambda_{nm}r) \tag{10}$$

Examining the left side of equation (10), it can be seen that

$$\sum_{k=1}^{D}\exp\frac{-i\hat{n}2\pi k}{D} = \begin{cases} D \text{ if } \dfrac{n}{D} = \text{integer} \\ 0 \text{ if } \dfrac{\hat{n}}{D} \neq \text{integer} \end{cases}$$

Then, because $\hat{n}$ is a dummy index

$$\Gamma(r)D = R_0 c\sum_{n=-\infty}^{+\infty}\sum_{m=0}^{\infty} 4in\pi A_{nm}R_n(\lambda_{nm}r) \tag{11}$$

Using the orthonormal properties of the cylinder function, we obtain

$$A_{nm} = \frac{D}{4i\pi R_0 cn\eta_{nm}}\int_{\mu}^{1.0}\Gamma(r)rR_n(\lambda_{nm}r)\,dr \tag{12}$$

where η_{nm} is the norm of $R_n(\lambda_{nm}r)$ between μ and 1 given by

$$\eta_{nm} = \frac{1}{2\lambda_{nm}^2}\left[(\lambda_{nm}^2 - n^2)R_n^2(\lambda_{nm}) - (\lambda_{nm}^2\mu^2 - n^2)R_n^2(\lambda_{nm}\mu)\right] \tag{13}$$

From the definition of the velocity potential it can be shown that the pressure is expressed as

$$P = -c^2 \frac{\partial \phi}{at} \tag{14}$$

neglecting steady duct flow. Using equations (1), (12), and (14), the rms pressure can be expressed as

$$P_{z=0} = \sum_{n=-\infty}^{+\infty} \sum_{m=0}^{\infty} \frac{\rho c D M_n}{4\sqrt{2\pi} R_0 \eta_{nm}} R_n(\lambda_{nm} r) \int_{\mu}^{1.0} \Gamma(r) r R_n(\lambda_{nm} r)\, dr \tag{15}$$

The integral in equation (15) can be integrated if the radial distribution of unsteady circulation is known.

Different mechanisms are involved in the pure-tone generation in fans and compressors. These different mechanisms vary in importance from configuration to configuration and, in a single design, from speed to speed (ref. 2). In general, there are two major kinds of fan-compressor blade passing frequency noise-generating mechanisms: those relating to the rotating blade row alone and those that are a result of the interaction of moving blade rows with adjacent stationary blade rows.

Rotor-alone noise arises from the rotating steady-pressure field that surrounds each blade as a consequence of its motion. In the absolute reference frame, this pressure field appears as a source pulsating with a frequency equal to that of the rotor blade passing frequency. One can see that for rotor-alone noise, the circulation input in equation (15) is equal to the steady circulation around the airfoil that can be calculated from the steady aerodynamics of the turbomachinery.

The interaction-related noise may result from different sources: viscous wake interaction, potential field interaction, or wake vortex interaction. The unsteady circulations resulting from these different interactions can be determined (refs. 1 and 2) and input in equation (15).

COMPARISON WITH EXPERIMENTAL DATA

A few experimental checks on the analytical model were presented in reference 1. Some additional correlations with experimental data are presented in the following paragraphs.

CF700 and CJ805-23 Fans

Both these General Electric aft fans are currently used in commercial applications. The CF700 powers the Falcon business jet, and the CJ805-23 powers the Convair 990 aircraft. Both fans were tested on the noise site at Edwards Air Force Base, and the measurements were taken on a 250-ft arc around the engine with microphones placed 10° apart. The sound-power levels were calculated from the measurements. The com-

parisons between the analytical and experimental results for both fans are shown on figures 2 and **3.** The agreement is extremely good.

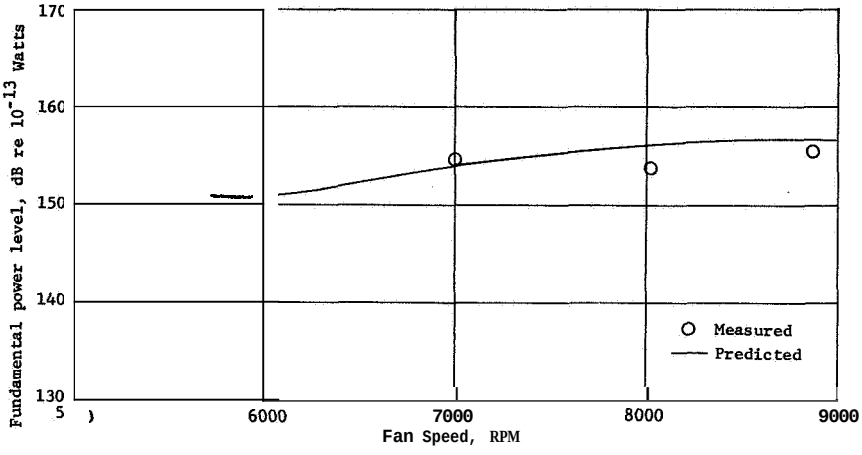

FIGURE 2.—Comparison between measured and predicted data on the CF700 fan.

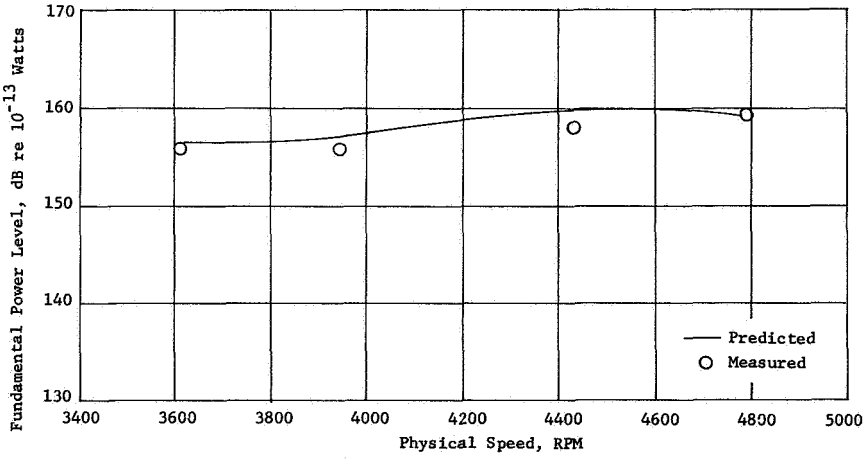

FIGURE 3.—Comparison between measured and predicted data on the CJ805-23 fan.

Two-Stage Low-Speed Fan

A two-stage fan was modified by General Electric under a **NASA** contract, **NAS 3–11166** (see ref. **3).** The outer panel of the fan first stage was eliminated, and the vehicle was transformed into a two-stage low-speed fan. The vehicle was tested at the General Electric Peebles test site. Measurements were taken in the far field along a 250-ft arc along

three different operating lines. Some of the data are compared with the analytical results in figure 4. Very good agreement was obtained.

LF336A Lift Fan

A lift fan was tested under a NASA contract, NAS 2–4970, at Edwards Air Force Base. The fan was tested in a horizontal position, and measure-

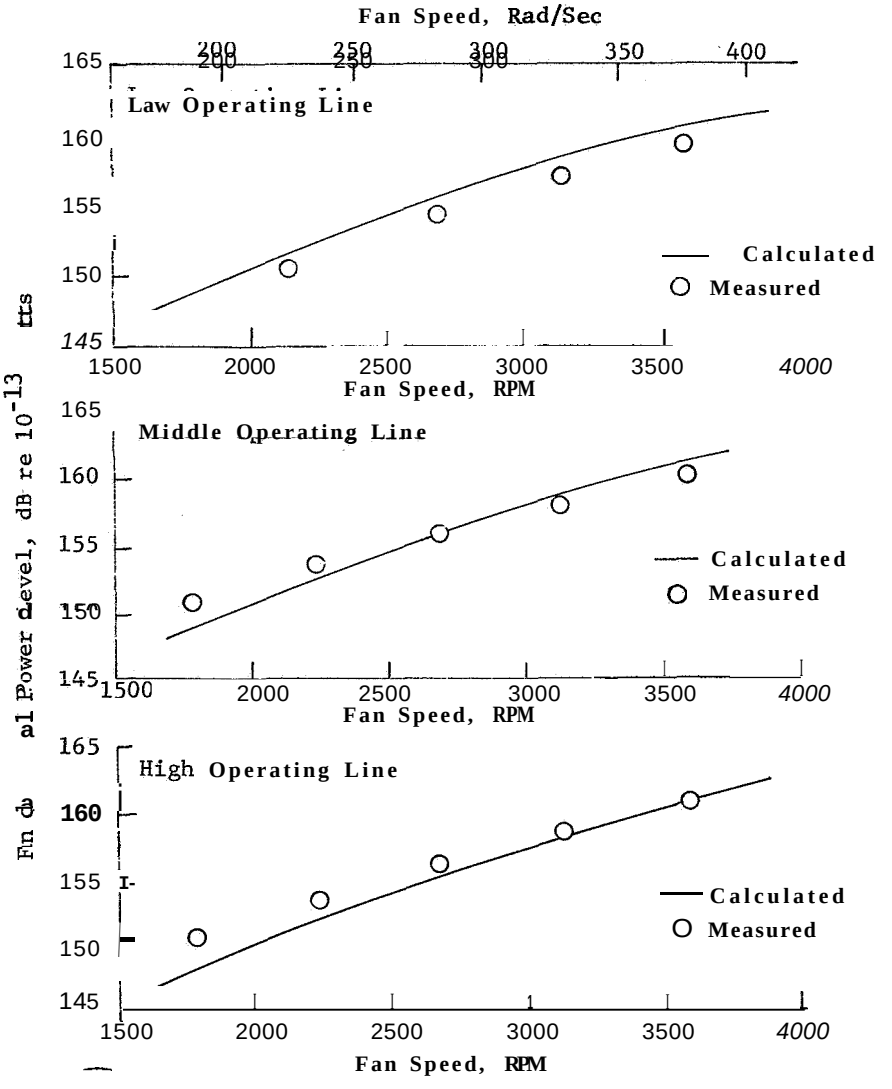

FIGURE 4.—Comparison between measured and predicted data on the second stage of a low tip speed fan noise demonstrator engine.

ments similar to the ones described previously were taken in the far field. A comparison of analytical and experimental results is shown in figure 5. They agree within 2.5 dB.

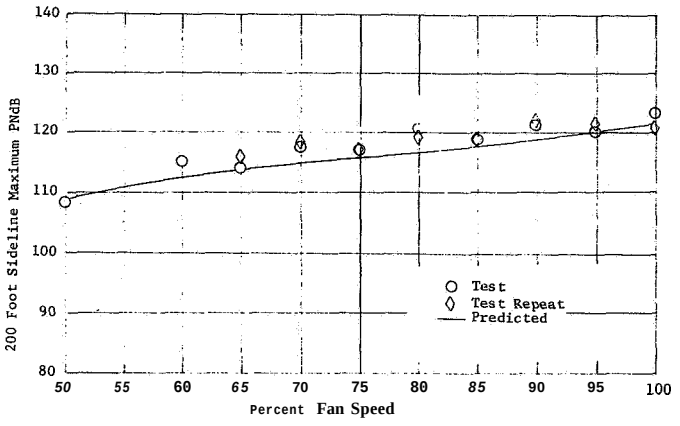

FIGURE 5.—Comparison between measured and predicted maximum 200 ft sideline PNdB for the LF336A fan.

NASA Langley Fan Configurations

A series of fan configurations were tested by Copeland et al. (ref. 4) in an anechoic chamber at Langley NASA Research Center. The blade passing frequency noise generated by the different configurations was analytically predicted, using the model described earlier. The comparison with the experimental data obtained along a 10-ft arc in the anechoic chamber is shown in figure 6. Again, the agreement is very good.

We can see that an analytical model can be constructed that relates the noise mechanisms in a fan-compressor to the basic aerodynamics of the turbomachmery. It does permit the parametric investigation of the effects of number of vanes, blades, pressure ratio, blade loading and diffusion factor, tip speed, and blade axial spacing on blade passing frequency noise (see ref. 2) and represents a versatile tool in the design of quiet fans and compressors.

PARAMETRIC STUDY OF ROTOR-ALONE NOISE

It can be seen from equation (15) that the sound-pressure levels generated by a rotor alone are a direct function of the circulation around the blade row. The larger the circulation, the higher the pure-tone levels. This is consistent with aircraft propeller experience. A study has been made to investigate these effects parametrically from a turbomachinery viewpoint. Some of the results are shown in figures 7 through 10.

371-986 O-LT-70—18

CONFIGURATION 1: IGC-rotor (62 vanes, 53 blades) spacing: 0.535 chord

Measured (NASA Langley) 132 dB

Calculated 132.2 dB

CONFIGURATION 2: Rotor-OGV (53 blades, 62 vanes) spacing: 0.535 chord

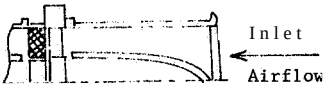

Measured (NASA Langley) 123 dB

Calculated 123.5 dB

CONFIGURATION 3: IGV-Rotor-OGV (62 vanes, 53 blades, 62 vanes)
Spacing: (I-R) 0.535 chord, (R-O) 0.535 chord

Measured (NASA Langley) 132 dB

Calculated 132.8 dB

CONFIGURATION 4: IGV-Rotor-OGV (62 vanes, 53 blades, 62 vanes)
Spacing: (I-R) 6.25 chord, (R-O) 0.535 chord

Measured (NASA Langley) 124 dB

Calculated 124 dB

FIGURE 6.—Comparison of measured and calculated PWL's for NASA 14.75-in.-diameter fan (ref. 4).

(1) Figure 7 shows that for a constant pressure ratio, sound-power levels generated by the rotor alone decrease as the design speed goes up. This results from the fact that the rotor loading, and consequently the circulation, goes down.

(2) Figure 8 shows that if the tip speed is held constant and the pressure ratio is increased, the fundamental frequency sound-power levels increase.

(3) Figure 9 shows that an increase in rotor diffusion factor is translated into a higher noise generation.

(4) Figure 10 shows that as the number of rotor blades is increased, the sound-power levels generated decrease. This seems to indicate that a high blade design is favorable. The optimum number could, however,

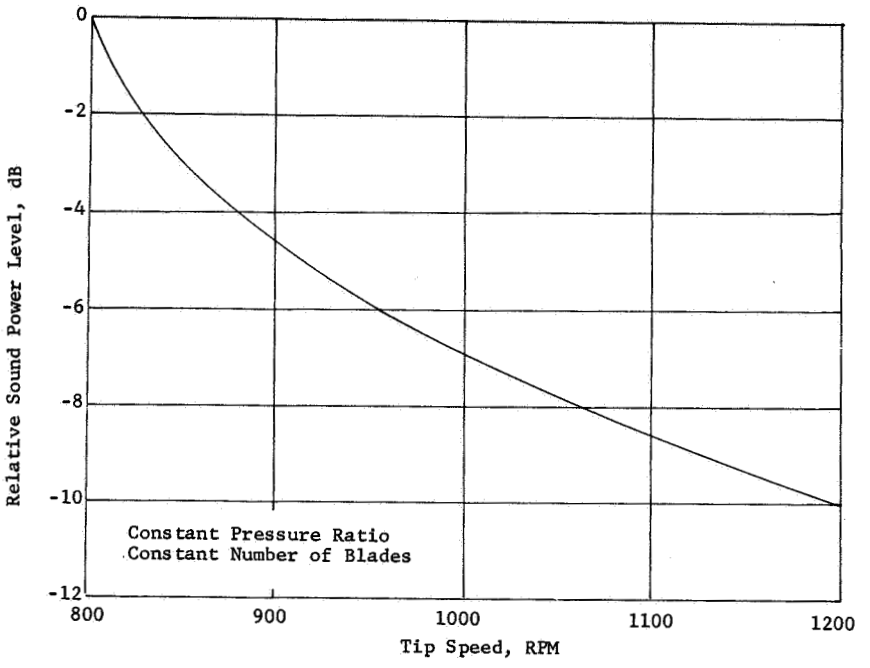

FIGURE 7.—Effect of tip speed on rotor-alone blade passing frequency noise.

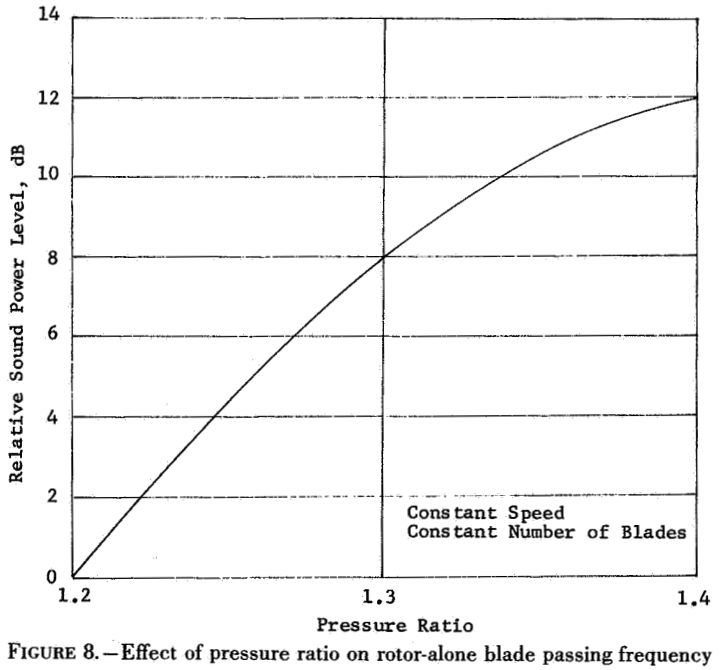

FIGURE 8.—Effect of pressure ratio on rotor-alone blade passing frequency noise.

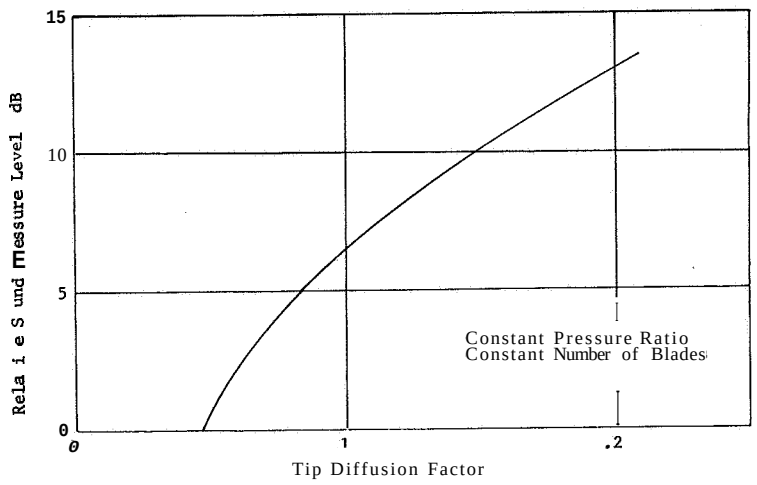

FIGURE 9.—Effect of diffusion factor on rotor-alone blade passing frequency noise.

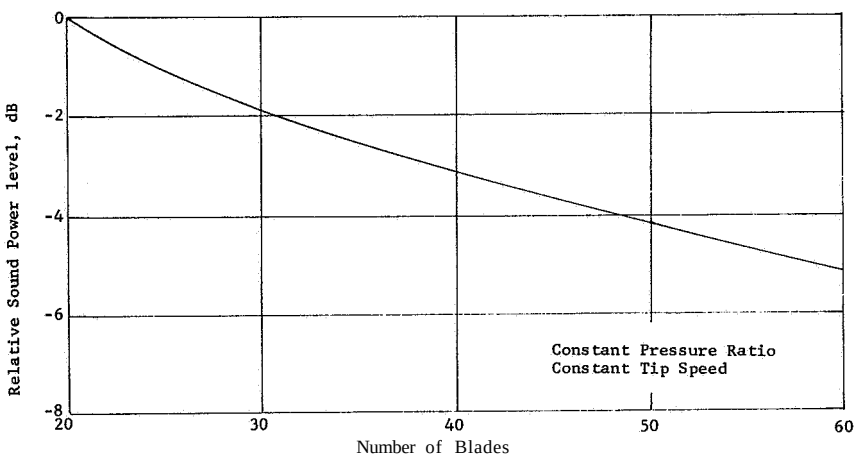

FIGURE 10.—Effect of number of blades on rotor-alone blade passing frequency noise.

vary from engine to engine due to psychoacoustic considerations. This subject will be discussed briefly in a later section.

PARAMETRIC STUDY OF INTERACTION NOISE

A parametric study was carried out to determine the functional relationship between the pure-tone noise generated in the fan by the wake interactions and the primary turbomachinery aerodynamic and geometric parameters. This study was restricted to fans and compressors without inlet guide vanes that, at the present time, tend to produce lower noise

levels than comparable machines with inlet guide vanes. The study was also directed toward designs incorporating large blade row spacings, where the wake, and not the potential interaction, is the major source of noise.

Pressure Ratio Effect

In an initial study, the tip speed of the machine and the fan geometry (number of blades and vanes, spacing-chord, etc.) were kept constant. Different designs with pressure ratios varying from **1.2** to **1.4** were investigated. When the pressure ratio is increased at a particular speed, more turning has to be done in the blade row and the loading goes up. This is translated into an increase of the coefficient of unsteady upwash and, consequently, in an increase of pure-tone levels. It can be seen from figure **11** that when the fan design pressure ratio is increased from **1.2** to **1.4,** the fundamental blade passing frequency power levels increase about 8 dB for a fan of constant size and **4** dB for a fan of constant thrust. These results indicate that pressure ratio is an important parameter that cannot be neglected. The use of simple correlation formulas that do not take this effect into account may lead **to** erroneous results.

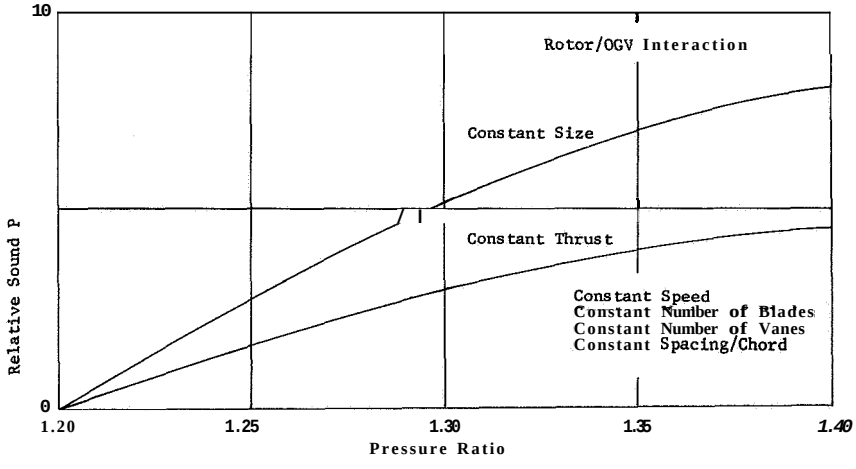

FIGURE 11.—Effect of pressure ratio on interaction noise generated at the blade passing frequency.

Tip Speed Effect

A study was done to investigate the effects of tip speed on the pure tones generated by fans of the same pressure ratio and geometry (number of rotor blades and outlet guide vanes, spacing-chord ratio). The results are shown in figure **12.** The analysis indicates that the pure-tone power levels at a constant pressure ratio are lower for a high-speed,

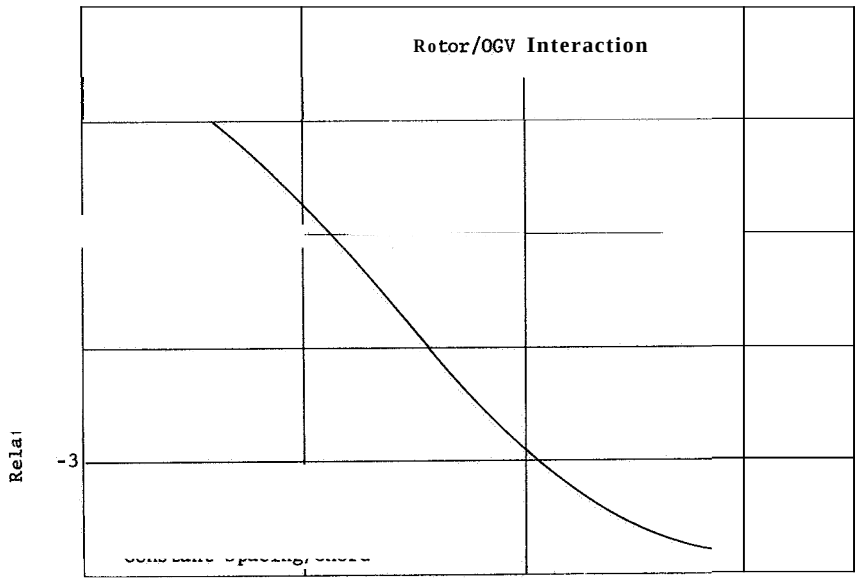

low-loading machine. This can be explained by the fact that for a constant pressure ratio the designs with high tip speed will have a lower rotor turning, which will result in lower pure-tone power levels. It does seem that the concept of noise increasing with speed can be quite misleading. It is true that the pure-tone levels rise as the speed is increased on a particular vehicle, but so do the rotor loading and stage pressure ratio. It does look as if it is not the speed but the higher work the stage is doing that is generating higher pure-tone power levels. It can be seen from figure 12 that for a particular design pressure ratio, a higher speed can lead to a pure-tone reduction.

Number of Rotor Blades Effect

The number of rotor blades is an important parameter in the noise generation and can easily be modified (within certain vibration and aerodynamic bounds) to suit the acoustic designer. Whether fan designs should be oriented toward a high or a low number of blades depends upon the engine size. The number of blades and the engine rpm will determine the pure-tone frequency, which should be kept out of the critical area of the NOY curve. Therefore, the size, as well as the blade-tip speed of the fan, must be known before a final selection of the number of blades

can be made. An investigation can be made, however (if we restrict ourselves to physics and leave out psychoacoustics for the moment) of the effect of the number of blades on the sound-power levels generated at the blade passing frequency. In the following study the pressure ratio, tip speed, blade row spacing, and the vane-blade ratio were kept constant, and the number of blades were varied from 20 to 80. The results are shown in figure 13. It can be seen that a design incorporating a high number of blades will reduce the fundamental frequency tones. The fan size and rpm will determine the optimum configuration from a PNdB viewpoint.

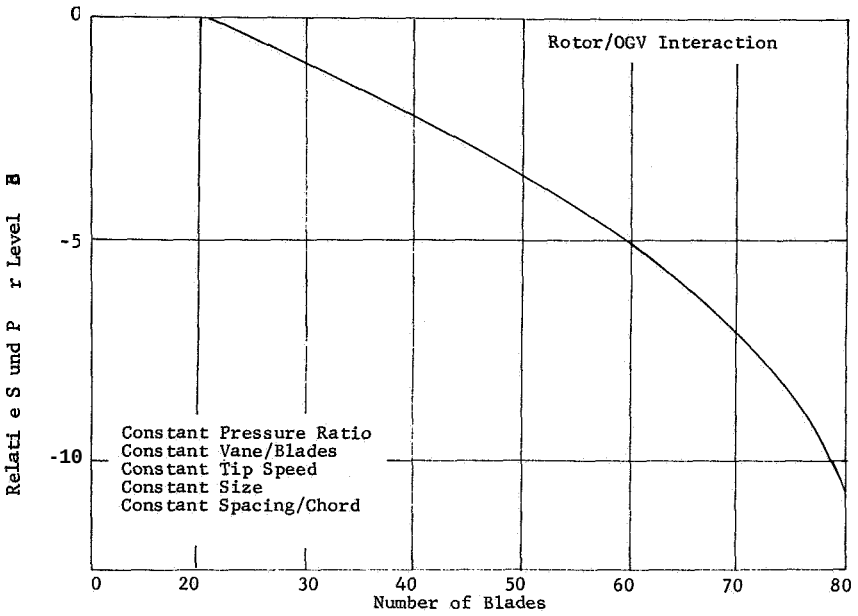

FIGURE 13.—Effect of number of blades on interaction noise generated at the blade passing frequency.

Vane-Blade Ratio Effect

The subject of vane-blade ratio effect on pure-tone noise has been quite controversial in the past. It was shown in references 5 and 6 that under ideal conditions in controlled experiments, a judicious vane-blade ratio selection did lead to operation below cutoff speed, and as a result, a major portion of the generated sound energy did not propagate in the duct. Different high speed experimental investigations have shown, however, that the cutoff phenomena are definitely not as sharp in an actual machine. The analysis of the sound generation shows, on the other hand, that the number of interaction diametral modes (or in other terms, the vane-blade combination) has a major effect on the blade

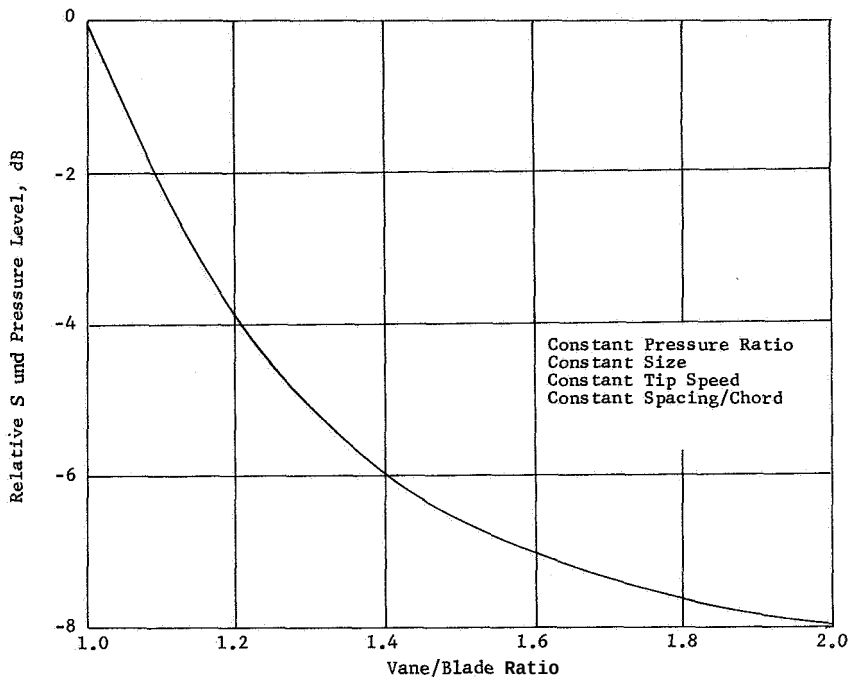

FIGURE 14.—Effect of vane-blade ratio on interaction noise generated at the blade passing frequency.

passing frequency tones. Figure **14** shows that a high vane-blade ratio can be beneficial not only from a sound-transmission, but from a sound-generation, viewpoint as well.

Blade Row Spacing Effect

It is well known that increasing the spacing between blade rows will decrease the interaction noise. Several experimental investigations have determined the reduction in pure-tone levels that can be obtained when the blade row spacing is increased. Some of the results have been summarized by Lowson in reference 7. An examination of figure **3** of reference 7 shows, however, how inconsistent those results are. Some researchers show a 2-dB reduction in sound-pressure levels (SPL) per doubling of the axial separation, while others prescribe **4** or even ***6*** dB SPL. This inconsistency can be explained by the facts that, first, several other parameters besides axial spacing are involved in the interaction process; and second, that the concept of "per doubling" is not strictly correct. It can be shown analytically (see refs. 8 and **9)** that geometric quantities like the solidity σ_1 of the upstream blade row and the blade chords, as well as aerodynamic quantities, such as the drag coefficient C_D and air exit angle, are of major importance in the wake interaction decay. These parameters

vary from one configuration to another, and ignoring them is bound to lead the designer to inconsistent conclusions. Also, it can be seen that the wake decay is not a simple function of blade row spacing and will not result in a constant ratio per doubling of the axial spacing; that is, the absolute spacing is the important parameter in comparing the effects of spacing changes.

In the present study a particular rotor-OGV (outside guide vane) configuration was chosen and the spacing varied from 0.1 to 2.0 spacing-chord ratio. The results are shown in figure 15. It can be seen that an appreciable reduction in pure-tone power levels can be obtained with large blade row spacjngs.

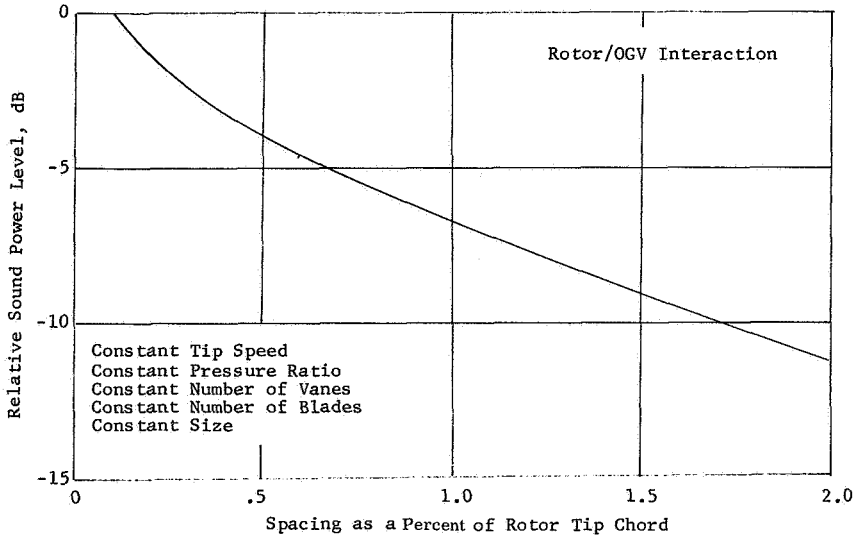

FIGURE 15. — Effect of spacing on interaction noise generated at the blade passing frequency.

SUMMARY AND CONCLUSIONS

Some theoretical methods have been developed to predict fan and compressor sound-power levels generated at the blade passing frequency. These prediction techniques have been used to study the effects of different aerodynamic and geometric parameters on fan and compressor noise. The results indicate that low sound-power levels will be obtained for low-pressure ratios, low rotor blade loadings, low rotor diffusion factors, high numbers of rotor blades, high vane-blade ratios, and large blade row spacings.

An appreciable reduction in pure-tone levels can be obtained by judicious selection of design parameters. This reduction of noise at the source can be quite attractive and should be incorporated in low noise fan and compressor designs.

REFERENCES

1. BENZAKEIN, M. J.; AND KAZIN, S. B.: A Theoretical Prediction of Aerodynamically Generated Noise in Fans and Compressors. Paper presented at meeting, Acoust. Soc. Am., Nov. 1968.
2. BENZAKEIN, M. J.; AND KAZIN, S. B.: Fan/Compressor Noise Reduction. Am. Soc. Mech. Engrs., Paper 69–GT–9, Mar. 1969.
3. MOTSINGER, R., ET AL.: Low Tip Speed Fan Noise Demonstration Program. NASA CR–72456, 1968.
4. COPELAND, W. L.; CRIGLER, J. L.; AND DIBBLE, A. C., JR.: Configuration of Downstream Stator to the Interaction Noise of a Single-Stage Axial Flow Compressor. NASA TN D–3892, 1967.
5. TYLER, J. M.; AND SOFRIN, T. G.: Axial Flow Compressor Noise Studies. S.A.E. Trans., 1961, pp. 309–332.
6. SPERRY, W. C.; AND BENZAKEIN, M. J.: Experimental Results of Vane/Blade Number Effects on Compressor Noise. Paper presented at 13th Annual International Gas Turbine Conference, Am. Soc. Mech. Engrs., Mar. 17, 1968.
7. LOWSON, M. V.: Compressor Noise Reduction. Paper presented at meeting, Acoust. Soc. Am., Nov. 1966.
8. SEARS, W. R.: Some Aspects of Non-Stationary Airfoil Theory and Its Practical Application. J. Aeron. Sci., vol. 8, no. 3, Jan. 1941.
9. KEMP, N. H.; AND SEARS, W. R.: Aerodynamic Interference Between Moving Blade Rows. J. Aeron. Sci., vol. 20, 1953, pp. 585–598.

SOME FEATURES OF AN EDGE-TONE FLOW FIELD*

K. Karamcheti
Stanford University
Stanford, Calif.

A. B. Bauer
Douglas Aircraft
Long Beach, Calif.

W. L. Shields
Air Force Office of Scientific Research
USAF

G. R. Stegen
Colorado State University
Fort Collins, Colo.

J. P. Woolley
Stanford University
Stanford, Calif.

A brief review of the nature of edge tones and the theories of their generation will be given. A number of experiments dealing with the details of the flow associated with edge tones and with the role of the various features, such as the mean velocity profile and the stability characteristics of the jet, will be described. The experimental results and their implications to the theories will be discussed.

INTRODUCTION

An edge tons is a tone of discrete sound produced when a thin jet of gas or liquid issuing from a slit impinges on a wedge-shaped edge or a rigid cylinder placed at a short distance from the slit (fig. 1). Edge tones were discovered nearly a century ago by Sondhaus (ref. 1) and have been the object of several investigations. The edge tone is a typical example of a class of problems in aerodynamic sound generation by free shear layers, such as separated boundary layers, thin jets, and wakes,

*The studies at Stanford, which were started in 1960, were supported by NSF during the period 1961–66. Since January 1965, they have been supported by NASA under NASA Grant NGR 05–020–275.

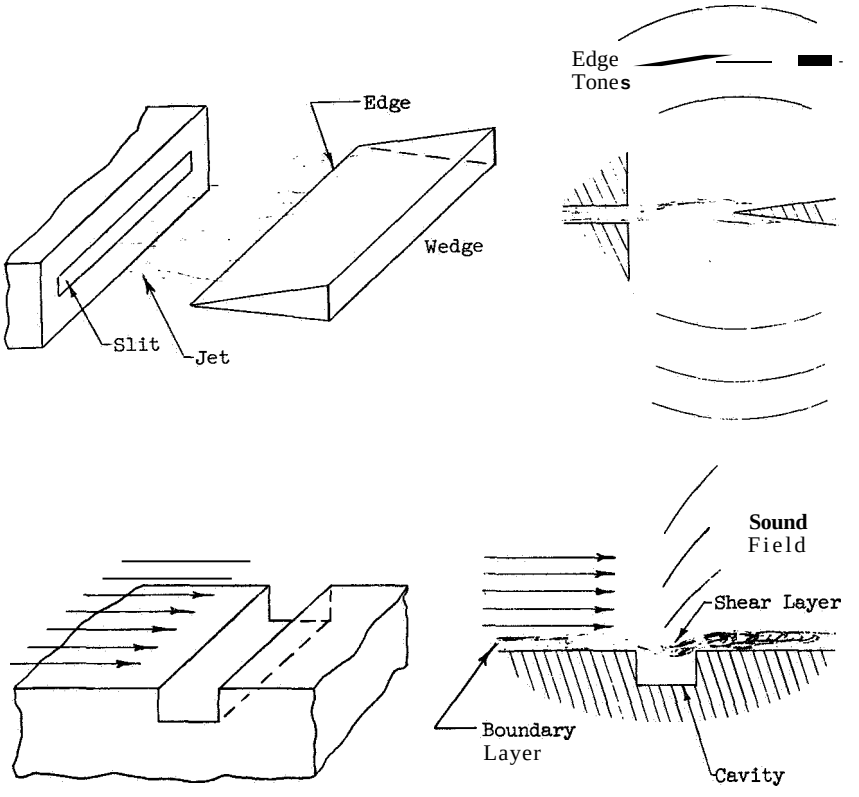

FIGURE 1. —Edge-tone production.

impinging on rigid surfaces. For instance, the production of sound by high-speed (subsonic or supersonic) flow of air past a cavity in a solid surface is a similar phenomenon (fig. 2). Such sound generation was observed and studied by Krishnamurty Karamcheti (refs. 2 and 3). A picture of an edge-tone flow is shown in figure 3.

Several experimental studies aimed at understanding the fluid mechanics underlying edge-tone generation have been carried out over a period of time at Stanford. Important aspects of these studies form the subject of this paper. A description of the main features of the edge-tone phenomenon and a brief review of the past experimental and analytical investigations of the problem will be given in this paper. A description and discussion of present' studies will follow. For detailed presentation of the studies, reference may be made to Karamcheti and Bauer (ref. 4), Shields and Karamcheti (ref. 5), Stegen and Karamcheti (ref. 6), and Woolley and Karamcheti.'

[1] J. P. Woolley and K. Karamcheti: Jet Stability and the Edge Tone. Dept. of Aeronautics and Astronautics, Stanford University. To be published.

FIGURE 2.—Sound radiation from a high-speed flow.

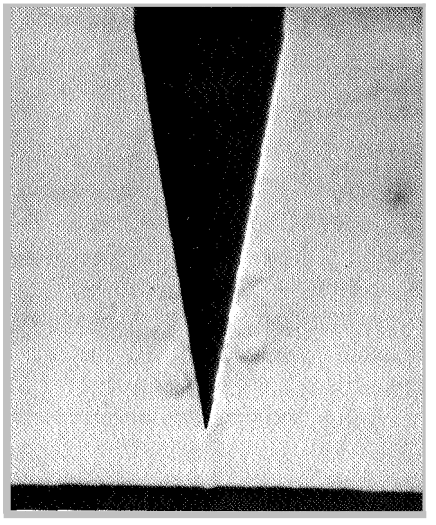

FIGURE 3.—An edge-tone flow field.

NATURE OF THE PROBLEM AND BACKGROUND

Main Features of Edge-Tone Operation

Experimental observations show that there are several main features of edge-tone operation, as illustrated in figure 4.

(1) When the mean speed $\bar{U}$ of the jet at the slit is maintained constant, there is a minimum edge distance h, i.e., from edge to slit, at which sound production commences. This distance is known as the minimum breadth.

(2) At a fixed mean speed, the frequency of the edge tone decreases gradually as the edge distance is increased over the minimum breadth. This frequency decreases until a certain edge distance is reached where the edge tone will suddenly jump to a new, higher frequency or mode of operation. The new mode of operation is known as stage 2; the first mode, as stage 1. As the edge distance is further increased, the frequency of stage 2 again decreases with distance until another jump in frequency takes place, and the edge tone is said to operate in stage 3. The appearance of the higher stages depends on the experimental conditions. At large edge distances, the edge tone is lost in the appearance of irregular or turbulent flow. When the edge tone is operating in the second or higher stage, and the edge distance is decreased, the frequency will increase until a certain edge distance is reached where the tone will jump down to the next lower stage. The distance at which this occurs does not coincide with the distance where the jump in frequency from

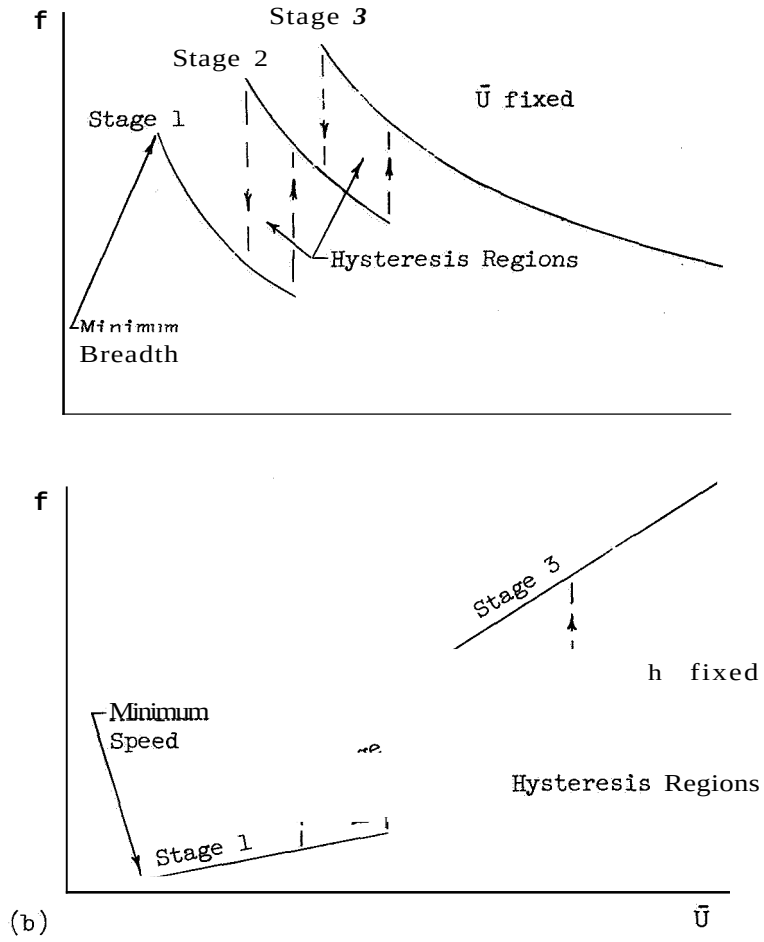

FIGURE 4—Edge-tone generation dependent on (*a*) minimum breadth and (*b*) minimum width.

one stage of operation to a higher one takes place as the edge distance is increased. Thus, the edge tone exhibits hysteresis regions of operation.

(3) In any given stage, the frequency is almost inversely proportional *to* the edge distance.

(4) At a fixed edge distance, there is a minimum mean speed below which no edge tone appears.

(5) If, at a fixed edge distance, the mean speed is increased gradually, the frequency of the tone increases until a certain value of the mean speed is reached at which a jump to a higher frequency and stage of operation will take place. As the speed is further increased, still higher frequencies and stages of operation will appear until the phenomenon is again limited to irregular or turbulent flow. When the mean speed is

decreased, the frequency decreases, and jumps to lower stages occur. Hysteresis regions are also associated with the frequency jumps between stages as the mean speed is changed.

(6) In any given stage, the tone frequency is approximately proportional to the mean speed.

(7) The sound field associated with the edge tone exhibits directional properties characteristic of a dipole field.

Review of Experimental Investigations

Edge tones have been the object of a large number of experimental and theoretical investigations. A complete review of past work will not be undertaken here, but some of the more important work pertinent to present purposes will be presented. Reviews of the literature on edge tones and related topics were given by Brown (ref. 7), Nyborg et al. (ref. 8), and Powell (ref. 9).

Brown (ref. 10), using an air jet, made stroboscopic measurements of the edge-tone frequency characteristics and carried out photographic studies of the jet flow in the edge-tone field. To make the jet visible, smoke was added to the jet. Nyborg et al. (ref. 8), using an air jet, made measurements of the frequency and intensity of edge tones by traversing a microphone in the sound field. Powell (ref. 9), using a hot wire and a microphone, measured the frequency and intensity of the edge tones produced with an air jet. Nyborg (ref. 11), Brackenridge and Nyborg (ref. 12), and Gross (ref. 13) made frequency and flow visualization studies for the case of edge tones generated by the motion of a jet of water impinging on a wedge.

Richardson (ref. 14), using hot-wire anemometers, made a few measurements of the mean-velocity field and the wavelength of the jet oscillations. He concluded that the ratio of the edge distance to the wavelength was approximately equal to the number of the stage in which the edge tone was operating.

Essential Physical Features Underlying Edge-Tone Generation

Various theories have been proposed to explain the generation of edge tones, to derive a formula for the frequency of the tone, and to explain the reasons for the jumps in frequency. We shall review later some of the specific theoretical ideas put forth recently. Here, we summarize the essential physical factors that underlie edge-tone generation.*

(1) Edge-tone production is accompanied by oscillations of the thin jet. The explanation for the occurrence of these oscillations lies in the natural

---

* The physical features underlying the sound production from surface cutouts in high-speed flow, as described by Krishnamurty Karamcheti (ref. 3), are similar to those underlying the production of edge tones.

instability of the jet to a certain range of disturbance wavelengths or frequencies. This range of disturbance wavelengths may be determined from a study of the stability characteristics of the jet.

(2) The wedge plays an important role in the edge tone because the tone does not appear when the wedge is removed from the jetstream. The nature of the flow processes occurring at the wedge is, therefore, an important factor in the edge-tone production. A study of these flow processes is essential for understanding the mechanism of the sound generation.

(3) The oscillating jet and its interaction with the wedge produce a fluctuating flow field outside the jet. This outside flow field in turn affects the motion of the jet. The coupling between them should be such that it selects and maintains, for the oscillation of the jet, a definite frequency out of the band of frequencies at which the jet is unstable.

A comprehensive theory of edge tones should, therefore, include the stability characteristics of the jet, the details of the outside flow, and the details of the coupling between the outside flow and the oscillating jet. Development of such a theory is a difficult task.

Review of Theoretical Investigations

Recent theories of edge tones, as given by Curle (ref. 15), Nyborg (ref. 11), and Powell (ref. 9), will now be reviewed. A review of the earlier ideas can be found in their work.

Curle's Theory

Curle (ref. 15) was concerned with deriving a formula for the frequency and explaining the jumps in the frequency. If, in the jet, disturbances of frequency f and wavelength λ are propagating with a uniform convection velocity u_c, the frequency is given by

$$f=\frac{u_c}{\lambda}$$

Once u_c and λ are determined in terms of the parameters of the problem, a formula for the frequency results. The following paragraphs outline Curle's method for obtaining λ and u_c.

(1) On the basis of the measurements by Brown (ref. 10) of the wavelength in the disturbed jet of an edge-tone system, it is asserted that the wavelength λ and the slit-edge distance h are connected by the relation

$$\frac{h}{\lambda}=n+\frac{1}{4}$$

where n is an integer denoting the stage of operation of the edge tone. Brown measured the wavelength from smoke pictures of the

disturbed jet. This relation is given theoretical justification by assuming the following feedback mechanism for a sustained edge-tone operation.

The oscillating jet is idealized as being bounded by two sets of propagating discrete vortices, as in the manner of a von Kármán vortex street (fig. 5). These jet vortices originate at the slit. They are very weak and diffuse when formed but build up as they propagate downstream through the jet. The wavelength of these propagating disturbances is taken as the distance between the centers of any two consecutive vortices on the same side of the jet.

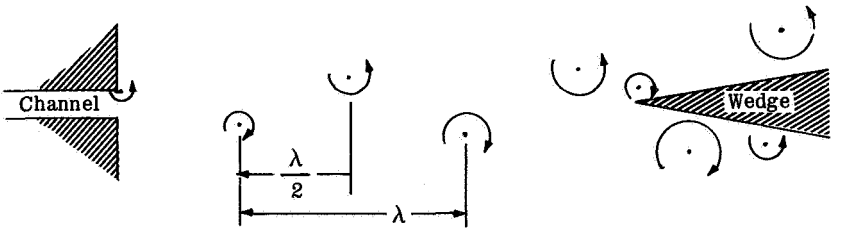

FIGURE 5.—Feedback mechanism for sustained edge-tone operation.

It is then suggested that the interaction of the oscillating jet with the edge produces additional vortices alternately above and below the edge. The vortices so formed on each side of the wedge are assumed to fall in line with the jet vortices on the corresponding side so as to form a stable configuration, like a von Kármán street, downstream of the edge. It is argued that the shedding of a vortex from the edge will take place when a jet vortex is situated, as shown in figure 5, one-quarter wavelength from the edge. If the jet vortex is in the top row, the transverse velocity, i.e., normal to the centerline of the edge, at the edge at the instant considered is a maximum and is directed upward. An edge vortex is then assumed to be shed at that instant from the upper side of the edge (fig. 5).

It is further argued that the formation and shedding of the vortex from the top side of the edge generates an embryo jet vortex simultaneously, as shown in figure 5, at the top of the slit. In a similar fashion when a vortex is shed from the bottom side of the edge, an embryo jet vortex is simultaneously formed from the bottom of the slit. As these embryo vortices leave the slit and move downstream, new ones originate at the slit periodically because of the periodic shedding of the edge vortices.

Because the simultaneous formation of the vortices at the edge and the slit takes place only when the edge is one-quarter wavelength from a jet vortex, it follows that

371-986 0-LT-70—19

$$h=A\left(n+\frac{1}{4}\right)$$

where n is an integer.

(2) Next, an expression for the convection velocity u_c is obtained by using the theory of Savic (ref. **16)** and the experimental results of Brown (ref. **10)** jointly. This expression is given as

$$\frac{u_c}{\bar{U}}=\frac{1}{2}\left(1-\frac{\lambda}{30d}\right)$$

where $\bar{U}$ is the mean velocity of the jet at the slit and **d** is the width of the slit.

(3) The formula for the edge-tone frequency is then given as

$$f=\frac{1}{2}\bar{U}\left(\frac{n+\frac{1}{4}}{h}-\frac{1}{30d}\right)$$

which, in view of the underlying considerations, applies only when $h \geqslant 10d$.

(4) It is suggested that the stage n of the edge tone is such that A is near that wavelength (out of the band of wavelengths for which jet disturbances are amplified) for which jet vortices receive maximum amplification. It is argued that the jumps in frequency always occur so that A becomes closer after the jump to the A of maximum amplification than before.

Nyborg's Theory

To develop a theory for the self-maintained oscillations of the jet in an edge-tone system, Nyborg (ref. **11)** considered the problem of determining the shape of the centerline of the jet on the basis of a simple model. This led him to an integral equation for the displacement of the jet centerline at the edge. The solution of this equation permits a set of discrete frequencies for the self-maintained oscillation of the jet. Nyborg's formulation is outlined in the following paragraphs.

(1) By describing the centerline of the jet by $y=\eta(x, t)$ (fig. **6),** one observes that $\eta(x, t)$ is the y-coordinate of a fluid particle that was at the slit at the time $t-6$, where δ is the time it takes for the particle to travel from the slit to the point x, η. Assuming that u, the x-component of the velocity of the particle, is a function of x only, one obtains

$$\delta=\int_0^x \frac{d\xi}{u(\xi)}$$

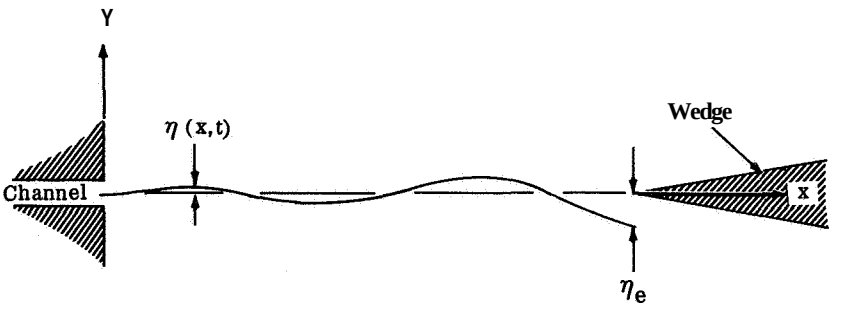

FIGURE 6.—Nyborg description of jet centerline.

(2) If v denotes the y-component of the velocity of the particle, we have

$$\eta(x, t) = \int_{t-\delta}^{t} v(\tau)\, d\tau$$

because v at the slit is assumed to be zero. This relation may be rewritten, by integrating the parts, as

$$\eta(x, t) = \int_{t-\delta}^{t} (t-\tau) \frac{dv}{d\tau}\, d\tau$$

where $dv/d\tau$ is the transversal acceleration. This relation forms the basis of Nyborg's theory.

(3) The transversal acceleration is proportional to the transversal pressure gradient; i.e., to the pressure difference across the jet. This pressure difference at the point x is assumed to be a function $\phi(\eta_e)$ of the instantaneous value of the jet deflection $\eta_e(\tau)$ at the edge multiplied by a function $g[h-x(\tau)]$ of the instantaneous distance $h-x(\tau)$ of the particle from the edge. Then

$$\eta(x, t) = \int_{t-\delta}^{t} (t-\tau) g[h-x(\tau)]\phi[\eta_e(\tau)]\, d\tau$$

(4) In particular, for the deflection at the edge we obtain

$$\eta_e(t) \equiv \eta(h, t) = \int_{t-\delta_0}^{t} (t-\tau) g[h-x(\tau)]\phi[\eta_e(\tau)]\, d\tau$$

where

$$\delta_0 = \int_0^h \frac{dx}{u(x)}$$

which is the required integral equation.

Assuming some trial functions for g and ϕ, Nyborg demonstrates that the solution of these integral equations leads to a set of discrete frequencies for self-maintained oscillations of the jet.

Powell's Theory

Powell (ref. 9) developed a theory to explain in detail, for the first time, the role of the various physical factors that underlie the mechanism of edge tones. His theory, although partly qualitative and partly quantitative, is the most comprehensive and convincing to date. It is, therefore, necessary to review his work in sufficient detail to bring out the important aspects that still need verification or further study.

Powell uses the following method to describe the sequence of events in an established edge-tone operation.

(1) A disturbance in the jet, at the location of the edge, is signified by the crossflow v_e at the edge in the absence of the edge. This velocity, which is periodic, may be represented in complex notation by

$$v_e = V_e e^{i\omega t}$$

where ω is the circular frequency.

(2) The interaction of this disturbance with the edge gives rise to a fluctuating force field $F(t)$ acting on the edge. In terms of v_e we can express $F(t)$ as

$$F(t) = \eta_s e^{i\phi_s} v_e$$

where $\eta_s e^{i\phi_s}$ is an effectiveness factor giving the amplitude and phase changes between v_e and $F(t)$.

(3) The force on the edge, or equivalently the force on the fluid because of the edge, produced a flow field in the medium outside the jet. The effect of this flow field is represented by the crossflow $v_0(t)$ at the slit of the jet nozzle when the nozzle is absent. The relation between $F(t)$ and $v_0(t)$ is represented by another effectiveness factor $\eta_t e^{i\phi_t}$ so that

$$v_0(t) = \eta_t e^{i\phi_t} F(t)$$

(4) The actual disturbance in the jet at the slit, in the presence of the jet nozzle, is then said to be related to $v_0(t)$ by another factor $\eta_d e^{i\phi_d}$. Thus, the actual disturbance in the jet represented by the crossflow component $v_0(t)$ at the slit is

$$v_0'(t) = \eta_d e^{i\phi_d} v_0(t)$$

(5) This disturbance as it moves downstream through the jet is amplified and appears as $v_e(t)$. Thus, if $qe^{i\phi_q}$ denotes the amplification factor involving, as before, both amplitude and phase changes

$$v_e(t) = qe^{i\phi_q} v_0'(t)$$

For a sustained edge tone, on the basis of the above relations,

$$q\eta_d\eta_t\eta_s e^{i(\phi_q+\phi_d+\phi_t+\phi_s)} = 1$$

which requires the changes in the amplitude and phase around the circuit to be consistent.

Powell then proceeds to determine the moduli (viz, q and the η's) and the arguments (viz, the ϕ's) characterizing the various effectiveness factors. It is here that hydrodynamical considerations enter the picture crucially.

First, on the basis of some experimental evidence and Lighthill's theory (refs. 17 to 19), it is argued that the fluid force acting on the edge is such that the radiated sound field is of a dipole character. A formula is given relating the sound pressure at a point in the field to the force $F(t)$ acting on the edge. This relation was verified experimentally. It is, therefore, asserted that the effect of the fluid action at the edge can be represented by a distribution of dipole sources along the edge, with the dipole normal to the center line of the undisturbed jet. It is then argued that a good approximation for the effectiveness factor between $F(t)$ and $v_0(t)$ is obtained by taking

$$\eta_t = \frac{1}{4\pi\omega\rho h^2\sqrt{h^2+\frac{b^2}{4}}}$$

and

$$\phi_t = -\frac{\pi}{2}$$

where ρ is the density of the medium and b is the width of the slit.

In considering the effectiveness of the motion $v_0(t)$ in disturbing the jet, it is assumed that a phase reversal is involved yielding

$$\phi_d = -\pi$$

It is then demonstrated that the amplitude factor η_d may be computed by conformal transformation. The result, however, is strongly dependent on the geometry of the apparatus at the slit; e.g., the lip angle and the depth d.

In relating the disturbances $v_e(t)$ and $v_0'(t)$ in the jet, it is assumed that the disturbance originating at the slit propagates downstream with a uniform convection velocity and constant wavelength, although its magnitude receives nonuniform amplification. Thus, if λ is the wavelength of the disturbance, we have

$$\phi_q = -2\pi \frac{h}{h}$$

With regard to the factor q, which gives the amplification of the disturbance through the jet in the distance h, it is pointed out that it depends on the amplitude and frequency of the original disturbance at the slit and on the Reynolds number of the jet at the slit.

In relating the force on the wedge to the velocity $v_e(t)$, it is argued that

$$\phi_s = 0$$

and

$$\eta_s = c_1 \rho \bar{U} b d$$

where c_1 is a constant. Note that $\rho \bar{U} b d$ is the mass flow.

On the basis of these detailed relations for the various effectiveness factors, the consistency conditions on the phase and amplitude changes around the edge-tone cycle may be written as

$$\frac{h}{h} = n + \frac{1}{4} \qquad \text{n, an integer}$$

and

$$q = \frac{1}{c_1 \eta_d} \frac{4\pi\omega h^2}{\bar{U} b d} \sqrt{h^2 + \frac{b^2}{4}}$$

The frequency of the jet disturbance is given by

$$\omega = 2\pi f = 2\pi \frac{u_c}{\lambda}$$

$$= 2\pi \frac{n + \frac{1}{4}}{h} u_c$$

where u_c is the convection velocity of the disturbance.

It is noted that various combinations of the quantities $\bar{U}$, b, d, w, and h can lead to the same value of the amplification q. As stated before, q is dependent on the frequency and the original amplitude of the disturbance and on the Reynolds number of the flow. Similarly, the con-

vection velocity **also** depends on these parameters. It is at this stage that the stability characteristics of the jet are brought into the picture. A qualitative description of the growth through the jet of small disturbances is then presented. Asserting that the amplification q computed from the above relation should correlate with the q given by the stability characteristics of the jet (note that c_1 and η_d are not known explicitly), it is shown how, from such correlation criteria, there would follow the minimum orifice-edge distance, the frequency jumps, the hysteresis regions, and other observed features of the edge tone.

Remarks

The recent theories of edge tones consider the mechanism of their generation as a feedback mechanism. The theories differ in the importance attributed to the details underlying the various elements of the cycle of an established edge-tone operation. Nyborg's theory is based on a simple model and considers only the interaction between the oscillating jet and the fluctuating pressure field, outside the jet, produced by the displacement of the jet at the edge. His analysis leads to a set of discrete frequencies of jet oscillation and to shapes of the jet centerline that are similar to some obtained experimentally. His theory, however, uses no fundamental hydrodynamic considerations. In particular, it takes no account of the stability characteristics of the jet. Consequently, it does not explain how to obtain the fluctuating pressure field, and why the frequency jumps occur. Inadequate as it is, Nyborg's analysis does indicate that in developing a sufficiently accurate or comprehensive theory of edge tones, one should take into account the role of the fluctuating pressure field just outside the oscillating jet. This was not considered in the other theories.

The theories of Curle and Powell are similar. Both emphasize the role of the stability characteristics of the jet and of the interaction of the oscillating jet with the edge. For the action at the edge, Curle assumes specifically vortex shedding, while Powell concerns himself only with the overall fluctuating force acting on the edge. It is of interest to note that Gross (ref. **13)** finds that the feedback mechanism envisaged by Curle does not meet the necessary condition on the amplitude changes around the cycle of operation. He argues that the effect of the edge vortices is propagated by viscous shear waves and that such waves may be greatly attenuated, particularly in water, over distances of the order of the slit-edge distance.

An important result of the theories of Curle and Powell is the so-called phase criterion

$$\frac{h}{\lambda}=n+\frac{1}{4} \qquad n, \text{ an integer}$$

which is also the basis of their formula for the edge-tone frequency

$$f=\frac{n+\frac{1}{4}}{h}u_c$$

The value of the integer n represents the stage of the edge tone. Both Curle and Powell indicate that the convection speed u_c depends on the wavelength of the disturbance in the jet. Because, in general, the speed u_c varies with distance downstream, the speed in the frequency formula represents an average speed over the slit-edge distance.

The only experimental information on the phase criterion is that indicated by Brown's measurements of the wavelength from smoke pictures of the oscillating jet. Some exploratory hot-wire measurements by Richardson (ref. 15) indicated that h/λ is nearly equal to n instead of $n+1/4$. This result, however, is not considered in the development of the theories.

EXPERIMENTAL APPARATUS AND TECHNIQUES

In light of past experimental observations and of the physical factors underlying the mechanism of edge tones, the following parameters influencing the phenomenon may be listed: the Reynolds number $R=\bar{U}d/\mu$ at the slit; the mean velocity profile at the slit; the ratio b/d, where b is the width of the slit; the ratio h/d; the external shape of the nozzle through which the jet issues; the shape of the object on which the jet is allowed to impinge; and a representative mach number of the jet flow, if the jet fluid is a gas.

For the present experiments it was decided to use air as the jet fluid but to keep the jet velocities sufficiently small so that the jet motion is incompressible. Thus, the mach number is eliminated as a parameter in the problem. Furthermore, b, d, and the external shape of the nozzle were kept fixed.

The edge-tone field may be described by the frequency and intensity of the tones. In the present experiments frequency was the only concern. Introducing the nondimensional frequency, the so-called Strouhal number

$$S=\frac{fh}{\bar{U}}$$

one notes that for the conditions envisaged here S is a function of R, h/d, the mean-velocity profile at the slit, and the shape of the edge.

For many of the experiments, a parabolic mean-velocity profile was maintained, and a wedge of fixed shape was used. In such a case, S is a function of R and h/d only.

Edge-Tone Apparatus

The general features of the edge-tone system used in the investigations are shown in figure 7. The details of the edge-tone generator are shown in figure 8. The jet is formed by blowing air through a two-dimensional channel. The entrance section of the channel is rounded and begins in a settling chamber that contains damping screens. The speed of the nozzle flow for fully developed parabolic profile was calculated for the static pressure drop measured between two points along the channel. For other profiles, such as a uniform profile resulting when the jet is formed by discharge through a sharp-edged slit, the mean speed is determined from the pressure drop across the slit (orifice). The velocity profiles (distributions) were obtained from hot-wire measurements.

Hot-Fire Equipment

Hot-wire anemometry with associated electronic instruments has been exclusively used to make all measurements. These measurements consisted of the mean and fluctuating velocity fields, instantaneous velocity fields, phase relations between fluctuations at different points of the flow field, and spatial variation of the amplitudes of the fluctuating velocity components. During the course of the investigations both constant current and linearized constant-resistance hot-wire anemometry employing single and x-probe (crosswires) sensors were used. For some measurements such as the phase relations and the instantaneous velocity fields, simultaneous use of two hot-wire probes was employed.

For details concerning the measurement techniques, reference may be made to the reports cited already.

RESULTS AND DISCUSSION

In this section we present some of the salient results of our investigations and point out their implications.

Frequency Versus Edge Distance

The overall details of the edge-tone operation with a wedge as shown in figure 7 at a Reynolds number of 704 are given in figure 9 in which the nondimensional frequency $S=fh/\bar{U}$ is plotted against the nondimensional wedge distance h/d. The velocity profile is parabolic.

It is seen that for $h/d<2.46$, no edge tone exists. In the range $2.46 \leqq h/d \leqq 6.14$ of edge distances, stage 1 operation occurs with a Strouhal number of about 0.48. The distance $h/d=2.46$ represents the minimum breadth. As h/d is increased above 6.14, stage 2 appears with S in the neighborhood of 1.1. Stage 2 continues to exist as long as h/d stays between the limits 5.13 and 9.05. At the same time, as shown by the flagged circles in figure 9, stage 1 also exists at a slightly reduced S, near

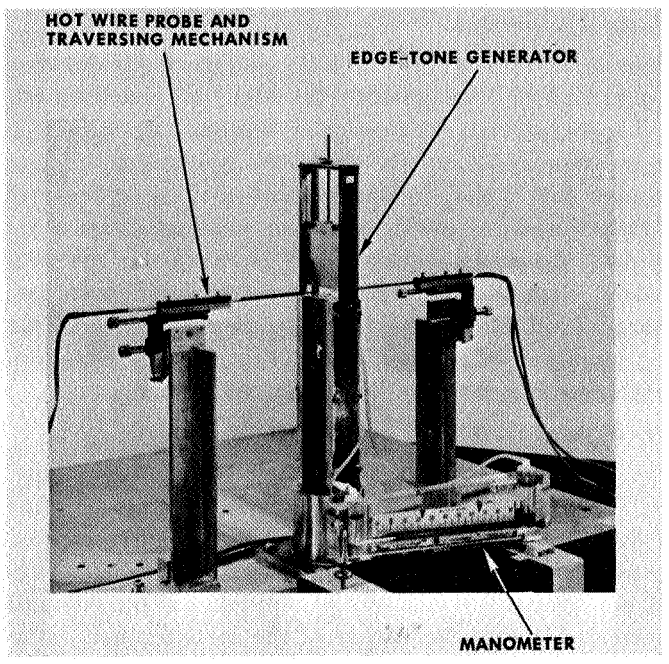

FIGURE 7.—Experimental apparatus.

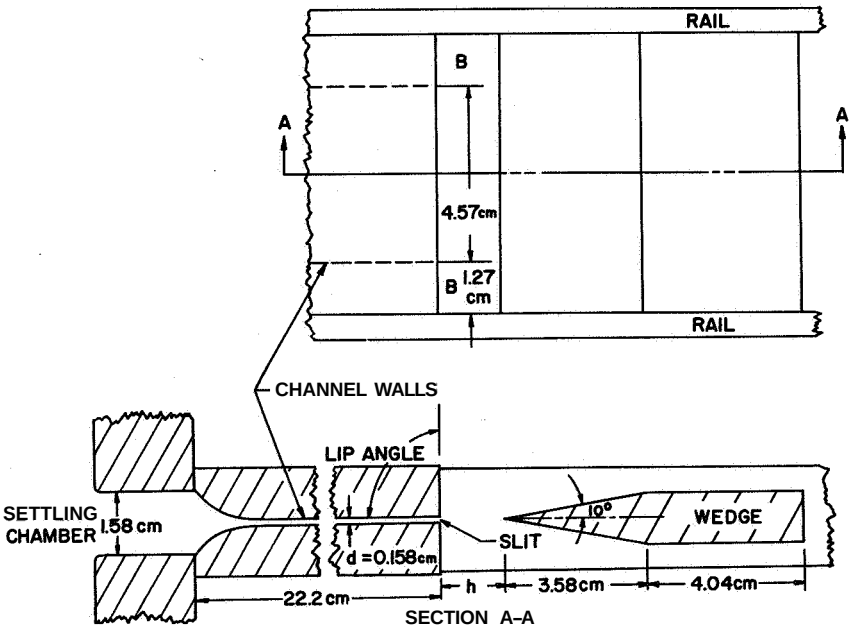

FIGURE 8.—Layout of channel and standard wedge.

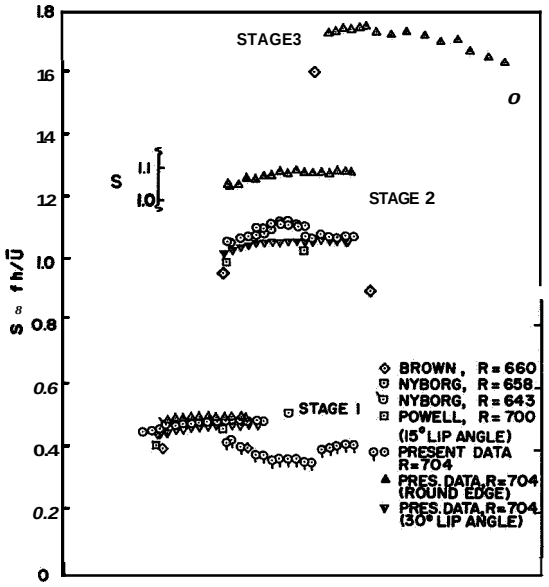
STAGE3
STAGE 2
STAGE 1
S
1.1
1.0
BROWN, R = 660
NYBORG, R = 658
NYBORG, R = 643
POWELL, R = 700
(15° LIP ANGLE)
PRESENT DATA
R = 704
PRES. DATA R=704
(ROUND EDGE)
PRES. DATA R=704
(30° LIP ANGLE)

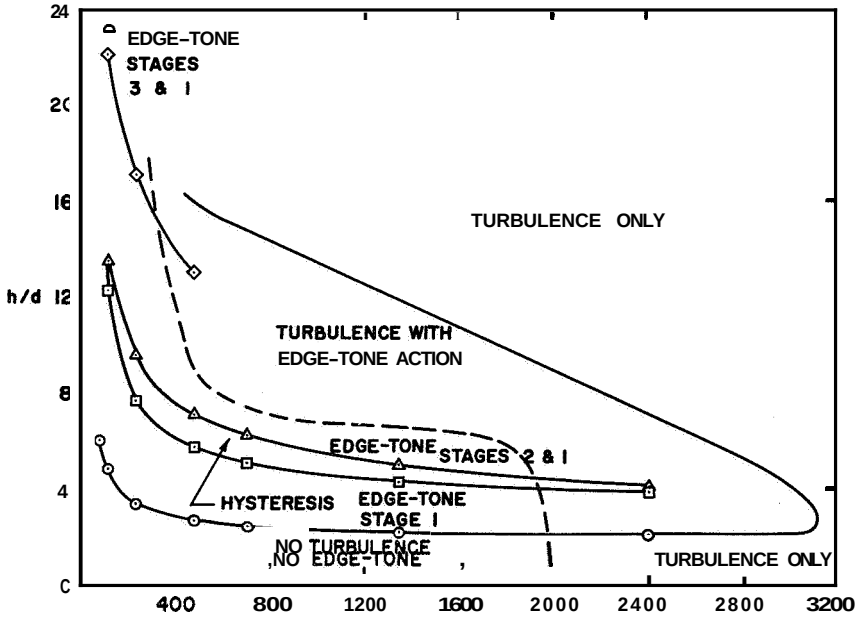
EDGE-TONE
STAGES
3 & 1
TURBULENCE ONLY
TURBULENCE WITH
EDGE-TONE ACTION
EDGE-TONE STAGES 2 & 1
HYSTERESIS
EDGE-TONE
STAGE 1
NO TURBULENCE
NO EDGE-TONE
TURBULENCE ONLY
h/d
400
800
1200
1600
2000
2400
2800
3200

$S=0.4$. To jump back to stage **1** operation alone, it is necessary to reduce h/d to less than **5.13.** Thus, region $5.13 \leq h/d \leq 6.14$ forms a hysteresis loop. No definite edge-tone operation could be observed for $h/d > 9.06$ because at these distances an irregular flow pattern or turbulence had gradually emerged as h/d was increased.

The hot-wire signals of stage **1,** as shown by the oscilloscope traces, were usually very smooth and nearly sinusoidal. However, such simplicity was lacking in stage **2,** for stage **1** always existed along with stage **2** and the frequency ratio of the stages was not usually an integer.

In figure 9 are included measurements of Brown (ref. 10), Powell (ref. 9), and Nyborg (ref. 8). For a discussion of minor differences exhibited between these data and the data of this paper, reference should be made to Karamcheti and Bauer (ref. **4).**

Edge-Tone Activity at Different Reynolds Numbers

Figure **10** gives the regions of edge-tone operation with a wedge and parabolic profile as a function of h/d and **R.** The line with the circular data points denotes the minimum breadth, the minimum value of h/d, for stage **1** oscillation. Above this, shown by the square data points, is the minimum value of h/d at which stage **2,** always accompanied by stage **1,** will operate. The next higher line, shown by the triangular data points, is the maximum h/d at which stage **1** will operate alone. The region between the square and the triangular points is the hysteresis region where either stage **1** alone or stages **1** and **2** together will operate. The mode of operation is always determined by the past history of h/d and **R** as long as the rates of change of h/d and **R** are reasonably slow. That is, if h/d and/or R are increasing as the hysteresis region is entered, stage **1** will continue to exist alone. If h/d and/or R are decreasing as the region is entered, both stage **2** and stage **1** will continue to exist.

In a similar fashion, the diamond points give the minimum h/d at which stages **3** and **1** together will operate. Above this, at $R=121$, is a half-circle data point at the largest h/d where stages **2** and **1** will operate. Thus, another hysteresis region exists at $R=121$. At the larger values of R for which data were taken, the hysteresis region could not be conveniently located.

Data were also taken at $R=80$, although only stage **1** could be measured. At this Reynolds number small drafts or acoustic disturbances in the building interfered with the edge-tone operation.

In general, as h/d was increased to the region above the dotted line, the edge tone was obscured by the appearance of turbulence. That is, at the lower values of R, where R was less than about **2000,** the hot-wire signal for the values of h/d above the dotted line became more difficult to interpret. Added to the sinusoidal edge-tone waves was a rather rough and nonperiodic "turbulent" signal, which became more dominating as

$S=0.4$. To jump back to stage **1** operation alone, it is necessary to reduce h/d to less than **5.13.** Thus, region $5.13 \leq h/d \leq 6.14$ forms a hysteresis loop. No definite edge-tone operation could be observed for $h/d > 9.06$ because at these distances an irregular flow pattern or turbulence had gradually emerged as h/d was increased.

The hot-wire signals of stage **1,** as shown by the oscilloscope traces, were usually very smooth and nearly sinusoidal. However, such simplicity was lacking in stage **2,** for stage **1** always existed along with stage **2** and the frequency ratio of the stages was not usually an integer.

In figure 9 are included measurements of Brown (ref. 10), Powell (ref. 9), and Nyborg (ref. 8). For a discussion of minor differences exhibited between these data and the data of this paper, reference should be made to Karamcheti and Bauer (ref. **4).**

Edge-Tone Activity at Different Reynolds Numbers

Figure **10** gives the regions of edge-tone operation with a wedge and parabolic profile as a function of h/d and **R.** The line with the circular data points denotes the minimum breadth, the minimum value of h/d, for stage **1** oscillation. Above this, shown by the square data points, is the minimum value of h/d at which stage **2,** always accompanied by stage **1,** will operate. The next higher line, shown by the triangular data points, is the maximum h/d at which stage **1** will operate alone. The region between the square and the triangular points is the hysteresis region where either stage **1** alone or stages **1** and **2** together will operate. The mode of operation is always determined by the past history of h/d and **R** as long as the rates of change of h/d and **R** are reasonably slow. That is, if h/d and/or R are increasing as the hysteresis region is entered, stage **1** will continue to exist alone. If h/d and/or R are decreasing as the region is entered, both stage **2** and stage **1** will continue to exist.

In a similar fashion, the diamond points give the minimum h/d at which stages **3** and **1** together will operate. Above this, at $R=121$, is a half-circle data point at the largest h/d where stages **2** and **1** will operate. Thus, another hysteresis region exists at $R=121$. At the larger values of R for which data were taken, the hysteresis region could not be conveniently located.

Data were also taken at $R=80$, although only stage **1** could be measured. At this Reynolds number small drafts or acoustic disturbances in the building interfered with the edge-tone operation.

In general, as h/d was increased to the region above the dotted line, the edge tone was obscured by the appearance of turbulence. That is, at the lower values of R, where R was less than about **2000,** the hot-wire signal for the values of h/d above the dotted line became more difficult to interpret. Added to the sinusoidal edge-tone waves was a rather rough and nonperiodic "turbulent" signal, which became more dominating as

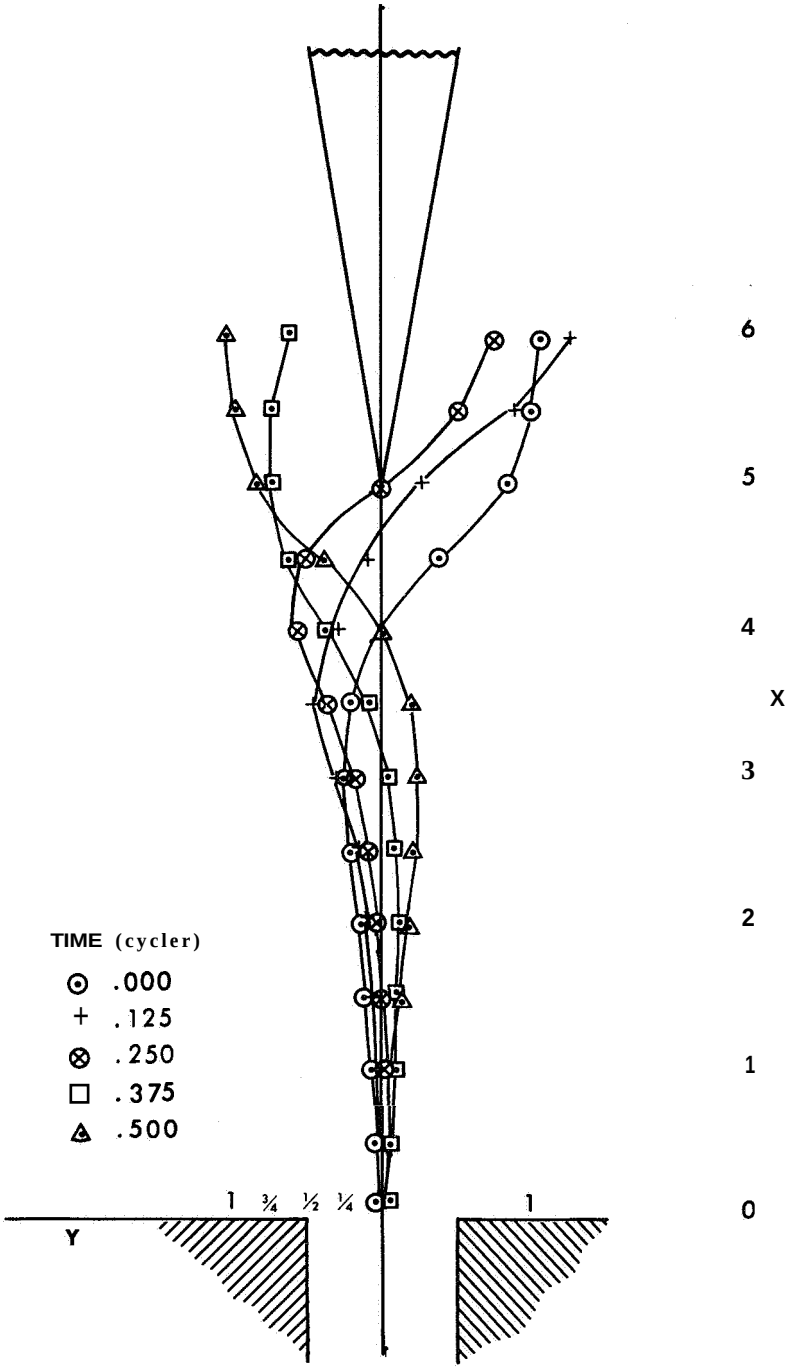

FIGURE 11.—Edge-tone jet centerline motion.

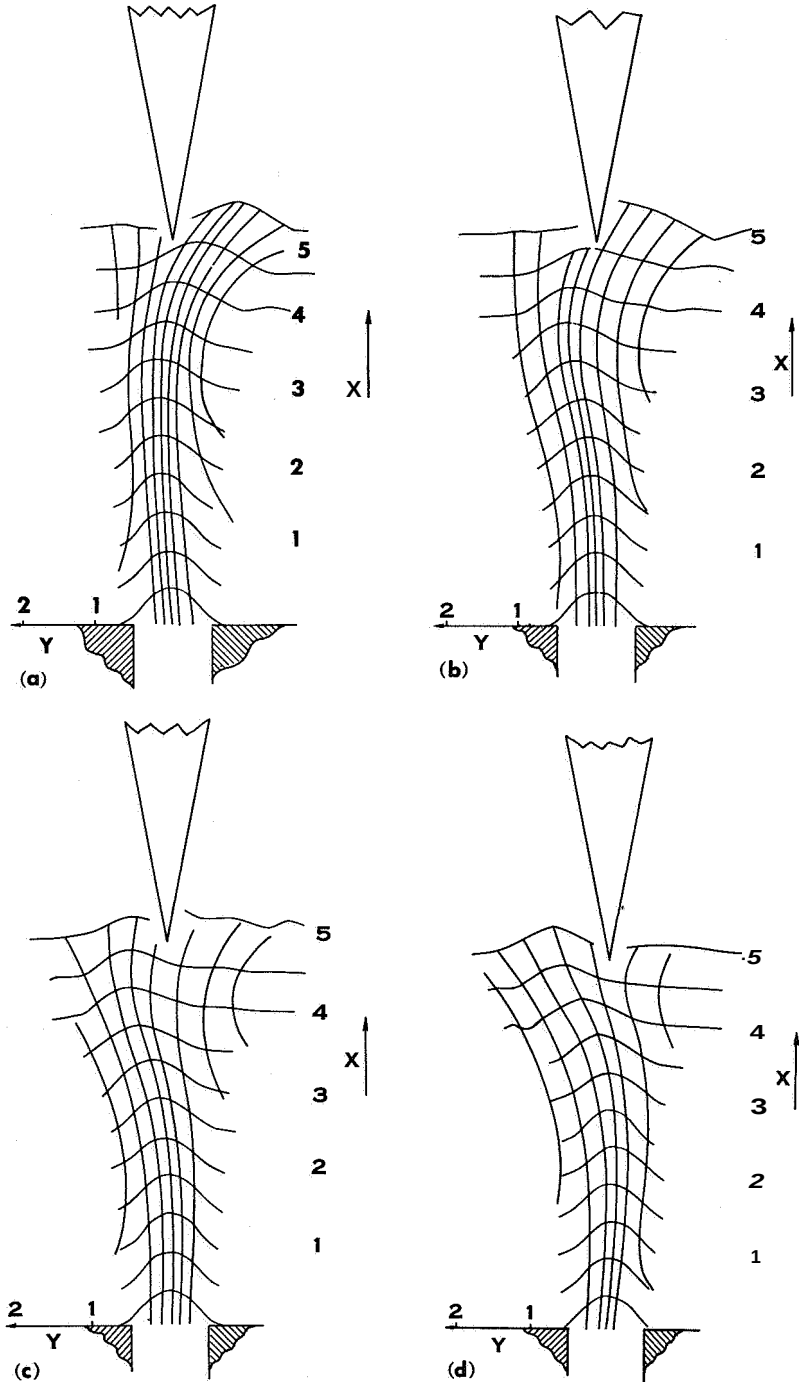

FIGURE 12.—Edge-tone streamlines: *(a)* $T=0$; *(b)* $T=1/8$; *(c)* $T=1/4$; *(d)* $T=3/8$.

h/d increased. For h/d above the solid line, no edge-tone action that could be sensed was observed.

Motion of the Jet Centerline

Earlier streamline flow visualization studies of the edge-tone jet have focused attention upon the gross lateral motion of the jet and the way that disturbances proceed along the jet. This jet motion has been idealized by Nyborg (ref. **11)** as the motion of the jet centerline. Figure **11** shows the motion of the jet centerline during an edge-tone cycle in stage **1** operation at $R=630$ and $h/d=5$ with a parabolic profile. The jet centerline is here defined as the point at which the local flow speed is maximum.

Streamline Patterns

Past studies of the edge tone have encountered considerable difficulties because it has not been clear how one should interpret the wavy disturbances of the edge-tone jet that are observed in the streamline pictures. Karamcheti and Bauer (ref. **4)** have shown that serious errors may be introduced by assuming, based on streamline pictures, that a single disturbance wavelength and propagation velocity can be chosen that are appropriate throughout the edge-tone jet. Measurements of the instantaneous velocity components in the edge-tone flow field enable the construction of instantaneous streamline pictures during an edge-tone cycle. Such pictures, for the same conditions mentioned in the previous section, are shown in figure 12. Included in the figure are the mean velocity profiles. It is seen that there is a strong tendency for the basic jet profile to be preserved in the edge-tone operation. In spite of the distortion occurring near the edge, a satisfactory physical picture of the edge-tone process can be obtained by considering gross lateral oscillations of the jet.

Phase Relations

Phase measurements were made with respect to the fluctuation in magnitude of the total velocity vector and the fluctuating transversal velocity component along the centerline of the edge-tone generator normal to the plane of the undisturbed jet.

In describing the results of the phase measurements, the phases at various spatial locations are expressed in terms of the phase at the slit. The angle in degrees by which the phase at a given location lags behind that at the slit is denoted by θ.

A typical result of the phase survey for the fluctuation in magnitude of the total velocity vector is shown in figure **13.** The edge tone is operating in stage **1** and the mean velocity profile is parabolic. In the figure the number denotes local phase angle divided by 2π. This number denotes, at the same time, the phase in terms of the period of oscillation. It is seen that the phase angle is a complicated function of the spatial location. In the jet region, the phase increases monotonically in the downstream

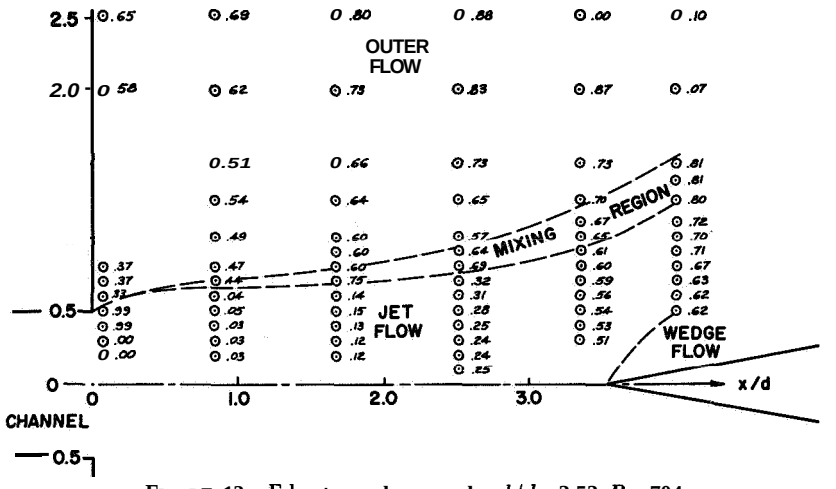

FIGURE 13.—Edge-tone phase angles, $h/d=3.53$, $R=704$.

direction while it changes relatively little with y. Just above the mixing region and for $2 \leq x/d < h/d$, changes in $\theta/2\pi$ are small. The phase change from the slit to the edge, as shown by the results, is in striking contrast to the value of *1.25* given by the theories.

Typical results for the phase variation along the centerline of the fluctuating transversal velocity component are shown in figure **14.** These measurements were made in the transition region where either stage **1** or stage *2* can be separately maintained. We note that there is a difference between the stages in not only the magnitude but also the spatial variation of phase. In stage *2* the phase varies linearly with x for $x/h > 0.25$, while in stage **1** the variation is not linear. Again, the theory is not substantiated by these results. According to the theoretical motions $\theta(x)/2\pi$ is a straight line from the origin to the point $x=h$ and $\theta(h)/2\pi$ is equal to *1.25* for stage *1* and *2.25* for stage *2.* Neither is the case. Thus, we conclude that the relations assumed in the theory for the average convection speed and the average wavelength are inappropriate.

Growth of the Fluctuating Transversal Velocity Component

The amplification of disturbances through the jet, as pointed out before, is one of the important factors underlying the mechanism of edge-tone operation (ref. 9). We present now some experimental results for the growth of the transverse velocity along the centerline of the edge-tone system. The measured quantity is the root-mean-square value, denoted by v_{rms}.

In presenting the results we plot the data as In $(v_{\mathrm{rms}}/U_{\mathrm{C}})$, where the

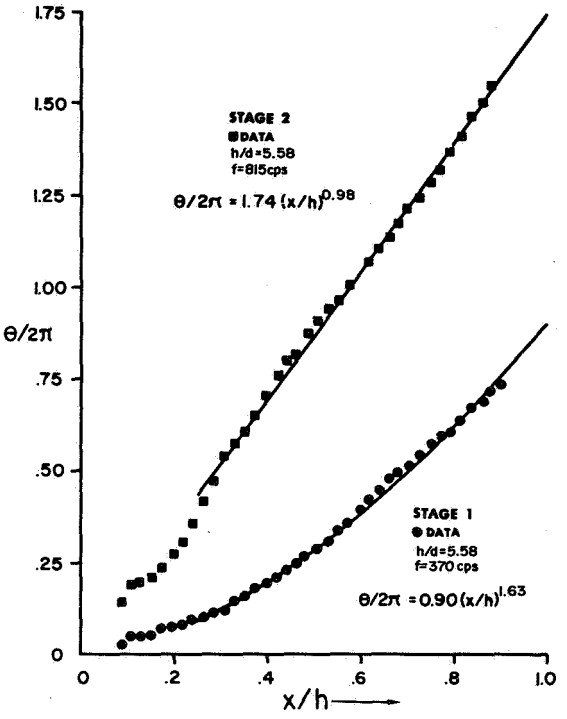

FIGURE 14.—Comparison of phase in stages 1 and 2.

centerline exit velocity U_{C_L} has a constant value of **9.00** m/sec. This is motivated by the linear stability theory of free jets, in which it is assumed that disturbances grow exponentially.

Experimental observations with a free jet show that disturbances initially grow exponentially. Later, the amplitude tends to level off, showing no further increase. This behavior is attributed to nonlinear effects resulting from the large amplitude **of** the developed disturbance. In the jet of the edge-tone system we observe that the amplitude of the disturbances are large compared to the local stream speed, even close to the slit ($x/d \approx 1/2$). It is of interest to determine whether the amplitude of these initially large disturbances will tend to level off.

Figure **15** shows the variation **of** v_{rms} with x/h. It is seen that we may approximately represent v_{rms} by a single function of x/h. The growth **of** the disturbances during stage 2 operation is shown in figure **16.** Once again, v_{rms} may be represented **by** a single function of x/h, which is different from that for stage **1** operation. It is seen that in either case v_{rms} does not grow exponentially. **No** leveling **off** is observed for stage 1 while it appears to occur for stage 2 as $x/h \rightarrow$ **1.** The explanation **of** the frequency jumps, following Powell's ideas, on the basis **of** these observed growth rates is unclear.

371-986 O-LT-70—20

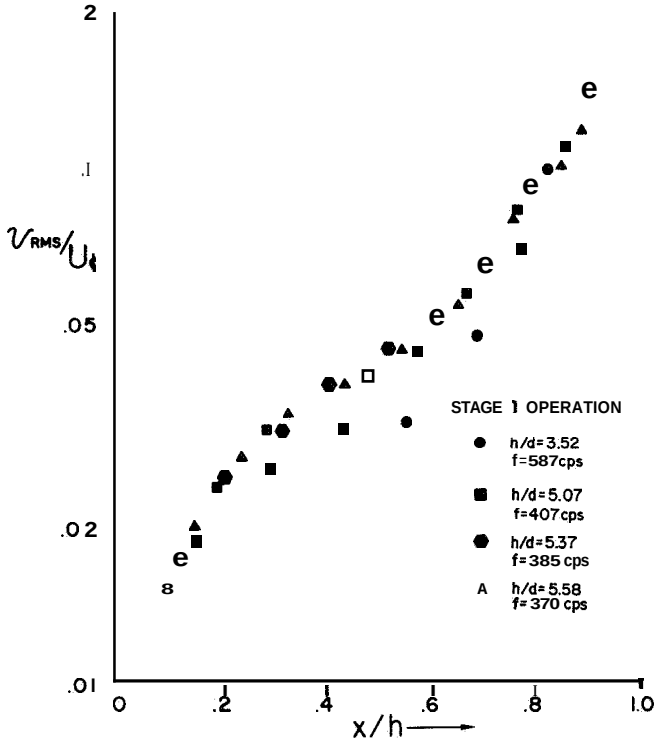

FIGURE 15.—Growth of disturbances during stage 1 operation.

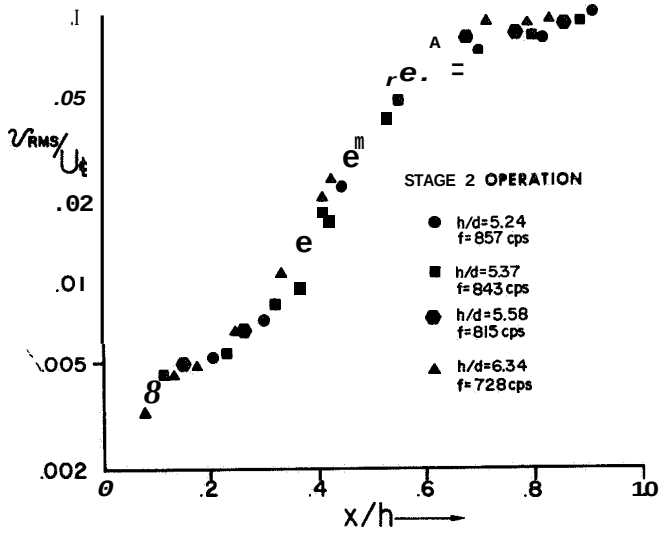

FIGURE 16.—Growth of disturbances during stage 2 operation.

Propagation Speed and Wavelength

To account for the observed variation of phase along the centerline, one may assume that a disturbance originates at the slit and propagates downstream with a varying convection velocity $c(x)$ and a varying wavelength $\lambda(x)$. Their relation to $\theta(x)$ is given by

$$c(x) = \frac{f}{\frac{d}{dx}\left(\frac{\theta(x)}{2\pi}\right)}$$

$$\lambda(x) = \frac{1}{\frac{d}{dx}\left(\frac{\theta(x)}{2\pi}\right)}$$

Using these relations and the experimentally observed $\theta(x)$, one may compute $c(x)$ and $\lambda(x)$. This has been done and the results are shown in figures 17 and 18, respectively, for stage 1 and 2 operations. In the same figures are included similarly computed results for the case of the free jet, in the absence of the edge, excited externally by the sound of frequencies equal to those occurring in the edge-tone operation. This affords a comparison between the propagation speeds in the free jet and in the edge-tone jet and an appreciation of the role of the free-jet stability properties.

We note that the edge-tone propagation speeds in stage 1 exhibit significant spatial variation and differ markedly from those of the free jet.

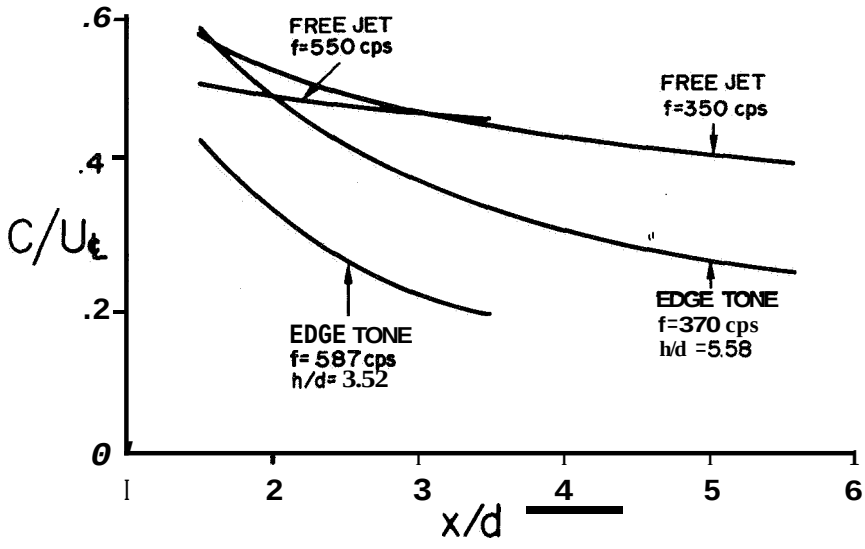

FIGURE 17.—Comparison of stage 1 and free-jet propagation speeds.

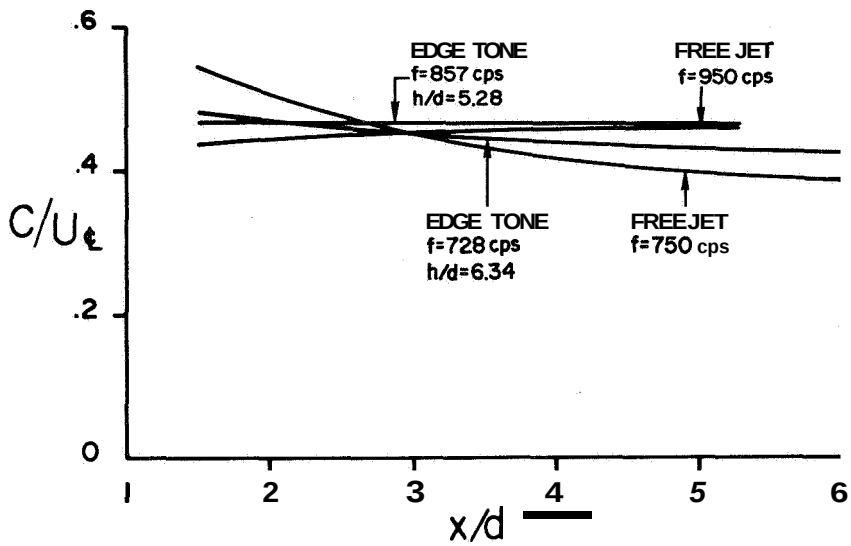

FIGURE 18.—Comparison of stage 2 and free-jet propagation speeds.

In stage 2, however, the edge-tone speeds are nearly constant and are close to the free-jet speeds. These observations require theoretical clarification.

Effects of Velocity Profile and Edge Shape

Experiments were conducted with a uniform mean-velocity profile instead of the parabolic profile using the standard 20° wedge as an edge. The edge tone produced by both velocity profiles was also examined using a rigid cylinder for the edge. The results for the Strouhal number at the minimum breadth are compared in figure 19 for the various cases. The corresponding Strouhal number for the von Kármán vortex street from a cylinder is much higher than the values observed here. In general, the edge-tone characteristics remained the same under these changed conditions. However, some quantitative differences were observed.

The major observed effect of the velocity profile change was on the minimum breadth for an edge-tone stage. The uniform jet consistently required a smaller edge distance to initiate the edge tone. Investigations of the phase velocities and amplification rates have not been completed.

There are two significant differences between the wedge and cylinder edges. First, the minimum breadth was higher for the cylinder than for the wedge. As a qualitative note to the latter, it was observed that the acoustic output of the wedge was considerably greater than that of the cylinder, particularly at higher Reynolds numbers.

There was also a significant combined effect of the edge type and velocity profile which may be observed from figure 19. For the uniform

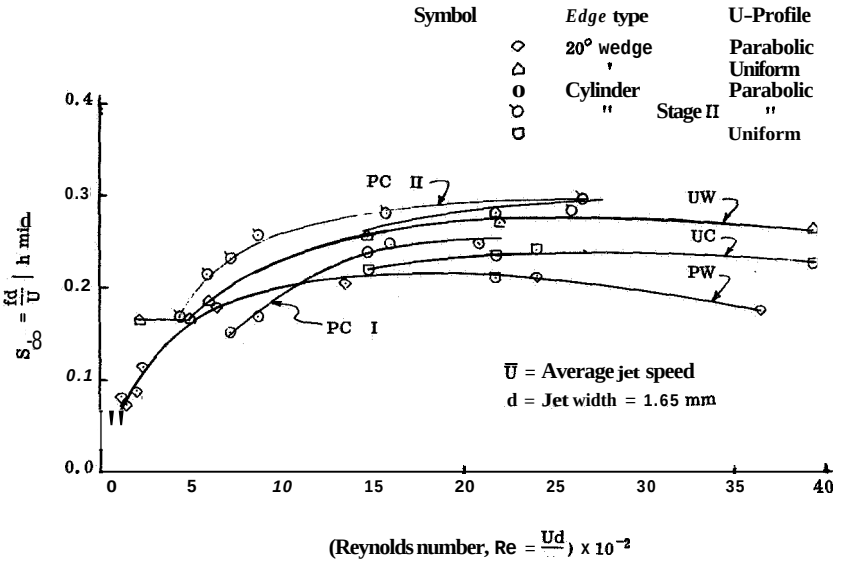

FIGURE 19.—Initial Strouhal numbers.

velocity profile, the frequencies were generally lower for the cylinder than for the wedge throughout the Reynolds number range investigated. The same is true for the parabolic profile in the low Reynolds-number range. However, the cylinder frequencies exceed those for the wedge above a Reynolds number of approximately 1000.

Here is firm evidence of the effects of both edge-type and jet-exit velocity profile upon the edge-tone phenomenon.

Jet Stability and Strouhal Number at Minimum Breadth

In figure 20 are shown the experimentally observed Strouhal numbers at the minimum breadth for the case of a parabolic mean velocity profile. These are compared with the amplification versus Strouhal number curve obtained by Sato (ref. 20) for an externally excited free parabolic jet. It is noted that the initial frequencies for both cylinder and wedge at low Reynolds numbers correspond closely to the frequency that receives maximum amplification by the jet. As the Reynolds number is raised, however, the initial frequencies increase toward the upper neutral (zero amplification) frequency.

The effects of Reynolds number on the Strouhal number and on the minimum breadth h_0/d are significant results. An explanation of these effects lies to a large extent in the stability characteristics of the jet. The Reynolds number affects these characteristics directly through the shape of the mean velocity profile at the slit. The disturbance created by the edge, and peculiar to the edge type, is amplified and transmitted

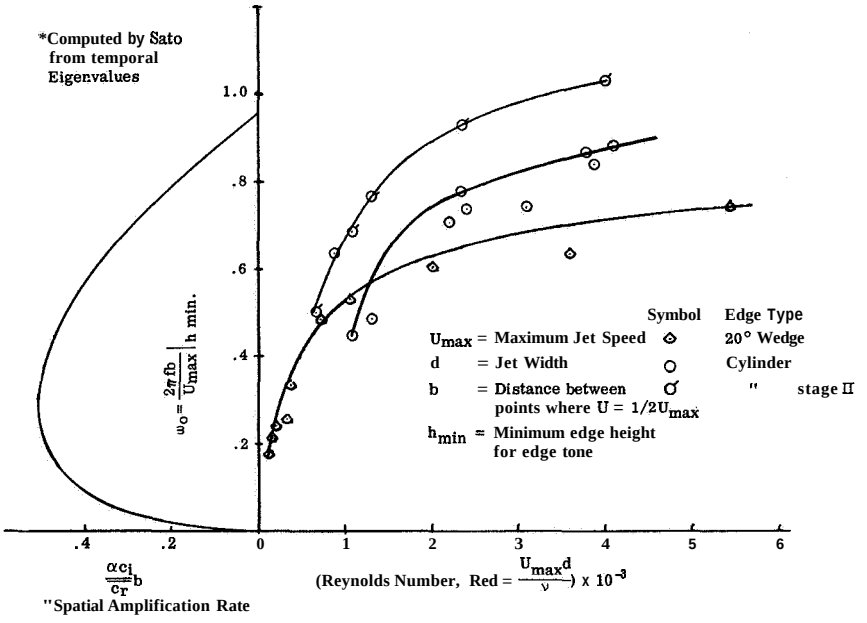

FIGURE 20.—Initial edge-tone frequencies for a parabolic jet compared to eigenvalue amplification rates.

by the jet according to its stability characteristics. It should, however, be borne in mind that the fluctuating flow field outside the jet, produced by the oscillating jet with the edge, also plays a part in deciding the minimum breadth.

Edge-Tone Suppression

During the course of the experimental study, it was found that the edge tone could be suppressed and stopped by placing two plates normal to the centerline of the undisturbed jet in the outside flow region. Consequently, experiments were made to determine for any given downstream station the location of the plates at which the edge tone is just stopped. Such measurements were made for stage 1 operation at a Reynolds number of 704 with a fixed edge distance h/d equal to 4.00. The results are shown in figure 21. The plates were 0.66 mm thick, 5.7 cm wide, and 8.5 cm long in the y-direction and were located symmetrically on opposite sides of the jet. The location of the plates at which the edge tone for the top plate was just suppressed is shown by the dotted curve in the figure. A similar curve below the jet for the bottom plate is not shown in the figure. For values of y_p in the region between the curves, there is no edge tone from the wedge. Suppression of the edge tone could be achieved even with a single plate.

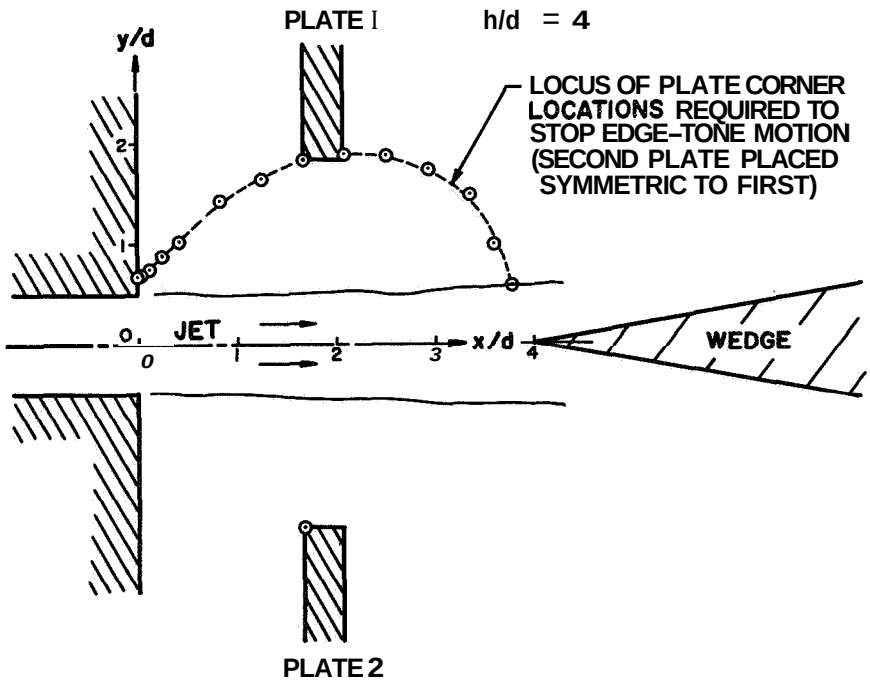

FIGURE 21.—Edge-tone suppression experiment.

REFERENCES

1. SONDHAUS, C.: Ueber die beim Ausstromen der Luft entstehenden Tone. Ann. Phys. (Leipzig), vol. 91,1854, pp. 126 and 214.
2. KARAMCHETI, KRISHNAMURTY: Acoustical Radiation From Two-Dimensional Rectangular Cutouts in Aerodynamic Surfaces. NACA TN 3487, 1955.
3. KARAMCHETI, KRISHNAMURTY: Sound Radiation From Surface Cutouts in High-Speed Flow. Ph. D. Thesis, Cal Tech, 1956.
4. KARAMCHETI, K.; AND BAUER, A.: Edge-Tone Generation. SUDAAR Rept. 162, Dept. of Aeronautics and Astronautics, Stanford Univ., 1963.
5. SHIELDS, W. L.; AND KARAMCHETI, K.: An Experimental Investigation of the Edgetone Flow Field., SUDAAR No. 304, Dept. of Aeronautics and Astronautics, Stanford Univ., 1967.
6. STEGEN, G. R.; AND KARAMCHETI, K.: On the Structure of an Edgetone Flow Field. SUDAAR No. 303, Dept. of Aeronautics and Astronautics, Stanford Univ., 1967.
7. BROWN, G. B.: The Mechanism of Edge-Tone Production. Proc. Phys. Soc. (London), vol. 49, 1937b, p. 508.
8. NYBORG, W. L.; BURKHARD, M. D.; AND SCHILLING, H. K.: Acoustical Characteristics of Jet-Edge and Jet-Edge-Resonator Systems. J. Acoust. Soc. Am., vol. 24, 1952, p. 293.
9. POWELL, A.: On the Edgetone. J. Acoust. Soc. Am., vol. 33, 1961, p. 395.
10. BROWN. G. B.: The Vortex Motion Causing Edge Tones. Proc. Phys. Soc. (London), vol. 49, 1937a, p. 493.

11. NYBORG, W. L.: Self-Maintained Oscillations of the Jet in a Jet-Edge System. J. Acoust. Soc. Am., vol. 26, 1954, p. 174.
12. BRACKENRIDGE, J. B.; AND NYBORG, W. L.: Transverse Oscillations in a Liquid Jet. Paper presented at the 56th meeting of the Acoust. Soc. of Am., 1958. Abstract in J. Acoust. Soc. Am., vol. 31, p. 114A.
13. GROSS, M. J.: Underwater Edge Tones. Acustica, vol. 9, 1959, p. 164.
14. RICHARDSON, E. G.: Edge Tones. Proc. Phys. Soc., vol. 43, 1931, p. 394.
15. CURLE, N.: The Mechanics of Edge Tones. Proc. Roy. Soc. (London), ser. A, vol. 216, 1953, p. 412.
16. SAVIC, P.: On Acoustically Effective Vortex Motion in Gaseous Jets. Phil. Mag., vol. 32, 1941, p. 245.
17. LIGHTHILL, M. J.: On Sound Generation Aerodynamically. Proc. Roy. Soc. (London), ser. A, vol. 211, 1952, p. 564.
18. LIGHTHILL, M. J.: Sound Generated Aerodynamically. Proc. Roy. Soc. (London), ser. A, vol. 267, 1962, p. 147.
19. LIGHTHILL, M. J.: Jet Noise. The Wright Brothers Memorial Lecture. Inst. Aerospace Sci., Jan. 21, 1963,
20. SATO, H.: The Stability and Transition of a Two-Dimensional Jet. J. Fluid Mech., vol. 7, 1959, p. 53.

PROPAGATIQN AND ATTENUATIQN OF SOUND IN A SOFT-WALLED ANNULAR DUCT CONTAINING A SHEARED FLOW

P. Mungur and H. E. Plumblee
Lockheed-Georgia Co.
Marietta, Ga.

The objective of this study is to extend the anaiysis of Mungnr and Gladwell to determine effects of flow, radial mean shear, and wall impedance on the propagation of sound in an infinite length, round, annular duct. A linearized first-order perturbation of the equations that govern fluid mass continuity and momentum, as well as the assumption of constant entropy and a perfect-gas equation of state, is used to describe fluctuating pressure and velocity variations. A propagating wave form of solution is assumed in the axial direction, and in the absence of mean swirl or mean radial flow, the resulting partial differential equation can be separated. The differential equation that describes pressure and velocity variations in the radial direction is solved numerically using a Runge-Kutta integration scheme.

INTRODUCTION

A recent conference at NASA Langley Research Center (ref. 1) highlighted research related to noise reduction of fanjet engines. At this conference NASA personnel and contractors described research funded as a result of growing concern by the public and the FAA on fanjet noise generation, sound propagation through the fan duct, methods of treating the duct with acoustic liner material, effects of sound pressure on the acoustic properties of the liner material, and radiation of sound from the fanjet engine duct to the surrounding community.

One of the areas where technological development is needed is the propagation of sound through a fan duct after application of acoustic liner materials. An analytical treatment of sound propagation in the fan duct is very involved because of the many complicating physical effects that interact with and modify the sound field. Briefly, the problem involves effects of flow and flow gradients, complex and nonlinear acoustic wall impedance, variable duct geometry, finite duct length with the resulting acoustic reflections from the duct end, and energy distribution in the propagating acoustic modes.

A classical treatment of sound propagation in a rectangular duct with hard walls was done by Rayleigh (ref. 2) about 100 years ago. Later Morse

(refs. **3** and **4)** treated the propagation of sound through circular and rectangular ducts with finite wall admittance. Then, when it became apparent that pure-tone sound radiation from turbofan engines was a problem that would have to be dealt with, two important studies were made by Tyler and Sofrin (ref. **5)** and Morfey (ref. **6).** Tyler and Sofrin solved for duct mode propagation in an annular, hard-walled duct. They also calculated radiation, but did not include effects of end reflections. Morfey calculated the radiation impedance of a thin annular duct for the plane and higher order angular acoustic modes and determined effects of termination impedance on propagation through the duct. In **1966,** Doak (ref. **7)** and Vaidya (ref. 8) studied propagation and attenuation of sound in circular and annular ducts with nearly rigid walls for the general case of higher order modes, and in **1968,** Rice (ref. **9)** solved for the modal propagation and attenuation constants in a soft-walled duct and then combined the modes to represent a plane pressure distribution at the duct entrance. Attenuation for the plane pressure distribution was then calculated. This compared favorably with limited experimental data. Flow and shear were not included.

Effects of flow have been studied by Vaidya (ref. **10),** Ingard (ref. 11), Morse and Ingard (ref. 12), Pridmore-Brown (ref. 13), Tack and Lambert (ref. 14), and Mungur and Gladwell (ref. **15).** Vaidya (ref. **10)** has studied the effect of mean flow on the modal propagation of sound in a finite length annular duct. Ingard (ref. **11)** studied the effect of mean flow on the transmission, reflection, and attenuation of sound in the presence of a plane boundary. Morse and Ingard (ref. **12)** included a study of effects of mean flow on sound propagation in a hard-walled rectangular duct. Pridmore-Brown (ref. **13)** considered sound propagation in a rectangular soft-walled duct in the presence of a sheared flow, but the solution was not valid near the wall. Tack and Lambert (ref. **14)** performed an analysis for sound propagation between semi-infinite soft walls, but the solution was limited to plane-mode propagation. Also, the solution contained a singularity at zero mach number, which limited the usefulness of the approach.

Recently Mungur and Gladwell (ref. **15)** have obtained numerical solutions for sound propagation in a rectangular hard-walled duct in the presence of a sheared flow. This solution avoids the difficulties in the Pridmore-Brown and Tack and Lambert analyses near the wall.

SOUND PROPAGATION IN A FINITE-LENGTH DUCT WITH FLOW

Although in the succeeding sections an analysis for an infinite length duct only is presented, it is actually the propagation in a finite length duct that ultimately must be determined. In general, the usual assumption in accounting for the end of a finite duct is to assume that it is ter-

minated in a radiation impedance. Any termination impedance different from the modal impedance will result in a reflection and standing waves in the duct. The normal assumption in calculating the effect of finite length is to assume that two propagating waves exist and travel in opposite directions and that in the presence of flow the upstream and downstream propagation constants are different. The form of the pressure wave in the finite length duct may be taken as

$$P(r,\theta,z,t) = [P_1(r,\theta)e^{-\gamma_1 z} + P_2(r,\theta)e^{\gamma_2 z}]e^{j\omega t} \tag{1}$$

For walls with finite admittance, the propagation constants γ_1 and γ_2 are complex and contain the attenuation constant. In the presence of a uniform flow, the axial velocity, from the axial momentum relationship, can be shown to be

$$u(r,\theta,z) = \frac{1}{\rho_0 C}\left[\frac{K_1}{1-MK_1}P_1(r,\theta)e^{-\gamma_1 z} - \frac{K_2}{1+MK_2}P_2(r,\theta)e^{\gamma_2 z}\right] + B_1 e^{-j\frac{k}{M}z} \tag{2}$$

where P_1 and P_2 are functions of r and 8, M is the mach number of the flow in the positive direction of z, K_1 and K_2 are the normalized propagation wave vectors (γ_1/jk) and (γ_2/jk), the computation of which will be described in the next sections, k is the wave number ω/c, and B_1 is a constant that can be determined if the impedance of the source is specified. In the presence of shear, equation (2) should contain two extra terms involving the derivative with respect to r of P_1 and P_2.

At the wall:

$$z = L \qquad P_L = \zeta_L \mu_L \tag{3}$$

where $\zeta_L = Z_L/\rho c$ is the specific acoustic termination impedance ratio. If this is specified and equations (1) and (2) are substituted in equation (3), P_2 can then be calculated in terms of P_1 together with a phase angle. It is evident that the phase angle is primarily a function of the impedance of the termination and indirectly a function of the source impedance through coupling via the flow as expressed by the third term in equation (2). Thus the sound field inside a duct of finite length can be obtained by the superposition of wave solutions for an infinite duct.

THE GOVERNING WAVE EQUATION IN PRESENCE OF FLOW AND SHEAR

The main object of the problem is to calculate the attenuation of the sound wave as it propagates down a round, annular duct in the presence of flow and shear. The governing wave equation is therefore required in cylindrical coordinates (fig. 1).

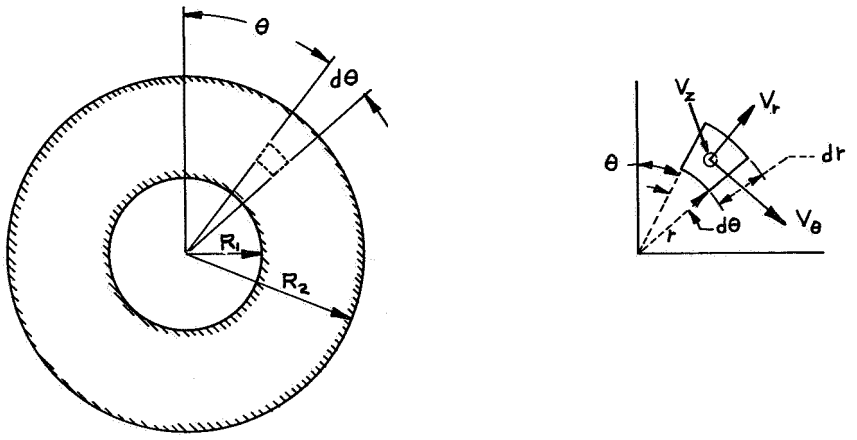

FIGURE 1.—Cylindrical coordinate system used for wave equation.

The three components of the Navier-Stokes equation in this coordinate system are, in the absence of body forces, as follows:

In the axial or z-direction:

$$\rho\left(\frac{\partial v_z}{\partial t}+v_r\frac{\partial v_z}{\partial r}+\frac{v_\theta}{r}\frac{\partial v_z}{\partial \theta}+v_z\frac{\partial v_z}{\partial z}\right)$$
$$=-\frac{\partial P}{\partial z}-\left[\frac{1}{r}\frac{\partial}{\partial r}(r\tau_{rz})+\frac{1}{r}\frac{\partial}{\partial \theta}(\tau_{\theta z})+\frac{\partial}{\partial z}\tau_{zz}\right] \tag{4}$$

In the radial or r-direction:

$$\rho\left(\frac{\partial v_r}{\partial t}+v_r\frac{\partial v_r}{\partial r}+\frac{v_\theta}{r}\frac{\partial v_r}{\partial \theta}-\frac{v_\theta^2}{r}+v_z\frac{\partial v_r}{\partial z}\right)$$
$$=-\frac{\partial P}{\partial r}-\left[\frac{1}{r}\frac{\partial}{\partial r}(r\tau_{rr})+\frac{1}{r}\frac{\partial \tau_{r\theta}}{\partial \theta}-\frac{\tau_{\theta\theta}}{r}+\frac{\partial \tau_{rz}}{\partial z}\right] \tag{5}$$

In the circumferential or 8-direction:

$$\rho\left(\frac{\partial v_\theta}{\partial t}+v_r\frac{\partial v_\theta}{\partial r}+\frac{v_\theta}{r}\frac{\partial v_\theta}{\partial \theta}+\frac{v_r v_\theta}{r}+v_z\frac{\partial v_\theta}{\partial z}\right)=-\frac{1}{r}\frac{\partial p}{\partial \theta}$$
$$-\left[\frac{1}{r^2}\frac{\partial}{\partial r}\left(r^2\tau_{r\theta}\right)+\frac{1}{r}\frac{\partial \tau_{\theta\theta}}{\partial \theta}+\frac{\partial \tau_{\theta z}}{\partial z}\right] \tag{6}$$

Here τ_{rz}, $\tau_{\theta z}$, τ_{zz}, τ_{rr}, $\tau_{r\theta}$, and $\tau_{\theta\theta}$ are the viscous stresses.

The equation of continuity of mass is

$$\frac{\partial \rho}{\partial t}+\frac{1}{r}\frac{\partial}{\partial r}(\rho r v_r)+\frac{1}{r}\frac{\partial}{\partial \theta}(\rho v_\theta)+\frac{\partial}{\partial z}(\rho v_z)=0 \tag{7}$$

which may be rewritten as

$$\frac{\partial \rho}{\partial t}+v_z\frac{\partial \rho}{\partial z}+v_r\frac{\partial \rho}{\partial r}+\frac{v_\theta}{r}\frac{\partial \rho}{\partial \theta}+\rho\left(\frac{\partial v_z}{\partial z}+\frac{\partial v_r}{\partial r}+\frac{1}{r}\frac{\partial v_z}{\partial \theta}\right)+\rho\frac{v_r}{r}=0 \tag{8}$$

Although, in the applications of most interest here, viscosity does not contribute significantly to the total attenuation, it is relatively important only in the boundary layers where the velocity gradient may be large (ref. 11), it does play an important role in governing the boundary conditions. Detailed consideration of the role of viscosity is beyond the scope of this paper; the main object here is to calculate the attenuation of the sound waves caused by the finite admittances of the walls. The viscous shear stresses are therefore neglected in what follows.

A further simplification in the analysis results from the assumption that the mean flow is in the axial direction only and uniform in that direction. Thus there is no mean swirl and the mean values of $\partial v_z/\partial \theta$, $\partial v_z/\partial z$, v_θ, and v_r are all zero. Therefore, only mean shear in the radial direction is permitted. If equations (4), (5), (6) and (8) are perturbed to first order and linearized by subtracting time-averaged quantities and neglecting products of fluctuating quantities, the following equations are obtained:

$$\rho_0\left[\frac{\partial v_z}{\partial t}+v_r\frac{\partial V_z}{\partial r}+V_z\frac{\partial v_z}{\partial z}\right]=-\frac{\partial p}{\partial z} \tag{9}$$

$$\rho_0\left[\frac{\partial v_r}{\partial t}+V_z\frac{\partial v_r}{\partial z}\right]=-\frac{\partial p}{\partial r} \tag{10}$$

$$\rho_0\left[\frac{\partial v_\theta}{\partial t}+V_z\frac{\partial v_\theta}{\partial z}\right]=-\frac{1}{r}\frac{\partial p}{\partial \theta} \tag{11}$$

and

$$\frac{\partial \rho}{\partial t}+V_z\frac{\partial \rho}{\partial z}+\rho_0\left(\frac{\partial v_z}{\partial z}+\frac{\partial v_r}{\partial r}+\frac{1}{r}\frac{\partial v_\theta}{\partial \theta}\right)+\rho_0\frac{v_r}{r}=0 \tag{12}$$

where V_z is the mean axial flow velocity, $\partial v_z/\partial r$ is the mean shear, ρ_0 is the mean density, and v_z, v_r, v_θ, p, and **p** now represent first-order fluctuating quantities.

Differentiation of equations (9), (10), and (11) with respect to z, r, and 0, respectively, and subsequent addition of these gives

$$\rho_0\left[\frac{\partial}{\partial t}\left(\frac{\partial v_z}{\partial z}+\frac{\partial v_r}{\partial r}+\frac{1}{r}\frac{\partial v_\theta}{\partial \theta}\right)+z\frac{\partial V_z}{\partial r}\frac{\partial v_r}{\partial z}+V_z\frac{\partial}{\partial z}\left(\frac{\partial v_z}{\partial z}+\frac{\partial v_r}{\partial r}+\frac{1}{r}\frac{\partial v_\theta}{\partial \theta}\right)\right]$$
$$=-\left(\frac{\partial^2 P}{\partial z^2}+\frac{\partial^2 P}{\partial r^2}+\frac{1}{r^2}\frac{\partial^2 P}{\partial \theta^2}\right) \tag{13}$$

Equation (12) may be rewritten in the form

$$\left(\frac{\partial v_z}{\partial z}+\frac{\partial v_r}{\partial r}+\frac{1}{r}\frac{\partial v_\theta}{\partial \theta}\right)=-\frac{1}{\rho_0}\left(\frac{\partial \rho}{\partial t}+V_z\frac{\partial \rho}{\partial z}\right)-\frac{v_r}{r} \tag{14}$$

If this is substituted in equation (13), one obtains

$$-\frac{\partial^2\rho}{\partial t^2}-V_z\frac{\partial^2\rho}{\partial z\,\partial t}-\frac{\rho_0}{r}\frac{\partial v_r}{\partial t}+\rho_0 z\frac{\partial V_z}{\partial r}\frac{\partial v_r}{\partial z}-V_z\frac{\partial^2\rho}{\partial z\,\partial t}-V_z^2\frac{\partial^2\rho}{\partial z^2}-\rho_0\frac{V_z}{r}\frac{\partial v_r}{\partial z}$$
$$=-\left(\frac{\partial^2 P}{\partial z^2}+\frac{\partial^2 P}{\partial r^2}+\frac{1}{r^2}\frac{\partial^2 P}{\partial \theta^2}\right) \tag{15}$$

Because no viscous effects are included, the entropy of the system can be taken to be conserved if it is also assumed that the thermal conductivity of the fluid is negligible. Under these conditions the pressure and the density fluctuations are adiabatically related by

$$P=\rho c^2 \tag{16}$$

where c is a constant, the mean speed of sound in the fluid.

In equation (15), if p is replaced by P/c^2 from equation **(16)** and the radial momentum relationship of **(10)** is used, one obtains

$$\frac{1}{c^2}\frac{\partial^2 P}{\partial t^2}+2\frac{M}{c}\frac{\partial^2 P}{\partial z\,\partial t}+M^2\frac{\partial^2 P}{\partial z^2}-2\rho_0 c\frac{\partial M}{\partial r}\frac{\partial v_r}{\partial z}-\nabla^2 P=0 \tag{17}$$

where $M=V_z/c=$ mach number of the flow and ∇^2 is the Laplacian operator in cylindrical coordinates:

$$\nabla^2=\frac{\partial^2}{\partial r^2}+\frac{1}{r}\frac{\partial}{\partial r}+\frac{1}{r^2}\frac{\partial^2}{\partial \theta^2}+\frac{\partial^2}{\partial z^2}$$

For harmonic waves propagating in the positive z-direction (downstream), the variation of the fluctuating quantities with time and z can be taken in the form $e^{j\omega t-\gamma z}$. Thus

$$\left(\frac{\partial}{\partial t}+V_2\frac{\partial}{\partial z}\right)=j\omega-\gamma V_z$$
$$=j\omega(1-MK) \tag{18}$$

where $K=\gamma/j\omega/c$ is the normalized z-component of the wave vector.

By using equation (18), equation **(10)** may be rewritten as

$$v_r=-\frac{1}{j\rho_0\omega(1-MK)}\frac{\partial P}{\partial r} \tag{19}$$

Writing ω/c as k, the wave number, and using equation *(19)* in equation (17), one obtains

$$k^2(1-MK)^2P+\frac{2K}{1-MK}\frac{\partial M}{\partial r}\frac{\partial P}{\partial r}+\nabla^2P=0 \tag{20}$$

or, if the terms in the Laplacian are written out explicitly,

$$\frac{\partial^2P}{\partial r^2}+\frac{1}{r}\frac{\partial P}{\partial r}+\frac{2K}{1-MK}\frac{\partial M}{\partial r}\frac{\partial P}{\partial r}+k^2[(1-MK)^2-K^2]P+\frac{1}{r^2}\frac{\partial^2P}{\partial\theta^2}=0 \tag{21}$$

This is the wave equation in cylindrical coordinates governing the propagation of small amplitude sound waves in the presence of a radially sheared, axially uniform mean flow. With the exception of the second and the last terms, equation *(21)* is similar to that derived in reference [15] for a semi-infinite duct in rectangular coordinates. The second term occurs because of the characteristic radial spreading in cylindrical coordinates, and the last term is the result of the inclusion in this analysis of possible pressure variations in the circumferential direction. The third term represents the direct refracting effect of the shear on the sound wave, whereas the usual uniform mean flow convection effects are included in the fourth term. It must be recalled that the above analysis permits variation of the mean flow along the radius only; it is therefore, strictly speaking, limited to a duct of constant area of cross section. The absence of coupling terms involving cross-differentiation with respect to θ and other coordinates results from the neglect of swirl and the resulting equation *(21)* is therefore separable in θ.

Now, let

$$\frac{\partial^2P}{\partial\theta^2}=-(k_\theta)^2P \tag{22}$$

where k_θ is the circumferential component of the wave vector.

This gives

$$P(\theta)=\left.\begin{matrix}\cos k_\theta\theta\\ \sin k_\theta\theta\end{matrix}\right\} \tag{23}$$

The coordinate 8 is periodic, repeating after 2π radians, but the pressure must be single valued, therefore the magnitudes of k_θ are restricted to integers. These may be denoted by m, and physically m is the number of diametral nodes of the mth mode. If the duct contains radial splitters that are lined with nonrigid materials, then k_θ may be complex. If the splitters are rigid, however, then an analysis similar to that given here can be applied.

Equation *(21)* now becomes

$$\frac{d^2P}{dr^2}+\frac{1}{r}\frac{dP}{dr}+k^2\left[(1-MK)^2-K^2-\frac{m^2}{k^2r^2}\right]P=\frac{-2K}{1-MK}\frac{dM}{dr}\frac{dP}{dr} \tag{24}$$

In the absence of shear, the term on the right-hand side vanishes, and as the mach number inside the square bracket is also independent of r, the equation becomes Bessel's equation and has the usual Bessel and Neumann function solutions. However, with the shear terms included, equation *(24)* is a second-order differential equation with variable coefficients **of** nonstandard form for which analytical solutions are not readily available in general. If the walls are not rigid, the coefficients are not only variable but also complex because K must be complex to satisfy the boundary conditions. Before solving equation (24), it is convenient to express it in terms of nondimensionalized parameters and coordinates.

The choice of a normalizing parameter for a coordinate depends on the sort of problem being analyzed. Broadly, three categories of sound propagation may be distinguished: inside a single cylinder, outside a cylinder, and within the annulus between two cylinders. The coordinate r can be normalized as $rL=X$, where L is some typical length, depending on the category of the problem. The other parameters that have already been normalized are M, the flow mach number, and K, the axial component of the wave vector normalized with respect to k, the total wave vector.

In terms of the new coordinate X, equation *(24)* becomes

$$\frac{d^2P}{dX^2}+\left(\frac{1}{X}+\frac{2K}{1-MK}\frac{dM}{dX}\right)\frac{dP}{dX}+(kL)^2\left[(1-MK)^2-K^2-\frac{m^2}{(kL)^2X^2}\right]P=0 \tag{25}$$

and (kL) now becomes the dimensionless frequency parameter.

One more parameter that must be specified is the hub-tip ratio; i.e., the ratio of the inner radius to the outer radius of the annulus. This can be denoted by $\epsilon=R_1/R_2$.

For sound propagation inside a single cylinder and outside a cylinder, one would choose $L=R_1$ and $L=R_2$, respectively. In the present analysis, however, it is convenient to use $L=R_2-R_1$, in particular, this facilitates comparisons with propagation in a rectangular duct.

ANALYTICAL SOLUTION FOR THE SPECIAL CASE OF UNIFORM FLOW

The assumption that the flow profile is uniform simplifies the problem by making the shear factor (dM/dx) vanish, and the wave equation

to be solved reduces to a standard differential equation, namely:

$$\frac{d^2P}{dX^2}+\frac{1}{X}\frac{dP}{dX}+\left(k_r^2-\frac{m^2}{X^2}\right)P=0 \tag{26}$$

where

$$k_r^2=(kL)^2[(1-MK)^2-K^2] \tag{27}$$

which is independent of X.

The solution to equation **(26)** has been given in numerous references, for instance, reference **16.** It is

$$P=B_2J_m(k_rX)+B_3N_m(k_rX) \tag{28}$$

where B_2 and B_3 are constants to be determined from the boundary conditions. $J_m(k_rX)$ and $N_m(k_rX)$ are, respectively, the Bessel and the Neumann functions of mth order.

Equation (28) must be combined with equation **(23)** and the term $e^{j\omega t-\gamma z}$ to completely define the modal pressure fields. From equations **(19)** and **(28),** the radial velocity is

$$V_r=-\frac{k_r}{j\rho ckL(1-MK)}[B_2J'_m(k_rX)+B_3N'_m(k_rX)] \tag{29}$$

where the primes denote differentiation with respect to the argument.

Let the magnitudes of X at the surfaces of the inner and the outer walls be denoted by σ_1 and σ_2 respectively. In terms of E, the hub-tip ratio

$$\sigma_1=\frac{R_1}{L}=\frac{R_1}{R_2-R_1}=\frac{\mathrm{E}}{1-\epsilon} \qquad \sigma_2=\frac{R_2}{L}=\frac{R_2}{R_2-R_1}=\frac{1}{1-\epsilon}$$

Case of Rigid Walls

If the walls are rigid, the radial velocity must be zero at each wall, and it follows that

$$B_2J'_m(k_r\sigma_1)+B_3N'_m(k_r\sigma_1)=0 \tag{30}$$

and

$$B_2J'_m(k_r\sigma_2)+B_3N'_m(k_r\sigma_2)=0 \tag{31}$$

From equations **(30)** and **(31),** one obtains

$$J'_m(k_r\sigma_1)N'_m(k_r\sigma_2)-J'_m(k_r\sigma_2)N'_m(k_r\sigma_1)=0 \tag{32}$$

which is the eigenequation, the roots of which yield real values of k_r, each defining a particular radial mode, henceforth denoted by the subscript n.

371-986 0-LT-70—21

Thus the complete pressure field for the (m, n) mode may be written as

$$P_{mn}=B_{2,mn}[Jm(k_{r,mn}X)+Q_{mn}(k_{r,mn}\epsilon)N_m(k_{r,mn}X]\cos m\theta e^{j\omega t-\lambda_{mn}z} \tag{33}$$

where

$$Q_{mn}(k_{r,mn}\epsilon)=\frac{J'_m(k_{r,mn}\sigma_1)}{N'_m(k_{r,mn}\sigma_1)} \quad \text{or} \quad \frac{J'_m(k_{r,mn}\sigma_2)}{N'_m(k_{r,mn}\sigma_2)}$$

and is a function of $k_{r,mn}$ and ϵ only. This equation gives the same result as that obtained previously by Sofrin and Tyler (ref. **5**).

Case of Nonrigid Walls

Let the normalized specific admittance ratio of the inner and the outer walls be denoted by A_1 and A_2. Although the assumption that the flow profile is uniform simplifies the wave equation to the extent that it admits a simple analytical solution of the form defined by equation (28), nevertheless it does create an unrealistic situation at the boundary. The suppression of the shear makes slip at the wall inevitable. In the next section a numerical solution to the complete wave equation is presented in which shear is taken into account, and the mean slip situation is thus avoided. In the present situation of mean flow, because of the relative motion between the wall and the fluid, continuity of particle displacement must be used instead of continuity of particle velocity. In references *15* and **11** it has been shown that in the presence of slip

$$V_{r(\text{wall})}=V_{r(\text{medium})}/(1-MK) \tag{34}$$

Replacing $V_{r(\text{wall})}$ by AP/ρ_0C and using equation (19) gives

$$\frac{A_1}{\rho_0C}[B_2J_m(k_r\sigma_1)+B_3N_m(k_r\sigma_1)]$$
$$=\frac{-k_r}{j\rho_0CkL(1-MK)^2}[B_2J'_m(k_1\sigma_1)+B_3N'_m(k_r\sigma_1)] \tag{35}$$

at the inner wall and

$$\frac{A_2}{\rho_0C}[B_2J_m(k_r\sigma_2)+B_3N_m(k_r\sigma_2)]$$
$$=\frac{-k_r}{j\rho_0CkL(1-MK)^2}[B_2J'_m(k_r\sigma_2)+B_3N'_m(k_r\sigma_2)] \tag{36}$$

at the outer wall, the n subscripts being omitted for simplicity.

The eigenequation can be obtained by eliminating B_2 and B_3 from equations **(35)** and **(36)** and is

$$\frac{A_1 jkL(1-MK)^2 J_m(k_r\sigma_1)+k_r J'_m(k_r\sigma_1)}{A_1 jkL(1-MK)^2 N_m(k_r\sigma_1)+k_r N'_m(k_r\sigma_1)} - \frac{A_1 jkL(1-MK)^2 J_m(k_r\sigma_2)+k_r J'_m(k_r\sigma_2)}{A_2 jkL(1-MK)^2 N_m(k_r\sigma_2)+k_r N'_m(k_r\sigma_2)}=0 \tag{37}$$

Because A_1 and A_2 will in general be complex for nonrigid walls, k_r, which is obtained from the roots of equation (37), will also be complex. It may be noted that, unlike the rigid wall case, the values taken by k_r are not independent of the frequency parameter kL. Numerical methods can be used to solve the complex roots of equation **(37).** This is not done here because in the next section, the complete wave equation including shear is solved numerically. Vaidya (ref. 8) has proposed an alternative approximate solution to this problem if the walls are either nearly pressure release **or** nearly rigid. In his study, expressions are derived for propagation and attenuation coefficients for small perturbations ($k\sigma_2|A| \gg m\pi$ or $k\sigma_2|A| \ll m\pi$) from the classical boundary conditions.

NUMERICAL SOLUTION OF THE GENERAL CASE OF PROPAGATION IN PRESENCE OF FLOW AND SHEAR

As has been pointed out in the section on the governing wave equation in presence of **flow** and shear, the presence of shear and nonrigid walls makes the wave equation a second-order differential equation with variable and complex coefficients. For realistic flow profiles, analytical solutions are not available; however, one can still resort to a numerical solution. **A** method developed in reference *15,* making use of the fourth-order Runge-Kutta integration technique (ref. 17), is extended here to yield a solution in the form of a system of transferred matrices. The admittances of the walls are brought in in the form of boundary constraint matrices and coupled to the transfer matrices to yield the eigenequation.

The equation to be solved, equation (25), may be rewritten as

$$\frac{d^2P}{dx^2}+a(x)\frac{dP}{dx}+b(x)P=0 \tag{38}$$

where

$$a(x)=\left[\frac{1}{x}+\frac{2K}{1-MK}\frac{dM}{dx}\right] \tag{39}$$

and

$$b(x)=(kL)^2[(1-MK)^2-K^2]-\frac{m^2}{x^2} \tag{40}$$

For given flow and shear profiles, the coefficients $a(x)$ and $b(x)$ could have been evaluated for any value of x if the value of K were known, but the whole object of the analysis is to determine the value of K. Although other numerical techniques may be possible, an obvious route is to use a trial-and-error method in the hunt for the eigenvalue.

It is convenient, for the numerical work, to reduce the second-order equation **(38)** to two first-order equations. Let

$$P = Y_1 \tag{41}$$

and

$$\frac{dP}{dx} = Y_1' = Y_2 \tag{42}$$

Then

$$\frac{d^2P}{dx^2} = Y_2' = -b(x)Y_1 - a(x)Y_2 \tag{43}$$

Note that Y_1, Y_2, and their derivatives are complex functions. In complex matrix notation

$$\begin{bmatrix} Y_1 \\ Y_2 \end{bmatrix}' = \begin{bmatrix} 0 & 1 \\ -b & -a \end{bmatrix} \begin{bmatrix} Y_1 \\ Y_2 \end{bmatrix} \tag{44}$$

Let the independent coordinate x in the region where the solution is required be divided into n steps. Then the solution, as given by the generalized Runge-Kutta method, is

$$\mathbf{Y}^{(r+1)} = \mathbf{Y}^{(r)} + \frac{h}{6}\left[\mathbf{m}^{(1)} + 2\mathbf{m}^{(2)} + 2\mathbf{m}^{(3)} + \mathbf{m}^{(4)}\right] \tag{45}$$

where

$$\begin{aligned}
&\mathbf{Y}^{(r)} = Y(rh) \equiv [Y_1(rh),\ Y_2(rh)] \\
&\quad h = \text{step size} \\
&\mathbf{m}^{(1)} = f(x_r,\ \mathbf{Y}^{(r)}), \\
&\mathbf{m}^{(2)} = f(x_r + \tfrac{1}{2}h,\ \mathbf{Y}^{(r)} + \tfrac{1}{2}h\mathbf{m}^{(1)}) \\
&\mathbf{m}^{(3)} = f(x_r + \tfrac{1}{2}h,\ \mathbf{Y}^{(r)} + \tfrac{1}{2}h\mathbf{m}^{(2)}) \\
&\mathbf{m}^{(4)} = f(x_r + h,\ \mathbf{Y}^{(r)} + h\mathbf{m}^{(3)})
\end{aligned} \tag{46}$$

and $f(x, \mathbf{Y})$ is defined by the right-hand side of equation **(44).**

The functions $\mathbf{m}^{(1)}$ through $\mathbf{m}^{(4)}$ can all be expressed in terms of $f(x, \mathbf{Y}^{(r)})$ and $\mathbf{Y}^{(r)}$ by using equation **(46),** and it follows that the second term on the right-hand side of equation **(45)** may be expressed in terms of a square matrix and a column matrix. Thus the magnitudes of the

functions at the first step may be expressed in terms of those at the initial step, that is, at the first boundary, by using equation **(45).**

Thus

$$[\mathbf{Y}]_1 = [\mathbf{Y}]_0 + [A_0][\mathbf{Y}]_0$$
$$= [A_{t10}][\mathbf{Y}]_0 \tag{47}$$

where the subscript 1 and 0 refer to the first and zero steps, and $[A_{t10}]$ is a matrix formed by adding the identity matrix to $[A_0]$ and will be the first of a system of transferred matrices.

The solution at the second step is

$$[\mathbf{Y}]_2 = [\mathbf{Y}]_1 + [A_1][\mathbf{Y}]_1$$
$$= [A_{t21}][\mathbf{Y}]_1 \tag{48}$$

Substituting equation **(47)** in equation (48), one obtains

$$[\mathbf{Y}]_2 = [A_{t21}][A_{t10}][\mathbf{Y}]_0$$
$$= [A_{t20}][\mathbf{Y}]_0 \tag{49}$$

In this way one may proceed to the nth step and write

$$[\mathbf{Y}]_n = [A_{tn0}]\,[\mathbf{Y}]_0 \tag{50}$$

where $[A_{tn0}]$ is the final transferred matrix.

The Boundary Conditions and the Eigenequation

If equation **(50)** is rewritten in terms of its components, one obtains

$$\begin{bmatrix} Y_1 \\ Y_2 \end{bmatrix}_n = [A_{tn0}] \begin{bmatrix} Y_1 \\ Y_2 \end{bmatrix}_0 \tag{51}$$

Because Y_1 stands for the pressure and Y_2 for the derivative of the pressure, then, at each of the two boundaries, Y_2 may be expressed in terms of Y_1 and the corresponding wall impedance. From equation **(19)**

$$Y_2 = -j\rho_0 ckL(1 - MK)V_r \tag{52}$$

If A_0 and A„ represent the normalized specific admittance ratios of the walls at the zeroth and the nth step, respectively, one may write

$$(Y_2)_0 = -jA_0kL(1 - MK)^2(Y_1)_0 \tag{53}$$

and

$$(Y_2)_n = -jA_n kL(1-MK)^2(Y_1)_n \tag{54}$$

Note that the values of M used in equations **(53)** and **(54)** are those computed at the walls so that these would be zero if a realistic flow profile is used, corresponding to no mean slip. Equation **(51),** if equations **(53)** and **(54)** are used to eliminate Y_2, becomes

$$\begin{bmatrix} 1 \\ BN \end{bmatrix}^{[Y_1]_n} = \begin{bmatrix} A_{tn0} \end{bmatrix} \begin{bmatrix} 1 \\ B0 \end{bmatrix}^{[Y_1]_0} \tag{55}$$

$$= [T0]^{[Y_1]_0} \tag{56}$$

where

$$BO = -jA_0 kL(1-MK)^2$$

$$BN = -jA_n kL(1-MK)^2$$

and the column matrices $\begin{bmatrix} 1 \\ BN \end{bmatrix}$ and $\begin{bmatrix} 1 \\ B0 \end{bmatrix}$ will be referred to as constraint matrices. **[TO]** is the matrix formed by multiplying $[A_{tn0}]$ and $\begin{bmatrix} 1 \\ B0 \end{bmatrix}$.

If equation **(56)** is partitioned, one obtains

$$(Y_1)_n = T0(1, 1)\ (Y_1)_0 \tag{57}$$

and

$$BN(Y_1)_n = T0(2, 1)(Y_1)_0 \tag{58}$$

so that

$$[(BN)T0(1, 1) - T0(2, 1)](Y_1)_0 = 0 \tag{59}$$

Equation **(59)** is the eigenequation and expresses the interaction of the boundaries with each other and with the frequency because the transferred matrix $[A_{tn0}]$ in equation **(55)** is a function of the frequency. Each propagating mode in the duct will have a value of K that will satisfy equation **(59).** Once these eigenvalues have been determined, the mode shapes can be obtained by computing the magnitudes of the function Y_1 and Y_2 for each step. For walls of finite admittance, K in general will be complex so that the eigenvalue hunt will have to be done in bath the real and the imaginary frequency planes. A computer program has been written that finds complex values of K that satisfy equation **(59)** given a frequency parameter, a hub-tip ratio, a flow and a shear profile, and a value of m, and finally computes the corresponding mode shapes. The decay coefficient of each mode is obtained from the imaginary part of the corresponding value of K.

NUMERICAL STUDIES

The analysis described in the previous sections has been used to perform several parametric studies on propagation and attenuation.

Primary attention has been directed toward the study of the effect of sheared flow on mode shapes, propagation, and attenuation constants in annular and rectangular ducts with rigid and nonrigid walls, However, effects of a few other parameters are also shown.

Because the method of determining the solution involves finding eigenfunctions that satisfy the differential equation for sound propagation in the duct, it is of interest first to show a typical set of modes. Figures **2** and 3 illustrate the (0, 1) and (0, 2) pressure and radial velocity modes for complex wall admittance. The values of the boundary and flow conditions are not included in these charts because the charts are included only to demonstrate the character of the pressure modes. In the computer analysis, the pressure is assumed to be $1.0 + j0.0$ at the inner wall; therefore the mode shapes always retain this value at the inner wall. The radial velocity is obviously related to the pressure at the boundaries by the wall admittance.

Figure **4** shows the downstream attenuation in dB per width in a soft-walled rectangular duct for individual modes plotted against mach number for three boundary-layer thicknesses, 1.5 percent, 5 percent and 12.5 percent, and mean flow. The boundary-layer profile used is a quarter sine wave restricted to a region quoted as a percentage of the total width between the walls. The initial increase and the subsequent decrease in the attenuation with mach number illustrate the opposing effects of refraction and convection. The increase in the attenuation with increasing boundary-layer thicknesses is the result of the effect of shear refracting the sound wave toward the walls for downstream propagation.

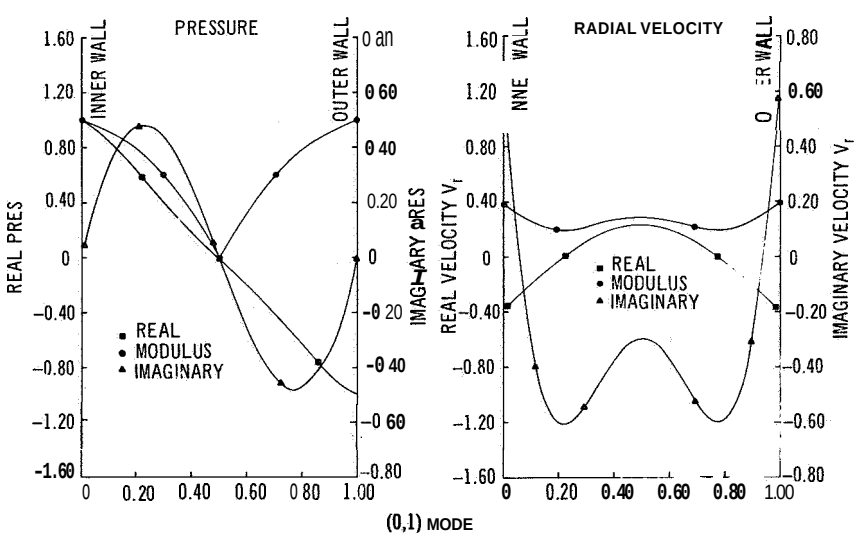

FIGURE 2.—Typical mode shape for rectangular duct with finite wall admittance containing a sheared flow.

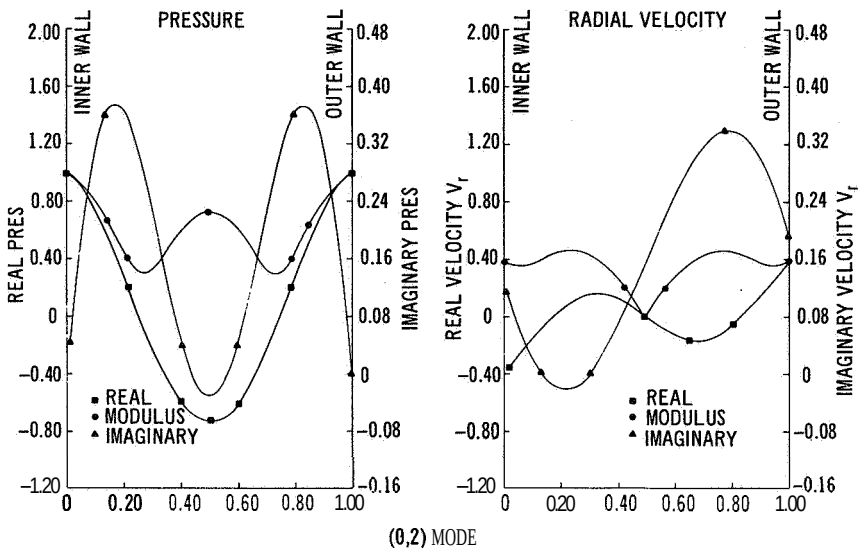

FIGURE 3.—Typical mode shape for rectangular duct with finite wall admittance containing a sheared flow.

As the mach number increases, the convective effects increase and result in a gradual reduction in the attenuation. Although the attenuation in dB per width is higher for the higher order modes, the percentage increase caused by the shear effect is higher for the lower order modes, as seen in the next figure. This effect will be higher still for higher frequencies.

Because there has been some controversy concerning the boundary condition that should be used for the case of mean flow, attenuation is shown for two possible mean-flow boundary conditions, continuity of particle displacement and continuity of particle velocity. The ratio of pressure to rate of change of pressure for each of these boundary conditions is

$$\frac{P}{\frac{\partial P}{\partial r}} = \frac{Z_{\text{wall}}}{j\rho_0 ckL(1-MK)^2} \quad \text{for continuity of particle displacement} \tag{60}$$

$$\frac{P}{\frac{\partial P}{\partial r}} = \frac{Z_{\text{wall}}}{j\rho_0 ckL(1-MK)} \quad \text{for continuity of particle velocity} \tag{61}$$

Examination of the effect of boundary-layer thickness would lead one to believe that the assumption of continuity of particle displacement is physically more consistent with the shear flow solution, which, because

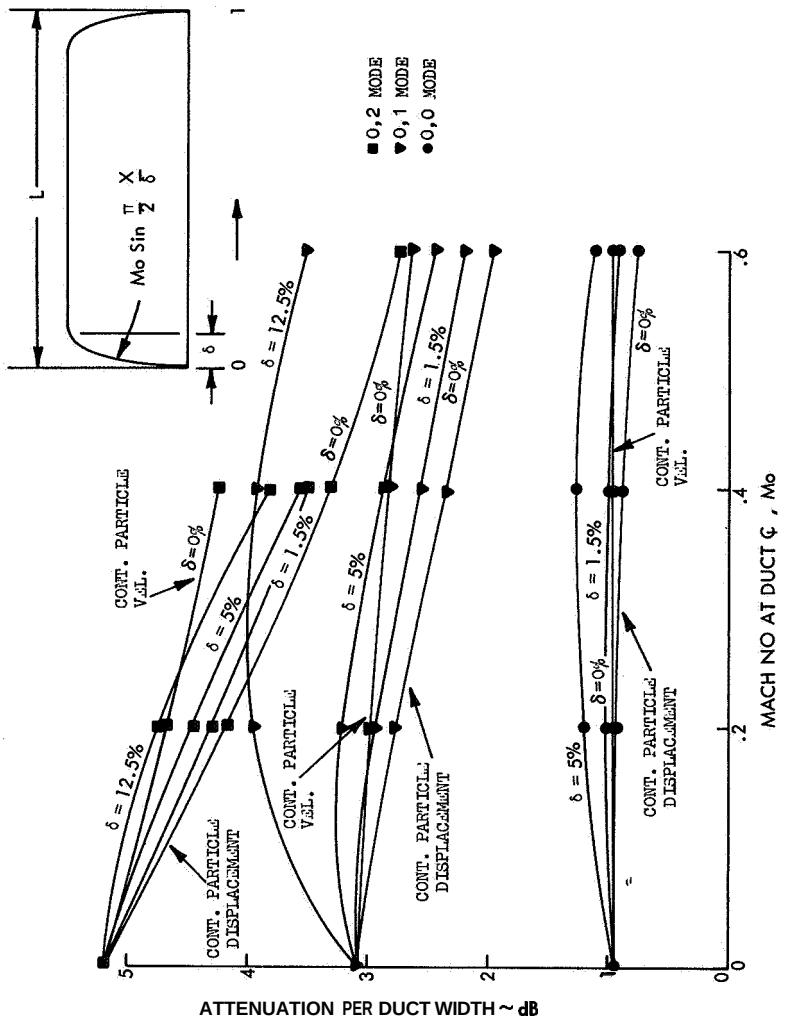

FIGURE 4.—Effect of mach number and shear layer thickness on mode attenuation in rectangular duct. Duct height/width = 2.0, vertical mode number $m = 0$, $kL = 5\pi$, wall admittance $A_0 = A_n = 0.345 - j0.138$.

of zero mean velocity at the boundary, does not require a mean-flow interaction in the boundary value. (See discussion after eq. (54).)

Figure 5 is included to show the relative magnitude of change in attenuation coefficient (the imaginary part of K) from both flow and shear because the dB scale in figure **4** is somewhat misleading. It also includes the attenuation coefficients for the continuous particle velocity boundary condition. Two general conclusions can be drawn from examination of figure 2. First, the change in mode attenuation is more drastic for the (0, 0) mode than for the higher order modes; and second, for realistic boundary-layer thicknesses, the attenuation could be 1 to 2 dB more or less than calculated using the mean-flow assumption according to the direction of flow. This second conclusion is drawn from one frequency,

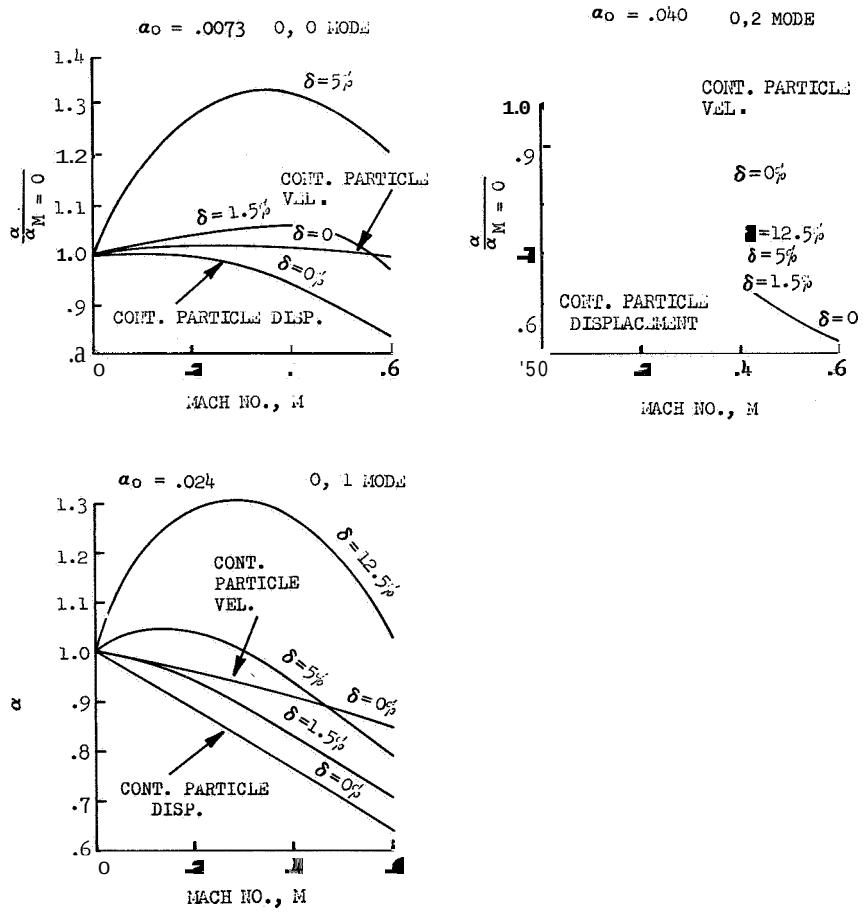

FIGURE 5.—Effect of mach number and wall shear on normalized attenuation coefficients for rectangular duct. (Duct parameters same as in fig. 4.)

one wall impedance, and one duct geometry. More parameter variations must be made to ascertain fully the potential magnitude of the effect of shear on linear attenuation.

It is also of interest to show the effect of the sheared flow on the natural mode shapes in a rigid-walled duct. This is shown in figure 6(*a*) for several laminar flow profiles. The modulus of the mode shapes for the (0, 0) and

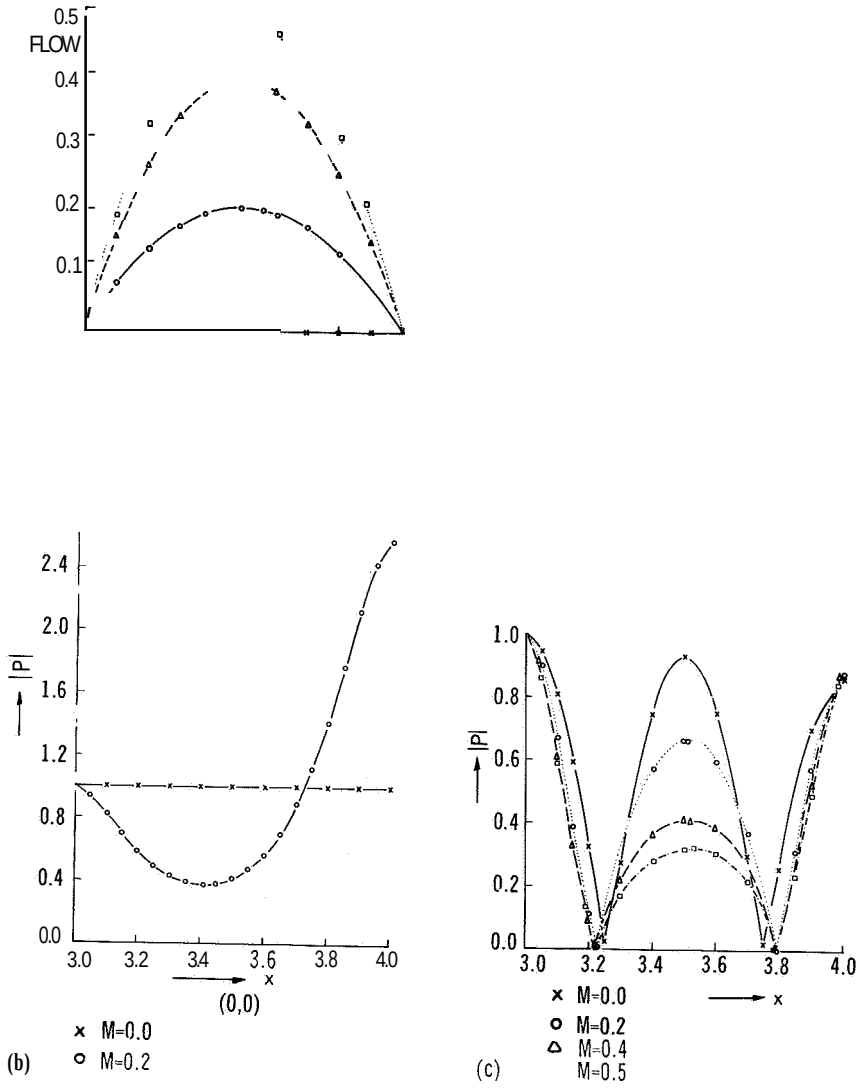

FIGURE 6.—Effect of sheared flow in mode shapes in rigid-walled annual duct. HTR = 0.75, $kL = 5\pi$, $A_0 = A_n = 0.0 + j0.0$, (*a*) flow profiles for annular duct, (*b*) (0,1) mode, and (*c*) (0,2) mode.

(0, 2) modes is shown for variations in centerline mach number of the laminar flow profile. The (0, 0) mode shape for the same wall conditions is shown in figure 7 for propagation against the sheared flow.

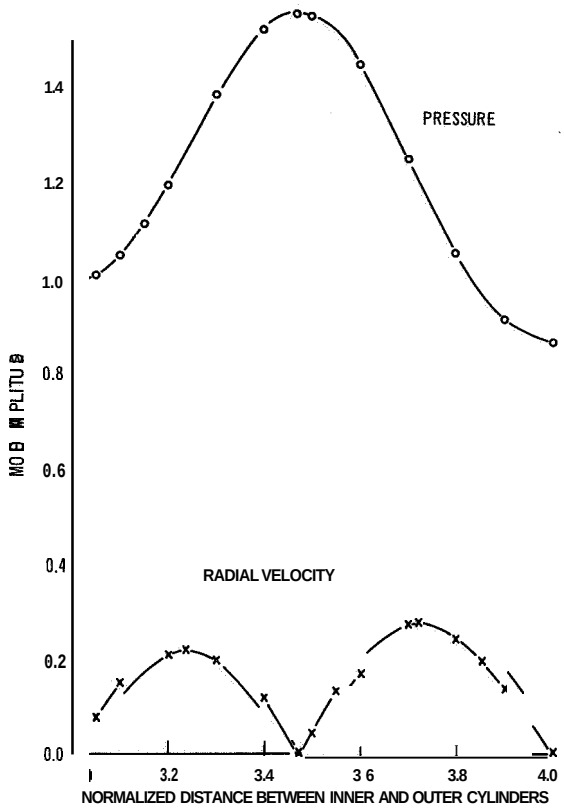

FIGURE 7.—First mode (0,0) for propagation against sheared flow in annular duct.
HTR = 0.75, $M = 0.2$, $A_0 = A_n = 0.0 + j0.0$, $kL = 2\pi$.

Figure 8 shows the effect of hub-tip ratio on the propagation and attenuation coefficients for individual modes. For hub-tip ratios above 0.4, there is very little change in the attenuation coefficients. The results suggest that one must be careful in applying measurements made from rectangular ducts (equivalent to very large hub-tip ratios) to design silencers with small hub-tip ratios.

Figures 9 and 10 show the effects of wall resistance and reactance on the mode shapes. Also, the propagation constants are included in figure 9. These calculations are for no-flow conditions.

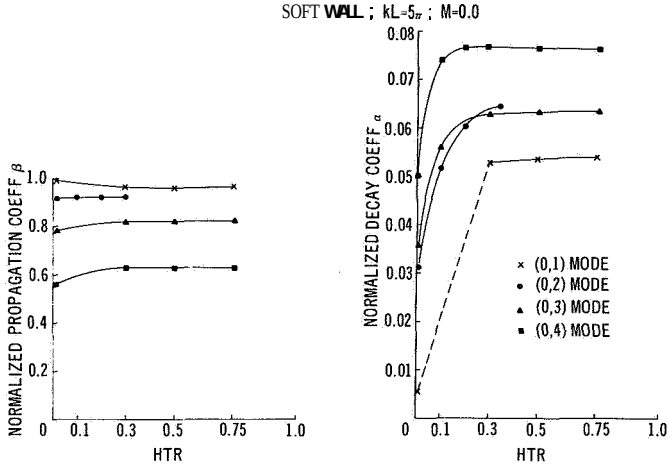

FIGURE 8.—Effect of hub-tip ratio on propagation constants, $K=\alpha+j\beta$.

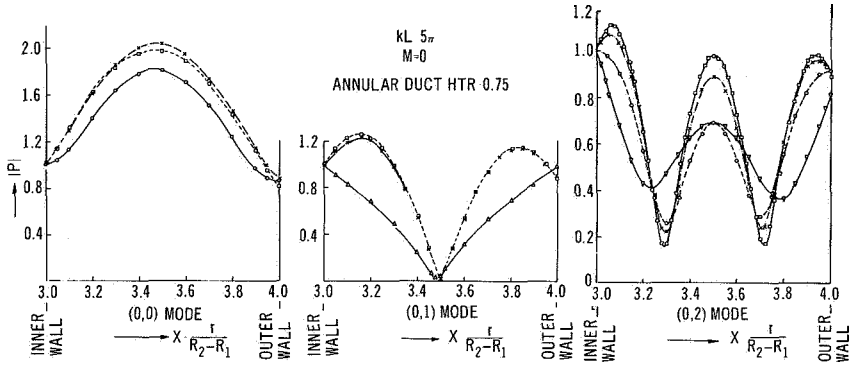

Z	a_n	β_n	α	Z	α_n	β_n	α
2.5−jo.0	Θ0.0106	0.9858	0.333	2.5−j1.0	A 0.057	0.9664	1.785
2.5+j1.0	× .007	.9877	.226	2.5+1.0	× .024	.9520	.754
2.5+j2.0	□ .007	.9890	.163	2.5+2.0	□ .016	.9545	.507

$Z=R+jx$	α_n	β_n	α
2.5−j2.0	▽ 0.037	0,9570	1.178
2.5−j0.0	Θ .061	.8966	1.918
2.5+j1.0	× .040	.8861	1.264
2.5+j2.0	□ .026	.8865	.82

FIGURE 9.—Effect of wall reactance on pressure mode shape. Z = wall impedance, α_n=attenuation constant, β_n=propagation constant, and α=dB per duct width

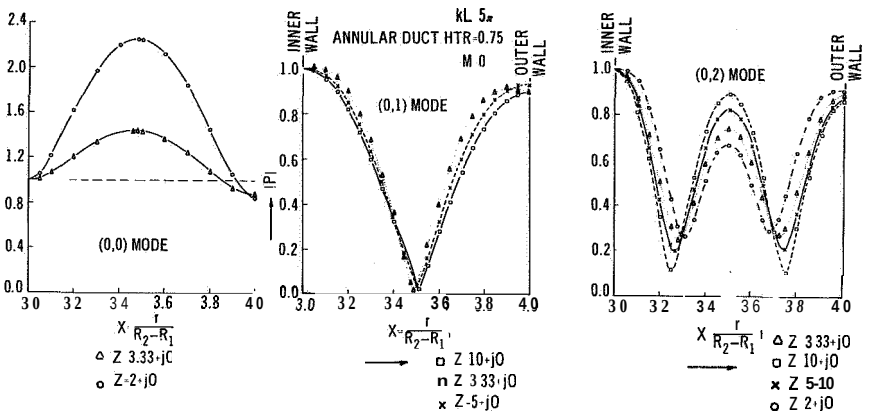

FIGURE 10.—Effect of resistance on pressure mode shape.

CONCLUSIONS

A theory has been developed that includes the effect of mean radial shear on the propagation and attenuation of sound in a uniform-geometry, acoustically lined duct. A numerical analysis technique has been developed for determining some illustrative solutions.

These preliminary numerical studies show that shear is potentially a major parameter in calculating sound propagation in lined ducts. Some results indicate the danger of using data obtained in rectangular duct experiments for design of annular duct acoustic liners, without a comparison of the data with both rectangular and annular duct theory.

REFERENCES

1. Progress of NASA Research Relating to Noise Alleviations of Large Subsonic Jet Aircraft. NASA SP–189, 1969.
2. RAYLEIGH, J. W. S.: The Theory of Sound. Dover Pub., Inc., 1945.
3. MORSE, P. M.: The Transmission of Sound Inside Pipes. J. Acoust. Soc. Am., vol. 11, 1939, p. 205.
4. MORSE, P. M.: Vibration and Sound. McGraw-Hill Book Co., Inc., 1948.
5. TYLER, J. M.; AND SOFRIN, T. G.: Axial Flow Compressor Noise Studies. SAE Trans., vol. 70, 1962, p. 309.
6. MORFEY, C. L.: Rotating Pressure Patterns in Ducts: Their Generation and Transmissions. J. Sound Vib., vol. 1, 1964, pp. 60–87.
7. DOAK, P. E.: Noise in Axial Flow Fans. Research Memo 139, Inst. Sound Vib., 1966.
8. VAIDYA, P. G.: Some Aspects of the Theory of Propagation of Periodic and Transient Sounds in Absorbent Ducts and in Rooms With an Open Window. Ph. D. Thesis, Univ. of Southampton, England, 1969.
9. RICE, E. J.: Attenuation of Sound in Soft Walled Ducts. NASA TM X–52442, 1968.
10. VAIDYA, P. G.: Noise in Axial Flow Fans. M.S. Thesis, Univ. of Southampton, England, 1966.

11. INGARD, U.: Influence of Fluid Motion Past a Plane Boundary on Sound Reflection, Absorption, and Transmission. J. Acoust. Soc. Am., vol. 31, 1959, pp. 1035–1036.
12. MORSE, P. M.; AND INGARD, U.: Theoretical Acoustics. McGraw-Hill Book Co., Inc., 1968.
13. PRIDMORE-BROWN, D. C.: Sound Propagation in a Fluid Flowing through an Attenuating Duct. J. Fluid Mech., vol. 4, 1958, p. 393.
14. TACK, D. H.; AND LAMBERT, F. F.: Influence of Shear Flow on Sound Attenuation in Lined Ducts. J. Acoust. Soc. Am., vol. 38, 1965, p. 655.
15. MUNGUR, P.; AND GLADWELL, G. M. L.: Acoustic Wave Propagation in a Sheared Fluid Contained in a Duct. J. Sound Vib., vol. 9, 1969, pp. 28–48.
16. JAHNKE, E.; AND EMDE, F.: Tables of Functions. Dover Pub., Inc., 1945.
17. HILDEBRAND, F. B.: Introduction to Numerical Analysis. McGraw-Hill Book Co., Inc., 1956.

III

INLET DUCT NOISE, BOUNDARY LAYER NOISE, DIAGNOSTIC TECHNIQUES

Chairman: **P. J. WESTERVELT**

311-986 0-LT-70—22

BASIC AIRCRAFT NOISE RESEARCH AT THE LANGLEY RESEARCH CENTER

Philip M. Edge, *Jr.*, and Harvey H. Hubbard
NASA Langley Research Center
Hampton, Va.

A brief description is given of that part of the Langley basic research program that relates primarily to aircraft noise. Included are studies of propulsion noise sources; duct treatment, propagation and radiation; effects of noise on structures and humans; and the effects of the atmosphere on aircraft ground runup and fly-over noise attenuation.

INTRODUCTION

Aircraft types	Problem areas		
	Aircraft structure	Aircraft interior	Airport community
General aviation..			✓
Current commercial			✓
V/STOL transport...	✓	✓	✓
STT..	✓	✓	✓
HST	✓	✓	✓

aircraft, the main problem is the noise that radiates into the communities near airports. The structural integrity and interior noise problems can be adequately controlled for current general aviation and commercial aircraft by special attention to design details. For the jumbo-jet class of transport aircraft, there may be particular concern for the interior noise environments because of the large dimensions of the passenger compartments.

With regard to future vehicles such as V/STOL and supersonic and hypersonic transports (SST and HST), community noise problems will be very significant, as will those problems of interior noise and structural integrity. As an example, it is projected that the external noise characteristics of the V/STOL transport may be a dominant factor in its design and will determine its success in commercial operations. It is also anticipated that noise transmission and structural integrity problems on future SST and HST vehicles will be especially severe at the rear of the aircraft where both the engine and the boundary-layer noise loads are most intense.

The Langley basic aircraft noise research program covers many areas. Propulsion noise source studies relate to the noise from jet exhausts, fans and compressors, and propellers and rotors. These studies include generation, prediction, and reduction considerations, and constitute a major portion of the Langley program. Duct acoustics involves propagation phenomena in ducts and the performance of absorptive treatments. Boundary-layer noise studies relate to the nature of the associated loads on structures and the predictions of those loads. These topics are dealt with in another paper of the conference by Harold B. Pierce and William H. Mayes.[1] Structural response research emphasizes noise transmission and sonic fatigue for flight structures and noise transmission and transient vibrations for building structures. Human factor studies relate primarily to the effects of noise on annoyance and task performance. Noise propagation through the atmosphere involves the ground-to-ground and air-to-ground situations that are significant in the radiation of noise from aircraft takeoffs and landings and ground operations into communities near airports.

PROPULSION NOISE SOURCES

Jet-exhaust-noise research projects are categorized under geometric arrangements and flow considerations. Geometric arrangement studies involve the basic noise characteristics of peripheral slot nozzles that are of interest for application to ground-effect machines and of straight-slot nozzles of the type incorporated in jet-augmented flap devices. This latter work is supported under a grant with the University of Tennessee.

---

[1] *See* p. 337.

The phenomenon of acoustic shielding of one jet by another is of interest in connection with the prediction of the noise from multitube nozzles and from multiengine airplanes. Pertinent model jet measurement studies at the Langley Research Center involving Boeing Co. personnel and equipment have recently been completed.

Flow considerations involve the establishment of jet-noise source locations and the effects of velocity profile, density, and flow additives on noise radiation. The establishment of the location of noise sources in the jet is a subject of a cooperative program with the Boeing Co. Velocity profile studies are currently focused on evaluation of possible beneficial directivity effects. The effects of jet density on the noise from jets has been under study at the Lockheed-Georgia Co. and is the subject of another paper of the conference, by H. E. Plumblee.[2]

The idea of adding substances to the flow to change the mixing patterns of the jet or absorb acoustic energy is the subject of several grant- and contract-supported studies. Secondary air addition is under study at Syracuse University; the addition of solid particles, at New York University; the addition of ionized particles as a tool in controlling the body forces of the jet, at Pennsylvania State University; and evaluations of foams as damping media are beginning at Thompson Ramo Wooldridge, Inc. Detailed results from the Syracuse University and New York University studies are presented in other papers of this conference by D. Dosanjh, Amr N. Abdelhamid, and James C. Yu;[3] and L. Arnold and S. Slutsky,[4] respectively.

Propeller and rotor noise research are important research items. The ducted propeller, which is under consideration for some operational STOL and general aviation applications, is being studied both from the standpoints of the noise loads on the internal duct structure and its far-field noise radiation. A theory has been developed for predicting the noise at any location inside the duct and for predicting the oscillating structural loads particularly on the inside duct surfaces. The coupling of resonators to the duct is being considered as a means of reducing the far-field noise radiation in experimental and analytical work being done by the Bell Aerosystems Co.

Blade loading variations as a functions of azimuth angle around the propeller or rotor disk can occur as a result of several phenomena such as nonuniform in-flow and variation of the in-flow angle. Such in-flow angle effects are being evaluated over a range of operating conditions by the application of recently developed theory.

Rotor-noise source identification is under study at the University

---

[2] *See* p. 113.
[3] *See* p. 63.
[4] *See* p. 137.

of Southampton in both analytical and experimental studies. Some modifications of existing helicopters to reduce the radiated noise are being evaluated in overflight measurement studies. The phenomenon of unloading the rotor in flight by the activation of winglike lifting devices is also being evaluated.

Fan and compressor noise studies (fig. **1)** include considerations of the sources as well as the propagation of the noise along the duct and into the radiation field. Noise generation and prediction are considered both for a rotor alone and for a rotor and stator in combination in which interference effects are significant. In this connection the Lowson noise prediction method is being applied by Wyle Laboratories to compressors whose noise radiation characteristics and operating conditions are known. The need to consider the load as distributed on the blade rather than concentrated at a point is also being studied. With regard to duct effects, consideration is given to finite length, the axial velocity of airflow, hard and absorptive walls, the axial variation of cross section, and inlet geometry.

Duct treatment studies involve the properties and behavior of candidate materials and the development of associated research capabilities. Results suggest that several different types of materials may be appropriate for use as duct acoustic treatment in jet-engine nacelles. At the present time there is not sufficient information concerning the acoustic or structural performance of these materials to permit the design of an optimum duct lining. Such designs are complicated by adverse environmental factors and aerodynamic flow interactions. Under development are advanced experimental capabilities for evaluating acoustic behavior of such materials at various angles of incidence and sound field modal patterns; at extremely high noise levels; and in the presence of airflow, including interactions with the boundary layer. Three of the contracts

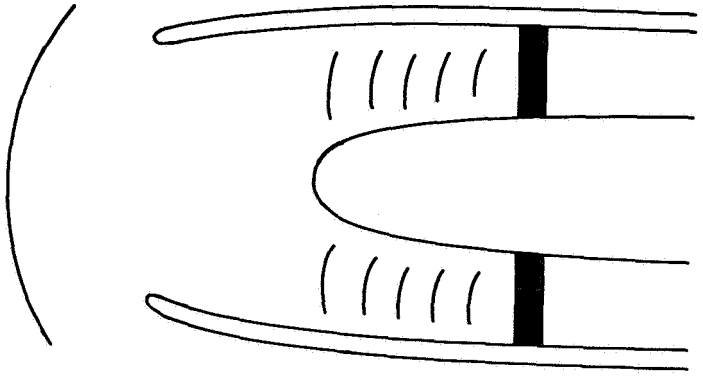

FIGURE I.—Fan and compressor noise

are held by Robert W. Benson & Associates, Ling-Temco-Vought Research, and Pennsylvania State University.

The use of such materials as fiber metal, for instance, in airplane structures is difficult because of the fact that it does not have a linear stress strain curve and may be particularly susceptible to sonic fatigue damage. Several structural evaluations including fatigue and static strength behavior have been conducted. Test equipment is under development to simulate the combined intense noise and elevated temperature conditions under which these materials must perform for basic sonic fatigue test purposes.

BUILDING RESPONSES

The manner in which buildings respond to aircraft flyover noise excitation is an important consideration in inside observations as suggested in figure 2. Involved are such phenomena as noise transmission losses of house structures; the vibration responses of house components such as rooms, walls, panels, and windows; and vibration induced interior noise. Houses respond differently to aircraft noise, and research may lead eventually to improved designs for noise-resistant structures.

HUMAN REACTIONS

The problems involving human responses are being studied from two points of view: the annoyance of people residing in communities near airports and the possible interference of noise with task performance for persons in noise and vibration environments. The subjective annoyance reaction studies include both laboratory and overflight situations

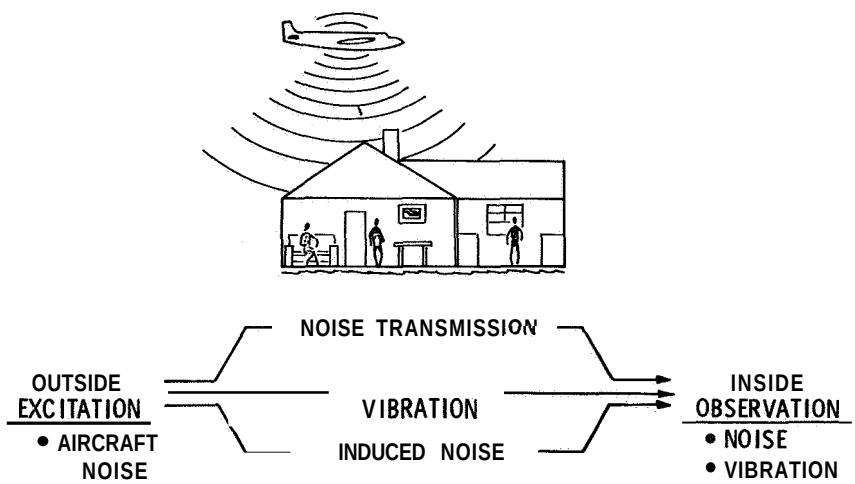

FIGURE 2. —Building responses.

and the involvement of human-subject juries. In addition, such items as sleep interference, the significance of personality traits, and the significance of other sociometric factors are included. The definition of noise and vibration environments in various flight vehicles is underway, and this work is complemented by psychomotor studies to evaluate the effects of noise on the performance of tasks requiring both manual and mental dexterity. Contract studies are being performed at Bolt, Beranek & Newman, Inc., Stanford Research Institute, and North Carolina State University.

NOISE PROPAGATION

An adequate knowledge of the propagation losses and the way in which the atmosphere is involved in aircraft flyover noise and ground to ground propagation is not available, but both acoustic and atmospheric data are being accumulated systematically. Such factors as surface conditions, atmospheric temperature, and humidity gradients are being evaluated by Bolt, Beranek & Newman, Inc., with regard to their effects on noise propagation from aircraft at altitudes up to about 3000 feet. The objective of such research is the correlation of the acoustic and atmospheric data in order to evaluate propagation losses and to develop usable prediction methods, which are vital to the design, operation, and noise certification of aircraft.

DESCRIPTION OF HYPERSONIC BOUNDARY LAYER NOISE FLIGHT MEASUREMENT PROGRAM

Harold B. Pierce and William H. Mayes
NASA Langley Research Center
Hampton, Va.

A proposed reentry flight experiment for which detailed aerodynamic measurements will be made provides the opportunity for a basic boundary-layer noise study. This paper deals with the need for boundary-layer noise information in the hypersonic-speed range and describes a research program designed to obtain this information.

Illustrated in figure 1 are the sources of flow-induced noise loads for a flight vehicle. The fluctuating pressure loads on the surface of the vehicle

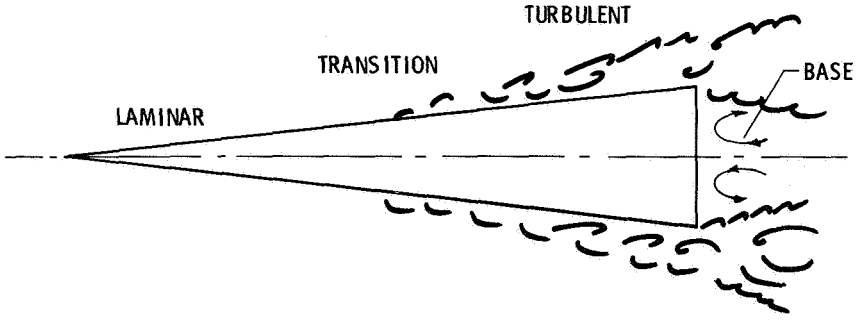

FIGURE 1.—Schematic diagram indicating various flow regimes pertinent to boundary layer induced noise loads for a flight vehicle.

depend on the type of flow; that is, whether it is laminar, transitional, or turbulent. On the vehicle base, the fluctuating pressure loads are caused by the separated flow of the wake.

Anticipated problem areas for future high-speed flight include structural integrity and interior environment. The fatigue loads caused by the fluctuating acoustic pressures may determine design requirements for the skin of hypersonic cruise and logistic resupply vehicles. Fluctuat-

ing base pressures are an important design consideration for vehicles such as the Viking Mars Lander. With regard to the interior environment, the vibrations and noise transmitted through the structure can adversely affect components in guidance systems; in the case of manned vehicles the effectiveness of flightcrews may be compromised by such factors. The lack of reliable data may thus lead to vehicle overdesign in an effort to assure mission success.

NATURE OF THE PROBLEM

The severity of flow-induced responses for flight vehicles is suggested by the data of figure 2, which were measured on an Air Force LORV–6

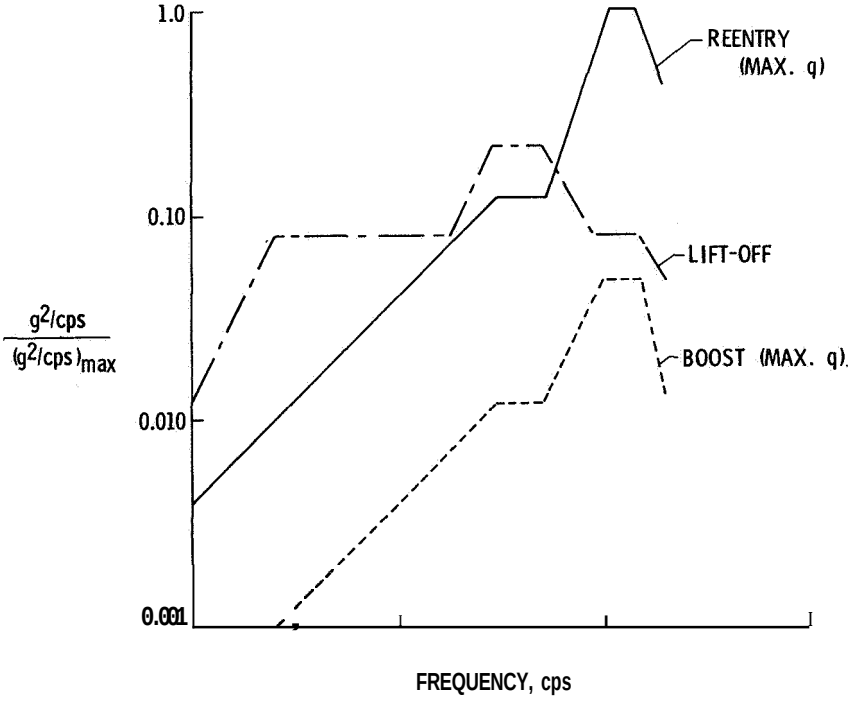

FIGURE 2.–Vibration spectra measured on an Air Force LORV 6 vehicle during launch and reentry phases of flight.

vehicle (ref. 1). In this figure, the maximum dynamic pressure reentry vibration spectrum is compared with similar spectra obtained at liftoff and during the boost-phase maximum dynamic pressure. It can be seen that the reentry vibration spectrum has a peak value markedly higher than those associated with the engines at liftoff and the airflow during boost.

Unfortunately, these high levels of vibrations are not readily predictable. because there is little acoustic loading information available for

the high-velocity conditions of reentry. To obtain such acoustic information, a definitive experiment to measure both acoustic data and related aerodynamic data is necessary. The measurements desired in an experiment of this type include acoustic measurements, as well as necessary related aerodynamic parameters. Acoustic measurements include the levels or magnitudes, frequency spectra, and spatial correlations. It is noted that each point on the acoustic-level time history represents a summation of the randomly fluctuating pressures over the entire frequency spectrum. In addition to the acoustic levels, both the frequency spectra and spatial correlations are important considerations with respect to the vibration modes of the vehicle structure. To properly associate the acoustic data with related local aerodynamic parameters, measurements of mach number, dynamic pressure, Reynolds number, and boundary-layer thickness are essential.

The status of acoustic data and the prediction theory for hypersonic speeds are our next concern. In figure 3, measurements and predictions

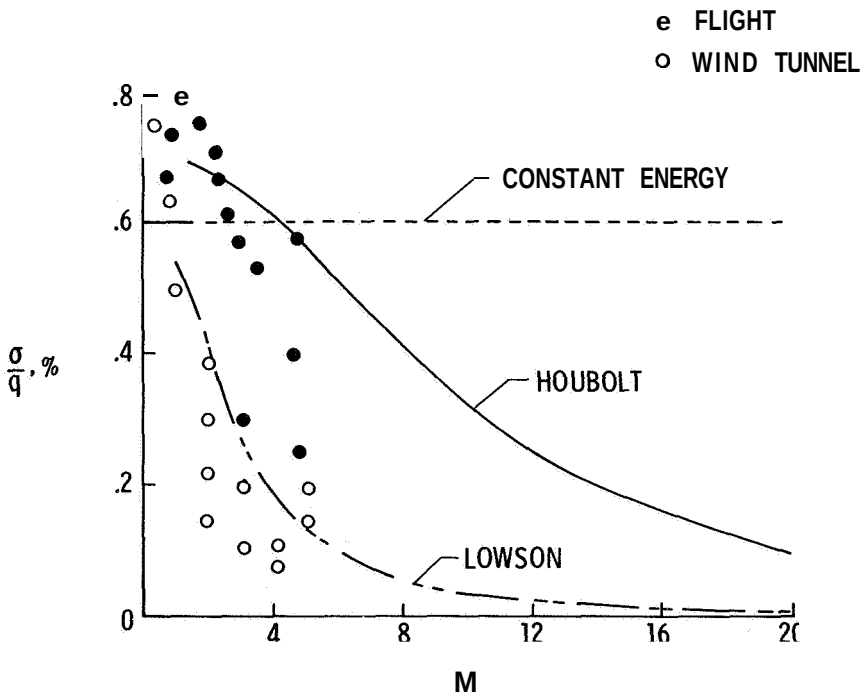

FIGURE 3. —Summary of experimental and theoretical acoustic loadings for **a range of mach numbers.**

of the root-mean-square values of acoustic loading σ expressed as a percentage of dynamic pressure q are plotted as a function of mach number. The points represent the available supersonic experimental

data (refs. 2 and 3) and the curves represent three prediction theories (refs. 4 and 5).

The experimental data include wind-tunnel (open symbols) and flight data (solid symbols). The wind-tunnel data were obtained from tests on different configurations in several facilities, and the flight data include results from the X–15, XB–70, and the Scout vehicle. There is an order-of-magnitude scatter in both the wind-tunnel data and in the flight data. Although the reasons for this scatter are not fully understood, it is believed that the various experimental techniques used and the uncertainties about the local flow conditions would partly account for it.

There is substantial subsonic experimental data (not shown) to indicate that the acoustic loading values are about 0.6 percent of the dynamic pressure (ref. 5). The constant energy prediction is simply an extrapolation of these subsonic data to hypersonic speeds. The Houbolt and Lowson theories were developed especially for the high-speed range. Each is semiempirical in nature, with Houbolt's theory being primarily influenced by fragmentary flight data at low-supersonic speeds, while Lowson's was influenced by fragmentary low-supersonic mach-number wind-tunnel data. The predicted acoustic loading values differ markedly at high mach numbers for the three methods, and these lead to widely different vehicle structure surface-weight estimates.

Some simplified estimates of the skin-surface weights for hypersonic cruise vehicles have been made, and the results are tabulated in table I.

TABLE I. – *Relative Unit Surface Weight*

M	Constant energy		Houbolt		Lowson	
	Fatigue	Noise reduction	Fatigue	Noise reduction	Fatigue	Noise reduction
0.8	1.0	1.0	1.0	1.0	1.0	1.0
3.	2.2	2.2	2.1	2.0	1.3	1.0
12"	8.0	2.0	4.0	.8	1.0	.1

Dynamic pressure has been shown to be a strong factor in acoustic loading, and some vehicles reach very large dynamic pressures in their normal mach number and altitude operating ranges, as illustrated in figure 4. Shown in this figure are values of dynamic pressures for current aircraft and for proposed supersonic and hypersonic cruise vehicles

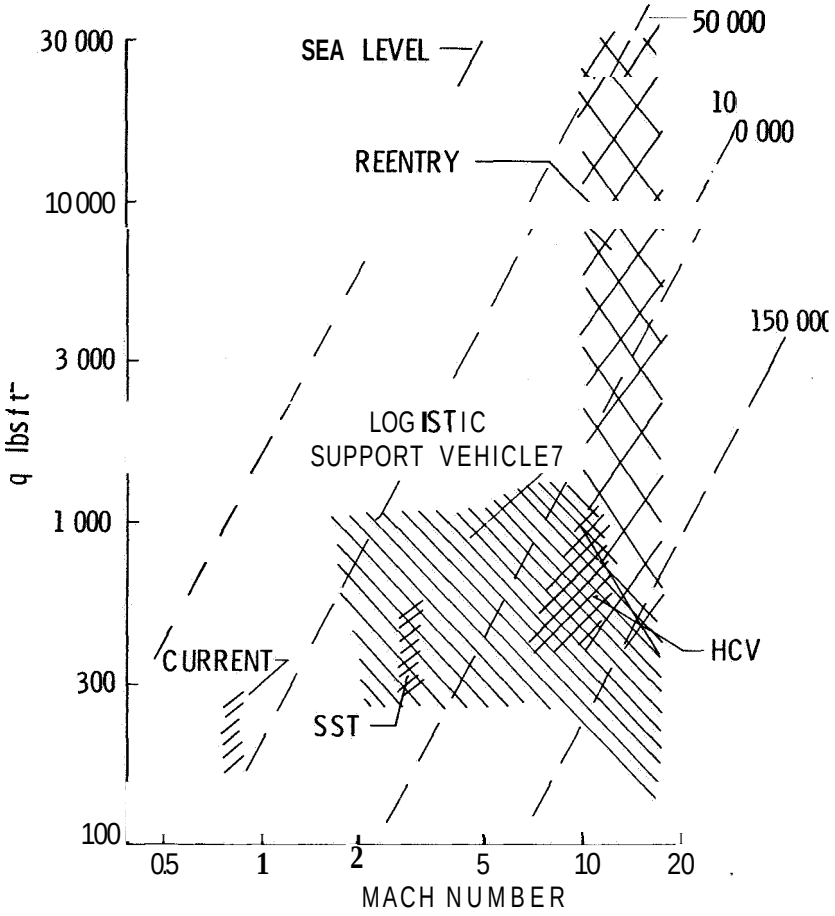

FIGURE 4.—Dynamic pressures associated with the operations of several types of flight vehicles.

Also shown is the operating range for the reentry-type vehicles that have dynamic pressures on the order of 30000 lbs/ft². This latter type of vehicle would be used for the proposed experiment.

PROPOSED FLIGHT EXPERIMENT

The sketches of figure 5 indicate the nature of the vehicle and some of the instrumentation. The vehicle is a slender cone having a length of

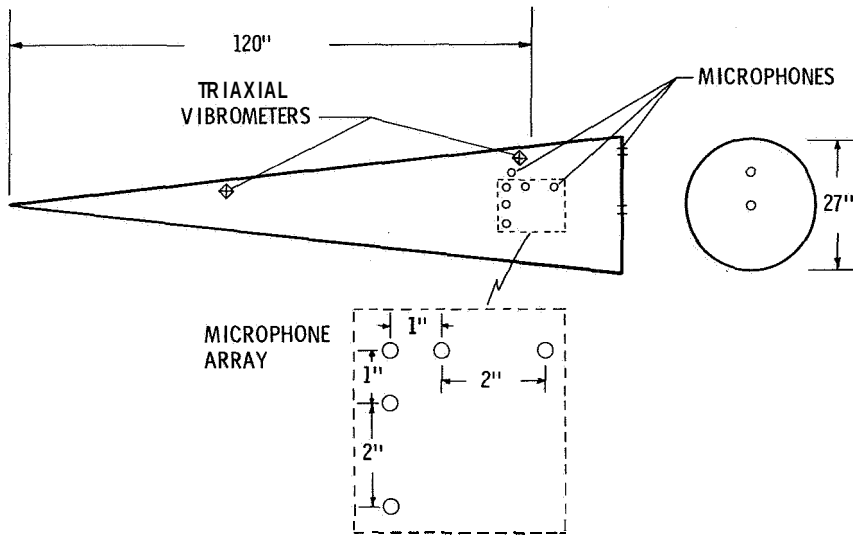

FIGURE 5.—Schematic diagram showing the shape and dimensions of the flight vehicle and location of instrumentation for a proposed hypersonic boundary layer noise experiment.

about 12 ft, a base diameter of 27 in., and a transpiration cooled nose tip. It would operate at a mach number of approximately 20 and at Reynolds numbers up to 500 million based on length from leading edge to the measuring point. Because an aerodynamic heating experiment is also included on the vehicle, there is extensive instrumentation to obtain pressure and temperature patterns over the entire vehicle, boundary-layer thickness, Reynolds numbers, mach numbers, and dynamic pressures.

The types and locations of the acoustic and vibration sensors are shown schematically. The magnitudes and spectra of the acoustic loads will be determined with a high-frequency (200000-Hz), wide-dynamic-range transducer ported to the vehicle surface. Two microphones having a 10000-Hz frequency range are ported to the base. The microphone array as shown in the inset sketch will be used to determine the correlation or spatial distribution of the loading. It consists of five ported microphones of the type previously developed for reentry flights (ref. 6). These microphones have about 5000-Hz response and provide phase information required to determine the correlation of the fluctuating pressure loads. Triaxial vibrometers located forward and aft will be used to determine the associated vehicle dynamic responses.

CONCLUDING REMARKS

A review of boundary-layer noise research indicates that prediction theories, which have been established by low-speed wind-tunnel and

flight data, differ markedly at hypersonic speeds where valid data are not available. A proposed experiment has been described for the purpose of obtaining basic boundary-layer noise information at hypersonic flight speeds. This experiment includes measurements of skin-surface pressures, vehicle base pressures, and vehicle vibrations along with detailed measurements of local aerodynamic flow parameters. The information obtained would be valuable for evaluating existing theories and for establishing reliable methods for predictions of acoustic loadings for a variety of advanced high-speed vehicles.

REFERENCES

1. JOHNSON, R. I., ED.: Boundary Layer Technology Flight Test Experiment. Re-Entry Systems, GE, Jan. 1969.
2. SPEAKER, W. V.; AND AILMAN, C. M.: Spectra and Space-Time Correlations of the Fluctuating Pressures at a Wall Beneath a Supersonic Turbulent Boundary Layer Perturbed by Steps and Shock Waves. NASA CR–486, May 1966.
3. BIES, DAVID ALAN: A Review of Flight and Wind Tunnel Measurements of Boundary Layer Pressure Fluctuations and Induced Structural Response. NASA CR–626, Oct. 1966.
4. HOUBOLT, JOHN C.: On the Estimation of Pressure Fluctuations in Boundary Layers and Wakes. Technical Information Series no. 66SD296, GE Missile and Space Division, Aug. 3,1966.
5. LOWSON, M. V.: Prediction of Boundary Layer Pressure Fluctuations. Wyle Laboratories (AFFDL TR–67–167, ASTIA no. AD 832715), Apr. 1968.
6. HELLER, HANNO H.; AND WIDNALL, SHELIA E.: Dynamics of an Acoustic Probe for Measuring Pressure Fluctuations on a Hypersonic Re-Entry Vehicle. J. Acoust. Soc. Am., vol. 44, no. 4, Oct. 1968.

PROPAGATION OF WAVES IN AN ACOUSTICALLY LINED DUCT WITH A MEAN FLOW

Edward J. Rice
NASA Lewis Research Center
Cleveland, Ohio

An analytical model is presented that describes the propagation of an initially plane pressure wave in an acoustically lined cylindrical duct with a uniform steady gas flow.

The theory predicts an optimum wall impedance for which a maximum sound-power attenuation is obtained. These optimum conditions are a function of duct geometry, sound frequency, and the steady flow mach number. The maximum possible sound-power attenuation was found to be independent of mach number, although the wall impedance at which this attenuation is obtained was dependent upon mach number.

Previous work with this model without steady flow has indicated that it is a useful technique for optimizing acoustic liner design at least for broadband noise. The present paper concentrates mainly on the differences between the zero and finite mach number theory. Both negative and positive mach numbers are considered to simulate acoustic liners in the fan inlet and exhaust ducts, respectively.

This paper presents an analytical model that may provide a technique for the optimum design of an acoustic liner for broadband noise attenuation in a duct with steady flow. A complete parametric study of the model without steady flow was presented in reference 1. This paper will therefore concentrate on the differences observed when the model was extended to include the effects of a uniform steady flow.

Reference 2 provides a comparison of the no-flow model with experimental data. Two inlet suppressors were tested on a 5-65 turbojet engine operated at very low inlet mach number. The agreement between theoretical and experimental sound-power attenuations was excellent in the portion of the noise spectrum containing the broadband noise. Further experimental verification of the extended theory at high mach number is still required.

The present theory is a limiting case of the theory found in references 3, 4, and 5 where concentration was centered on the refraction of sound by a boundary layer. The uniform steady flow profile assumed in this paper has the advantage that it is still simple enough to perform a complete parametric study of the variables involved in an acoustic liner design. Corrections due to boundary-layer refraction can then be considered in the acoustic liner design if they are of sufficient importance.

SYMBOLS

B_j	coefficient for the jth characteristic function of acoustic pressure
c	speed of sound, fps
D	duct diameter, ft
dB_{max}	maximum possible sound power attenuation for a given η and LID, dB
E	acoustic power, ft-lb_f/sec
E_{jk}	acoustic power contribution of the jth and kth pressure or velocity solutions, ft-lb_f/sec
f	sound frequency, Hz
i	$\sqrt{-1}$
I	acoustic power flux, lb_f/sec/ft
I_{jk}	acoustic power flux contribution of the jth and kth pressure or velocity solutions, lb_f/sec/ft
J_n	Bessel function of the first kind, of order n
L	duct length, ft
L/D	duct-length-to-diameter ratio
M	uniform steady flow mach number
p	acoustic pressure, $\sum_j p_j$, psi
p_j	acoustic pressure contribution of jth characteristic function, psi
p_j^*	complex conjugate of p_j, psi
Q_j	$1-M(\tau_j-i\sigma_j)$
r	radial coordinate, ft
r_w	duct radius, ft
t	time, sec
v_j	acoustic particle velocity contribution of jth characteristic function, fps
v_{rj}	radial component of v_j, fps
v_{xj}	axial component of v_j, fps
v_r	radial component of acoustic particle velocity, $\sum_j v_{rj}$, fps
v_x	axial component of acoustic particle velocity, $\sum_j v_{xj}$, fps
x	axial coordinate
Z	liner acoustic impedance, $lb_m/ft^2/sec$
α_j	complex eigenvalue of jth radial characteristic solution
η	frequency parameter, Df/c
θ	specific acoustic resistance
θ_m	optimum value of θ
$\theta_{m,0}$	optimum value of θ for $M=0$
ζ	density, lb_m/ft^3

σ_j, τ_j	transmission parameters for jth characteristic function (see eq. (6))
χ	specific acoustic reactance
χ_m	optimum value of χ
$\chi_{m,0}$	optimum value of χ for $M=0$
ω	circular frequency, rad/sec
$(\ )^*$	complex conjugate

ANALYTICAL MODEL

The geometry and the assumptions upon which the present theory is based are shown in figure 1. The acoustic liner is located on the outer

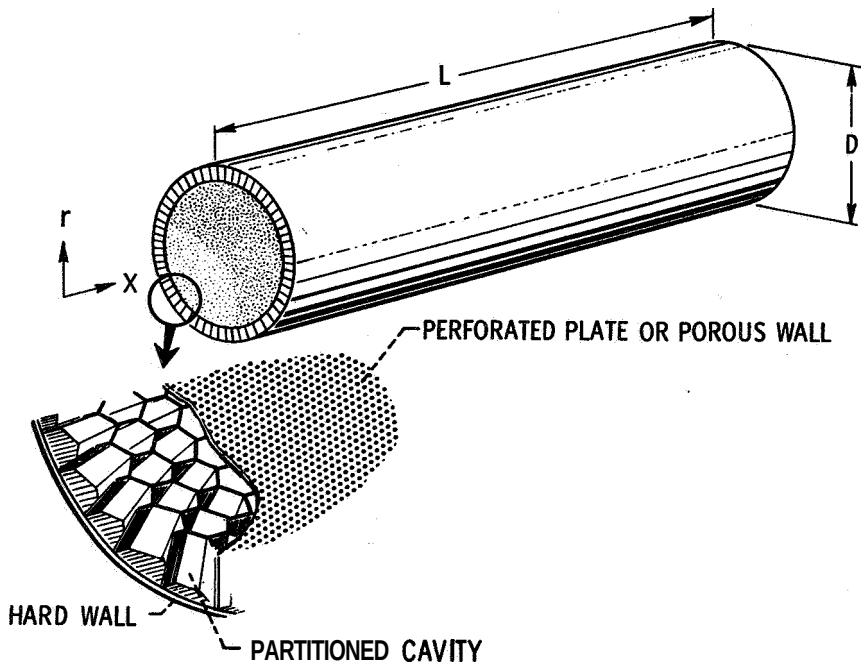

FIGURE 1.—Analytical model. Assumptions: linearized equations, uniform steady flow, no end reflections, uniform wall impedance, plane pressure wave at duct entrance. Results: pressure and velocity at any point in duct, sound power attenuation. Parameters: Df/c, L/D, wall resistance, wall reactance, steady flow mach number.

radius of a cylindrical duct. The expanded view of the liner shows a perforated plate mounted upon a honeycombed backing cavity forming an array of Helmholtz resonators. This construction is shown only as an example of how a wall of low acoustic impedance might be obtained. The essential requirements of the wall to satisfy the assumptions of the present model are as follows. The hole spacing is small compared to the

sound wavelength so that the wall impedance is uniformly distributed. Waves cannot run in the back cavity, and the wall is point reacting.

The sound-pressure waves will enter the duct at $x=0$ and run in the positive x-direction. A positive mach number will indicate steady flow in the positive x-direction thus simulating a fan exhaust condition. A negative mach number simulates a fan inlet.

Additional assumptions made in the analysis are as follows. The sound-pressure level in the duct is sufficiently small that the linearized wave equation may be used. The steady flow in the duct is uniform with radius and length. The duct is properly terminated or of sufficient length such that no end reflections occur. The wall impedance is uniform and does not change with length. This last assumption can be relaxed by matching the solutions at the joining planes of several short ducts within which the wall impedance can be considered not to vary.

The linearized wave equation with uniform steady flow is (ref. 6)

$$\nabla^2 p=\frac{1}{c^2}\frac{\partial^2 p}{\partial t^2}+\frac{2M}{c}\frac{\partial^2 p}{\partial x\,\partial t}+M^2\frac{\partial^2 p}{\partial x^2} \tag{1}$$

With the left side of equation (1) expressed in cylindrical coordinates, the axisymmetric, separable solutions for acoustic pressure that are periodic in time can be written as

$$p_j=B_j e^{i\omega t}J_0\left(\alpha_j\frac{r}{r_w}\right)e^{-\frac{\omega}{c}(\sigma_j+i\tau_j)x} \tag{2}$$

The j subscript indicates an infinite number of characteristic solutions are available. The complete solution for pressure is then

$$p=\sum_j p_j \tag{3}$$

The acoustic particle velocity that is periodic in time and exponential in x corresponding to each of the characteristic solutions in pressure is

$$v_j=\frac{i}{\zeta\omega Q_j}\nabla p_j \tag{4}$$

where

$$Q_j=1-M(\tau_j-i\sigma_j) \tag{5}$$

and again the velocity is built up by the summation of the infinite number of characteristic solutions.

The damping and transmission parameters in equation (2) are related to the mach number and radial eigenvalues by

$$\sigma_j + i\tau_j = \frac{-iM + \sqrt{(1-M^2)\left(\frac{\alpha_j}{\pi\eta}\right)^2 - 1}}{1-M^2} \tag{6}$$

where

$$\eta = Df/c \tag{7}$$

The eigenvalues α_j and pressure coefficients B_j in equation (2) must be evaluated by the use of boundary conditions imposed at the acoustic liner surface and the duct entrance. Both α_j and Bj may be complex numbers.

Boundary Conditions

At the acoustic liner surface $(r=r_w)$, each characteristic solution must be compatible with the wall-impedance condition. The wall impedance must be specified by some independent method.[1] The wall impedance is defined as the ratio of acoustic pressure to acoustic velocity normal to the wall (in this case, radial velocity). Thus the acoustic impedance is given by

$$Z = \left(\frac{p_j}{v_{rj}}\right)_{r=r_w} \qquad j = 1, 2, 3, \ldots \tag{8}$$

When equations (2) and (4) are used in equation (8), the boundary condition can be expressed as

$$\frac{Z}{\zeta c\eta} = \frac{i\pi J_0(\alpha_j)}{\alpha_j J_1(\alpha_j)} Q_j \tag{9}$$

Equation (9) can then be solved for each of the α_j. Q_j also contains α_j through σ_j and τ_j, which renders the system nonorthogonal. For $M=0$, Q_j equals 1 and the solutions are orthogonal.

It should be noted that the wall-boundary condition as expressed in equation (9) uses the particle-velocity continuity concept rather than the continuity of particle-displacement concept, first applied to duct propagation by Ingard (ref. 7) and later used in references 4 and 5. The particle-displacement boundary condition was developed by Miles (ref. 8) and Ribner (ref. 9) to describe the acoustic behavior of the interface between two gases traveling at different velocities. This interface behaves like a wave traveling along a yielding but impervious membrane separating the two gases. It is not clear that an unmovable but permeable surface such as a perforated plate over honeycombed cavities should behave in the same way.

If continuity of particle displacement is used at the liner wall, Q_j will appear in equation (9) to the second power.

---

[1] *See* p. 357.

The second boundary condition involves specifying the pressure wave at the lined duct entrance $(x=0)$. It is assumed here that this pressure wave is plane and periodic. This condition can be written as

$$p=\sum_j p_j=e^{i\omega t} \qquad (x=0) \tag{10}$$

Using equation **(2)** in equation **(10)** yields

$$\sum_j B_j J_0\left(\alpha_j \frac{r}{r_w}\right)=1 \tag{11}$$

Multiplying by $rJ_0\left(\alpha_k \frac{r}{r_w}\right)$ and integrating from $r=0$ to r_w transforms equation **(11)** into

$$\sum_j B_j \int_0^{r_w} rJ_0\left(\alpha_j \frac{r}{r_w}\right) J_0\left(\alpha_k \frac{r}{r_w}\right) dr=\int_0^{r_w} rJ_0\left(\alpha_k \frac{r}{r_w}\right) dr \tag{12}$$

If the system of solutions were orthogonal (as when $M=0$), the integral on the left of equation **(12)** would equal zero except for $k=j$. A single equation would then result for each of the B_j. However, for nonzero mach number all of the integrals in equation **(12)** may be nonzero. The result is an infinite number of linear equations each containing all of the B_j's. The system of equations can be truncated at the number of terms that provides sufficient accuracy. For the results presented in this paper, the first **10** characteristic functions were used.

Sound-Power Attenuation

The sound-power flux in the axial direction for the present case of uniform steady flow can be written as

$$I=pv_x+\frac{M}{2}\left[\frac{p^2}{\zeta c}+\zeta c(v_x^2+v_r^2)\right] \tag{13}$$

This can be obtained by substitution of the first-order continuity and momentum equations into the energy equation carried to the second order, with only time-varying terms considered.

Because the pressures and velocities in equation **(13)** are summations of complex quantities, the jkth term of the sound power flux can be written:

$$I_{jk}=\frac{1}{2}\text{Real}\left\{p_j^* v_{xk}+\frac{M}{2}\left[\frac{p_j^* p_k}{\zeta c}+\zeta c(v_{xj}^* v_{xk}+v_{rj}^* v_{rk})\right]\right\} \tag{14}$$

where p_j^* is the complex conjugate of the jth term in the pressure series.

The jkth term in the sound power series is then

$$E_{jk}=2\pi\int_0^{r_w} rI_{jk}\,dr \tag{15}$$

The sound power E is then obtained by summing equation (15) over j and k.

The sound power can then be calculated at $x=0$ and $x=L$ and the sound power attenuation then is given by

$$\text{dB}=10\log_{10}\left[\frac{E_{x=L}}{E_{x=0}}\right] \tag{16}$$

RESULTS OF THE THEORETICAL MODEL

In figure 2 a particular example of the propagation of sound in a duct with finite wall impedance is presented as an illustration of the results

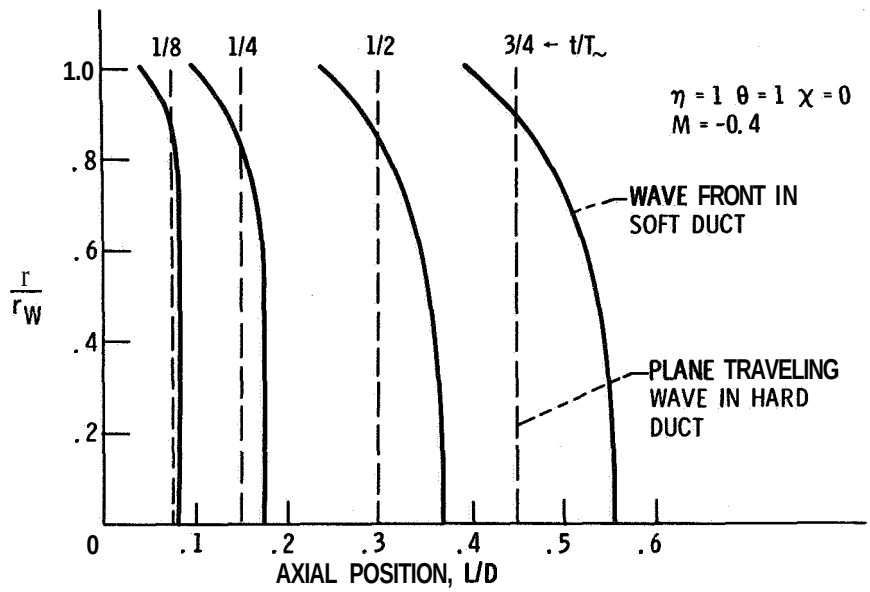

FIGURE 2.—Comparison of wave propagation in hard and soft duct.

of the theory. Radial position is normalized by the wall radius, and axial position is given in duct diameters. This example is for a wall specific resistance of 1, reactance of zero, $\eta=1$, and $M=-0.4$. The solid lines represent lines of constant phase for the pressure after four elapsed times given in fractions of a period. For comparison, the progression of the same initial pressure wave in a hard-walled duct is

given by the dashed lines for the same elapsed times. It can be seen that although the pressure wave begins as a plane wave at the duct entrance, it does not remain one as it moves down the duct. Distortion of the wave at the duct wall starts immediately at the duct entrance. As the wave travels down the duct, the distortion grows toward the axis. Very close to the duct entrance, the pressure wave is still plane near the axis but is propagating at greater than the speed of sound relative to the steady flow.

The most important result of the theory is illustrated in figure 3. Here contours of constant sound-power attenuation are plotted in the

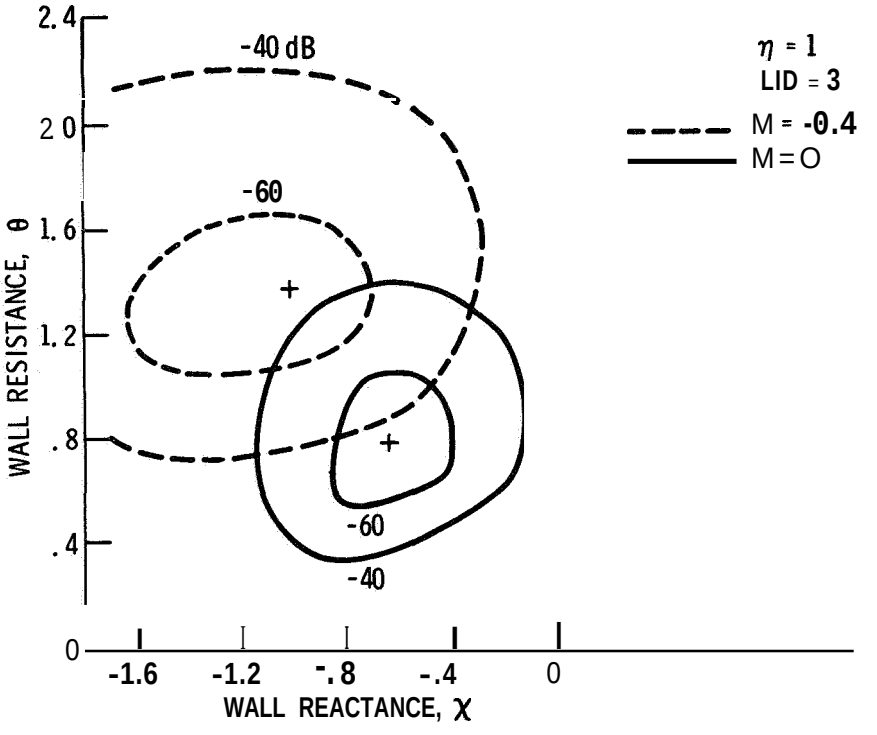

FIGURE 3.—Effect of mach number on sound power attenuation contours.

acoustic liner specific impedance plane. These contours are for the special case of $\eta = 1$, $L/D = 3$, and thus are for a particular geometry and sound frequency. Negative reactance here means a stiffness-controlled reactance dominated by the back cavity compressibility effects.

The two sets of sound-power attenuation contours shown are for $M = 0$ and $M = -0.4$. In each case the location of the maximum possible attenuation is shown by the + symbol near the center of the contours.

It can be seen that a considerable shift in the optimum liner impedance has occurred between $M = 0$ and $M = -0.4$. This type of shift is quite

general for all cases of practical interest. When compared to the zero-mach-number theory of reference 1, the optimum impedance is shifted so that negative mach number requires higher resistance and more negative reactance, while positive mach number requires lower resistance and a reactance closer to the liner resonance point. For very low values of η ($\eta < 0.5$) and high positive mach numbers, the optimum reactance can become positive.

The next two figures will show the magnitude of the maximum sound-power attenuation and the optimum wall impedance for which it is obtained.

In figure 4 the maximum possible sound-power attenuation normalized by L/D is plotted against the frequency parameter $\eta = Df/c$. Positive and negative mach numbers are considered for the two cases of $L/D = 1$ and 2. First consider the case of $L/D = 1$, with $M = -0.4$ shown by the solid line and $M = +0.5$ shown by the circles. It is seen that the results for the two mach numbers are coincident. The zero mach-number results (ref. 1) also coincide precisely with the $M = -0.4$ results. The same is true for the second case shown with $L/D = 2$. Thus the quite unexpected conclusion is that the maximum possible sound-power attenuation is independent of mach number.

The reader should be aware that an acoustic liner can be made to operate at the optimum impedance only at one sound frequency, whose value will depend upon the duct geometry and the acoustic liner con-

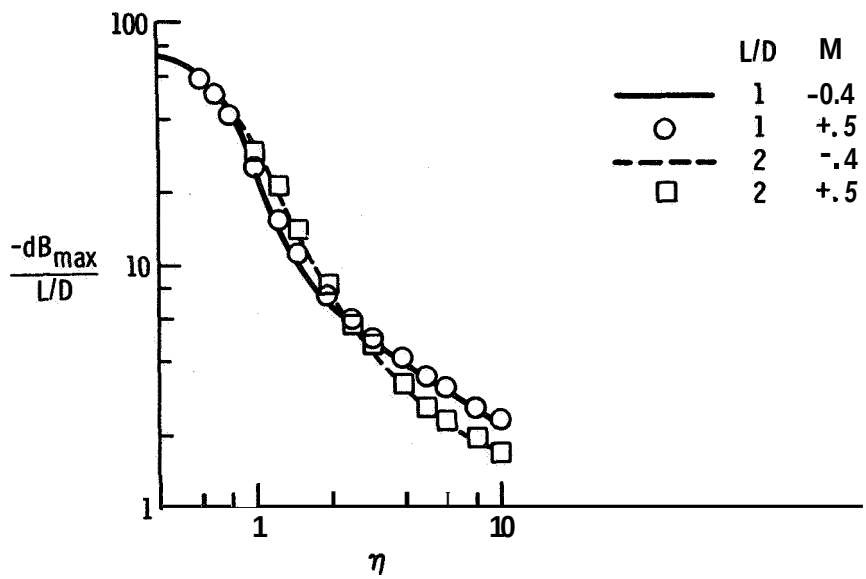

FIGURE 4—Maximum attenuation for positive and negative mach number.

struction.[2] For wall impedance that is large compared to optimum values, the approximate solution

$$\mathrm{dB} \approx \frac{-17.4(L/D)\theta}{(1+M)(\theta^2+\chi^2)} \tag{17}$$

will be valid. Equation (17) can be derived in a way analogous to that of reference 6. In reference 6, however, the quantity $(1+M)^2$ appears to be the result of the continuity of displacement boundary condition used there. From equation (17) it is seen that for operation far off optimum, the attenuation is certainly a function of mach number.

In figure 5 the optimum acoustic liner specific resistance (θ_m) and reactance $(-\chi_m)$ have been multiplied by $(1+M)$ and plotted against the frequency parameter η. This simple transformation can be seen to relate the nonzero mach number $(M=+0.5)$ optimum impedance to the results of the zero-mach-number theory. The approximate relationships can thus be written as

$$\theta_m \approx \frac{\theta_{m,0}}{(1+M)} \qquad \chi_m \approx \frac{\chi_{m,0}}{(1+M)} \tag{18}$$

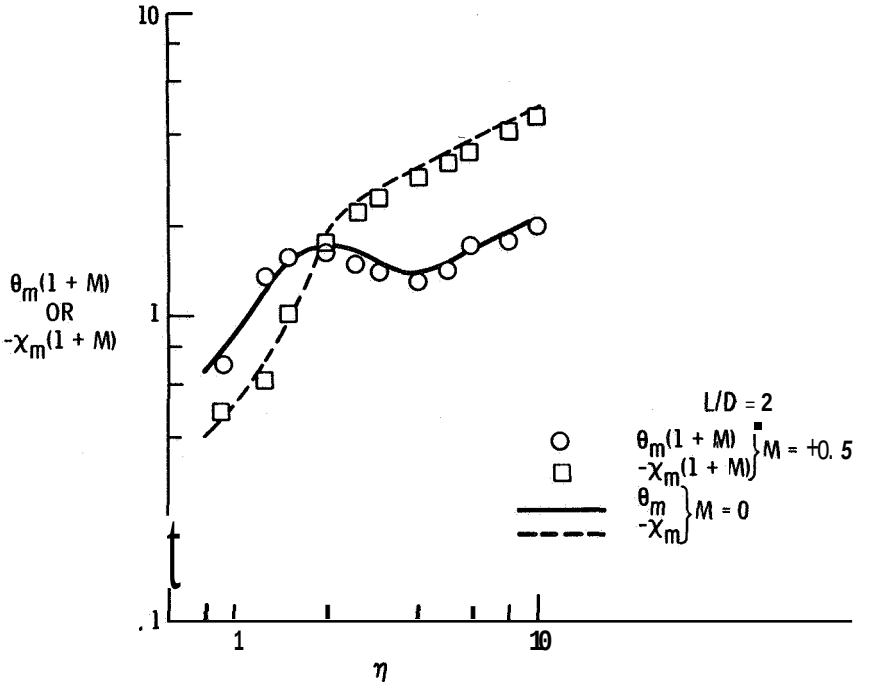

FIGURE 5.—Effect of mach number on wall impedance locus for maximum attenuation.

[2] See p. 357.

where $\theta_{m,0}$ and $\chi_{m,0}$ are for zero-mach number. Equations (18) will adequately relate the results with steady flow to the more extensive zero-mach-number results reported in reference 1 over the range of variables that are of practical interest. As stated previously for $M > 0$ and $\eta < 0.5$, χ_m can become positive. In this case the second of equations (18) will not hold because for $M = 0$, $\chi_{m,0}$ is always negative.

CONCLUDING REMARKS

An analytical approach for the determination of the optimum impedance of acoustic liners with a uniform steady flow has been presented here. This represents an extension of the work in reference 1, which was for zero-mach number. The zero-mach-number theory has been partially verified by the work presented in reference 2. The present theory for nonzero mach number must yet be verified by experimental evidence. Work along this line is proceeding at the present time.

REFERENCES

1. RICE, E. J.: Attenuation of Sound in Soft Walled Circular Ducts. Symposium on Aerodynamic Noise. NASA TM X-52442. May 1968. Also, AFOSR-UTIAS Symposium on Aerodynamic Noise. Univ. of Toronto Press, 1969.
2. FEILER, C. E.; RICE, E. J.; AND SMITH, L. J.: Performance of Inlet Sound Suppressors. Proceedings of the Conference on Progress of NASA Research Relating to Noise Alleviation of Large Subsonic Aircraft. NASA SP-189, 1968, pp. 53-57.
3. PRIDMORE-BROWN, D. C.: Sound Propagation in a Fluid Flowing Through an Attenuating Duct. J. Fluid Mech., vol. 4, 1958, pp. 393-406.
4. MUNGUR, P.; AND GLADWELL, G. M. L.: Acoustic Wave Propagation in a Sheared Fluid Contained in a Duct. J. Sound Vib., vol. 9, 1969, pp. 28-48.
5. TACK, D. H.; AND LAMBERT, R. F.: Influence of Shear Flow on Sound Attenuation in a Lined Duct: J. Acoust. Soc. Am., vol. 38, 1965, pp. 655-666.
6. MORSE, P. M.; AND INGARD, K. U.: Theoretical Acoustics. McGraw-Hill Book Co., Inc., 1968.
7. INGARD, UNO: Influence of Fluid Motion Past a Plane Boundary on Sound Reflection, Absorption, and Transmission. J. Acoust. Soc. Am., vol. 31, 1959, pp. 1035-1036.
8. MILES, J. W.: On the Reflection of Sound at an Interface of Relative Motion. J. Acoust. Soc. Am., vol. 29, 1957, pp. 226-228.
9. RIBNER, H. S.: Reflection, Transmission, and Amplification of Sound by a Moving Medium. J. Acoust. Soc. Am., vol. 29, 1957, pp. 435-441.

CURRENT UNDERSTANDING OF HELMHOLTZ RESONATOR ARRAYS AS DUCT BOUNDARY CONDITIONS

John F. Groeneweg
NASA Lewis Research Center
Cleveland, Ohio

The problem of specifying a duct-wall geometry having an acoustic impedance that satisfies a maximum attenuation condition is considered. In particular, the current understanding of the impedance behavior of a duct lining composed of an array of Helmholtz resonators is examined. Available impedance data and predictions are compared for conditions of the type experienced in engine fan ducts; namely, high sound-pressure levels, simultaneous excitation at more than one frequency, and mean flow past the wall. This review points to the changes in impedance produced by mean flow and broadband excitation as the phenomena most urgently requiring further research.

SYMBOLS

b	cavity depth
c	speed of sound
c_D	orifice discharge coefficient
d	orifice diameter
D	duct diameter
f	frequency
K	see equation (2)
L	lined duct length
M_∞	mean duct mach number
M_0	peak orifice mach number
p	pressure
t	orifice thickness
v_0	orifice velocity
δ	orifice end correction
ζ	specific acoustic impedance for a resonator array
θ	specific acoustic resistance
λ	wavelength
ν	gas kinematic viscosity
ρ	gas density
σ	open area ratio (orifice area to wall area)
χ	specific acoustic reactance
ω	angular frequency

INTRODUCTION

The problem of describing sound attenuation in soft-walled ducts is usually divided into two parts. In the first parr, the wall boundary condition is specified in terms of an acoustic impedance and the wave propagation is then analyzed. The results sought are the values of wall impedance that maximize attenuation. Before such results can be used, the second part of the problem must be solved; that is, a wall construction having the desired impedances must be specified.

This essential operation of relating wall impedance to geometric parameters and acoustic and flow variables is the subject of this paper. In particular, the current understanding of Helmholtz resonator arrays is reviewed. This basic wall geometry is of practical interest and also illustrates, at least qualitatively, the type of impedance behavior exhibited by other types of porous walls backed by resonant cavities. Calculated impedances are compared with available data to summarize what is known and to point out areas requiring further research.

MAXIMIZING SOUND ATTENUATION

Some features of the problem of matching wall-impedance behavior to maximum attenuation conditions for a duct are shown in figure 1.

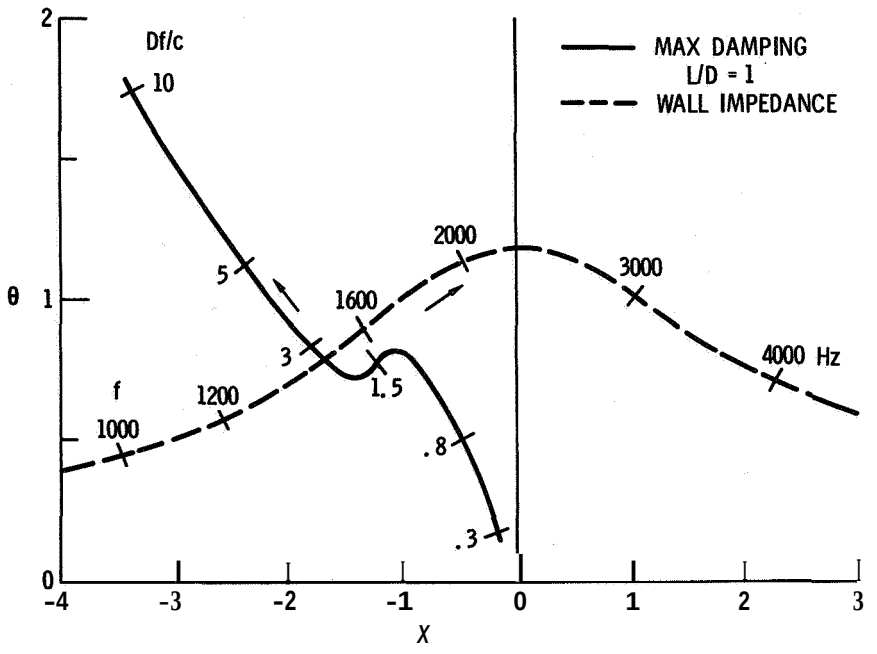

FIGURE 1.– Locus of maximum damping with superimposed wall impedance, for $\sigma = 0.054$, $t = 0.05$ in., $d = 0.052$ in., $b = 0.5$ in., and 145 dB.

A locus of maximum damping based on the propagation analysis of Rice[1] and a calculated wall-impedance characteristic for a Helmholtz resonator array are superimposed in the resistance-reactance plane. The propagation analysis indicates that maximum damping is achieved at larger negative reactances as the frequency parameter Df/c is increased. On the other hand, the wall reactance increases with frequency causing the wall-impedance locus to intersect rather than trace the maximum damping locus. As a result, damping is maximized only at the intersection point and only if the frequencies on the two curves are matched by adjusting duct diameter or resonator dimensions. Qualitatively similar reactance behavior is observed for any facing material covering resonant cavities. In any case, maximizing the damping in a given frequency range can only be accomplished if the wall-impedance characteristic is known.

HELMHOLTZ RESONATOR ARRAYS

Geometric parameters and variables associated with the duct environment that determine the impedance of Helmholtz resonator arrays are illustrated in figure 2. The mathematical boundary condition used in

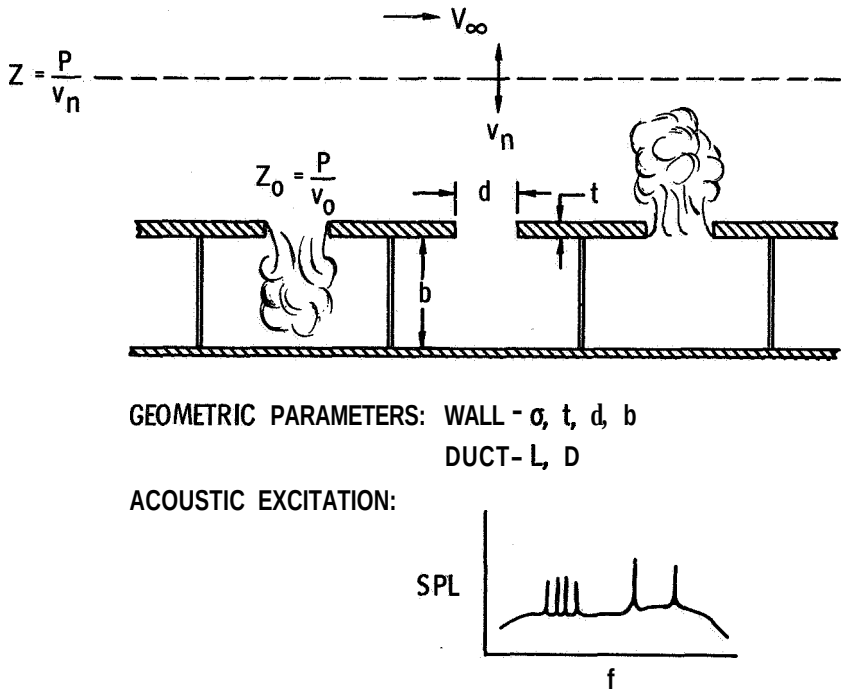

FIGURE 2.—Helmholtz resonator arrays.

[1] See p. 345.

propagation analyses is a uniform wall impedance that corresponds to the ratio of acoustic pressure to normal acoustic particle velocity fluctuations at some distance from the perforated wall. A separate acoustic impedance Z_0 may be defined for each orifice. The single-orifice impedance is related to the uniform impedance for the array by the ratio of orifice area to wall area, which is the open area ratio σ. This result is based on first-order continuity arguments to arrive at $v_n = \sigma v_0$. If the cavity partitions are thin, wall area and cavity cross-sectional area are nearly equal so that σ, cavity depth b, and orifice diameter d together specify cavity volume. In practice, the ratio of orifice thickness to diameter is usually less than 1. The two important duct dimensions are the lined length L and duct diameter D.

In addition to geometric parameters, the wall impedance depends on the acoustic and flow environment. The excitation spectrum in figure 2 shows discrete frequency spikes superimposed on a broadband level and is typical of spectra occurring in engine fan ducts. Impedance of Helmholtz resonators, particularly the resistance, is nonlinear in the sense that it depends on pressure amplitude. At high amplitudes, turbulent jets are formed alternately on the low-pressure or exit sides of the orifices. It is the turbulent dissipation of the jet kinetic energy that constitutes the primary dissipation mechanism. The mean flow in the duct, indicated by V, also affects wall behavior. Amplitude, flow, and frequency effects will receive most of the emphasis in the following discussion.

IMPEDANCE EQUATIONS

The following is a set of semiempirical equations for the impedance of Helmholtz resonator arrays:

Specific impedance for an array:

$$\zeta = \frac{Z_0}{\rho c \sigma} = \theta + i\chi \tag{1}$$

Resistance:

$$\theta = \frac{\sqrt{8\nu\omega}}{\sigma c}\left(1 + \frac{t}{d}\right) + \frac{K}{C_D^2}\frac{|v_0|}{\sigma c} \tag{2}$$

Reactance:

$$\chi = \frac{(t+\delta)\omega}{\sigma c} - \cot\left(\frac{\omega b}{c}\right) \tag{3}$$

Orifice velocity:

$$|v_0| = \frac{|p|}{\rho c \sigma (\theta^2 + \chi^2)^{1/2}} \tag{4}$$

The resistance equation (eq. (2)) contains two terms, the first of which represents viscous dissipation in the oscillatory boundary layer at the

wall and in the orifices (ref. 1). The second term, containing the magnitude of the orifice velocity v_0, is the nonlinear term that dominates at higher pressure amplitudes. It has been obtained from quasi-steady arguments based on the Bernoulli equation (ref. 2) and from a second-order fluid mechanic analysis based on the assumption that all the kinetic energy of the jets formed at high amplitudes is dissipated (refs. 3 and 4). Values of the factor K of 0.37 and 0.43 have been obtained experimentally (ref. 5) and analytically (ref. 3), respectively. The discharge coefficient C_D, which depends on σ and v_0, has been obtained' from steady flow measurements as a first approximation (ref. 5). Calculated values presented in this paper take $K/C_D^2 = 1$ for simplicity.

The reactance expression (eq. (3)) has two terms corresponding to orifice inertia and cavity reactance. An end correction 6 is added to the orifice thickness to account for the inertia contributed by oscillating the mass of gas in the vicinity of the orifice entrance and exit. Besides depending on orifice diameter and open area ratio (ref. 1), 6 also decreases with increasing amplitude and mean flow. The cotangent form of cavity reactance allows for distributed inertia and compressibility in the cavity. For small values of the argument $\omega b/c$, cot $(\omega b/c) \approx c/\omega$ b, and the compliance dominates.

To use equation (2) for resistance, orifice velocity must be known. With few exceptions, as in reference 1, pressure amplitudes rather than orifice velocities are measured. Therefore, the definition of impedance is used in equation (4) to give peak orifice velocity in terms of peak pressure. Thus, for a given geometry, pressure amplitude, and frequency, equations (2), (3), and (4) may be solved simultaneously for resistance and reactance. Effects of amplitude on 6 and effects of mean flow past the wall on 6 and θ have not been specified in these three equations.

PRESSURE AMPLITUDE EFFECTS

The variable that has received the most attention in the literature is pressure amplitude. Figure 3 shows the effects on impedance of amplitude as indicated by peak orifice mach number.

Three types of data appear: (1) pressure-phase data (ref. 5), which refer to impedances obtained by measuring the pressure oscillations at the perforated wall and in the cavity and the phase angle between the two; (2) anemometer data (ref. 2), which refer to hot-wire measurements of orifice velocity oscillations that were combined with measured pressure fluctuations to give impedance directly from the definition (eq. (1)); and finally, (3) the standard impedance. tube measurements (ref. 1), which were made with the cavity depth b adjusted to a quarter wavelength.

For comparison with the measurements, the resistance was calculated from equations (2), (3), and (4) at the conditions given for the pressure-

311-986 0-LT-70 — 24

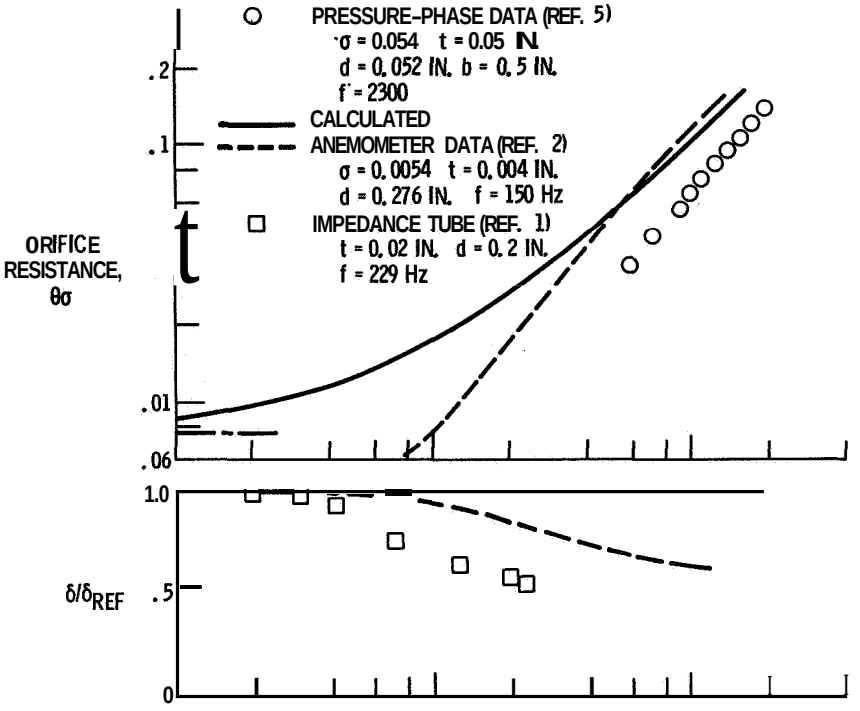
PRESSURE-PHASE DATA (REF. 5)
σ = 0.054 t = 0.05 IN.
d = 0.052 IN. b = 0.5 IN.
f = 2300
CALCULATED
ANEMOMETER DATA (REF. 2)
σ = 0.0054 t = 0.004 IN.
d = 0.276 IN. f = 150 Hz
IMPEDANCE TUBE (REF. 1)
t = 0.02 IN. d = 0.2 IN.
f = 229 Hz
ORIFICE RESISTANCE, θσ
.2
.1
.01
.06
1.0
δ/δREF
.5
0

and 6) is that the inertia contribution of the mass on the exit side of the orifice is removed under conditions of turbulent jet formation. A quantitative description of the process is not available at present.

MEAN FLOW EFFECTS

Trends in orifice resistance and reactance that are similar to those obtained with pressure amplitude are observed in the presence of a mean flow past the wall. The dependence on mean flow mach number is shown in figure 4, where the reference conditions θ_{ref} and δ_{ref} are for $M_\infty = 0$. All the values shown are from two types of experiments. The impedance-tube, flow-duct apparatus (refs. 7 and 8) is a standard impedance tube that is mounted with its axis perpendicular to a flow duct in such a way that the sample is flush with the duct wall. In this arrangement there is no well-defined back cavity because it is replaced by the flow duct. Values of resistance and reactance were obtained without a sample at zero flow. These so-called radiation corrections were subtracted from the impedance values measured with flow. This procedure assumes the radiation correction is independent of sample geometry and flow, which can lead to considerable uncertainty, particularly for low-impedance samples. The data inferred from flow-duct

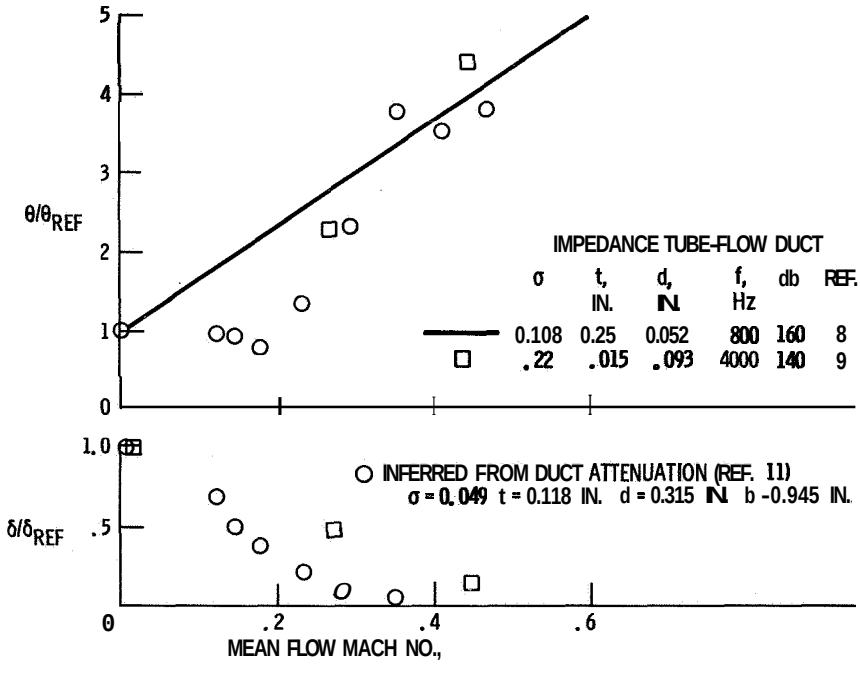

FIGURE 4. —Effect on impedance of mean flow past the resonators.

attenuation spectra (refs. 9 and 10) are based on the assumption that propagation influences on the spectra are negligible compared to the effects of wall impedance. The validity of this assumption depends on the duct flow, geometry, and frequency: and should be investigated. In short, a reliable experimental technique for measuring impedance with flow needs to be developed. The pressure-phase method appears to offer some promise (ref. 5).

Two mechanisms have been proposed to account for the increase in resistance with mean flow. Both involve ways in which the orifice velocities are increased. The first (ref. 11) suggests that velocity fluctuations in the turbulent boundary layer associated with mean flow increase the effective orifice velocity and produce an effect on resistance analogous to that produced by a steady bias velocity through the perforated wall. The second hypothesis (ref. 12) attributes increased orifice velocities to an increased effective pressure difference across the orifice produced by the flow. A reduced mean static pressure is assumed to exist around the jets formed on the duct side of the orifice. This is based on the idea that the jet experiences a surface pressure analogous to the mean pressure distribution around a cylinder in crossflow. A pressure increase at the orifice entrance when flow proceeds into the cavities might also be realized by making the flow stagnant as it turns into the orifice. At present, analytical results and experimental data to test these concepts are not available. Considering the substantial increases in resistance indicated by the limited data in figure 4, further investigation of this effect is urgent.

The decrease in orifice reactance with the end correction approaching zero is more pronounced for flow than for amplitude. Strong flow past the wall appears to completely eliminate the inertia contribution of the gas immediately outside the orifices on the duct side. The significance of these reactance changes for thin orifices is evident when the problem of matching wall impedance for maximum damping is considered as discussed in connection with figure 1. The interaction between these qualitatively similar effects on impedance produced by amplitude and flow also deserves study.

FREQUENCY EFFECTS

Moving now to a consideration of frequency effects, figure 5 shows the variation of resistance with frequency at a constant amplitude of 160 dB with no mean flow. The calculated curve peaks at the resonant frequency of 2270 Hz where orifice velocity is a maximum. Pressure-phase data for the same geometry as the data in figure 3 are plotted in

---

[2] *See* p. 345.

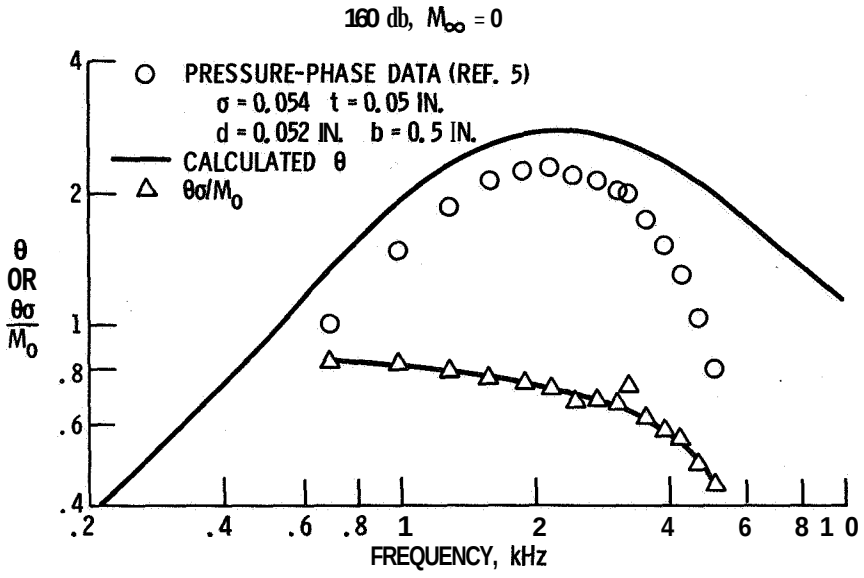

FIGURE 5.—Resistance as a function of frequency.

figure 5. As before, the pressure-phase data lie below the calculated values. They differ by roughly a constant multiplier up to resonance, after which the difference increases. This divergence beyond the peak is emphasized by the plotted ratio of orifice resistance to-peak orifice mach number for the data as represented by the triangles. From an empirical point of view, this behavior can be interpreted as a frequency-dependent discharge coefficient. Physically, the peak particle displacements in the orifice decrease with increasing frequency and become of the same order as the orifice thickness or diameter in this case. When this occurs, it is likely that the orifices are no longer operating in a turbulent jet regime. Phase diagrams describing various regimes of orifice behavior have been experimentally determined (ref. 13) and depend in general on orifice diameter, thickness, frequency, and peak velocity, or displacement. However, the results have not been quantitatively correlated in terms of orifice geometry.

With respect to the frequency dependence of cavity reactance, the behavior in the vicinity of $b = \lambda/2$ should be investigated experimentally. Here cot $(\omega b/c)$ becomes indeterminate and should probably be modified to include a distributed resistance to reflect the. fact that turbulent dissipation of the jet occurs throughout the cavity.

The case of practical interest, i.e., when the resonators are excited by a spectrum of pressure amplitudes, will now be considered. Because the resonators behave nonlinearly, superposition does not apply and

frequency interaction effects can be expected. A simple illustration of resistance being affected by simultaneous excitation at two frequencies, a fundamental and its second harmonic, is given in figure 6. Resistance was measured at a fundamental frequency f_1 by the pressure-phase method using 10-Hz bandwidth filters centered on f_1. The sound-pressure level of the fundamental excitation was held constant at 135 dB and θ_{ref} refers to the resistance with no excitation at the second harmonic. As the amplitude of the second harmonic is increased and becomes greater than 135 dB, the resistance at the fundamental increases. The calculated curve, which somewhat overpredicts the effect, is obtained by inserting the magnitude of the overall sound-pressure level for the two frequencies in equation (4). This procedure of using overall sound pressure to calculate the impedance under conditions of broadband excitation has received limited confirmation by the ability to predict attenuation for some lined engine inlets (ref. 14). However, methods for predicting and measuring impedance under conditions of excitation by amplitude spectra, such as those encountered in engine fan duct, deserve more investigation.

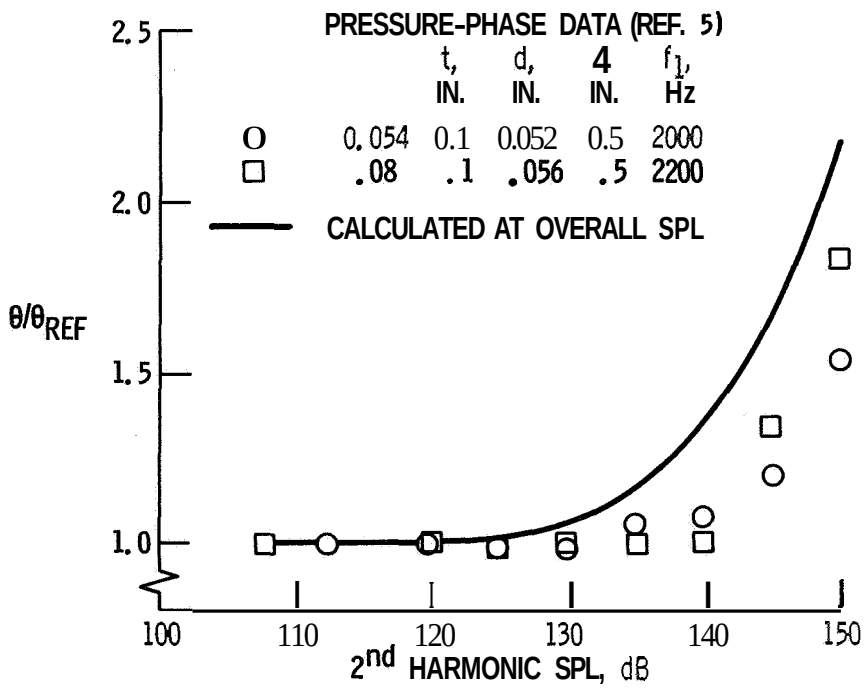

FIGURE 6.—Resistance for simultaneous excitation at the fundamental and second harmonic frequencies, 135 dB at fundamental.

CONCLUDING REMARKS

The ability to specify wall constructions that correspond to particular impedances is essential if propagation analyses are to be used for sound attenuation predictions. This review of the impedance behavior of Helmholtz resonator arrays shows that pressure amplitude effects have received the most attention. The key role of orifice velocity as related to the nonlinear dependence of resistance on pressure amplitude has been clearly established. However, basic experimental techniques and analyses are needed to clarify wall-impedance behavior under conditions representative of those encountered in aircraft-engine-noise problems. In particular, the impedance phenomena associated with mean flow past the lined wall and an acoustic excitation spectrum consisting of broadband noise with superimposed discrete frequencies deserve special research emphasis.

REFERENCES

1. INGARD, UNO: On the Theory and Design of Acoustic Resonators. J. Acoust. Soc. Am., vol. 25, no. 6, Nov. 1953, pp. 1037–1061.
2. INGARD, UNO; AND ISING, HARMUT: Acoustic Nonlinearity of an Orifice. J. Acoust. Soc. Am., vol. 42, no. 1,1967, pp. 6–17.
3. SIRIGNANO, WILLIAM A.; AND HARRJE, DAVID T.: Nonlinear Aspects of Combustion Instability in Liquid Propellant Rocket Motors. NASA CR-77672, June 1966, pp. 31–40.
4. ZINN, BEN T.: A Theoretical Study of Nonlinear Damping by Helmholtz Resonators. AIAA Paper 69–481,1969.
5. GARRISON, G. C.; SCHNELL, A. C.; AND BALDWIN, C. D.: Suppression of Combustion Oscillations With Mechanical Damping Devices. Rept. no. PWA FR–3210, Pratt & Whitney Aircraft, Apr. 15, 1969.
6. WESTERVELT, P. J.: Acoustical Impedance in Terms of Energy Functions. J. Acoust. Soc. Am., vol. 23, no. 3, May 1951, pp. 347–348.
7. GARRISON, G D.: A Study of the Suppression of Combustion Oscillations with Mechanical Damping Devices. Rept. no. PWA FR–2596, Pratt & Whitney Aircraft, Nov. 20,1967.
8. FEDER, ERNEST; AND DEAN, LEE WALLACE: Analytical and Experimental Studies for Predicting Noise Attenuation in Acoustically Treated Ducts for Turbofan Engines. Rept. no. PWA–3486, Pratt & Whitney Aircraft, NASA CR-1373, 1969.
9. PHILLIPS, BERT: Effects of High Wave Amplitude and Mean Flow on a Helmholtz Resonator. NASA TM X–1582, 1968.
10. MECHEL, F.; MERTENS, P.; AND SCHILZ, W: Research on Sound Propagation in Sound Absorbent Ducts with Superimposed Air Streams. AMRL-TDR-62-140, vol. III, Physik. Inst., Univ. Gottingen, West Germany, Dec. 1962.
11. INGARD, UNO: Absorption Characteristics of Nonlinear Acoustic Resonators. J. Acoust. Soc. Am., vol. 44, no. 4, 1968, pp. 1155–1156.
12. SIRIGNANO, W. A.; AND TONON, T. S.: Nonlinear Aspects of Combustion Instability in Liquid Propellant Rocket Motors. NASA CR-72426, June 1968.

13. INGARD, UNO; AND LABATE, S.: Acoustic Circulation Effects and the Nonlinear Impedance of Orifices. J. Acoust. Soc. Am., vol. 22, no. 2, Mar. 1956, pp. 211–218.

14. FEILER, CHARLES E.; RICE, E. J.; AND SMITH, L. JACK: Performance of Inlet Sound-Suppressors. Proceedings of the Conference on Progress of NASA Research Relating to Noise Alleviation of Large Subsonic Jet Aircraft. NASA SP–189, 1968, pp. 53–57.

ACOUSTIC RESEARCH ACTIVITIES AT MARSHALL SPACE FLIGHT CENTER

Gilbert A. Wilhold
NASA Marshall Space Flight Center
Huntsville, Ala.

The science of acoustics studies the generation, propagation, and reception of sonic energy. Noise generation for the purpose of this paper is defined as the basic noise-source characteristics associated with jet and rocket exhaust flow fields and the sources of pressure fluctuations developed on the vehicle during flight. Propagation includes energy dissipation, refraction, reflection, diffraction, and high amplitude or nonlinear effects. Reception is not included in this survey.

The acoustic research activities at Marshall Space Flight Center (MSFC) include all the areas noted above. The goal of this survey paper is to review and present those research programs at MSFC that are in accord with the technological objectives of this conference.

The acoustic research activities at MSFC in the two basic areas of noise generation and propagation will be summarized in this paper. Noise generation will be subdivided into noise generation of jet and rocket exhausts and in-flight fluctuating pressures.

SYMBOLS

dB	$10 \log \overline{p^2}/p_{ref}^2$
p	acoustic pressure N/m^2
$\overline{p^2}$	time average of the square of the acoustic pressure; i.e., mean squared pressure, N^2/m^4
p_{ref}	reference pressure, 0.00002 N/m^2
f	frequency, Hz
Δf	bandwidth= $f_u - f_L$, Hz
f_u	upper frequency limit, Hz
f_L	lower frequency limit, Hz
SPL_{OA}	sound-pressure level overall magnitude, dB
$SPL_{1/3}$	sound-pressure level in a 113-octave frequency band, dB
SPL_{OB}	sound-pressure level in an octave frequency band, dB
$CPSD(f)$	correlated acoustic pressure spectral density between two spatial points at a given frequency. N^2/m^4 Hz

$\Box^2$	d'Alembertian operator $=\nabla^2-\frac{1}{C_0^2}\frac{\partial^2}{\partial t^2}$
∇^2	Laplacian operator $=\frac{\partial^2}{\partial X_1^2}+\frac{\partial^2}{\partial X_2^2}+\frac{\partial^2}{\partial X_3^2}$
t	time, sec
X	spatial coordinate, m
C_0	isentropic speed of sound, m/sec
Q	mass flow rate, kg(mass)/sec
$\nabla\cdot$	divergence $=\frac{\partial}{\partial X_1}+\frac{\partial}{\partial X_2}+\frac{\partial}{\partial X_3}$
F	body force, N
ρ	density, kg(mass)/m^3
$\mathbf{q}$	fluid particle velocity, m/sec
i, k	subscripts, designating the ith and kth direction, respectively
$\tau_{i,k}$	viscous fluid stress, N/m^2
R	distance from apparent source to point on the vehicle surface, m
X_0	distance from midpoint of vehicle in exhaust plane to apparent source, m
$A(f)$	proportional to the apparent acoustic power' density, for a given frequency, radiated back toward the vehicle from an apparent source, N^2/m^2 Hz
T	thrust of one engine, N
D	exit diameter of one engine, m
V	exit velocity of rocket exhaust, m/sec
n	number of rocket engines
fD/V	Strouhal number, nondimensional frequency
ϕ	angle between ground and centerline of deflected exhaust stream, deg
θ	angle in ground plane measured from projection of centerline of deflected exhaust on ground plane, deg
η	acoustic efficiency factor $A_{OA}/W_M=0.005$ for large boosters, nondimensional
A_{OA}	overall acoustic power, W
W_M	mechanical power of rocket exhaust, W
$A'(f)$	the apparent monopole acoustic power spectral density radiated in the ground plane for a given frequency f, W/Hz

ACOUSTIC ENVIRONMENTS OF ROCKET EXHAUSTS

The most disturbing byproduct of static tests and launch-site space-vehicle operations is the acoustic noise field generated by the exhaust

flow of the rocket motors. This noise field is generated during the period prior to launch of a rocket and also during the static (restrained) firing tests of the rocket booster and its stages.

Providing a physical feeling for the amount of acoustical power generated during the operation of a rocket motor is difficult. However, if the acoustic power of the Saturn V vehicle at launch (about 2.0×10^8 W) were converted to electrical power, it would supply enough electrical power to light about 200 000 average homes, assuming about 10^3 W would completely light up an average home. If the acoustic power were converted to mechanical power, it would lift an auto (1 ton weight at the surface of the Earth) at a rate of about 50000 mph. These crude analogies reveal the magnitude of the tremendous acoustic power that must be considered with respect to space vehicles. Although much lower in total magnitude, current and future jet aircraft are also beginning to create significant noise fields that result in aircraft design and location problems (refs. 1 and 2).

The resultant noise problem is so great that it dominates the structural and electronic design considerations of the rocket and the ground-support equipment (GSE). It also presents an operational hazard to astronauts, to static-site and launch-site personnel, and to the communities surrounding these sites. The subjective aspects of the psychological and physiological reactions to this intense noise field are extremely difficult to assess. Of course, as rockets grew in size, the magnitude and compbxities of the problems associated with the noise field grew proportionately.

All aspects of the noise problem should be defined at the earliest possible point in the research, development, and operation of current and future space vehicle systems. It is obvious that the impact of noise on the systems, and hence total cost, will be much greater if a fix-instead-of-cure attitude is taken with respect to this important design consideration.

Importance and Definition of Noise Fields

Acoustic problems enter into almost all aspects of the design considerations for a proposed space-vehicle system. They influence the static-site and launch-site firing locations, orientation, and operations; the structural integrity of the space vehicle itself; the design specifications for the space-vehicle electronic systems; and the structural and electronic integrity of the GSE. Additionally, they create vibration problems that must be considered if GSE and space-vehicle structural and electronic components are to be properly and adequately designed. Therefore, they dictate the existence of adequate acoustic and vibration test facilities necessary for qualification testing. These tests involve

great expenditures of manpower and money. Another problem is that the Saturn class of space vehicles have pushed current facility capabilities to the limit in size and achievable acoustic pressure levels.

Acoustic levels are expressed in a logarithmic manner, i.e., in decibels (re 0.00002 N/m^2). As the overall level becomes high, an error in the dB level represents a 'proportionately larger error in the absolute acoustic pressure value. An error at high levels results in penalties because of overdesign and qualification testing. When the overall acoustic levels were much lower, these considerations were not so critical. Current noise levels, however, are such an annoyance that the decision to build new vehicle configurations is being made on the basis of anticipated noise levels. Such bases of decision clearly point out the need for timely, accurate estimates of the noise levels associated with a given space vehicle or jet aircraft.

It is necessary to provide an estimate of the overall magnitude and the spectral and spatial decomposition of the acoustic energy to define the acoustic field. This is provided by giving, at a point of observation, the overall sound-pressure level (SPL_{OA}); the spectral characteristics of the acoustic pressure, usually in 1/3-octave $SPL_{1/3}$ or full octave band SPL_{OB} values against frequency; and the cross-power spectral characteristics (CPSD) of the acoustic pressure, usually 1/3- or full-octave band levels reduced to spectrum values. These are the quantities used by the various structural and electronic system engineers for proper design and test criteria. For engineering purposes the above quantities provide the terms of an acoustic field definition, and the efforts of the acoustician should be oriented toward using them. However, because of difficulties that will be discussed later, the last quantity, the CPSD, is usually missing in the first estimates for a given configuration.

Prediction Methods

The acoustic field around a rocket exhaust is divided into three regions: the far field, the midfield, and the near field. The far field is that part of the radiated noise field that appears to be coming from a single point in a highly directional manner. The far field includes distances on the order of 50 to 100 nozzle diameters or so. The midfield is the part of the radiated field that appears to be coming from a spatially extended source in a highly directional manner. The midfield involves distances on the order of 5 wavelengths or so. The near field is the fluctuating pressure field that is not all radiated and is highly frequency dependent. This involves distances within a wavelength or so.

The goal of the aerodynamicist, as stated above, is to estimate the detailed characteristics of the noise field in each of the above regions. Such characteristics would include an accurate definition of the overall

energy and the spectral and spatial decomposition of the acoustic field. Currently this is not possible. To overcome the problem, efforts are being channeled into both theoretical and practical work. Theories are being advanced to explain the actual noise-generating mechanisms of hot rocket-exhaust flows, and improvement of the methods used for predicting noise levels is also being sought.

The wave equation for acoustic motions (assuming linear approximations) can be written most generally as (ref. 3)

$$\Box^2 p \equiv \nabla^2 p - \frac{1}{C_0^2}\frac{\partial^2 p}{\partial t^2} = -\frac{\partial Q}{\partial t} + \nabla \cdot \mathbf{F} - \frac{\partial^2(\rho \mathbf{q}_i \mathbf{q}_k - \tau_{ik})}{\partial x_i \, \partial x_k} - \frac{\partial^2}{\partial t^2}\left(\frac{p}{C_0^2} - \rho\right)$$

The right-hand terms will vanish in a source-free, homogeneous, isentropic medium at rest; i.e., far from the source. In the confined region where the violent exhaust flow exists, they become appreciable and may be regarded as sound sources. This representation provides some insight into the mechanism of sound generation:

$\partial Q/\partial t$, for example, represents an unsteady injection of fluid, i.e., pulsating mass flow through the nozzle exit area, a monopole-type radiation.

$\nabla \cdot \mathbf{F}$ is the spatial variation of body force; i.e., it can represent pulsating thrust force across the nozzle exit, a dipole-type radiation.

$\partial^2/\partial x_i \, \partial x_k(\rho \mathbf{q}_i \mathbf{q}_k)$ represents sound generation caused by momentum fluctuations including the Reynolds stress. This term is a major noise source in turbulent flow and turbulent jets and represents quadrupole radiation.

$\partial^2/\partial x_i \, \partial x_k(\tau_{ik})$ is the sound generation term caused by fluctuations of viscous stress. It is generally negligible.

$\partial^2/\partial t^2(p/C_0^2 - \rho)$ may represent the effect of entropy and temperature fluctuations. It can be monopole or quadrupole in nature, depending on the influence of convection properties of flow.

The relative importance of the above terms to the noise field generated by hot-rocket-exhaust flow fields is the subject of much debate, and a great deal of effort is being expended to determine their relative importance. It must be stated that detailed knowledge of these quantities does not exist, and hence a theoretical estimation of the radiated acoustic field of a free (undeflected) hot rocket exhaust cannot be made at this date (ref. 4).

Hence model and full-scale test data and the principles of dynamic similarity must be used to generate prediction techniques. These methods are computerized at MSFC, but will provide only spectra and overall SPL. Cross-correlation characteristics cannot be estimated from these prediction methods at this time. Prediction techniques of the mid-field, near field, and far field will be discussed next.

The first prediction method is used to compute the midfield noise levels for the vehicle surface of the static (restrained) booster and launch pad. This method considers the flow stream to consist of apparent sources of a single frequency (fig. 1) distributed at apparent locations in the stream with respect to the nozzle-exit plane. These apparent sources are considered statistically independent of one another. Hence their effect at the vehicle surface can be combined, **i.e.**, their mean square pressure values added directly, to calculate the overall value. The apparent source strength and location are evaluated from measured spectra taken from full-scale and model data and normalized for dynamically similar conditions. Their apparent characteristics—strength and location—are purely arbitrary; i.e., they can be adjusted simultaneously to give the same results. If the source is arbitrarily moved farther away, its strength is increased to maintain the measured value being used to generate the model, which is why they are called apparent.

From sets of dynamically similar experimental data, the apparent source strengths and locations are solved simultaneously and then nondimensionalized by dividing the acoustic power by the mechanical power of the system to give nondimensional source strength and dividing

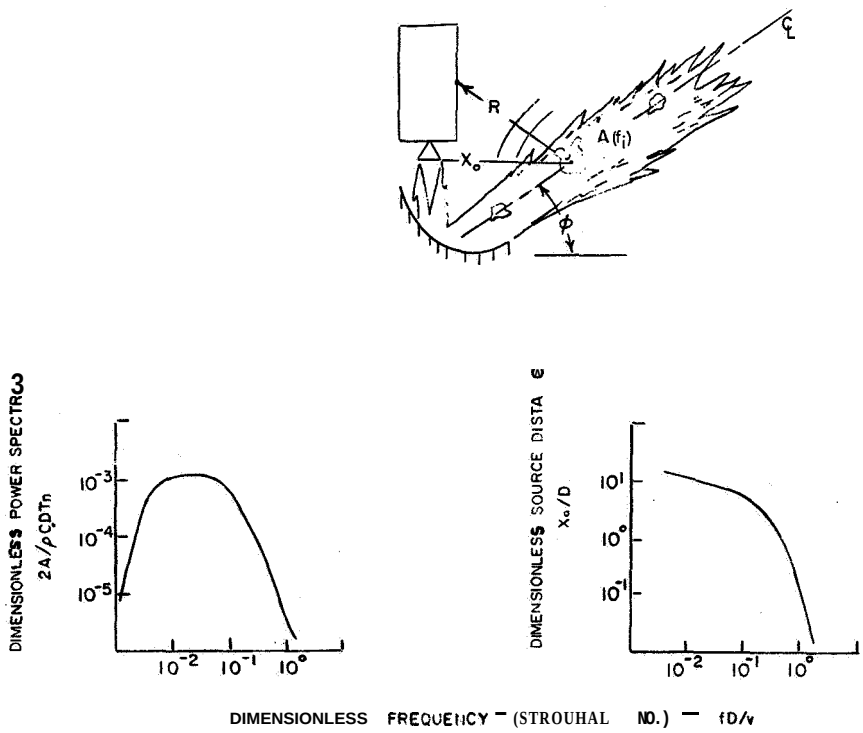

FIGURE 1.—Vehicle apparent source model.

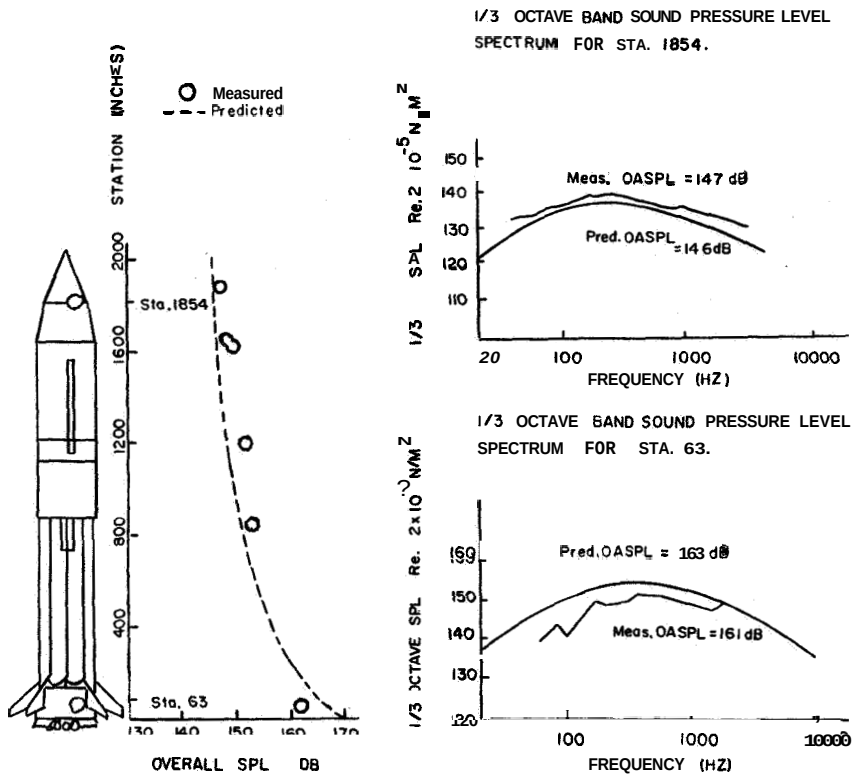

FIGURE 2. — On-pad acoustic levels for Apollo-Saturn IB flight vehicle AS–203.

the apparent source distance by the exit nozzle diameter to give nondimensional location. These empirically derived quantities are then plotted against nondimensional frequency. The nondimensional curves can then be used to estimate the acoustic field for future vehicles with similar characteristics. For example, the split-flow condition of launch is assumed to consist of two streams replaced by such apparent source characteristics and their effects then combine. See figure 2 for a comparison of predicted and measured results.

The curves generated above for bell-nozzle deflected flow cannot arbitrarily be applied to nozzles of different configuration, e.g., the slotted-ring engine, and caution must be used when applying such curves to very high speed flows; e.g., 10000 to 20 000 fps. New curves must be generated for new conditions. Clustering effects, exit plane-to-deflector distance, and all the important scaling factors influence the limitations of such a prediction model. These methods do not provide correlation characteristics.

New prediction models, definition of the limitations of the above models, and studies of the noise-generation mechanisms of hot rocket

Type of measurement	Location	Frequency range	Number
a. Meteorological (Ane.)	External	Static	12
b. Acoustic:			
Amplitude	External	20–200 kc	100
Phase	External	20–20 kc	60
c. Temperature	External	Static	100
d. Pressure	External	Static	100
e. Humidity Sensor	External	Static	1

Current experiments:

1. Study of the effects of cone- or bell-shaped nozzles upon the radiated pressure field.
2. Evaluation of meteorological characteristics on acoustic data.

Planned experiments:

1. Saturn V launch configuration to define the S–IC on-pad acoustic environment, specifically the cross-correlation characteristics.
2. Sound-source location study utilizing phase correlation techniques.
3. Definition of source characteristics for various types of expanding flows with a given nozzle configuration.
4. Evaluation of engine cluster geometry upon external acoustic field.

B. Thermoacoustic simulation facility (pressure, 1500 psi; temperature, 1500°F):

Type of measurement	Location	Frequency range	Number
a. Temperature	Internal	Static	Traversing
b. Pressure			
c. Gas Composition (alphatron)			

exhausts are being made at the MSFC new and unique Acoustic Model Test Facility (AMTF) (table I) and the Thermoacoustic Simulation Facility (table I). The AMTF is a self-contained highly flexible facility with its own blockhouse control center, data acquisition system, thrust-reaction structure, and propellent storage system, which includes conventional and exotic propellent capabilities. The AMTF exhausts over a hard surface and encloses an acoustically clean area with minimum interference by thrust-reaction structure. It was designed specifically

for acoustic testing and experimentation and even includes capabilities for acquiring detailed meteorological conditions during a test.

Correlation characteristics of the radiated acoustic field of the rocket or jet exhaust can be scaled (ref. 5). It is important, however, to have the reflecting surfaces of the vehicle or structure of interest present if proper correlation characteristics are to be obtained. These surfaces influence the correlation characteristics appreciably in certain frequency ranges. An experiment to measure correlation characteristics for launch conditions will be performed at the MSFC AMTF on a scale model of the Saturn V vehicle. It is hoped that the results of this test can be nondimensionalized and applied to dynamically similar configurations of other vehicles.

The midfield acoustic fields on the ground are much more difficult to compute because there exists a different apparent source distribution and set of power characteristics for every radius. Here the source appears as a spatially extended one, and hence this geometric effect, which appears different for each radius, must be taken into account. By using a 180° sector in the ground plane, a series of apparent source models are generated for chosen radii at various angular orientations around the deflected exhaust system. These are stored on the computer for extrapolation to dynamically similar conditions.

The spatial distribution of the noise source is not only important to the midfield region but even more significant with respect to the near-field region. In addition to the geometric effect of a spatially distributed source, the primary mechanisms of noise generation in the flow field become significant factors in determining the fluctuating pressure field

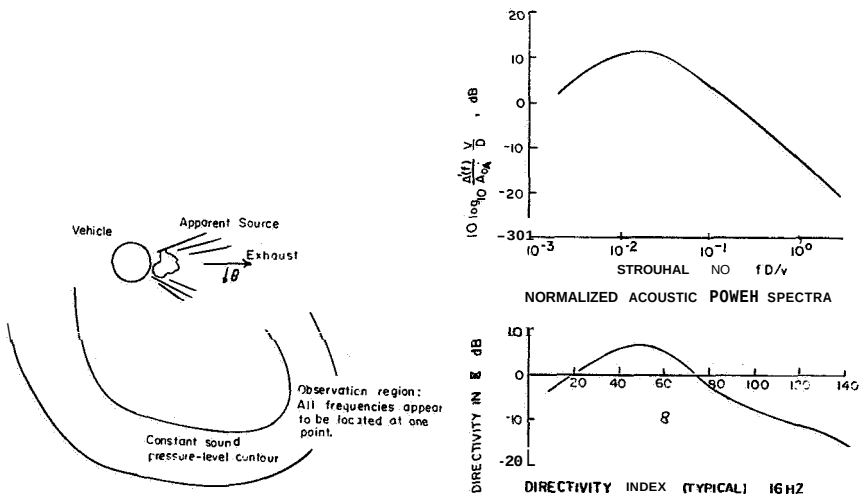

FIGURE 3.—Far-field ground plane apparent source model.

371-986 0-LT-70-25

in the near field. As stated above, detailed knowledge of these mechanisms does not exist at this time. Currently there is not enough experimental data available to attempt to generate an adequate prediction model for this region (ref. 6).

In the far-field region (fig. 3), all the sources for the different frequencies appear to be located at a single point. Again, experimental data and similarity principles are used to generate apparent source characteristics. These apparent characteristics are monopole source strength and directivity effects; i.e., the deviation from the perfect symmetrical radiation of the assumed monopole. The apparent source strength for each frequency is normalized to the overall acoustic power, which is calculated by multiplying an acoustic efficiency factor η (0.005 for high thrust systems) by the total mechanical power of the rocket-exhaust system. The efficiency factor η is derived from many sets of experimental data (ref. 7).

The acoustic SPL at an observation point is then computed for the monopole source in the conventional manner for a homogeneous, isotropic medium for 1/3-octave or octave center band frequencies, a relatively straightforward and easy calculation, because all the monopole sources appear to be at a single point. Corrections are then applied to account for the directional properties of the source by using directivity curves, such as those shown in figure 3, that account for the deviation of the source from a monopole as a function of angular position around the vehicle. Such directivity curves are generated for each center frequency. After application of the directivity corrections, the resultant sound pressure spectrum, 1/3-octave or octave, represents the best estimate of the acoustic field at that point. It can then be summed in the usual way to obtain an overall SPL. This approach is applicable to all dynamically similar configurations. Where distances become appreciable, absorption and attenuation effects must be taken into account. Typical results for the Saturn V vehicle static firing condition for the Huntsville, Athens, and Decatur, Ala., areas are shown in figure 4.

The above technique was modified for use in computing the far-field ground acoustic field as the space vehicle flies through its boost phase (ref. 8). The effects of vehicle velocity and exhaust plume changes on the apparent source characteristics were evaluated, and a new set of apparent source characteristics derived, which allows the estimation of the far-field ground acoustic field from holddown to the end of the boost phase flight period. These fields are calculated by computer as a function of time at any desired observation point on the ground plane. Typical results of these estimates are presented in reference 9 and figures 5 and 6.

One of the major restrictions on the estimation of the far-field noise

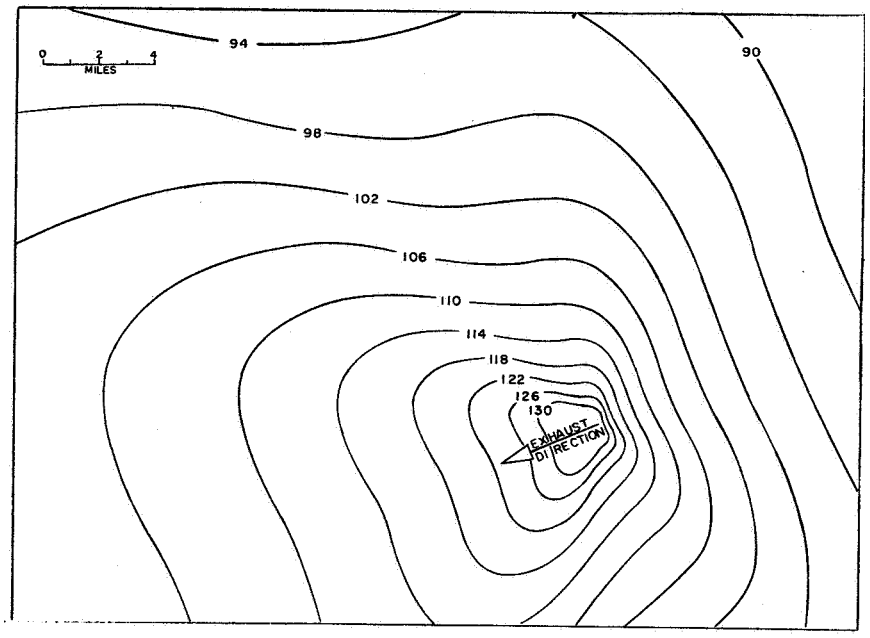

FIGURE 4.—Constant overall sound pressure level contours Saturn V S-IC static firing.

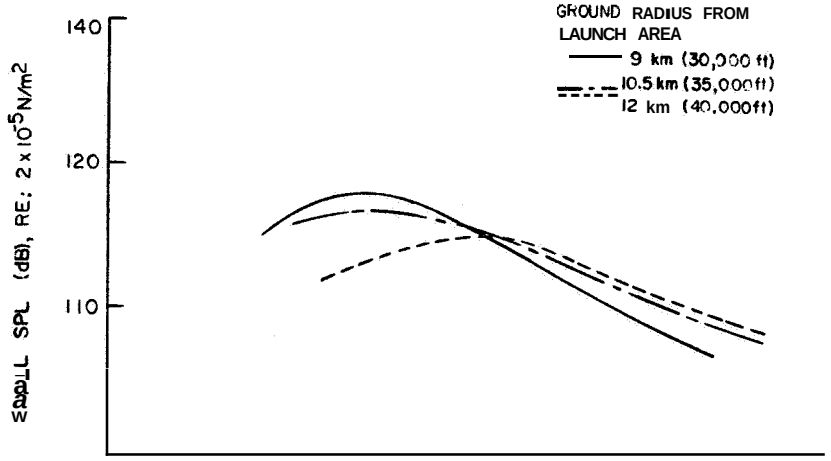

levels by the far-field techniques is the assumption of a homogeneous, isotropic propagational medium. For this case it is sufficient to derive the apparent source characteristics for the ground plane only. If the propa-

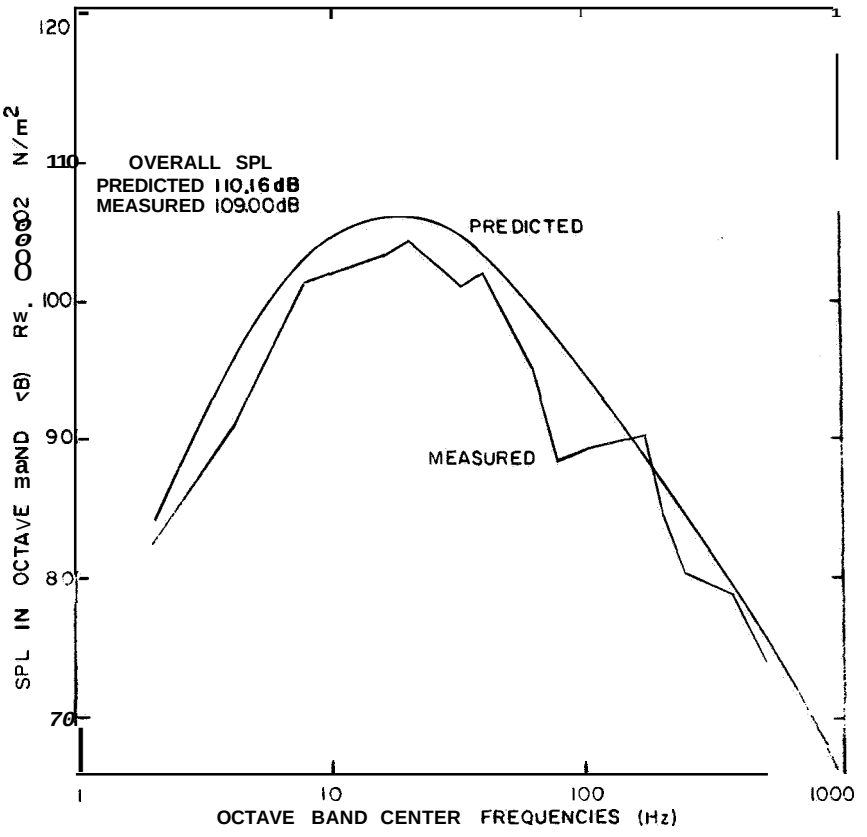

FIGURE 6.–Measured acoustic data from SA–5 flight (Saturn I vehicle) with predicted noise levels at 5.148 km.

gational medium is inhomogeneous, however, the acoustic energy arriving at an observation point on the ground plane may be the result of refraction. The three-dimensional radiation characteristics of the source then become important. To generate a prediction model for these conditions, three-dimensional apparent source characteristics are derived from experimental data and coupled with a modified ray acoustic approach using a linear layer model for the inhomogeneous atmosphere (ref. 10). This model estimates the sound-field spectrum caused by the refracted energy but is still limited by the restrictions on ray acoustics. For instance, one of the major restrictions is that the sound-pressure level at a focal point becomes infinite. The atmospheric inhomogeneities therefore play a prominent role in restrictions on the operational procedures of static-test-firing boosters because high acoustic energy levels can be refracted into surrounding highly populated communities. If

meteorological conditions indicate this is the case, the firing must be postponed until the conditions change.

IN-FLIGHT FLUCTUATING PRESSURES

Theoretical estimates of the in-flight fluctuating pressure field on the vehicle are not as good as those of the noise radiated from the rocket exhaust. Limitations in both areas are the result of lack of information about the physical processes occurring within the region of violent fluid flows. Present macroscopic and quantized theories of these physical processes fail to provide adequate explanations.

The extreme irregularity of aerodynamic surfaces of most modern space vehicles, among other factors, prevents detailed analytical description of the steady or mean flow parameters. But knowledge of these parameters is of paramount importance to the basis of any theory for the prediction of the in-flight fluctuating pressure field. Indeed, the estimation of the steady-flow parameters constitutes the first step in determining the areas where intense in-flight noise fields will occur.

Prediction Methods

To attack this problem, we classify the critical flow regions as the turbulent boundary layer, the region of separated flow, the region of oscillating shock waves, and protuberance noise (fig. 7). Only the turbulent boundary layer has seen significant analytical advances. The other two flow regimes create fluctuating pressure fields for a majority of locations on the vehicle that are usually of an order of magnitude more severe than those created by the turbulent boundary layer and exhaust-generated noise fields. Physical parameters of interest in this problem are the overall pressure magnitude and the spectral and spatial decomposition. Reynolds-number effects are anticipated for all the above sources.

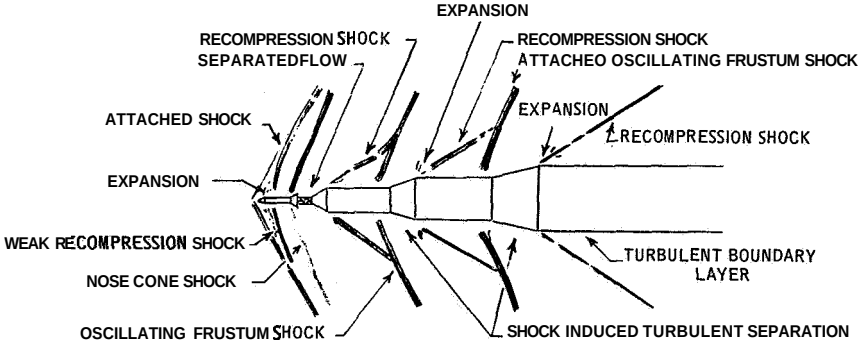

FIGURE 7. —Aerodynamic noise.

M. K. Bull has advanced a theory that allows analytical estimation of the overall magnitude of the spectral and spatial distribution of the fluctuating pressure field within an attached turbulent boundary layer (ref. 11). These characteristics are estimated from an empirically evaluated spatial cross-correlation function. Bull's theory states that the turbulence–mean-shear interaction is the main mechanism contributing to the turbulent boundary-layer noise. It is first necessary, however, to establish the vehicle locations where this type of flow will exist during flight before Bull's theory can be applied. This again emphasizes the need to establish the mean-flow profiles.

Scarcity of experimental data chiefly affects the development of hypotheses in the other, more important, critical-flow regimes. Efforts to obtain data for these problems have given rise to a series of wind-tunnel experiments on cone cylinder step configurations, measuring programs for the Saturn family of vehicles in the R&D phase, proposals for scale-model flight vehicles, experiments to be conducted on aircraft, and consideration of many unconventional modes of testing. But serious disadvantages exist for each of these approaches. Instrumentation, background noise, and scaling problems plague the wind-tunnel experiments. A sufficiently large number of flight measurements on full-scale vehicles cannot be obtained in the detail necessary to describe the noise phenomena. Scale-model launch vehicles, on the other hand, require stringent instrumentation specifications and are very costly.

Because the theoretical models cannot suitably estimate the in-flight noise levels, scale-modeling techniques are used. To establish the in-flight noise level of a specific vehicle, a rigid scale model of it is placed in the wind tunnel after dynamic-pressure transducers have been strategically located on it. A series of tests then explores the expected mach number and angle-of-attack range of the full-scale vehicle. The mean square pressure values and their spectra, measured in this manner, are then extrapolated to the full-scale vehicle for the prescribed flight trajectory. This operation has to be carried out for each new configuration or configuration change.

The trend in vehicle development has been toward larger and larger boosters, but wind-tunnel facilities remain the same size. This fact causes acute technical problems in scaling and in providing adequate instrumentation. For instance, because the size and flow capabilities of the tunnel facilities remain the same while the full-scale booster size grows, the full-scale flow fields often cannot be simulated dynamically; i.e., the full-scale mach-number and Reynolds-number variation cannot be deduced from the scaled test. Because these are the primary scaling parameters, uncertainties arise in the scaling procedures. For example, it is not yet known how the size of the separated flow regions will be

affected by mach-number and Reynolds-number variations or how these size variations are reflected in the noise-generating mechanisms. Besides these scaling problems, how the oscillating shock and the correlation functions will scale is not known.

The facility-to-booster-size ratio also generates stringent instrumentation requirements. As the boosters grow larger, the scaling procedures demand the scaled frequency range of interest to increase. For current space boosters, this frequency range is approaching the zero-to-100-kc range. Studying the correlation function in such a frequency range requires very stringent phase specifications for the data-acquisition and reduction systems. Moreover, as the boosters grow larger and the size of tunnel facilities remains constant, the spatial regions of interest in the scaled domain become very small. Spatial variations in the fluctuating pressure field, of primary interest, necessitate very small transducers. The high-frequency requirement creates problems of pressure cancellation across the transducer surface, which also makes very small transducers necessary. Besides these problems, the wind tunnels are inherently noisy and generate background interference with the acoustic environment generated by the scale-model vehicle.

Although engineering estimates of the overall mean fluctuating pressure levels and their spectral distribution may be obtained by suitable wind-tunnel tests, the main goal, the cross-correlation function, cannot be accurately evaluated from most tests. Another consideration

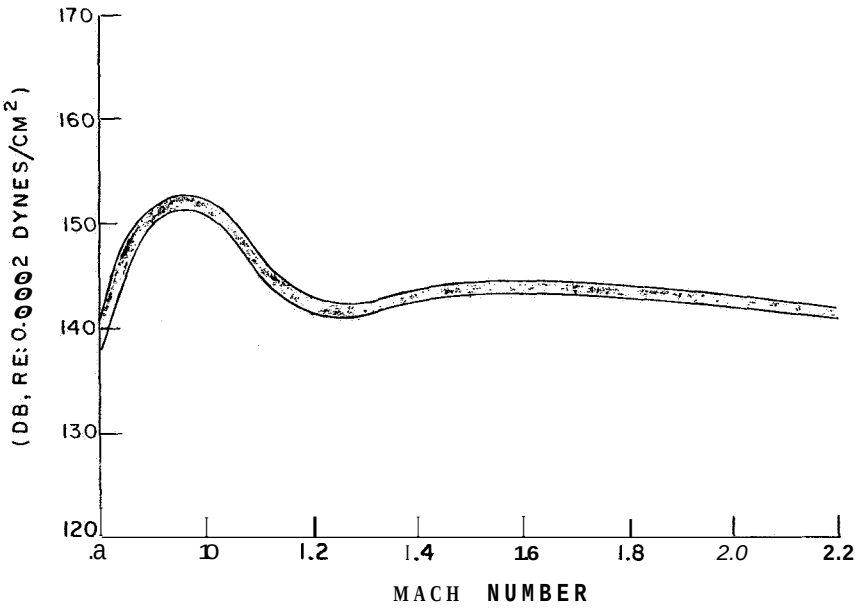

FIGURE 8.—Overall sound pressure level versus mach number at station 2852, $\alpha = 0°$.

is that much time elapses before the knowledge of these tests becomes available because each new configuration requires a complete series of tests and extensive reduction of extremely large volumes of information.

Figure 8 presents, for Saturn V, an example of the results of present empirical prediction techniques. The SPL shown represents the best estimates that can currently be made. They are limited by the various shortcomings that we have discussed earlier for the prediction techniques.

SUMMARY

Noise-prediction problems and improvements can be summarized as follows. Present theories are wholly inadequate for supplying necessary engineering information. The obstacles to the development of adequate theories are being removed in a well-organized, step-by-step procedure. However, such development requires a great deal of fundamental and technological work. Experimental and analytical efforts to achieve a better understanding and description of the stress tensor for prediction of exhaust noise are being made. Methods to establish the mean flow conditions over irregular aerodynamic surfaces are also being studied. The generation of a limited reliable set of basic in-flight data is being attempted for the Saturn V. These data will help guide the development of adequate noise-prediction theories for the oscillating shock and separated flow fields. Acquisition of data from aircraft experiments and comparison of it to suitably scaled wind-tunnel data are helping us to understand scaling law and wind-tunnel effects.

A combination of current prediction techniques can in most cases provide engineering estimates of most of the static-firing and launch SPL for current Saturn-type vehicles. Any deviation in design of future vehicles, however, will require scale-model testing to establish a set of reference data for extrapolation. Wind-tunnel testing is necessary to determine the in-flight noise levels, but deficiencies occur because of the limitations of data-acquisition systems and scaling procedures.

New and perhaps revolutionary experimental approaches to in-flight and other acoustic field problems are being sought. For instance, NASA-Marshall has constructed an acoustic model research facility to solve many of the current problems with engine-generated noise. The only one of its kind designed explicitly for such work, this facility will accommodate scaled models of any type of single and clustered engines with total thrust levels up to 70 000 lb and will be able to fire horizontally as well as vertically. Variations in exit plane to deflector spacings will also be permitted. Its other features include exotic propellant capabilities, a self-contained high-frequency data-acquisition system, and an acoustically clean area. This facility has its own blockhouse control center and

will be operated on a noninterference basis. Both applied engineering and basic research information will be generated at the facility.

Advances are also being sought in data acquisition and reduction. Methods for economically reducing and analyzing large volumes of correlation data are being investigated. Such techniques appear to be feasible, though still far in the operational future. Concentration in the data-acquisition and instrumentation areas is also being encouraged to provide systems to measure extreme noise fields and levels.

Aerospace noise problems will continue to grow, and current efforts to provide economical and suitable designs of vehicle systems must be oriented toward solving this growing problem.

Current MSFC research programs designed to accomplish this goal within the areas of noise generation and propagation are varied. The problem of noise generation in jet and rocket exhausts has been subdivided into the following studies and their respective objectives:

(1) Development of apparent source prediction models to normalize apparent source characteristics (reference, source strength, location, efficiency, and directivity) for the developmenr of models to predict near-field (including vehicle), midfield, and far-field noise levels caused by undeflected and deflected single and multiple exhaust flows

(2) Correlation characteristics of the acoustic pressure field on the Saturn **V** vehicle for launch conditions to measure the spatial and temporal correlation characteristics of the acoustic pressure field on a scale model **of** the Saturn **V** vehicle for various conditions during launch

(3) The variation in source Characteristics of a high-thrust hot rocket exhaust because of changes in chamber pressure to define the changes in acoustic efficiency, source strength, and directivity because of variation of chamber pressure of a very high-thrust rocket engine (J–2 engine) re approximately 10^5 lb

(4) Studies of the basic description of hot and cold subsonic and supersonic flow fields to define the mean and turbulent flow characteristics of cold and hot subsonic and supersonic exhaust flow fields

(5) Entropic effects of noise generation by hot exhaust flows to define the noise-generation mechanisms associated with regions of high entropy production in an exhaust flow

(6) Spectral techniques in jet noise theory to obtain a new insight into the basic jet noise-generation mechanisms described by Lighthill's theory by transforming his equation into the wave number and frequency domain

(7) Isolation and identification of the flow regions of a jet generating acoustic energy to define the noise-generation characteristics of various regions of subsonic and supersonic exhaust flow fields

Research in noise generation caused by in-flight fluctuating pressures

has been divided into the following studies and objectives:

(1) Separated flow, and shock wave and turbulence interactions at interstage regions to define the fluctuating pressures and their spatial and temporal correlation characteristics of the separated flow in the region of a cylinder-cone-cylinder junction

(2) Transonic and low supersonic three-dimensional protuberance study to examine the spatial and temporal con-elation characteristics of a flow field induced by three-dimensional protuberances during transonic and low supersonic mach numbers

(3) Scale-model Saturn **V** 4 percent AEDC wind-tunnel test to define spatial and temporal correlation characteristics of the Saturn **V** vehicle during flight

(4) Extrapolation of wind-tunnel data to full-scale vehicles to delineate the major effects of violating the mach number and Reynolds number similarity parameters caused by wind-tunnel testing

The problem of noise propagation has been separated into the following studies and objectives:

(1) Atmospheric attenuation of low-frequency noise to define the atmospheric absorption of low-frequency noise by use of Saturn static firing data

(2) Ground attenuation to define the ground absorption effects on an acoustic wave

(3) Wave propagation through heterogeneous media to analytically calculate the acoustic intensity at caustic points

(4) Evaluation of acoustic intensity at focal points from data from static firings to verify methods used for estimating acoustic intensities at caustic points

(5) Far-field acoustic intensity change because of variation of atmospheric parameters to determine the sensitivity of the far-field intensities with respect to variation in atmospheric parameters

(6) An explicit solution of Burgers' equation to analytically define wave propagation in a thermoviscous medium

(7) Measurement of the characteristics of a high-amplitude pressure wave to verify experimentally the explicit, analytic solution to Burgers' equation

CONCLUSIONS

Knowledge of the basic noise-generating mechanisms of a free (undeflected) hot rocket-exhaust flow field is extremely limited. Even less basic knowledge exists for the deflected condition.

Prediction techniques exist and are computerized for estimation of the overall and spectral characteristics of the acoustic field at the vehicle surface caused by the rocket-exhaust flow for static firing and launch

conditions. Cross-correlation characteristics, and, therefore, realistic structural response values, cannot be calculated at this time. Experimental efforts are underway to overcome this problem.

Techniques are available and computerized for estimating the ground-plane midfield acoustic fields in terms of overall characteristics and spectra.

The near-field fluctuating pressure levels for a hot rocket exhaust cannot be estimated. There is an acute lack of experimental data for this region. Also, the details of noise-generation mechanisms are not yet known.

Methods are available and programed to estimate the exhaust flow noise, ground-plane far-field environments for a homogeneous, isotropic medium for both restrained (static and launch) firing and in-flight conditions, with the in-flight conditions given as a function of time, and an inhomogeneous medium, restrained firing only.

New, unique, and extremely flexible experimental facilities for studying acoustic fields and noise-generation mechanisms for any type of rocket or jet propulsion systems are available at MSFC.

Estimates of overall and spectral characteristics can be made for the in-flight fluctuating pressures for flight vehicles.

Although these methods, when used correctly, provide fairly reliable estimates of the acoustic environments, each has severe restrictions and limitations. Extreme caution, therefore, must be used when applying them to new situations; i.e., supersonic transport, jumbo jets, and/or the space shuttle.

At the extremely high SPL generated by current space vehicles, small errors in dB values result in large errors in structural response analyses.

The importance of obtaining accurate estimates of the acoustic fields at the earliest possible time during the R&D phase of space vehicle or large jet aircraft is of vital importance and cannot be overemphasized. The solution of this problem will save great expenditures of money and manpower resources. Dynamic test facility capabilities for qualifying vehicle and ground-support structures and equipment are dictated directly by the magnitude and characteristics of the generated acoustic fields.

REFERENCES

1. GOLOVIN, NICHOLAS: **Alleviation of Aircraft Noise. Astronaut. Aeron., Jan. 1967, p. 71.**
2. RICHARDS, E. J.: **Aircraft Noise—Mitigating the Nuisance. Astronaut. Aeron., Jan. 1967, p. 34.**
3. T. YAO-TSU WU: **Introductory Lectures on Hydro-Acoustics. Schiffstechnik, Forschungshefte fur Schiffbau und Schiffsmaschinenbau, Sept. 1966, p. 93.**
4. FFOWCS WILLIAMS, J. E.: **Possible Effects in Rocket Exhaust Noise. Tech. Memo 67-8, Wyle Laboratories, Oct. 1967.**

5. CLARKSON, B. L.: Scaling of the Near Field Pressure Correlation Patterns Around a Jet Exhaust. Acoustical Fatigue in Aerospace Structures, Trapp and Forney, eds., Syracuse University Press, 1965, p. 19.
6. OLLERHEAD, J. B.: On the Prediction of the Near Field Noise of Supersonic Jets. NASA CR–857, Aug. 1967.
7. GUEST, S. H.: Acoustic Efficiency Trends for High Thrust Boosters. NASA TN D–1999, July 1964.
8. WILHOLD, G.; GUEST, S.; AND JONES, J.: A Technique for Predicting Far Field Acoustic Environments Due to a Moving Rocket Sound Source. NASA TN D–1832, Aug. 1963.
9. GUEST, S.; AND JONES, J.: Far Field Acoustic Environmental Predictions for Launch of Saturn V and a Saturn V MLV (Modified Launch Vehicle) Configuration. NASA TN D–4117, Sept. 1967.
10. JONES, J.: Sound Pressure Estimations From a Point Directional Acoustic Source Radiating in an Inhomogeneous Medium. Aero-Astrodynamics Research Review, no. 3, NASA TM X–53389, Oct. 1965, p. 2.
11. BULL, M. K.: Space Time Correlations of the Boundary Layer Pressure Field in Narrow Frequency Bands. ASD–TDR–62–722, 1963.

ONE-SHOT MEASUREMENTS OF THE DECAY OF SUPERSONIC AERODYNAMIC TURBULENT STRUCTURES

B. H. Funk
NASA Marshall Space Flight Center
Huntsville, Ala.
and
H. A. Cikanek, Jr.
Northrop Corp.
Huntsville, Ala.

The purpose of this paper is to briefly summarize a diagnostic technique that provides the means for measuring the time history of the decay of turbulent structures from one time history of information. That is, each point on the decay envelope is computed from the same sample of flow disturbances.

This technique is readily applicable both to conventional instrumentation and to the laser-schlieren optical remote-sensing system used here. The statistical correlation of schlieren signals eliminates the necessity for tracers and potentially represents the simplest of the remote-sensing systems employing optical correlation.

These qualitative experimental results were obtained at Marshall Space Flight Center during an in-house wind-tunnel test that was conducted to assess the feasibility of applying optical correlation to supersonic turbulent flows. The details of this test and the mathematical description of the one-shot statistical correlation technique are presented in a NASA TM. (See reference.)

DISCUSSION

Figure 1 shows the plan view of a wind-tunnel test section. A single laser beam is passed through, and is normal to, the turbulent boundary layer on a thin plate. After passing through the test section, the beam is reflected downstream from mirror $M1$ to mirror M2, where it is reflected back across the flow, parallel to the first pass, such that the disturbances intersecting the beam upstream at time t again intersect it at a later time $t+\tau$. The photodetector $D1$ monitors the resulting time history, which is amplified and then filtered.

If it is assumed, for the present, that the statistical properties of the turbulence across the test section are two dimensional and stationary,

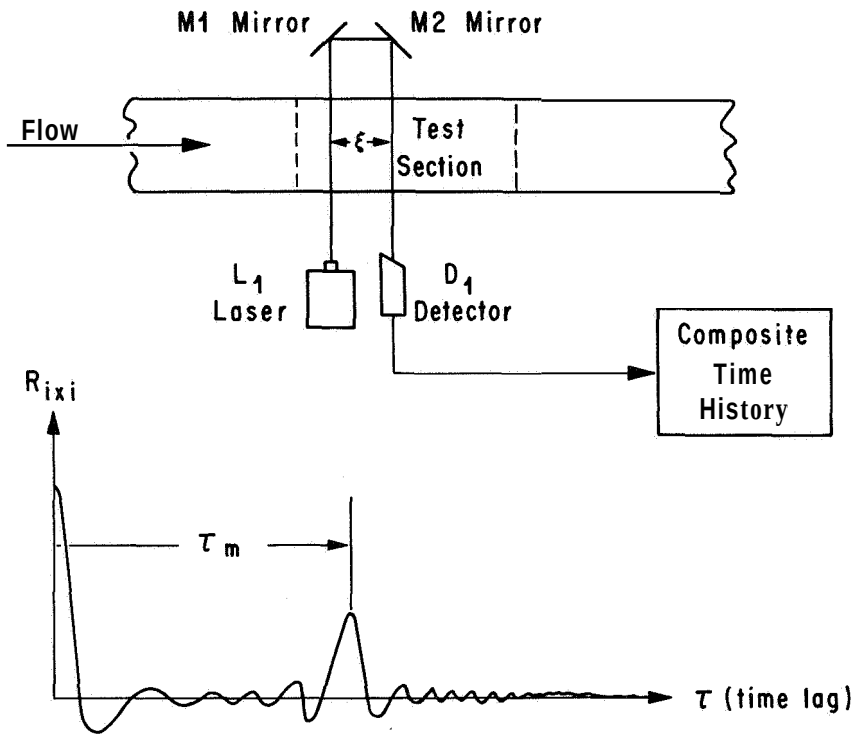

FIGURE 1. — The one-shot autocorrelation for determination of convection speed in two-dimensional turbulence.

the autocorrelogram of this composite[1] time history will exhibit two peaks[2] of correlation. The larger of these occurs at zero time delay and is characteristic of all autocorrelograms of random time histories. The second peak occurs at a time delay τ_m corresponding to the most probable transit time of disturbances between the two stations where the beam passes through the test section. This peak emerges from the computation because the same (or similar) random signal is contained in the time history twice at different times. We refer to such a time history as a composite time history, and its autocorrelogram as a one-shot autocorrelogram.

In figure 2, two additional features that extend the range of application of the one-shot autocorrelation have been introduced. Here, two detectors monitor the light of two parallel laser beams directed through the turbu-

[1] The word "composite" is used here to imply a time history of random data composed of the algebraic sum of one or more random time histones of data.

[2] The reference of the word "peak" implies the maximum positive peak in a local region on the correlogram.

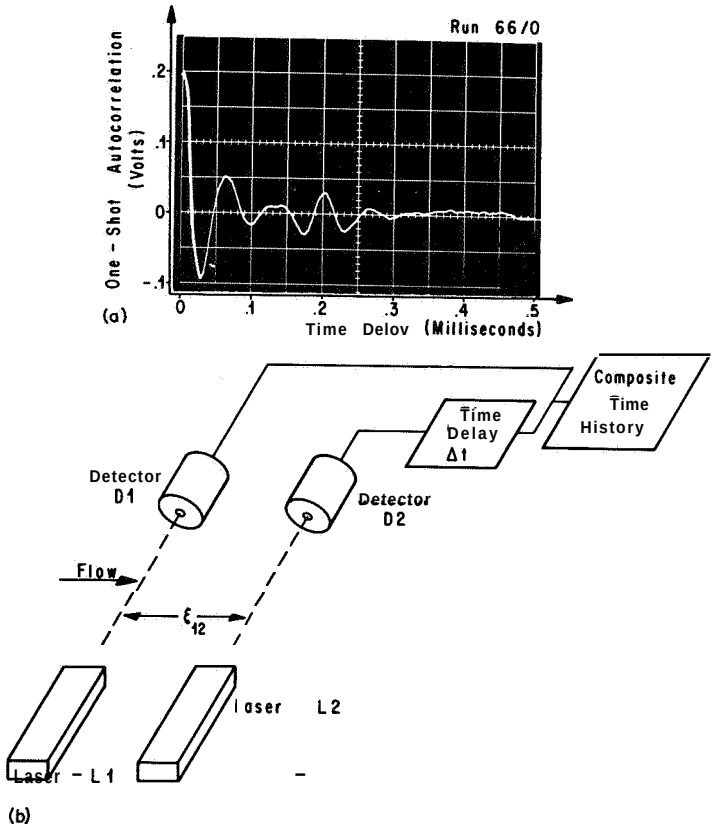

FIGURE 2.—One-shot autocorrelation with induced time delay, *(a)* time history and *(b)* schematic.

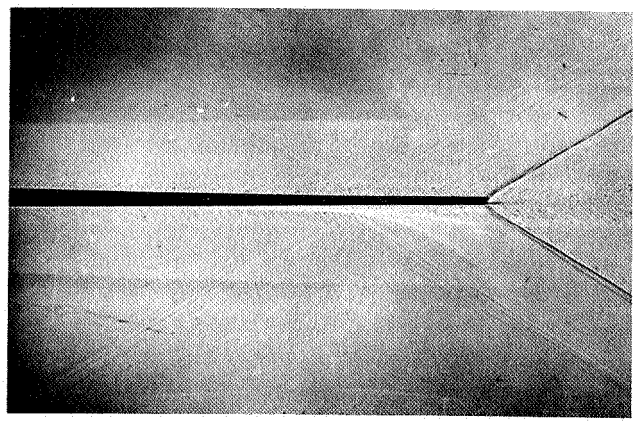

FIGURE 3.—Shadowgraph of;flow field generated by the thin plate model.

lence at the same locations just shown for the single beam (fig. 2(*a*)). The two time histories are added electronically to form a composite that is equivalent to the composite of the single-beam case (fig. 2(*b*)). This arrangement was used primarily to reduce the sensitivity of the single-beam geometry to facility-induced noise (mechanical and acoustical excitation).

The arrangement shown in the schematic of figure 2 was used to experimentally verify the theory. The beams were passed through the turbulent boundary layer on the thin plate (fig. 3). The plane formed by the beams was 0.20 in. above the surface of the plate, and the beams were separated by a distance of 3.90 in. in the direction of flow. The stagnation conditions were approximately atmospheric and the free-stream mach number was 2.0.

The one-shot autocorrelogram of the composite time history was computed during the run. Figure 2 shows a photograph taken immediately thereafter from an online oscilloscope. The secondary peak at 0.2 msec corresponds to a speed of 1510 fps (the supersonic free-stream speed was 1660 fps). A known time delay may be introduced into the downstream time history to avoid peak interference when the beam separation is small.

The schlieren sensing mode was used for this measurement in combination with the parallel-beam geometry. However, the one-shot technique is not restricted by the sensing mode or the beam geometry. That is, the method can be applied to three-dimensional flows using crossed beams, or other suitable beam geometries. The reason is that the one-shot method requires only that the composite time history contain at least two statistically correlated random signals that sufficiently lag one behind the other in time. This generalization is evident from the following statement of the one-shot autocorrelation as it applies to the analysis of random time histories exhibiting statistical stationary:

> The autocorrelogram of a single composite time history composed of the sum of two or more statistically correlated random signals that sufficiently lag one behind the other in time will exhibit a correlation peak for each possible pair of the signals.

Schlieren signals were retrieved for optical correlation by passing two (or more) parallel laser beams through the turbulent boundary layer shown in figure 3. The beams were normal to the test section, and the plane formed by the beams was approximately parallel to the surface of the thin-plate model. A knife edge was placed in each beam allowing approximately 50 percent of the laser light to fall on the respective photodetectors of the beams (fig. 4).

A disturbance passing through one of these beams will deflect it. The deflection is proportional to the component of the gradient of the index

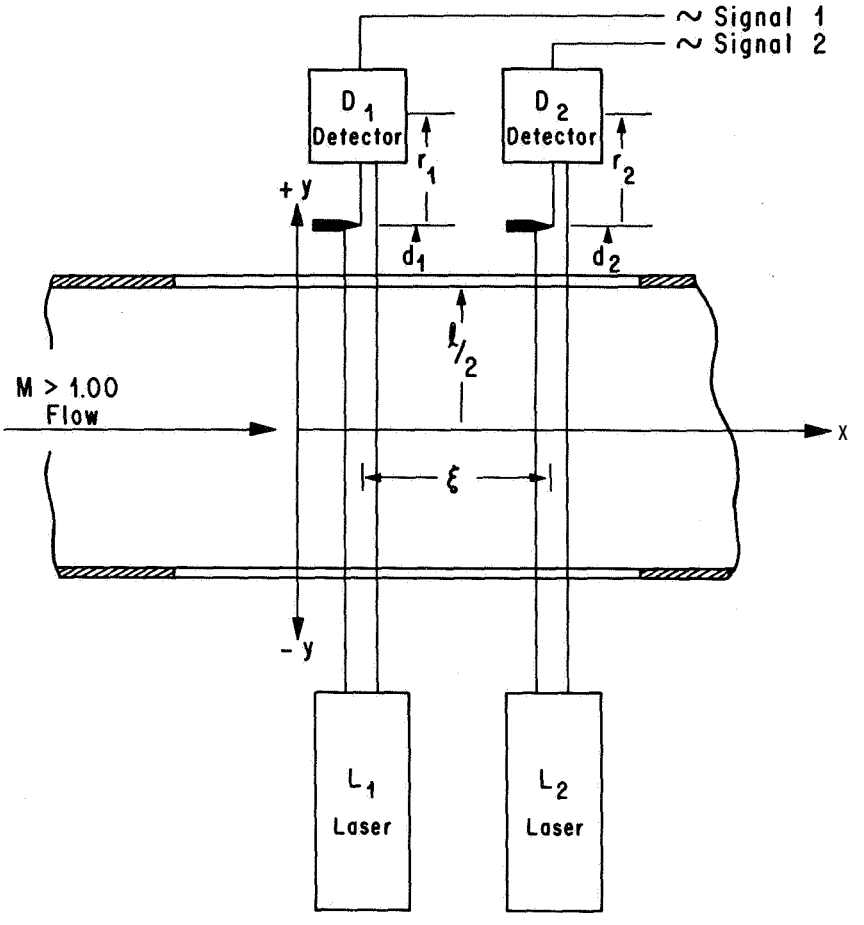

FIGURE 4.—Parallel-beam arrangement for remote acquisition of 7-in. BWT data.

of refraction that is normal to the beam. The x-component of the deflected rays of light along the knife edge, inside the laser beam, produces fluctuations in the amount of light monitored by the photodetector. This time history of luminous energy is converted into an ac electrical signal that is amplified and carefully filtered for computation.

The one-shot method may be extended by the introduction of additional beams. The schematic shown in figure 5(*a*) differs from the former two-beam cases in that the downstream laser beam has been split. One-half of the beam is reflected upstream and then across the test section. All three beams lie in the same plane, are parallel, and are normal to the flow.

371-986 0-LT-70-26

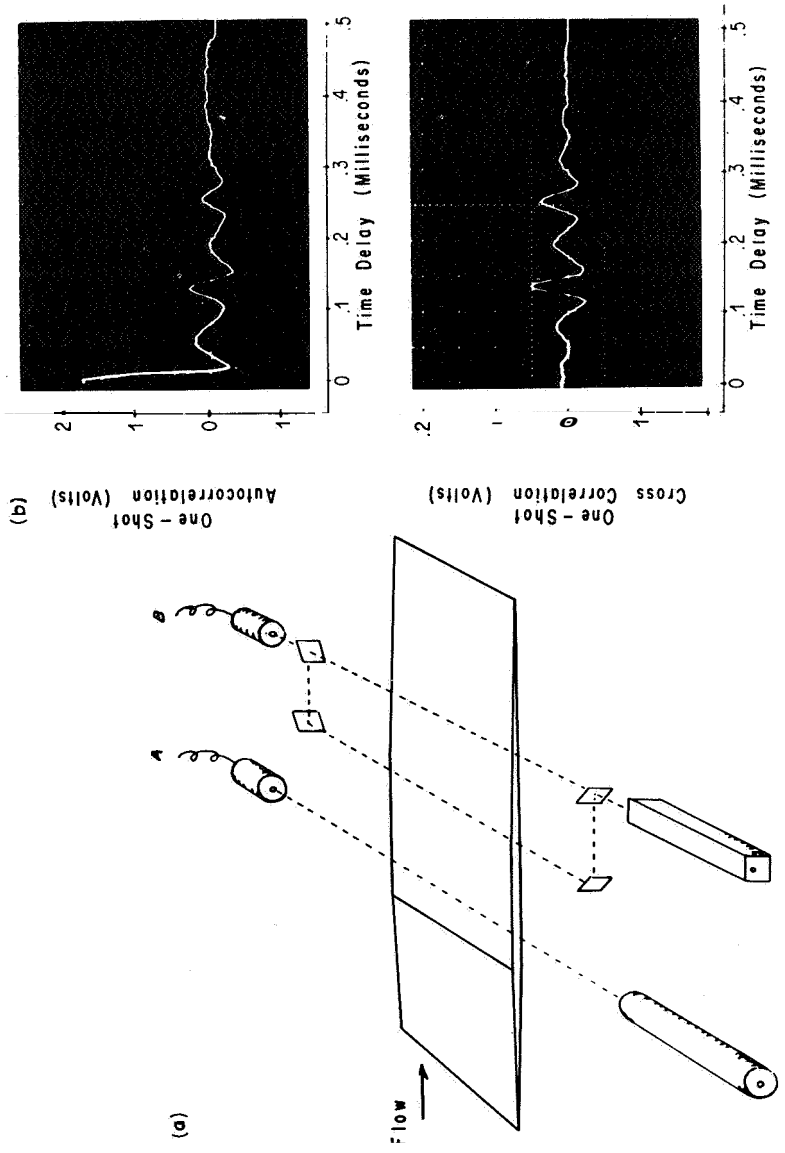

FIGURE 5.—One-shot correlation profiles measured in a supersonic turbulent boundary layer, (*a*) schematic and (*b*) autocorrelogram.

The information contained in the two downstream beams is added optically to form a composite time history that is monitored by the downstream detector B. The upstream beam passes directly into the photodetector A. With these three beams directed through the turbulent boundary layer shown in the previous figure, the time histories of detectors A and B were electronically added to form a composite containing all three time histories. The one-shot autocorrelogram of this composite is shown in the upper half of figure 5(*b*).

Next, the time history of detector A was cross-correlated with the composite time history of detector *B* containing the individual time histories of the two downstream beams. This cross-correlogram is shown at the lower half of figure 5(*b*). We referred to this type of cross-correlation as a one-shot cross-correlation and its correlogram as a one-shot cross-correlogram.

The one-shot cross-correlation for application to random time histories exhibiting statistical stationarity may be summarized as follows:

> The cross-correlation of a single time history with a composite time history, with the single time history containing a random signal that is statistically correlated to two or more random signals contained in the composite, will result in a cross-correlogram exhibiting peaks of cross-correlation between the signal in the separate time history and each of the signals in the composite, the signals in the composite sufficiently lagging behind each other in time.

Referring to both of the correlograms in figure 5, we see that the peak at 0.135 msec represents the correlation between the upstream beam and the center beam. The peak at 0.254 msec (approximately in the center of the grid) represents the correlation between the upstream beam and the last downstream beam. The slope of a straight line connecting these two peaks is a first approximation to the decay history of turbulent structures computed from the same sample of disturbances. Better

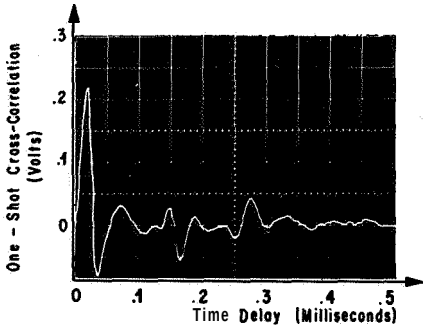

FIGURE 6.—One-shot cross-comelogram with three time histories in the composite.

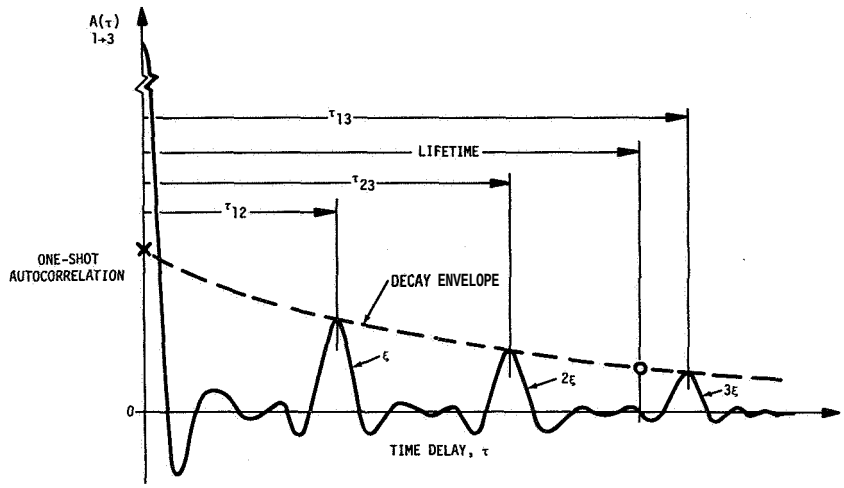

FIGURE 7. — One-shot autocorrelation of the decay of turbulent structures.

approximations of the decay history can be obtained by adding more beams to the composite.

Figure 6 shows a one-shot cross-correlogram of a four-beam arrangement. The knife edge for the second beam was reversed. This reversal changed the sign of the correlated signal and inverted the second peak. The other two peaks are located near the origin and near the center of the grid. The absolute magnitude of these peaks at their respective time delays provides three points on the decay envelope. Inverting the correlation peak by reversing one of the knife edges provides experimental evidence supporting the argument that the sensing mode is schlieren.

Figure 7 is a schematic of a one-shot autocorrelogram of a three-beam arrangement. Knowledge of the signal-to-noise ratio at zero beam separation and the magnitude of the mean-squared value of each of the signals is sufficient for computing the approximate initial position on the decay envelope. In the figure, this point is marked with an "x."

Proceeding from the origin in the positive (τ) direction in figure 7 and referring to the three-beam geometry previously shown, we see that the first peak at τ_{12} represents the correlation between the upstream beam (beam 1) and the center beam (beam 2). The next peak at τ_{23} represents the correlation between beam 2 and the last downstream beam (beam 3). If the turbulence is homogeneous, this peak defines an additional point on the decay envelope; otherwise, this secondary peak can be used to provide information about the change of the decay process with respect to the change in initial position from which the decay envelope is measured. The last peak represents the correlation between the first and third beams.

CONCLUSION

The one-shot autocorrelogram of a three-beam arrangement can provide four points describing the decay envelope computed from a single time history containing information retrieved from the same sample of turbulence. A four-beam arrangement can provide seven such points if none are destroyed by overlapping. Other features of this one-shot method are as follows:

(1) Provides means for determining the most probable flow direction, as well as speed, from one time history of information

(2) Eliminates phase-matching errors, reduces facility run time, and minimizes instrumentation because only one time history is necessary

(3) Provides means for visual online display of the decay history as the data are being retrieved and computed from the same sample of disturbances

REFERENCE

FUNK, B. H.; AND CIKANEK, H. A.: Optical Probing of Supersonic Aerodynamic Turbulence With Statistical Correlation. NASA TM X-53850, June 9, 1969.

NOISE MEASUREMENTS IN WIND TUNNELS

David H. Hickey
NASA Ames Research Center
Moffett Field, Calif.

Paul T. Soderman
Army Aeronautical Research Laboratory

and

Mark W. Kelly
NASA Ames Research Center
Moffett Field, Calif.

The feasibility of using the Ames 40- by 80-ft wind tunnel as a noise research facility was determined by comparison of noise measurements in the free field and the wind tunnel. Background noise levels from the wind-tunnel airflow and drive system were measured. Corrections for sound reflection from the wind-tunnel walls were derived from noise measurements of a point source in the free field and in the wind tunnel. Noise data from a helicopter rotor in the wind tunnel, corrected for wind-tunnel reverberation, agreed well with flyover noise data. Results of this investigation indicate that, within limits prescribed by background noise level, wind tunnels can be useful noise research facilities.

INTRODUCTION

Experimental noise research is usually conducted in outdoor test facilities or in anechoic chambers. In both cases, the relationship between the noise generator and the receiver is constant and usually in the far field. Analysis of results is thus straightforward but does not give an accurate representation of flyover noise because the effects of forward speed (such as compressibility, asymmetric loading, inflow turbulence, and Doppler shift) are not represented. Noise measurements in actual flyovers provide proper representation of these effects, but it is difficult to control the experiment and make accurate measurements. A noise generator in a wind tunnel provides most of the necessary flyover-noise-generation features and provides a controlled environment. Other advantages include the ability to vary model (or noise generator) and test

parameters without regard to flying qualities, the opportunity for a noise evaluation of unconventional research models (such as V/STOL models), and a probable reduction in overall test cost. Of course, most wind tunnels are not designed for noise measurements; they are reverberant chambers or ducts that tend to amplify the free-field noise. Unless special care is taken, wind-tunnel drive-system noise and wind noise on the microphones may mask the noise to be measured. When the noise source is large with respect to the test section, it may be physically impossible to have the separation between the noise source and the microphone that is required for far-field measurements.

In view of the potential advantages of near- or far-field noise measurements in wind tunnels, an exploratory investigation was begun to evaluate the feasibility of performing aerodynamic noise studies in the Ames 40- by 80-ft wind tunnel. This paper summarizes the results of this investigation. Calibrations of the noise properties of the wind-tunnel test section and comparisons of helicopter-rotor noise measured in flight and in the wind tunnel are presented.

MODEL AND FACILITIES

The noise measurements were taken in the Ames 40- by 80-ft wind tunnel during an aerodynamic investigation of two 48-ft-diameter Bell Helicopter Co. rotors. The rotors are described in references 1 and 2.

The Ames 40- by 80-ft wind tunnel has a test section 40 ft high and 80 ft wide. Maximum air velocity in the test section is about 200 knots. Six 6-bladed fans operating up to 290 rpm (630-fps tip speed) drive the wind tunnel. The wind-tunnel entrance cone, test section, and diffuser are constructed of metal plate. The rectangular portions of the rest of the circuit are constructed of fiber-coated corrugated metal. The closed circuit of the wind tunnel is 0.6 mile long.

DISCUSSION

The work described in this paper was a cooperative effort by Bell Helicopter Co., the U.S. Army Aeronautical Research Laboratory at Ames, and the Ames Research Center. Bell Helicopter personnel measured helicopter rotor noise in the wind tunnel and in flight (refs. 1 and 2), while NASA personnel performed the acoustic calibration of the wind-tunnel test section.

Background Noise

Figure 1 shows the overall sound-pressure level and broadband noise of the 40- by 80-ft wind tunnel (with an empty test section) as a function of airspeed. The wind-tunnel noise consists of the tunnel drive fan

harmonics, noise from an auxiliary compressor, and broadband noise. Above 300 Hz, the wind-tunnel noise is primarily broadband noise. Figure 2 shows the same overall wind-tunnel background noise data and the measured sound pressure levels of two 48-ft-diameter helicopter rotors operating at several advance ratios and advancing tip mach numbers. With the thin-tip rotor, the noise up to tip mach numbers of 0.85 is near the level of the tunnel background noise and would have to be corrected for this background noise. The standard-rotor noise level is well above the background noise, so no corrections are necessary. Figure 3 shows the frequency spectrum of wind-tunnel and rotor (standard-tip) noise. The wind-tunnel noise level was well below any of

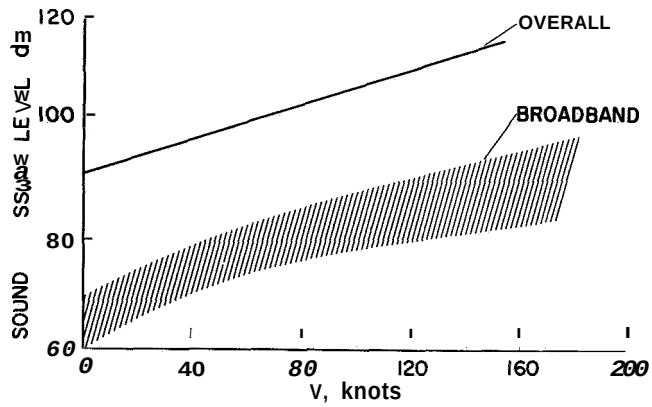

FIGURE 1.—Ames 40- by 80-ft wind tunnel noise level.

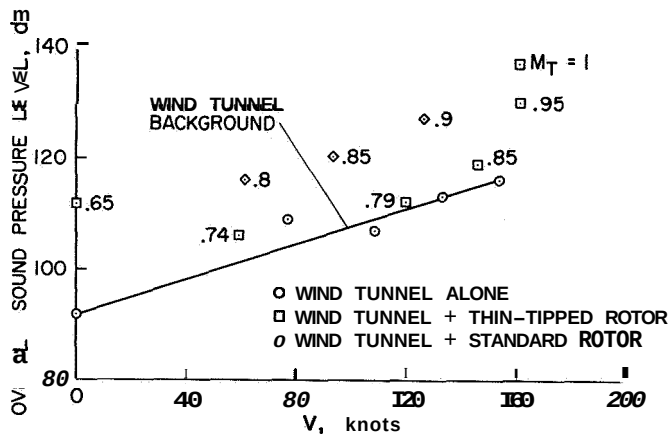

FIGURE 2.—Background noise level in Ames 40- by 80-ft wind tunnel.

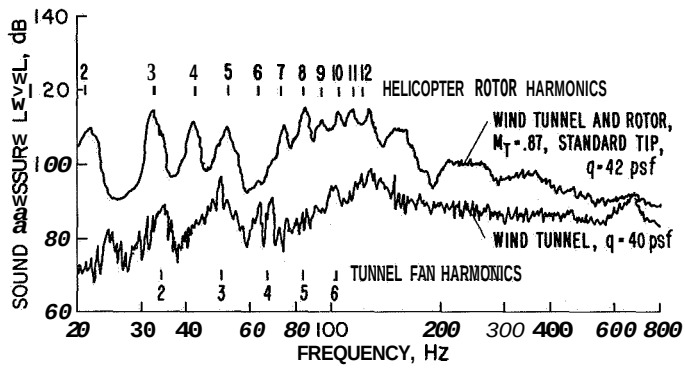

FIGURE 3.—Noise spectrum with and without a rotor.

the important rotor noise contributions. This was not the case for the thin-tipped rotor at low tip mach numbers, however. For that case the wind-tunnel drive fan and rotor harmonics were out of phase so that at some frequencies the wind tunnel was noisier than the rotor. The fan rotational noise was approximately equal to the broadband noise up to a free-stream velocity of about 100 knots. Above 100 knots, rotational noise was dominant. Up to about 100 knots, any noise source with spectrum sound-pressure levels of 95 to 100 dB will dominate the background noise. Above 100 knots, 95- to 100-dB sound-pressure level will be above the background noise only if the frequency is 300 Hz or above. Noise generated by advanced propulsion systems designed to be quiet may fall within the wind-tunnel background noise level; thus noise research in this facility will have to be carefully screened to assure the acquisition of useful information. This problem is not peculiar to the 40- by 80-ft wind tunnel. Recent measurements in an Ames 7- by 10-ft wind tunnel indicated noise levels similar to those measured in the 40- by 80-ft wind tunnel. For small wind tunnels having fan-blade harmonics at higher frequencies, the fan-blade harmonics can possibly be attenuated with techniques currently being explored for application to turbofan engine inlets.

Wind-Tunnel Noise Calibrations

The noise measurement area includes the wind-tunnel entrance cone, test section, and diffuser. The geometry of the measurement area suggests both enclosure and duct noise propagation characteristics. In view of the complicated shapes involved, it was decided to obtain the wind-tunnel noise characteristics experimentally. The noise of a point source was measured in the free field and in the wind tunnel. Some of these measurements made along the centerline of the wind tunnel are

shown in figure 4. Figure 4 also shows the location of the helicopter rotor and microphone used for measurements to be discussed later. The discrepancy between free-field and wind-tunnel measurements was smaller in the wind-tunnel diffuser than in the test section or entrance cone. Figure 5 shows the noise spectrum in the free field and wind tunnel for several microphone positions. In the first position, 50 feet upstream from the speaker, the general effect of the wind tunnel was to increase noise

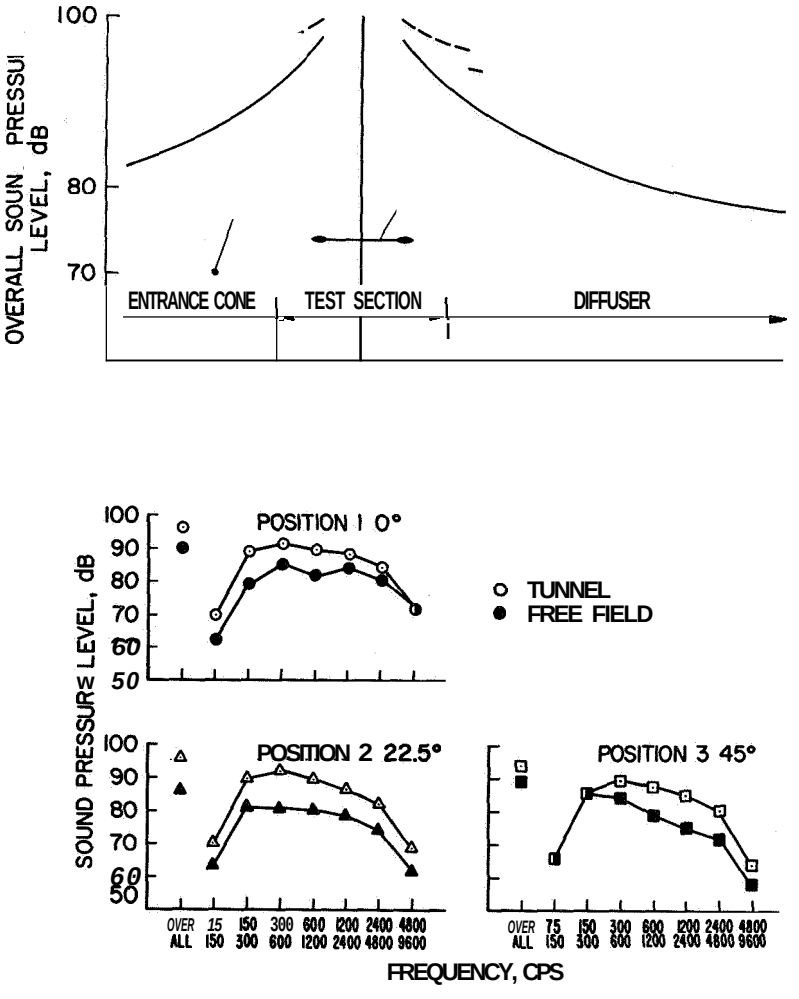

FIGURE 5.—Frequency response on 50-ft radius.

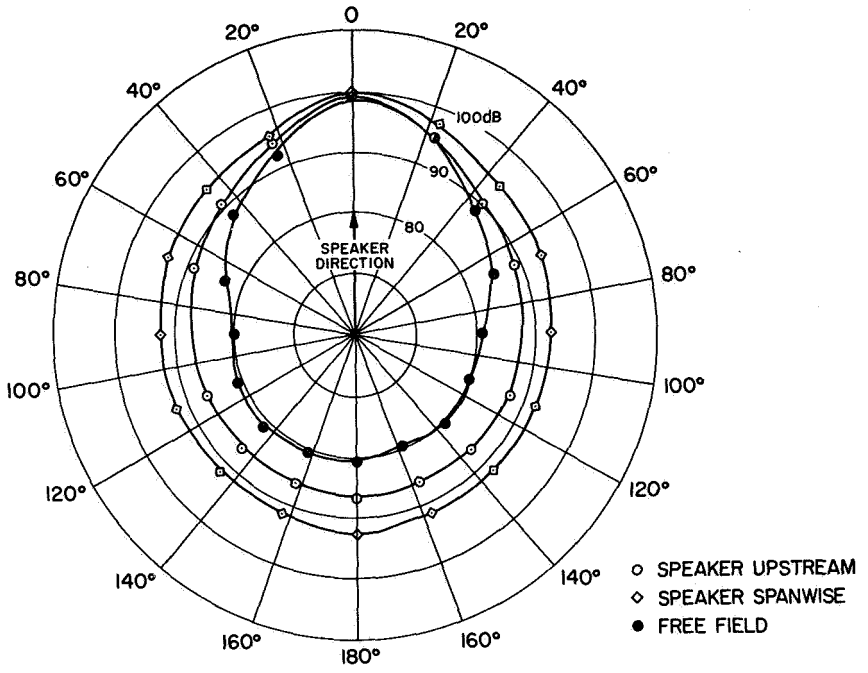

FIGURE 6.—Directional white noise source, radius=20 ft.

in all octaves except the highest. In the second position the effect was essentially the same. In the third position (about 5 ft from the wall), however, the middle octaves were amplified, while the lower octaves were not. These results indicate octave-band analysis is feasible for measurements in a large portion of the wind-tunnel section. Figure 6 shows the noise of a single speaker measured in the free field and in the wind tunnel. The wind-tunnel walls, whether the speaker was oriented streamwise or spanwise, tended to lessen directivity by enforcing the noise in the low-level areas. With the speaker oriented across the wind tunnel, directivity was reduced from 20 dB outside to 8 dB inside the wind tunnel. The maximum noise value did not change with speaker orientation. Wind-tunnel measurements of directivity will be suspect unless the source is very directional.

Comparison of Rotor Noise as Measured in the Wind Tunnel and in Flight

Helicopter rotor noise was measured in the wind tunnel and in flight (see fig. 4 for rotor and microphone locations). Figure 7 shows these measurements for the thin-tip rotor. Frequency spectrums were similar,

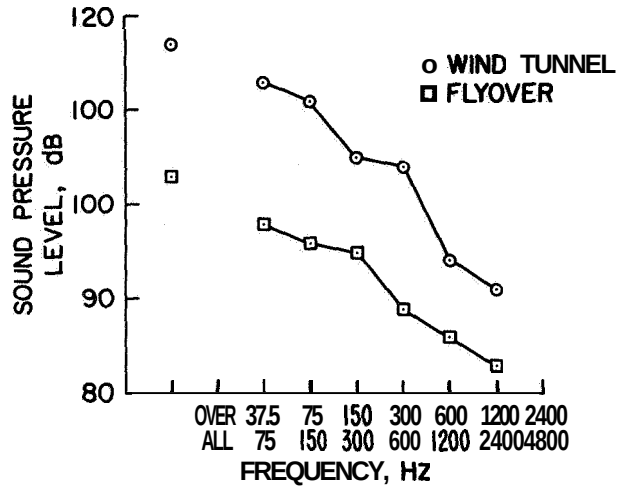

FIGURE 7.—Comparison of uncorrected wind-tunnel and flight-test results.

but the noise measured in the wind tunnel was 8 to 15dB higher than that measured in flight. The wind-tunnel data were corrected according to the wind-tunnel calibration and for a difference in distance, but not for tail rotor noise (in the flight measurements) or directivity. These corrected data are shown in figure 8. Except for one octave band, the corrected wind-tunnel and the flight data agreed within 5 dB. Corrections for tail rotor noise would improve the correlation only slightly because blade slap, which is in the same octave bands, was the dominant noise source. The correlation is good considering the large corrections to the wind-tunnel data, which were derived from data with a point source in the center of the wind tunnel, and the difficulty in obtaining accurate flight data. These results indicate that the probability of obtaining meaningful far-field noise measurements is high if the wind-tunnel background noise is sufficiently low and corrections are known for the reverberant field in the wind tunnel.

Wind-Tunnel Test Results

Use of a wind tunnel as a noise-measuring range permits the investigation of the effects of flight parameters and model or aircraft configurations independently of handling qualities or aircraft flyability. This section of the paper will illustrate the type of noise data that can be obtained during the aerodynamic test of a propulsion system. Figure 9 shows the variation of noise with helicopter rotor collective pitch for several advancing tip mach numbers. As collective pitch was changed, cyclic

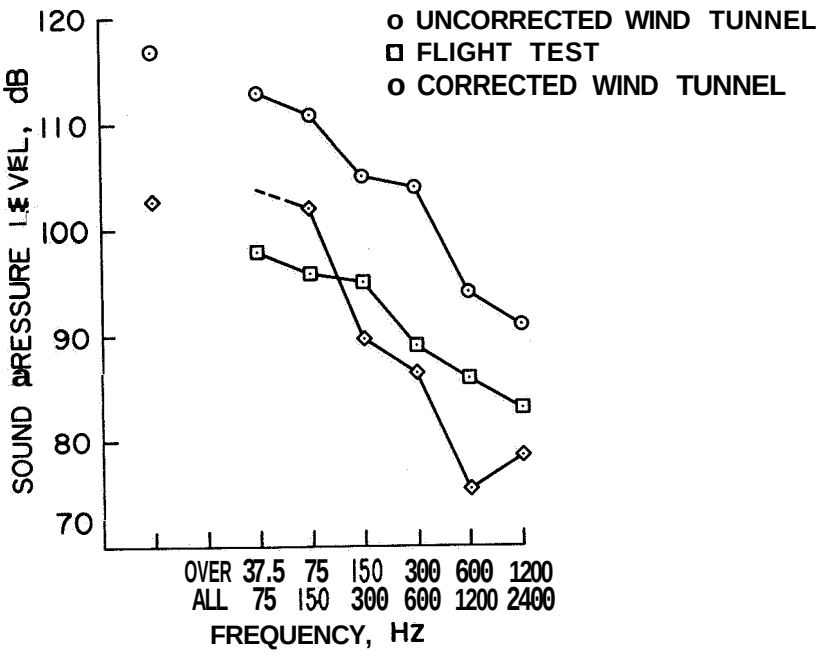

FIGURE 8. —Comparison of corrected wind-tunnel and flight-test results.

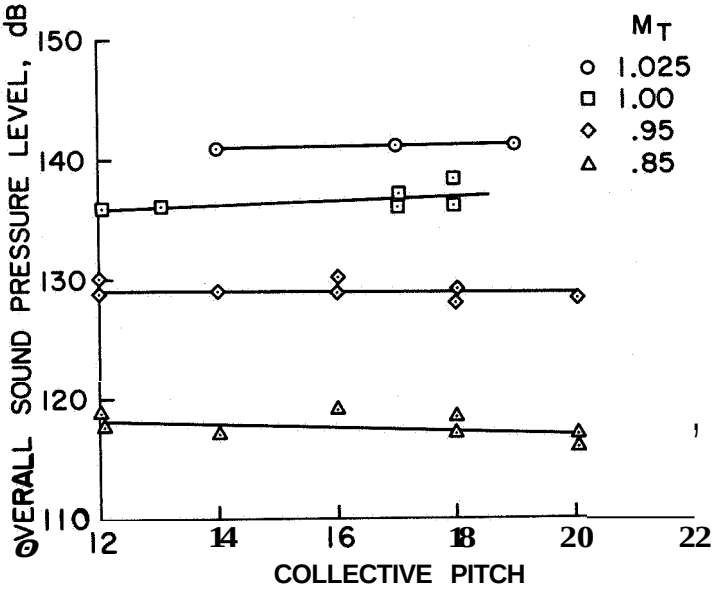

FIGURE 9. —Effect of collective pitch on noise, thin-tip rotor.

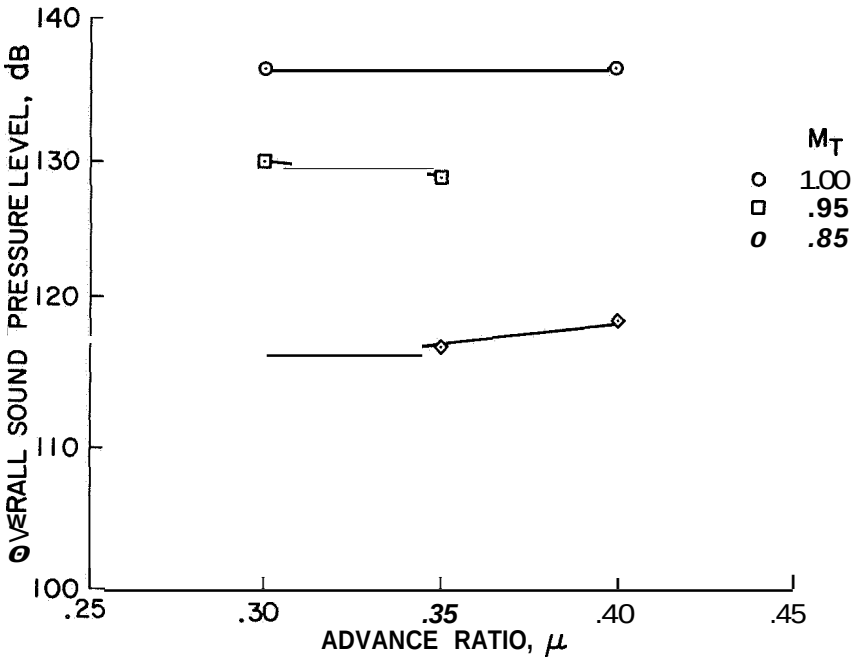

FIGURE 10.—Effect of advance ratio on noise, thin-tip rotor.

pitch was changed to give zero flapping. The most surprising aspect of these results is that noise did not change with collective pitch (blade loading) because of the dominance of compressibility noise. At lower tip mach numbers, noise did change with collective pitch. Figure 10 shows noise as a function of advance ratio for several tip mach numbers that were only slightly affected by advance ratio. In fact, data in figures 9 and 10 indicate the overriding noise generated by this high-speed rotor is primarily a function of tip mach number and, therefore, compressibility effects. Results such as these are easily obtained during a wind-tunnel investigation, but would be costly and difficult to obtain in flyover situations because the environment is difficult to control during flight tests and independent variations of parameters such as advance ratio and mach number are not possible.

CONCLUDING REMARKS

A limited investigation of the Ames 40- by 80-ft wind tunnel as a noise research tool has been conducted. The study of the background noise and reverberation characteristics of the wind tunnel indicates that the probability of making meaningful far-field noise measurements is high if limita-

tions from the magnitude and spectrum of the background noise are recognized and the data are corrected for the effects of the enclosure. It has been shown that rotary-wing aircraft noise can be studied. Additional experiments are required to evaluate the wind-tunnel noise characteristics with multiple noise sources (multiengine models) and when the noise source is positioned away from the wind-tunnel centerline. The wind-tunnel background noise characteristics presented here may be representative of a class of subsonic wind tunnels. It is suggested that background noise level should be a major design criterion for future subsonic wind tunnels.

REFERENCES

1. Cox, C. R.: Full Scale Helicopter Rotor Measurements in the Ames 40- by 80-Foot Wind Tunnel. Rept. 576–099–052, Bell Helicopter Co., July 1967.
2. Cox, C. R.: Rotor Noise Measurements in Wind Tunnels. Proc. Third CAL/AVLabs Symposium, vol. 1, June 1969.

SURFACE-PRESSURE FLUCTUATIONS ASSOCIATED WITH AERODYNAMIC NOISE

Charles F. Coe
NASA Ames Research Center
Moffett Field, Calif.

The three basic sources of random surface-pressure fluctuations associated with aerodynamic noise are attached boundary-layer turbulence, separated flow turbulence, and oscillating shock waves. Investigations dealing with these three flow regions have been numerous. (See references 1 to 3 for an appropriate lengthy bibliography.) A review of the literature indicates, however, that the required statistical information to describe surface-pressure fluctuations is reasonably complete only for subsonic attached turbulent boundary layers. Investigations at transonic and supersonic speeds have primarily included measurements of pressure-fluctuation intensities and very limited analysis of power spectra and/or spatial correlation. With the exception of results in references 1 and 2, these latter forms of analysis have only been published for attached flow.

An extensive investigation of surface-pressure fluctuations underlying attached and separated turbulent boundary layers and shock waves has been undertaken at NASA-Ames Research Center. This research hopes to improve the statistical description of the random-pressure fluctuations at transonic and supersonic mach numbers and to improve the understanding of the mechanism of the turbulent flows. Another objective is eventually to derive empirical expressions that will adequately describe the unsteady pressure fields in the different flow regions. The first reporting of results by Chyu and Hanly (ref. 1) compared the statistical properties of surface-pressure fluctuations in attached supersonic flow with previously published subsonic data. They also showed data obtained in supersonic separated flow induced by a 45" frustum and compared the results with attached-flow data. More recently, the results obtained on several models have been studied to investigate the scaling and spatial correlation of surface pressure fluctuations in separated flow at supersonic mach numbers.[1] This paper intends to describe the overall scope of the research program and to illustrate a few typical results.

[1] These results will be reported in a forthcoming NASA TN.

371-986 0-LT-70—27

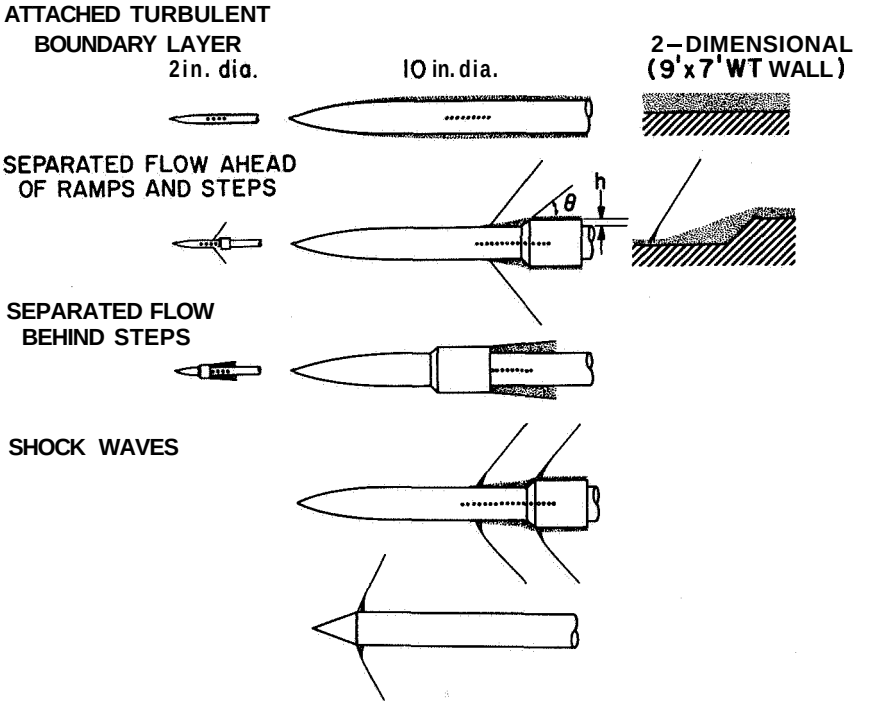

FIGURE 1.—Configuration investigated.

SCOPE OF RESEARCH

Sketches of models used for the investigation (fig. 1) illustrate the initial scope of the research program. The basic configurations were 2-in.- and 10-in.-diameter ogive cylinders and the Ames 9- by 7-ft wind tunnel wall to investigate attached turbulent boundary-layer noise. Cone frustums ahead of axisymmetric rings and two-dimensional wedges of different height and a variety of angles from 15° to 90° were added to the cylinders and walls to investigate the regions of separated flow and shock waves. The different model sizes and tunnel wall provide large variations of the thicknesses of both the attached and separated boundary layers to investigate scaling relationships. The thicknesses of attached boundary layers, for example, varied from approximately 0.16 in. on the 2-in.-diameter model to 4.0 in. on the wind-tunnel wall. Separated-flow lengths ahead of the 45° frustums and an 8-in.-high 45° wedge varied from 1.6 to 35 in. Data were also obtained from cone cylinders to compare shock-wave characteristics at transonic mach numbers with the detached frustum shock waves at supersonic speeds.

The surface-pressure fluctuations were measured with 1/8-in.-diameter pressure transducers that were flush mounted in longitudinal,

lateral, and diagonal arrays. In addition, detailed static-pressure distributions and boundary-layer measurements were obtained. Tests have been conducted at zero angle of attack at transonic and supersonic mach numbers to 2.5. As tests and analysis of data have progressed, results have shown that a serious problem exists with wind-tunnel turbulence and background noise at all frequencies in transonic wind tunnels and, as other investigators have also shown, possibly at lower frequencies in supersonic wind tunnels. As a result of this problem, a separate investigation of the wind-tunnel background noise has been undertaken. The initial analysis of data from the original investigation has concentrated on results obtained in the 9- by 7-ft supersonic wind tunnel. In addition, the scope of the original research program has been extended to include the reduction and analysis of the aerodynamic noise data obtained from the XB–70 flight research program. This work is being done as a cooperative effort with NASA-Flight Research Center and was expected to provide valuable flight data for correlation with wind-tunnel results. Unfortunately, a major part of the pressure-fluctuation data at supersonic speeds was unlike data measured beneath attached boundary layers by other investigators. Another serious problem requiring additional investigation was therefore indicated.

TYPICAL RESULTS

Characteristics of Flow in Vicinity of Detached Shock Wave

Some results of the investigation illustrate the characteristics of the flow in the vicinity of a detached shock wave ahead of a 45° wedge at supersonic numbers. A typical longitudinal distribution of the broadband pressure fluctuations and corresponding power spectra representing each of the three flow regions of interest, the attached boundary layer, separated boundary layer, and shock wave, are shown in figure 2. The characteristic features of the broadband pressure fluctuations $\sqrt{\overline{p^2}}/q$ shown in the inset figure are the low intensities of the attached boundary layer, the high-intensity peak at the shock, which occurs where the slope of the mean static-pressure distribution is maximum, and the plateau level corresponding to the plateau region of the static-pressure distribution.

The power spectra show the distinct differences in shapes and mean-square amplitudes that distinguish each of the flow regions. Shock spectra are characterized by a very steep slope and high intensities at low reduced frequencies, $f\delta_0/U_\infty$ (δ_0 is the boundary-layer thickness immediately ahead of the detached shock wave). The frequency range of these data obtained on the wall of the 9- by 7-ft wind tunnel was from 10 Hz to 20 kHz. The separated-flow spectra were at least one decade lower than the shock spectra at low frequencies. Having a less steep

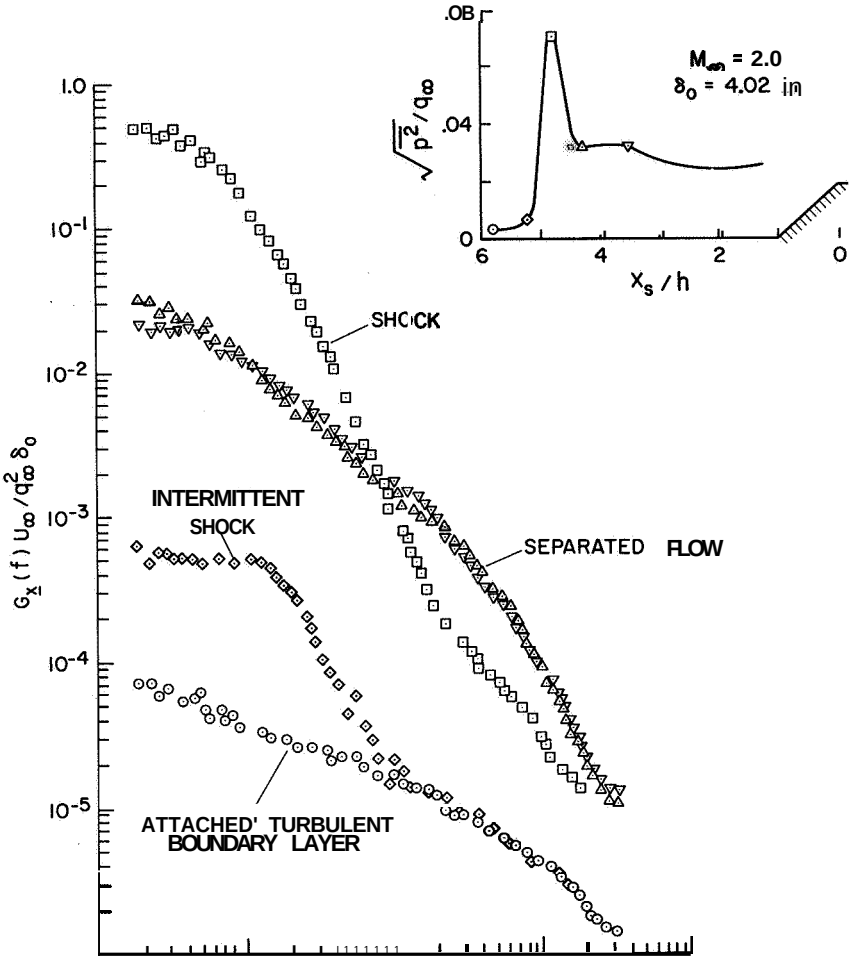

.08
.04
0
$\sqrt{\overline{p^2}}/q_\infty$
M_∞ = 2.0
δ_0 = 4.02 in
6
4
2
0
X_s/h
1.0
10^{-1}
10^{-2}
10^{-3}
10^{-4}
10^{-5}
$G_x(f)\,U_\infty/q_\infty^2\,\delta_0$
SHOCK
INTERMITTENT SHOCK
SEPARATED FLOW
ATTACHED' TURBULENT BOUNDARY LAYER

oscillation. Only the very-low-frequency components of the pressure fluctuations are increased in intensity, while the intermediate and high frequencies retain the intensities of the attached boundary layer.

Correlation of Pressure Fluctuations Between Shock Wave and Adjacent Attached and Separated Flow

The extent of the interaction between the shock oscillations and the pressure fluctuations in the adjacent attached and separated flow regions is shown in figure 3. The coherence functions $\gamma(\xi_1, f)$ and cor-

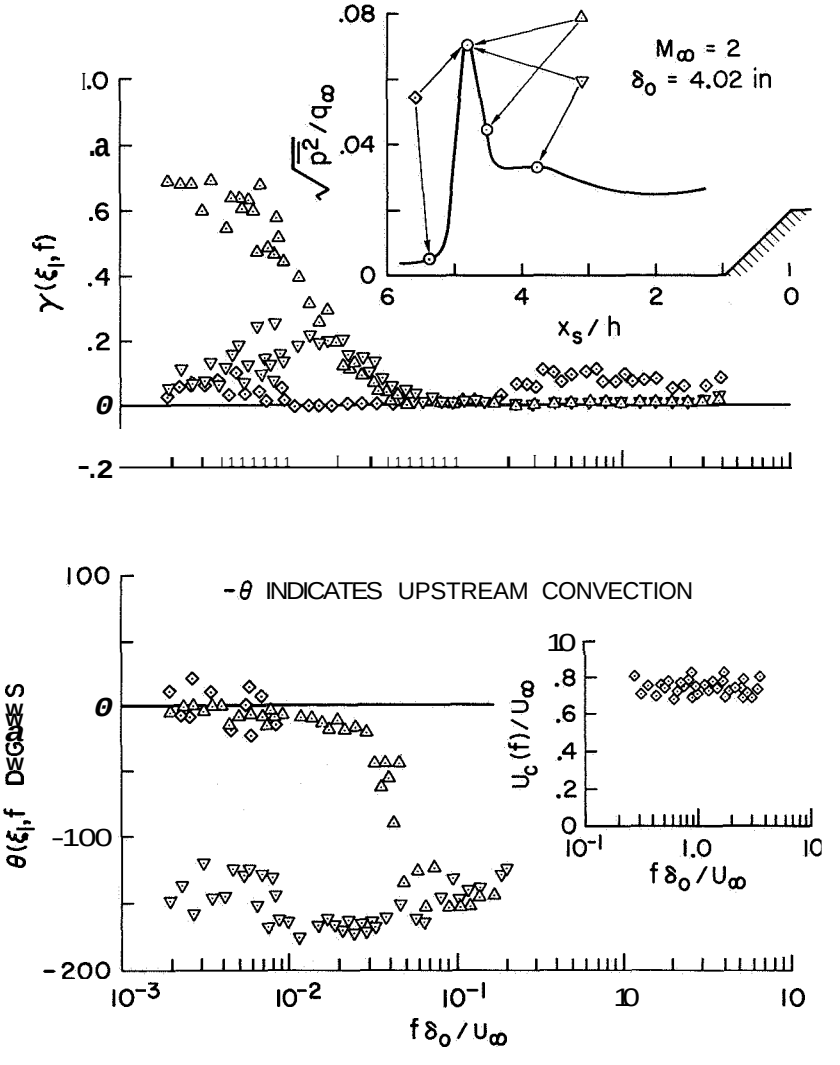

FIGURE 3.—Correlation of pressure fluctuations between shock wave and adjacent attached and separated flows.

responding phase angles $\theta(\xi_1, f)$ represent the cross-spectra of the pressure fluctuations measured by the transducer pairs that are indicated by the corresponding symbols in the broadband distribution of $\sqrt{\overline{p^2}}/q$. For the shock-wave separated-flow case, the results indicate that the pressure fluctuations were related only at reduced frequencies $f\delta_0/U_\infty < 0.04$. For the case shown, the corresponding frequency was approximately 200 Hz. At these low frequencies the coherence diminished rapidly with distance downstream from the shock wave; however, a small amount of coherence, less than 0.2, persisted well into the separated region downstream of the shock wave. The negative phase angles show that the convection of the mean related turbulence was upstream from the separated region to the shock wave, indicating that the turbulence generated within the separated region has a predominating influence on the shock oscillations at low frequencies. For the shock-wave attached-flow case, the results indicate only a small amount of coherence at very low frequencies, undoubtedly resulting from the occasional excursion of the shock wave to the upstream transducer station, no coherence at intermediate frequencies, and then a small amount of coherence (about 0.1) at frequencies $f\delta/U_\infty > 0.2$ (corresponds to approximately 1000 Hz). At these higher frequencies, when there is some Coherence, the phase angles can be converted to narrowband convection velocities. The points shown in the inset figure are scattered somewhat because of the low coherence but indicate convection characteristics, U/U_∞ between 0.7 and 0.8, which are similar to those measured for an attached boundary layer. The similarity of convection characteristics indicates that the higher frequency turbulent eddies that prevail near the wall within an attached turbulent boundary layer persist into the region of the shock wave. These data are compatible with Kistler's results (ref. 4), which illustrate the alternating characteristic of shock-oscillation time histories between attached and separated flow.

Nondirnensionalization of Power Spectra in Separated Flow

Several geometric and flow parameters have been considered for the nondimensionalization of the measured characteristics of the pressure fluctuations. Typical scaling of spectral measurements obtained on the different models in separated flow ahead of the 45" frustums and 45" wedge is shown in figures 4 and 5. The spectra, which are reproduced directly from CRT plots, are not readily identified individually, but the effectiveness of the parameters in reducing the spread of the data can be seen.

The scaling of spectral measurements obtained on the different models at $M=2.0$ is illustrated in figure 4. The spectrum selected for each model represented the approximate average of the measurements and

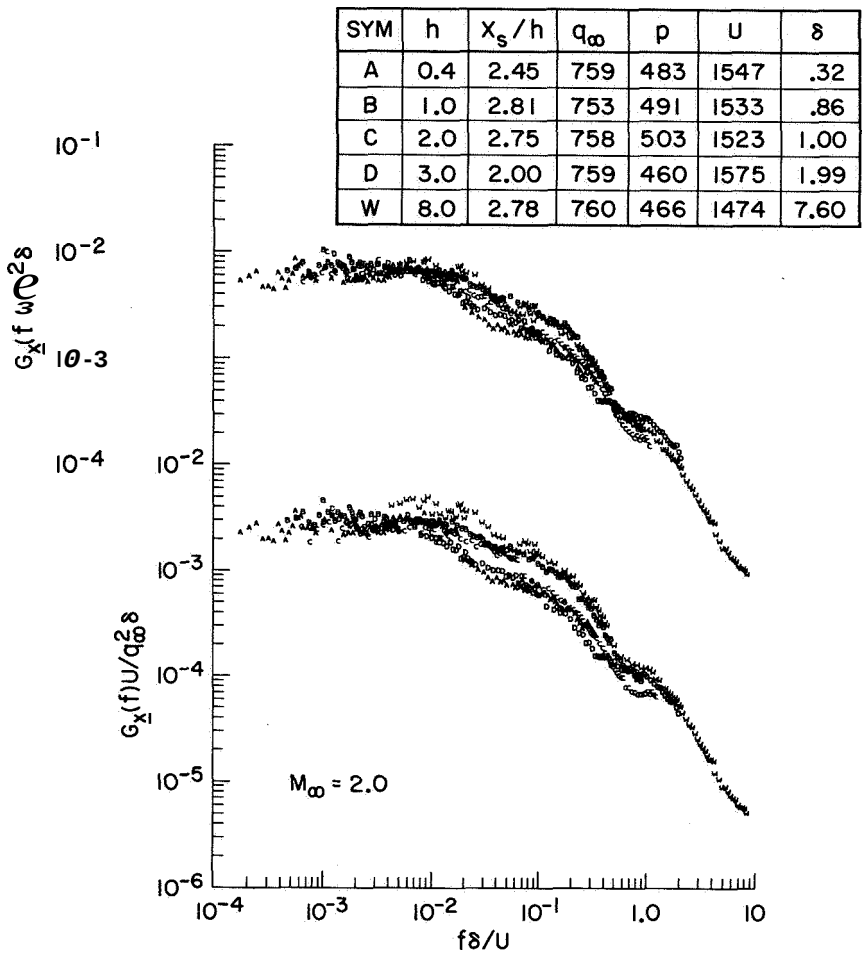

SYM	h	X_s/h	q_∞	p	U	δ
A	0.4	2.45	759	483	1547	.32
B	1.0	2.81	753	491	1533	.86
C	2.0	2.75	758	503	1523	1.00
D	3.0	2.00	759	460	1575	1.99
W	8.0	2.78	760	466	1474	7.60

FIGURE 4.—Scaling of power spectra of pressure fluctuations in separated flow, $M_\infty = 2.0$.

in most cases was obtained near the center of the region of separated flow. Frequency has been nondimensionalized by the local boundary-layer thickness δ and velocity U, and a comparison is made between free-stream dynamic pressure q_∞ and local static pressure p for scaling the mean-square amplitude. The closeness of fit of the irregularities in the shape of the spectra illustrates the effective scaling of frequency by the parameter $f\delta/U$. Comparison of the two groups of data shows that the spread of the mean-square amplitudes was less when scaled by local static pressure than by free-stream dynamic pressure. These differences in the scaling of the spectra are reflected in the different mean-static pressure measurements obtained on the axisymmetric and two-dimensional models.

SYM	M	h	X_s/h	q_∞	p	U	δ
A	1.6	0.4	2.95	896	805	1300	.36
B		3.0	2.00	896	856	1278	2.07
C	2.0	1.0	2.81	753	499	1539	.86
D		8.0	2.78	760	566	1474	7.60
W	2.5	1.0	2.81	538	237	1771	.80
X		8.0	2.78	540	284	1716	7.10

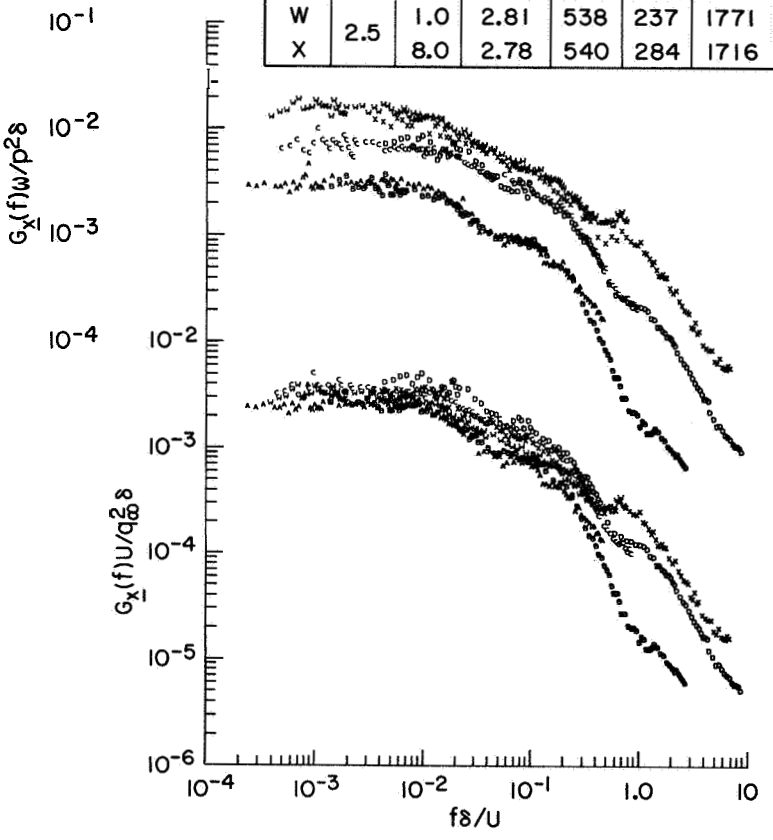

FIGURE 5.—Effect of mach number on separated-flow-power spectra.

The effective scaling of spectra by the local static pressure only applies at constant mach numbers. Figure 5 shows additional spectral measurements obtained at mach numbers from 1.6 to 2.5. The results show a closeness of fit at each mach number that is considered remarkable for random dynamic data obtained on different models, but there was a significant variation of the nondimensionalized spectral levels with mach number. The least effect of mach number was obtained when the spectra were nondimensionalized by q_∞. The curves approach a collapsed form at reduced frequencies $f\delta/U < 0.4$; however, for $f\delta/U > 0.4$

the power spectra increased with mach number. This mach-number effect was previously observed by Chyu and Hanly (ref. **1)** and was attributed to the fact that at high frequencies the predominant turbulent eddies attain supersonic convection speeds. The turbulent eddies are therefore more sensitive to the variation of mach number.

Spatial Correlation of Pressure Fluctuations in Attached and Separated Flow

Chyu and Hanly (ref. 1) presented the power, cross-spectra, and space-time correlations **of** fluctuating pressures underlying the attached boundary layer on the 10-in.-diameter ogive cylinder and the separated boundary layer ahead of the 2-in.-high frustum. Among other things, they investigated the cospectral and quadspectral density and coherence as functions of a wave-number parameter $f\xi_1/U_c(f)$, where ξ_1 is the longitudinal separation distance of pressure transducers and $U_c(f)$ is the convection velocity as a function of frequency. Illustrative coherence functions are shown in figure **6.** The results indicate a similarity between the coherence measurements in attached and separated flow at supersonic mach numbers if the velocity term is $U_c(f)$. In separated flow, $U_c(f)$ varies significantly with frequency. The general trends of the data are also similar to the subsonic-flow measurements by Bull (ref. 5**).** The envelope of the coherence functions for various spatial distances

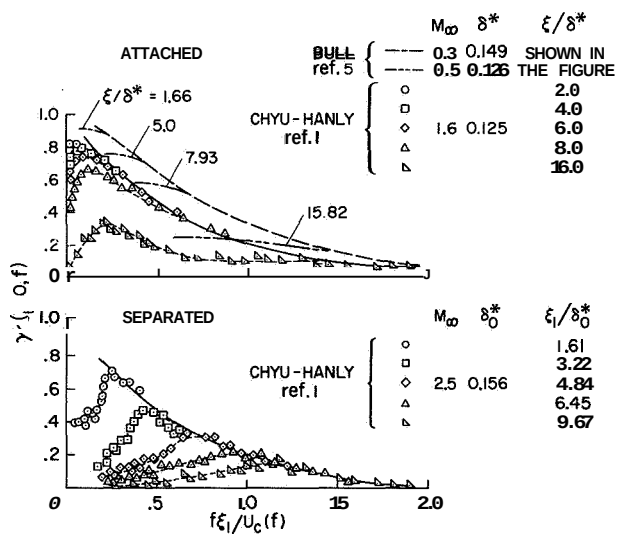

FIGURE 6.—Longitudinal coherence of pressure fluctuations in attached and separated flows.

ξ_1/δ decreases exponentially with increasing frequency.[2] The envelope, however, unfortunately represents the coherence only at high frequencies. Consequently, a different representation of the spatial correlation is being investigated that involves the determination of a decaying exponential of the form

$$|G(\xi_1, f\delta/U|_{\text{norm}} = e^{-\xi^{\alpha_1}}$$

The normalized moduli of the cross-spectral densities $|G(\xi_1, f\delta/U|_{\text{norm}}$ for available or selected transducer spacings ξ_1 (longitudinal) and ξ_2 (lateral) are curve fitted to the exponential function by the method of least squares to obtain a nondimensional attenuation-coefficient function $\alpha(\xi_1, f\delta/U)h$.[2] To date, only separated-flow data have been analyzed to obtain the attenuation coefficients; however, this form of analysis will be extended to include the attached-flow case.

Figure 7 shows the attenuation-coefficient function measured in separated flow on the 10-in.-diameter model with the 2-in.-high frustum shoulder. The function is shown to be reasonably independent of the number of moduli, the transducer spacing, or the reference locations involved in the curve fitting. These results indicate that the flow is relatively homogeneous within the limited area of the separated-flow region where the measurements were obtained. It appears that the attenuation coefficients decreased slightly at higher frequencies as the larger transducer spacings were used in the analysis. The variation is considered insignificant, however, in light of the state of the structural part of the problem of predicting response to random turbulence. Attenuation coefficients obtained from transducer arrays oriented longitudinally, diagonally, and laterally to the free-stream flow indicate that the decay of correlated turbulence was independent of orientation at $f\delta/U < 0.06$. The predominant turbulence is therefore nonconvective at the lower frequencies, and contours of equal spatial correlation would be circular. At $f\delta/U > 0.06$, the attenuation coefficients were progressively lower as the angularity of the transducer orientation changed from lateral to longitudinal, indicating extended correlation in the direction of free-stream flow.

A comparison of the attenuation-coefficient functions obtained on the different models is shown in figure 8. The results indicate that the

---

[2] The attenuation-coefficient form of presentation of the spatial correlation was introduced by Dr. Richard D. Rechtien, University of Missouri, Rolla, Mo., while supported by NASA grant NGR 26-003-026.

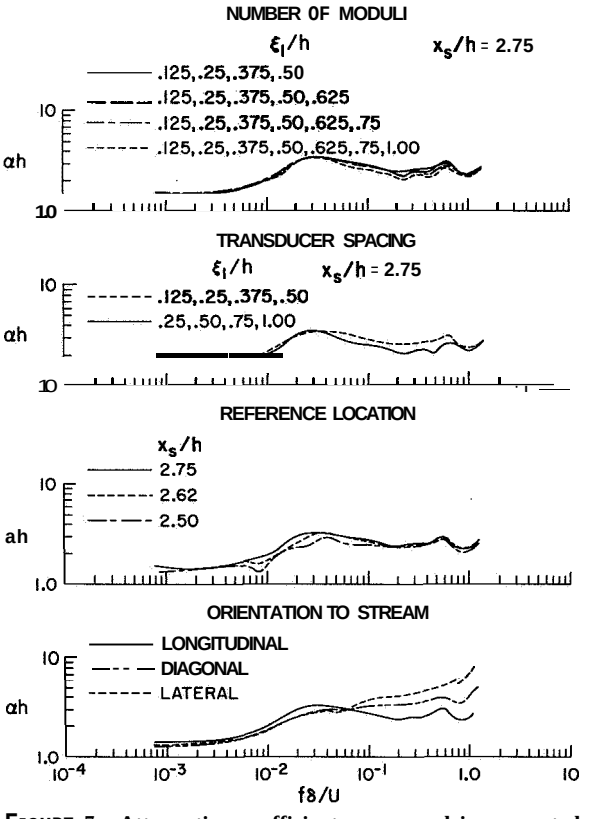

FIGURE 7.—Attenuation coefficients measured in separated flow on 10-in.-diameter model ahead of 2-in.-high 45° frustum, $M_\infty = 2.0$.

frequency-dependent characteristics of the decay of correlated turbulence are effectively scaled by $f\delta/U$. The nondimensionalized attenuation coefficients were in relatively good agreement at $f\delta/U < 0.04$ and at $f\delta/U > 0.5$. Between these two nondimensional frequencies, agreement continued in the general shape of the attenuation curves, but a larger spread in the data, up to a factor of 2, existed. In spite of this greater spread of data in the intermediate frequency range, it is believed that a single curve could be drawn and an expression derived to adequately represent the attenuation-coefficient function. Additional analysis of fluctuating pressures is in progress to determine whether the characteristics remain consistent when the separated region is induced by different frustum and wedge angles.

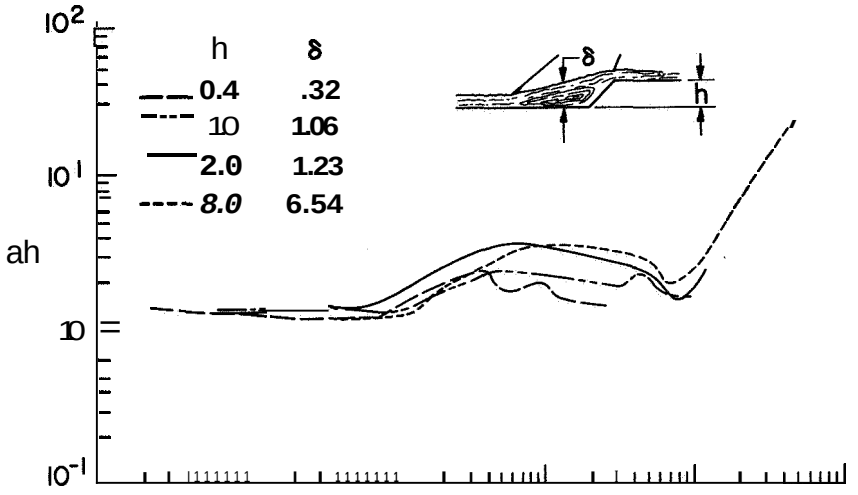

Environmental and Test Technique Problems

As previously mentioned in the section entitled "Scope of Research," problems have been encountered with wind-tunnel background noise and with pressure-fluctuation measurement techniques. A few specific examples of results, including XB–70 flight data, follow that are related to these problems.

Wind-Tunnel Background Noise

Analysis of data obtained in wind tunnels has disclosed that results can be seriously affected by the environmental noise and/or turbulence. The noise environment in a slotted or porous transonic test section often exceeds the levels of aerodynamic noise induced by turbulence on models. In wind tunnels with smooth nonporous walls (subsonic or supersonic), the effects of tunnel noise are more subtle but have been suspected of influencing the lower frequency content of attached turbulent boundary-layer noise.

Figure 9 illustrates a problem of evaluating supersonic wind-tunnel noise and its effects. Power spectra of pressure fluctuations are shown that were measured beneath a laminar and two turbulent boundary layers of different thicknesses at $M=2$ in the 9- by 7-ft wind tunnel. It can be noted that the mean-square intensity from the laminar boundary layer exceeded the intensities from the attached boundary layer at low frequencies. Because subtraction of the laminar spectrum from the

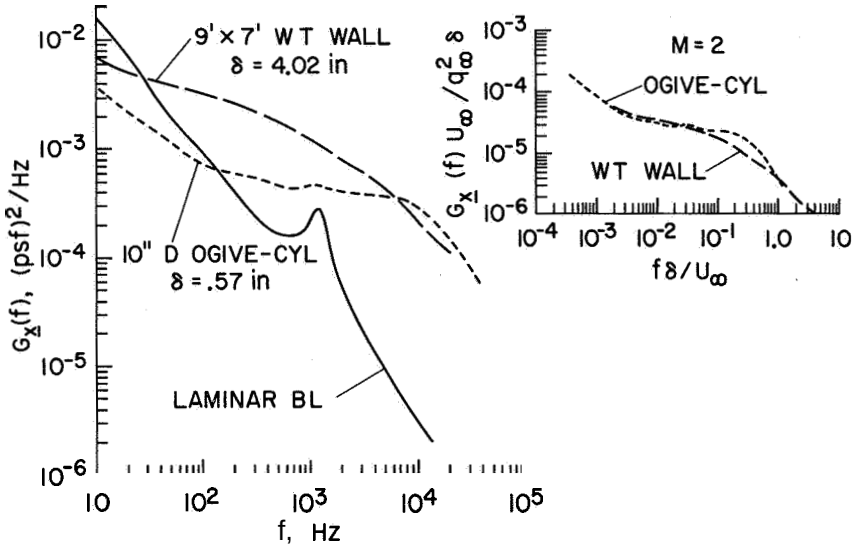

FIGURE 9.—Comparison of spectra of pressure fluctuations underlying laminar and turbulent attached boundary layers in the Ames 9- by 7-ft wind tunnel.

attached spectra would yield negative power, the question of whether the laminar spectrum adequately represents the environmental turbulence and/or noise arises. If so, it would be indicated that the background noise is attenuated significantly as it propagates through a turbulent boundary layer. It is interesting to note in the inset figure that the two attached boundary-layer spectra scale reasonably well even though they include an undetermined contribution from the background noise at low frequencies. Such results indicate a need for further study of wind-tunnel background-noise calibration techniques and a need to quantitatively evaluate the effect of turbulence and velocity gradients on the propagation of noise through a turbulent boundary layer.

Effect of Transducer Flushness

Some inconsistencies in pressure-fluctuation measurements beneath attached boundary layers have prompted the investigation of the effects of the smoothness of a transducer installation. Figure 10 shows the intensity of the pressure fluctuations measured by a transducer as it was moved in and out from a flush position in the **9**- by 7-ft wind-tunnel wall and the effect on the fluctuations measured downstream at a distance of **0.118 6.** The results also show the effects on the coherence and convection-velocity measurements. It can be seen that a very small discontinuity in the surface $y/\delta < \pm 0.001$ was sufficient to significantly affect the rms intensities at the location **of** the movable transducer.

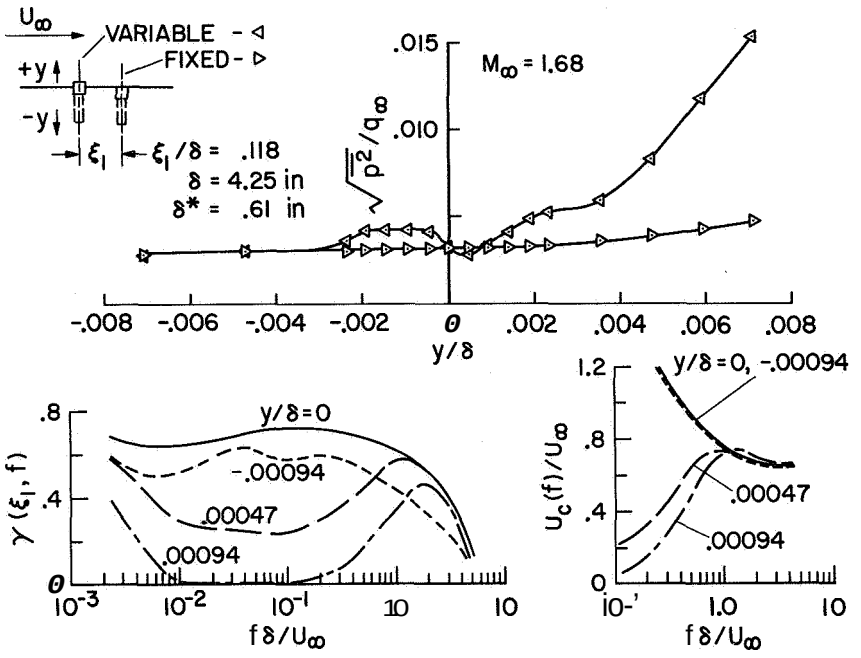

FIGURE 10.—Effect of the flushness of a transducer mounting on the measurement of wall pressure fluctuations.

Very small changes in transducer flushness even more drastically affected the coherence and narrowband convection-velocity measurements. The results show that a transducer protruding approximately 0.0005 6 introduced sufficient turbulence near the wall to predominate in the convected-related turbulence at $f\delta/U_\infty < 1.0$. A submerged transducer at $y/\delta \simeq -0.001$ introduced turbulence locally that affected the coherence throughout the frequency range, but apparently convection of turbulence between the transducers was negligible. Such extreme sensitivity of the flow to instrumentation interference undoubtedly accounts for much of the experimenter's difficulty in obtaining consistent and reliable aerodynamic noise measurements, particularly those involving spatial correlation.

Pressure-Fluctuation Measurements on the XB-70

Figure 11 shows a comparison of surface-pressure fluctuations measured in attached flow on the XB–70 by various investigators as a function of mach number. The two sets of XB–70 flight data indicated *(A)* and *(B)* represent results obtained from arrays of two different types of pressure transducers mounted on the underside of the fuselage about 20 ft from the nose. Some *(A)* transducers were installed on all aero-

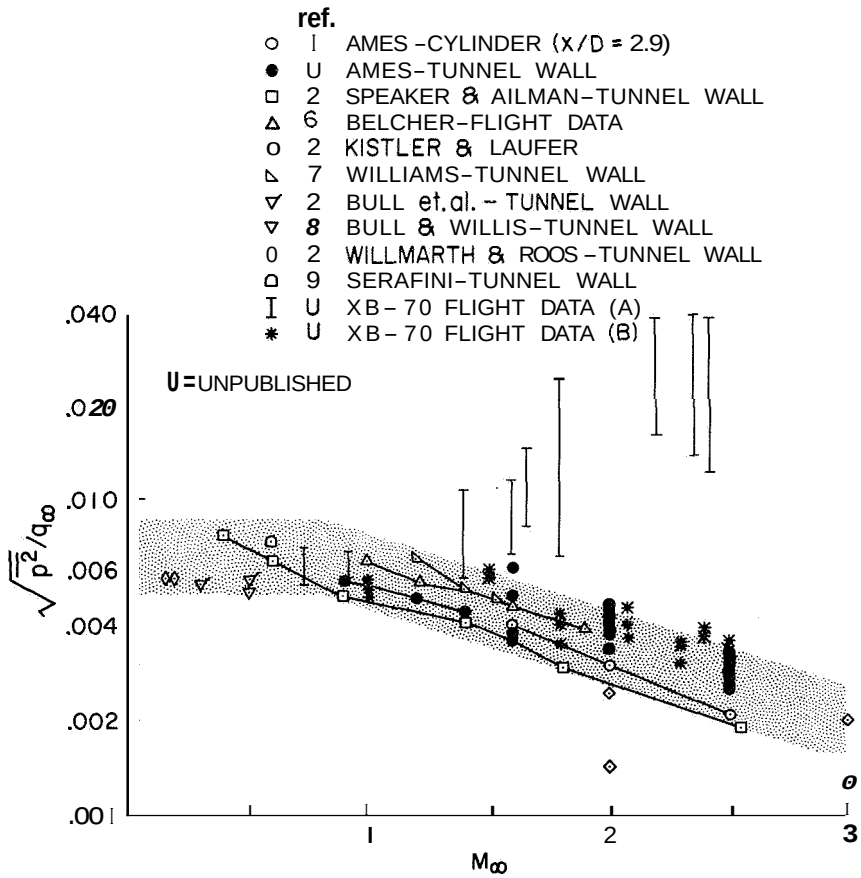

FIGURE 11.—Comparison of pressure fluctuations measured on XB-70 and by various investigators (refs. 1, 2, and 6 to 9).

dynamic-noise flights throughout the flight research program, while the *(B)* transducers were used only on the last supersonic flight. If the **XB-70** fight data *(A)* are disregarded, most of the remaining data fit within an envelope having a spread of about **80** percent, which in itself does not speak well of the present methods **of** measuring fluctuating pressures. If the **XB-70** flight data *(A)* are considered, there is even a more radical difference in pressure-fluctuation measurements at supersonic mach numbers. The **XB-70** flight data *(A)* agreed subsonically with other data but were up to one decade higher than other data at $M=2.4$. The corresponding spectra of the *(A)* data at supersonic mach numbers also differed greatly from attached boundary-layer-like spectra and appeared like the typical shock spectrum shown in figure 2.

The reasons for the large differences between the XB–70 flight data (A) and (B) still have not been identified, although the shock-wave-like spectrum implies a local flow interference. Calibration of the two types of transducers in still-air environments over the flight range of temperature, pressure, and vibration have not yielded any accountable differences in performance. Because such large differences in the pressure fluctuations have been measured by two supposedly acceptable transducer systems, it is important for future applications that the reasons for the discrepancies be resolved. Tests that include the installation of some XB–70(A) transducers in the 9- by 7-ft wind tunnel are now in progress.

CONCLUDING REMARKS

The discussion above has only touched on highlights of the work in progress to investigate pressure fluctuations associated with aerodynamic noise. Analysis of data obtained in regions of attached and separated flows and shock waves is continuing, and significant results will be reported as they become available. In addition, the investigation of wind-tunnel background noise and other test technique problems are in progress to improve the reliability and establish practical limits of aerodynamic noise data acquisition in wind-tunnel facilities.

REFERENCES

1. CHYU, W. J.; AND HANLY, R. D.: Power and Cross-Spectra and Space-Time Correlations of Surface Fluctuating Pressures at Mach Numbers Between 1.6 and 2.5. AIAA paper no. 68–77, Jan. 1968.
2. SPEAKER, W. V.; AND AILMAN, C. M.: Spectra and Space-Time Correlations of the Fluctuating Pressures at a Wall Beneath a Supersonic Turbulent Boundary Layer Perturbed by Steps and Shock Waves. NASA CR–486, 1966.
3. LOWSON, M. V.: Prediction of the Inflight Fluctuating Pressures on Space Vehicles. Rept. WR 65–26, Wyle Laboratories, Dec. 1965.
4. KISTLER, A. L.: Fluctuating Wall Pressure Under a Separated Supersonic Flow. J. Acoust. Soc. Am., vol. 36, no. 3, Mar. 1964, p. 543.
5. BULL, M. K.: Wall Pressure Fluctuations Associated With Subsonic Turbulent Boundary Layer Flow. J. Fluid Mech., vol. 28, pt. 4, 1967, p. 719.
6. BELCHER, P. M.: Predictions of Boundary-Layer Turbulence Spectra and Correlations for Supersonic Flight. Paper presented at Fifth Int. Congr. Acoust. (Liege, Belgium), Sept. 1965.
7. WILLIAMS, D. J. M.: Measurements of the Surface Pressure Fluctuations in a Turbulent Boundary Layer in Air at Supersonic Speeds. AASU Rept. 162, Dec. 1965.
8. BULL, M. K.; AND WILLIS, J. L.: Some Results of Experimental Investigations of the Surface Pressure Field Due to a Turbulent Boundary Layer. AASU Rept. 199, Nov. 1961.
9. SERAFINI, J. S.: Wall-Pressure Fluctuations and Pressure Velocity Correlations in a Turbulent Boundary Layer. NASA TR R–165, 1958.

OPTIMUM LINING CONFIGURATIONS

H. K. **Liu**
A. J. Martenson
General Electric Research and Development Center
Schenectady, N.Y.

A method has been developed to predict the effects of acoustic lining in axially symmetric ducts of arbitrary shape with a moving medium. It is not necessary to assume that the duct is infinitely long, and the method will yield the directivity pattern as well as the acoustic distribution in the duct. It is assumed that a large set of unknown acoustic sources is distributed over the surface of the duct. The values for these sources are determined by using a set of linear, algebraic equations that satisfy the boundary conditions. Calculation of the acoustic pressure anywhere inside or outside of the duct then becomes a simple summation process. Experimental validation of the method is presented. An extension is proposed by which the optimum distribution of wall impedance may be found.

INTRODUCTION

One of the most effective ways to silence the noise radiated from fans and compressors is to install acoustic lining in the inlet or exit ducts. The selection of the best lining is still a somewhat uncertain process because of certain limitations in present technology.

Linings are often tested in the laboratory with a standing wave tube in which the acoustic wave moves normal to the absorbing surface. Under these conditions, the characteristic impedance would be the most effective energy absorber. A large improvement over this procedure is effected when the lining is tested in a duct with a moving medium. This type of testing is closer to reality because boundary-layer effects are approximated and the acoustic waves are moving parallel to the absorbing surface. The effectiveness of the lining is judged by its ability to absorb acoustic energy as the waves move down the duct. A rotating, many-lobed source in a circular duct should be used for the best simulation. This is still no substitute for an engine test because the actual shape of the duct may be important. Also, the expense of fabricating and

installing lining, especially for a circular duct, prohibits a large parametric study to arrive at the optimum lining configuration.

The problem is complicated still further by the expectation that the optimum lining configuration is likely to have different impedances at various positions in the duct. The angle of incidence between the incoming wave and the normal to the wall will vary from place to place, as will the boundary-layer thickness. It is clear that an analytical approach to the problem is needed.

This paper reports some of our progress and results concerning the task of developing the best lining configuration. We have developed a tool that makes it possible to predict the effects of a particular lining configuration in a duct of any axially symmetric shape with a moving medium. This analysis is limited to discrete frequency studies and does not account for any real fluid effects such as turbulence or boundary layers. Boundary-layer effects are very important and it is, therefore, proposed that the results of this study be applied in the following way. The inside boundary of the duct with its distributed impedance as modeled in the digital computer is actually the edge of the boundary layer. When an optimum impedance distribution has been obtained, it must be remembered that this impedance is actually the impedance at the edge of the boundary layer and results from the combined effects of the boundary layer and the lining itself. The determination of the impedance of the lining alone may be considered as a separate analytical problem or may be solved experimentally by measuring the impedance at the edge of the boundary layer in a model that approximates the flow regime. This would certainly be a simpler test than the ones mentioned earlier because there is no need to model the actual acoustic situation existing in the engine.

The method for calculating acoustic pressures in ducts of arbitrary shape will now be outlined.[1] This outline will be followed by a discussion of a method for optimizing the lining impedance.

We will use the techniques that were originally developed for sonar studies and extend them to include the moving medium and acoustic linings. Chen and Schweikert (ref. 1) solve a very general class of acoustic transmission problems using the concept of a distributed acoustic source over the boundary of the body. The approach is basically an extension of potential flow theory with the addition of phase effects necessary for acoustic studies. It is necessary to extend Chen and Schweikert's analysis to apply it to the moving medium, soft walls, and rotating patterns.

---

[1] A. J. Martenson and H. K. Liu: Propagation of the Discrete Frequency Noise in Axisymmetric Ducts of Arbitrary Shape. To be published in J. Acoust. Soc. Am.

THEORY

Assuming small acoustic pressure and a homogeneous medium, the following wave equation suffices to describe the potential in the field (ref. 2):

$$\left[\frac{1}{r}\frac{\partial}{\partial r}\left(r\frac{\partial}{\partial r}\right)+\frac{1}{r^2}\frac{\partial^2}{\partial\phi^2}+(1-M^2)\frac{\partial^2}{\partial z^2}-\frac{2M}{c}\frac{\partial^2}{\partial z\,\partial t}-\frac{1}{c^2}\frac{\partial^2}{\partial t^2}\right]\Phi=0 \qquad (1)$$

$$\text{pressure}=p'=\left(\frac{\partial\Phi}{\partial t}+V_z\frac{}{\partial z}\right. \qquad (1a)$$

where

c	acoustic velocity
t	time
ϕ, r, z	cylindrical coordinates as shown in figure 1
M	steady mach number of the fluid in the $+z$ direction
Φ	velocity potential
ρ_0	fluid density
V_z	steady velocity in the z-direction

Figure 1 shows the coordinate system.

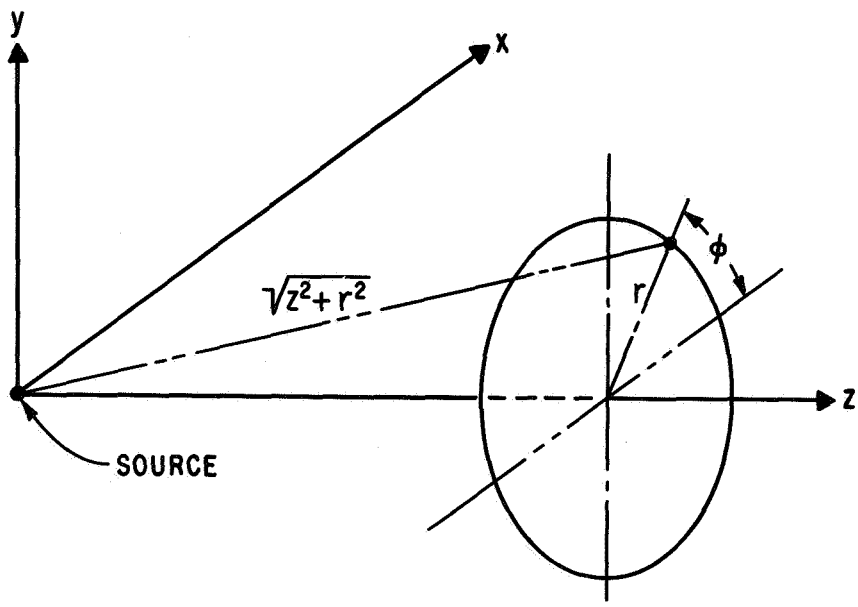

FIGURE 1. – Cylindrical coordinate system.

Consider an acoustic source located at the origin of the coordinate system. With an infinite homogeneous medium, the potential in the field is distributed as follows (ref. 2):

$$\Phi=\frac{A'e^{-i(\omega t-\nu R_0)}}{R_0^*}=\hat{\Phi}'(z,r)e^{-i\omega t} \tag{2}$$

where

$$R_0=\frac{-Mz+[z^2+(1-M^2)r^2]^{1/2}}{1-M^2} \tag{3}$$

$$R_0^*=\left[\frac{z^2}{1-M^2}+r^2\right]^{1/2} \tag{4}$$

$r^2=x^2+y^2$

$\hat{\Phi}'=\dfrac{\hat{A}'e^{i\nu R_0}}{R_0^*}$

$\nu=\omega/c$

$\hat{A}'=$ source strength

$\Lambda=$ complex number

Relation (2) satisfies the differential equation (1).

A series of terms of the same form as equation (2) will be used to obtain the solution when the boundary is present. Obtaining the solution will be done by introducing a set of acoustic source points near the boundary and summing their effect.

Replace the boundary by a set of distributed, acoustic source points of unknown strength as illustrated in figure 2. Considering a point ξ somewhere in the acoustic field, the velocity potential may be expressed as follows:

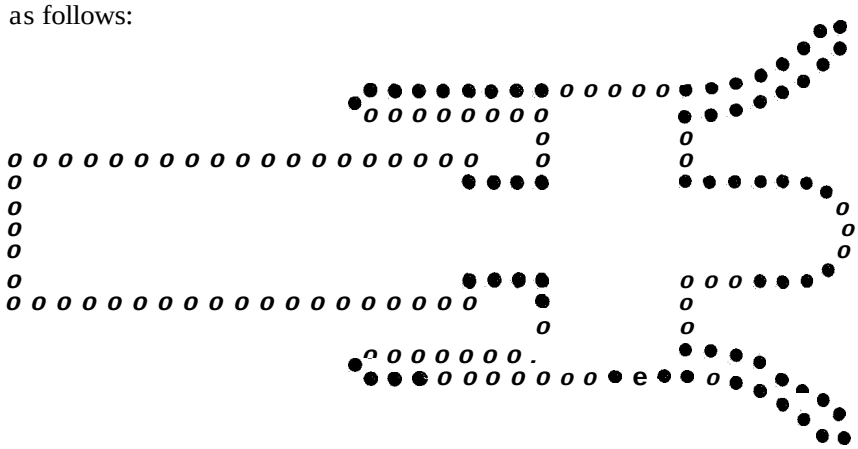

FIGURE 2.—Distributed source points.

$$\hat{\Phi}'_{\xi}=\int_S\int \hat{A}'(s)\frac{e^{i\nu R}}{R^*}ds \tag{5}$$

where S denotes the total surface of sources and $\hat{A}(s)$ is the source strength per unit area. R and R^* are defined as follows:

$$\begin{aligned} R&=\frac{-(z-z')M+\sqrt{(z-z)^2+(1-M^2)[(x-x')^2+(y-y')^2]}}{1-M^2}\\ R^*&=\sqrt{\frac{(z-z')^2}{1-M^2}+(x-x')^2+(y-y')^2}\end{aligned} \tag{6}$$

Because the wave equation is linear, it is satisfied by relation (5). The objective is to determine the unknown source strength distribution $\hat{A}(s)$, such that the boundary conditions are also satisfied. The surface of sources S will be placed immediately inside the boundary B of the originai body. It would be possible to place S on B, but relation *(5)* would become more complex if pressure or velocity is calculated on the boundary because the expression becomes indeterminate as ds and R" approach zero.

A boundary condition must be defined for every point on the boundary B. This condition may be a statement of normal velocity, pressure, or acoustic impedance. Let us assume that the normal velocity at the exterior of B is given by

$$u=\hat{U}(s)\,e^{i(m\phi-\omega t)}$$

where m is the number of lobes.

Because of the rotating pressure field, it is logical to assume a source of the following type:

$$\text{Source strength per unit area}=\hat{A}'e^{-i\omega t}=Ae^{i(m\phi-\omega t)}$$

According to the definition of the velocity potential, the outward normal derivative of potential can be written as follows:

$$\frac{\partial\Phi}{\partial N}=-u \tag{7}$$

where

$$\Phi=\hat{\Phi}'e^{-i\omega t}=\hat{\Phi}e^{i(m\phi-\omega t)}$$

Substitute equation (5) into equation (7) and consider point j on the surface B. Assume that B encloses S. (Good results have been obtained with spacings between S and B as small as 1/100 of a wavelength.)

$$\hat{U}_j = -\int_S\int \hat{A}(s)\,\frac{\partial}{\partial N_j}\left[\frac{e^{i\nu R}}{R^*}\right] ds \tag{8}$$

where N_j is the unit vector normal to the boundary at point j.

The boundary will be described by a set of short rings. Each ring is paired with another ring of uniform source strength immediately inside the boundary (with a phase variation of $e^{im\phi}$). The boundary conditions of each ring will be satisfied only at discrete points at the midpoint of the ring. Therefore, j in equation (8) takes on a finite number of values:

$$\hat{U}_j = -\sum_{k=1}^{K} \hat{A}_K \frac{\partial}{\partial N_j}\left[\frac{e^{i\nu R_{kj}}}{R^*_{kj}}\right] \Delta s_k \tag{9}$$

In like manner, equation (5) (for a rotating lobed pattern) may be expressed as follows:

$$\hat{\Phi}_j = \sum_{k=1}^{K} \hat{A}_k \left[\frac{e^{i\nu R_{ij}}}{R^*_{ij}}\right] \Delta s_k \tag{10}$$

This can be used with equation (1a) to obtain the acoustic pressure at j:

$$\hat{P}_j = \rho_0 \sum_{k=1}^{K} \hat{A}_k \left[-i\omega + V_z \frac{\partial}{\partial Z_j}\right] \frac{e^{i\nu R_{kj}}}{R^*_{kj}} \Delta s_k \tag{11}$$

where $p'_j = \hat{P}_j e^{i(m\phi - \omega t)}$

For the impedance condition at j, we must have

$$Z_j = -\frac{P_j}{U_j} \qquad \hat{P}_j + \hat{Z}_j \hat{U}_j = 0$$

The minus sign is introduced here because we are interested in the ratio of pressure to velocity in the fluid, and impedance is usually defined as this ratio for the Iiaing. A positive resistance will then indicate energy absorption at the surface.

By substituting equations (9) and (11) into the above, we obtain

$$\sum_{k=1}^{K} \hat{A}_k \left[-i\omega\rho_0 + V_z\rho_0 \frac{\partial}{\partial Z_j} - Z_j \frac{\partial}{\partial N_j}\right] \frac{e^{i\nu R_{kj}}}{R^*_{kj}} = 0 \tag{12}$$

The $\hat{A}_k$ values represent a set of K unknowns. Equation (9), (11), or (12), or a combination of these equations, then gives the needed matrix which can be solved for $\hat{A}_k$. Although equation (11) was written to describe the pressure at point j on the boundary, it may also be used to calculate the pressure at any other position in the acoustic field.

Experience has shown that four or five boundary points per wavelength on B will give good results. Sometimes, as few as three points per wavelength will suffice. More will be needed near points of discontinuity in the surface and especially near the edges of thin shells. It is possible to guess the accuracy of the solution by looking at the phase angles along some line parallel to the surface in the near field. A continuous change in phase will usually indicate that sufficient detail was used. With insufficient detail, a random phase distribution is obtained.

RESULTS

The equations described here were programed for the General Electric *635* computer. An acoustic model of a jet engine was built for experimental verification. This device consists of a wooden pipe with **24** sound sources located on the outer periphery and radiating inward toward the axis of the device. The sources can be phased in such a way as to produce rotating lobed patterns similar to those produced in an actual jet engine (fig. 3).

Figure **4** shows a comparison between the calculated and measured pressure distributions inside the duct at a frequency above cutoff. The results show a pronounced standing-wave pattern because the frequency of **700** Hz is only slightly higher than the cutoff frequency **(630 Hz).** The calculations agree quite well with the experimental results. Small differences near the mouth of the duct may be caused by room reflections because the model was not tested in an anechoic chamber.

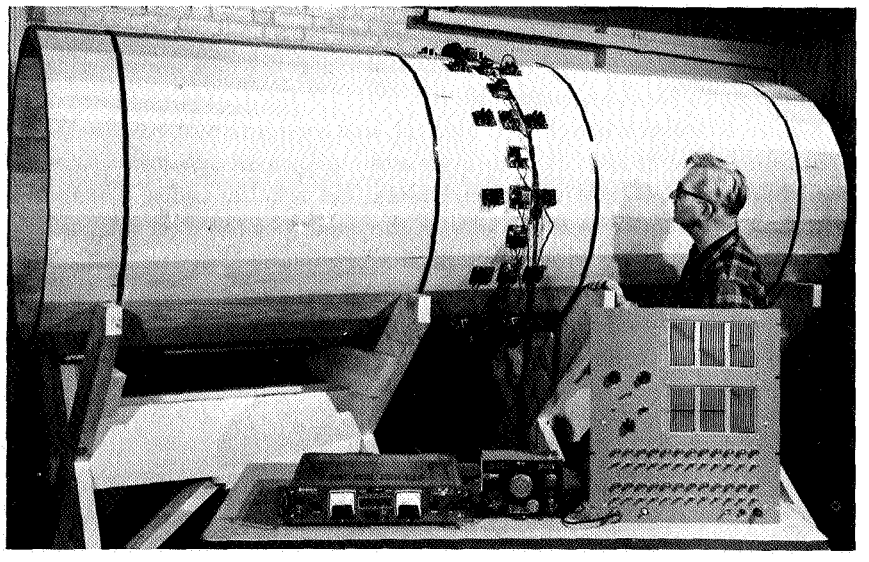

FIGURE 3.—Phased speaker model.

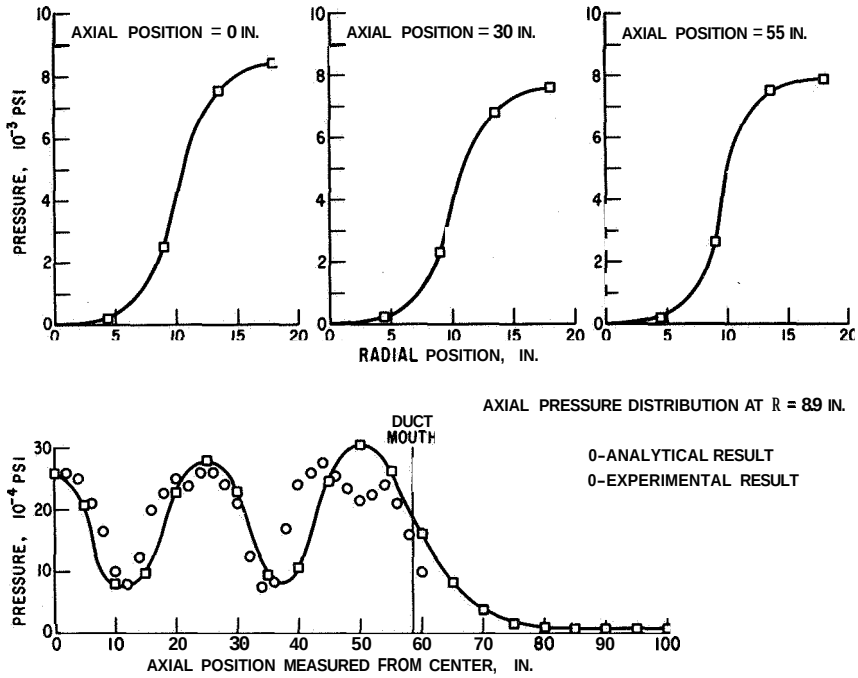

FIGURE 4 – Phased speaker model results. Four lobes, 700 Hz (above cutoff), no acoustic lining.

Figure **5** shows a similar comparison at a frequency below cutoff. Here the agreement was not nearly as good. Differences are probably the result of the fact that the acoustic pressures are extremely low below cutoff, and small effects such as extraneous noise sources and unwanted transmission paths become important.

Figure 6 summarizes the analytical and experimental results for the four-lobed case at 1000 Hz. Analysis and experiment agree exceptionally well both for the axial and radial plots. No reliable radial distribution could be obtained experimentally at the mouth of the duct because the levels were too low here. Most of the attenuation on the half radius occurred during the initial **10** or **15** in. of duct length. Notice that the lining completely eliminated the standing wave pattern.

Experimental validation under flow conditions has not as yet been attained.

OPTIMIZATION

It is logical to extend this work to obtain the optimum distribution of lining impedance. We have shown how to write equations for normal velocity and pressure at the boundary. Because acoustic intensity is equal to the product of normal velocity and pressure, it is not difficult

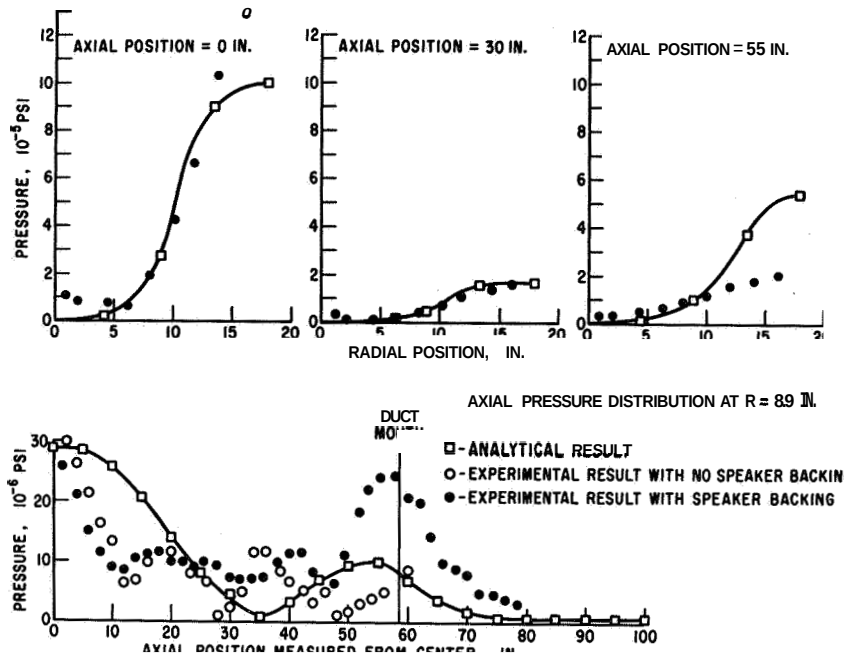

FIGURE 5.—Phased speaker model results. Four lobes, 600 Hz (below cutoff), no acoustic lining.

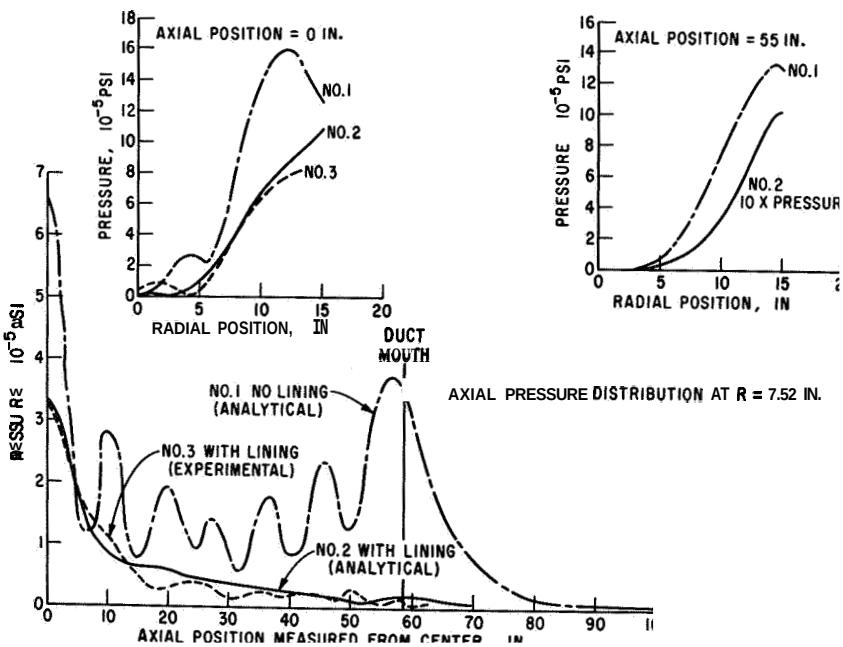

FIGURE 6.—Phased speaker model results. Four lobes, 1000 Hz. Lining impedance $=\rho c(2.4+2.4i)$.

to predict the energy flow into the lining as a function of the lining impedance and the unknown source strength $\hat{A}_k$. By maximizing the energy flow across the boundary, it is possible to write a set of K equations to solve for the $\hat{A}_k$ values. The ratio of pressure to normal velocity would then be the optimum impedance. This is the area of our current research.

REFERENCES

1. CHEN, L. H.; AND SCHWEIKERT, D. G.: Sound Radiation From an Arbitrary Body. J. Acoust. Soc. Am., vol. 35, no. 10, Oct. 1963, pp. 1626–1632.
2. BLOKHINTSEV, D. I.: Acoustics of a Nonhomogeneous Moving Medium. NACA TM 1399, Feb. 1966.

SPECTRAL TECHNIQUES IN JET NOISE THEORY*

S. P. Pao
Wyle Laboratories
Huntsville, Ala.
and
M. V. Lowson
Loughborough University of Technology
England

The present report emphasizes the evaluation of the noise field by spectral methods. Thus the turbulence field is described by its wave-number and frequency characteristics rather than in space and time. One representation is simply the Fourier transform of the other, but it does seem that spectral methods offer considerable simplicity and possibly greater insight into the problem.

INTRODUCTION

The advent of jet and rocket propulsion introduced a new form of noise caused by the high-speed turbulent exhaust flows that characterize these engines. The noise from jet and rocket engines can cause both community noise and structural fatigue problems. In spite of considerable noise-control effort, jet-engined aircraft are still a major source of noise in communities near airports. Rocket-engine test schedules are also often controlled by potential community noise problems. Both aircraft and rocket vehicles have experienced fatigue failures in regions close to the engine because of the intense noise levels occurring near the exhaust. Thus, there are many problems in jet and rocket noise that still require solutions.

The problems are complicated by several factors. Although the noise field is clearly related in some way to the turbulence, a wide variety of fluctuating mechanisms can be postulated as possible fundamental causes. Controversy still exists as to whether the supersonic or subsonic portions of an exhaust flow are responsible for the major part of the noise.

*This work was sponsored by NASA Marshall Space Flight Center under contract NAS8-21060.

In some circumstances, noise generated within the engine can be important, while in other circumstances noise radiated far downstream by instability mechanisms could be significant. At the present time the real contribution of both of these sources in a full-scale case is unknown. The effects of noise caused by combustion, or even the effects of mean jet temperature, are still essentially undetermined. Conflicting evidence is available regarding the possible significance of shocks in supersonic flow. Even such an apparently straightforward case as coaxial jet mixing has been found to cause almost insuperable problems of prediction with current techniques. Thus it seems that new methods are required.

The major part of the published theoretical work on exhaust noise has attempted to calculate the noise field by evaluation of the appropriate retarded time integrals. Such evaluation requires knowledge of the fourth derivative of a fourth-order correlation function in the turbulent flow. Not surprisingly, estimation of this function is difficult, but some success has certainly been achieved using this approach.

Most of the results previously found in jet-noise theory can be rediscovered by a very simple spectral approach and will be presented in the report. The simplicity is thought to be an important advantage. The present work has also enabled direct estimates, which will be discussed in a later section, of the noise to be made. The work also suggests some experimental measurements of turbulence that appear to be particularly relevant to the noise problem.

THE LIGHTHILL EQUATION

The clearest way to understand the mechanisms underlying noise generation by turbulent flows is by use of the basic equation first derived by Lighthill (ref. 1). This equation has been the basis for virtually all work on exhaust noise to date and can be derived in a straightforward way from the mass and momentum conservation equations in fluid mechanics:

$$\frac{\partial \rho}{\partial t}+\frac{\partial \rho v_i}{\partial x_i}=Q \tag{1}$$

and

$$\frac{\partial \rho v_i}{\partial t}+\frac{\partial \rho v_i v_j}{\partial x_j}+\frac{\partial p_{ij}}{\partial x_j}=F_i \tag{2}$$

where Q is a rate of mass introduction per unit volume and F_i is the external force per unit volume. The nonhomogeneous wave equation

$$\frac{\partial^2 \rho}{\partial t^2}-c_0^2\frac{\partial^2 \rho}{\partial x_i^2}=\frac{\partial Q}{\partial t}-\frac{\partial F_i}{\partial x_i}+\frac{\partial^2 T_{ij}}{\partial x_i \partial x_j} \tag{3}$$

with

$$T_{ij}=\rho v_i v_j+p_{ij}-c_0^2\rho\delta_{ij}$$

is the Lighthill equation. Each term on the right-hand side of equation (3) gives the effects of a different acoustic source mechanism. The first, $\partial Q/\partial t$, gives the effect of mass introduction. Examples include pulse jets, sirens, tip jet rotors, and the random mass fluctuations that can occur across the exit plane of a jet exhaust. The second term, $\partial F_i/\partial x_i$, gives the effect of external fluctuating forces that can act on the air. Examples include compressors, propellers, helicopter rotors, and the random fluctuating forces that exist on the exhaust lip or on any body in a turbulent airstream. The third term, $\partial^2 T_{ij}/\partial x_i \partial x_j$, incorporates several different effects. T_{ij} is generally referred to as the "acoustic stress tensor." The most significant fluctuation of the acoustic stress tensor will be caused by the turbulent velocity fluctuations, which affects the $\rho v_i v_j$ product. The effects of viscous stresses and thermodynamic fluctuations are contained in the remaining terms of T_{ij}, which will be discussed later in further detail. In a free jet-exhaust flow with constant mass flow, the noise will be derived solely from the quadrupole term.

However, there are limitations to the Lighthill equation. Only the wave propagation in the ambient fluid is considered, and the right-hand side of equation (3) is considered as known, although it also contains the fluctuating density. Indeed, the Lighthill equation can be rewritten so that all possible effects of varying density are brought onto the left-hand side of equation (3). This was done by Phillips (ref. 2). Unfortunately, the resulting equation is very difficult to solve even for the simplest type of acoustic source. Thus, in most work to date, the effects of mean flow inhomogeneity have been tacitly ignored, and the Lighthill equation is inevitably solved by means of the homogeneous retarded potential solution to the wave equation, with the right-hand side assumed known.

The overall acoustic effects of inhomogeneities may be estimated by simple arguments. Consider a geometrical acoustic type of approximation to the inhomogeneous solution, in which the speed of sound at any location is considered to be the sum of the local speed of sound and the local convection velocity. Thus, the effective local speed of sound for an eddy moving at mach 1 can actually be double the homogeneous value usually assumed. Sound may then be considered to travel along some ray path bent in accordance with the local effective speed of sound. For very-low-frequency sound, with wavelengths much greater than the jet dimension, the effect of ray bending will be negligible. Thus the first-order solution to the Lighthill equation may be expected to apply either at low frequencies or low exhaust velocities ($M \ll 1$). Again at high frequencies when the inhomogeneity has a scale much greater than the wavelength, the Lighthill equation will apply locally. Thus it should predict overall power correctly if a local wave equation is used. On the other hand, the directionality pattern of the noise in this case must be modified substantially because of the surrounding refraction zone. But at mid-

frequencies, where inhomogeneity scale and wavelength are of the same order, no definite rules can be laid down. The redirectioning of sound due to refraction has been studied by numerous authors and may in reality be the principal cause of the observed directionality pattern of jets.

THESPECTRAL ANALOGY

If the right-hand side of equation **(3)** is written **as** G to represent any source term, the solution of equation **(3)** in Helmholtz form is

$$\rho(\mathbf{x}, t) = \frac{1}{4\pi c^2} \int \left[\frac{G(\mathbf{y}, t)}{r} \right] d\mathbf{y} \tag{4}$$

where x and y denote the coordinates of the sources. The brackets around the source function require that G must be evaluated at a retarded time

$$t' = t - r/c \tag{5}$$

It is of particular interest to study the spectral form of this solution. The Fourier transformation pair relating G and its wave number frequency spectrum G are

$$\hat{G}(\mathrm{k}, w) = \int \int G(\mathbf{x}, t) \exp -2\pi i(\mathbf{k} \cdot \mathrm{x} + \omega t) d\mathbf{x}\, dt \tag{6}$$

and

$$G(\mathbf{x}, t) = \int \int \hat{G}(\mathbf{k}, w) \exp 2\pi i(\mathbf{k} \cdot \mathbf{x} + \omega t) d\mathbf{k}\, d\omega \tag{7}$$

In addition, we choose to use the far-field approximation

$$r = r_1 - (\mathbf{y} \cdot \mathbf{r})/r_1 \tag{8}$$

in which we assume that the source region is small compared with the distance between the source and receiver and that r_1 is a reference distance between the receiver and the center of the source. By substituting equations (5) and ***(8)*** into equation (7) and using equation (7) as the integrand in equation (4), we have

$$\rho(x, t) = \frac{1}{4\pi c^2 r} \int \hat{G}\left(-\frac{\omega \mathbf{r}}{c r_1} \omega\right) \exp 2\pi i \omega \left(t - \frac{r_1}{c}\right) d\omega \tag{9}$$

from which we can easily identify its Fourier counterpart

$$\rho(\mathbf{x}, \omega) = \frac{\exp -2\pi i \omega r_1/c}{4\pi c^2 r_1} \hat{G}\left(\frac{-\omega \mathbf{r}}{c r_1}, \omega\right) \tag{10}$$

Equation (10) is a key result, which does not appear to be widely known, although it was first found by Kraichnan (ref. **3)** in **1953.**

Now the spectral form of the source terms can be found from equation (6) as

$$\hat{G}(\mathbf{k}, \omega) = \hat{\dot{Q}}(\mathbf{k}, \omega) + 2\pi i k_i \hat{F}_i(\mathbf{k}, \omega) - 4\pi^2 k_i k_j \hat{T}_{ij}(\mathbf{k}, \omega) \tag{11}$$

By defining the scalar components of

$$\hat{T}_{rr} = \left(\frac{r_i}{r_1}\right)\left(\frac{r_j}{r_1}\right)\hat{T}_{ij}$$

and

$$\hat{F}_r = \left(\frac{r_i}{r_1}\right)\hat{F}_i \tag{12}$$

the far-field noise is represented by

$$\hat{\rho}(\mathbf{x}, \omega) = \frac{-\exp\{-2\pi i \omega r_1/c\}}{2c^2 r_1}\left\{\frac{\hat{\dot{Q}}}{2\pi} + \frac{i\omega}{c}\hat{F}_r + 2\pi\frac{\omega^2}{c^2}\hat{T}_{rr}\right\} \tag{13}$$

in which all the spectra are evaluated at $(\omega \mathbf{r}/cr, \omega)$. In the above analysis, all spectra are first order and simply the Fourier transforms of the original functions. For random functions, this representation does not give a meaningful result and, as is well known, a second-order or mean-square power spectrum must be defined. In such circumstances the far-field noise shall be represented as

$$\overset{M}{\rho}(\mathbf{x}, \omega) = \frac{1}{4c^4 r_1^2}\left\{\frac{\overset{M}{\dot{Q}}}{4\pi^2} + \frac{\omega^2}{c^2}\overset{M}{F}_r + 4\pi^2\frac{\omega^4}{c^4}\overset{M}{T}_{rr}\right\} \tag{14}$$

Equations (13) and *(14)* reveal that the noise radiation mechanism is very selective, namely, for each frequency, only one corresponding wave number in the turbulence component is responsible for the source. Furthermore, for dipole and quadrupole sources, only the component in the direction of emission is responsible for the sound production.

So far, we have assumed that the sound source is stationary with respect to the receiver. The effects of a source in uniform motion shall be shown here with the aid of a wave-number frequency diagram. On this diagram, figure *1*, a point source with a single frequency ω_0 is represented by a straight line parallel to the k-axis. Lines of constant slope represent constant speeds of particle motion or wave propagation in the direction of k. Furthermore, all the waves propagated in the free ambient fluid shall satisfy the relation $\omega/k = c_0$. For a stationary point source, the wave number which matches the frequency ω_0 is k_0 as shown in figure 1. However, when the source is moving with velocity V, the sound-producing wave number has shifted from k_0 to k, as indicated by the intersection of the source motion line V and the sound propagation line c_0. The shift is the Doppler relation

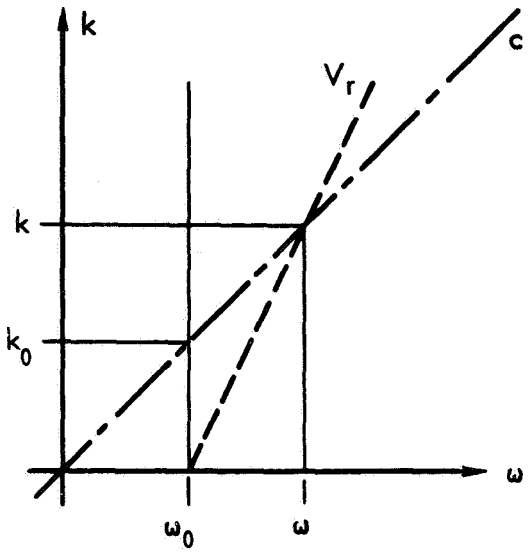

FIGURE 1.—Location of sound-radiating element of a moving source in the wave-number frequency space, subsonic case.

$$k=\frac{k_0}{1-M_r} \qquad M_r=V/c \tag{15}$$

At the same time the far-field sound frequency has shifted from ω_0 to $\omega=\omega_0/(1-M_r)$.

The amplitude of the sound radiated may also be found by a simple argument. Figure 2 shows an enlarged version of figure **1** in which the incremental values are specifically displayed. For the stationary case the sound in the frequency increment $\delta\omega$ is given by the part of the wave-number spectrum lying in δk_1. But in the moving case the wave-number region of interest is δk_2 wide. The ratio of the amplitudes is thus $\delta k_2/\delta k_1$, which is $1/1-M_r$.

However, in general, there is no reason to suppose that the value of G at k will remain equal to the value at k_0, so the $(1-M_r)^{-1}$ factor cannot be applied alone, except in the monopole case. Equation **(11)** shows how dipole (force) and quadrupole (acoustic stress) fields would vary as k and k^2, respectively. This variation should be included in the estimation of the amplitude. Thus, equation **(14)** for the sound can be written, to include the effects of motion, as

$$\overset{M}{\rho}(\mathbf{x},\omega)=\frac{1}{4c^4r_1^2(1-M_r)}\left\{\frac{\overset{M}{\dot{Q}}}{4\pi^2}+\frac{\omega_0^2}{c^2(1-M_r)^2}\overset{M}{F}_r+\frac{\omega_0^4}{c^4(1-M_r)^4}\overset{M}{T}_{rr}\right\} \tag{16}$$

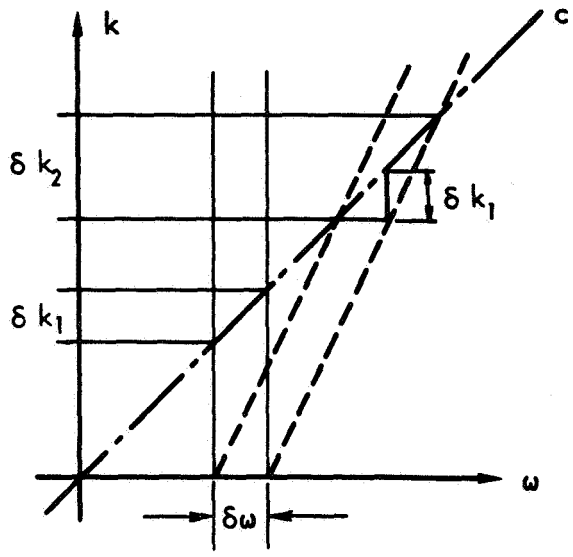

FIGURE 2.—Enlargement of figure 1.

where ω_0 is the frequency in the moving axes, and all the spectra are evaluated at $\{-\omega_0 \mathbf{r}/cr_1(1-M_r), \omega_0\}$. Thus, we have recovered the well-known dependence of random monopole, dipole, and quadrupole sources on $(1-M_r)$ to the $-1, -3$, and -5 power, respectively.

It is appropriate here to show a realistic jet turbulence spectrum in the wave-number frequency plane as obtained by Wills (ref. 4). Figure 3 shows a typical case where contours of equal values of the spectrum function have been plotted. Here both the frequency and the convective speeds are shown in separate sets of logarithmic coordinates. The vertical segment of the spectral pattern near $U = 1000$ fps should be the sound-emitting part of this turbulence structure. Clearly, in this case at a jet convection velocity of 200 fps, very little sound would be radiated. At higher subsonic speeds the whole pattern slides sideways to the right, and more sound would be radiated. At transonic convection speeds the sound source is given by values lying through the maximum region of the spectrum, and at supersonic speeds, the sound source strength again decreases. Hence future theory may predict that the transonic region produces most of the sound for a supersonic jet.

The results found so far suggest that the sound field of any prescribed turbulence field can be found directly from its wave-number frequency spectrum. Thus, the problem now hinges on the spectral estimation of the turbulence. More specifically, equation (16) showed that calculation of the sound radiated by a jet required knowledge simply of $\overset{M}{T}_{ij}(\mathbf{k}, \omega)$ at the points $(-\omega_0 \mathbf{r}/cr(1-M_r), \omega_0)$ in the wave-number frequency space. Definition of these terms requires further manipulations.

371-986 O-LT-70—29

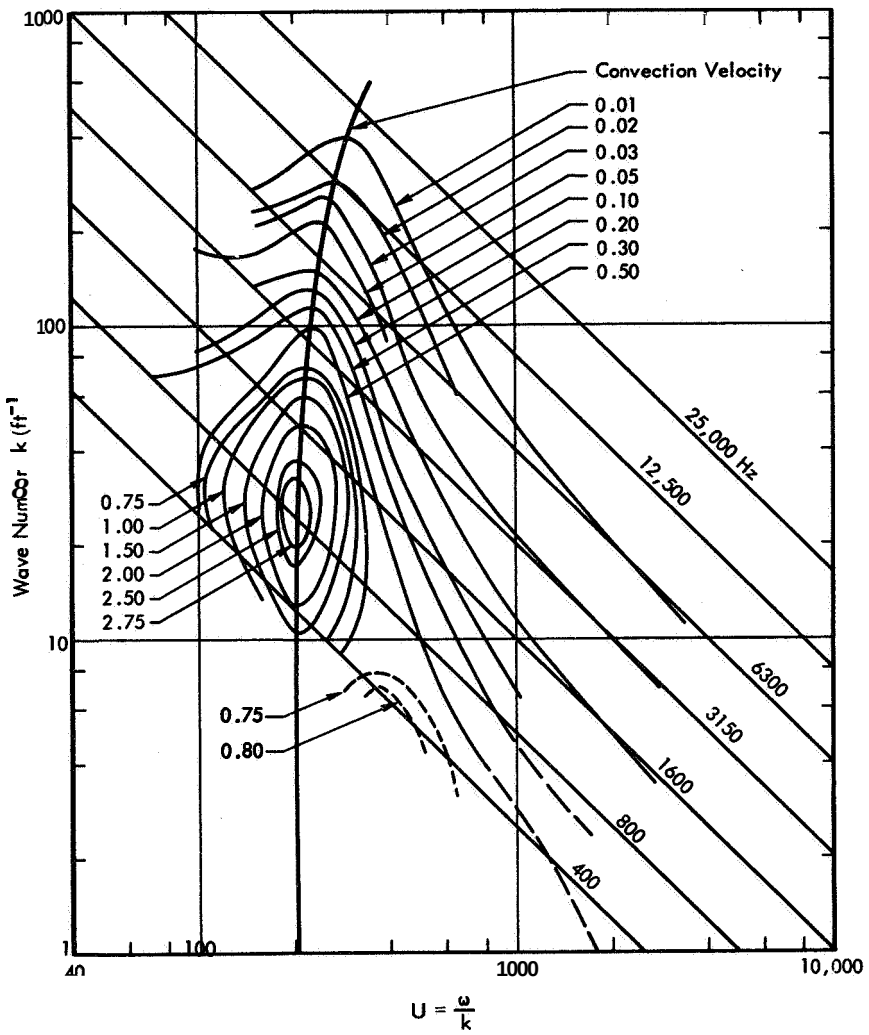

FIGURE 3.—One-dimensional wave-number phase velocity spectrum of the longitudinal fluctuating velocity component in the mixing region of a round jet.

The equation for the acoustic stress tensor is

$$T_{ij}=\rho v_i v_j+p_{ij}-c_0^2\rho\delta_{ij}$$

Obviously this term contains the effects of momentum fluctuations, viscous stress, and thermodynamic fluctuations. In general, the viscous stress is small compared to the other effect and can safely be ignored.

It is common in jet-noise theory to split the velocity v_i into mean and fluctuating parts $v_i=U_i+u_i$, thus

$$\rho_0 v_i v_j = \rho_0 (u_i U_j + u_j U_i + u_i u_j)$$

in which the mean value $U_i U_j$ has been omitted because it does not contribute directly to the sound. Upon contraction, $v_i U_j$ cannot be distinguished from $U_i u_j$, so that the first two terms may be construed as a single contribution that is caused by the interaction of the turbulence and mean shear (T−M). The last term, $u_i u_j$, gives the sound caused only by turbulence-turbulence interactions. These two contributions will be defined as the shear noise and self-noise, respectively.

In spectral form the shear-noise source is given as

$$\hat{G}_{SH}(\mathbf{k}, \omega) = -4\pi i \rho_0 k_i s_{ij} \hat{u}_j(\mathbf{k}, \omega) \tag{17}$$

where $s_{ij} = \partial v_i / \partial x_j$ are constants. This expression clearly indicates that the shear noise is an interaction of the shear gradient and the turbulence. The interaction process is very selective; each shear-gradient component reacts with only one component of the turbulence. Because of its dependence on the first power of k, the shear noise has an essentially dipole source character.

Finally, the assumption of constant gradient is not essential. If the gradients were not constant, the noise source spectrum would be a convolution of the turbulence spectrum with the velocity gradient. In such a case, every frequency of sound is generated by a band of wave numbers, and every wave-number component of the turbulence generates a band of shear noise in the far field.

The construction of the self-noise source is relatively straightforward. If the velocity fluctuation spectrum $\overset{M}{u}_r$ were given, the noise source can be represented by a convolution integral:

$$\overset{M}{T}rr(\mathbf{k}, \omega) = \int_l \int_\sigma \overset{M}{u}_r(l, \sigma) \overset{M}{u}_r(\mathbf{k} - l, \omega - \sigma)\, dl\, d\sigma \tag{18}$$

The self-noise source has the character of a longitudinal quadrupole. In the case of an isotropic turbulence model, the self-noise source itself has a spherically symmetric directivity pattern.

Upon close examination, important qualitative conclusions can be drawn from the thermodynamic portion of the turbulent stress tensor as defined by Lighthill. By adding and subtracting $c^2 \rho \delta_{ij}$, the thermal term be rewritten as

$$G_{TH} = \rho\{U^2 + (c^2 - c_0^2)\delta_{ij}\} + \{p_{ij} - c^2 \rho \delta_{ij}\}$$

in which c is the local speed of sound in the jet. After using some elementary relationships in thermodynamics, the expression can be reduced to the following form:

$$\hat{G}_{TH}(k,\omega)=\left\{(\gamma-1)c_p(T_t-T_0)\delta_{ij}+\left(\frac{3-\gamma}{2}\right)U^2\right\}\hat{d\rho}+\{p/c_v\}\,\delta_{ij}\hat{ds} \tag{19}$$

Of particular importance is that the high speed of sound in a hot jet does not contribute directly to the sound. Only the density and entropy fluctuations have first-order effects on the noise production.

A simple turbulence structure shall be introduced to demonstrate some further details of sound-generation mechanism by means of the present theory. For this purpose a simple homogeneous isotropic turbulence structure is chosen in the moving frame of reference:

$$\overset{M}{u}_{ij}(\mathbf{k},\omega)=\frac{a^3\beta\bar{u}_0^2}{\pi^2}\{(ka)^2\delta_{ij}-a^2k_ik_j\}\exp-\{(ka)^2+(\beta\omega)^2\} \tag{20}$$

where $\bar{u}_0^2$ is the mean turbulence intensity, a is the integral spatial scale, and β is the integral time scale. Experimental results suggest that $\bar{u}_0^2\simeq 0.09U^2$ and $\mathrm{a}=a/cM\beta\simeq 0.20$ to **0.35** (ref. **5).**

By using this turbulence model, the noise emission from a round jet has been computed. The resulting formulas for the shear noise are

$$I(\mathbf{x}_0,\omega_n)=\frac{a^5\beta\rho\bar{u}_0^2(\cos^4\theta+\cos^2\theta)}{2\pi^2c^5r^2(1-M\cos\theta)^5}\left(\frac{\partial U_1}{\partial x_2}\right)^2\int_{0.707\omega_n}^{1.414\omega_n}\omega^4\exp$$

$$-\frac{\omega^2a^2}{c^2}\frac{1}{\{(1-M\cos\theta)^2}+\frac{1}{\alpha^2M^2}\}d\omega \tag{21}$$

$$I(\mathbf{x}_0)=\left(\frac{\partial U_1}{\partial x_2}\right)^2\frac{3\sqrt{\pi}\rho\bar{u}_0^2\alpha^4M^4a(\cos^4\theta+\cos^2\theta)}{16\pi^2cr^2\{(1-M\cos\theta)^2+\alpha^2M^2\}^{5/2}} \tag{22}$$

which provide the octave band and overall sound intensities. As noted before, the shear noise has an essential dipole directivity pattern. The directivity pattern as given in the above formulas agrees with that given by Ribner (ref. **6)** in **1964,** although it is derived by different approaches. However, the predicted wave spectrum depends on

$$\{(1-M\cos\theta)^2+\alpha^2M^2\}$$

to the $-5/2$ power instead of the $-3/2$ power as expected from a dipole source. This effect is the result of the choice of the turbulence model. The spectrum in the low-wave-number region follows a k^2 law, which artificially raises the power dependence from $-3/2$ to $-5/2$. In actual measurements of jet turbulence, the spectrum in this region is usually flat.

It is interesting to investigate the noise-source distribution in the wave-number frequency space. Figure 4 shows the turbulence intensity

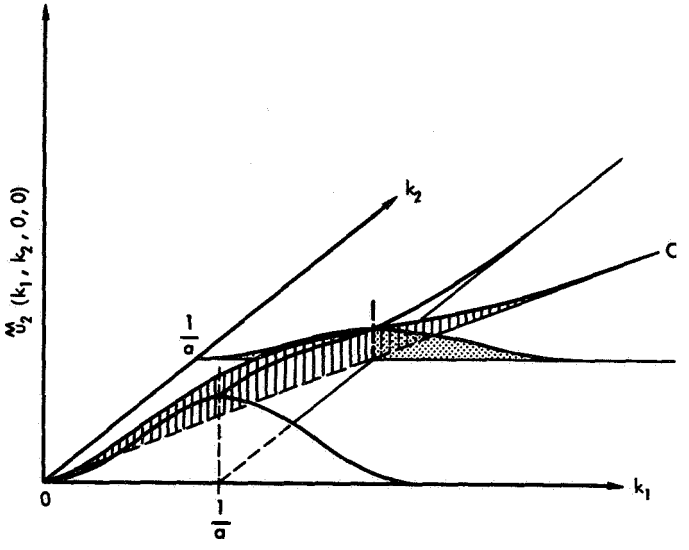

FIGURE 4.—Distribution of spectral intensity of $\overset{M}{u}_2(\mathbf{k}, \omega)$ in the k_1, k_2-plane.

distribution in the k_1, k_2-plane. The wave number k_3 is set to zero for simplicity of representation. A vector **OC** is drawn along the direction of emission of the noise. In this figure, the source intensity is given along **OC** and several other representative sections. It is clear that the shear noise is zero in the transverse direction k_2 and reaches a maximum in the axial direction k_1.

An important feature not represented in figure 4 is the location of the noise source in the wave-number space where the most intense sound radiation occurs. The definition of the turbulence structure (eq. (20)) consists of separable wave-number and frequency factors. The peak turbulence intensity in the wave-number space is determined entirely by the wave-number component. However, the most intense part of the turbulence spectrum does not necessarily generate the most intense sound. In the formulation of shear noise (eq. (21)), one may detect two separable factors also. In particular, the frequency factor is

$$f(\omega) = \omega^2 \exp - (\beta^2\omega^2)$$

The variation of turbulence intensity with wave number along section **OC,** and the factor $f(\omega)$, are plotted in figure 5 to the common abscissa $k = \omega/c(1 - M \cos 6)$. Their product, plotted on the same figure, is proportional to the shear-noise intensity. The peak of f (~)s located at

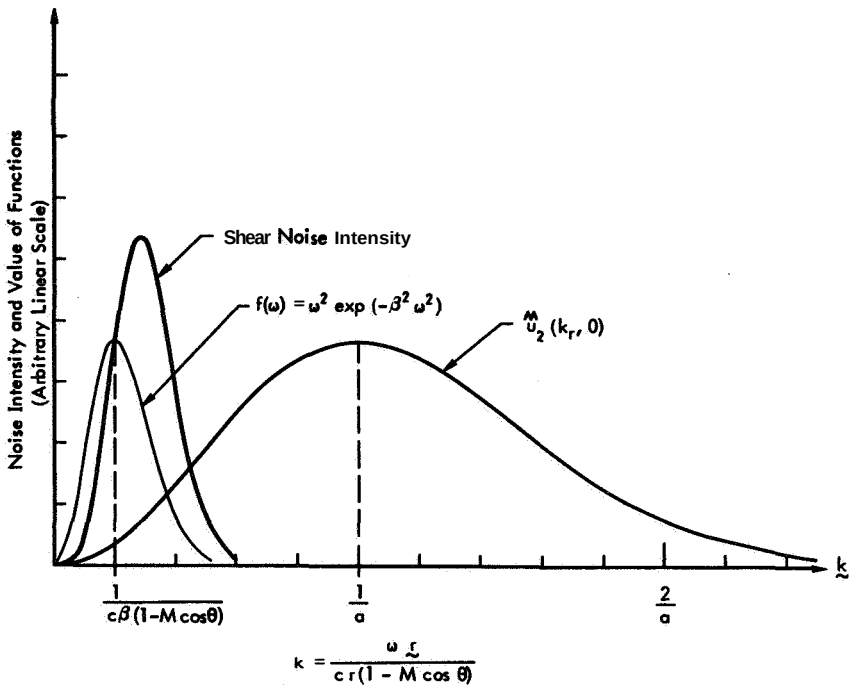

FIGURE 5.—Location of the peak shear noise production region on the wave number axis.

$\omega = \beta^{-1}$. Because the intensity of the turbulence varies with k^2 in the low-wave-number range, its product with $f(\omega)$ produces a peak of shear noise at a frequency $\omega = \sqrt{2}\beta^{-1}$. The conclusion reached by this analysis shows that the location of sound of peak noise relative to the wave-number space is dominated by the frequency factor in the case of shear noise.

The predicted self-noise octave band and overall intensities are given by

$$I(\mathbf{x}_0, \omega_n) = \frac{\rho \bar{u}_0^4 a^3 \beta}{4c^5 r^2 (1 - M \cos\theta)^5} \int_{0.707\omega_n}^{1.414\omega_n} \omega^4 \exp -\frac{1}{2}\frac{\omega^2 a^2}{c^2}\left\{\frac{1}{(1 - M\cos\theta)^2} + \frac{1}{\alpha^2 M^2}\right\} d\omega \tag{23}$$

$$I(\mathbf{x}_0) = \frac{3\sqrt{2\pi}\rho u_0^4 \alpha^4 M^4}{8acr^2\{(1 - M\cos\theta)^2 + \alpha^2 M^2\}^{5/2}} \tag{24}$$

The self-noise-source spectrum exhibits a different character than the shear-noise source. Because the self-noise-source spectrum is derived from a self-convolution of the model velocity fluctuation power spectrum, it has a gaussian distribution. Most of the energy is therefore

concentrated in the low-wave-number range. If the noise-source term is broken down into its spatial and time factors, the time factor is found to decide the location of the peak noise frequency. The frequency factor

$$f(\omega) = \omega^4 \exp\left(-\frac{1}{2}\beta^2\omega^2\right)$$

has a peak located at $\omega = 2/\beta$ that is exactly one octave above the corresponding peak of frequency factor of the shear noise. Because the sound source depends on the self-convolution of the second-order spectrum in the longitudinal direction and the sum of square of the same spectrum in the transverse directions, the strength of the noise source is relatively insensitive to the assumed form of the turbulence structure as long as the total power remains the same. In view of this property, one may expect that a simple model of turbulence may provide a good prediction of the self-noise.

Far-field noise radiation prediction has been made and compared with the experimental results given by Mangiarotty et al. (ref. 7). One particular case where $M = 0.80$ is presented here. Figures 6 and 7 show that overall levels are predicted to within 5 dB over the whole acoustic field. This is thought to be a significant result. It will be observed that the spectral shape prediction of the theory is considerably less accurate. However, the present work used a much simplified spectral model for analytic convenience, and many improvements are clearly possible.

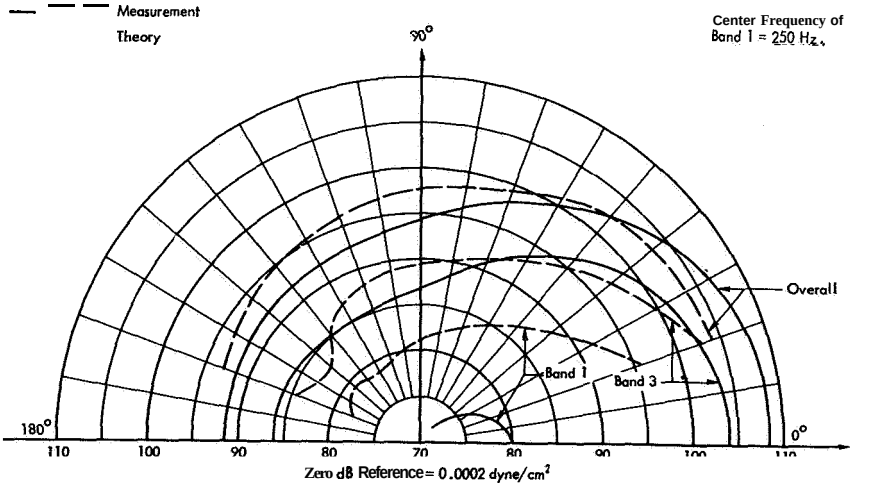

FIGURE 6.—Comparison of theoretical jet noise prediction with experimental measurements by Mangiarotty et al. Jet diameter= 2.86 in., exit mach number=0.80. Sound-pressure levels are measured and computed at points 6 ft away from the jet nozzle (ref. 7). Overall noise and octave bands 1 and 3.

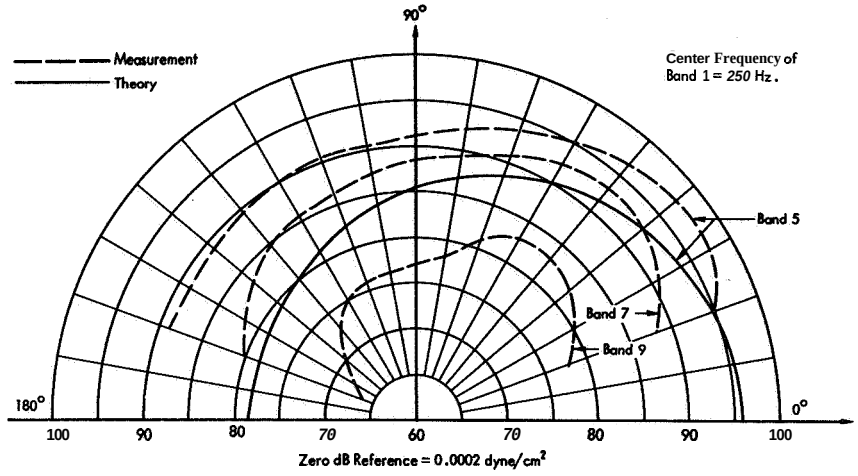

FIGURE 7.—Comparison of theoretical jet noise prediction with experimental measurements by Mangiarotty et al. Jet diameter = 2.86 in., exit mach number = 0.80. Sound pressure levels are measured and computed at points 6 feet away from the jet nozzle (ref. 7). Octave bands 5, 7, and 9. Predicted noise levels for bands 7 and 9 are below 50 dB; these curves are not shown in this figure.

The prediction and experimental data agree well in the octave bands where the peak-noise intensities occur. But for high-frequency bands the predictions are very poor. In the chosen model of turbulence, the frequency spectrum drops off much faster than any actual turbulence structure.

CONCLUSION

We find from this analysis that the noise-generation mechanism is intimately connected with the fine structure and dynamics of the turbulence. To predict or control noise radiation from jet exhaust flows, further efforts must be made to understand the jet turbulence structure. A full description of the four-dimensional space and time variation of turbulence seems essential. The following quantities for subsonic jet-noise prediction must be defined by the application of the present theory:

(1) The fourth-order spectrum $\overset{M}{T}_{rr}(\mathbf{k}, \mathbf{w})$ for various values of r-orientation

(2) The mean flow velocity profile $U_1(y_2)$

(3) The transverse velocity fluctuation spectrum $\overset{M}{u}_2(\mathbf{k}, \mathbf{w})$

(4) The turbulence intensity profile of the jet $\bar{u}_0^2(y_2)$

Some data on all these parameters exist except for the transverse spectrum, which is important for the shear-noise estimation and justifies careful experimental study.

Although extensive data on jet turbulence are available in the literature, most are not applicable to predictions of jet noise. The reason is either that the measured turbulence component is not directly related to sound-generating elements, or that the measurement is not sufficiently accurate in the low-wave-number range to render meaningful sound radiation estimates. The only exception so far is the experimental work by Chu (ref. 8), which was specifically designed according to basic jet-noise theory. Chu measured the space-time correlation functions of T_{rr} and u_r in several orientations of **r**. His work has contributed significantly toward resolving the very difficult problem of measuring full three-dimensional jet turbulence structure. However, in the process of data reduction the important information of the spectral content is not preserved.

In addition to the above-mentioned general shortcomings of existing data on jet turbulence, one important aspect has been ignored altogether. It is a familiar fact that the turbulence intensity across the jet is non-uniform. This spatial inhomogeneity of the turbulence structure has a profound influence on the spectrum of the turbulence according to theories of spectral analysis. This effect is particularly important for the low-wave-number range, where most sound is generated. The inhomogeneity must therefore be considered thoroughly in further theoretical work.

REFERENCES

1. LIGHTHILL, M. J.: On Sound Generated Aerodynamically. I. General Theory. Proc. Roy. Soc., ser. A, vol. 211, 1952, pp. 564–578.
2. PHILLIPS, O. M.: On the Generation of Sound by Supersonic Turbulent Shear Layers. J. Fluid Mech., vol. 9, 1960, pp. 1–28.
3. KRAICHNAN, R. H.: The Scattering of Sound in a Turbulent Medium. J. Acoust. Soc. Am., vol. 25, 1953, pp. 1096–1104.
4. WILLS, J. A. B.: On Convection Velocity in Turbulent Shear Flows. J. Fluid Mech., vol. 20, 1964, p. 417.
5. DAVIES, P. O. A. L.; BARRATT, M. J.; AND FISHER, M. J.: Turbulence in the Mixing Region of a Round Jet. A.R.C. 23, 728–N300–FM 3181, 1962.
6. RIBNER, H. S.: The Generation of Sound by Turbulent Jets. Vol. 8 of Advances in Applied Mechanics. Academic Press, Inc., 1964, pp. 103–182.
7. MANGIAROTTY, R. A.; ET AL.: Acoustic and Thrust Characteristics of the Subsonic Jet Efflux From Model Scale Sound Suppressors. Part I. Unheated Jets. Rept. no. D6–15071, vol. II, The Boeing Co., 1966.
8. CHU, W. T.: Turbulence Measurements Relevant to Jet Noise. UTIAS Rept. no. 119, Inst. for Space Studies, Univ. of Toronto, 1966.

ACKNOWLEDGMENTS

The authors wish to thank Dr. J. E. Ffowcs Williams for valuable discussions.

MATHEMATICAL ASPECTS OF NONLINEAR WAVE PRQPAGATION

Ervin Y. Rodin
Washington University
St. Louis, Mo.

The increasing use of analytical approximations of the Navier-Stokes equations, such as the Burgers' and the Korteweg-de Vries equations, makes imperative the study of the correlations between equations of this type and the physical mechanisms that they describe. We discuss here, in particular, Burgers' equation. It is shown that the initial-value problem for this equation yields an explicit explanation of the interaction between the thermoviscous mechanism of the medium and an imposed excitation; that from this, it is possible to obtain some exact solutions for important boundary value problems, which are analogs of Fay's considerations of 1931; and that the mathematical restrictions imposed on any solution of Burgers' equation by the second-order nature of this equation can easily be removed, to restore some of the generality of the Riemann-Earnshaw formulations.

During the last century both Riemann and Earnshaw presented what are now the classical solutions to the pair of equations

$$\begin{aligned} &\bar{v}_t + \bar{v}\bar{v}_{\bar{x}} + \frac{2}{\gamma-1} a a_{\bar{x}} = \epsilon \bar{v}_{\bar{x}\bar{x}} \\ &a_t + \bar{v} a_{\bar{x}} + \frac{\gamma-1}{2} a \bar{v}_{\bar{x}} = 0 \end{aligned} \tag{1}$$

In the set of equations (1), $\bar{v}$ is particle velocity, a is sound speed, y is the ratio of specific heats, E a diffusion constant, while t and $\bar{x}$ are time and the space variables, respectively.

The Riemann-Earnshaw solution was obtained, however, only for the case of vanishing viscosity, $\epsilon = 0$.

In 1956, with the appearance of Lighthill's paper (ref. 1), an argument was made available, which reduced the set of equations (1) to a single equation

$$v_t + v v_x = \delta v_{xx} \tag{2}$$

Lighthill did this by using some clearly defined approximations and by rearranging and redefining both the independent and dependent variables in (1). For instance, the best that could now be said about x in equation (2) is that it has a spacelike character: It is the variable of a moving coordinate system.

The principal reason for wanting to reduce the system of equations (1) to equation (2) is that exact solutions are available for the latter. Therefore, equation (2) still incorporates the very important effects of time dependence, nonlinearity, and viscosity and does not seem to be an unreasonable tool.

The solution of equation (2) proceeds through a direct transformation into the linear diffusion equation. Specifically, if one has to solve for equation (2) a problem defined by

$$v(x, 0) = f(x) \qquad -\infty < x < \infty \tag{3}$$

the solution is very simple (refs. 2 and 3).[1]

Condition (3), however, describes only an initial-value problem while, practically speaking, a boundary-value problem is more important. It turns out, however: that if we specify the conditions

$$\begin{aligned} v(x, 0) &= f(x) \qquad 0 \leqslant x < \infty \\ v(0, t) &= g(t) \qquad t > 0 \end{aligned} \tag{4}$$

then solving equation (2) becomes a complicated matter and leads to the solution of a rather unpleasant integral equation.

The question of the meaning of the set of conditions (4) if x is a variable in a moving frame may be raised at this point also. The answer is that the Lighthill approximation is only one of many (refs. 3 and 4) for the system of equations (1), and that entirely different approaches may be necessary (ref. 2). The reason is that Lighthill considered the infinite medium only and his approximations, therefore, are valid only there.

There have been three essentially different attempts to circumvent the difficulty of solving equation (2) with the set of conditions (4). One attempt replaced the first of the set of conditions (4) by a condition of infinity. The second one essentially linearized governing equation (2). The third attempt, perhaps the most ingenious of them (ref. 2), replaced equation (2) with

$$v_x - vv_t = \delta v_{tt}$$

---

[1] E. Y. Rodin: On Some Approximate and Exact Solutions of Boundary Value Problems for Burgers' Equation. J. Math. Anal. Appl., to be published in 1969.

[2] Ibid.

Obviously, the change of sign in the second term is unimportant. What is significant is the interchanging of the two independent variables of equations (1), allowing in this way for the treatment of a problem like equation (3) but prescribed on a boundary.

An obvious difficulty with this approach is that no initial conditions can be prescribed. There are other difficulties also; e.g., phenomenological ones. Yet, the results of this theory are excellent, and one should like to understand why.

The clue, it appears, lies in the fact that an initial value problem for the diffusion equation that, through a transformation, solves **(2)** is equivalent to a special boundary value problem for the same equation. Schematically and specifically:

$$v(x, 0) = f(x) \Longleftrightarrow \begin{cases} v(0, t) = a(t) \\ v_x(0, t) = b(t) \end{cases} \tag{5}$$

In other words, specification of the left-hand side of equation (5) is completely equivalent to the specification, on the right. There is a unique $a(t)$ and $b(t)$ for a given $f(x)$, and vice versa.

If we now attempt to find a solution for equation **(2)** with a specification in terms of the right-hand side of equation (5) (still on $-\infty < x < \infty$, of course), we obtain

$$v(x, t) = \frac{-2\delta \sum_{n=1}^{\infty} \frac{K^{(n)}(t)}{\delta^n} \frac{x^{2n-1}}{(2n-1)!} + \sum_{n=0}^{\infty} \frac{[a(t)K(t)]^{(n)}}{\delta^n} \frac{x^{2n}}{2n!}}{\sum_{n=0}^{\infty} \frac{K^{(n)}(t)}{\delta^n} \frac{x^{2n}}{2n!} - \frac{1}{2\delta} \sum_{n=0}^{\infty} \frac{[a(t)K(t)]^{(n)}}{\delta^n} \frac{x^{2n+1}}{(2n+1)!}} \tag{6}$$

where

$$K(t) = \exp\left[\frac{1}{2\delta} \int D(t)\, dt\right] \tag{7}$$

with

$$D(t, \delta) = D(t) = \begin{vmatrix} a(t) & 2\delta \\ b(t) & a(t) \end{vmatrix} \tag{8}$$

Here, as I mentioned, $a(t)$ and $b(t)$ can be related to any given initial condition. A new, significant quantity appears here, relation (8). I called it the determinant of nonlinear diffusion in reference 3, and observed the following concerning the solution (6). Dissipation with time is still an exponential phenomenon, as in the linear case, but here it is rather complicated. As a result, the analytical solution presents the well-known nonlinear interaction among the various harmonics.

But still, equation (6) seems to represent a situation that is somewhat Pirandelloesque, a solution in search of a problem. Fortunately, however, this is not quite so. Besides the fact that this solution can be applied immediately to any situation that I might term "Lighthillian," the consideration of piston-driven propagation, defined by a boundary value problem of the type

$$v(g(t), t) = g'(t) \tag{9}$$

can be solved approximately by equation (6) because equation (9) can be expanded into a Taylor series and the terms retained are exactly the ones used in equation (6).

Indeed, if this is done, we can recover from equation (6), as a special case, the analog of the classical solution of Fay (ref. 5).[3]

To conclude, I should like to point out yet another, completely new, way of solving equations (1) approximately for given boundary conditions.

This method is the accidental discovery that if u is any solution of equation (2), any solution v of the ordinary nonlinear differential equation

$$u^2\left[\frac{v_x}{u}+\frac{v}{2}\right]_x = v^2\left[\frac{v_x}{v}+\frac{v}{2}\right]_x \tag{10}$$

is a solution of equation (2) also. But because equation (10) allows for the prescription of one boundary condition, our problem can be solved approximately; and the solution will be of the form

$$v=\frac{u^2+\alpha u-2u_x}{u+\alpha}$$

with u a solution of equation (2) and α depending on the boundary condition.

REFERENCES

1. LIGHTHILL, M. J.: Surveys in Mechanics, G. K. Batchelor and R. M. Davies, eds., Cambridge Univ. Press, 1956, pp. 250–351.
2. BLACKSTOCK, D. T.: J. Acoust. Soc. Am., vol. 36, 1964, p. 534.
3. RODIN, E. Y.: NASA CR-643, Nov. 1966.
4. SU, C. H.; AND GARDNER, C. S.: J. Math. Phys., vol. 10, 1969, p. 536.
5. FAY, R. D.: J. Acoust. Soc. Am., vol. 3, 1931, p. 222.

[3] Ibid.

INVESTIGATION OF PRESSURE PROBE RESPONSE IN UNSTEADY FLOW

Thomas E. Siddon[1]
University of Toronto
Canada

The measurement of pressure or density variations in unsteady flows such as turbulence poses problems that, to date, are largely unresolved (refs. 1 and 2). Accurate measurement of the fluctuating (ac) pressure or density is of particular importance to aerodynamic noise research in view of the role played by pseudo-sound in the noise-generation process (e.g., see ref. 3). Elsewhere in these proceedings a method of remote optical probing is described that enables the determination of spatially and temporally averaged properties of the density field (L. N. Wilson et al.).[2] The present article describes a more conventional approach concerned with inflow measurements of the fluctuating pressure. A particular objective was the exploration of the possibility of correcting for the error in such measurements instantaneously, using a specially devised error-compensating probe. A more extensive account of this work is given in reference 4.

INTRODUCTION

The problem is illustrated with the aid of figure 1. If a fast-responding static pressure probe is placed in an unsteady flow, the pressure P_m detected at the pressure sensing holes will not equal the true pressure P_t that would have occurred in the absence of the probe. The error arises from aerodynamic interaction between probe and flow and depends on both the probe geometry and properties of the adjacent velocity field. For convenience, we separate the instantaneous pressure into a steady dc part, or static pressure, and an unsteady ac part, the fluctuating pressure:

$$P(t)=\bar{P}+p(t) \tag{1}$$

In general, both $\bar{P}$ and p will be measured incorrectly. The errors are not necessarily small. For example, the error in p could be as large as p itself in certain circumstances.

[1] Presently at University of British Columbia, Vancouver, Canada.
[2] See p. 147.

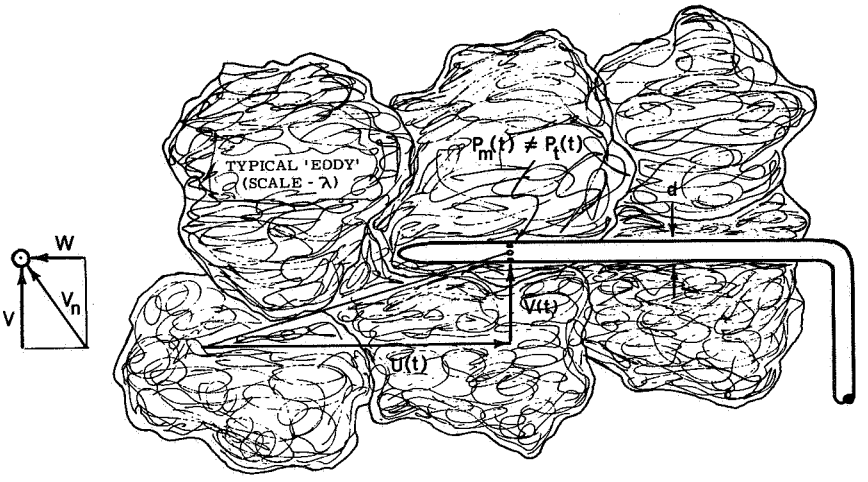

FIGURE 1.—Conventional static pressure probe in unsteady flow.

BACKGROUND

To predict the errors analytically is a formidable task, and little progress has been made from this approach. Rather, certain empirical relations have come to be accepted in which the error is presumed to depend on the fluctuating (ac) cross velocity v_n normal to the probe axis. Goldstein (ref. 5) suggested that the steady pressure $\bar{P}$ as measured by a static probe in a turbulent stream would be overestimated according to

$$\bar{P}_m - \bar{P}_t \simeq +(1/4)\rho\overline{v_n^2} \tag{2}$$

Fage (ref. 6) reported measurements which supported this equation; however there is some reason to question his findings (ref. 4). Similar expressions have been used for the error in fluctuating pressure (refs. 7 and 8). For instance, Strasburg (ref. 7) proposed that

$$p_m(t) - p_t(t) \simeq +(1/4)\rho(v_n^2 - \overline{v_n^2}) \tag{3}$$

The work of Barat (ref. 9) and Toomre (ref. 10) provides a more general description of the crossflow error. It is shown that the error depends on a coefficient (denoted by B here) that may be positive or negative depending on whether the scale or wavelength of the turbulence is smaller or larger than the probe diameter:

$$\bar{P}_m - \bar{P}_t \simeq B\rho\overline{v_n^2}$$
$$\downarrow$$
$$\underbrace{-1/2 \leqslant B}_{\lambda \gg d \text{ large scale}} \leqslant \underbrace{+1/2}_{\lambda \ll d \text{ small scale}} \tag{4}$$

At the large wavelength limit the situation is rather like uniform potential crossflow about an infinite cylinder. An average of the circumferential pressure distribution leads to a negative error, with $B=-1/2$. At the other extreme, when the scale is very small, the stagnation effect of individual eddies leads to a positive error with $B=+1/2$. Experiments by Bradshaw and Goodman (ref. 11) show qualitative agreement with this picture. It now appears that the large-scale condition is likely to be encountered in many practical situations. Hence, the widely accepted Goldstein correction is misleading.

EMPIRICAL ANALYSIS

Strictly speaking, the interaction error is defined by integrating the Navier-Stokes equations over the distorted velocity field and the surface of the probe. To evaluate this integral for a general unsteady situation would be virtually impossible. In the present work, extended forms of the empirical error equations were postulated and later substantiated. An incompressible flow was assumed, the properties of the undisturbed velocity field being regarded as more or less uniform over distances much larger than the probe diameter (large-scale hypothesis). Using an approach similar to that of Strasburg (ref. 7), the pressure error was expended in a power series of the instantaneous velocity components U, V, and W:

$$P_m(t)-P_t(t)=a_1U+a_2U^2+a_3V+a_4V^2+a_5W+a_6W^2+a_7UV+\ldots \tag{5}$$

(Terms involving fluid acceleration are disregarded here; see ref. 4.) The variables are separated into steady and fluctuating parts:

$$U(t)=\bar{U}+u \qquad V(t)=\bar{V}+v \qquad W(t)=\bar{W}+w \qquad P(t)=\bar{P}+p$$

This step, together with symmetry conditions and dimensional considerations (ref. 4), leads to two separate error equations: one for the error in static pressure and a second for the error in fluctuating pressure:

$$\bar{P}_m-\bar{P}_t\simeq A\rho(\bar{U}^2+\overline{u^2})+B\rho(\bar{V}_n^2+\overline{v_n^2}) \tag{6}$$

$$p_m(t)-p_t(t)\simeq A\rho(2u\bar{U}+u^2-\overline{u^2})+B\rho(2v\bar{V}+2w\bar{W}+v_n^2-\overline{v_n^2}) \tag{7}$$

where $\bar{V}_n^2=\bar{V}^2+\bar{W}^2 \qquad v_n^2=v^2+w^2$

The coefficients A and B prescribe the magnitude of errors arising from axial-flow and crossflow effects, respectively. It must be stressed that these equations are based on the assumption of quasi-steady flow,

371-986 O-LT-70—30

with the acceleration terms being neglected. Nevertheless, for unsteady flows in which the energy-bearing spectral content is concentrated at low frequencies, such that λ/d is relatively large (on the assumption of a frozen convected pattern of turbulence), these equations should provide an adequate description of the error. Earlier experience with the aerofoil turbulence probe (refs. *12* and **13)** confirmed that quasi-steady assumptions remain valid for a wide range of frequencies if the probe can be made small enough.

By careful shaping of the probe, coefficient A can be made much smaller than B, in which case the equation for fluctuating pressure error becomes

$$p_m(t) - p_t(t) \simeq B\rho(2v\bar{V} + 2w\bar{W} + v^2 - \overline{v_n^2}) \tag{8}$$

This equation is fundamental to the error-compensating scheme to be described. Note that for a probe alined with the mean flow direction, $\bar{V}$ and W will be zero.

ERROR COMPENSATION

A miniature probe was developed to measure the unsteady quantities p_m, v, and w instantaneously and simultaneously at a near-common point in the flow. By analog solution of the error equation (8), it was then possible to obtain an improved estimate of the true pressure p_t. The system is shown schematically in figure *2*.

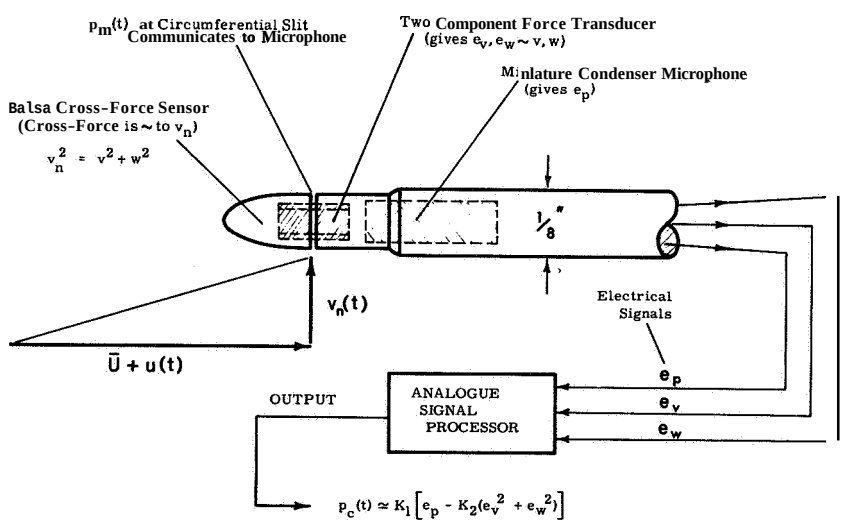

FIGURE 2. —Error-compensating pressure probe.

A prime requirement was that the probe be small, and a nominal diameter of 1/8 in. was selected as the minimum practical size. A second criterion was that the unsteady quantities should be converted into electrical signals by sensors that would respond uniformly over a wide-frequency range. For the pressure measurement a special miniature transducer was designed. This was housed inside the probe to monitor the apparent pressure developed at a circumferential slit located near the nose of the probe. A novel technique was devised for monitoring the components of cross-velocity. This involved a simple extension of the very successful aerofoil probe concept (refs. 12 and 13). The nose-piece of the probe was mounted on a four-element piezoelectric beam that afforded a measurement of two orthogonal components of cross-force. For moderate levels of turbulence these components of force are linearly related to the cross-velocity components v and w, if the frequency is not too high. Extensive calibration of the pressure and velocity sensors indicated linear response that was well matched over a frequency range from 10 Hz to 5000 Hz. Electrical signals from the sensors were fed to an analog system built up of Philbrick operational components. This system computed the corrected pressure instantaneously.

The cross-sectional area of the probe was increased slightly at a point about 3 diameters downstream of the nose. This shaping trick was employed to minimize the probe sensitivity to axial-flow fluctuations (i.e., to minimize the coefficient A by offsetting the error caused by nose curvature). Figure 3 shows a closeup view of the probe tip, together with other devices used in the investigation.

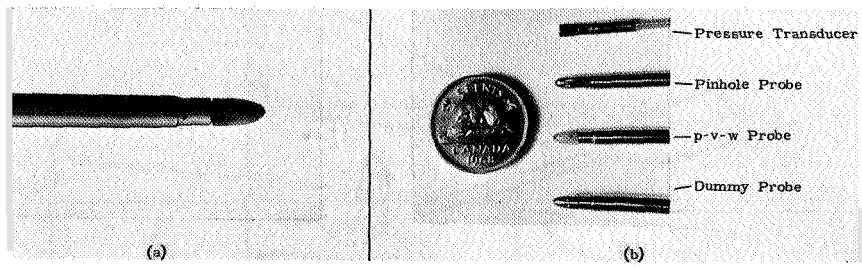

FIGURE 3.—Closeup detail of the probes. (*a*) The pv-w probe, (*b*) associated devices.

THE EXPERIMENTS

To substantiate the empirical error functions and to test the error-compensating scheme, a number of experiments were undertaken in a variety of unsteady flows. Here we will give only a partial description; a more complete account is to be found in reference 4.

Rotating Nozzle Flow

One of the more unique experiments involved a contrived rotating-nozzle flow. The basic configuration is depicted in figure 4. A nozzle was rotated in a bearing, with the nozzle passageway inclined at an angle θ_0 to the axis of rotation. Airflow passing through the nozzle was caused to swirl. A probe positioned in the flow as shown experiences constant pressure, but a sinusoidally fluctuating crossflow. An apparent pressure fluctuation is registered that is entirely caused by crossflow interaction with the probe. The simultaneous oscilloscope traces illustrate the sinusoidal nature of p_m, v, and w (fig. 5; signals are unfiltered).

Reference to the error equation helps describe the situation. From geometrical considerations

$$v(t) \simeq U_0 \sin \theta_0 \sin \omega t$$

$$w(t) \simeq U_0 \sin \theta_0 \cos \omega t$$

With proper choice of coordinates, $\bar{V} = U_0 \sin \alpha$ and $\bar{W} = 0$. The true fluctuating pressure p_t must be zero for reasons based on symmetry. With these restrictions, the error equation (8) takes a very simple form:

$$p_m(t) \simeq 2B\rho[U_0 \sin \alpha]v(t) \tag{9}$$

If the equation is valid, a plot of p_m versus $\sin \alpha$ should be linear; from the slope the error coefficient B may be found. Figure 6 shows such a plot,

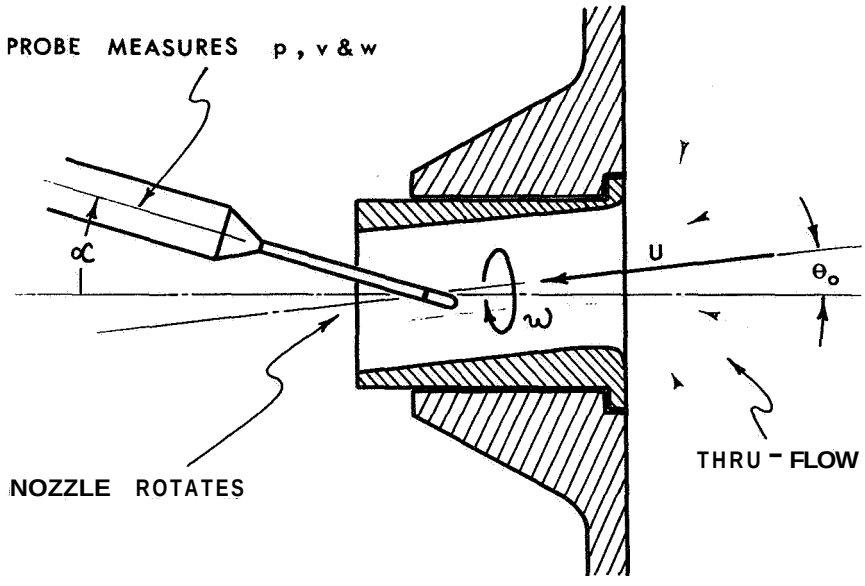

FIGURE 4.—Schematic of rotating inclined nozzle flow.

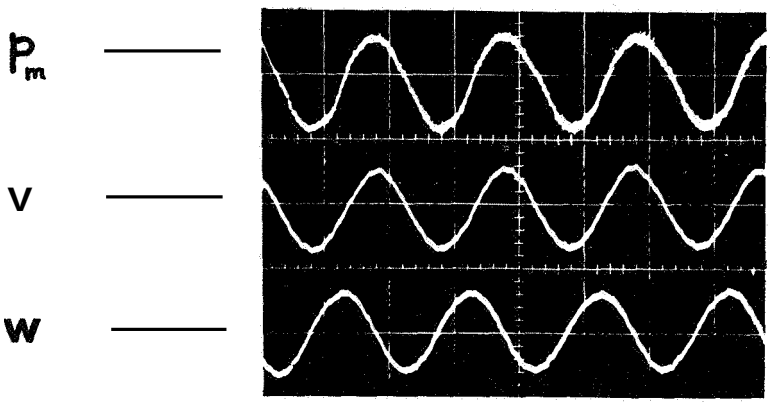

FIGURE 5.—Pressure and velocity signals of p-v-w probe in nozzle flow. Pressure signal is spurious effect of crossflow.

obtained for various values of flow velocity. The expected linearity was observed for values of α up to about 20". The error coefficient turned out to be negative and almost equal to $-1/2$.

The oscilloscope traces in figure 7 depict a successful attempt at error compensation. The upper trace is the spurious measured pressure. The middle trace is the error term as computed with the analog compensation system. Subtraction of the two led to the bottom trace, indicating that the true fluctuating pressure was zero, as expected.

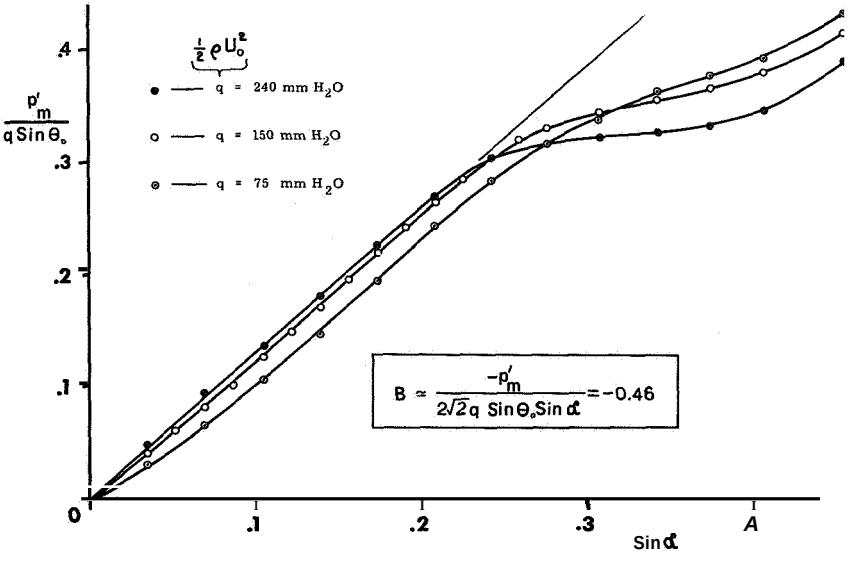

FIGURE 6.—Determination of error coefficient B with rotating inclined nozzle.

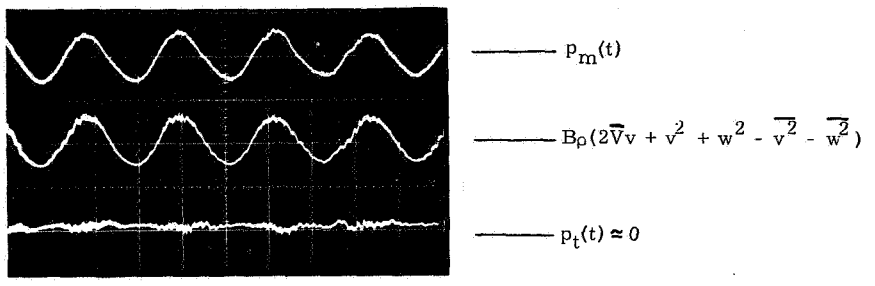

FIGURE 7. —Cancellation of crossflow error in rotating inclined nozzle flow.

Turbulent Channel Flow

A series of measurements were carried out in turbulent channel flow. The probe was mounted in a duct of 8-in. by 12-in. cross section at a point where the turbulence was fully developed. To minimize spurious pressure fluctuations of acoustic nature, the duct was lined with acoustical tile. Preliminary measurements indicated that turbulence levels were about 3 percent on the duct centerline and that effective turbulence wavelengths were some 40 times larger than the probe diameter in the frequency range of dominant spectral content.

A novel technique was devised for evaluating the error coefficient. The probe was placed on the duct centerline at angle of attack α (inset on fig. 8). With $\bar{V} \simeq \bar{U} \sin \alpha$ and $\bar{W} = 0$, equation (8) takes the form

$$p_m - p_t \simeq B\rho(2v\bar{U} \sin \alpha + v^2 + w^2 - \overline{v^2} - \overline{w^2}) \tag{10}$$

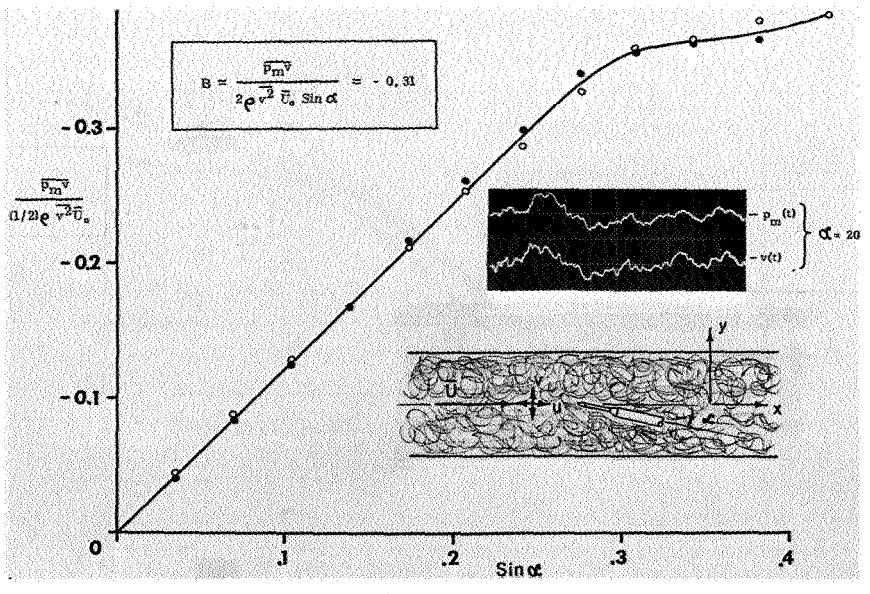

FIGURE 8. —Determination of error coefficient B in turbulent channel flow.

Multiplying through by v and time averaging gives

$$\overline{p_m v} - \overline{p_t v} \simeq B\rho(2\overline{v^2}\bar{U} \sin \alpha + \overline{v^3} + \overline{vw^2}) \tag{11}$$

Because of symmetry conditions at the duct centerline, the correlations $\overline{p_t v}$, $\overline{v^3}$, and $\overline{vw^2}$ must be zero. The result is

$$\overline{p_m v} \simeq 2B\rho\overline{v^2}\bar{U} \sin \alpha \tag{12}$$

If this expression is valid, a plot of $\overline{p_m v}$ versus sin a should be linear; from the slope, B may be determined. Figure 8 depicts such a plot. The correlations $\overline{p_m v}$ were evaluated with a Princeton Applied Research signal correlator. Here again the expected linearity was observed. In fact the curve bears close resemblance to the corresponding rotating-nozzle result. From the slope, B was evaluated as about $-1/3$. The oscilloscope traces inset on figure 8 illustrate the high degree of correlation between p_m and v when a is large.

Distributions of root-mean-square (rms) pressure were obtained by traversing the probe across the duct. The data are shown in figure 9 in which the lowermost curve gives the direct uncorrected pressure. The middle curve is the corrected pressure as computed by the error-compensating system with $B = -1/3$. The rotating-nozzle value $B = -0.46$

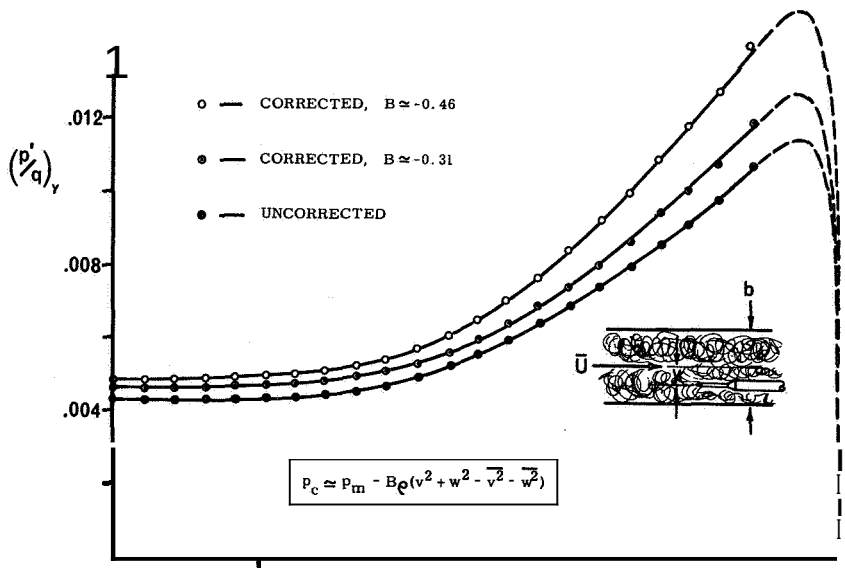

FIGURE 9.—Profiles of root-mean-square pressure p' in turbulent channel flow.

was also tried, resulting in the uppermost curve (in this case the error is probably overcorrected). The notable feature of these data is that correction consistently increased the rms pressure levels but not by a substantial amount, about 10 percent in the central region of the duct.

A typical comparison of spectral density for the corrected and uncorrected pressure is given in figure 10. Over most of the frequency range below 1000 Hz the correction increased the spectrum level by a constant 20 percent for the case with $B=-0.46$. There is some uncertainty about the data at very low frequencies because of the presence of tunnelborne (acoustic) pressure. At the high-frequency end, the condition $A \gg d$ breaks down and the correction loses validity. Nevertheless at 1000 Hz the spectrum is more than 20 dB down from its peak value; thus the correction to overall rms pressure is not likely to be affected significantly by the apparent spectral discrepancy at higher frequencies.

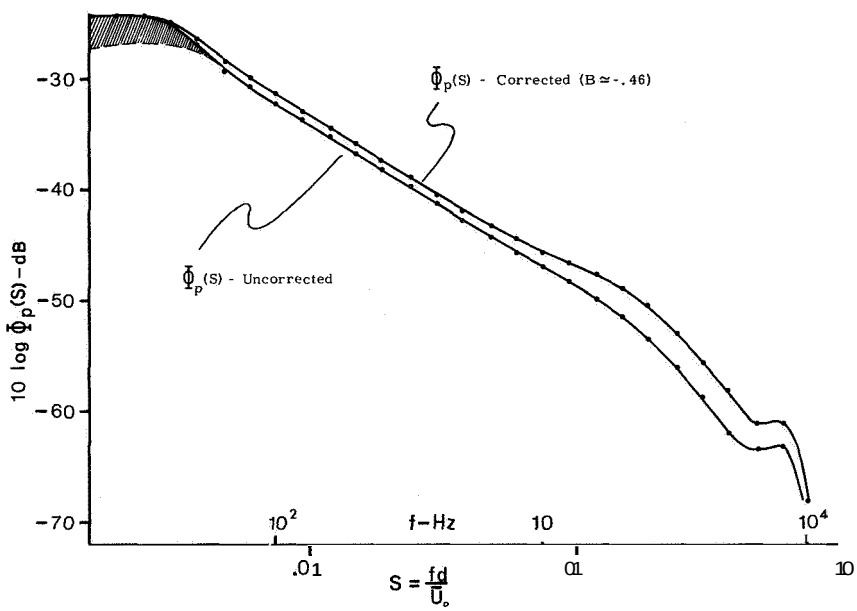

FIGURE 10.—Spectral density of fluctuating pressure at duct centerline.

CONCLUSIONS

Similar measurements to those already reported were carried out in other sorts of turbulent flow. For example, figure 11 gives typical profiles of rms pressure for a round turbulent jet. Complete details are to be found in reference 4. Here it is sufficient to note that consideration of the overall results allows the following generalizations to be made:

(1) Values of the error coefficient B were consistently negative, ranging between $-1/3$ and $-1/2$. This suggests that the large-scale hypothesis is realistic in many circumstances.

(2) The correction to rms pressure level was generally small, i.e., less than 20 percent of the uncorrected pressure. However, the correction did not always increase the pressure. Sometimes it had the opposite effect.

(3) In certain cases the waveforms of corrected and uncorrected pressure differed noticeably, even though the rms levels were nearly equal.

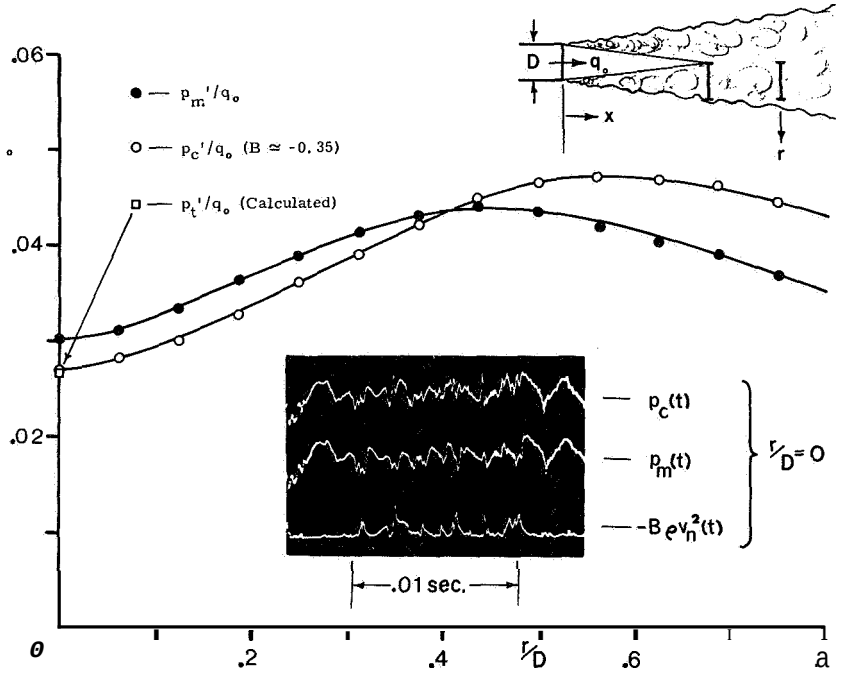

FIGURE 11. –Profiles of root-mean-square pressure p' in 4 in. round jet $(x/D=6)$.

The present study has been handicapped by an absence of standards with which to make comparison; i.e., there are no documented measurements of the true fluctuating pressure, free of probe error. Thus the results are not conclusive. Nevertheless it is felt that the feasibility of an error-compensating scheme has been demonstrated and that new insights have been gained that were hitherto unattainable.

REFERENCES

1. GINOUX, J. J., ed.: Round Table Discussion. Paper presented at meeting on The Mechanism of Noise Generation in Turbulent Flow, sponsored by AGARD Fluid Mechanics Panel. (Rhode-Saint-Genese, Belgium), Apr. 1–5, 1963. (Limited distribution.)
2. CORCOS, G. M.: Pressure Measurements in Unsteady Flows. Inst. of Engineering Research Rept., ser. 183, no. 1, Univ. of California, Jan. 1962.
3. RIBNER, H. S.: Aerodynamic Sound From Fluid Dilatations—a Theory of the Sound From Jets and Other Flows. UTIA Rept. 36, Inst. for Aerospace Studies, Univ. of Toronto, 1962.
4. SIDDON, T. E.: On the Response of Pressure Measuring Instrumentation in Unsteady Flow (An Investigation of Errors Induced by Probe-Flow Interaction). UTIAS Rept. 136, Inst. for Aerospace Studies, Univ. of Toronto, Jan. 1969.
5. GOLDSTEIN, S.: A Note on the Measurement of Total Head and Static Pressure in a Turbulent Stream. Proc. Roy. Soc., ser. A, vol. 155, 1936, p. 570.
6. FAGE, A.: On the Static Pressure in Fully Developed Turbulent Flow. Proc. Roy. Soc., ser. A, vol. 155, 1936, p. 576.
7. STRASBURG, M.: Measurements of the Fluctuating Static and Total Head Pressures in a Turbulent Wake. David Taylor Model Basin R&D Rept. 1779, 1963.
8. KOBASHI, Y.: Measurements of Pressure Fluctuations in the Wake of a Cylinder. J. Phys. Soc. Japan, vol. 12, 1957, p. 533.
9. BARAT, M.: Influence de la Turbulence sur les Prises de Pression Statique. Compt. Rend., vol. 246, 1953, p. 1156.
10. TOOMRE, A.: The Effect of Turbulence on Static Pressure Measurements. A.R.C. 22010, 1960.
11. BRADSHAW, P.; AND GOODMAN, D. G.: The Effect of Turbulence on Static Pressure Tubes. R.&M. No. 3527, A.R.C., 1963.
12. SIDDON, T. E.; AND RIBNER, H. S.: An Aerofoil Probe for Measuring the Transverse Component of Turbulence. AIAA J., Apr. 1965, pp. 747–749.
13. SIDDON, T. E,: A Turbulence Probe Utilizing Aerodynamic Lift. UTIAS Tech. Note 88, June 1965.

ACKNOWLEDGMENT

The author is indebted to Prof. H. S. Ribner, who suggested this work and provided valuable counsel during its course. The use of research facilities at the Institute for Aerospace Studies, University of Toronto, is gratefully acknowledged. The project was supported by the Air Force Office of Aerospace Research, U.S. Air Force, and by the National Research Council of Canada.

IV

PANEL AND OPEN DISCUSSION

Chairman: H. S. RIBNER

Some Comments on Possible Back-Reaction Effects of Acoustic Fields on Aerodynamic Sound Sources

P. E. Doak
Lockheed-Georgia Co.
Marietta, Ga.

In my contribution to this panel discussion, I would like to draw attention to one aspect of the aerodynamic noise problem that has, as yet, barely been mentioned, either in this conference or in previous work. The problem may have been ignored in the past mainly because it has been unimportant in past and current problems. However, several remarks at this conference have reinforced my belief that it is not always going to be unimportant. The remarks I am referring to are those of Dr. Martenson and of Professor Westervelt, who have suggested certain situations in which acoustic back reaction on an aerodynamic sound source may be appreciable. This possibility can be placed in a somewhat more general context.

Professor Sears has described the ways in which the aerodynamicist can contribute to our understanding of aerodynamic noise by further development of techniques for predicting the unsteady pressure, or force, distributions on blade cascades in compressible flow. Acousticians certainly want all such predictions that can be made. However, we acousticians have allowed Professor Sears and his aerodynamicist colleagues to believe that these aerodynamic forces can be calculated without reference to the acoustic field. Further, we have allowed them to believe that these aerodynamic forces can then be used by us acousticians as acoustic-source distributions that will remain unaffected by the sound field that they produce.

I think that there are three good reasons for saying, at this stage of our knowledge of aerodynamic sound generation, that the range of validity of such an assumption needs to be carefully examined in the next stages of our research.

First, examination of the mass, linear momentum, and energy transport equations of a compressible fluid shows that the assumption is not universally valid. Acoustic motion of a fluid does not occur independently

of turbulent motion, for the two are coupled through nonlinear terms of the equations.

Second, Dr. Martenson has pointed out that when an acoustic mode of a duct is excited by a fan at a frequency near the cut-on frequency of the mode, the acoustic mode can provide a very large reactive load on the fan and thus possibly affect the acoustic source strength of the fan.

Third (and this is the point which I wish to develop a little further, especially for the benefit of the aerodynamicists present), in other branches of acoustics, the concept of a source impedance is well understood and plays an essential role in descriptions of the acoustic fields produced by acoustic sources or equivalent acoustic sources. Recently, for example, the source impedance of ventilating fans has been of interest in connection with pure-tone noise production by such fans in relatively reverberant rooms.

A simple example can be used to illustrate the general nature of the back reaction of an acoustic field on a source producing it. Suppose a simple harmonic force Fe^{iwt} acts on a piston, or material element, in a fluid. In general, the piston may have an internal mechanical impedance Z_M, and so, in the absence of the acoustic field in the medium surrounding it, one could write as an equation of motion of the pistor.:

$$Z_M u = F$$

where ue^{iwt} is the velocity of the piston. In the presence of the acoustic field, however, there will be an additional force on the piston Spe^{iwt}, where S is a piston area and pe^{iwt} is the acoustic pressure on the piston. This pressure, in turn, is expressible in terms of the specific acoustic impedance "seen" by the piston and the velocity amplitude u of the piston. Further, this acoustic impedance generally can be thought of as having two elements in parallel: namely, a specific radiation impedance Z_R associated with the radiation of acoustic energy by the source and a (for want of a better phrase) nonradiative specific impedance Z_{NR} not associated with the radiation of acoustic energy by the source to large distances. This nonradiative impedance, for example, could be regarded as that provided to the source by the presence of a duct liner or other potentially sound-suppressing device.

Thus, taking into account the acoustic load on the source, the equation of motion above becomes of the form

$$F = \left(Z_M + \frac{SZ_R}{1 + Z_R/Z_{NR}}\right) u$$

The mean rate at which the force does work is then (where the bar denotes "complex conjugate of" and Re denotes "real part of")

$$\frac{1}{2}\mathrm{Re}\,(F\bar{u}) = \frac{1}{2}\mathrm{Re}\,(Z_M)\,|u|^2 + \frac{1}{2}\mathrm{Re}\left(\frac{SZ_R}{1+Z_R/Z_{NR}}\right)|u|^2$$

In this description, then, the acoustic power produced by the source appears proportional to the mean-square velocity amplitude of the source. Alternatively, it can be expressed as proportional to the mean-square applied force, which is

$$\frac{1}{2}\left|F\right|^2 = \frac{1}{2}\left|\left(Z_M + \frac{SZ_R}{1+Z_R/Z_{NR}}\right)\right|\left|u\right|^2$$

In this form, it is

$$\frac{1}{2}\mathrm{Re}\,(F\bar{u}) = \frac{\frac{1}{2}|F|^2}{\left|Z_M + \dfrac{SZ_R}{1+Z_R/Z_{NR}}\right|}\left\{\mathrm{Re}\,(Z_M) + \mathrm{Re}\left(\frac{SZ_R}{1+Z_R/Z_{NR}}\right)\right\}$$

In brief, the important aspects of this relationship that are relevant in the present context are as follows.

The acoustic load is negligible only when the internal source impedance Z_M is much greater in magnitude than the total acoustic impedance $SZ_R/(1+Z_R/Z_{NR})$. Although this is often the case for sound generated by motion of relatively massive objects such as loudspeaker diaphragms or aircraft structure, there is good reason to suppose, following the conjecture by Ira Dyer in the early 1950's, that it is not the case for many important aerodynamic sound sources such as fan rotor or stator rows. Also, one would suppose that a turbulent eddy, as a sound source, would have a relatively low internal impedance. These ideas at present remain conjectures. Fundamental theoretical and experimental work is needed to define and measure the internal source impedances of representative aerodynamic sound sources.

In determining the effectiveness of a given force as a producer of acoustic power, in addition to showing the importance of the ratio of the internal source impedance to the total acoustic impedance, the preceding expression also shows that the nonradiative part of the acoustic impedance "seen" by the source can affect the acoustic power radiated, as well as the radiation impedance. When Z_R is much smaller than Z_{NR}, the radiated acoustic power tends to be independent of the nonradiative impedance; but the opposite is true when Z_{NR} is much smaller than Z_R. In general physical terms, this means that the acoustic power output of an applied force can be drastically reduced by providing a device that acts as a pressure release. At the same time, the real part of the impedance provided by this device must be smaller, relative to the magnitude of its total impedance, than is the case for the radiation impedance.

COMMENTS ON SUPERSONIC JET NOISE

H. T. Nagamatsu
General Electric Research and Development Center
Schenectady, N.Y.

Further analytical and experimental studies should be made to determine sound propagation at the jet exit and in the supersonic mixing region. The available acoustic data for supersonic jets indicate that the greatest noise source from a supersonic jet is located in the vicinity of the transition from supersonic to subsonic velocity on the axis; i.e., just ahead of the sonic location. Both analytical and experimental studies should be conducted to resolve the flow phenomena that cause this large noise generation at this particular location. It is not very clear at present the importance of source, dipole, and quadrupole strengths on the noise generation for supersonic jets. No experimental data are available on the distribution of the quadrupole and its strength even for a subsonic jet. To achieve large jet-noise reduction for subsonic and supersonic jets, it is important to know the actual noise-generation mechanism within the subsonic and supersonic jets. In this respect the role of mach waves from supersonic eddies on the total acoustic radiation from supersonic jets is not well defined. Optical photographs indicate the presence of mach waves, but the power spectra are broadband for a parallel flow nozzle and do not indicate large acoustic power at the frequency determined from the spacing of the mach waves and the ambient velocity of sound.

The contribution of the shock waves that are present for a convergent nozzle at supersonic jet mach numbers on the noise generation and on the overall sound-power output requires additional investigations. It was observed for a mach-1.5 jet from both a convergent and a parallel flow nozzle, each with a throat diameter of 2 in. and with ambient-temperature air, that the difference in the overall power levels between these jets was only 3 dB. While the shock waves from the convergent nozzle were numerous, the contribution of these waves to the total sound generation was not as great as anticipated.

Controlled investigations for supersonic jets at elevated temperatures should be conducted to resolve the effects of jet mach number, velocity,

and density on the distribution of the acoustic sources and on the total acoustic power output. For this purpose, additional near-field acoustic data, the corresponding impact pressure fluctuations, and turbulent velocity, density, and pressure fluctuations within the jet at various distances from the jet exit should be obtained. Besides the jet total temperature, the effects of velocity and temperature gradients on the noise generation from subsonic and supersonic jets should be investigated. If there are large effects on the noise generation, a jet-noise suppressor can be developed to make use of this fact. The attenuation of sound through a supersonic jet is also not well understood. This information will be useful in the multitube suppressor for supersonic jets. By conducting intensive theoretical and experimental research on the supersonic jet-noise phenomenon, the knowledge regarding the noise sources and methods of decreasing the noise from subsonic and supersonic jets will alleviate the jet-noise problem.

COMMENTS ON STATUS AND PROBLEM AREAS IN JET NOISE RESEARCH

H. S. Ribner
University of Toronto
Canada

PHYSICS OF JET NOISE

There is a need to come to a consensus concerning the physics of jet-noise generation. Even for the simplest case, the round subsonic jet, there are a number of competing mathematical descriptions, e.g., references **1** to **17.**[1] Their equivalence, where it exists, should be brought out and their differences resolved. We ought to emphasize the common core of what can be considered established and direct our major effort toward the more uncertain areas.

We are ready to agree that the basic mathematical formalism of Eighthill (ref. **1)** is valid, while reserving for ourselves the right to some differences in its applications and developments. Certain alternative formulations by means of inner and outer expansions, e.g., references 12 and **13,** confirm the Lighthill results to a high degree. Thus, there would appear to be no further need for reexamination of the foundations.

The analytical developments together with specially devised experiments have thrown a fair amount of light on the physics of jet noise (fig. **1**). The eddy noise generators give rise to a basic directional pattern, which is modified by convection of the eddy sound sources and refraction of the sound waves by the jet-flow and jet-temperature profiles (refs. 6 and **7).**

There appears to be a consensus that the convection and refraction effects are very powerful and account for much of the directional pattern. Researchers generally agree on an analytical formula for the convection effect, and the refraction effect can be established either by special experiments with sound sources injected into a jet (refs. **18** and **19)** or (very recently) by computer programs.[2]

---

[1] See also p. 435.
[2] Unpublished work of L. K. Schubert, University of Toronto.

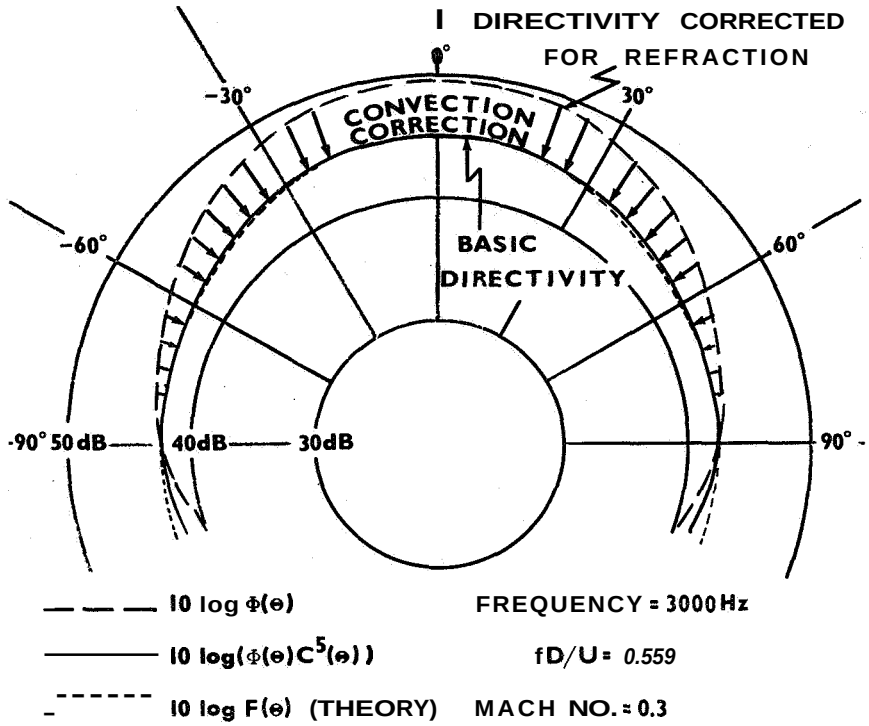

FIGURE 1.—Jet noise in terms of a basic pattern, not very directional, that is powerfully modified by convection of the eddy sound sources and refraction of the sound in passing through the jet (ref. 22).

My personal view is even stronger. I think that convection and refraction normally dominate the directional pattern of jet noise (refs. 7 and 20). These are competing effects and by themselves are sufficient to define almost completely the well-known lobes of maximum intensity at about 40° to the jet axis. If convection and refraction effects are corrected out of jet-noise data measured in our laboratory, the residual patterns of basic directivity are not very directional (e.g., fig. 2 of ref. 19).

There is agreement on certain features of the basic directivity. The pattern is a superposition of two: a fairly nondirectional self-noise from the turbulence alone and a strongly directional shear noise from interaction between the turbulence and the mean flow. The shear noise has a more-or-less figure-of-8 pattern, with one lobe pointing downstream and the other upstream. Some workers have concluded that the shear noise is the stronger of the two, which implies a rather directional basic pattern. Our own studies, both experimental and theoretical, suggest that the shear noise is merely comparable with the self-noise on the average, so that the combined pattern is not very directional. For full resolution

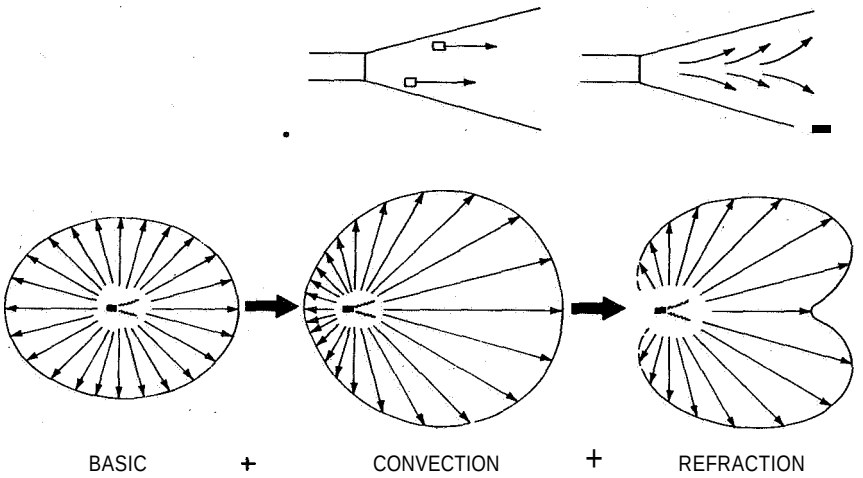

FIGURE 2.—Comparison of experimental and theoretical basic directivity of jet noise at low mach number (ref. 19).

of this point, the contributions of convection and refraction to cited experimental data will have to be established unimpeachably, which is a difficult task.

FREQUENCY SPECTRUM AND DOPPLER SHIFT PARADOX

Different but probably equivalent arguments (refs. 7 and 15) lead to the notion that the shear-noise spectrum is well below, e.g., an octave, the self-noise spectrum in dominant frequency content. Thus the low-frequency shear noise is beamed downstream as the figure-of-8 pattern, with the high-frequency self-noise dominant at the sides. This is compatible with the observation that the sound progressively deepens in pitch as one moves from the side of a jet toward the rear.

But because the turbulent eddies—the sound sources—are being swept to the rear, we would expect a compensating rise in pitch there from Doppler shift. Experimentally we find that this is almost completely canceled out by selective refraction; the high frequencies are strongly refracted away from the the axis of the jet, leaving the low frequencies to dominate near the axis (refs. 20 to 22).

NOISE EMISSION PER UNIT LENGTH OF JET

For a long time the noise emission from unit length of a subsonic jet was taken to be constant (x^0 law) for the first four to eight diameters, followed by a very sharp decay (x^{-7} law) according to similarity arguments (refs. 2, 4, and 23), supported by some experimental data (refs. 24

and 25). More recent arguments[3] (ref. 26) throw doubt on the similarity underlying the x^0 law. Some data[4] suggest the theory that the emission per unit length rises monotonically to a peak at as much as 15 diameters from the nozzle before the abrupt decay. Supersonic jets are, in fact, known to emit in this fashion (ref. 27).

This is a point that should be resolved for subsonic jets by suitable experiments. As a caution, we note that Potter's very neat scheme of progressive insertion of a jet through a hole (ref. 27) fails for subsonic jets, although it is highly successful for supersonic ones; the wall containing the hole appears to add considerable masking noise through an interference effect.[5]

EFFECT OF JET TEMPERATURE

The effect of jet temperature on jet noise needs to be resolved. The early work of Rollin (ref. 28) indicates no appreciable effect. More recent work of Plumblee (ref. 29)[6] indicates a significant noise reduction for very high temperatures. Simple theory indicates the noise power reduction should go as the density ratio squared $(\rho_j/\rho_0)^2$ for the same efflux velocity and nozzle area. This follows if we postulate no sound from entropy fluctuation and no changes in the mixing dynamics. Experimentally it works very well for jets of foreign gases mixing with air, where the density ratio (ρ_j/ρ_0) refers to two different gases at the same temperature. But where (ρ_j/ρ_0) refers to the same gas at two different temperatures, we obtain conflicting results. Because of the practical implications this point should be cleared up.

SUPERSONIC JETS

The foregoing remarks were directed primarily at subsonic jet noise. Less is known about the noise from supersonic jets and rockets. Yet this is an urgent current problem posed by the supersonic transport. The theories seem good enough in predicting the efficiency versus mach number and the major directional features (refs. 3, and 6 to 10). For example, the intensity peaks in a direction normal to the mach cones of the moving eddies.

All theories of flow-noise generation are predicated on knowledge of the turbulent flow characteristics. Such knowledge is singularly deficient for supersonic jets and mixing layers. Extensive measurements with

---

[3] J. E. Ffowcs Williams: Some Open Questions on the Jet Noise Problem. Dept. of Math., Imperial College, London. (Unpublished paper.)

[4] L. Maestrello: Unpublished research. The Boeing Co., Seattle.

[5] See p. 161.

[6] See also p. 113.

hot film sensors, airfoil probes (ref. 30), and more exotic devices (e.g., refs. **31** and **32)** are required.[7] We need to know mean flow profiles and turbulence quantities such as rms values, scales, spectra, and space-time correlations for velocity, density, and temperature fluctuations. Establishing valid inferred values of velocity, density, and temperature from the raw probe data will be no mean task, because all these factors influence the readings of the data.

The relative contributions of velocity, density, and entropy fluctuations to the noise of supersonic jets are not yet well established. Nor is the significance of shock-turbulence interaction (refs. **33** to **36).** For a supersonic nozzle operating near the design condition, for weak shocks only, the contribution appears minor.

JET MUFFLERS

The development of jet-noise mufflers has been largely ad hoc. This is not to say that those involved (e.g., the basic patent holders Westley, Lilley, and **A.** D. Young) have not been influenced by theoretical concepts, but that a well-documented, rational theory of muffler behavior is lacking and is urgently needed. **As** remarked earlier, there is still much diversity among the views concerning the mechanism of noise generation in a much simpler situation: the simple unmuffled round jet. The corrugated and multitube mufflers produce a far more complicated flow field, and so far, I know of no promising type of analysis.

Relatively crude phenomenological theories have been developed at Rolls-Royce and Boeing, and by Lee et al. (ref. **37)** and Eldred et al. (ref. **38)** (cf. also ref. **34).** In the absence of more fundamental approaches, these are all that we have. More experiments are required to measure the fluid dynamics of the muffler nozzle mixing process. These fluid dynamic data should serve to guide the assumptions of the theories or to provide a basis for alternate theories. The phenomenological theorists and fundamentalists need to communicate more with each other for mutual benefit. Improved phenomenological theories can result in the short term, and fundamental theories in the long term.

For experimental assessment of the acoustical performance of mufflers, we should agree on some ground rules. The thrust loss owing to the muffler should always be stated. Very large silencing ΔdB is meaningless if associated with a large thrust loss. If the muffler merely throttles down the jet velocity at constant nozzle area, the U^8 law alone would yield a quieting $\Delta \mathrm{dB} = 40 \log_{10}$ (thrust ratio). I would like to see muffler quieting corrected to a constant thrust basis by use of this formula.

In the case of supersonic jets, we can refer to standard unsuppressed

---

[7] *See* p. 147

jets that fit on established predictive curves (e.g., the SAE method). Relatively shock-free jets with properly designed converging-diverging nozzles will meet this test. But choked flows, especially cold flows, and flow speeds well off the nozzle design mach number can produce what Lighthill calls disintegrated jets (ref. 1) with a strong shock structure. A screech phenomenon involving acoustic feedback (refs. 40 to 44), probably triggered by shock-turbulence interaction, makes such jets extremely noisy. Since the standard jets can be achieved by proper design, it would seem that muffler performance (that is, ΔdB provided by. the muffler) should always be assessed relative to the standard jet-noise level. Impressive reductions assessed relative to a nonstandard noisier jet would be of little significance.

REFERENCES

(An attempt has been made to cite relevant references known to the author in a list of reasonable length. The tabulation is far from exhaustive, and there are many important omissions.)

1. LIGHTHILL, M. J.: Jet Noise. AIAA J., vol. 1,1963, pp. 1507–1517.
2. LILLEY, G. M.: On the Noise From Air Jets. ARC 20, 376–N40–FM2724, British A.R.C., 1958.
3. PHILLIPS, O. M.: On the Generation of Sound by Supersonic Turbulent Shear Layers. J. Fluid Mech., vol. 9, 1960, pp. 1–28.
4. POWELL, A.: Similarity Considerations of Noise Production From Turbulent Jets, Both Static and Moving. Rept. SM–23246, Douglas Aircraft Co., 1958. Abridged in J. Acoust. Soc. Am., vol. 31,1959, pp. 812–813.
5. POWELL, A.: Vortex Sound. Dept. of Eng. Rept. 61–70, Univ. of Calif. (Los Angeles), 1961.
6. RIBNER, H. S.: Aerodynamic Sound From Fluid Dilatations—A Theory of the Sound From Jets and Other Flows. UTIAS Rept. 86, Inst. for Aerospace Studies, Univ. of Toronto, 1962.
7. RIBNER, H. S.: The Generation of Sound by Turbulent Jets. Vol. 8 of Advances in Applied Mechanics, Academic Press, Inc., 1964, pp. 103–182.
8. RIBNER, H. S.: Eddy Mach Wave Noise From a Simplified Model of a Supersonic Mixing Layer. UTIAS TN 146, Inst. for Aerospace Studies, Univ. of Toronto, 1969.
9. FFOWCS WILLIAMS, J. E.: The Noise From Turbulence Convected at High Speed. Phil. Trans. Roy. Soc. London, ser. A, vol. 255, 1963, pp. %9–503.
10. FFOWCS WILLIAMS, J. E.; AND MAIDANIK, G.: The Mach Wave Field Radiated by Supersonic Turbulent Shear Flows. J. Fluid Mech., vol. 21,1965, pp. 641–657.
11. KOTAKE, S. G.; AND OKAZAKI, T.: Jet Noise. Bull. Japan Soc. Mech. Engrs., vol. 7, no. 25,1964, pp. 153–163.
12. OBERMEIER, F.: Berechnung aerodynamisch erzeugter Schallfelder mittels der Methode der Matched Asymptotic Expansions. Acustica, vol. 18,1967, pp. 238–240.
13. LAUVSTAD, V. R.: On Non-Uniform Mach Number Expansion of the Navier-Stokes Equations and Its Relation to Aerodynamically Generated Sound. J. Sound Vib., vol. 7, 1968, pp. 90–105.
14. BSCHORR, O.: Analyses of Jet and Boundary Layer Noise. ICAS Paper no. 68–43, paper presented at Proc. 6th Congress Internat. Council of Aeronaut. Sciences, Sept. 1968.

15. CSANADY, G. T.: The Effect of Mean Velocity Variations on Jet Noise. J. Fluid Mech., vol. 26, pt. 1, 1966, pp. 183–197.
16. KRISHNAPPA, G.: Some Studies on Jet Noise. Ph. D. Thesis, Dept. of Mech. Eng., Univ. of Waterloo, Ontario, Canada, May 1967.
17. JONES, I. S. F.: Fluctuating Turbulent Stresses in the Noise Producing Region of a Jet. J. Fluid Mech., vol. 36, pt. 3, 1969, pp. 529–543.
18. ATVARS, J.; SCHUBERT, L. K.; GRANDE E.; AND RIBNER, H. S.: Refraction of Sound by Jet Flow or Jet Temperature. NASA CR–494, May 1966. Supersedes UTIAS TN 109, 1965.
19. GRANDE, E.: Refraction of Sound by Jet Flow and Jet Temperature. Extension of Temperature Range Parameters and Development of Theory. NASA CR–840, Aug. 1967. (Supersedes UTIAS TN 110, 1966.)
20. RIBNER, H. S.: Quadrupole Correlations Governing the Pattern of Jet Noise. UTIAS Rept. 128, Inst. for Aerospace Studies, Univ. of Toronto, Nov. 1967. Revised in J. Fluid Mech., vol. 38, Aug. 14, 1969, pp. 1–24.
21. RIBNER, H. S.: The Elusive Doppler Shift in Jet Noise. Reports of the Sixth International Congress on Acoustics, Dr. V. Kohasi, ed., vol. IV, pt. F, 1968, pp. F-97–F-100.
22. RIBNER, H. S.: Jets and Noise. Can. Aeron. and Space Inst., vol. 14, Oct. 1968, pp. 282–298.
23. RIBNER, H. S.: On the Strength Distribution of Noise Sources Along a Jet. UTIAS Rept. 51, Inst. for Aerospace Studies, Univ. of Toronto, 1958. Abridged in J. Acoust. Soc. Am., vol. 30, 1958. p. 876.
24. SANDERS, N. D.; AND LAURENCE, J. C.: Fundamental Investigation of Noise Generation by Turbulent Jets. SAE Trans., vol. 65, 1957, pp. 244–249.
25. DYER, I.: Distribution of Sound Sources in a Jet Stream. J. Acoust. Soc. Am., vol. 31, 1959, pp. 1011–1021.
26. JONES, I. S. F.: Scale Pertinent to Noise Prediction for the First Few Diameters of a Jet. AFOSR–UTIAS Symposium on Aerodynamic Noise, Univ. of Toronto Press, 1969.
27. POTTER, R. C.: An Experiment To Locate the Acoustic Sources in a High Speed Jet Exhaust Stream. J. Acoust. Soc. Am., vol. 42, Nov. 1967, p. 1214(A).
28. ROLLIN, V. G.: Effect of Jet Temperature on Jet-Noise Generation. NACA TN 4217, 1958.
29. PLUMBLEE, H. E., JR.: The Effect of Exhaust Temperature on Jet Noise Generation. J. Acoust. Soc. Am., vol. 42, Nov. 1967, p. 1214(A).
30. SIDDON, T. E.; AND RIBNER, H. S.: An Aerofoil Probe for Measuring the Transverse Component of Turbulence. AIAA J., vol. 3, no. 4, Apr. 1965, pp. 747–749.
31. SIDDON, T. E.: On the Response of Pressure Measuring Instrumentation in Unsteady Flow. UTIAS Rept. 136, Inst. for Aerospace Studies, Univ. of Toronto, 1969.
32. FISHER, M. J.; AND KRAUSE, F. R.: The Crossed-Beam Correlation Technique. J. Fluid Mech., vol. 28, 1967, pp. 705–717.
33. LIGHTHILL, M. J.: On the Energy Scattered From the Interaction of Turbulence With Sound or Shock Waves. Proc. Cambridge Phil. Soc., vol. 49, pt. 3, 1953, pp. 531–551.
34. RIBNER, H. S.: Shock-Turbulence Interaction and the Generation of Noise. NACA TN 3255, 1954, or NACA Rept. 1233, 1955.
35. RIBNER, H. S.: Acoustic Energy Flux From Shock-Turbulence Interaction. J. Fluid Mech., vol. 35, pt. 2, 1969, pp. 299–310.
36. LOWSON, M. V.: Shadowgraph Visualization of Noise From Cold Supersonic Jets. Research Staff Rept. WR-67–3, Wyle Laboratories, Jan. 1967.
37. LEE, ROBERT; ET AL.: Research Investigation of the Generation and Suppression of Jet Noise. Navy Bureau of Weapons contract no. 59–6160–c, Flight Propulsion Lab. Dept. (Cincinnati), General Electric Co., 1961.

38. ELDRED, K.; ET AL.: Suppression of Jet Noise With Emphasis on the Near Field. Rept. ASD–TDR-6–578, Flight Dynamics Lab., Aeron. Systems Div., AF Systems Command, Wright-Patterson AF Base, Feb. 1963.

39. MIDDLETON, D.; AND CLARK, P. J. F.: Assessment and Development of Methods of Acoustic Performance Prediction for Jet Noise Suppressors. UTIAS TN 134, Inst. for Aerospace Studies, Univ. of Toronto, 1969.

40. POWELL, A.: On the Mechanism of Choked Jet Noise. Proc. Phys. Soc. London, ser. B, vol. 66, 1953, pp. 1039–1056.

41. MERLE, MARIE: Emissions Acoustiques Associées aux Jets d'Air Supersoniques. J. Mecan., vol. 4, 1965, pp. 305–317.

42. WESTLEY, R.; AND WOOLLEY, J. H.: An Investigation of the Noise Fields of a "Choked" Axi-Symmetric Air Jet. AFOSR–UTIAS Symposium on Aerodynamic Noise. Univ. of Toronto Press, 1969.

43. WESTLEY, R.; AND WOOLLEY, J. H.: The Near Field Sound Pressures of a Choked Jet During a Screech Cycle. Preprint no. 42, AGARD Conference Proceedings on Aircraft Engine Noise and Sonic Boom, May 1969.

44. POLDERVAART, L. J.; WIJNANDS A. P. J.; AND VINK, A. T.: The Photographic Evidence of the Feedback Loop of a Two-Dimensional Screeching Supersonic Jet of Air. Reports of the Sixth International Congress on Acoustics, V. Kohasi, ed., vol. IV, pt. F, 1968, pp. F–101 – F–104.

General Remarks

COMMENTS ON THE PREDICTION OF NOISE FROM PROPELLERS AND ROTORS

I. E. Garrick
NASA Langley Research Center
Hampton, Va.

Dr. W. R. Sears has suggested at this conference and also in his Von Kármán lecture (ref. 1) that most of the noise produced by airfoils in motion, such as propeller blades, helicopter rotors, and fan stages, can be predicted reasonably well, at least for subsonic speeds, from the forces given by classical unsteady airfoil theory. In this regard, we are gratified by the reference he has made to the usefulness of our work of long ago (ref. 2). We would, however, indicate that experience has shown many differences between calculation and measurement even for subsonic propellers with airloads that are relatively steady. This is particularly true for the higher harmonics of multibladed propellers. In the case of helicopter rotors, the difficulty lies particularly in defining the unsteady airloads because the higher harmonics of the noise spectrum appear to be extremely sensitive to small variations in the loading. This point was emphasized recently by Lowson and Ollerhead (ref. 3), Wright (ref. 4), and Sadler and Loewy (ref. 5), and in fact is indicated in the treatise of Morse and Ingard (ref. 6). Thus, the noise output of rotating blades can be considerably modified by interactions with asymmetrical flow, wind, turbulence, vibration, separated flows, and vortices. To confirm a theory, fairly detailed knowledge of the airload distribution around the rotor disk is required. In this regard, the obvious lack of basic experimental information in the detail required is a formidable task for future researchers. Effects of the unsteady flow that may seem minor for fan stages may be much more significant for helicopter rotors.

An additional remark in connection with the paper, "Unsteady Airfoil Response" by R. A. Arnoldi,[1] is appropriate here with reference to the noise effects of thickness of the blades, effects often neglected. The linear theory distributes the pressures and loading equally to both surfaces of the airfoil and does give a relatively good account of the total

[1] *See* p. 247

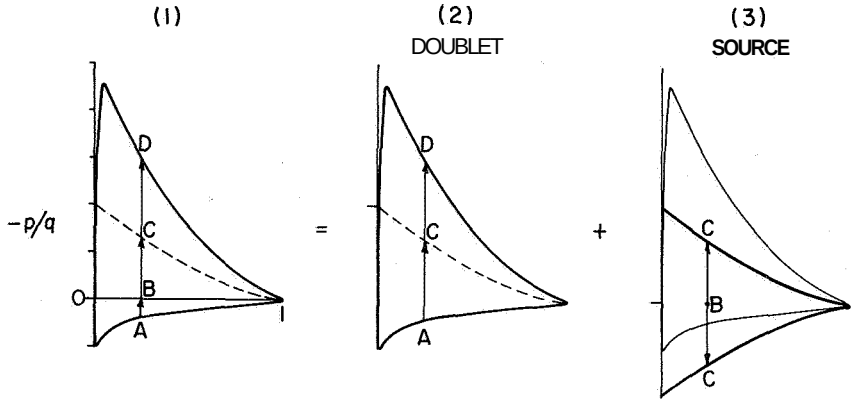

FIGURE 1.—Pressure distribution separated into loading and compression effects and represented by doublet and source distributions.

actual loading. However, the noise associated with effects of thickness may be taken well into account by closer examination of the individual pressure distributions over each surface. This may be clarified by figure 1. Let the actual pressure distributions over the upper and lower (or front and rear) surfaces over a section of the blade be given as in (1). The distributions may be separated into the sum of those in (2) and (3). In (2) we separate the loading into two equal parts and represent it by a doublet distribution appropriately placed over the disk and proportional to strengths AC or CD. In (3), however, we account for the noise caused by the piston or compression effect of thickness by an appropriate source distribution by letting the difference in pressure levels BC between the ambient free stream values at B and the midpressure values at C be proportional to the strength of the source distribution. This procedure was briefly mentioned in reference 2.

REFERENCES

1. SEARS, W. R.: Aerodynamics, Noise, and the Sonic Boom. 1968 von Kármán Lecture. AIAA J., vol. 7, no. 4, Apr. 1969, pp. 577–586.
2. GARRICK, I. E.; AND WATKINS, CHARLES E.: A Theoretical Study of the Effect of Forward Speed on the Free-Space Sound-Pressure Fjeld Around Propellers. NACA Report 1198, 1954.
3. LOWSON, M. V.; AND OLLERHEAD, J. B.: A Theoretical Study of Helicopter Rotor Noise. J. Sound Vib., vol. 9, no. 2, Mar. 1969, pp. 197–222.
4. WRIGHT, S. E.: Sound Radiation From a Lifting Rotor Generated by Asymmetric Disk Loading. J. Sound Vib., vol. 9, no. 2, Mar. 1969, pp. 223–240.
5. SADLER, S. GENE; AND LOEWY, ROBERT G.: A Theory for Predicting the Rotational and Vortex Noise of Lifting Rotors in Hover and Forward Flight. NASA CR–1333, May 1969.
6. MORSE, P. M.; AND INGARD, K. U.: Theoretical Acoustics. McGraw-Hill Book Co., Inc., 1968, p. 738.

COMMENTS ON DR. BENZAKEIN'S REMARKS ON FAN NOISE AND FAN DESIGN SPEED

Arthur W. Goldstein
NASA Lewis Research Center
Cleveland, Ohio

Dr. Benzakein's statement with supporting calculations that rotor discrete tone emission, caused by the rotation of the rotor pressure pattern, will decrease with increasing rotor design speed (pressure ratio and mass flow constant) is an important one with which I disagree. As shown below, the effect of design speed on rotor input-to-duct oscillation is negligibly small. Because of the smallness of this effect and the reduced transmission of the duct below cutoff, the subsonic rotor shows an advantage for low levels of far-field noise originating in rotation of the rotor pressure field. Other advantages of low-speed design are reduced broadband radiation from the rotor and absence of shock noises resulting from wave rotation, oscillation, and interaction with turbulence.

One acoustic advantage of high-speed design is obtained from the reduced level of the range of steady pressures on the blade surfaces and the resulting reduced wakes discharged from the blades. This, in turn, reduces the level of radiation from the outlet guide vanes that intercept these wakes. Some compensation for this effect may be obtained by increasing the rotor solidity near the tips and the axial spacing between the rotor and the outlet guide vanes.

Theoretical considerations therefore indicate advantages for both the high-speed and low-speed designs; empirical data will be required to decide which is quieter.

The intensity of the transmitted sound for zero-order radial mode (most easily transmitted) in an annular duct of low height is obtained for the skewed dipoles by Morfey (see reference) as

$$I_2 = (T\alpha/8\rho c)\,|P_z + (m/\alpha ka)P_y|^2$$

above cutoff and

$$I_2 = (T|\alpha|/8\rho c)\,|P_z + (m/\alpha ka)P_y|^2 \exp\,(-2|\alpha|kz)$$

below cutoff

where

I_2	intensity of transmitted sound
T	energy transmission coefficient of duct
ρ	gas density
c	sonic speed
m	order of angular mode (integer $n \times$ number of rotor blades B)
k	wave number $(k=\omega/c)$
w	frequency (of sound) $w=m\Omega$
Ω	rotor angular velocity
αk	$\sqrt{k^2-m^2/a^2}$
a	radius of annulus
U	Ωa, rotor linear speed
P_z	axial component of dipole force representing blade
P_y	rotational component of dipole force representing the blade

This equation also assumes no gas velocity effects on the acoustics. The rotor input term (aside from the duct transmission properties) is

$$|P|^2=|P_z+(m/\alpha ka)P_y|^2=|P_z+P_y/\sqrt{U^2/c^2-1}|^2$$

Because P is perpendicular to the relative velocity vector W, averaged over the rotor intake and output values, then

$$P_z=-P_y(W_{y1}+W_{y2})/2W_z$$

The power equation

$$UP_y=\dot{m}\Delta H$$

(where m is mass flow, and ΔH, rise in stagnation enthalpy of gas passing through fan) permits determination of discharge velocity vector so that with the momentum equation

$$P_y=\dot{m}(W_{y2}-W_{y1})$$

and

$$W_{y1}=-U$$

we obtain finally

$$P_y=m\Delta H/U \qquad P_z=\dot{m}\Delta H(1-\Delta H/2U^2)/W_z$$

$$|P|^2=(\dot{m}\Delta H/W_z)|(1-\Delta H/2U^2)+(W_z/U)/\sqrt{U^2/c^2-1}|^2$$

The factor $\dot{m}\Delta H/W_z$ is the same for all comparable designs, and the speed effect can be shown for a fan designed for a pressure ratio of 1.5,

an efficiency of 0.85, and an axial mach number of 0.6, as summarized in table I.

U/c	0.8	0.9	1.2	1.4
Axial: $(1-\Delta H/2U^2)$	0.44	0.56	0.75	0.82
Rotational: $\frac{W_z}{U}\Big/\sqrt{\frac{U^2}{c^2}-1}$	$1.25i$	$1.53i$	.75	.44
Resultant	1.32	1.63	1.50	1.26

The speed effect is seen to be negligible, and the variation of transmission indicates that low speeds are to be preferred for reduction of this specific type of fan noise.

REFERENCE

MORFEY, C. L.: Rotating Pressure Patterns in Ducts: Their Generation and Transmission. J. Sound Vib., vol. 1, 1964, pp. 60-87.

NEW AVENUES FOR BOUNDARY-LAYER ACOUSTICS RESEARCH

R. I. Johnson and H. Saunders
General Electric Co.
Philadelphia, Pa.

SYMBOLS

$\bar{p}$	root-mean-square pressure, psf
q	dynamic pressure, psf
P_0	tunnel stagnation pressure, psia
dB	decibels $= 20 \log_{10} \frac{\bar{p}}{p_{ref}}$, where $p_{ref} = 0.0002\ \mu$bar
M	machnumber
T_W	model surface temperature, °R
T_0	tunnel stilling chamber temperature, °R

Subscripts

1	local conditions
∞	free stream

INTRODUCTION

The recent availability of extremely small and sensitive acoustic sensors (piezoelectric and condenser type) have opened new avenues for turbulent boundary layer research. This new measurement scheme complements the previously accepted measurement techniques (schlieren photos, thermal measurements, and static pressure measurements) and offers promise of improving our understanding of the boundary-layer characteristics. Acoustic phenomena associated with the boundary layer emerge in a number of different areas:

(1) Structurally induced vibration caused by fluctuating pressures in wakes as well as boundary layers

(2) Boundary layer transition from laminar to turbulent flow

(3) Correlation between test facilities of transition Reynolds numbers by tunnel wall radiated noise

(4) Relationship between free stream disturbances and transition

(5) Correlations between shear, heat-transfer rates, and acoustic pressures

In recognition of these considerations, a wind-tunnel test program was conducted at mach number 4.0 to obtain preliminary data on model boundary-layer acoustics. From the analysis of the data, new insights into boundary-layer acoustic phenomena were developed, and several promising avenues for further productive research identified. Some of the striking features of this data are:

(1) Acoustic amplitudes during transition that are significantly higher than in fully turbulent flow

(2) Spectral content differences between tripped and naturally induced turbulent flow at the same location

(3) Turbulent flow acoustic amplitudes at $M = 4$ higher than theoretical predictions

(4) Power spectra indicative of a filtered addition of radiated noise from the tunnel walls.

The discussion presents a brief description of our test program and the data evaluation.

VEHICLE MODEL AND SENSOR INSTALLATION DESCRIPTION

The data reported here were taken in AEDC's Tunnel A at $M_\infty = 4.0$ with varying stagnation pressures. The model on which the acoustic sensors were mounted was a cylinder (as shown in fig. 1) with forebodies of varying bluntness ratio. The figure shows the location of microphones along the cylinder and the types used at each station. In addition to the acoustic sensors, temperature and pressure sensors were also installed along the length of the cylinder. The temperature gages were used to determine the point of transition of the boundary layer from laminar to turbulent flow. For some tests, a ring of spherical boundary-layer trips was installed on the forebody to produce turbulent flow along the cylinder.

One of the basic test objectives was to determine the differences between various installation techniques of microphones. Figure 2 presents a sketch of the techniques employed in this test series. Only one type of microphone, the 1/4-inch-diameter Bolt, Beranek & Newman piezoelectric device, was tested under the flush, straight port and 90" bend port configurations shown in figure 2. In tests where the surface heat-transfer rates and temperatures are low, the flush-mounted arrangement is normally employed. For high heat-transfer rate regions (such as a reentry flight test), the ported arrangement is used to protect the crystal from thermal effects. Both straight and bent ports have been flight tested.

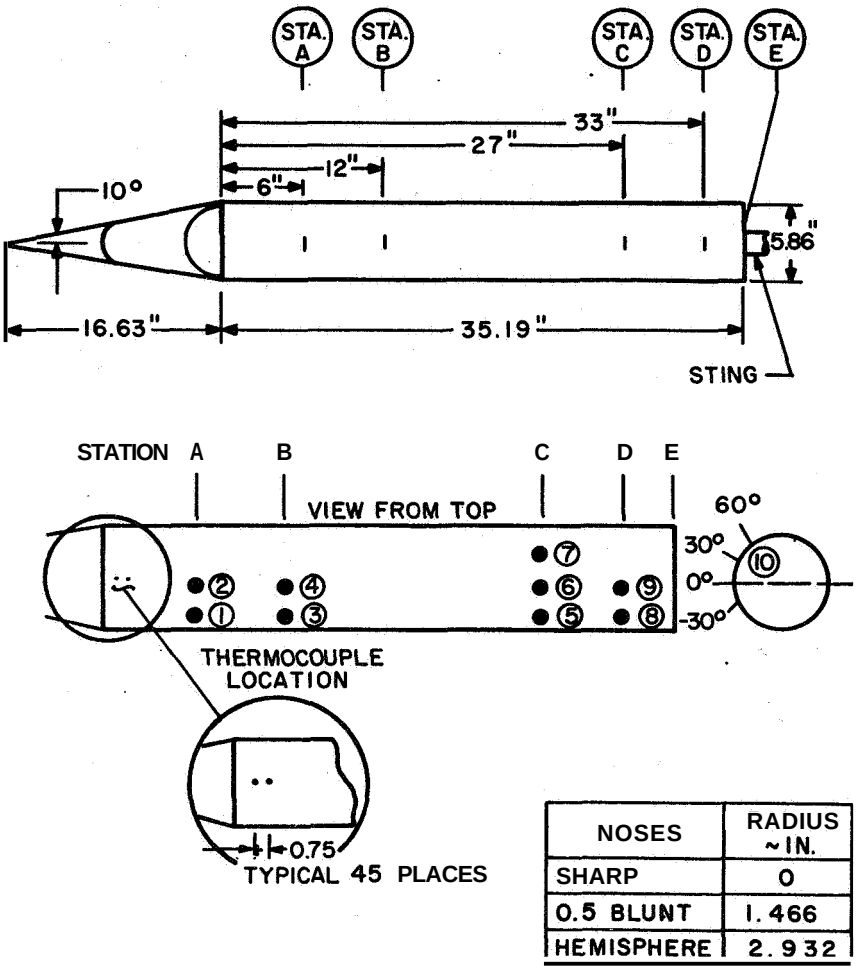

NOSES	RADIUS ~IN.
SHARP	0
0.5 BLUNT	1.466
HEMISPHERE	2.932

FIGURE 1.—Test model configurations.

Channel	Station	Sensor type	Installation
1	A	Backface crystal	Backface.
2	A	BBN 1/4-in.-diameter acoustic (model 450X)	Flush.
3	B	CRL 1/2-in.-diameter acoustic (model SD-129)	Straight port.
4	B	BBN 1/4-in.-diameter acoustic (model 450X)	Straight port.
5	C	B&K 1/4-in.-diameter acoustic (model 4136)	Straight port.
6	C	BBN 1/4-in.-diameter acoustic (model 450X)	90° bend port.
7	C	Endevco accelerometer	Backface.
8	D	CRL 1/2-in.-diameter acoustic (model SD-129)	Straight port.
9	D	BBN 1/4-in.-diameter acoustic (model 450X)	Flush.
10	E	ARC 5/16-in.-diameter acoustic (model LC70)	Flush.

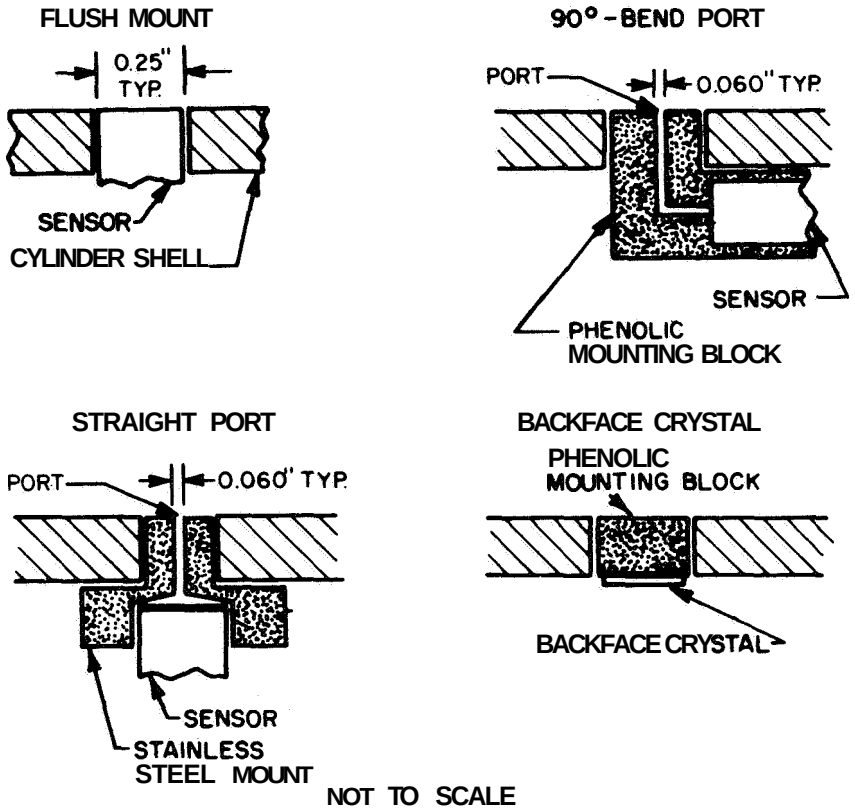

FIGURE 2.—Acoustic sensor installation techniques.

The latter configuration normally has a lower frequency response capability (because of its longer port), but does tend to reduce the sensitivity of the crystal to motions of the shell to which it is mounted; i.e., shell accelerations are in the plane of the crystal, not normal to it.

Detailed comparisons of the measurements from each microphone and the installation technique are described in reference 1. For our tests, it did not appear that the vibration isolation of the bent port outweighed the disadvantage resulting from its lower Helmholtz frequency when compared to a straight port arrangement.

Although the sensors were calibrated at only one frequency (1000 Hz), their response out to approximately 5000 Hz was expected to be flat. However, as described in reference 1, significant differences were observed in the low-frequency spectra of two different-size sensors at the same location. This observation indicates that the previously accepted procedure for calibration of ported sensors is inadequate for compressible flow. In addition, it would be well to determine how the calibration varies with mach number and boundary-layer thickness.

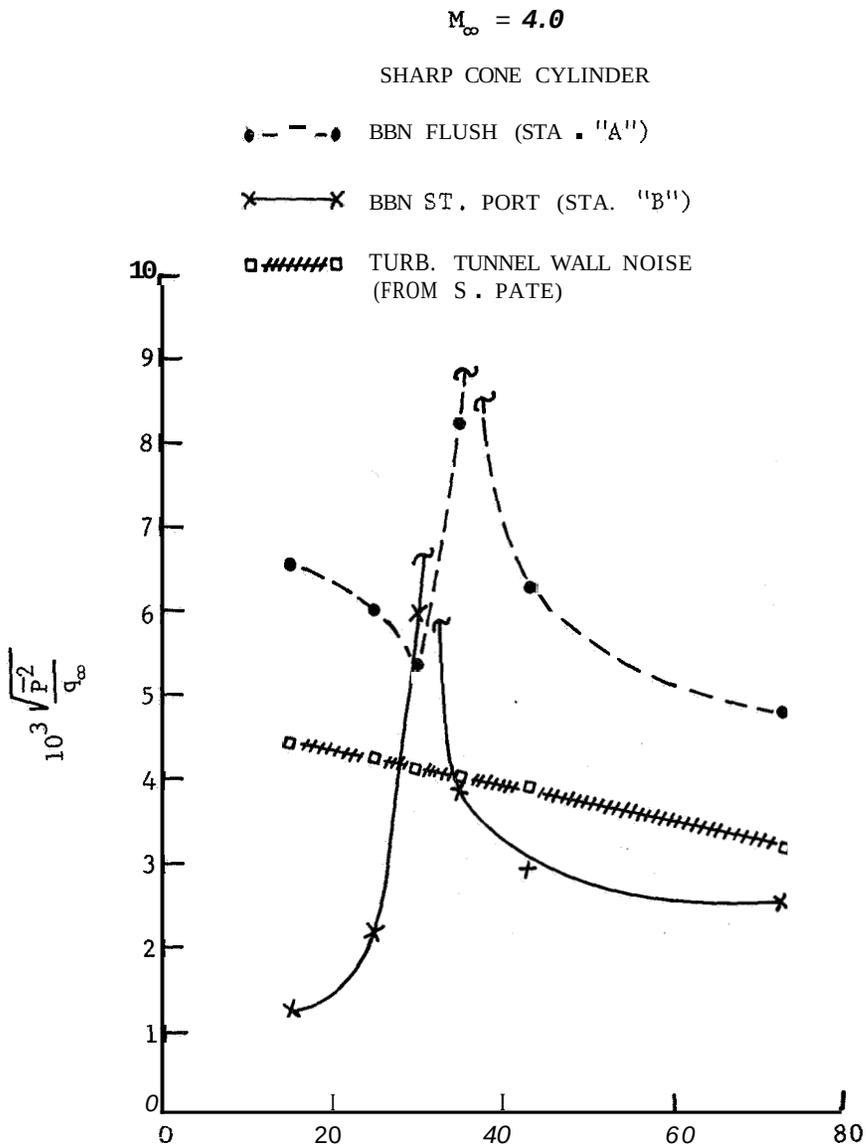

FIGURE 3.—Overall sound pressure versus tunnel stagnation pressure (flush and ported sensors).

AMPLITUDE AND SPECTRA OF ACOUSTIC PRESSURES

Figure 3 presents the variation in overall sound amplitude with tunnel stagnation pressure at two locations on the model. Data from the flush and straight-ported installations of the BBN sensor are shown. As the

stagnation pressure increases, the flow over the two sensors changes from laminar to turbulent. By correlating with the thermal data, the onset of turbulence, end of transition, can be shown to occur simultaneously with the peak in sound-pressure level around 30- to 35-psi stagnation pressure. This fact, that the sound-pressure level during transition may be higher than in fully turbulent flow, has been observed in other test programs.

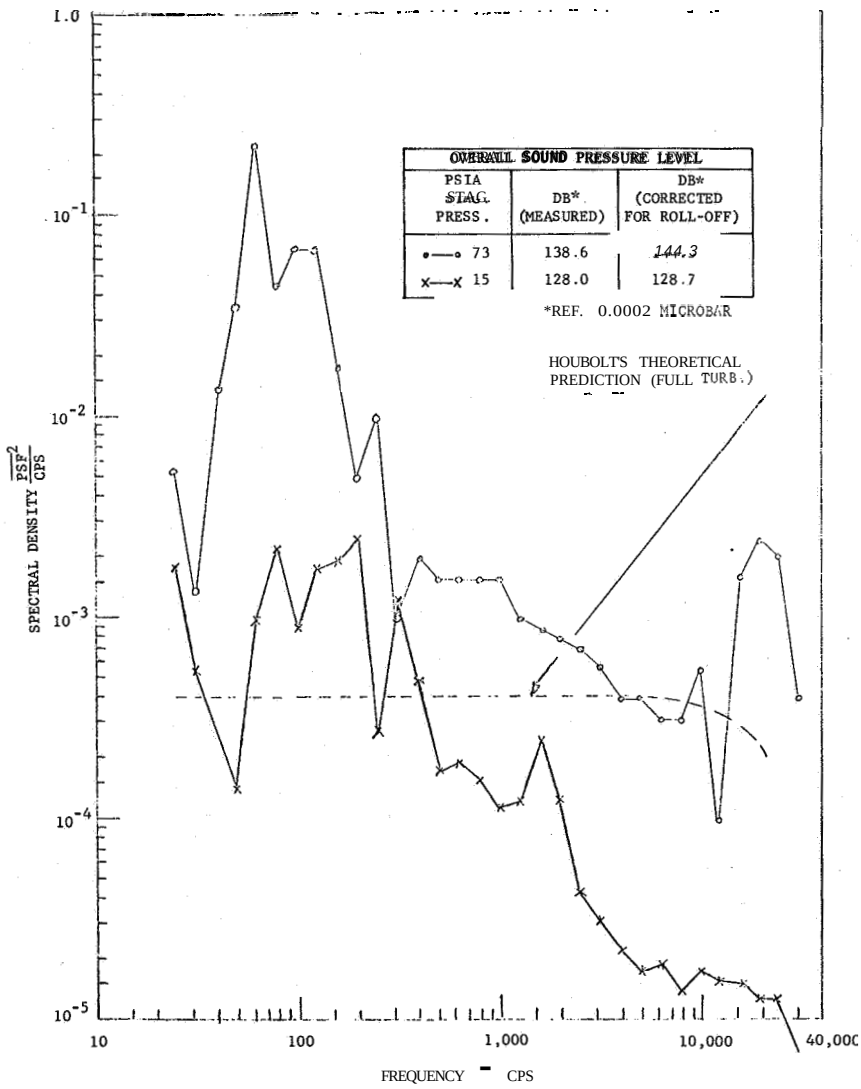

FIGURE 4.—Acoustic power spectra (laminar and turbulent flow, flush sensor).

Qualitative agreement with this acoustic phenomenon (peaking above the turbulent level during the transitional phase) has been obtained with thin-film heat-transfer rate measurements (ref. 2). Further examination of the correlation of thermal and acoustic spectra as the flow shifts from laminar to turbulent may well provide insight into the basic characteristics of turbulence in a boundary layer.

In figure 3, the nondimensional amplitude of wind-tunnel wall noise is shown taken from a separate test by Pate and Schueler (ref. 3). These measurements were obtained with a flush-mounted B&K microphone. They are representative of but not necessarily equal to the magnitude of radiated wall noise during our test because they were taken at a different time with a different model installed in the test section.

Figure 4 presents the power spectra of the acoustic pressure for the flush-mounted sensor in both laminar ($P_0 = 15$ psia) and turbulent flow ($P_0 = 73$ psia). The dominant high-frequency content of the turbulent noise is readily seen; however, the large values of acoustic pressure at low frequencies (< 400 Hz) in both laminar and turbulent flow indicates that there may well be a contribution to these data from the turbulent boundary layer on the tunnel wall. If there is a contribution from the tunnel wall, one would expect this to occur at high frequencies as well as low; therefore, because the laminar curve does not indicate this, the shock surrounding the model may act as a frequency-sensitive filter to the radiated noise.

Study of this phenomenon, possibly by measurement of the spectra as one moves across a model shock from the free stream and down into the boundary layer, would aid in determining if free stream disturbances of discrete frequencies can affect boundary-layer transition. In addition, it would enable us to identify the amplitude and spectral content of the radiated wall noise in the acoustic data and, by subtraction, obtain a more accurate prediction of the acoustic environment expected during a flight test.

TRIPPED VS. UNTRIPPED TURBULENT FLOW

The data exhibited in this section, although of a preliminary nature, show that the dynamic traits of tripped flow are different from the naturally induced turbulent flow in both the high- and low-frequency regimes. An 0.5 bluntness ratio forebody model was tested with and without trips at a stagnation pressure of 42 psi. Figure 5 shows the location of the trip rings and heat-transfer-rate measurements for tripped and untripped flow. Figure 6 indicates the vast difference in sound spectra at the low- and high-frequency ends between the tripped and untripped flow, even though the heat-transfer rates are coincident and indicative of fully turbulent flow. These data were taken with a 90"

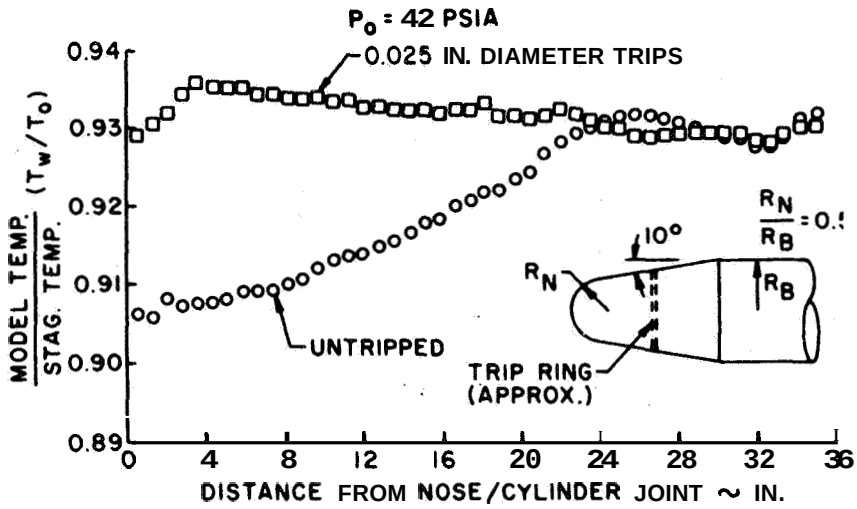

FIGURE 5. – Temperature distribution along model (tripped and untripped flow).

bend ported BBN sensor 27 in. aft of the cylinder-forebody joint. This difference is further exemplified by noting that there was an 8-dB difference in the overall sound-pressure level between tripped and untripped flow. The main question arising is whether or not the naturally induced turbulent boundary layer in flight can be faithfully simulated by an artificially induced turbulent boundary layer in the wind tunnel.

BASE-PRESSURE MEASUREMENTS

Base-pressure measurements have been a source of disagreement for a number of years. These disagreements may be due, at least in part, to the difference in dynamic response characteristics of the various static sensors used. As shown in figure 7, the aft sound-pressure levels caused by the wake may be as much as 30 percent of the static pressure. Because the base pressure contributes to a vehicle's drag, neglecting these oscillating pressures can cause erroneous predictions in the vehicle's performance.

NONDIMENSIONAL PRESSURE FLUCTUATION VS. MACH NUMBER

Figure 8 depicts the variation of overall sound-pressure level with mach number. This graph presents the pertinent wind-tunnel and flight data and semiempirical prediction methods. The most striking feature is the wide difference between the measured wind-tunnel test data. S. Pate (ref. 11) shows a large difference in acoustic levels between the

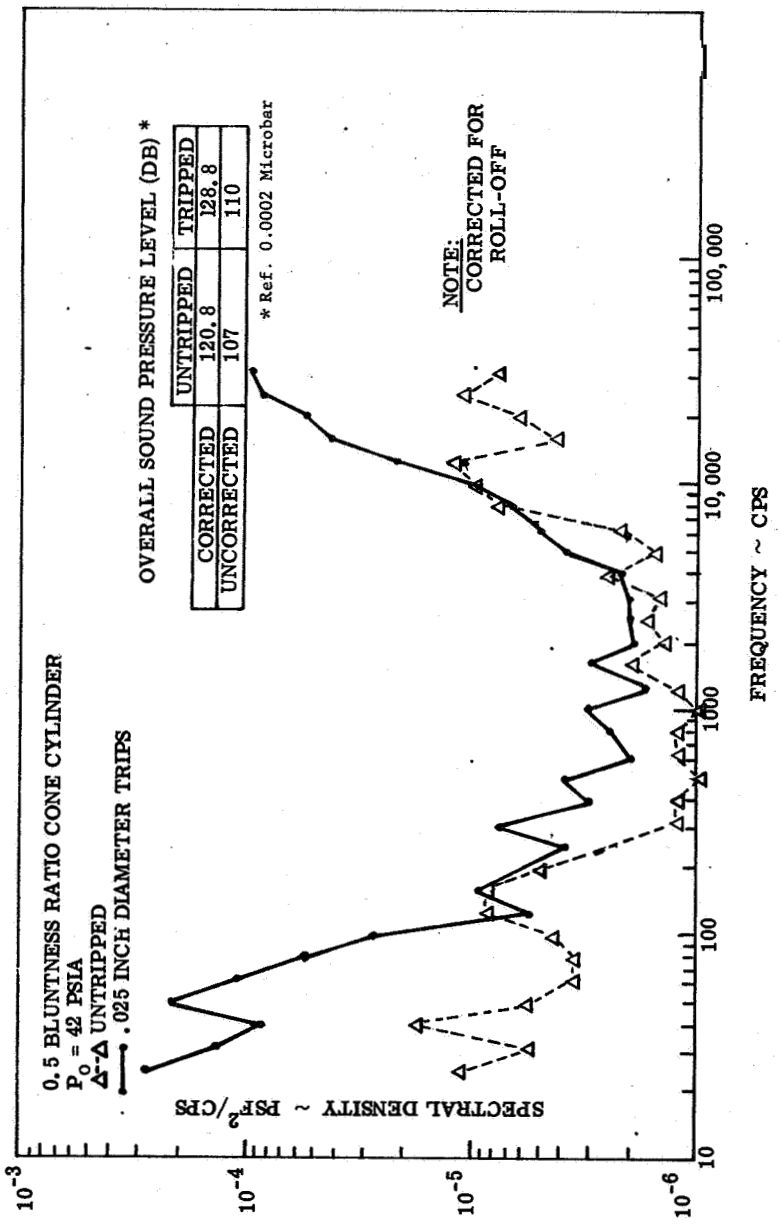

FIGURE 6.—Acoustic power spectra (tripped and untripped flow, 90° bend ported sensor).

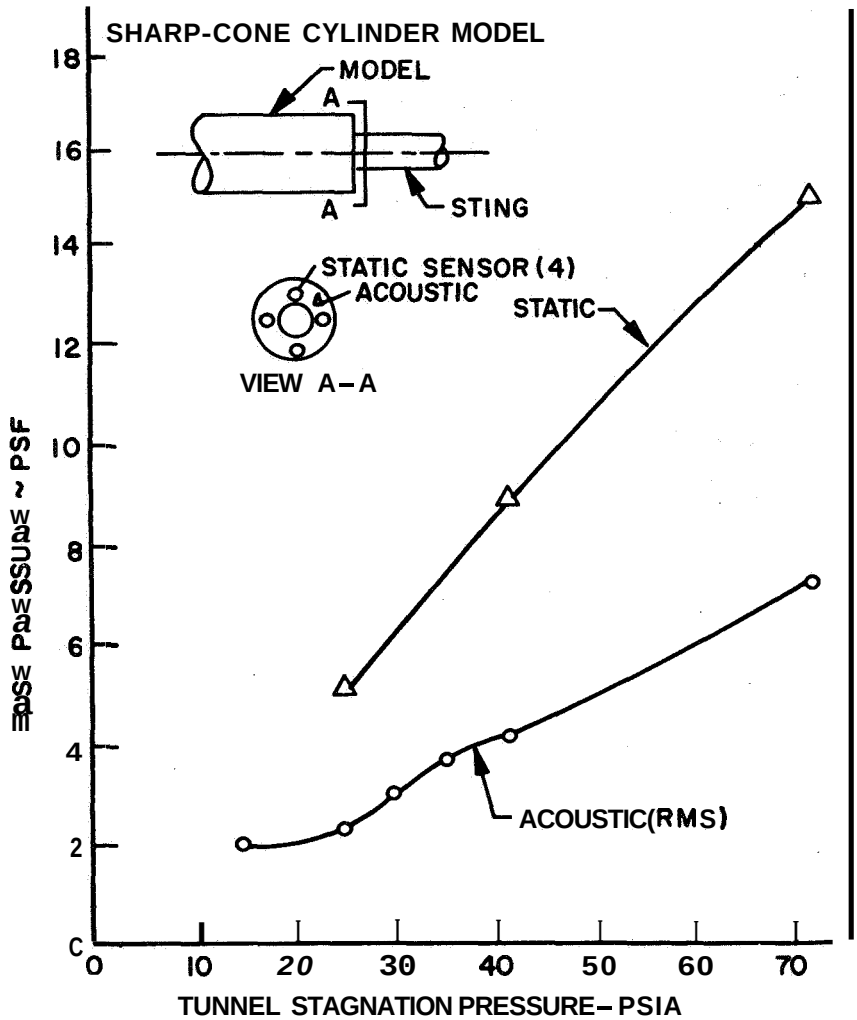

FIGURE 7.—Acoustic and static base pressure versus tunnel stagnation pressure (flush sensor).

end of transition and full turbulence. Because the high values of sound pressure in the transitional regime appear to have a greater fraction of their energy in the low-frequency regime, the component vibrations induced by the transitional noise may exceed the values in fully turbulent flow.

Drs. J. C. Houbolt (ref. 9) and M. Lowson (ref. 10) derive analytical methods for predicting $\sqrt{\bar{p}^2}/q$ in fully turbulent flow, but even here there are large differences. Clearly, there is a good deal of conflicting data at low mach numbers and a dearth of data at hypersonic mach numbers.

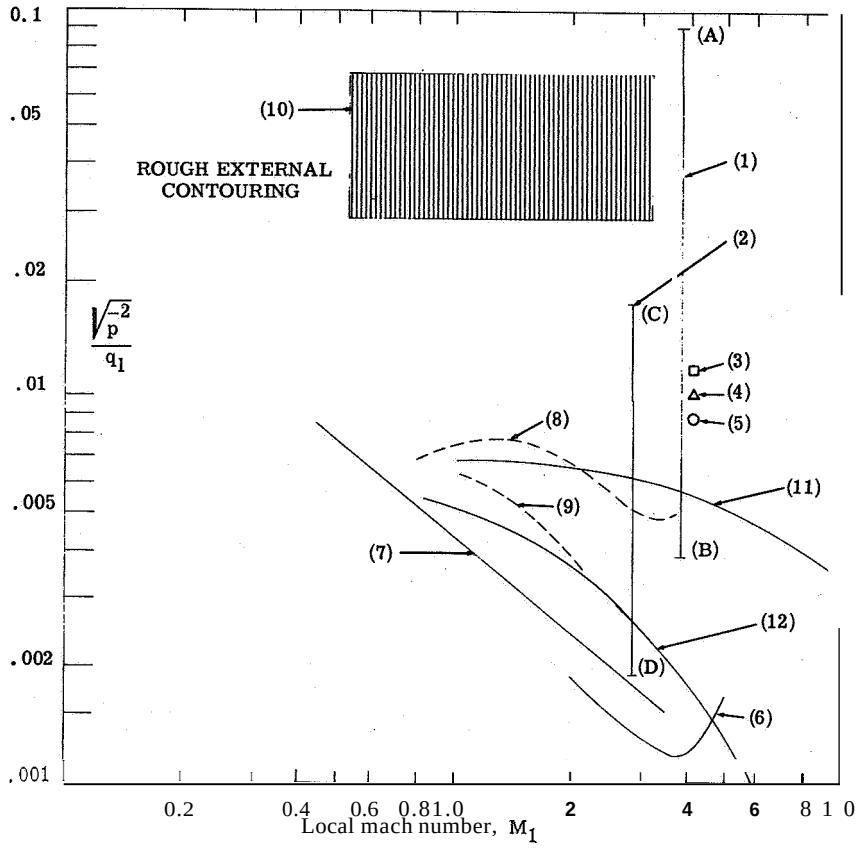

WIND TUNNEL

(1) Pate (AEDC)-Trans. to full turb. (A-B)
(2) Pate (AEDC)-Trans. to full turb. (C-D)
(3) Johnson et al-BBN 90° Bend port
(4) Johnson et al-BBN Straight port
(5) Johnson et al-BBN Flush
(6) Kistler and Chen
(7) Speaker and Ailman

FLIGHT TEST

(8) Hilton (Scout)
(9) Belcher (XB-70)
(10) Mayes (Mercury)

PREDICTION METHODS

(11) Houbolt
(12) Lowson (Flat plate)

FIGURE 8. – Overall sound pressure versus mach number (refs. 4 to 10).

SUMMARY

As a result of the testing described in the previous sections, there appear to be certain areas for further acoustic research that offer substantial promise. These areas and their most apparent direct application for the data obtained from their investigation are as follows:

(1) Interaction of tunnel noise and model shocks:

(a) Free-stream disturbance effects on transition

(b) Correlation between flight and wind tunnel measurements

(2) Compressible flow calibration of ported sensors: Accurate data in high thermal environment flight tests

(3) Base pressure measurements (acoustic versus static): Accurate base drag predictions

(4) Tripped versus untripped turbulent acoustic spectra:

(a) Subscale simulation techniques for full-scale turbulent flow

(b) More accurate prediction of flight performance from wind-tunnel data

(5) Amplitudes and spectra of transitional boundary of layer noise: Structural design requirements

(6) Correlation of acoustic and heating spectra: Improved understanding of turbulent boundary-layer characteristics

While the testing accomplished at the AEDC facility was certainly not all inclusive, it is clear that there are many fruitful avenues for acoustic research the investigation of which would provide data of practical value to both theoreticians and developers of flight hardware.

REFERENCES

1. JOHNSON, R. I.; MACOUREK, M. N.; AND SAUNDERS, H.: Boundary Layer Acoustic Measurements in Transitional and Turbulent Flow at $M_\infty = 4.0$. AIAA Paper no. 69-344, 1969.
2. OWEN, F. K.: Transition Experiments on a Flat Plate at Subsonic and Supersonic Speeds. AIAA Paper no. 69-9, 1969.
3. PATE, S. R.; AND SCHUELER, C. J.: An Investigation of Radiated Aerodynamic Noise Effects on Boundary Layer Transition in Supersonic and Hypersonic Wind Tunnels. AIAA Paper no. 68-375, 1968.
4. KISTLER, A. L.; AND CHEN, W. S.: The Fluctuating Pressure Field in a Supersonic Turbulent Boundary Layer. J. Fluid Mech., vol. 16, 1963, pp. 41-64.
5. SPEAKER, W. V.; AND AILMAN, C. M.: Spectra and Space Time Correlations of the Fluctuating Pressures at a Wall Beneath a Supersonic Turbulent Boundary Layer Perturbed by Steps and Shock Waves. NASA CR-486, 1966.
6. HILTON, D. A.: Preflight Aerodynamic Noise Measurements on a Scout Launch Vehicle. NASA TN D-1818, 1963.
7. BELCHER, P. M.: Predictions of Boundary Layer Turbulence Spectra and Correlations for Supersonic Flight. Paper presented at the Fifth International Acoustical Congress (Liege, Belgium), 1965.

8. MAYES, W. H.: Boundary Layer Pressure Fluctuations on the Mercury Capsule. Personal communication, Jan. 1969. Also, GARRICK, I. E.; HILTON, D. A.; AND HUBBARD, H. H.: Recent Free Flight Boundary Surface Aerodynamic Noise Measurements. AGARD Rept. 467, Apr. 1963.
9. HOUBOLT, J. C.: On the Estimation of Pressure Fluctuations in Boundary Layers and Wakes. GE 66SD296, Aug. 1966.
10. LOWSON, M. V.: Prediction of Boundary Layer Pressure Fluctuations. AFFDL-TR-167, Apr. 1968.
11. PATE, S. R.; AND BROWN, M. D.: Acoustic Measurements in Supersonic Transitional Boundary Layers. Paper presented at 15th National Instrument Society of America Aerospace Symposium, May 1969.

371-986 O-LT-70—33

GENERAL COMMENTS

Hwachii Lien
AVCO System Division
Wilmington, Mass.

The following research topics were not discussed at the Basic Noise Research Conference but are believed to be important for future study.

COMBUSTION NOISE

The sound radiated from the combustion flame is considered to arise mainly from a statistical distribution of monopole sources that are coupled to the combustion instability. For low mach-number flows, the intensity of combustion noise is usually higher than the aerodynamically generated sound. Therefore, understanding the mechanism of combustion noise generation and transmission should be the first approach to the solution of jet-noise-reduction problems. In noise generation and transmission by combustion flame, sound-sound interaction plays an important role in the steepening of sound waves. Also contributing to the energy transfer from other modes (ref. 1) to the acoustic mode is the production of both vorticity and sound modes, through vorticity-vorticity interaction; sound scattering and vorticity convection, resulting from sound-vorticity interaction; sound scattering, with vorticity generation; heat convection, caused by vorticity-entropy interaction; and other minor effects resulting from entropy-entropy interaction. In addition to those nonlinear interaction problems, many fundamental aspects of studies have never been carefully investigated. In this connection, for example, the study of the directionality of the combustion noise radiation may be undertaken by modifying the omnidirectional field of monopole radiation with coupled convection and fluctuation of the individual sound sources by the burning flow. Another analytical study of interest would be the investigation of the combustion noise frequency spectrum. It has been reported (ref. 2) that the wavelength of the maximum sound level for combustion noise is 70 to 100 times the jet diameter, but the wavelength for unignited aerodynamic noise is only three to seven times the jet diameter. This difference in noise characteristics must be explained by physicochemical investigation.

CHEMICAL ADDITIVES

The introduction of chemical additives into the burning flow creates many important effects, such as heat and mass release, alternation of flow properties that may change the fluctuation level, and change in combustion velocity. Undoubtedly, these effects are related to the noise problems, and the importance of the research work related to the effect of chemical additives in the flow is evident. For example, a study is very much needed to clarify the counteracting effects on sound intensity of turbulence intensification (ref. 3) and temperature rise associated with chemical heat release. Future research should also include a search for chemical additives that can reduce the turbulent fluctuation or even relaminarize the flow.

REENTRY EXPERIMENTS

The application of acoustic probes for boundary-layer transition detection has been successfully conducted for several reentry flights (ref. 4). A sudden change in turbulent pressure fluctuations at transition is observed and correlated, and the measurements indicate very rapid response, superior to the response of thermocouple detection techniques. This instrumentation technique, when correlated with the data from

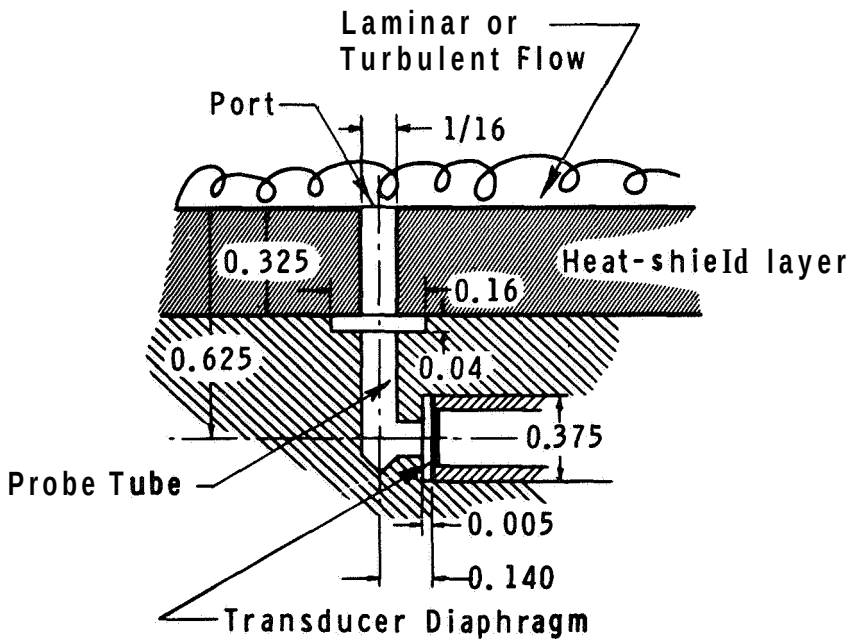

FIGURE 1.—Transition-detector configuration (ref. 4).

vibration sensors, can be extended to study the reentry boundary-layer noise characteristics and the wall response to the turbulent transition. However, many technical problems related to the theory of instrumentation, such as the effect of the frequency response of the acoustic coupler (existing between the port and the transducer, see fig. 1) and the effect of heat-shield ablation on the response of the acoustic probe, need to be studied.

REFERENCES

1. CHU, B. T.; AND KOVASZNAY, L. S. G.: Non-Linear Interactions in a Viscous Heat-Conducting Compressible Gas. J. Fluid Mech., vol. 3, 1958, p. 494.
2. SMITH, T. J. B.; AND KILHAM, J. K.: Noise Generation by Open Turbulent Flames. J. Acoust. Soc. Am., vol. **35,** 1963, p. 715.
3. ESCHENROEDER, A. Q.: Intensification of Turbulence by Chemical Heat Release. Phys. Fluids, vol. **7,** 1964, p. 1735.
4. STARR, E. A.; AND MYERS, R. H.: Acoustic Measurement of Transition on Re-entry Vehicles. Paper presented at 15th National Aerospace Instrumentation Symposium, Instrument Society of America (Las Vegas), May **5–7,** 1969.

COMMENTS ON SOME UNSOLVED PROBLEMS IN JET-NOISE RESEARCH

G. M. Lilley
University of Southampton
England

In spite of some preliminary work of I. S. F. Jones and others, the measurement of the equivalent acoustic-source distribution and strength in low- and high-speed jets has not yet progressed very far. Arguments still exist as to the relative magnitudes of shear noise and self-noise. Information on correction velocities in jet mixing regions is available, but no certainty exists as to how these apply to the dominant acoustic sources in a jet and to what degree the assumption of a constant convection mach number is applicable for the purpose of estimating noise radiation in intensity, directivity, and spectrum. Recently Ffowcs 'Williams and Hawkings (ref. 1) and I (ref. 2) independently presented papers in which acceleration of the equivalent acoustic sources was introduced. This is an aspect of jet-noise studies that has not been treated so far, and further consideration should be given to such acceleration effects as outlined in the preceding references.

So far, an adequate treatment of refraction of generated noise at high frequency in high-speed hot jets has yet to be formulated. Studies of this phenomenon in the "Water Table" experiments of Ffowcs Williams and others could help to elucidate this problem, which is primarily associated with changes in directivity and intensity in the downstream arc, especially in the region close to the jet axis.

SUBSONIC JETS

The effect of the sharpness of the jet lip on the intensity of jet noise has been questioned by Ffowcs Williams and others, and therefore a careful experiment to explore the effect of jet-exit geometry should be undertaken. It is known that such effects are of importance in choked jets in connection with the "screech" phenomenon, where a bluff base interferes with the incident external sound wave and so modifies the feedback cycle.

In the conference the structure of static jets has continually been mentioned, but no reference has been made to changes imposed by an external flow. Few studies of turbulent structure of jets in the presence of an external flow have been undertaken, and data on space-time correlations and their changes with external speed are urgently needed.

SUPERSONIC JETS

In this important field of jet-noise research, I feel we must distinguish between the noise from parallel supersonic jets in the absence of shock waves and the noise of choked jets. The former case represents a continuation of subsonic jet noise, although when the sources are corrected at supersonic speeds with respect to the external speed of sound, strong mach-wave emission results. Some important new results in this area are quoted in the references mentioned above and should be further explored. Choked jet studies, including the phenomenon of screech, needs further attention for the detailed fluid mechanics of mixing region shock cell interaction are not well understood. Again, the effect of an external flow on choked jet noise needs exploring. The distribution of equivalent noise sources in choked jets and the effect of jet-temperature ratio and jet-to-external-velocity ratio needs urgent attention.

JET-NOISE SUPPRESSORS

The mechanism by which jet-noise suppressors such as corrugated, multitube and toothed nozzles work is not well understood. In few cases have detailed studies been made of the global changes in the flow structure as a result of the addition of the suppressor. Further reduction in noise at low-thrust penalties for both low- and high-speed jets demands more adequate understanding of the mechanism by which noise suppressors work and, in particular, the changes in the distribution and strength of the equivalent noise sources.

The proposal from New York University for noise suppression by the use of additives is timely and should be followed up. The mechanism by which additives in water reduce turbulent intensity in shear flows is not understood, and further work in this area could be helpful in understanding the nature of additives in gaseous jets. The use of additives could benefit noise reduction by reducing turbulent intensity, by providing a medium for sound absorption, or by a combination of both methods. In the past, the use of additives has been shown to be prohibitive because of the excess of mass required. The newer schemes presumably invoke confidence that the mass of material required is minimal.

A vital problem in all suppressor schemes is the lack of knowledge of the flow structure of the jet mixing region and its dependence on the basic jet parameters. Further fluid mechanic research on turbulent jet stability needs to be undertaken with a view to the determination of the large-scale structure of the turbulent flow in the mixing region. Some work on these lines is in progress at the University of Southampton.

REFERENCES

1. FFOWCS WILLIAMS, J. E.; AND HAWKINGS, D. L.: Theory Relating to the Noise of Rotating Machinery. A.R.C. 29.821, N.558, Jan. 1968.
2. LILLEY, G. M.: Physics of Aerodynamic Noise. AGARD Meeting (St. Louis), 1969.

SOME COMMENTS ON THE USE OF ADDITIVES (SMALL SOLID PARTICLES) IN THE JET NOISE PROBLEM*

J. T. C. Liu
Brown University
Providence, R.I.

Prof. Lee Arnold of New York University has presented an interesting paper [1] at this conference. I would like to point out certain references that may be of some interest. The late Paul S. Epstein (ref. 1) considered the attenuation of sound the result of velocity interactions of the gaseous medium with freely suspended spheres that were either a rigid solid, an elastic solid, or a viscous liquid. This work was later extended to include heat transfer between the gas and the spheres (ref. 2) and was subsequently shown to be in good agreement with the experiments of Zink and Delsasso (ref. 3) in a limited frequency range. Several recent theories have appeared (refs. 4, 5, and 6). Culminating all this are the experiments of Temkin and Dobbins (refs. 7 and 8) that verified the theoretical calculations. The more recent work of Marble and Wooten [2] took the effects of mass transfer between the particles and gas into account. The recent renewed interest in this area since the latter part of the last decade has been related to solid-propellant rocket motors in which it was observed that, at times, high-frequency instabilities could be stabilized by the addition of metallic powders to the propellant (refs. 9, 10, and 11). This technical interest generated a body of investigations of the dynamics of a gas carrying small solid particles. Some of the salient features and further references may be found in the papers by Marble (refs. 12, 13).

*These comments were prepared through the sponsorship of NASA grant no. NGR 40-002-009.

[1] See p. 137.

[2] F. E. Marble and D. C. Wooten: Sound Attenuation in a Condensing Vapor. Aerospace Research Laboratories Report (1969), to be published.

Professor Arnold's frequent quotations of the papers by Saffman (ref. 14) and Michael (ref. 15) necessitate some caution about the interpretation of certain statements and formulations found in these papers. These authors considered the low-speed hydrodynamic stability of plane-parallel dusty gas flow, in which the dust and gas are in equilibrium in the mean flow, and velocity interactions occur in the perturbed flow. When the flow is termed "stabilized" if coarse dust is present because the coarse dust does not respond to the perturbations, the kind of instability being stabilized must be more specifically identified. For instance, for the plane Poiseuille flow problem, which is what Saffman (ref. 14) and Michael (ref. 15) were concerned about, or for nearly parallel flows with solid boundaries in general, the instability arises as a result of viscous instability. That is, the periodic vorticity generated at the wall by the presence of traveling wavy disturbances and the subsequent diffusion of this vorticity away from the wall set up the phase shift between the velocity components of the Reynolds shear stress in such a way that the mechanism of energy conversion from the mean flow to the disturbances become favorable. When this energy supply overpowers the viscous dissipation, instability takes place. If the flow is seeded with coarse dust, then $\omega\tau \rightarrow \infty$ is implied, where ω is the disturbance frequency and τ is the characteristic time required for the dust to come to local equilibrium with the gas motion. In this high-frequency range, the viscous diffusion sublayer is too thin to contain any dust to effect a stabilization. When $\omega\tau = 0(1)$, some relative stabilization takes effect. This occurs in two ways: one is, of course, the dissipation of total (gas plus dust) kinetic energy because of the work done by the dust-gas interaction; the other, more subtle, is the rearranging of the phase shift caused by dust-gas relaxation that decreases the gas Reynolds shear stress from its clean-gas value. However, in Saffman's and Michael's work, the overall (dust plus gas) Reynolds shear stress contributes to the energy conversion mechanism. The dust Reynolds shear stress, beginning with zero when $\omega\tau \rightarrow \infty$, is always positive and reaches equilibrium with the gas as $\omega\tau \rightarrow 0$. The result is that the overall Reynolds shear stress does not appreciably dip below the clean gas value if $\omega\tau = 0(1)$ and if the two-phase mass-per-unit-volume ratio becomes the same order. (See ref. 16 for further details of such a "physical calculation.")

Michael (ref. 15) used a perturbation procedure based on the assumption that the dust-to-gas mass per unit volume ratio is small. In this procedure the zeroth approximation reproduces the Orr-Sommerfeld equation for a clean gas, the first approximation produces the clean-gas Orr-Sommerfeld operation on the left-hand side, while the effect of dust-gas interaction is relegated to the right-hand side as a nonhomogeneous

term. The application of this procedure is proper if it is realized that in making the expansion for small dust concentration, the parameter $\omega\tau$ is not entirely innocent, but the retention of its order as $or \geqslant 0(1)$ is implied. Although the nonhomogeneous problem could be calculated numerically without difficulty to ranges of $\omega\tau < 0(1)$, the original implication that such an expansion procedure restricts consideration to the near-coarse dust regime must be kept in mind.

Wiggle disturbances in such a mixture have been considered. What about step disturbances? (For a more general description of disturbances in such a mixture with mass, velocity, and temperature interactions, see ref. 15.) For the present purposes, suppose only velocity and temperature interactions take place, and furthermore, to keep things simple, we are willing to set the velocity and temperature relaxation times equal and the gas and particle heat capacities equal. If the Ackeret problem, the small-perturbation problem in a supersonic uniform stream, is taken into consideration, one arrives at an Ackeret problem of relaxation, which dates back to Lord Rayleigh (ref. 17). Namely, in the present context, there is a "frozen" Ackeret problem (in which the mach number is based on the clean-gas speed of sound) that is differentiated with respect to the streamwise variable and divided by an appropriate relaxation length, plus an "equilibrium" Ackeret problem (with the mach number based on a speed of sound in an equilibrium two-phase mixture) equal zero. Then, à la Chu (ref. 18), Moore and Gibson (ref. 19), and Whitham (ref. 20), signals damp along the frozen mach wave and the bulk of the signal is eventually carried along the equilibrium mach wave but with a diffusive structure. This feature is, in fact, allied to a remark that Prof. Frank Moore of Cornell University has made concerning the possibility of using chemical energy for the dissolution of signals.

REFERENCES

1. EPSTEIN, P. S.: On the Absorption of Sound in Suspensions and Emulsions. Contributions to Applied Mechanics, Theodore Von Kármán Anniversary Volume. California Institute of Technology, 1941, p. 162.
2. EPSTEIN, P. S.; AND CARHART, R. R.: The Absorption of Sound in Suspensions and Emulsions. I. Water Fog in Air. J. Acoust. Soc. Am., vol. 25, 1953, p. 553.
3. ZINK, J. W.; AND DELSASSO, L. P.: Attenuation and Dispersion by Solid Particles Suspended in a Cas. J. Acoust. Soc. Am., vol. 30, 1958, p. 765.
4. CHOW, J. C. F.: Attenuation of Acoustic Waves in Dilute Emulsions and Suspensions. J. Acoust. Soc. Am., vol. 36, 1964, p. 2395.
5. CHU, B. T.; AND CHOW, J. C. F.: On a Macroscopic Theory of a Two-Phase Fluid. AIAA Paper no. 65-8, 1965.
6. TEMKIN, S.; AND DOBBINS, R. A.: Attenuation and Dispersion of Sound by Particulate Relaxation Processes. J. Acoust. Soc. Am., vol. 40, 1966, p. 317.
7. TEMKIN, S.; AND DOBBINS, R. A.: Measurements of Particulate Acoustic Attenuation. AIAA J., vol. 6, 1964, p. 1106.

8. TEMKIN, S.; AND DOBBINS, R. A: Measurements of Attenuation and Dispersion of Sound by an Aerosol. J. Acoust. Soc. Am., vol. 40, 1966, p. 1016.
9. ANGELUS, T. A: Unstable Burning Phenomenon in Double-Base Propellants. Vol. 1 of ARS Progress in Astronautics and Rocketry: Solid Propellant Rocket Research, M. Summertield, ed., Academic Press, Inc., 1960, p. 527.
10. PRICE, E. W.: Experimental Solid Rocket Combustion Instability. Tenth Symposium (International) on Combustion. The Combustion Institute (Pittsburgh), 1965, p. 1067.
11. DOBBINS, R. A.; AND TEMKIN, S.: Propagation of Sound in a Gas-Particle Mixture and Acoustic Combustion Instability. AIAA J., vol. 5, 1967, p. 2182.
12. MARBLE, F. E.: Dynamics of a Gas Containing Small Solid Particles. Proceedings of the Fifth AGARD Combustion and Propulsion Colloquium. Pergamon Press, Inc., 1963, p. 175.
13. MARBLE, F. E.: Some Gas Dynamic Problems in the Flow of Condensing Vapors. Astronaut. Acta, vol. 14, 1969, pp. 585--614.
14. SAFFMAN, P. G.: On the Stability of Laminar Flow of a Dusty Gas. J. Fluid Mech., vol. 13, 1962, p. 120.
15. MICHAEL, D. H.: The Stability of Plane Poiseuille Flow of a Dusty Gas. J. Fluid Mech., vol. 18, 1964, p. 19.
16. LIU, J. T. C.: On the Hydrodynamic Stability of Parallel Dusty Gas Flow. Phys. Fluids, vol. 8, 1965, p. 1939.
17. RAYLEIGH, J. W. S.: The Theory of Sound. Vol. II. Dover Pub., Inc., 1945, p. 25.
18. CHU, B. T.: Wave Propagation and the Method of Characteristics in Reacting Gas Mixtures With Applications to Hypersonic Flow. (WADC TN-57-213), Brown University Division of Engineering, May 1957.
19. MOORE, F. K.; AND GIBSON, W. E.: Propagation of Weak Disturbances in a Gas Subject to Relaxation Effects. J. Aerospace Sci., vol. 27, 1960, p. 117.
20. WHITHAM, G. B.: Some Comments on Wave Propagation and Shock Wave Structure With Application to Magnetohydrodynamics. Commun. Pure Appl. Math., vol. 12, 1959, p. 113.

COMMENTS ON NONLINEAR EFFECTS

Richard L. Moore
Douglas Aircraft Co.
McDonnell Douglas Corp.
Long Beach, Calif.

Before beginning my comments, I would first ask if anyone possesses experimental data supporting the use of the linearization procedures in aircraft jet engines.

Since no affirmative answer was received from the participants at the conference with respect to this matter, this comment will point out reasons for believing that this analysis must be treated nonlinearly and some implications for future research and engineering. Experiments at Douglas have found that compressor noise measured with a wideband system at a point 15 ft from the fan bypass duct exit of a DC–8 show peak amplitude of 0.15 psi and a rise time of approximately 20 μsec. Both of these observations can be used to infer that the compressor noise in the duct is composed of a series of shock waves passing down the duct.

This observation strongly suggests that wideband measurements must be made in the duct to obtain the peak overpressures of the traveling shock waves. The observation also suggests that the theoretical analysis of noise as the superposition of continuous waves, without regard to their phase relationships, is open to question.

For example, if the energy is contained in a series of pulses or shock waves whose time separation is, on the average, the fan blade passage frequency, Fourier analysis has shown that both harmonics and subharmonics are required to approximate the spacing of the waves. But the energy is really contained in the pulse, not in the fundamental or any of the harmonics. The effect of a Helmholtz resonator on a series of shock waves spaced at the fundamental frequency of the resonator will be entirely different from its effect on a small amplitude periodic wave. Thus, it is concluded that the attenuation of each individual shock wave during its passage through the duct should be measured as criteria of the best method of duct lining for acoustic treatment.

To do this will require the use of a controlled shock tunnel (instead of the acoustic generators presently in vogue), plus broadband acoustic recording equipment.

In addition to the fanjet engine, theoretical and experimental measurement of the scaling laws for jet noise must be developed to determine at what jet size and mach number (and aircraft mach number) the waves issuing from near the sonic point become finite amplitude waves. The standing waves observed near the sonic point propagate, at least initially, with the speed of the aircraft, and thus to a fixed observer represent sound as the aircraft passes.

Thus, the simulation of aircraft jet noise from small laboratory jets may well suffer from nonlinear effects unless experimental measurements can prove the contrary.

As a further comment, the effect of humidity on propagation of sound in a real nonuniform atmosphere remains an open and important problem. Its importance is more obvious to those who have tried to reduce aircraft flyover noise to a "standard day."

COMMENTS ON BASIC NOISE RESEARCH

P. M. Munger
University of Southampton
England

BOUNDARY CONDITIONS IN DUCT ACOUSTICS

In solving problems in duct acoustics in the presence of flow, a considerable number of assumptions are quite often made before the governing wave equation is amenable to analytic solutions. In most of the papers presented at the conference on propagation in ducts, the assumption that the mean flow is uniform across the duct has been made. This automatically assumes mean plug flow and makes slip at the walls inevitable. Although in practice there is no slip, the simplification of the problem requires that slip be taken into account to avoid contradiction of the original assumption of uniform flow.

When there is relative motion between the fluid and the walls, the basic continuity of displacement must be used instead of the continuity of velocity. This is the result of the existence of an extra convective term in the substantial derivative of the displacement. In the absence of relative motion, continuity of particle displacement also leads to continuity of particle velocity, as the following analysis will show.

Consider, for example, sound propagation in an acoustically lined cylindrical duct with uniform mean flow U. The acoustic particle displacement in the medium in the radial direction may be written as

$$\xi_m = E(r, \theta) e^{j\omega t - \gamma x}$$

where γ is the axial complex propagation wave vector, and $E(r, \theta)$ is the amplitude of the radial displacement. The radial acoustic particle velocity V_m of the fluid medium is given by

$$V_m = \frac{d\xi_m}{dt} = \frac{\partial \xi_m}{\partial t} + U \frac{\partial \xi_m}{\partial x}$$

371-986 O-LT-70—34

or

$$V_m = j\omega(1-MK)\xi_m$$

where

$$K=\frac{\gamma}{j\omega/c} \qquad \text{and} \qquad M=\frac{U}{c}$$

The wall velocity in the radial direction is obtained from ξ_w, the wall displacement in that direction. Thus

$$V_w=\frac{d\xi_w}{dt}=\frac{\partial\xi_w}{\partial t}=j\omega\xi_w$$

Using the basic continuity of acoustic displacement, one may write

$$\xi_w=\xi_m$$

at the wall, or

$$\frac{V_w}{j\omega}=\frac{V_m}{j\omega(1-MK)}$$

Thus

$$V_w=\frac{V_m}{(1-MK)}$$

It is clear that in the absence of relative motion, $V_w=V_m$. The term $(1-MK)$ in the denominator must be retained when slip is present. From here on, one continues in the usual way with the analysis by replacing V_w with the product of the local wall admittance and the acoustic pressure, and V_m with the radial pressure gradient at the wall and other terms, as prescribed by the radial momentum equation.

It has already been mentioned that, in practice, slip does not occur and the mean velocity at the wall is zero, but then the mean velocity profile cannot be uniform. Thus, one deduces that the use of a simplified wave equation (uniform flow) makes the boundary conditions unrealistic; on the other hand, using a realistic boundary condition (no slip) makes the assumption involved in writing a simplified wave equation invalid. The remaining alternative is to solve the more complete wave equation, taking the boundary layers into account.

Motivated by the above arguments, numerical techniques have been developed at Southampton University to solve the more complete wave equation.[1]

---

[1] *See* p. 305.

COMMENTS ON VARIATION OF TURBULENCE NOISE WITH FREQUENCY

Newell D. Sanders
NASA Lewis Research Center
Cleveland, Ohio

Lighthill's analysis shows that the sound power from a turbulent flow varies with the fourth power of the frequency and velocity as follows:

$$\text{Power} \approx \frac{\rho}{c^5}\omega^4 U^4 \tag{1}$$

where ρ is density, c is the speed of sound, ω is angular frequency, and U is the velocity of the flow.

On the other hand, a sphere oscillating in the second-order spherical harmonic (quadrupole) generates sound according to the following relation:

$$\text{Power} \approx (\rho c)\left(\frac{\omega r}{c}\right)^6 r^2 U_r^2 \tag{2}$$

where r is the radius of the sphere and U_r is a harmonic velocity at the surface of the sphere. Both equations result in the eighth-power law but disagree on the relative effects of frequency. We will explore this disagreement.

From the Lighthill development, the following sequence of approximate equations relate far-field density fluctuations to near-field disturbances:

Monopole:

$$\rho' \approx \frac{1}{c^2}\int \frac{1}{X}\frac{\partial Q}{\partial t}\,dy \approx \omega U$$

Dipole:

$$\rho' = \frac{1}{c^3}\int \frac{x_i}{X^2}\frac{\partial F_i}{\partial t}\,dy \approx \omega^2 U$$

Quadrupole:

$$\rho' = \frac{1}{c^4}\int \frac{x_i x_j}{X^3}\frac{\partial T_{ij}}{\partial t}\,dy \approx \omega^2 U^2$$

where

ρ' density fluctuations in far field
e speed of sound
X linear coordinate of far-field point
Q mass flow for monopole
F force for dipole
T_{ij} shearing stress for quadrupole
t time
Y linear coordinate of near-field point
U a near-field velocity

The third equation does not appear to follow in a direct sequence after the other two. Lighthill calls T_{ij} the quadrupole strength and says that T_{ij} is a shearing stress proportional to the square of the velocity because $T_{ij}=\rho U_i U_j$.

Acoustic fields of spherical harmonics show a regular progression as illustrated here:

Zero order (monopole):

$$U_f \approx i\left(\frac{\omega r}{c}\right)\frac{r}{R}U_r$$

$$\text{Power} \approx (\rho c)\left(\frac{\omega r}{c}\right)^2 r^2 U_r^2$$

First order (dipole):

$$U_f \approx -\left(\frac{\omega r}{c}\right)^2\left(\frac{r}{R}\right)U_r$$

$$\text{Power} \approx (\rho c)\left(\frac{\omega r}{c}\right)^4 r^2 U_r$$

Second order (quadrupole):

$$U_f \approx -i\left(\frac{\omega r}{c}\right)^3\left(\frac{r}{R}\right)U_r$$

$$\text{Power} = (\rho c)\left(\frac{\omega r}{c}\right)^6 r^2 U_r$$

nth order:

$$U_f \approx i^{(n+1)}\left(\frac{\omega r}{c}\right)^{n+1}\left(\frac{r}{R}\right)U_r$$

$$\text{Power} = (\rho c)\left(\frac{\omega r}{c}\right)^{2(n+1)} r^2 U_r^2$$

In these equations U_r is a fluctuating velocity in the near field at the surface of a sphere with radius r, and U_f is a fluctuating velocity in the far field. (See reference.) This sequence and Lighthill's sequence agree

on the effects of frequency for monopoles and dipoles. They disagree for quadrupoles as mentioned before. Another disagreement concerns the effect of near-field velocity. The spherical harmonic analysis shows a linear relation between near-field and far-field velocities; and, consequently, the power is proportional to the square of the velocity in all cases. Lighthill's analysis shows an extremely nonlinear characteristic for the quadrupole in which power is proportional to the fourth power of the velocity. Lighthill's solution prohibits linear superposition of solutions, whereas the spherical harmonic approach does allow linear superposition.

The foregoing discussion certainly leads one to believe that a fairly deep disagreement exists between the shear stress method of Lighthill and the shear-strain method using spherical harmonics.

REFERENCE

RAYLEIGH, LORD JOHN W. S.: The Theory of Sound. Vol. II, art. 323, eq. (13). Dover Pub., Inc., 1945.

COMMENTS ON EXTENSION OF THE RIEMANN-EARNSHAW SOLUTION TO MULTIDIMENSIONAL GAS FLOW

G. M. Schindler
Douglas Aircraft Co.
McDonnell Douglas Corp.
Long Beach, Calif.

INTRODUCTION

The discovery of the solution for traveling simple waves in one-dimensional isentropic gas flow by Riemann (ref. 1) and Earnshaw (ref. 2) more than a century ago was certainly an important step forward toward the deeper understanding of the nonlinear propagation mechanism of such waves. To describe the flow field inside and outside machinery of complex geometrical configuration, it would be desirable to have solutions of the same type available that involve more than just a single space coordinate. For this reason, the principal results that have been obtained recently in an attempt to solve the multidimensional gas flow problem are communicated (ref. 3).

PROBLEM FORMULATION AND SOLUTION

Given are the fluid dynamics equations in eulerian form for the n-dimensional, isentropic flow of a nonviscous gas:

$$\frac{\partial \rho}{\partial t}+\sum_{j=1}^{n}\frac{\partial \rho u_j}{\partial x_j}=0$$

$$\frac{\partial u_i}{\partial t}+\sum_{j=1}^{n}u_j\frac{\partial u_i}{\partial x_j}+\frac{1}{\rho}\frac{\partial p}{\partial x_i}=0 \qquad i=1,\ldots,n \tag{1}$$

$$p\cdot\rho^{-\gamma}=\text{constant}$$

$$\gamma=\text{constant}$$

Equations (1) are identically satisfied if

$$\rho=\Omega(p)=\rho_0\left(\frac{p}{p_0}\right)^{\frac{1}{\gamma}} \tag{2a}$$

$$u_i=U_i(p) \qquad i=1, \ldots, n \tag{2b}$$

$$\Omega^2(p)\sum_{j=1}^{n}[U_j'(p)]^2=\Omega(p) \tag{2c}$$

$$\left[\Omega(p)\sum_{j=1}^{n}U_j(p)U_j'(p)+1\right]t-\Omega(p)\sum_{j=1}^{n}U_j'(p)x_j=A(p) \tag{2d}$$

Here a prime denotes the derivative with respect to p, and $A(p)$ is an arbitrary function of p. Equation (2d) relates the pressure p with the time t and the space coordinates $x_1, \ldots, x_n$. It may be noted that this implicit expression for p involves a total of n arbitrary functions; namely, $(n-1)$ velocity components and $A(p)$. The remaining nth component of the particle velocity is determined by the constraint expressed in equation (2c). To verify that equations (2a)–(2d) solve equations (1), one should note that equation (2d) satisfies the system

$$\frac{\partial p}{\partial x_i}=-\frac{\Omega(p)U_i'(p)}{\Omega(p)\sum_{j=1}^{n}U_j(p)U_j'(p)+1}\frac{\partial p}{\partial t} \qquad i=1, \ldots, n \tag{3}$$

Replacing the spatial derivatives of p by the derivative with respect to time in equations (1), it follows immediately that the latter are identically satisfied if the constraint (2c) holds.

In the special case $n=1$, the constraint (2c) can be solved for $U_1'(p)=U'(p)$. Integration leads to the two Riemann invariants corresponding to the two different signs of $U(p)$. Because these two invariants are constant, they characterize respectively "forward-facing" and "backward-facing" simple waves. Equation (2d) reduces exactly to the Riemann-Earnshaw solution.

For steady flow, the factor of time t in equation (2d) has to vanish:

$$G(p)=\Omega(p)\sum_{j=1}^{n}U_j(p)U_j'(p)+1=0 \tag{4}$$

Substituting $\Omega(p)$ according to equation (2a) and integrating yields Bernoulli's equation.

From equations (2c) and (4), it follows that for unsteady one-dimensional flow and for steady two-dimensional flow, the particle velocity is completely determined. This explains why solutions to the flow problem in these two cases have been found (ref. 4). In all other cases the remaining velocity components ($n-1$ components for unsteady flow and

n—2 components for steady flow) assume the role of arbitrary functions, which follows from equation (2d).

REFERENCES

1. RIEMANN, B.: Abhandl. Ges. Wiss. Goettingen, Math. Physik. Kl. 8, 43, 1860.
2. EARNSHAW, S.: Trans. Roy. Soc. (London), vol. 150,1860, p. 133.
3. SCHINDLER, G. M.: Simple Waves in Multidimensional Gas Flows. DAC 5626, Douglas Aircraft Co., Long Beach, Calif., 1969.
4. COURANT, R.; AND FRIEDRICHS, K. O.: Supersonic Flow and Shock Waves. Ch. VI, Interscience Pub., Inc., 1948.

THE EFFECTS OF LONG-RANGE COHERENCE ON JET NOISE GENERATION

Peter J. Westervelt
Brown University
Providence, R.I.

We examine here the consequence of a most unconventional proposal with regard to the noise-generating mechanism of an axisymmetric jet with sonic velocity. The basic source is assumed to be the virtual source used to describe the parametric acoustic array (ref. 1). In this discussion we concentrate our attention on the directional properties of the acoustic emission, ignoring absolute magnitudes.

We chose the following form for the source strength density in which $U(x)$ is the unit function

$$q\alpha\{[-\alpha_c e^{\alpha_c x}][1-U(x)]+\alpha_a e^{-\alpha_a x}U(x)\}\delta(y)\delta(z)e^{ikx-i\omega t} \tag{1}$$

which corresponds to an exponential creation rate α_c left of the origin, an abrupt phase reversal at the origin and the exponential annihilation rate α_a to the right of the origin. The wave number k is related to the spectral component ω through $k=\omega/c$ with c the velocity of sound. It might be emphasized at this point that the density q has an axis of symmetry x corresponding to the jet axis.

The asymptotic pressure developed by such a source is proportional to

$$\frac{-\alpha_c}{i\alpha_c+k\sin^2\theta/2}+\frac{\alpha_a}{i\alpha_a+k\sin^2\theta/2}$$

which results in the following angular dependence for the far-field intensity

$$F(\theta)=\frac{(\alpha_c-\alpha_a)^2k^2\sin^4 8/2}{(\alpha_c^2+k^2\sin^4\theta/2)(\alpha_a^2+k^2\sin^4\theta/2)} \tag{2}$$

Of course, 8 is the angle made by the line of observation with the positive x-axis.

Long-range coherence implies that α_c and α_a are small compared to the wave number k. With this assumption and a further restriction that the annihilation and creation rates are not equal (otherwise there would be no radiation at all), we find the following results:

(1) Behind the jet $F(0)=0$

(2) At the angle of maximum emission $\theta_{\max}=\cos^{-1}[1-2k^{-1}\sqrt{\alpha_a\alpha_c}]$ and

$$F(\theta_{\max})=\frac{(\alpha_c-\alpha_a)^2}{\alpha_c\alpha_a}$$

(3) In the forward direction

$$F(\pi)=\frac{(\alpha_c-\alpha_a)^2}{k^2}$$

We see that the principal features of jet-noise directivity are reproduced in this simple model. Furthermore, the zero at $\theta=0$ appears with no effects of refraction playing any part. The zero is of course an exaggeration of the dip that occurs in real life and is not under any circumstances to be taken seriously. What I think should be learned from this analysis is the fact that the introduction of long-range correlation into the sources can result in powerful effects on their angular radiation patterns. This and related effects should certainly be taken into consideration in any future research program aimed at understanding and eventually controlling aerodynamic noise processes.

REFERENCE

WESTERVELT, P. J.: J. Acoust. Soc. Am., vol. 35, 1963, p. 535.

THE NONLINEAR ACOUSTIC IMPEDANCE OF ORIFICES

Peter J. Westervelt
Brown University
Providence, R.I.

I would like to make some comments pertaining to the very interesting report by Dr. John F. Groeneweg.

About 20 yr ago I made a detailed experimental and theoretical study of the nonlinear orifice (ref. 1) of which only a small part was then published (ref. 2). This work, which will soon be published in full, showed that the experimental discharge coefficients applicable to oscillatory flow differed significantly from the experimental steady-flow coefficients. A satisfactory theory of this phenomenon needs to be developed.

While theory and experiment agree quite well for superposed steady plus acoustic flow through the orifice, no satisfactory theory seems to exist for the important case involving crossflows.

REFERENCES

1. WESTERVELT, **P. J.: The Interaction of a Finite Amplitude Acoustic Wave with Small Obstacles and Orifices. Ph. D. Thesis, M.I.T., January 1951.**
2. WESTERVELT, **P. J.: Acoustical Impedance in Terms of Energy Functions. J. Acoust. Soc. Am., vol. 23, no. 3, May 1951, pp. 347–348.**

COMMENT ON PAPER BY DR. R. ARNOLDI

D. S. Whitehead
University of Cambridge
England

Dr. Arnoldi had mentioned the results of calculations in which the force on cascade blades had been found to be the result of wakes washed down from upstream obstructions (ref. 1). These results showed peculiar kinks as the phase angle between adjacent blades was varied. No physical reason for these kinks is known, but the accuracy of the calculations has since been confirmed by other workers.

Currently, these calculations were being extended to include the effect of compressibility of the fluid. The method used is an extension of that due to Lane and Friedman (ref. 2). Preliminary results showed that the technique of using an incompressible theory to get the blade force and then an acoustic dipole calculation to find the radiated sound worked sufficiently well away from a resonance or cutoff condition. However, near a resonance condition the lift force tended to zero, while the acoustic pressure perturbation tended to infinity. So far the calculations have only been done at low mach number, and the resonance effects were only observed over a very narrow range of mach numbers.

REFERENCES

1. WHITEHEAD, D. S.: Force and Moment Coefficients for Vibrating Airfoils in Cascade. R&M No. M–3254, British A.R.C., Feb. 1960.
2. LANE, FRANK; AND FRIEDMAN, MANFRED Theoretical Investigation of Subsonic Oscillatory Blade Row Aerodynamics. NACA TN 4136, 1958.

U.S. GOVERNMENT PRINTING OFFICE : 1970 O-LT—371-986